NASA Conference Publication 3260

28th Aerospace Mechanisms Symposium

Proceedings of a symposium
held at the Cleveland Marriott Society Center,
Cleveland, Ohio,
and cosponsored by NASA Lewis Research Center and
Lockheed Missiles and Space Company, Inc.
May 18–20, 1994

NASA Conference Publication 3260

28th Aerospace Mechanisms Symposium

Proceedings of a symposium
held at the Cleveland Marriott Society Center,
Cleveland, Ohio
and cosponsored by NASA Lewis Research Center and
Lockheed Missiles and Space Company, Inc.
May 18–20, 1994

National Aeronautics and
Space Administration

Office of Management

Scientific and Technical
Information Program

1994

CONTENTS

PREFACE

The proceedings of the 28th Aerospace Mechanisms Symposium, which was hosted by NASA Lewis Research Center, Cleveland, Ohio, and held at the Marriott Society Center, Cleveland, Ohio, on May 18, 19, and 20, 1994, are reported in this NASA Conference Publication. The symposium was sponsored by the National Aeronautics and Space Administration and Lockheed Missiles and Space Company, Inc.

The purpose of the symposium was to provide a forum for the interchange of information among those active in the field of mechanisms technology. To that end, 25 papers and 7 posters were presented on aeronautics and space flight, with special emphasis on actuators, aerospace mechanism applications for ground-support equipment, lubricants, pointing mechanisms, joints, bearings, release devices, booms, robotics, and other mechanisms for spacecraft. The papers were prepared by authors from a broad aerospace background, including the U.S. aerospace industry, NASA, and European and Asian participants.

The efforts of the review committee, session chairs, and speakers contributing to the technical excellence and professional character of the conference are especially appreciated.

SYMPOSIUM SCHEDULE

TUESDAY, 17 MAY 1994

7:00-9:00 EARLY REGISTRATION AND CHECK-IN

WEDNESDAY, 18 MAY 1994

7:30 Wednesday Authors' Breakfast
(2nd floor conference room at Cleveland Marriott Society Center)

8:30 REGISTRATION AND REFRESHMENTS
(Ballroom Foyer, Cleveland Marriott Society Center)

9:30 INTRODUCTORY REMARKS
Douglas A. Rohn, Host Chairman
NASA Lewis Research Center, Cleveland, Ohio
Stuart H. Loewenthal, General Chairman
Lockheed Missiles & Space Co., Sunnyvale, California

CENTER WELCOME
J. Stuart Fordyce, Deputy Director
NASA Lewis Research Center, Cleveland Ohio

10:00 SESSION I—SOLAR ARRAY/POWER TRANSFER
Fabio Fabbrizzi, Session Chair
Officine Galileo, Florence, Italy

Space Station Freedom Solar Array Containment Box Mechanisms
Mark E. Johnson, Bert Haugen, and Grant Anderson
Lockheed Missiles & Space Co., Sunnyvale, California

INSAT-2A and 2B Deployment Mechanisms
M.N. Sathyanarayan, M. Nageswara Rao, B.S. Nataraju, N. Viswanatha, M. Laxmana Chary, K.S. Balan, V. Sridhara Murthy, Raju Aller, and H.N. Suresha Kumar
ISRO Satellite Centre, Bangalore, India

Roll Ring Assemblies for the Space Station
J. Batista, J. Vise, and K. Young
Honeywell Satellite Systems Operation, Phoenix, Arizona

International Space Station Alpha's Bearing, Motor, and Roll Ring Module Development Testing and Results
David L. O'Brien
Rocketdyne Division, Rockwell International, Canoga Park, California

12:00 LUNCH

1:15 SESSION II—ROBOTICS/MASS PROPERTIES
Savi S. Sachdev, Session Chair
Spar Aerospace Ltd., Brampton, Canada

Design, Characterization, and Control of the Unique Mobility Corporation Robot
Virgilio B. Velasco, Jr. and Wyatt S. Newman
Case Western Reserve University, Cleveland, Ohio
Bruce Steinetz
NASA Lewis Research Center, Cleveland, Ohio
Carlo Kopf and John Malik
Unique Mobility, Inc., Golden, Colorado

Development of an Interchangeable End Effector Mechanism for the Ranger Telerobotic Vehicle
Robert Cohen and David Akin
University of Maryland, College Park, Maryland

Diamond Turning in the Production of X-Ray Optics
Steven C. Fawcett
NASA Marshall Space Flight Center, Huntsville, Alabama

Innovative Mechanism for Mass Properties of an Object
Kedron R. Wolcott
I-NET Inc., Kennedy Space Center, Florida
Todd A. Graham
NASA Kennedy Space Center, Florida
Keith L. Doty
University of Florida, Gainesville, Florida

3:15 BREAK

3:30-5:00 SESSION III—POSTER PREVIEWS
Larry Pinson, Session Chair
NASA Lewis Research Center, Cleveland, Ohio

Space Station Freedom Solar Array Tension Mechanism Development
Curtis Allmon and Bert Haugen
Lockheed Missiles & Space Co., Sunnyvale, California

Leveraging Metal Matrix Composites to Reduce Costs in Space Mechanisms
Ted Nye, Rex Claridge, and Jim Walker
TRW Space and Electronics Group, Redondo Beach, California

Design, Development, and Testing of a Lightweight Optical Sensor Cover System
Mike Hurley
Naval Research Lab, Washington DC
Scott Christiansen
Starsys Research Corp., Boulder, Colorado

Energy Absorber for the CETA
Clarence J. Wesselski
Lockheed Engineering and Sciences Co., Houston, Texas

Design, Characterization, and Control of the NASA Three Degree of Freedom Reaction Compensation Platform
Craig Birkhimer and Wyatt Newmann
Case Western Reserve University, Cleveland, Ohio
Benjamin Choi and Charles Lawrence
NASA Lewis Research Center, Cleveland, Ohio

Pip Pin Reliability and Design
Lane P. Skyles
Lockheed Engineering and Sciences Co., Houston, Texas

Intelligent Control of a Multi-Degree-of-Freedom Reaction Compensating Platform System Using Fuzzy Logic
Benjamin B. Choi and Charles Lawrence
NASA Lewis Research Center, Cleveland, Ohio
Yueh-Jaw Lin
University of Akron, Akron, Ohio

6:00-8:00 WELCOMING RECEPTION
(Ballroom Foyer, Cleveland Marriott Society Center)

THURSDAY, 19 MAY 1994

7:00 Thursday Authors' Breakfast
(2nd floor conference room at Cleveland Marriott Society Center)

8:00 SESSION IV—ACTUATORS/POINTING
William M. Logue, Session Chair
Martin Marietta Astronautics Group, Denver, Colorado

High Precision Moving Magnet Chopper for Variable Operation Conditions
Winfried Aicher and Manfred Schmid
Dornier GmbH, Friedrichshafen, Germany

Two-Axis Antenna Positioning Mechanism
Michelle Herald
Space Systems/Loral, Palo Alto, California
Leilani C. Wai
INTELSAT, Palo Alto, California

Design and Performance of the Telescope and Detector Covers on the Extreme Ultraviolet Explorer Satellite
James L. Tom
University of California, Berkeley, California

Pointing and Tracking Space Mechanism for Laser Communication
A. Brunschvig and M. de Boisanger
Matra Marconi Space, Toulouse, France

10:00 BREAK

10:15 SESSION V—BEARINGS
Roamer Predmore, Session Chair
NASA Goddard Space Flight Center, Greenbelt, Maryland

A Comparison of the Performance of Solid and Liquid Lubricants in Oscillating Spacecraft Ball Bearings
S. Gill
European Space Tribology Lab, Warrington, United Kingdom

Development of Long-Life, Low-Noise Linear Bearings For Atmospheric Interferometry
E.W. Roberts, R.B. Watters and S. Gill
European Space Tribology Lab, Warrington, United Kingdom
R. Birner, G. Lange and W. Posselt
Deustche Aerospace AG, Ottobrun, Germany

The Preliminary Evaluation of Liquid Lubricants for Space Applications by Vacuum Tribometry
W.R. Jones, Jr., S.V. Pepper, R. Jansen, et al.
NASA Lewis Research Center, Cleveland, Ohio
L.S. Helmick
Cedarville College, Cedarville, Ohio
M. Masuko
Tokyo Institute of Technology, Tokyo, Japan

Design of a High-Speed Reliable Ball Bearing
Herbert B. Singer and Erik Gelotte
The Charles Stark Draper Laboratory, Cambridge, Massachusetts

12:15 LUNCH

1:30 SESSION VI—BOOMS
Sandee Paige, Session Chair
The Aerospace Corp., El Segundo, California

MSAT Boom Joint Testing and Load Absorber Design
D.H. Klinker, K. Shuey, and D.R. St. Clair
Lockheed Missiles & Space Co., Sunnyvale, California

Special Test Equipment and Fixturing for MSAT Reflector Assembly Alignment
Jeffrey A. Young, Michael R. Zinn, and David R. McCarten
Lockheed Missiles & Space Co., Sunnyvale, California

Deployable and Retractable Telescoping Tubular Structure Development
M.W. Thomson
Astro Aerospace Corp., Carpinteria, California

3:00 BREAK

3:15 SESSION VII—LESSONS LEARNED
E.W. Roberts, Session Chair
European Space Tribology Lab, AEA Technology, Warrington, United Kingdom

Lessons Learned from Selecting and Testing Spaceflight Potentiometer
Ted Iskenderian
Jet Propulsion Laboratory, Pasadena, California

The Galileo High Gain Antenna Deployment Anomaly
Michael R. Johnson, Jet Propulsion Laboratory, Pasadena, California

6:00-10:00 Banquet at Crawford Museum
6:00 Buses depart from Cleveland Marriott Society Center
6:30-7:15 Social Hour—Car/Airplane Collection
7:15 Dinner in Rotunda
8:30 The Art of Restoration, David Holcomb
10:00 Return to Cleveland Marriott Society Center

FRIDAY, 20 MAY 1994

7:00 Friday Authors' Breakfast
(2nd floor conference room at Cleveland Marriott Society Center)

8:00 SESSION VIII—RELEASE/DAMPER
William Schneider, Session Chair
NASA Johnson Space Center, Houston, Texas

Implementation of Heaters on Thermally Actuated Spacecraft Mechanisms
John D. Busch and Michael D. Bokaie
TiNi Alloy Co., San Leandro, California

Payload Holddown Release Mechanism
Dale Chaput, Mark Visconti, Michael Edwards, and Tom Moran
G&H Technology, Inc., Camarillo, California

Advanced Release Technologies Program
Bill Purdy
Naval Research Lab, Washington DC

Load Limiting Landing Gear Footpad Energy Absorption System
Chris Hansen and Ted Tsai
NASA Johnson Space Center, Houston, Texas

10:00 BREAK

10:15 NASA LEWIS RESEARCH CENTER OVERVIEW
David J. Poferl
Director, Technical Services Directorate

10:45 PRESENTATION OF THE HERZL AWARD
Bowden Ward
NASA Goddard Space Flight Center, Greenbelt, Maryland

CLOSING REMARKS
Charles W. Coale, Organizational Chairman
Lockheed Missiles & Space Co. (Ret.), Sunnyvale, California

11:00 LUNCH AND CHECK-OUT

12:30 BUS LEAVES MARRIOTT FOR TOUR

1:00-3:00 NASA LEWIS FACILITY TOUR, THEN AIRPORT
Zero-G, Electric Propulsion, Advanced Communications Technology Satellite, Tribology, and others. Stops may change, depending on facilities operations.

SYMPOSIUM ORGANIZING COMMITTEE

Douglas A. Rohn, Host Chairman, NASA Lewis Research Center

Stuart H. Loewenthal	General Chairman	LMSC
Edward A. Boesiger	Operations Chairman	LMSC
Charles W. Coale	Organizational Chairman	LMSC (Ret.)
Obie H. Bradley, Jr.		NASA LaRC
Charles S. Cornelius		NASA MSFC
Michael Eiden		ESA/ESTeC
David F. Engelbert		NASA ARC
Alan C. Littlefield		NASA KSC
Edward C. Litty		JPL
Ronald E. Mancini		NASA ARC
Stewart C. Meyers		NASA GSFC
John W. Redmon, Sr.		NASA MSFC
John F. Rogers		NASA LaRC
William C. Schneider		NASA JSC
Donald R. Sevilla		JPL
Sterling W. Walker		KSC
Bowden W. Ward, Jr.		NASA GSFC

SYMPOSIUM ADVISORY COMMITTEE

Paul W. Bomke	JPL
Aleck C. Bond	NASA JSC (Ret.)
Thomas F. Bonner	Space Industries
H. Mervyn Briscoe	ESTeC (Ret.)
Kenneth C. Curry	JPL (Ret.)
Otto H. Fedor	LSOC (Ret.)
Harvey H. Horiuchi	JPL
Frank T. Martin	NASA GSFC (Ret.)
Alfred L. Rinaldo	LMSC (ret)
Nathan D. Watson	NASA LaRC (Ret.)

Edward A. Wegner, LMSC (Ret.), Publicity Coordinator

SPACE STATION FREEDOM SOLAR ARRAY CONTAINMENT BOX MECHANISMS

Mark E. Johnson, Bert Haugen, and Grant Anderson
Lockheed Missiles & Space Co.
Sunnyvale, California

Introduction

Space Station *Freedom* will feature six large solar arrays, called solar array wings, built by Lockheed Missiles & Space Company under contract to Rockwell International, Rocketdyne Division. Solar cells are mounted on flexible substrate panels which are hinged together to form a "blanket." Each wing is comprised of two blankets supported by a central mast, producing approximately 32 kW of power at beginning-of-life. During launch, the blankets are fan-folded and compressed to 1.5% of their deployed length into containment boxes (*figure 1*). This paper describes the main containment box mechanisms designed to protect, deploy, and retract the solar array blankets: the latch, blanket restraint, tension, and guidewire mechanisms.

Design Heritage

SAFE

The technologies and mechanisms used on the Space Station *Freedom* (SSF) wing were first demonstrated in 1984 on the Solar Array Flight Experiment (SAFE) aboard Shuttle mission STS-41D (*figure 2*). However, different requirements for SSF led to major differences in the implementations of the latch and blanket tensioning mechanisms, as well as the addition of a blanket restraint system. SAFE's smaller, single blanket design was latched and preloaded in a single containment box using cams and the initial motion of the extendable mast. In contrast, the two containment boxes of the much larger two-blanket SSF design (*figure 3*) were required to swing 90° into a more compact configuration for stowage aboard the Orbiter. The 90° rotation of the two boxes necessitated an all new design for the latch mechanism (see below). The smaller wing and very short operational life of SAFE allowed its tension mechanisms to be weight-optimized for low load at high stress, without concern for thermal cycles and related mechanism fatigue. Increased tension and life requirements for SSF, as well as limitations in the partially deployed mast capability, caused major redesign of the tension mechanism. In contrast, SSF's guidewire mechanisms are direct descendants of SAFE. Both designs use constant-force spring driven takeup drums to deploy and retract over 30 m (>100 ft) of wire rope. This cable passes through every other blanket hinge, guiding the fanfolding blanket during deployment and retraction. Finally, a new blanket restraint system was designed to accommodate the weight and size of the SSF blankets.

Milstar

Though a later design, Milstar's mechanisms have less in common with SSF than do SAFE's. The primary reason for this is that Milstar has no requirement to retract its

wing on-orbit. Its latch mechanism is preloaded on the ground and released by pyrotechnic pinpullers. The guidewire tension is required only during initial deployment, so may be provided by a small slip-clutch. Though the Milstar tension mechanism is similar to the SSF design in providing nominally constant force over a wide range of thermally induced blanket and mast motion, it was sized for only a fraction of the tension required by SSF.

Special Requirements

In addition to the typical requirements for spacecraft mechanism design which include vacuum, temperature extremes, zero gravity, light weight, and remote operation, the Space Station *Freedom* program dictated several unique requirements for the solar arrays that significantly impacted the design of the containment box mechanisms. The most onerous of these requirements was that for repeated deployments and retractions: 35 extension/retraction cycles and 15 unlatch/latch cycles over the operational life of the wing. This requirement resulted from a system level desire to retract the arrays to allow on-orbit servicing of the remainder of the electrical power system and to avoid excessive wing loads that potentially result from the plumes emitted by the Orbiter's thrusters impinging on a deployed wing. Not only did this requirement preclude the use of single action release devices from being used on the containment box, but it also necessitated the ability to passively restow and align 33 m (107 ft) of solar array blankets and the related tensioning hardware within the containment box to sufficient accuracy to allow relatching without damaging the solar array.

A second category of unique requirements were those necessary to allow assembly and servicing on-orbit by astronauts during Extra-Vehicular Activity (EVA). The two most significant items in this category were requirements for manual backup capability to the automated mechanisms and the ability to remove and replace an individual containment box on-orbit. In addition to necessitating additional mechanization for the EVA to bypass the automatic mode and manually actuate the latch, these requirements necessitated separable interfaces and consideration in the mechanism designs of EVA limitations and risks.

The final category of special requirements was the severe design life which included a four year storage requirement, a one year dormant condition on orbit in the stowed configuration, and a 15 year operational life in low earth orbit (LEO) with a significant Atomic Oxygen (AO) flux. The space station orbit required the mechanisms to withstand 87,000 thermal cycles during this exceptionally long life. Finally, the long life in the specified AO environment of LEO provided very severe constraints on the use of lubricants and non-metals.

Mechanism Descriptions

Latch Mechanism

Function & Requirements

When stowed for launch, the folded blanket is preloaded within the containment box. This prevents "chatter" between the blanket panels during the

vibratory/acoustic loading of ascent, as well as providing some measure of lateral restraint by inter-panel friction. The SSF latch mechanism is required to provide 24.9 ± 1.8 kN (5600 ± 400 lb) of preload (*figure 3*), distributed over eight locations on the containment box, using available motor output with 100% torque margin and a maximum of 20 seconds. It must capture and release the box cover anywhere from 0–9 cm (0–3.5 in) above the nominal compressed blanket stack height and be capable of 15 operations over a 15 year on-orbit life. It also must provide actuation force for the blanket restraint system and tension mechanisms.

Physical Description & Performance

To evenly distribute the preload into 17.2 kPa (2.5 psi) over the stowed blanket, there are eight latch points on the perimeter of the containment box, four per side (*figure 4*), and foam pads between the box and blanket. The motor drive assembly (*MDA*) is located at the inboard end of the box to minimize wire harness length and cantilevered mass. Its minimum output is 12 N-m (110 in-lb) at 180 RPM. This torque is transmitted by a *drive shaft* to tandem, opposing *ball screws* in the center of the box (*figure 5a*). The ball screws are lightly lubricated with a Braycote 600 grease plate, protected from AO by the box structure. Their support bearings are treated with a sputtered MoS_2 dry film solid lubricant. Small radial bearings support the extreme ends of the screws, while larger face-to-face mounted angular contact bearing pairs support the thrust loads (11.6 kN, or 2600 lb max). The thrust loads are reacted out locally by a common central bearing housing so that little load is transferred to the honeycomb panel mounting surface. *Ball nut flanges* on the ball screws are driven toward the center of the box during a latch operation. A pair of short *tie rods* are pinned between each ball nut flange and two arms of a *torque tube.* This slider-crank mechanism transforms the horizontal motion of the ball nut flanges into rotation of the torque tubes.

Each torque tube has two latch *hooks,* pivoted and sprung on lobes at each end (*figure 5b*). When the hooks engage *pivot pins* on the box cover, the rotation of the torque tube is transferred into vertical motion of the cover with a second crank-slider mechanism. There are four torque tubes but only two ball screws: the torque tubes furthest from the box center are driven by long *tie rods* from the central torque tubes. This method saved the weight and complication of a second pair of ball screws and associated support bearings.

The latches start in a self-locking, over-top-dead-center position. Unlatching turns the torque tubes, raising the latch hooks which are held against the cover pivot pins by *hook springs* (*figure 5c*). Some distance after the blanket preload is relieved, the hook springs are overpowered by a cam feature on the torque tube, swinging the hook out of the cover pins' path (during blanket extension). After the wing is retracted, the latch hooks are able to recapture the cover by reversing the motion.

Primary and redundant limit switches provide telemetry for the latched and unlatched positions, while hard stops protect against overtravel if the limit switches fail. Each pivot location features redundant pivot paths and lined bushings (PTFE impregnated) for controlled friction and low edge wear. The stowed preload is set at assembly by adjusting the length of the latch hooks with their central turnbuckles.

In the event of power loss or a failed motor, the latch mechanism may be operated by an astronaut using a rotary power tool. The *manual backup assembly* is located inline with the drive shaft, near the motor. A dog clutch transmits rotary power during nominal operation. This spring-loaded clutch may be disegaged by an astronaut using the *lever.* The mechanism is then driven by the astronaut's rotary power tool via a 1:1 miter gear pair. This gear mesh is never disengaged—it freewheels during nominal, motorized operation.

A kinematic analysis of the latch mechanism utilized conservative friction factors (0.30 for PTFE-lined bushings and MoS_2 surfaces, 90% efficient ball screws) and blanket compression characteristics (*figure 6*). The predicted performance satisfied the design requirements for 100% torque margin and < 20 seconds operation time (*figure 7*).

Blanket Restraint System

Function & Requirements

The Blanket Restraint System (BRS) for the SSF containment boxes is a spring actuated retractable pin mechanism designed to restrain the blanket within the containment box during launch then retract prior to solar array deployment on orbit. The functional requirements of the BRS include: restraint of the blanket during launch (with a maximum clearance ≤ 0.089 mm, or 0.0035 in, to limit transient impact loads), ability to retract in on-orbit environments, use of only the available latch drive motion for pin release, adequate telemetry to verify retraction, and reset capability during ground test with no access to the actuation system. The quantitative requirements are shown in Table 1. In addition, the multiple deployment/retraction requirement of the SSF wing requires that the BRS be resettable during ground test with minimal test operations interference. This turned out to be a driving requirement for the design of the mechanism.

Table 1: Blanket Restraint Pin Performance

Parameter	Requirement	Measured Value
Release force	≤ 222 N (50 lb)	58 N (13 lb) max
Allowable Sideload during retraction:	≥ 227 N (51 lb)	240 N (54 lb) min, 418 N (94 lb) max
Limit Load	> 5.8 kN (1,300 lb)	> 7.1 kN (1,600 lb)
Ultimate Load	> 12.5 kN (2,800 lb)	> 12.9 kN (2,900 lb)
Operational Temperature Range:	-73 to +37 C (-100 to +100°F)	-85 C (-121 °F) (hot case not tested)
Design Life: On-orbit In Test	≥ 1 retraction ≥ 50 retractions	not tested

Mechanism Description & Performance

Unlike previous smaller and lighter flexible solar arrays which relied on inter-panel friction to provide lateral restraint of their blankets during ascent, the SSF blankets are positively restrained during launch by a retractable pin system. This was required due to the weight of the folded SSF blanket assembly—over twice that of SAFE's and six times the weight of Milstar's. The use of friction alone to provide the

lateral restraint of the stowed blanket was not adequate for this system without undue compressive forces that threatened to crack solar cells and cause large weight penalties to the containment box structure and latch mechanism. Thus a non-pyrotechnic, retractable pin system was determined to be needed after efforts to either increase inter-blanket friction or provide "interlocking" panel segments were deemed unreliable or impracticable (largely due to the on-orbit retraction requirement).

The pin of the BRS extends through the honeycomb structure of the box and is inserted through slots machined in aluminum stiffeners in the blanket. Some slots are in the x direction resulting in only y lateral restraint while others are slotted in the y direction resulting in x direction lateral restraint. There are a total of seven pins per box assembly. Two pins restraint the blanket in the x direction and six restrain the blanket in the y direction (one stiffener hole is circular). The slots provide allowance for relative thermal growth between the glass/Kapton/fiberglass blanket assembly and the aluminum containment box to limit thermally induced pin loads. The BRS pin will be retracted within the containment box structure once on-orbit prior to the first solar array deployment.

The heart of the mechanism is a titanium *tapered pin* nested within a stainless (303) *"expandable" pin* (*figure 10 & 11*). The expandable pin is sectioned along its length to allow for expansion when the MoS_2 lubricated tapered pin is inserted. The pins are precision machined to calculated profiles such that the expandable pin will achieve (ideally) line contact with the tapered pin upon its complete insertion into the expandable pin. After wire Electrical Discharge Machining (EDM) of the expandable pin longitudinal slots and insertion of the tapered pin, the outer surface of the expandable pin is precision ground to 20.32 +0.00/-0.04 mm (0.800 +0.000/-0.0015 in) along its interface with the blanket assembly.

The pin assembly contains a 53 N/cm (30 lb/in) *spring* compressed to 222 ± 22 N (50 ± 5 lb) for extraction of the tapered pin from the expandable pin. This retraction allows the expandable pin to contract (a maximum of 2.5 mm, or 0.100 in, diameter at the tip) in order to relieve all sideload from the pin during retraction. At this point, a 10.5 N/cm (6 lb/in) *spring* compressed to 111 ± 22 N (25 ± 5 lb) retracts the entire expandable pin assembly from the blanket into the *mounting tube* assembly. This results in release of the blanket and allows unhindered deployment of the folded blanket assembly during mast extension. In ground testing, the system can be reset to the "extended" position to allow rethreading of the blanket over the "collapsed" pin. The unit then can be cocked into the expanded position, securing the blanket into position with minimal clearance. The blanket side loading on the expandable pin is transferred to the titanium tapered pin then through the mounting tube into inserts in the honeycomb structure.

The BRS assembly employs a *pin lock* attached by *actuation cables* to a *trip lever* on the latch mechanism (*figure 12*). During unlatch of the blanket box, the lever pulls open the pin lock door resulting in release of the system. In the event of a "stuck" pin, a lockout plunger prevents the pin lock from resetting. This will allow the pin to retract on its own if an unanticipated transient event (*e.g.*, unpredicted thermal gradients) causes an initial failure to retract.

When the pin fully retracts, it releases the *lockout plunger* to allow resetting the pins and pulls two additional plungers from redundant limit switches to close a series circuit. In addition to this electrical confirmation, a yellow 3.8 cm (1.5 in) long "visual indicator" protrudes out of the end of the mounting tube and will allow an astronaut to determine if any pins have failed to retract. The retracting expandable pin assembly is captured by a padded stop at the end of the mounting tube. An interface for a reset tool was designed into this stop so that all forces required to reset an expandable pin will be reacted into its mounting tube structure. No additional bracing on the ground support equipment or flight structure is required.

Tension Mechanism

Function & Requirements

When deployed, two tension mechanisms apply tension to the flexible, hinged blanket to maintain its flatness and achieve a minimum natural frequency of 0.085 Hz for the deployed wing. The load requirement is bounded by 245 N (55 lb) minimum for the frequency requirement, and 423 N (95 lb) maximum for blanket strength (hinge loading). The operational life requirements include 35 full stroke cycles for array extensions/retractions, and 87,000 partial stroke cycles for on-orbit thermal cycles (operational and ground test cycles are doubled for qualification testing). The blanket length tolerance and thermal distortions require the full stroke to be 71 cm (28 in), and the partial stroke 8–15 cm (3–6 in). In addition, strength limitations of the partially deployed mast require that the tension be limited to less than 53 N (12 lb) until after full mast extension.

Physical Description & Performance

Each tension mechanism is a spring-driven cable drum. A constant-force spring, while providing a convenient flat force profile, was unacceptably large when designed to withstand 200,000 fatigue cycles at the design load. Instead, a pair of power springs were utilized to provide a more weight and space efficient design. The nonconstant moment produced by these springs is converted to a nominally constant force by the increasing radius of a helical cable drum. Solid film (MoS_2) lubricated ball bearings are used in the cable drum and mechanism pulley to minimize friction at these points. A complete discussion of this mechanism is given in the paper "Space Station *Freedom* Solar Array Tension Mechanism Development."

The single blankets deployed by SAFE and Milstar are tensioned during mast extension, but SSF's large power requirements and stowage envelope constraints required a split blanket/twin box design. This introduced the possibility of differing blanket lengths. Such an imbalance would mean blanket tension loads may be applied to one blanket before the other, imparting unacceptable dynamic loading on the mast during the final seconds of deployment. The solution was a two-stage tension mechanism that provides full 333 N (75 lb) only for launch restraint and when the wing is completely deployed. This was accomplished by linking each tension mechanism with the motion of the latch mechanism ball screws.

Miscellaneous Mechanisms

To control the motion of the blanket during extension and especially retraction, three guidewire mechanisms on the box base pay out over 30 m (100 ft) of wire rope

attached to the box cover. A single constant-force spring powers each wire drum, producing 5.3 ± 0.9 N (1.2 ± 0.2 lb) over the considerable stroke. SAFE used multiple springs per mechanism, but the single spring design provides similar forces and reliability, saving the weight of additional spring drums, bearings, and associated fasteners. The mechanism's life requirements are similar to the tension mechanism. Reliable, even winding of the guidewire cable during retraction is ensured by a proper "fleet angle" (the angle over which the cable alternates when winding on the drum).

Other minor mechanisms on the box are an astronaut-operated soft dock mechanism, swing bolts, and an electrical connector separation mechanism where the box Orbital Replaceable Unit (ORU) interfaces with the rest of the wing. Proper stowage of a retracted and compressed blanket is maintained by small deployer bars and over 300 small extension springs at the extreme blanket ends.

Development Testing

Latch Mechanism Performance Test

This test was necessary to evaluate the overall function of the mechanism, including correlation of kinematic analysis & drag predictions, calibration & adjustment of the preload, capture & release of the box cover, proper motion of the drive train & linkages, and interaction of the limit switches & hard stops.

The test equipment consisted of a complete development latch mechanism (without the manual backup assembly). An aluminum plate and frame structure simulated the box base, and an offloaded aluminum plate simulated the box cover in zero gravity (*figure 4*). The folded blanket compression characteristics (*figure 6*) were simulated by a foam pad and appropriate spacers. A test motor with separate controller provided representative torque (up to 12.4 N-m, or 110 in-lb), though at 10% of flight motor speed (15 RPM). A torque reaction transducer measured motor output, and a single LVDT measured vertical cover motion. As for flight production, each latch hook featured a full bridge strain gauge for measuring the "axial" force in each hook (the offset pivot point at the hook end induces some bending).

The test successfully demonstrated the latch motion, adjustment, and operation. Torque measurements exceeded expectations by 0.2–0.9 N-m (2-8 in-lb, *figure 8*), but were well within the flight motor's capability with 83% torque margin. This discrepancy was attributed to additional losses in the drive train. There was slight rubbing on the cover pivots and hook spring leading to minor redesign of those components.

Blanket Restraint System Performance Test

The BRS was tested for both structural load capability as well as retraction performance. The development test employed both a full BRS pin assembly and a representative section of the containment box honeycomb (*figure 13*). The pin was loaded using 82 representative strips of "solar array blanket" with sections of aluminum stiffeners to simulate the blanket loading of the flight pins.

For retraction capability, the BRS demonstrated release at -73 C (-100 °F) with no internal binding due to thermal growth. The maximum sideload under which retraction reliably occurred was 418 N (94 lb). However, the minimum retraction of one pin assembly was just 240 N (54 lb). This was lower than expected and was attributed to internal pin loading caused by a shortening of the moment arm of the titanium pin due to pin bending during loading. The flight design was improved by providing a shoulder on the titanium pin to ensure the moment arm of the pin remains relatively constant and the internal loading more predictable.

The structural capability of the pin was very close to what was predicted. The yield of the system occurred in the titanium pin at 10.2 kN (2,300 lb) and was very benign. Ultimate failure occurred in the honeycomb insert bond line to the honeycomb and was evidenced by "crimpling" of the honeycomb around the insert.

As can be seen from the load vs. deflection curve (*figure 14*), there is a hysteresis in the system. This is due to the friction between the expandable and tapered pins. Calculations showed that this hysteresis indicated a relatively high effective friction coefficient between these members of 0.27. The development unit used Braycote 601 grease on the tapered pins with uncontrolled surface finishes. Improvements made for the flight units that will reduce the internal hysteresis and fiction include providing controlled surface finishes on the tapered expandable pins, increasing internal clearances and lubricating with sputtered MoS_2 (grease was used during development testing due to schedule constraints).

The lessons learned from the development testing included: the need for increased internal clearances between the tapered and expandable pins allow for minor pin bending; the need for a functional "break-in" test to allow initial wear of the pin stop; and the need for controlled surface finishes to improve internal friction properties.

Tension Mechanism Performance and Life Cycle Tests

The tension mechanism first exhibited unacceptable hysteresis and wear during the performance and life tests, leading to incorporation of power springs lubricated with sputtered MoS_2 and Bray oil. The paper "Space Station *Freedom* Solar Array Tension Mechanism Development" contains a full description of this test.

Integrated Box Mechanisms Performance and Life Cycle Test

Once the major box mechanisms had undergone development testing at the component level, they were assembled together on the latch mechanism test stand to verify correct interaction. The test configuration consisted of the latch, manual backup, two tension mechanisms BRS pin assemblies. Using the same instrumentation as previous latch testing, this test configuration underwent numerous simulations of all operational sequences: the combined unlatch/detension/BRS release sequence, tension wire extension, full tension application, detension sequence, tension wire retraction, and latch/tension sequence. The test indicated proper performance of the integrated mechanisms with only minor enhancements necessary to the BRS release hardware. These enhancements were to

provide adjustment of the release cables during assembly and to provide increased stroke from the torque tube lugs.

The set of mechanisms were exercised through 70 tension/detension cycles, and 30 latch/tension/unlatch/detension cycles—twice the on-orbit life requirement. At the end of the testing, all mechanisms were still functioning as designed. Post-test inspection of the mechanisms revealed no adverse wear but some organic wear debris on the ball screw assembly. The development ball screws were tested unlubricated, but were not cleaned of the residual coating applied by the supplier for storage. Flight ball screws will be thoroughly cleaned and lightly lubricated with Bray 601 grease plate.

Future Testing

Funding caps and system level redesign of the space station have delayed the qualification testing of the wing, including the containment box mechanisms, until late 1994 through 1995. The testing will include qualification of the tension mechanism at the component level to demonstrate performance, after exposure to severe random vibration, for twice the operational life cycles (100 extension/retraction cycles and 176,000 thermally induced cycles). The life cycling will be performed under full thermal and vacuum conditions in an accelerated life test. The guidewire mechanism will undergo similar life cycle testing. At the wing assembly level, the containment box mechanisms will be qualification tested for full functional performance of both automatic and manual backup modes before and after exposure to acoustic environments and periodically during operational life cycle testing (>100 full extension/retraction cycles and >50 unlatch/latch cycles). Life cycle testing at the wing level is being performed at ambient conditions due to the large size of the deployed array (7.6 by 33.5 m, or 25 by 110 ft, for the test configuration utilizing only one of the two containment boxes and blankets). Functional testing of the latch mechanism and blanket restraint system at the containment box and wing assembly level under thermal and vacuum conditions will be performed on a "protoqual" basis on each flight wing. This test will include a first motion demonstration of the wing extension as well as simulation of worst case containment box thermal gradients during the operation of the mechanisms.

Conclusion

The major containment box mechanisms for the Space Station *Freedom* solar array wing have been design, built, and undergone component and integrated development testing. Performance of the mechanisms and their interactions was successfully verified by the development testing and minor enhancements to the hardware have been incorporated. Production of qualification units has begun, to be tested during 1994. First flight is scheduled for 1997.

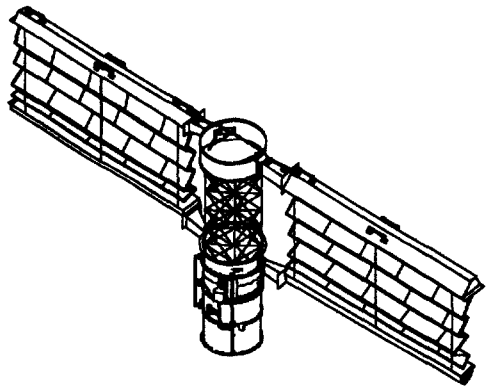

Figure 1: Space Station Freedom Solar Array Wing (Deploying)

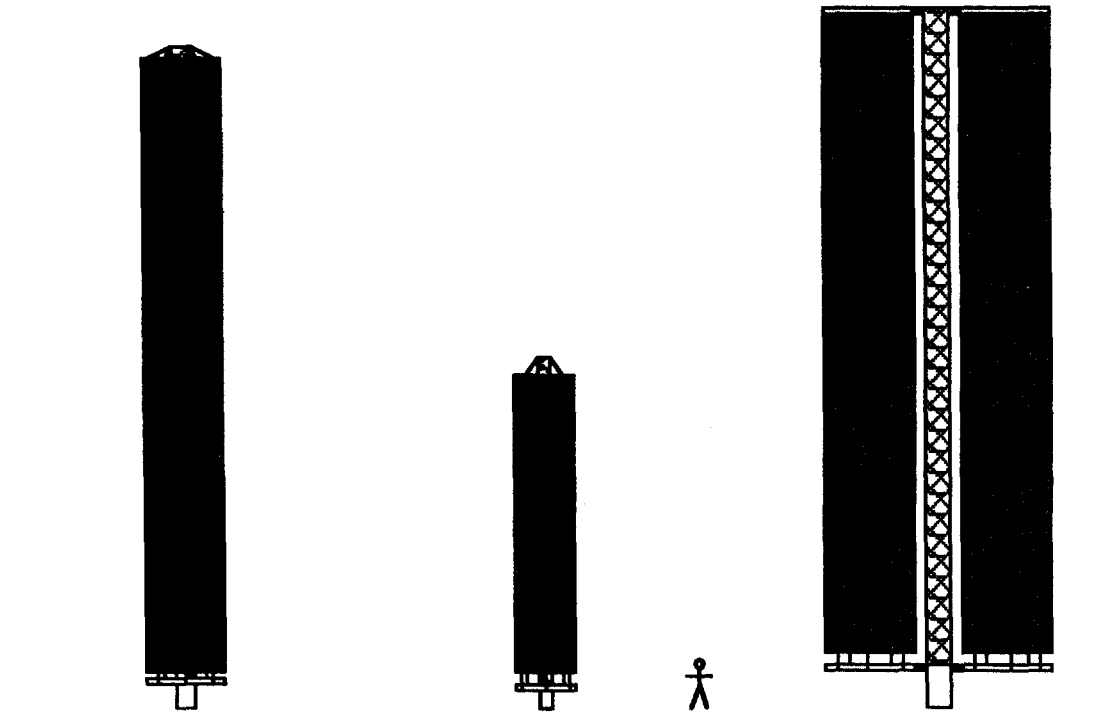

Figure 2: SAFE, Milstar, and SSF Solar Array Wings

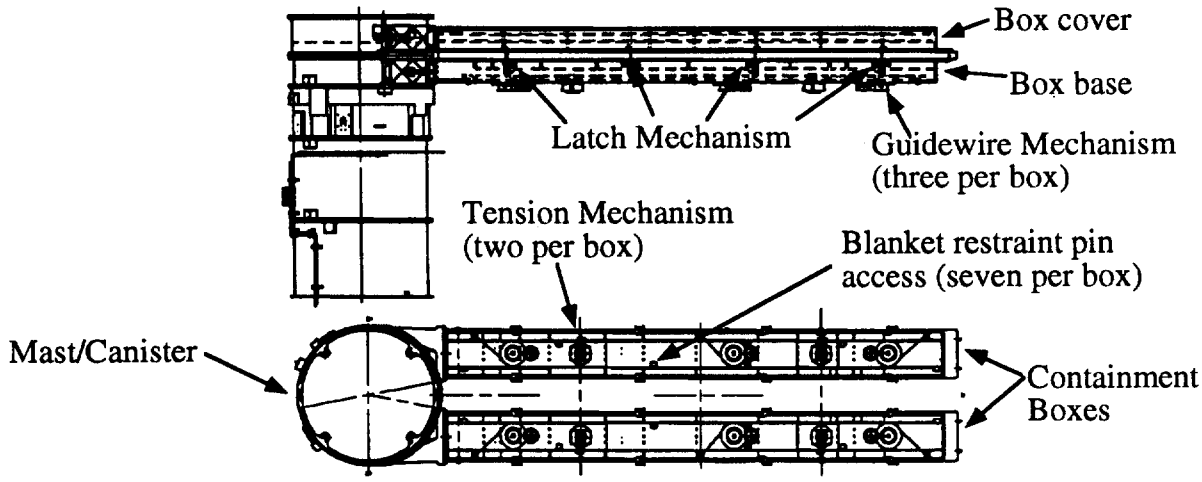

Figure 3: SSF Stowed Wing Layout

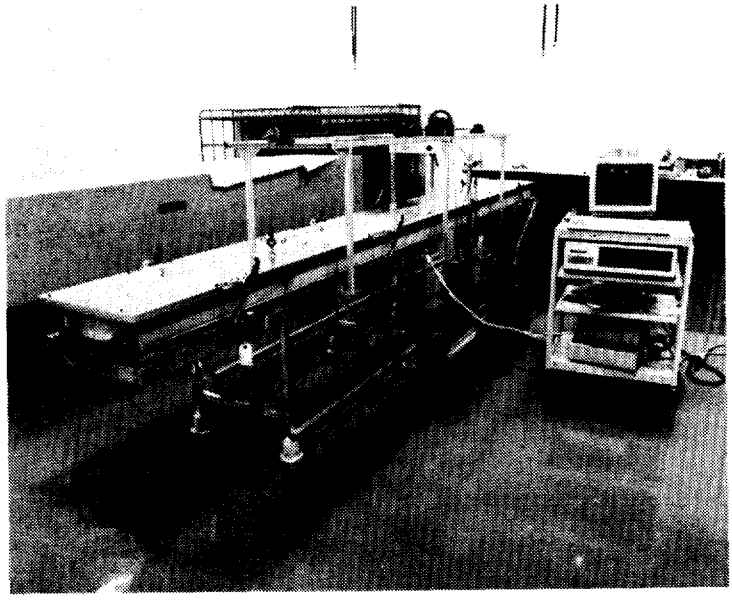

Figure 4: Latch Mechanism Development Test

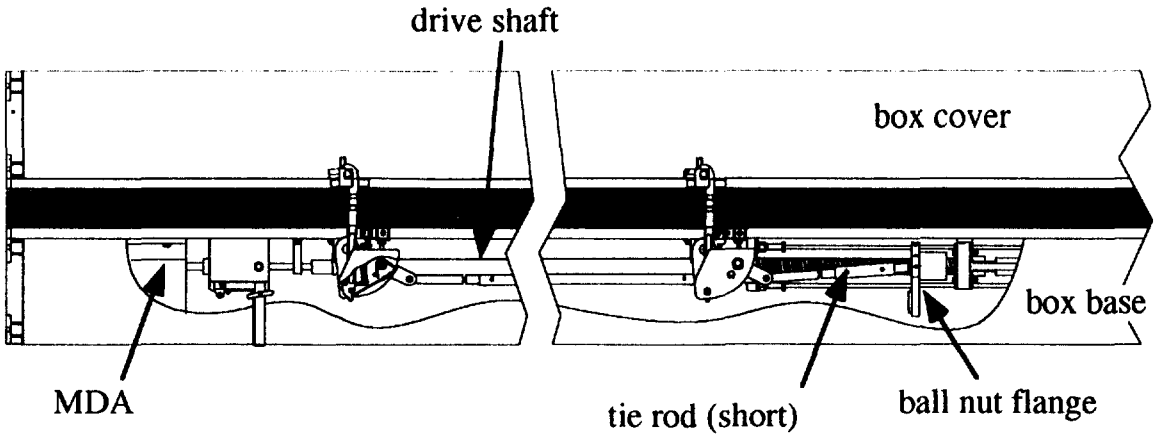

Figure 5a: Latch Mechanism Kinematics (Latched)

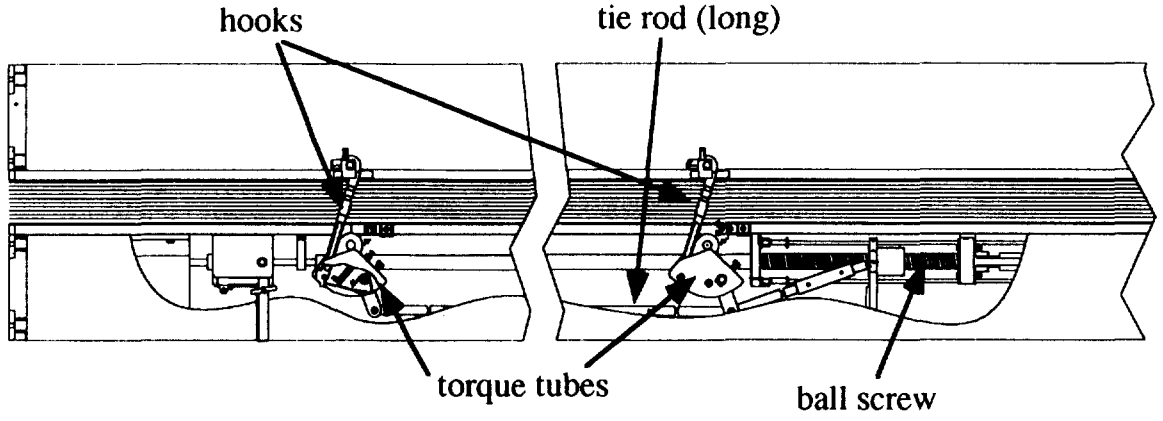

Figure 5b: Latch Mechanism Kinematics (Mid-operation)

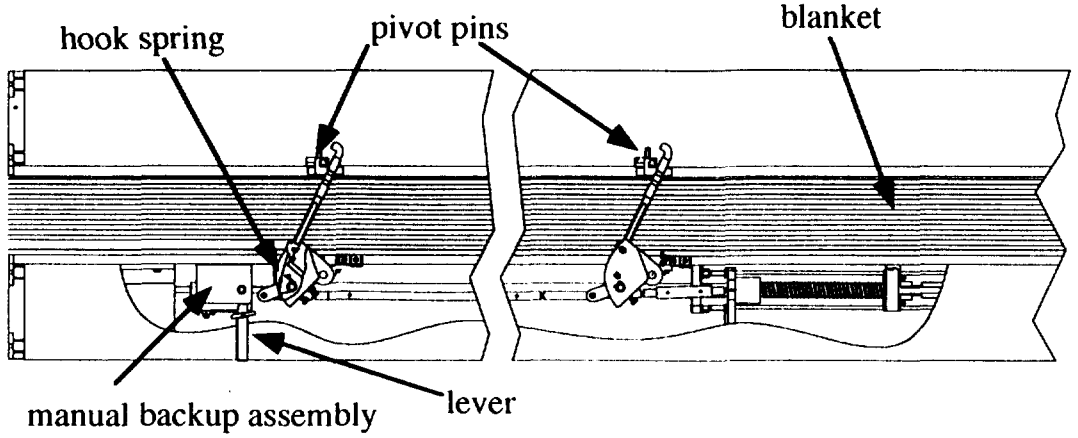

Figure 5c: Latch Mechanism Kinematics (Unlatched)

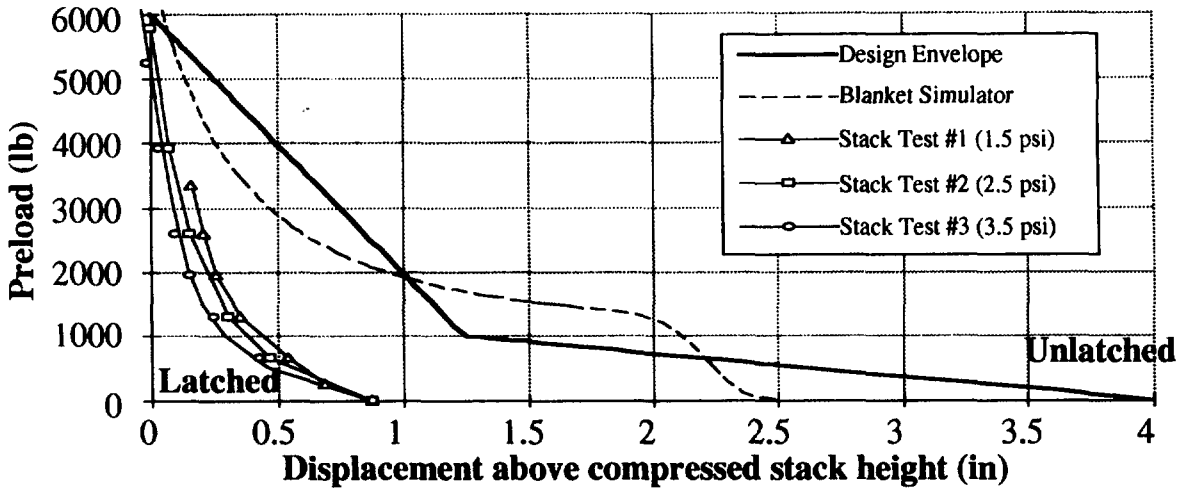

Figure 6: Blanket Compression Characteristics

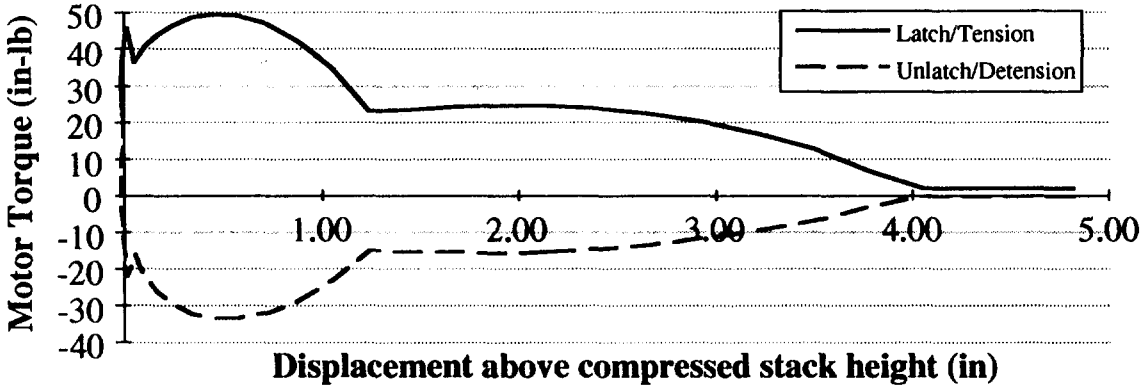

Figure 7: Latch Mechanism Performance Prediction

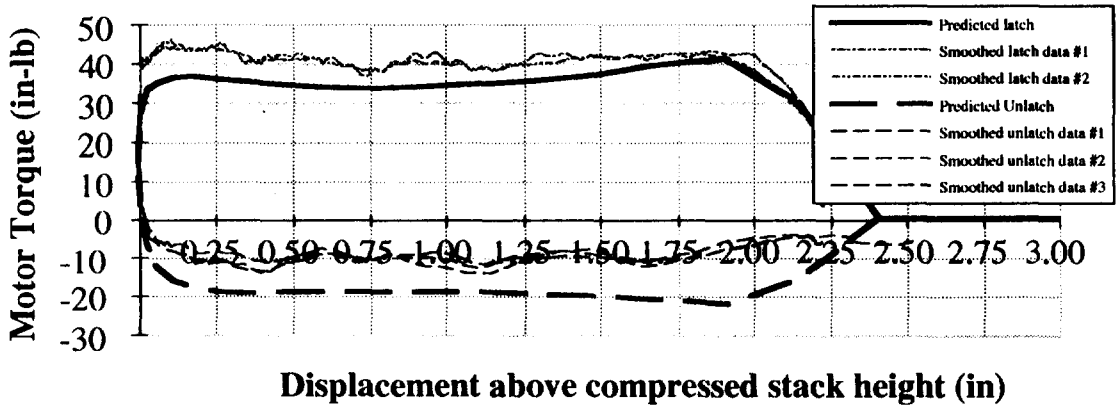

Figure 8: Latch Mechanism Development Test Results

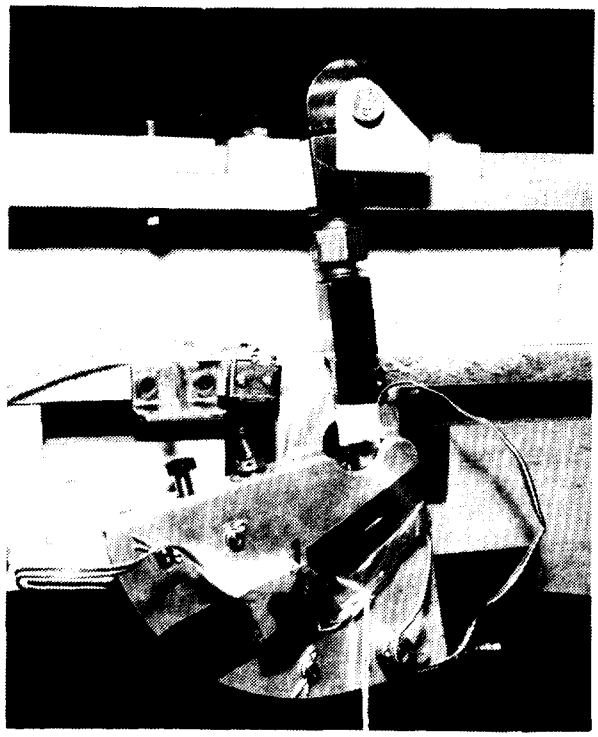

Figure 9: Development Latch Mechanism Hook

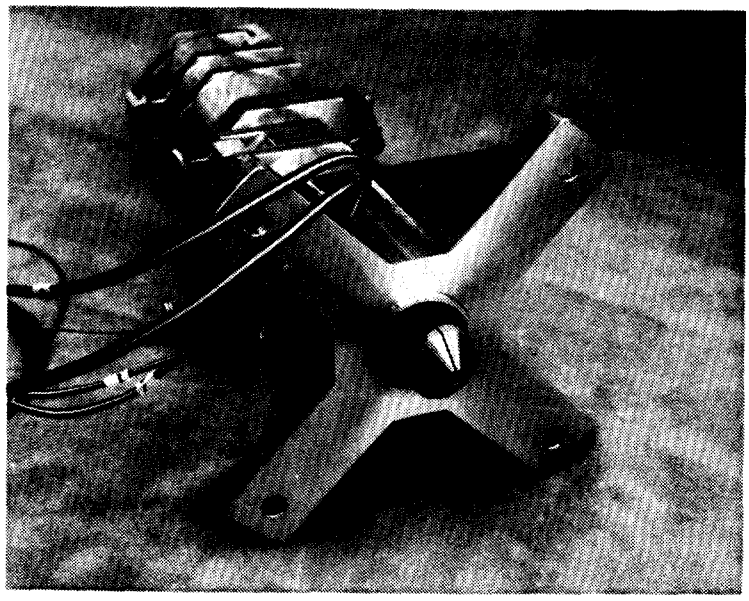

Figure 10: Blanket Restraint System Pin Assembly

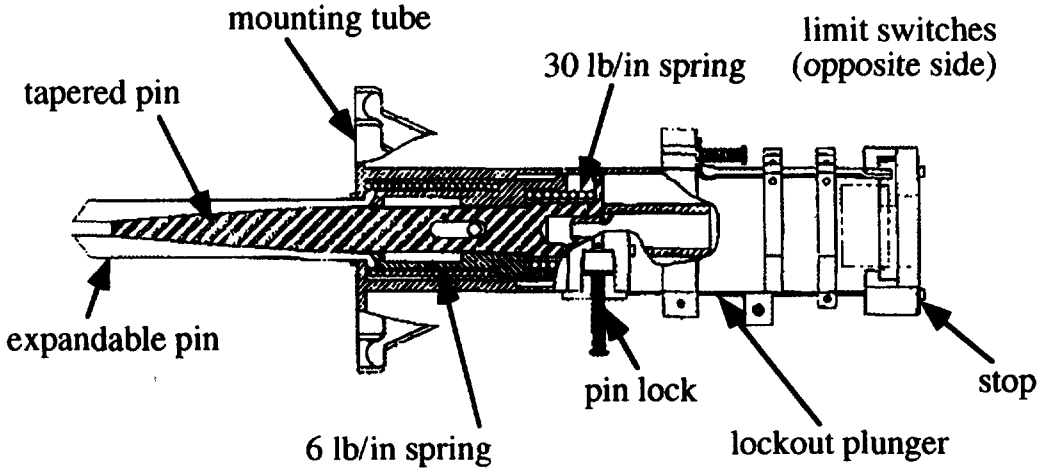

Figure 11: Blanket Restraint System Pin Assembly Cross-Section

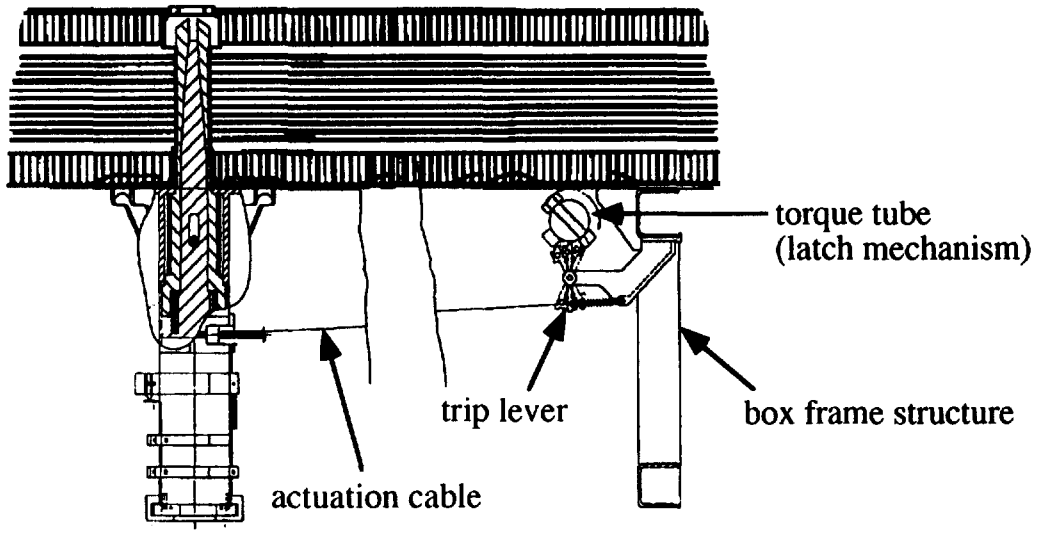

Figure 12: Blanket Restraint System Actuation

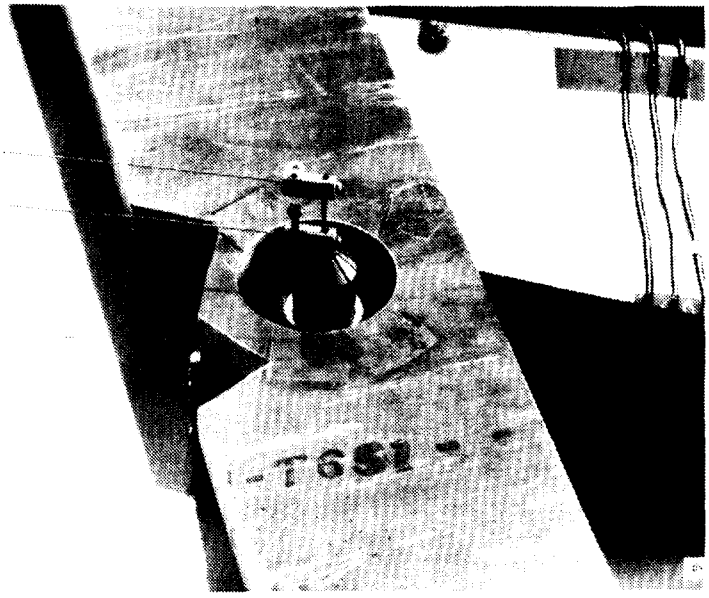

Figure 13: Blanket Restraint System Development Test

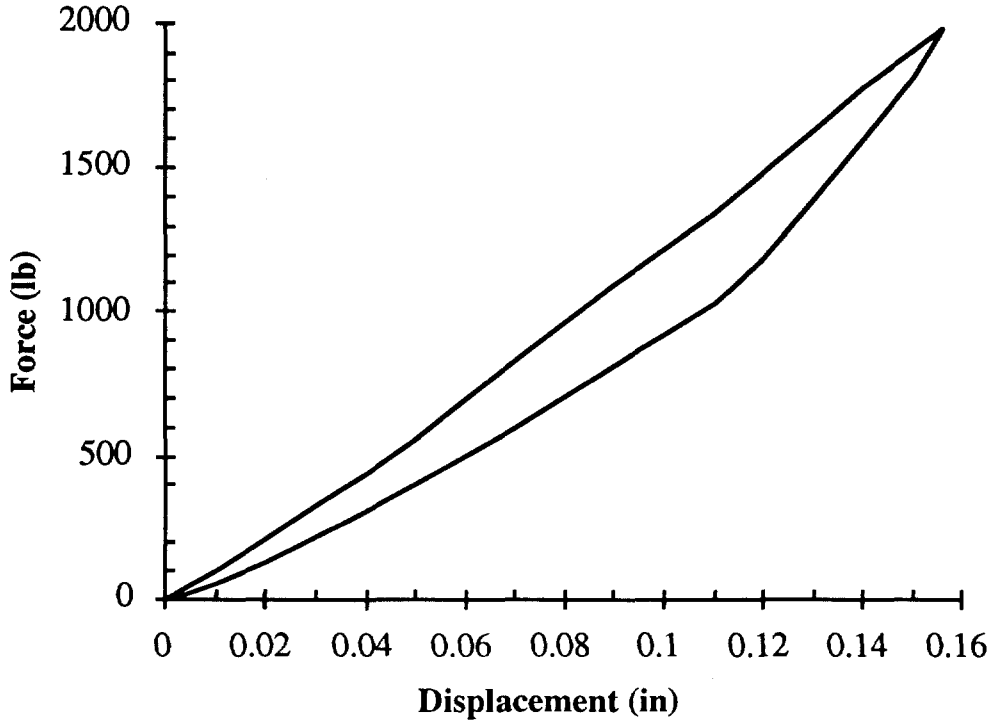

Figure 14: Blanket Restraint System Test Results

INSAT-2A and 2B DEPLOYMENT MECHANISMS

M.N. Sathyanarayan, M. Nageswara Rao, B.S. Nataraju,
N. Viswanatha, M. Laxmana Chary, K.S. Balan,
V. Sridhara Murthy, Raju Aller,
and H.N. Suresha Kumar
Spacecraft Mechanisms Group
ISRO Satellite Centre
Bangalore, India

ABSTRACT

The Indian National Satellite (INSAT) 2A and 2B have deployment mechanisms for deploying the solar array, two C/S band antenna reflectors and a coilable lattice boom with sail. The mechanisms have worked flawlessly on both satellites. The configuration details, precautions taken during the design phase, the test philosophy, and some of the critical analysis activities are discussed.

1.0 INTRODUCTION

The INSAT-2A and 2B are the first two indigenously built operational communication satellites. Both satellites are identical in their configuration and include mechanisms for deployment of a solar array, two C/S band antenna reflectors, and a coilable lattice boom with solar sail. Figure 1 shows the satellite with deployed appendages. All the mechanisms have functioned flawlessly on both INSAT-2A and INSAT-2B Spacecraft. All the deployment indications were seen unambiguously.

This article describes some of the special features of these mechanisms, precautions taken during design phase, the test philosophy, and the analyses that are behind the consecutive total successes. Some of the details which are common to all the mechanisms are highlighted below.

- Use of pyrocutters with simple designs, adequate margins, and mechanical and electrical redundancies.
- Minimizing the number of deployment phases in each mechanism and using simple configurations.
- Use of simple designs for the hold-down and release mechanisms.
- Provision of spring-actuated pushers at all separation planes to ensure a positive release and first motion.
- Provision of compensation features at hold-down interfaces/close control loops (CCL) and incorporation of flexibilities in hold-down bolts to account for differential thermal expansions.
- Meticulous and elaborate planning and implementation of the test and evaluation plan for each of the mechanisms at component level,

sub-assembly level, and system level, and establishment of dedicated test facilities.
- One-hundred percent participation by independent quality assurance teams.

2.0 SOLAR ARRAY DEPLOYMENT MECHANISM

2.1 CONFIGURATION

The solar array consists of a yoke, three large panels of 1.8m x 2.15m, and two small panels of 1.073m x 1.8m. The two small panels are stowed at the back side of the first large panel and are held down by a secondary hold-down loop. The yoke, first large panel with two stacked small panels, and the other two large panels are stowed on the spacecraft deck using six hold -own assemblies interconnected as shown in Figure 2. Figure 3 shows the array deployment in two stages, namely primary deployment and secondary deployment. Primary deployment consists of deployment of the yoke and three large panels, and secondary deployment consists of deployment of the two small panels. Three distinct advantages of this solar array configuration are:

- No need for partial deployment during transfer orbit by proper sizing of array. Transfer orbit power is obtained by orienting the south side of the Spacecraft to sun.
- 75% of power is available on deployment of large panel and the array is steerable after the first stage of deployment.
- Primary deployment is of accordion type which reduces the shock load considerably.

In any deployment mechanism configuration selection, the number of deployments should be kept at a minimum as this results in the reduction of pyrocutters. The availability of 75% of power at the end of the first stage of deployment itself is a positive aspect from a mission point of view. The choice of accordion type of deployment is preferred. The shock at each joint is minimized because the energy gets countered due to the change in direction of rotation between successive panels .

2.2 HOLD-DOWN BLOCK

Figure 4 shows a typical hold-down assembly. A flexible wire rope is used instead of a rigid rod used in most hold-downs [1]. The flexibility in hold down allows for minor misalignment due to assembly as well as thermal distortions and ensures positive release. Adding to the wire rope flexibility in the hold-down bolt, hinging has been included for smooth withdrawal and release of the long hold-down bolt.

In addition, in each of the hold-down base assemblies, a spring is provided to ensure the release of the hold-down lever/plunger elements immediately after cutting the hold down loop, even though the reaction forces in the hold down are enough for this release.

Prior to the deployment in the geostationary orbit, the array stack has to withstand the thermal loads expected during the transfer orbits. These loads can distort the panels and can cause hindrance to the deployment. To prevent the building up of thermal loads, a thermal slip provision is made in the hold-down block at the interface of panels, the details of which are shown in Figure 5.

The in-plane loads on the panels expected during launch do not exceed the friction loads acting at various interfaces. For generating the required frictional resistance at the outer-most panel hold-down block, at the next panel serrations at the interface, and at the first panel level, a grooved configuration has been used. Thus a graded friction has been adopted in the design.

At each of the interfaces between panels, spring-actuated pushers have been used to give first motion to the panels even though the springs at the hinges have enough margin over the frictional torque. These pusher springs are located away from the hinges, thus producing a large torque at the start of the motion for a small angular movement. However, this does not increase the deployment energy considerably and the value is about 3% of the deployment energy.

2.3 CLOSE CONTROL LOOPS (CCLs)

The CCLs are used to coordinate the deployment direction. Figure 6 shows a typical CCL. Each CCL consists of a preloaded wire rope loop passing over two pulleys mounted at the hinges. This CCL has the feature that the turn buckle and spring are combined. A compression spring is used instead of a tension spring to make the assembly compact. The loop has two springs, one on each side with a provision to adjust the preload. The temperature differentials expected in the orbit change the length of the wire rope. This change is absorbed by springs. The springs are also designed to maintain the preload in the loop well within the specified value. Thus it is ensured that the coordinated control is not affected.

2.4 SNUBBERS

The yoke is triangular in shape and supports two shunt regulators. This yoke is supported at three hinge points. The two-meter span beam of yoke has a low frequency, if unsupported. This frequency is increased by using

two preloaded snubbers. The snubbers are made of space-qualified silicone rubber. This design eliminates the need for a separate yoke hold down. Similar snubbers have been used to support the two small panels. This design has been successfully implemented to limit and damp the vibration amplitudes. The design has been validated through qualification tests at spacecraft level and its successful on-orbit performance.

2.5 SMALL PANEL HOLD-DOWN SYSTEM

A hold-down system shown in Figure 7 is a simple restraint mechanism without any rigid clamping. This is a unique, compact and simple design adopted in the system for small panel hold down and release system.

3.0 C/S BAND ANTENNA REFLECTORS DEPLOYMENT MECHANISM

INSAT-2 has two C/S-reflectors of size 1.772 m x 1.772 m each. These reflectors are stowed parallel to the East and West faces of the satellite deck and when deployed through 73.61°, the characteristic value of the paraboloid, they will have a northward tilt of 3.77° corresponding to the beam center of 22° N latitude. Figure 8 shows the stowed and deployed configurations.

3.1 HINGE LINE DEFINITION

The accuracies required on deployment of the reflectors were of the order of +0.02 deg over the above-mentioned angles of 73.61 deg and 3.77 deg. To accommodate the reflectors within the specified envelope in the stowed condition, the edges of the reflector must be kept parallel to the satellite faces. At the same time, in the deployed configuration, a 3.77 degree northward tilt was required at the end of deployment. This complex requirement was met by an accurate definition of the hinge line.

The stowed and deployed coordinates were considered. Intersection of spheres with appropriate solid geometry relations has been used for finding the hinge line. This line was further checked by using rotation transformation matrices to ensure that the stowed coordinates when rotated about the defined hinge line would give the required deployed coordinates of the reflector.

The defined hinge line had a tilt about two axes. Designing the hardware to meet this requirement and subsequent fabrication and inspection operations have been very challenging. A typical hinge is shown in Figure 9 with associated locking linkage and flexure. The double-tilt bracket seen in the figure was fabricated using CNC milling with appropriate programs. The inspection of this complex component has been carried out using a 3D

measuring machine. The hinge line defined by analysis has been implemented in the hardware and the pointing accuracies realized on assembly have been checked by using optical theodolites, autocollimation prisms, and associated accessories.

3.2 HOLD-DOWN MECHANISM

The C/S-reflector and solar array hold down and release mechanism concepts are similar. They include a provision for thermal slip at hold down and spring-actuated pushers at separation planes. The two hold downs used in this system are interconnected with a straight wire rope and a single cutter, unlike multiple explosive bolts used in other satellites, thus increasing the reliability of the system.

3.3 FLEXURE

Flexures have been used in the hinge outboard bracket to the CFRP antenna interface to take care of the effects of thermal differentials. These elements have been designed to have a low stiffness along the CFRP rib direction and high stiffness in the deployment direction to withstand the latch-up moment. A typical flexure can be seen in Figure 9.

3.4 LOCKING LINKAGE

Figure 9 also shows the locking linkage position in the hinge assembly. These linkages ensure a precise and positive locking for the reflector when it deploys through a predetermined angle of 73.61 deg. Based on range tests, if any change in this angle is required, a provision exists in this mechanism for fine tuning the opening angle by +0.5 deg from the nominal orientation. These linkages have been designed to take tensile load at latch-up, unlike the compression mode in designs used in other spacecraft.

4.0 SOLAR SAIL/BOOM

The coilable lattice boom with a conical-shaped sail balances the solar radiation torque acting on the solar array. The deployable boom is 14.95 m long and 0.26 m diameter. The solar sail at the end of the boom is 1.5 m diameter at the bottom, 0.79 m diameter at top, and 4.4 m long. Figure 10 shows the stowed and deployed configurations of the coilable lattice boom with sail. Stowed sail and boom are held down to the north panel using a launch restraint assembly and a preloaded tie rod. The boom in its stowed condition is housed inside a very compact canister, with the stowed height of the boom being 2% of its deployed length. The boom has self deploying capability but to control the rate of deployment, a lanyard type of deployment mechanism is used along with a drive motor with worm gear

speed reducer. A pyro bolt cutter is used for cutting the tie rod and releasing the hold down for on-orbit deployment. Six microswitches are used for monitoring the performance of the boom during deployment.

During the fabrication of boom, elaborate tooling and fixtures have been developed to ensure the boom geometry is well within the desired limits and the axis of the boom is maintained within +0.3 deg consistently for all models.

4.1 HINGE

The boom uses hinges with two degrees of freedom to connect the longerons with battens. The diagonals are connected to these hinges through spherical terminals as shown in Figure 11. These hinges are dry lubricated with MoS_2 on all the bearing surfaces to minimize friction and ensure a smooth deployment. The hinge parts have been configured for ease of assembly and disassembly for replacements, if required.

4.2 FIRST-MOTION SPRING ASSEMBLY

The characteristic of this type of boom is that the self deployment force at the start of deployment is low if both ends of the boom/longerons are stowed flat. Also, the friction at the end hinge assemblies is high. To overcome these problems and to aid the deployment of the boom in the initial phase, a wedge support with an 8° taper and a spring-actuated first-motion spring assembly are incorporated below each of the longeron end fittings at the base end. These features give a force of 7 kg over an initial plunger movement of 10 mm. A typical kick-off plunger assembly is shown in Figure 12. This design ensures base-end deployment, which is an essential feature for a trouble-free deployment.

4.3 LANYARD SPOOL ASSEMBLY

The boom with sail is released at a controlled rate using a lanyard. One end of the lanyard is attached to the tip plate of the boom with the other end wound on a spool that is driven by a DC motor through a worm gear speed reducer to preclude the possibility of the boom driving the motor. The lanyard is attached to the spool by an end hook that automatically gets released from the spool in the event of failure of the motor auto off feature at the end of deployment. This feature avoids the backwinding of the lanyard on spool.

4.4 AUTO-MOTOR-OFF SWITCH ASSEMBLY

Figure 13 shows this actuator. A spring-loaded lever dips into a recess provided in the lanyard spool soon after full deployment of the boom and in turn actuates two microswitches that cut off power to the DC motor. The design is such that the lever will not interfere in the rotation of the spool even when there is no lanyard on the spool.

4.5 GROUNDING TECHNIQUE OF SAIL

To minimize the build up of static charges on the large area solar sail surface, use of aluminized Kapton film with a conductive coating on the Kapton side and grounding it would have been a simple option. However, considering the prohibitive cost of this material, a special grounding technique has been developed and qualified. This technique involves the use of standard aluminized kapton film with conductive tabs at both top-mid and mid-bottom cone interfaces. This has resulted in considerable saving in cost. All the joints have undergone extensive static charge testing and qualified for the expected on-orbit conditions.

5.0 PYROCUTTERS

Pyro wire rope cutters are one of the critical elements for the successful functioning of the mechanisms. The pyrocutters used in the solar array and C/S band antenna were qualified earlier during the development of mechanisms for Indian Remote Sensing Satellites. The bolt cutter used for boom mechanism was developed during the INSAT-2 project. All pyrocutters have both electrical and mechanical redundancies with adequate margin of safety.

6.0 ANALYSIS

The analysis activities carried out for each of the above systems are discussed in brief. The deployment dynamics of the INSAT-2A and 2B Solar Array and C/S band antennae have been carried out in detail for both ground and on-orbit conditions. However, in case of 2A, the predicted deployment time did not match with the on-orbit deployment time. Hence a post launch analysis has been carried out using the high-speed camera data analysis obtained during ground tests of INSAT-2B. The updated initial velocity values were used for predicting the deployment times of the INSAT-2B primary array deployment, secondary array deployment, and the C/S band antennae. The predicted values are in close agreement with the on-orbit deployment time. The post-launch analysis is discussed in reference [2]. The mismatch between initial prediction and 2A on-orbit values has been assessed to be due to initial velocities imparted to the

system by the snubbers and spring-actuated pushers ,which give a small amount of energy into the system for a few milliseconds.

The hinge line definition which was discussed in C/S band antennae is an important analysis that has been carried out. Here an application of solid geometry, intersection of spheres, angle between lines, planes, and rotation transformations have been used in accurately defining a hinge line. The intersection of spheres results in a set of nonlinear algebraic equations. After obtaining the solution, it was checked thoroughly for required angular accuracies. The process was repeated iteratively until the accuracies required were met.

A best-fit paraboloid analysis has been carried out in defining the vertex shift, focal length changes, focus shifts, and corresponding tilts. A least-square fit was used. This is discussed in detail in reference [3].

One of the most fascinating analysis was the elasto-plastic analysis of the lanyard. The lanyard experiences a shock load from the release of the stowed energy of the boom, preloaded tie rod, tip plate, and launch restraint rods when the tie rod is cut. This energy was found to be greater than the elastic energy carrying capability of the lanyard. Consequently, the lanyard was found to yield. So an elasto-plastic analysis with a cumulative damage study was conducted. The number of cycles the lanyard could withstand before failure was found. Based on this analysis, the maximum number of allowable tests on the flight model lanyard was defined and implemented. This is discussed in detail in reference [4].

The shock analysis for the primary deployment, secondary deployment and C/S reflector has been carried out. This provides the basic input for the design of hinges.

The boom free vibration and thermal distortion study has been carried out. The deflection of the boom with sail from its nominal direction due to thermal differentials, superimposed with acceleration loads acting during controlling of satellite, has been found. The study has been carried out to ensure the sail middle cone does not come within the field of view of the VHRR cooler which is very sensitive to heat radiation.

7.0 TESTING

To ensure successful working of these mechanisms, a detailed test matrix and associated test plan was generated for all the critical components, subassemblies and assemblies. These were meticulously planned and implemented. A few of them are listed below.

- Strength and stiffness measurements
- Calibration of springs
- Characterization of harness loops
- Destructive and non-destructive testing of various boom elements
- Coupon testing of adhesive joints.
- Friction measurements.
- Alignment using autocollimation
- Fine-motion study using high-speed camera.
- Non-contact distance measurements using ECDS (Electronic Coordinate Determination System)
- Angular error measurement and correction.

Further, for the testing of the mechanisms, a few sophisticated or dedicated facilities have been established. These include:

- Zero-"g" fixture for solar array deployment.
- High-bay test facility for vertical deployment of boom with sail
- Water-trough facility for horizontal deployment of the boom.
- Electronic Coordinate Determination System for alignment and non-contact distance measurements.
- High-speed camera for measuring fast motions such as hold-down release.
- Air-bearing facility for Zero-"g" tests on C/S antenna reflectors.

One of the important tests used in the qualification of the Coilable Lattice Boom (CLB) was a stress rupture study of longeron. Stress rupture (static fatigue or delayed failure) is the failure under sustained loads over a long period of time. Stress rupture of glass fiber composites is controlled by surface defects of fiber, matrix failure due to visco-elastic deformation, etc. In an application like CLB of INSAT-2A/2B, it may become necessary to store the boom in a stowed condition for a long period due to various reasons during fabrication, testing and prelaunch phases. Typically, a storage life of about five years is specified under a flexural strain of 1.1% or a stress of 60 - 65 Kgf/mm^2. On the continuous longerons of the CLB, stress rupture data based on a 15-year study as a function of sustained stress versus life under tensile loading on composites is available in the literature. However, the type of loading in our application is flexural. Stress rupture behavior on longeron elements at 2% strain level has been verified by coiling on a mandrel of suitable size on the INSAT-2A boom structural model and storing for more than 4 years without any failure of longerons.

The two small panels are stowed at the back of the first panel. The pyrocutter used for cutting the hold-down cable is mounted in the back side of the solar cells on the first panel. To ensure that the solar cells on

the first panel are able to withstand the shock due to pyro, a few tests were conducted. Acceleration levels were measured and the solar cells mounted on first panel were found to be intact. With these tests, the use of a pyrocutter mounted on the first panel was cleared.

8.0 MISSION

Both the solar array and antenna are made of CFRP. As these panels will be facing sun before deployment, the temperature of the array can go beyond 70 deg C, the qualification temperature of the hinge interfaces. Hence, reorientation of the satellite is necessary to bring down the temperature of the array below 70 deg C. This is done to ensure that the hinge interface loads at latch-up are well within the limits to which the hardware was qualified. To minimize the thermal differential within the CCL wire rope, which in turn can produce change in tension of CCLs wire rope and consequently an increase in friction torque, a small tilt was given in the satellite. The tilt angles are 60 deg in the Roll-Pitch plane away from the sun to bring down the temperature, and 6 deg from the Roll-Pitch plane towards the earth-viewing face to avoid thermal differential within CCLs.

To facilitate monitoring deployments, an adequate number of microswitches have been used. In the solar array, and C/S band antennae, microswitches have been used for monitoring the cutting of wire rope, system first motion, and locking of hinges. The coilable lattice boom cutting of bolt, initial motion, motor-release function, and sail deployment have been monitored through microswitches. In case of any anomaly, sufficient data can be obtained through these indications for further analysis.

As can be expected, a mechanism would work better if temperatures close to laboratory conditions are created in space. This philosophy was adopted in the C/S band antennae deployment. The East reflector was deployed with the east face of the satellite facing sun, and the West reflector was deployed with the west face facing sun. With this, the temperatures of the hinges were close to 20 deg C. The solar sail boom was deployed when the temperature of the motor was around 20 deg C. This was adopted in both INSAT-2A/2B. All mechanism deployments were smooth and all indications were obtained unambiguously.

9.0 CONCLUSIONS

The configuration of the deployment mechanisms used in INSAT-2A and 2B has been discussed. Some of the design features are discussed. The thermal compensation features and flexibility in hold down have been discussed showing how thermal differentials have been taken care in the

design. The spring-actuated pushers give a large torque acting for a few milliseconds in the initial phase of deployment. Detailed analyses carried out to support the design and testing phases of the mechanisms have been brought out. The meticulously planned testing at various levels and development of dedicated test facilities has been highlighted. Wherever possible the mission sequence has been finalized so as to ensure that the temperature of the hinges is around room temperature for smoother performance of mechanisms.

REFERENCES

1. H. Brodersen and I. Rizos. "INTELSAT V SOLAR ARRAY," Proceedings of European Symposium on Photo-voltaic Generators in Space, ESTEC, Noordwijk, 11-13, (Sept. 1978), ESA SP 140, pp 209-217.

2. B.S. Nataraju and H.N. Suresha Kumar. "Post-launch analysis of INSAT-2A deployment mechanism." Doc. No. INTS-TR-MEC-03-90-189(0) (April 1993).

3. B.S. Nataraju, B.P. Nagaraj and H.S. Vijayalakshmi. "Best fit paraboloid and related geometric properties of C/S band reflector of INSAT-2 SP."
ISAC-INSAT-SPII-33-90-12-05-03
Doc. No. ---------- (Dec 1990)
INTS-TR-MEC-03-90-129 (0)

4. B.P. Nagaraj and B.S. Nataraju. "Dynamic analysis of lanyard of INSAT-II SP."
ISAC-INSAT-TS-II-33-90-11-05-04
Doc. No. ---------- (Nov 1990)
INTS-TR-MEC-03-90-115 (0)

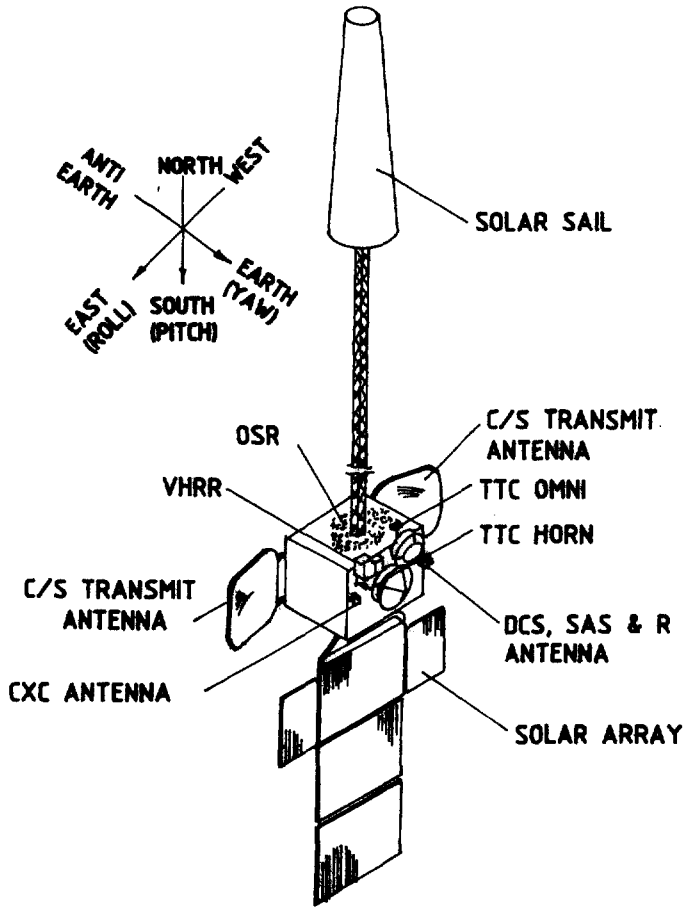

FIG.1 ONORBIT CONFIGURATION-INSAT-2 SPACECRAFT

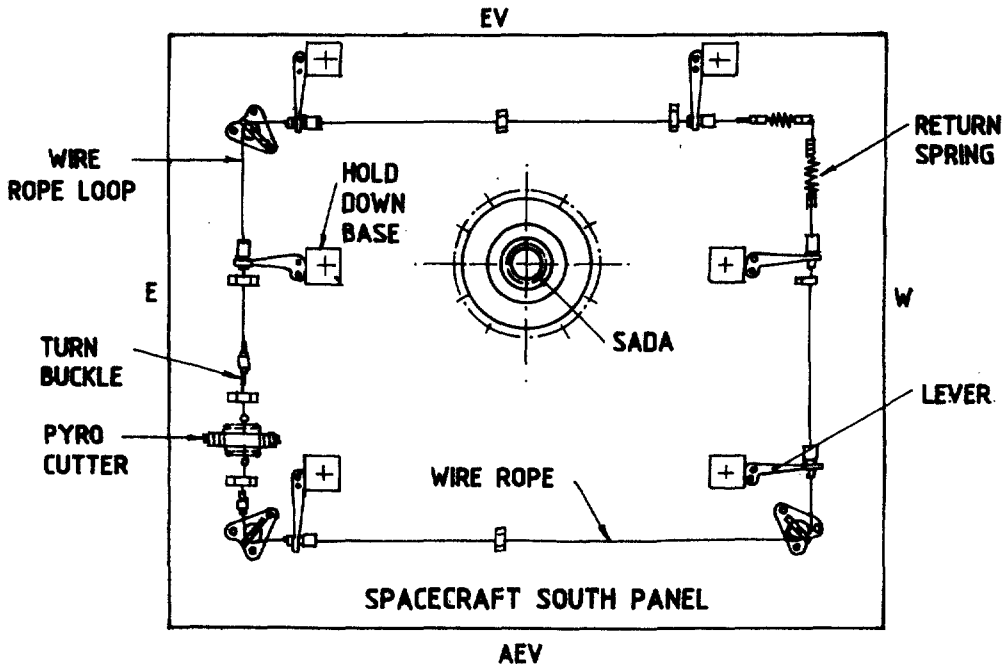

FIG.2 PRIMARY HOLD DOWN LOOP

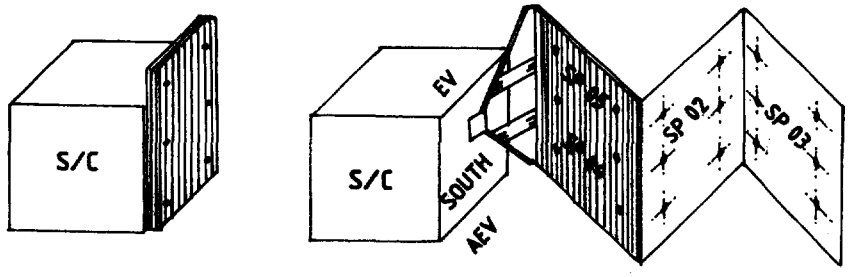

STOWED ARRAY PANELS DURING PRIMARY DEPLOYMENT

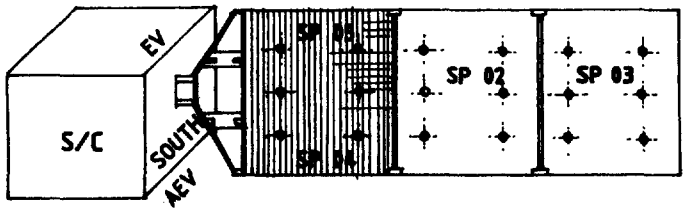

PRIMARY DEPLOYMENT OF SOLAR ARRAY
AT LATCH-UP

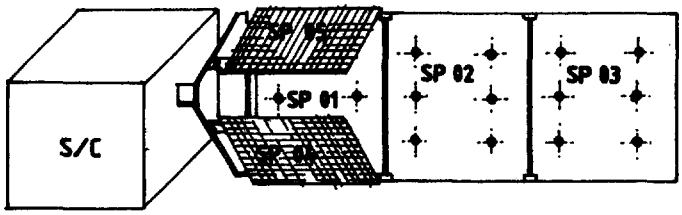

SIDE PANELS UNDER DEPLOYMENT

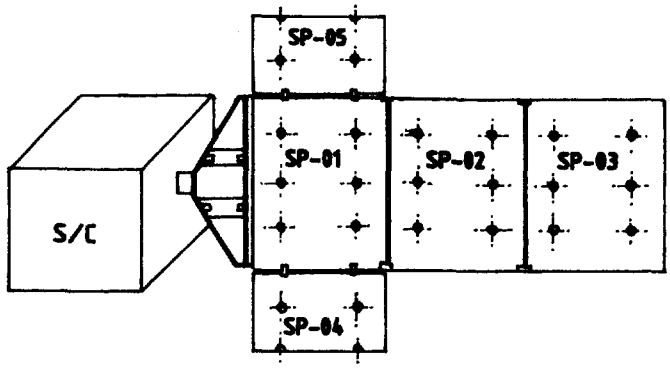

FULLY DEPLOYED SOLAR ARRAY

FIG.3 SOLAR ARRAY DEPLOYMENT SEQUENCE

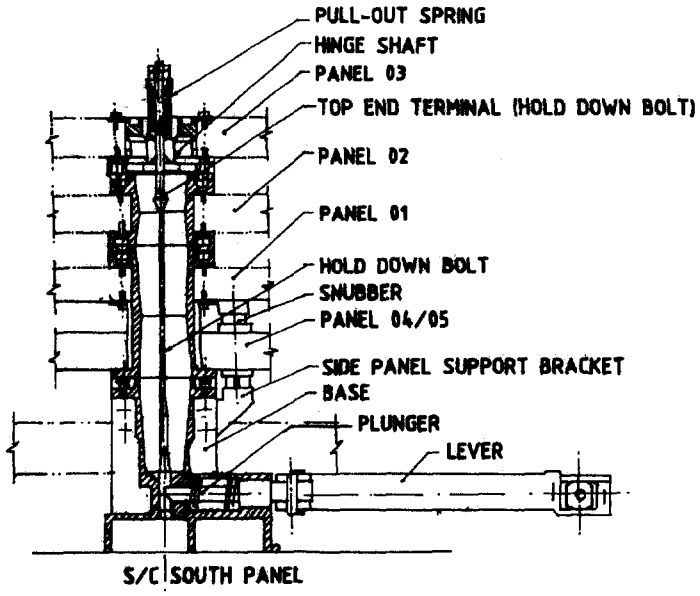

FIG.4 HOLD DOWN ASSEMBLY DETAILS

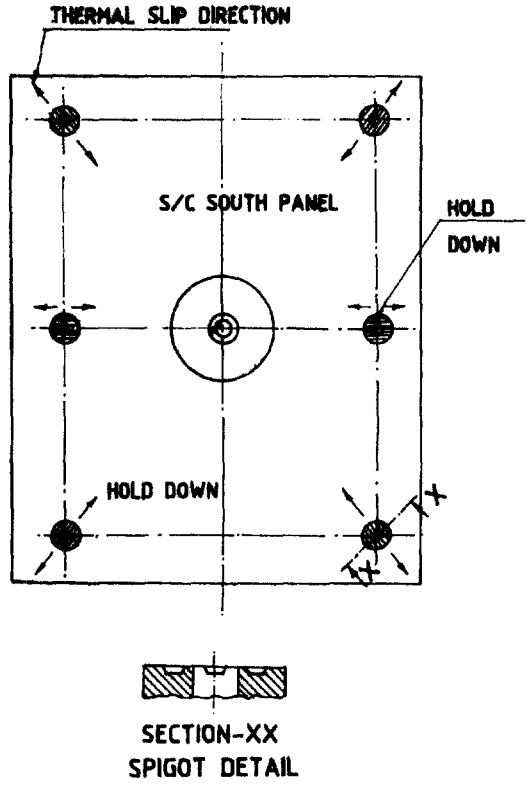

FIG.5 SOLAR PANEL STACK SPIGOT

LOCATIONS FOR THERMAL SLIP

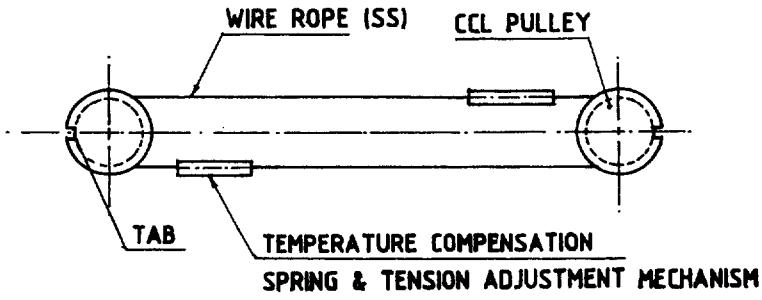

FIG.6 CLOSE CONTROL LOOP

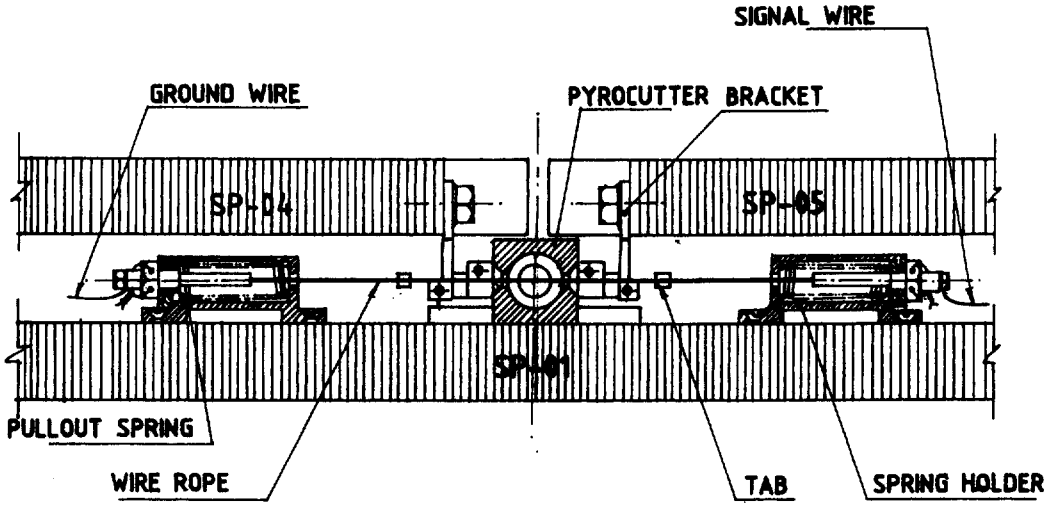

FIG.7 HOLD DOWN & RELEASE SYSTEM FOR HALF PANELS

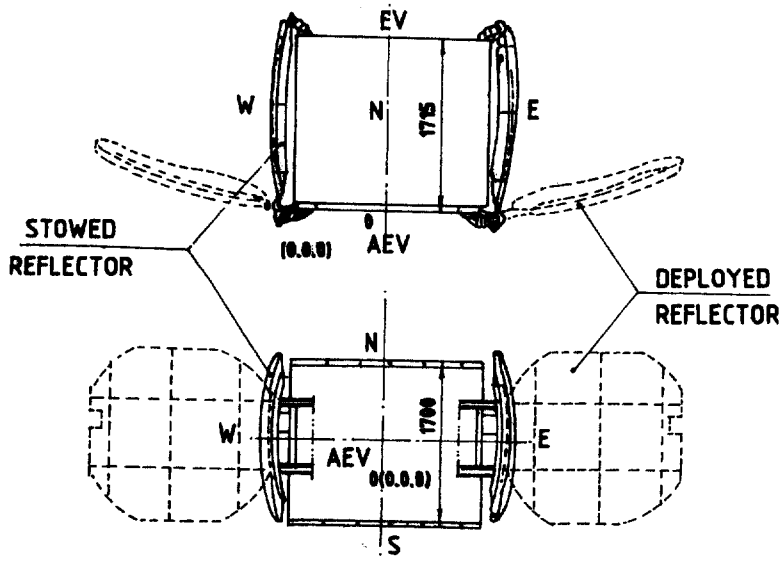

FIG.8 STOWED AND DEPLOYED CONFIGURATION OF C/S-REFLECTOR

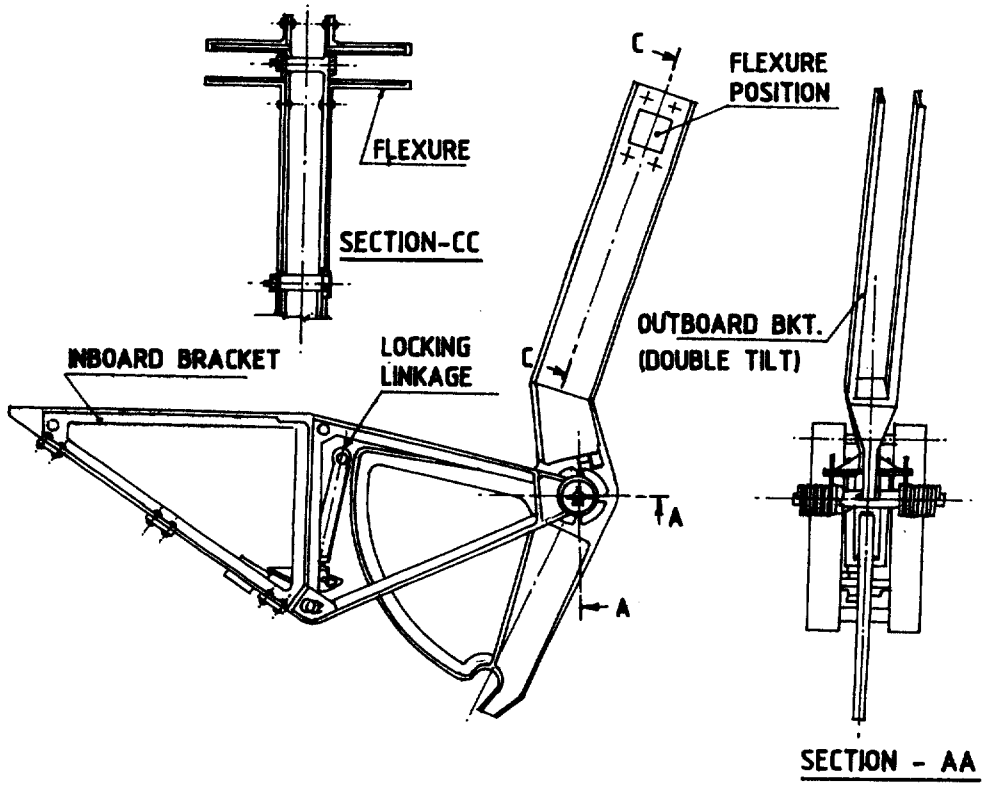

FIG.9 TYPICAL HINGE ASSEMBLY DETAILS

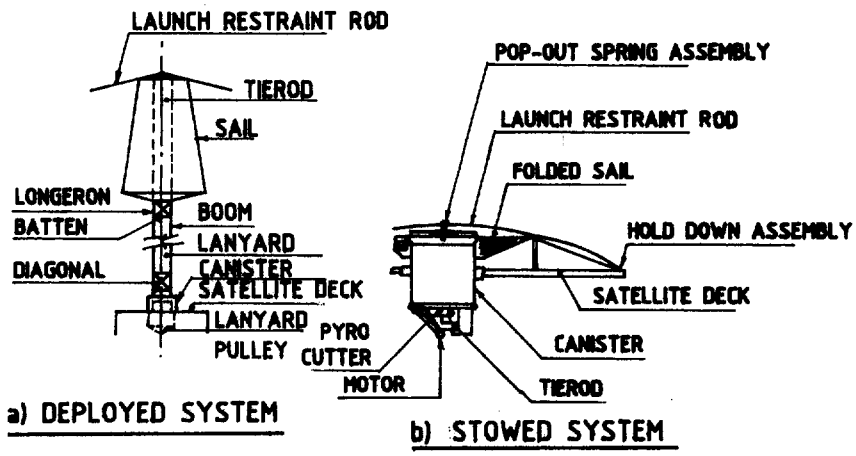

FIG.10 STOWED AND DEPLOYED CONFIGURATION OF SAIL BOOM

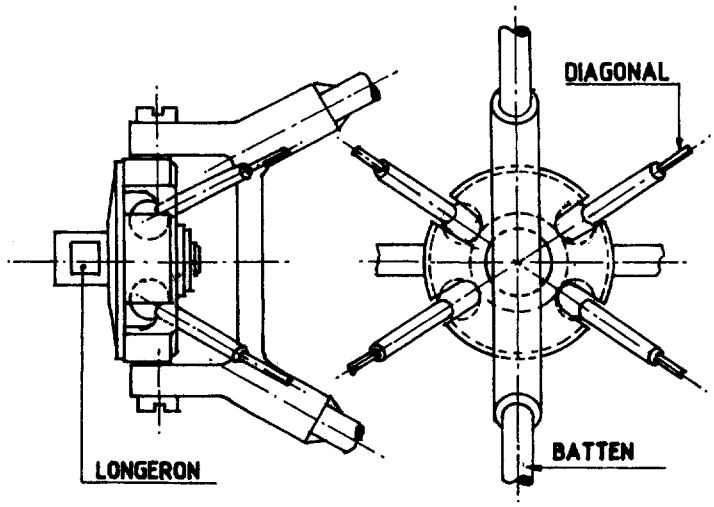

FIG.11 TWO DEGREE OF FREEDOM HINGE ASSEMBLY

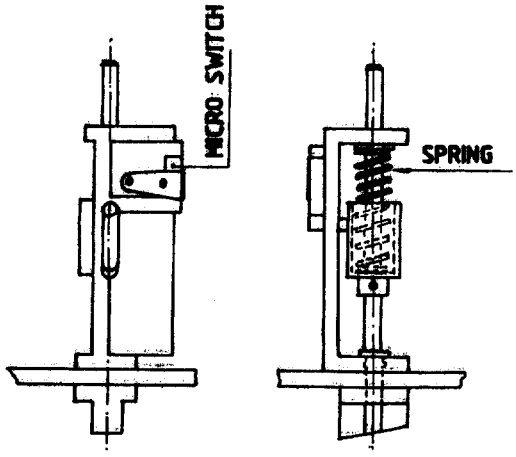

FIG.12 FIRST MOTION SPRING ASSEMBLY

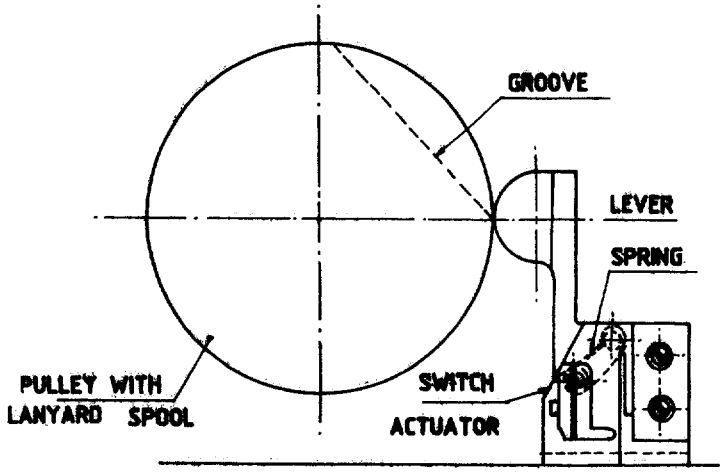

FIG.13 AUTO MOTOR OFF SWITCH ASSEMBLY

ROLL RING ASSEMBLIES FOR THE SPACE STATION

J. Batista, J. Vise, and K. Young
Satellite Systems Operation
Honeywell Inc.
Phoenix, Arizona

ABSTRACT

Space Station Freedom requires the transmission of high power and signals through three different rotational interfaces. Roll ring technology was baselined by NASA for rotary joints to transfer up to 65.5 kW of power for 30 years at greater than 99 percent efficiency. Signal transfer requirements included MIL-STD-1553 data transmission and 4.5 MHz RS250A base band color video. A unique design for each rotary joint was developed and tested to accomplish power and signal transfer. An overview of roll ring technology is presented, followed by design requirements, hardware configuration, and test results.

INTRODUCTION

Space Station Freedom required high-efficiency transfer of up to 65.5 kW of power for 30 years. Signal transfer with low electrical noise resistance was also required for communication and control. These primary requirements challenged the state of the art of the two existing electrical rotary transfer devices, slip rings and flex capsules. Table 1 shows that flex capsules are limited with respect to rotation and fatigue life. Slip rings have wear limitations due to sliding electrical contact, generate debris, and require lubrication.

Roll rings are a new technology developed to perform the same function as a slip ring/brush assembly, but by means of rolling instead of sliding electrical contact. Consequently, there is no measurable wear, lubrication is not required, and long fatigue life can be met. Two types of roll rings have been developed: one type for signal and low power, another for high-power applications.

The Space Station Freedom design featured three rotary joints. Figure 1 shows the location of the three rotary joints. The Solar Alpha Rotary Joint (SARJ) provides continuous rotation of the solar arrays to account for orbital rates and transfers 65.5 kW of power as well as signals. The Beta Gimbal (BG) rotates the solar arrays to track the seasonal changes of the sun angle and transfers 45 kW of solar array power, low power, and signal. The Thermal Radiator Joint (TRRJ) keeps the radiators pointed at deep space and transfers low power and signal. Each rotary joint incorporates a unique roll ring design.

This paper describes how roll rings have been designed and built to meet the challenges at each of the Space Station rotary joints. Test results are then presented to validate the designs.

ROLL RING BACKGROUND

The roll ring electrical signal/power rotary transfer device evolved from ball-bearing and electrical transfer technologies and has been under development since mid-1970. The device consists of two or more concentric conductive rings and at least one rolling, flexible, conductive element (Figure 2). The conductive element, or flexure, is fitted to, and captured in, the annulus space between the concentric rings. When the rings are suitably attached to two structures that are aligned with a common axis, the conductive flexure provides a precise, mechanically stable, electrical coupling between the two structures.

The theoretical torque of the roll ring is zero. Actual torque levels are very small and exist because the flexure and the ring grooves cannot be fabricated perfectly. The bulk of roll ring life testing has been conducted in a vacuum environment. This imposes the most severe conditions from a life and wear standpoint because water vapor is present in a laboratory environment and acts as a lubricant. The ring tracks and flexures are plated with a gold/cobalt alloy, which acts as a dry lubricant during vacuum operation and ensures the integrity of the electrical contact surfaces. The gold plating is backed by a nickel plating to enhance the wear life, reduce porosity in the gold plating, and act as a migration barrier to the copper in the base metal. Wear and flexure fatigue testing has been conducted to over 3.2×10^7 revolutions of the inner ring in a vacuum environment and 1.6×10^8 revolutions in air. The resultant wear debris of the latter unit was of extremely low volume and consisted of gold dust adjacent to the running tracks. In summary, the roll ring design exhibits low and consistent torque, has near zero wear debris, and has no time-related effects; thus, it is an excellent choice where long-life requirements are to be met.

Alignment considerations are taken into account by developing the geometrics of the ring grooves and the flexures such that the rolling dynamics and kinematics are stable. This stability is required not only to ensure that the flexure does not escape the ring grooves, but so that the flexure/ring contact tracks are uniform and predictable. The design that has evolved is tolerant of normal radial, axial, and angular misalignments such that two contact footprints are ensured at each inner and outer ring tracks independent of reasonable misalignments. The radial preload is controlled by the machined-in geometrics. No adjustments are required nor desired after assembly.

The relatively high radial preload between the flexure and the ring groove results in a contact pressure that is of significant magnitude to dispel accumulated organic films and/or lubricants should they somehow migrate or condense onto the track area. Because the mass of the flexure is low and the flexure preload is relatively high, the combination of these two attributes ensures high vibratory and mechanical shock integrity. Operating temperature ranges of -55 to 80 °C can be accommodated with the roll rings as well.

Roll ring electrical noise is identified as momentary, distinctly periodic but short (few milliseconds or less) resistance spikes. The resistive magnitude of these spikes is not related to current and is essentially the same for both air and vacuum

environments, remaining constant over running time. Peak noise resistance on circuits comprised of a single flexure range from 0.01 to 0.10 ohm.

Development of power roll ring technology for use on the Space Station was funded by NASA Lewis during the 1980s. Power roll rings were tested by NASA Lewis to the equivalent of 200 years of Space Station operation and have carried currents of 200 A per circuit and 500 VDC; transfer efficiencies of 99.9% were demonstrated.

The roll ring design offers flexibility in meeting system requirements because the design is based on modules containing sets of circuits. The number of modules can be increased or decreased due to system design requirements and are assembled into stand-alone units that can be individually tested. This design feature provides for separation of shielded and nonshielded circuit sets, high-voltage and low-voltage sets, low-current and high-current designs, and various other arrangements. Typically, power crossings are used for currents in excess of 5 A, while signal roll rings are employed where currents are less than 5 A.

HARDWARE DESCRIPTION

Roll Ring Description (General)

Signal and low-power applications utilize a multiple-crossing module design made up of inner and outer housings, as shown in Figure 3. The inner and outer housings consist of inner and outer contact rings, each encased in a dielectric epoxy material. Depending upon the application, each crossing utilizes one or more flexures. Multiple flexure designs employ parallel tracks in each contact ring. A typical signal module design utilizes a pair of flexures in parallel tracks and can transfer up to 10 A at 120 VDC. Isolation of 45 to 70 dB can be provided between crossings. Surge currents to 100 A, shock loads to 300g, and frequencies from DC to 200 MHz, have been tested. Assembly of roll ring modules is straightforward, requiring only installation of flexures between inner and outer housings.

Power crossings utilize a multiple-flexure design for high-power transfer. Each power crossing consists of an equal number of flexures and idlers, an inner and outer contact ring, and two idler guide tracks. A typical power crossing is depicted in Figure 4. Power is transferred from one contact ring, through multiple flexures, to a second contact ring. Idlers separate each flexure and are captured by idler guide tracks, which are in turn attached to the inner contact ring. Idlers allow contact velocities of each interfacing component to be matched, minimizing sliding and associated drag torque and wear. Operational drag torque less than 1.1×10^{-2} N-m (0.1 in.-lb) per crossing is a measure of near-zero interface sliding.

Utility Transfer Assembly

The Utility Transfer Assembly (UTA), Figure 5, provides high power and signal transfer across the SARJ. The UTA consists of three parts: the power section for transferring primary power, the signal section for transferring MIL-STD-1553 data, and dual resolvers for indicating rotational position. Angular contact bearings support the rotating assembly. Continuous rotation in either direction or alternating

UTA was designed for a rotational rate of 0.07 radian per minute. The resolvers are capable of providing angular position to within 175 milliradians. The unit is designed for random vibration levels of 12.6g rms and was tested to levels exceeding 6g rms. The UTA was designed to be Extravehicular Activity (EVA) replaceable. Handles, tether attach points, and EVA-compatible fasteners are provided. Figure 6 shows the fully assembled UTA development unit.

The power section consists of 24 crossings for transferring 65.5 kW at 160 VDC. Eleven crossings are used to transfer positive voltage, eleven transfer negative voltage, and two transfer case ground. Each crossing contains 14 flexures to distribute the power and 14 idlers to maintain flexure separation. Electrical power is brought to the inner and outer rings by 1/0 AWG, multistranded, superflex cable.

The signal section consists of four, 12-crossing signal modules. Redundancy is obtained by having single flexures run in parallel grooves for each crossing. Standard MIL-STD-1553 twin-axial cable is connected to both outer and inner module rings. Each module transfers positive, negative, and shield across the rotating interface. Twelve MIL-STD-1553 data buses, two RS-170A-3 video-plus sync circuits, and case ground are all transferred through the UTA's signal section. Drag torque contribution from signal crossings is negligible at 7×10^{-5} N-m per crossing.

Power and Data Transfer Assembly

The Power and Data Transfer Assembly (PDTA), Figure 7, provides low power and signal transfer across the TRRJ. The PDTA consists of two parts: the signal section for transferring power and data and dual resolvers for indicating rotational position. Angular contact bearings are again used to support the rotating assembly. The PDTA was designed for continuous rotation in either direction with a rotational rate of up to 0.52 radian per minute.

The PDTA was designed to be EVA replaceable. Handles and EVA-compatible fasteners are provided. Figure 8 shows the PDTA development unit.

The PDTA signal section consists of two, 12-crossing signal modules. Redundancy is again obtained by having single flexures run in parallel grooves for each crossing. Standard MIL-STD-1553 twin-axial wire is connected to both the outer and inner module rings. Each module transfers positive, negative, and shield across the rotating interface. Four MIL-STD-1553 data buses, 300 W of power at 160 VDC, and case ground are all transferred through the PDTA's signal section.

Beta Gimbal Roll Ring Subassembly

The Beta Gimbal Roll Ring Subassembly (BGRRS), Figure 9, transfers high power, low power, and signals across the BG. High-power transfer is handled by a source power module, while low power and signal transfer are handled by a secondary power module and a signal module, respectively. The BGRRS also

features fixed and floating duplex bearing pairs, a resolver/transformer assembly, and EVA interfaces. Figure 10 shows the BGRRS development unit.

The source power module is comprised of five power crossings that provide two source power circuits (two crossing each) and a source power ground (single crossing). Each power crossing is capable of transferring 113 A continuous current at 200 VDC. Chassis ground is carried from stator to rotor through the power ground crossing. Each of the five power crossings consists of 11 flexures, 11 idlers.

The secondary power module consists of six crossings that provide two secondary power circuits (two crossings each) and one DC control power circuit (two crossings). Each crossing utilizes three flexures in parallel paths and is rated at 6.3 A maximum current at 127 VDC.

The BGRRS signal module consists of six crossings that make up two MIL-STD-1553 circuits (three crossings each). Each crossing utilizes a pair of flexures in parallel paths. Each MIL-STD-1553 circuit consists of high- and low-signal leads and a shield. The shield is tied to chassis ground on the stator and rotor and is carried through the signal module on an individual crossing. The signal module is wired with standard twin-axial cable.

The platform interface connector plate allows for EVA removal and installation of the Beta Gimbal Assembly (BGA), the Orbital Replaceable Unit (ORU) into which the BGRRS assembles. The station connector plate is mounted on a flexible metal bellows to provide stiff torsional interface for the transfer of torque with little wind-up, while providing a flexible interface to accommodate mounting misalignments and runouts within the BGA. Four EVA-compatible connectors are installed on the rotor connector plate.

TEST RESULTS

All three roll ring development units were tested to qualification-level environments. Functional testing included drag torque, resolver error, MIL-STD-1553 word error rate, signal roll ring noise resistance, and power roll ring throughput resistance. During functional testing, the units were rotated in each direction at 70 milliradians per minute for the majority of test time and at up to 2π radians per minute for brief periods. Environmental testing included random vibration, thermal cycling, and thermal vacuum testing. A typical mechanical test setup for full functional testing is shown in Figure 11. Each unit was exposed to environmental test levels, described in Table 2.

Signal Roll Ring Noise Reduction

Noise testing has been the standard performance test for signal roll rings. As discussed in detail in Reference 3, a prime objective of roll ring development was reduction of noise spikes. To accomplish this, significant progress has been made in fabrication techniques, control of plating processes, plating purity, and cleaning processes. These improved techniques were developed during fabrication of the UTA and PDTA and implemented on the BGRRS roll rings. Progress in noise reduction is evident by the comparison made in Table 3. Noise spikes on UTA and

PDTA were attributed to signal module and flexure runouts and flexure size variation. These lessons were used to make improvements in flexure and module geometric control during fabrication. Improvements in machining, inspection, and cleaning techniques also were made. High-purity plating and elimination of metallic oxides from surfaces by stringent reduction of low-nobility metals in gold plating also contributed to improvements in noise reduction. The BGRRS benefited from the latest techniques as demonstrated by the noise resistance in Table 4.

Excellent resultant noise resistance is seen in Figure 12. This data shows actual noise graphs obtained after completion of BGRRS testing. The noise test results presented are for a pair of crossings connected in series at the rotating end of the roll ring to permit continuous rotation of the unit without cable binding. Noise testing was performed by looping 100 mA of current through all the roll ring pairs. Voltage peak detectors operating at 16 kHz detect the highest and lowest voltage over a 0.25-second span. Resistance is then calculated and plotted as noise.

Signal Roll Ring MIL-STD-1553 Word Error Rate

All three roll ring assemblies will become a part of the Space Station MIL-STD-1553 data bus. Table 4 summarizes MIL-STD 1553 test results. For the UTA, 43 separate tests were conducted for a total transmission of 85.5 billion words. Out of the 43 individual tests performed, two tests that transferred 1.1 billion words had 378 errors for a word/error ratio higher than the required 10^7; however, it should be noted that the UTA and PDTA were tested with all crossings (circuits) connected in series and, therefore, test results are the cumulative errors for all crossings. The test conducted was therefore much more severe than the required single-circuit transmission of data. The BGRRS was required to demonstrate compliance to MIL-STD-1553 while configured into a simulated Space Station data bus. Sixty-six different send/receive combinations were tested to determine if the presence of the roll ring assembly would affect the performance of the bus. During testing, source power and secondary power were also transferred while the unit rotated. The BGRRS passed each of the 66 individual tests. The largest number of errors observed for an individual test was 43 out of a specification limit of 55 errors. Table 4 gives a summary of the cumulative results for all 66 tests. The measured crosstalk isolation between individual data circuits for the three roll ring assemblies was between 66 to 70 dB at 2 MHz. This satisfied the 45-dB isolation requirement.

High-frequency (Video) Test

Two signal circuits designated for transfer of video on UTA were tested with the requirement that resolution be sufficient for cable identification. This objective was satisfied. Results showed that over the frequency of DC to 5 MHz, loss was 1 dB, isolation was -54 dB, and the signal-to-noise ratio was 72 dB. Relative chrominance-to-luminance variation demonstrated a gain of 1 IRE with a delay of -1.6 ns; between 5 to 200 MHz, the loss was -3 dB.

Power Roll Ring Resistance

The UTA successfully conducted 95 A through 24 crossings at ambient conditions and 76.5 A at 43 °C in a vacuum. Resistance for a pair of crossings in series was typically 1.9 milliohms at ambient conditions including the resistance of

the loop-back connector at the rotating end. The power transferred during this test was greater than the requirements shown in Table 5.

The BGRRS transferred 226 A across two parallel circuits (113 A per crossing). The circuits consisted of a parallel set of two power crossings, looped back at the rotating end, and back through across on the two power return crossings. Resistance for this parallel configuration, including 1.2 meters of size 1/0 wire for each crossing configured in parallel at the nonrotating side, was typically 1.43 milliohms at ambient temperature and pressure conditions. During thermal vacuum testing at the hot temperature of 60 °C, power crossing resistance measured 1.6 milliohms with wire temperatures at 88 to 93 °C.

Power Roll Ring In-Rush Fault

The BGRRS is required to survive a 1-millisec in-rush fault current pulse of 4500 A. Before the BGRRS unit was assembled, Reference 2 and its authors provided guidance for conducting a development test on a parallel arrangement of two power crossings within the BGRRS power module. The fault current was applied with the test item kept stationary and at ambient temperature and pressure. The actual in-rush fault applied was 5000 A, peaking at approximately 0.27 ms with a 1.0-ms period. Comparison of the pre- and post-fault resistance measurements indicate essentially no change in resistance and thus no damage to roll ring crossings. Disassembly and inspection showed all components to be normal with no detectable damage caused by the application of the fault currents.

The BGRRS development unit was then assembled with new crossing components and after all functional and environmental testing was completed, the BGRRS was subjected to the in-rush fault current test. Functional test results after application of the fault current were normal.

Drag Torque (UTA and PDTA)

The UTA had a 9.0 N-m drag torque after initial assembly, which increased to approximately 27.1 N-m during functional testing after X-axis vibration. This was considered a failure because the drag torque requirement was < 13.6 N-m. The unit was disassembled, inspected, and analyzed to determine the cause of the failure. The high drag torque was caused by two design problems:

1. The outer contact ring track geometry was spoiled by a twist in the ring caused by the radial clamping pressure of the heat transfer spring between the ring and the housing. This resulted in flexure interference and then higher drag torque.

2. The idler guide tracks had windows manufactured in them to reduce weight and to aid in assembling the power circuits. It was found that an idler got lodged in the window, causing a flexure to break, and created high drag torques. This created the 27.1 N-m drag torque.

The software for sizing power roll ring components was improved to allow complete analysis of geometric tolerances and to maximize rolling efficiency. Design modifications were made to the flexures, contact rings, and outer guide

tracks. The window size on the outer guide track was decreased. After the UTA was refurbished, drag torques remained low throughout the remaining tests with peaks at ambient conditions measured at 1.7 N-m.

On the PDTA, drag torque measurements were typically 0.35 N-m, well below the required 1.36 N-m.

Drag Torque (BGRRS)

Measurement of BGRRS drag torque became a problem. It was not possible to obtain accurate torque data with the original test setup, which featured an in-line strain gauge torque sensor. The torque sensor capability was 3.5 N-m and inherently had low torsional stiffness. Rotation of the BGRRS at the ultra low speed of 70 milliradians per minute caused the soft torque sensor shaft to wind-up and not release until the breakaway torque of the bearings was exceeded. This manifested as large torque oscillations on the torque plots. Cost and schedule constraints demanded a speedy solution, while maintaining as much of the original test setup as possible.

To eliminate the oscillation problem, the low stiffness torque sensor was removed and a stiffer force sensor setup was designed and fabricated in-house (Figure 11). Modifications to support the drive motor with bearings at each end were made. A lever arm was attached to the drive motor to translate force back into 222-N load cells. As the motor rotated the BGRRS, torque was reacted by the load cells and torque was derived from the force measurement. Lateral loads were minimized by use of a ball to provide point contact at each load cell. Calibration of the force sensor was accomplished by rotating a known weight at the end of a lever attached to the drive shaft (point C in Figure 11). The improved test setup allowed for temporary substitution of the original torque sensor in order to verify calibration.

BGRRS drag torque during thermal vacuum testing at the 70 milliradians per minute speed (including up to 0.15 N-m of fixture torque) was 0.85 to 1.13 N-m at the cold temperature of -29 °C. and 0.35 to 1.13 N-m at the high temperature of 60 °C. This met the <1.36 N-m requirement.

Electrical Characterization of UTA at NASA Lewis

Reference 1 reports the results of the electrical characterization of the UTA, using the Space Station Power Management and Distribution (PMAD) DC test bed at NASA Lewis. A summary of the reported results follows.

Impedance of the UTA was characterized. Inductance was found to be higher than anticipated, and a recommendation was made that roll ring inductance be considered in the design of the power network. Corona test results showed onset values above 1 kV.

Crosstalk coupling was determined to be largely capacitive, but attenuated so that power transients did not interfere with the MIL-STD-1553 data bus. Power-signal crossing coupling was measured to be -67 dB at 1 MHz. Signal-signal coupling was measured to be -71 dB at 1 MHz.

Verification was made that the UTA was capable of withstanding normal PMAD voltage and current transients. The MIL-STD-1553 data bus was active during transients, with no data bus errors recorded.

Electrical rolling noise resistance was found to be extremely low at 0.3 milliohm for the signal crossings.

CURRENT STATUS OF SPACE STATION ROLL RING ASSEMBLIES

As the configuration of the Space Station has evolved, numerous changes have been made to all three of the roll ring assemblies during the qualification design phase of the projects. All three units have completed qualification design. Procurement of qualification unit parts is almost complete as this paper is submitted for publication in December 1993.

CONCLUSIONS

Considerable progress has been made on roll rings for power and signal transmission during development of the UTA, PDTA, and BGRRS. Improvements in fabrication, process controls, and inspection techniques have been validated. Signal roll rings prove to be very suitable for MIL-STD-1553 data bus applications, video transmission, and low-power applications. High transfer efficiency and low drag torque of the power roll ring have been verified for Space Station applications.

REFERENCES

1. Yenni, E. J. "Electrical Characterization of a Space Station Freedom Alpha Utility Transfer Assembly." 27th Intersociety Energy Conversion Engineering Conference, 1992.
2. Yenni, E. J. and Birchenough, A. G. "Large Transient Fault Current Test of an Electrical Roll Ring." 26th Intersociety Energy Conversion Engineering Conference, 1991.
3. Smith, D. W. "Signal and Power Roll Ring Testing Update." 23rd Aerospace Mechanisms Symposium, 1989.
4. Renz, D. D. "Multi-Hundred Kilowatt Roll Ring Assembly Evaluation Results." 23rd Intersociety Energy Conversion Engineering Conference, 1988.
5. Porter, R. S. "A Rotating Electrical Transfer Device." 19th Aerospace Mechanisms Symposium, NASA, 1984.

ACKNOWLEDGMENTS

The authors are grateful to Ken Huck, Steve Jones, and Pete Jacobson for their contributions to the background and hardware description sections.

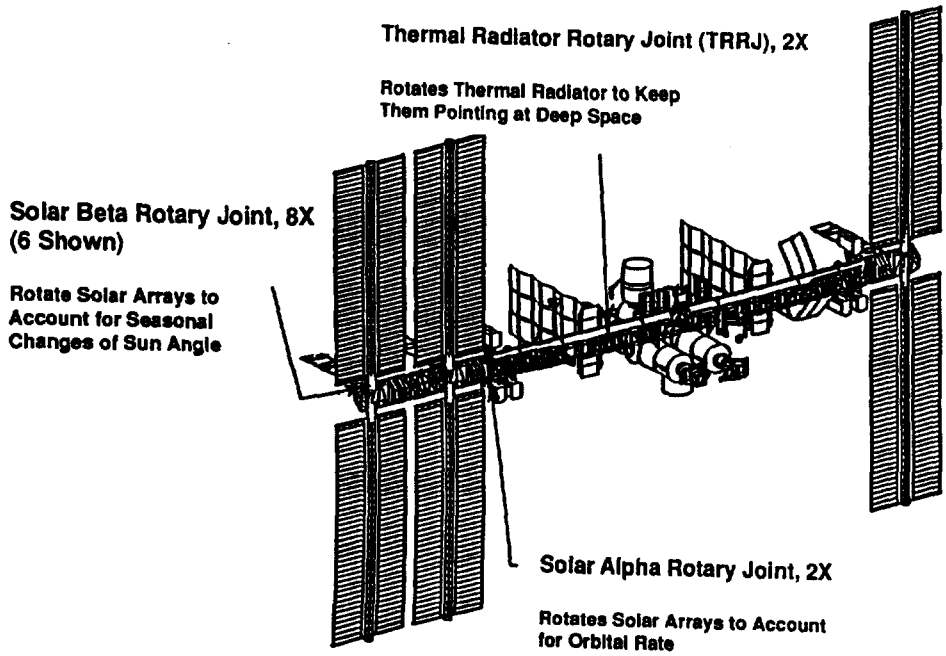

Figure 1. Roll Ring Locations on Space Station Freedom

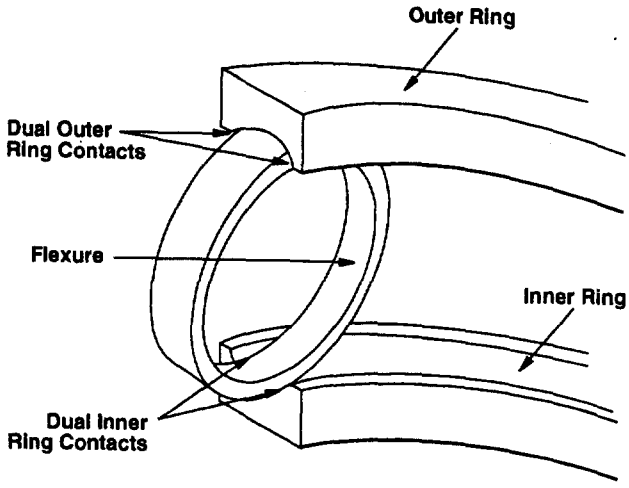

Figure 2. Signal Roll Ring

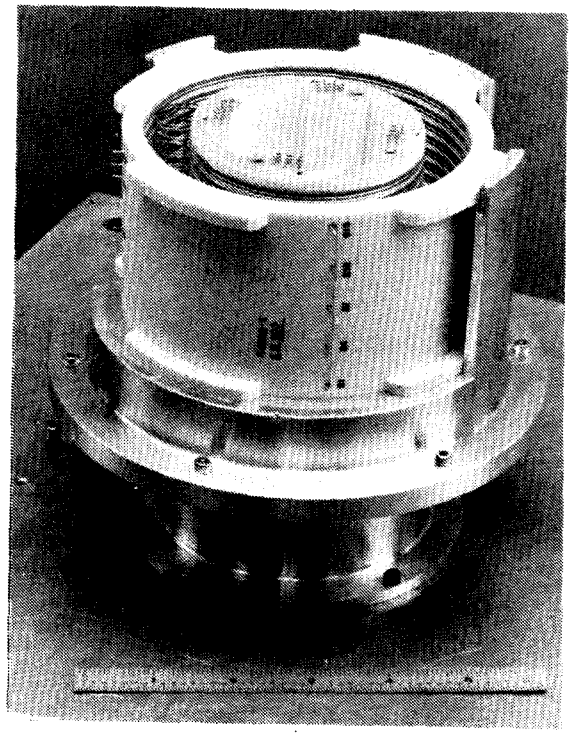

Figure 3. Signal Roll Ring Subassembly

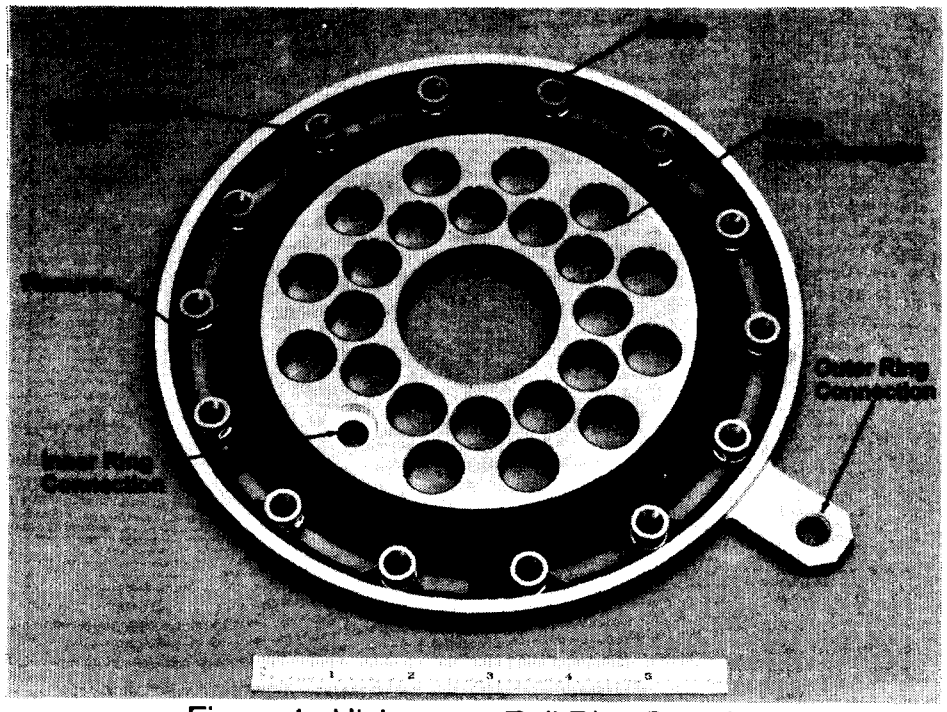

Figure 4. High-power Roll Ring Crossing

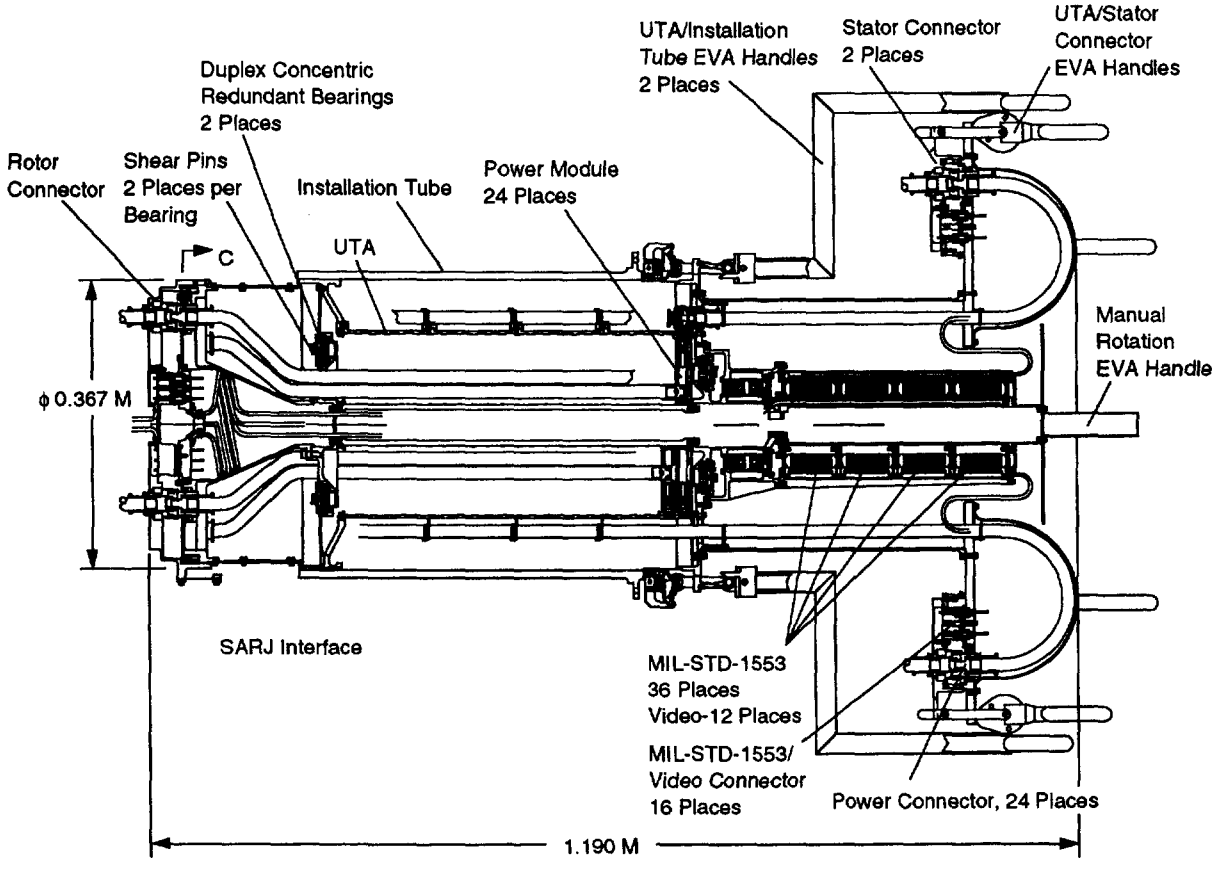

Figure 5. UTA Cross Section

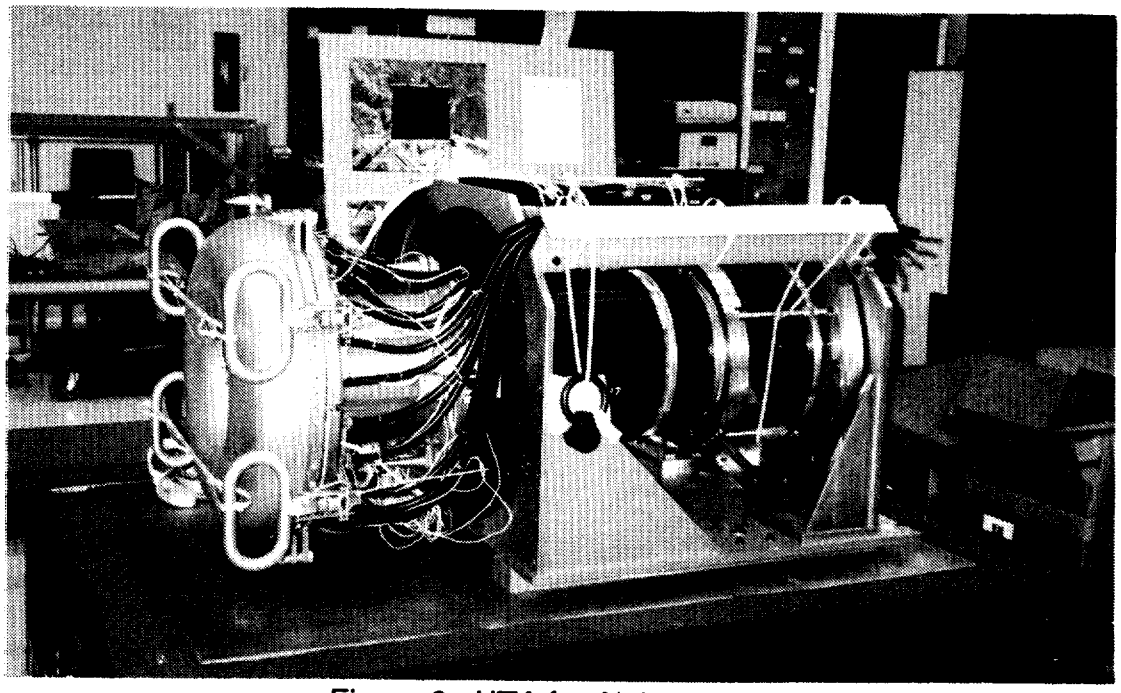

Figure 6. UTA for Alpha Joint

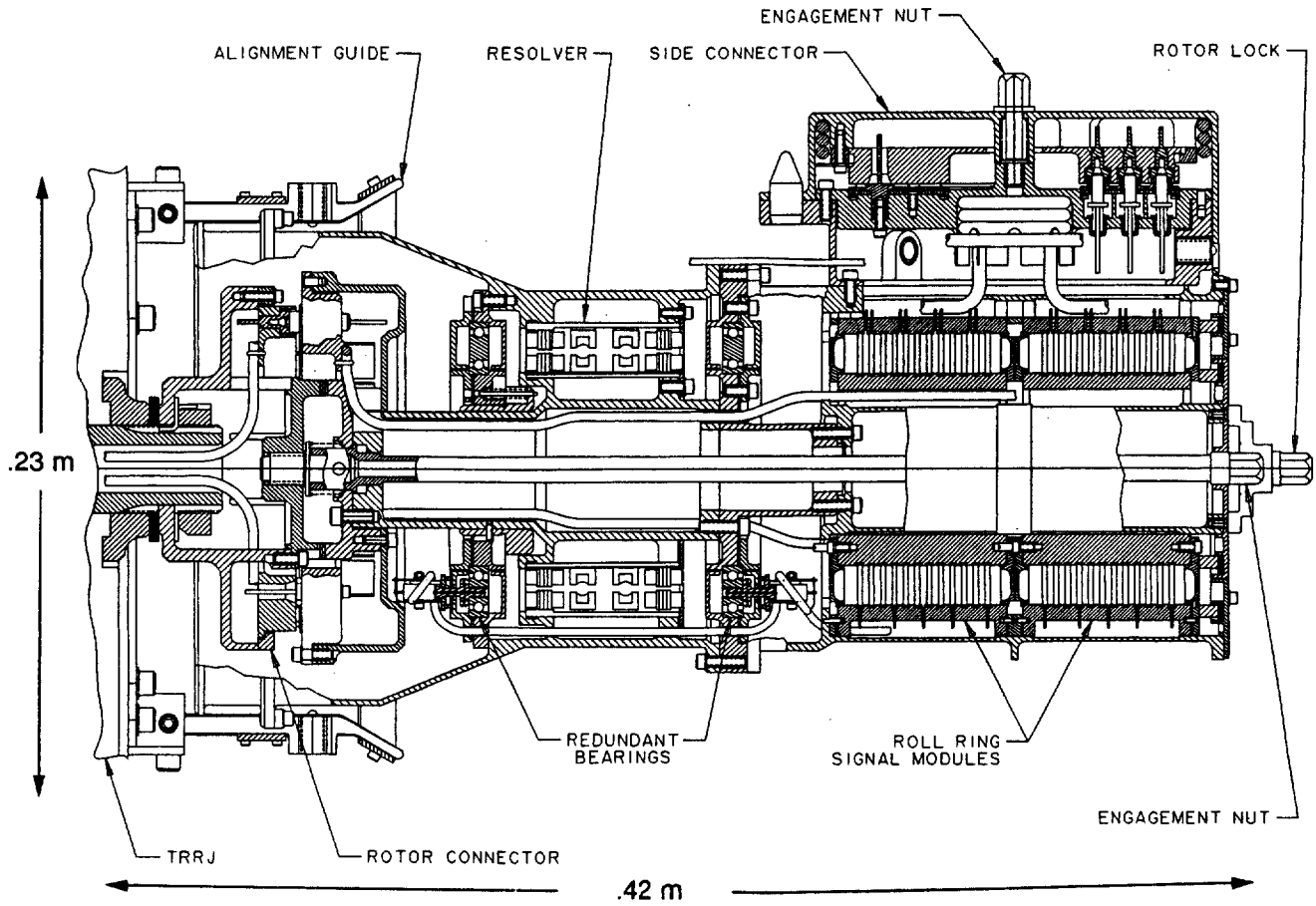

Figure 7. PDTA Cross Section

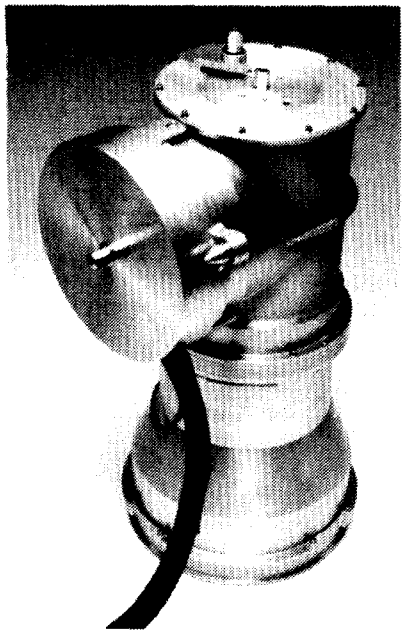

Figure 8. PDTA for Radiator Joint

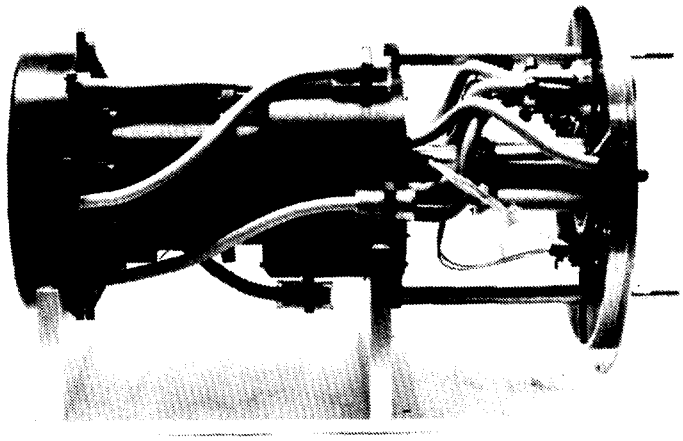

Figure 10. BGRRS for Beta Joint

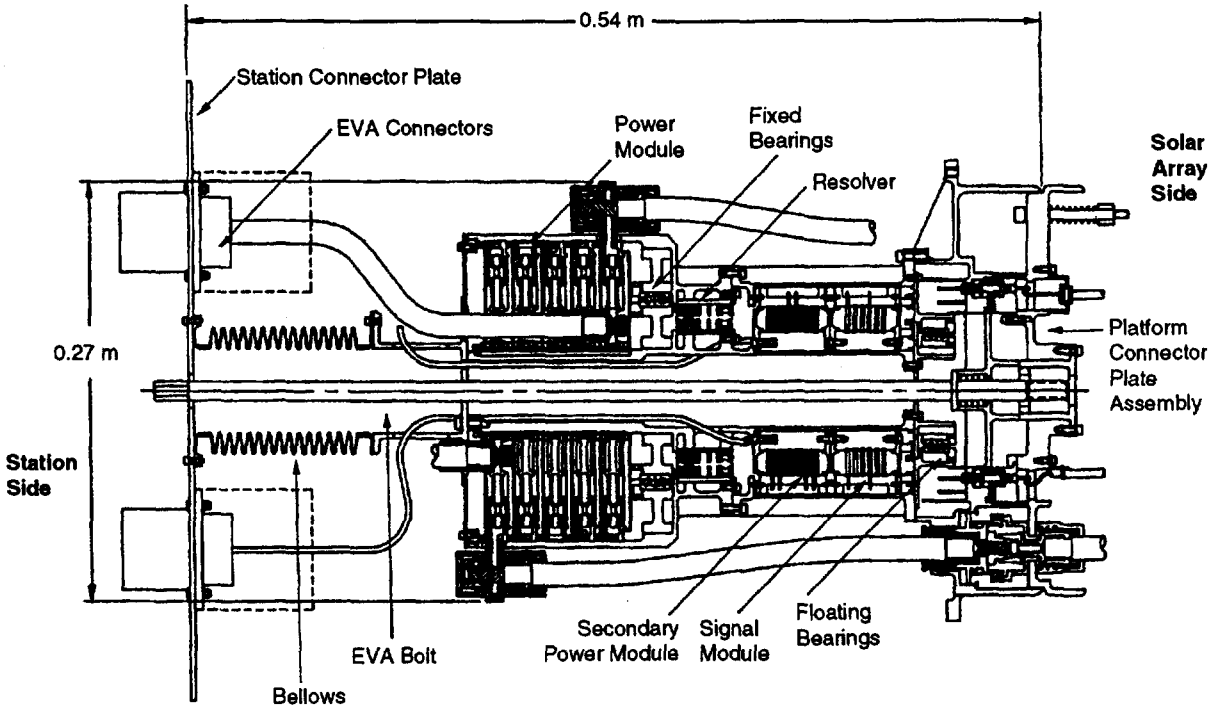

Figure 9. BGRRS Cross Section

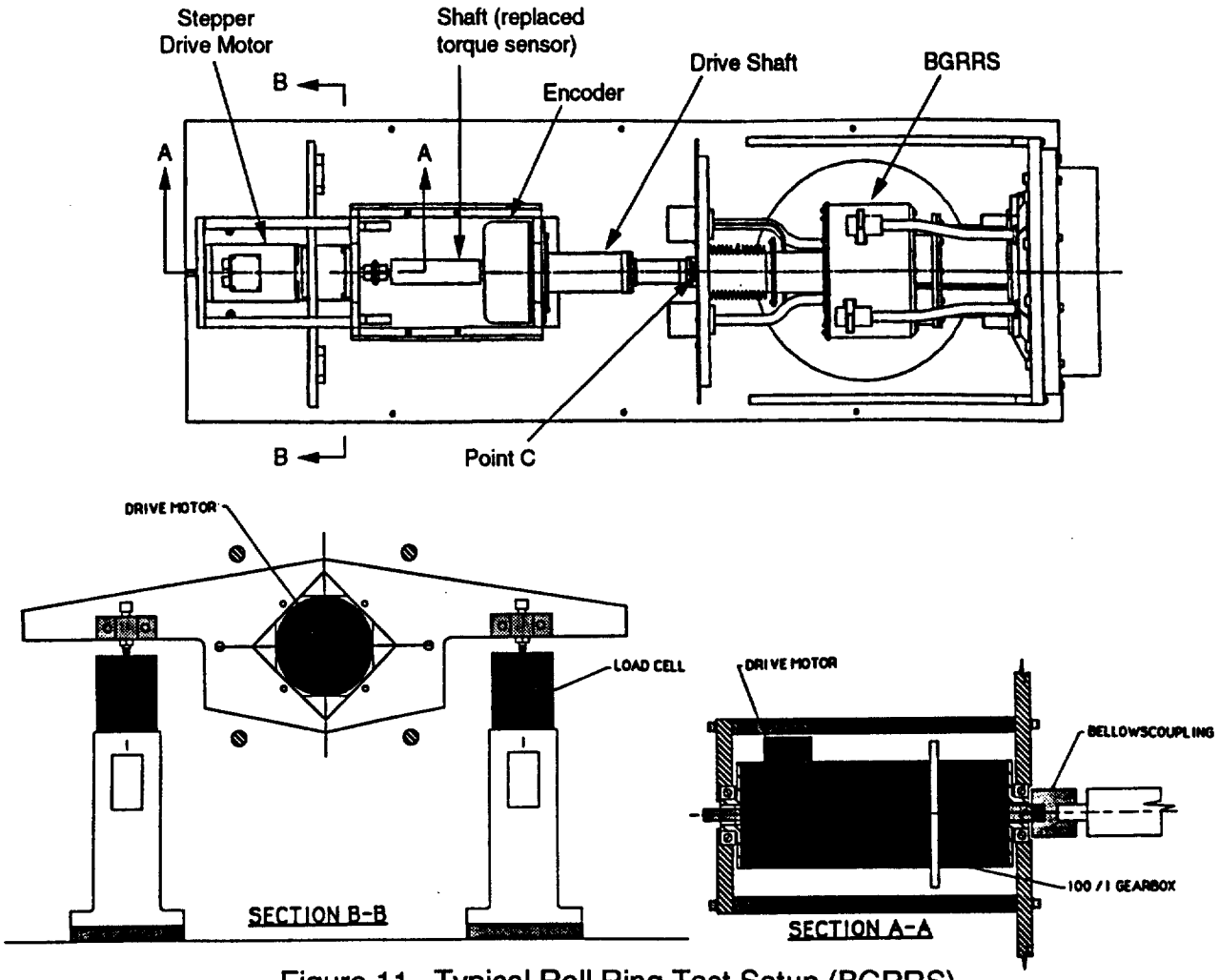

Figure 11. Typical Roll Ring Test Setup (BGRRS)

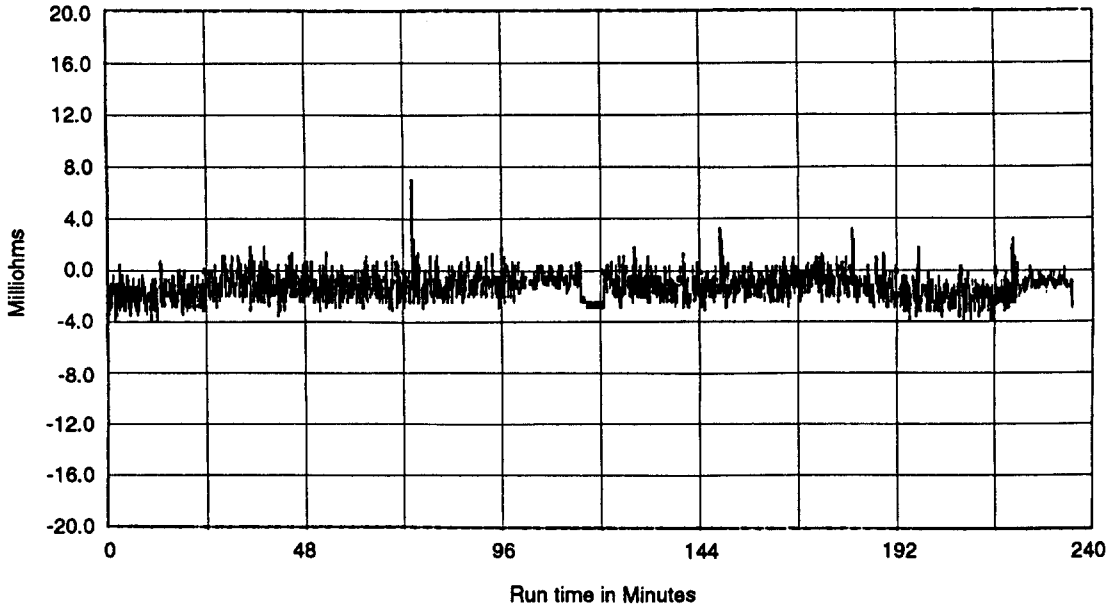

Figure 12. Noise Resistance

Table 1. Electrical Transfer Tradeoffs

Characteristic	Slip Ring	Flex Capsule	Roll Ring
Torque	T	0.05 T	0.2 to 0.005 T
Resistive noise (milliohms) at 0V A	30	Zero	10
Lubrication requirements (for vacuum)	Organic on A_u Graphite and M_oS_2 on Ag	None	None
Storage/standby	N_2 purge avoid air (H_2O)	Insensitive	Insensitive
Wear rate (in./in.)	10^{-10} initial; 6×10^{-11} final	None	Not measurable to 2×10^8 rev
Rotation	Continuous Revolutions	<±3 rev	Continuous Revolutions
Dither effects	Noise at debris piles	Fatigue limited	None
Assembly adjustments	Alignment and pressure	None	None
Run-in	Required/cleaning	None	None
High frequency	To 20 MHz (?)	To 20 MHz	to 150 MHz
Life	>200 M rev	Fatigue limited	>200 M rev

Table 2. Space Station Environment Test Level

Environment	UTA	PDTA	BGRRS
Random Vibration	Composite 6.2 grms Duration 90 sec	Composite 6.3 grms Duration 90 sec	Composite 12.2 grms Duration 180 sec
Thermal Cycle	-23 to 43 °C 9 cycles	-23 to 43 °C 6 cycles	-29 to 68 °C 12 cycles
Thermal Vacuum	-23 to 43 °C <1.33 millibar 3 cycles	-23 to 43 °C <1.33 millibar 3 cycles	-29 to 60 °C <1.33 millibar 3 cycles

Table 3. Roll Ring Noise Resistance

Unit	Background Noise (mΩ)	Peak Noise (mΩ) (3)	Current
UTA Signal (1)	<10 (13x) <20 (3x)	15-30 (4x) 15-50 (5x) 15-89 (1x) 15-143 (3x) 15-243 (1x) 20-300 (2x)	0.1 mA
PDTA Signal (1)	6-10	13-32 (1x) 18-66 (1x) 13-18 (1x) 18-347 (1x)	0.1 mA
BGRRS Signal (1)	2-4	5-9 (2x)	0.1 mA
BGRRS Low Power (2)	2	4-6 (2x)	2 A

Notes: 1. Signal Roll Rings have 2 flexures in parallel per crossing.
2. Low Power Roll Rings have 3 flexures in parallel per
3. Peak Noise levels seen by the number of circuits in parentheses, eg (4x).

Table 4. Signal Roll Ring Performance

Unit	Total Words Transmitted	Total Errors	Words Transferred Per Error	Requirement (words/error)
UTA	85.5×10^9	143	59.8×10^8	$>1 \times 10^7$
PDTA	17.7×10^9	97	18.2×10^7	
BGRRS	37.6×10^{10}	509	7.38×10^7	

Table 5. Space Station Roll Ring Requirements Matrix

Parameter	Requirement		
	UTA	PDTA	BGRRS
Data	12 1553 Buses (36 Crossings)	4 1553 Buses (12 Crossings)	2 1553 Buses (6 Crossings)
High-Power	24 Crossings 65.5 kW	–	5 Crossings, 45 kW
Low-Power	–	6 Crossings .3 kW each	6 Crossings, 0.8 kW each
Rotation	2∏ rad -0.0087 to 0.0087 rad/s	2∏ rad -0.0087 to 0.0087 rad/s	2∏ rad -0.10 to 0.10 rad/s
Positional Telemetry	Resolver, Redundant, 1.8 mrad Accuracy	Resolver, Redundant, 1.8 mrad Accuracy	Resolver, 1.5 mrad Accuracy
Drag Torque	<2.7 N-m	<1.4 N-m	<1.4 N-m
Weight	<136 kg	<16 kg	<24 kg

INTERNATIONAL SPACE STATION ALPHA'S BEARING, MOTOR, AND ROLL RING MODULE DEVELOPMENTAL TESTING AND RESULTS

David L. O'Brien
Rocketdyne Division
Rockwell International
Canoga Park, California

ABSTRACT

This paper presents the design and developmental testing associated with the bearing, motor, and roll ring module (BMRRM) used for the beta rotation axis on International Space Station Alpha (ISSA). The BMRRM with its controllers located in the electronic control unit (ECU), provides for the solar array pointing and tracking functions as well as power and signal transfer across a rotating interface.

INTRODUCTION

The BMRRM is part of the beta gimbal assembly (BGA), as shown in Figure 1. The BMRRM is located between the beta gimbal transition structure (which deploys the BGA and solar array away from the station) and the BGA platform. The sequential shunt unit, ECU and solar array are all attached to the BGA platform.

The beta rotation axis is the second of two axes required to allow maximum use of solar power for the electrical systems aboard the space station. The beta axis servocontrol compensates for both the seasonal and orbital changes in the station's orientation to the solar vector (line-of-sight). Under the ISSA program, nominal beta axis rotational rates vary from zero to 0.096 rad/d (five degrees per day). Shuttle docking (plume loads) and extravehicular / intravehicluar operations also define expected beta axis motions. The maximum allowable velocity is 0.076 rad/s (240 degrees per minute), although the default control parameters limit velocity to 0.025 rad/s. The beta gimbal was designed under the Space Station Freedom requirements, which had an additional requirement of alpha axis rotation in early flights, which is around 0.078 rad/min, (four degrees per minute). The leading design drivers of the BMRRM are the beta axis servocontrol, power and signal transfer through a rotating joint, and structural loading requirements. Small angle oscillations are also expected due to vibrational modes of the station.

BMRRM DESIGN

The BMRRM consists of two sets of angular contact bearings, a brushless dc torque motor, resolver, roll ring subassembly, antirotation latches, and a housing to hold the components together. The electronics to operate the motor, latches, and resolver are located in the ECU. A cross-sectional view of the BMRRM is shown in Figure 2. The bearings, motor, and roll ring are all concentric to each other. The

BMRRM's total mass is 63.5 kg, of which the roll ring is 27.2 kg, the motor 8.2 kg, and the bearings 5.4 kg.

The angular contact bearings provide structural stiffness about five axes. The bearing sets are separated by 0.5 m (20 inches), which accommodates bending loads. The outboard bearing set (toward the solar array) supports axial loading. The inboard set is free to move axially to accommodate thermal expansion and tolerance stacking. Each bearing set was consists of two 0.45 m diameter angular contact bearings mounted face-to-face and preloaded to 0.34 rad (18 degrees) contact angle.

A brushless dc motor provides the torque about the beta axis. Due to the low required torque of 1.4 N-m (12 in-lb) plus friction losses (less than 2 N-m), a direct drive motor was used. Eliminating a geared system helped pointing accuracy by reducing frictions losses, thus reducing station vibration disturbances on the inertially stable array. Eliminating the geared system also helped control stability by abolishing backlash, reduced power consumption due to lower frictions losses, reduced mass, and increased life (no gear wear). The motor is capable of providing 45 N-m torque (stall), resulting in about 8 to 1 torque margin. The motor is a 3-phase, Y-wound, 64-pole device about 0.4 m in diameter. Figure 3 shows an outboard view of the BMRRM with the motor and roll ring connector.

The resolver, which is located within the roll ring subassembly, provides arc-minute pointing accuracy knowledge for the proportional-integral-derivative (PID) closed servoloop. The PID servoloop is a digital controller located in the ECU. The BGA/BMRRM does not use inertia or solar sensing instruments. The pointing control comes from the station's guidance, navigation, and control system or the ground, via the photovoltaic controller unit. As a backup, the motor and controller are designed to allow open-loop stepping. The resolver pointing knowledge is also used for commutating the motor.

The roll ring subassembly provides bidirectional transfer of source power (212 A), secondary and dc control power (less than 8 A) and MIL-STD-1553B data signals. The roll ring, as being installed into the BMRRM, is shown on Figure 4. The transfer is across a rotating joint through slightly compressed multiple rotating flexures connecting the inner and outer conducting rings. The rotating flexures greatly reduce the sliding friction, allowing the BMRRM to be rotated with very low torques. Most of the BMRRM's torsional friction comes from the angular contact bearings.

There are two antirotation latches in the BMRRM each 1.77 rad (92.8125 degrees) apart. There are 64 holes in the BMRRM housing flange; therefore, by oscillating between the latches, 128 latching positions are available (every 0.05 rad or 2.8125 degrees). An antirotation latch is a paraffin actuated pull-pin device. When 15 Vdc power is applied by the ECU the paraffin solid-to-liquid phase change results in pulling the pin out of the latch hole and resets a toggle mechanism. The next time power is applied the paraffin actuator toggles the mechanism and allows the spring loaded pin to be pushed back into the latching hole.

The BMRRM can be replaced on-orbit. To facilitate this the roll ring contains a single input mating connector as shown in Figure 3. This connector includes all power, motor, latch, and resolver lines.

BMRRM TESTS AND RESULTS

Four series of tests were performed: component functional, system functional, thermal vacuum, and static structural. Both functional tests were performed in a clean room environment at Rocketydne, Rockwell International, Chatsworth facility. The thermal vacuum test was performed at Martin Marietta Aerospace, Denver. The static structural test was performed at Rocketydne, Rockwell International, Canoga facility. At the time of writing, 60 percent of the component and system functional tests were completed. The static structural test was fully completed. Results of the thermal vacuum and remaining functional tests will be presented at the conference.

Component Functional

The purpose of component functional testing was to verify the BMRRM design, ensure BMRRM assembly workmanship, verify the control model's component subroutines, and verify some component performance requirements. Component functional testing included friction, open-loop servo and position knowledge accuracy. The BMRRM was installed onto an electrical test set, as shown in Figure 5. The test set contained a torque cell, an external motor to rotate the BMRRM, motor voltage sensors, motor current sensors, and a motor controller (which simulates the ECU). The buildup and test sequence of the BMRRM is shown on Figure 6.

The friction tests measured the resulting torque of the main bearings, roll ring bearings, and motor clogging under several conditions. Conditions included constant velocity tests, initial torque tests, small angle dither tests, and open-loop sine wave voltage inputs. Due to the low rotational rates the BMRRM exhibited little viscous friction characteristics. Three rates were tested over a complete revolution: 0.076, 0.57, and 6.9 rad/min (4, 30, and 360 degrees per minute). The average steady-state friction torque for the three rates were 1.2, 1.3, and 1.9 N-m, respectively. However, over an operating range of zero to 0.078 rad/min the steady-state friction changes less then 1 percent. The small angle and initial torque tests show that there was no static friction involved. The friction closely resembles the Dahl model with a Dahl slope of 565 N-m/radian and a steady state torque between 1.1 and 1.8 N-m. Figure 7 compares the Dahl model and the friction test data for a 6.9 rad/min case. The friction "overshoot" shown was probably caused by motor static torque, which includes cogging as well as hysteresis effects. When the motor was tested independently a 1 N-m static friction was measured. Test set dynamics may also play a part in this overshoot, details of which will be presented at the conference.

Open-loop servo tests included back electromotive force (BEMF) and torque motor constant. The BEMF test measured the voltage outputs of each phase while the BMRRM was rotated at a constant 5.74 rad/m rate. The BEMF curves analysis will be presented at the conference. The data will state the amount of torque ripple caused by the motor. The torque motor constant test verifies controller motor power train, that is (1) motor torque, (2) motor to controller alignment, and (3) the controller current regulator. Prior to performing the torque motor constant test, the motor was aligned to the resolver by applying current through the +C -B phases. The windings were then rotated such that torque went to its stable zero (with constant current through the given phases, the windings have a sinusoidal torque curve with two zero

torques, one stable and one unstable). As shown in Figure 8, the torque constant test was within 2 percent of the theoretical maximum value.

Position pointing accuracy and related alignment tests verified the pointing knowledge requirements and provided the needed accuracy for commutating the brushless motor. Position accuracy tests to measure resolver accuracy over a revolution range in both rotating directions were performed. Figure 9 shows a typical resolver error plot. The resolver "zero" is adjusted mechanically to the alignment support equipment zero. The sinusoidal error is typical for resolvers and since the error is repeatable it can be biased within the controller software.

System Functional

System functional testing included proportional hold, step inputs, rate inputs, and latching. The latter three required the use of an inertia simulator. This support equipment simulates the large inertia (8200 kg m^2) and dynamic modes of the solar array, via electrical-mechanical means. At the time of writing the inertia simulator was not complete, thus no rate or latching tests and only limited step tests were performed. These tests will be completed prior to the conference and presented thereupon.

For the proportional hold test the BMRRM was locked down at a specific position and then commanded to move to various positions. Since only the proportional constant is used, the torque produced was proportional to the constant and the error angle: $T = K_t P (\Phi_{cmd} - \Phi_{actual})$. Figure 10 shows results for several command angles and two proportional constants. As shown the system is very linear, within 2 percent.

The step tests varied from 0.0025 degrees (typical for beta rotation) to as large as 180 degrees (faulted conditions), although 5 degrees and 30 degrees steps were the baseline testing conditions. These step tests only used the hardware itself as an inertia (less than 1/3000 th of the solar array inertia), thus the system reacted abruptly to the step inputs, often exceeding velocities expected on-orbit (peaked at 1000 degrees per minute). Three control algorithms were tested: proportional (P), proportional-derivative (PD), and proportional-integral-derivative (PID). A firmware error was discovered in the integral subroutine, thus the PID reacted similar to a PD controller. The P controller test data is compared to the simulation model in Figure 11. Generally the simulation models correlate to the test data within 50 percent. It is uncertain why the model deviates from the test data points, although two reasons have been proposed: (1) the friction model is invalid at the higher speeds and (2) the modeled hardware inertia was an assumption. The PD controller test data is compared to the simulation model in Figure 12. In the PD controller case, the simulation model correlated to the test data within 30 percent. The maximum velocity for the PD controller was below the terminal velocity (which is 1.5 A divided by the derivative coefficient for a frictionless system), which validated the speed control capabilities of this positional controller.

Environmental Testing

Static structural testing was performed to verify the stress and load-deflection models. The tests represented about 75 percent of the on-orbit bending loads and 400 percent of the on-orbit torsional and shear loads. The bending loads are the

main structural design driver. The BMRRM has very large torsional and shear safety factors, thus the 400 percent loading was required to amplify the deflection. Within the BMRRM the deflections generated were within 20 percent of expected values. No structural failures occurred.

Thermal vacuum/thermal balance (TVTB) testing was used primarily to verify the thermal math models. A hot and cold soak as well as transient test (emulating the 60 minute solar, 30 minute eclipse cycle) was performed. Two infrared heat lamp cages were utilized; one representing the solar flux, and the other, on the anti-solar side, representing an averaged albedo and earth IR flux. The TVTB testing showed warm BMRRM internal temperatures during the cold condition, around 5 to -13 C. Internal BMRRM hardware temperatures are limited to about -65 C. The initial design concern was that the internal temperatures may become too cold, thus a high absorptivity black painted surface was chosen. However, this 50 C margin will allow the design team to proceed with a less costly and more durable clear anodizing surface, rather than the baseline black painted surface. A 30 degree step test was planned for the ambient-ambient pressure, ambient-vacuum, cold-vacuum, and hot-vacuum conditions to measure thermally and vacuum caused differences in the servoloop. The ambient-vacuum test was successful, showing little difference between it and the ambient pressure test. However, an open developed in the B motor phase during the cold-vacuum case, which never closed even after the hardware was brought back to ambient temperature and pressure conditions. At the time of writing, the BMRRM has not been disassembled to determine where the open occurred. A step test using an external power supply and two of the three motor phases was performed during the cold-vacuum condition, although analysis is not yet complete.

CONCLUSIONS

All development testing program goals were accomplished, including:

1. The assembly and test sequence of Figure 6 was shown to be an acceptable hardware flow.
2. All component-level performance requirements were met, with the exception of the motor line open during cold thermal-vacuum testing. Once the root cause of the open is found a small design modification may be needed.
3. The system-level performance test results were within the tolerances expected, however additional testing with an inertia simulator is needed.
4. Data from the tests largely verify the control model's component friction, motor, and controller subroutines. Some additional minor friction testing is desirable to determine the cause of and model for small angle movements.
5. Data from both the static structural and thermal testing is approximate to what was expected.

Overall the BMRRM has proven to be a very tolerant, lightweight, high-accuracy rotating gimbal with minimal friction torque, and thus high rotating efficiency.

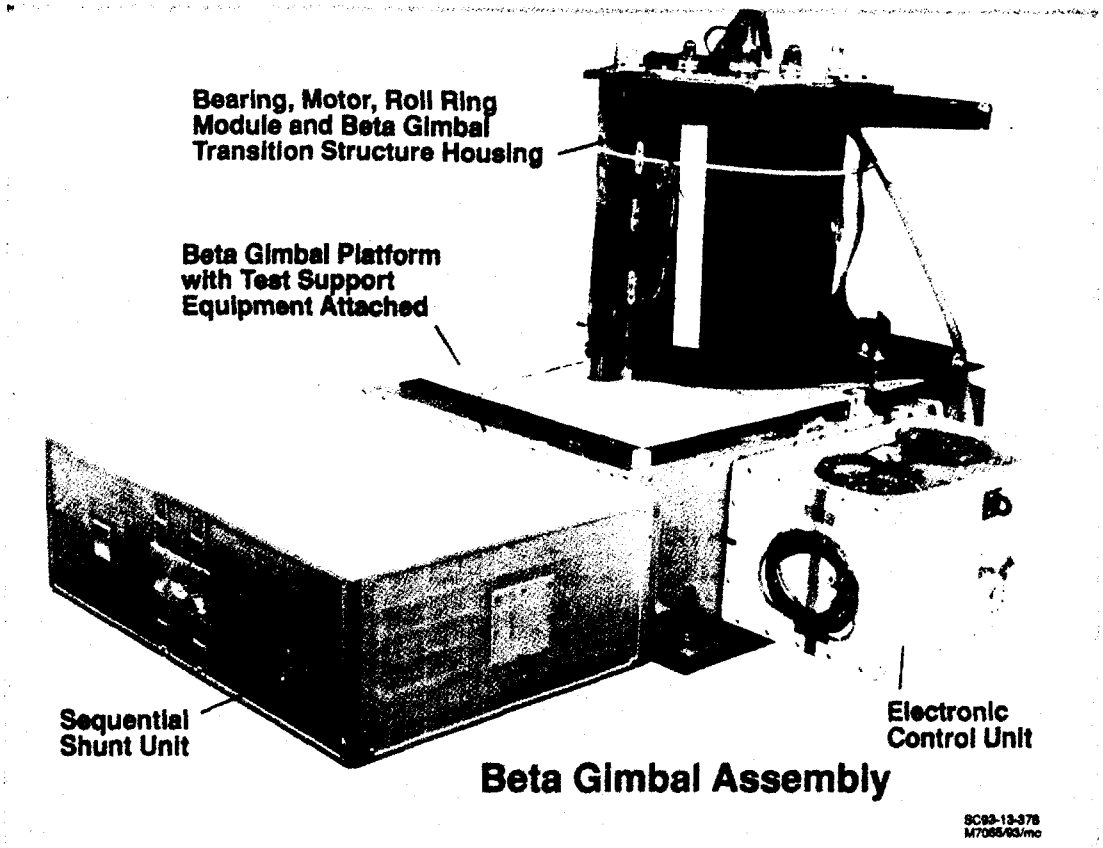

Figure 1. Beta Gimabal Assembly

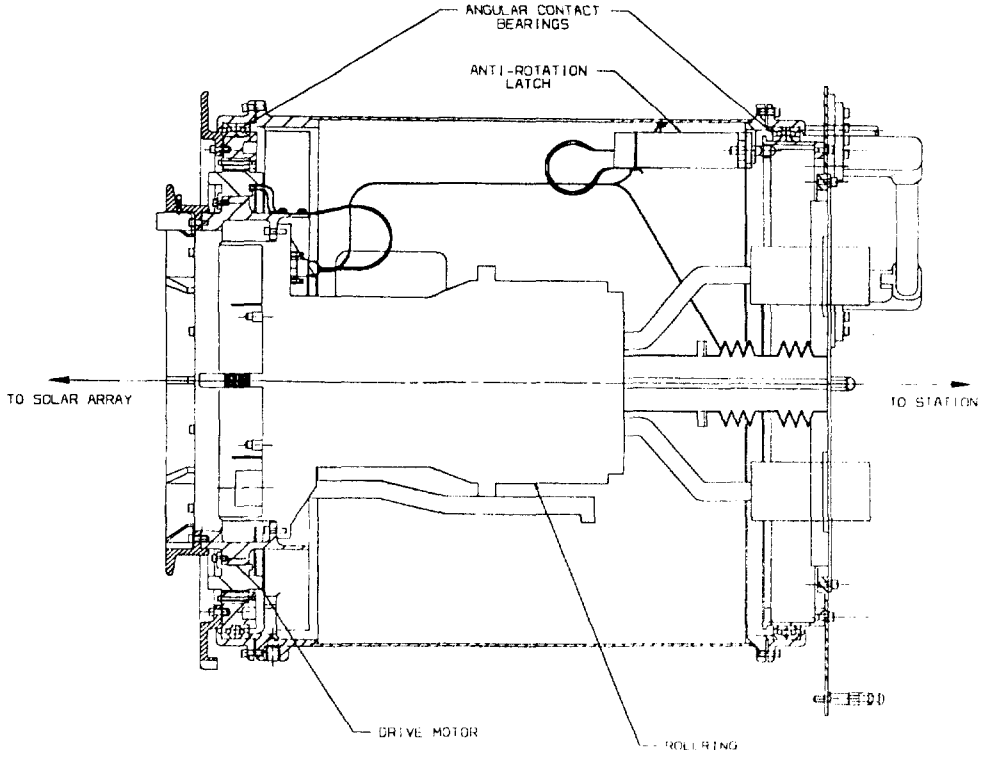

Figure 2. BMRRM Cross-sectional View

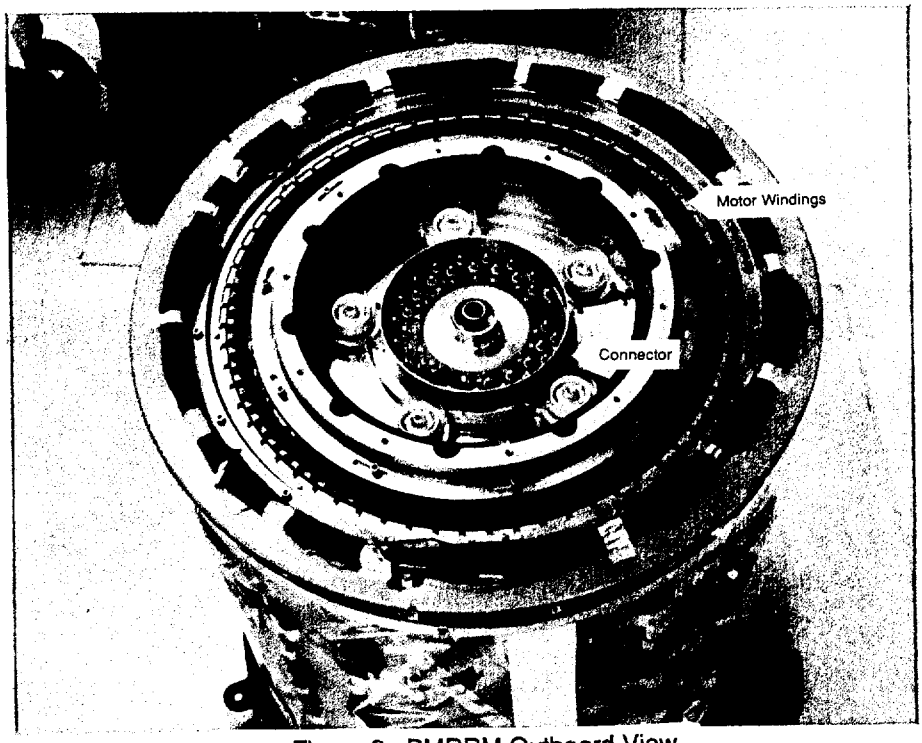

Figure 3. BMRRM Outboard View

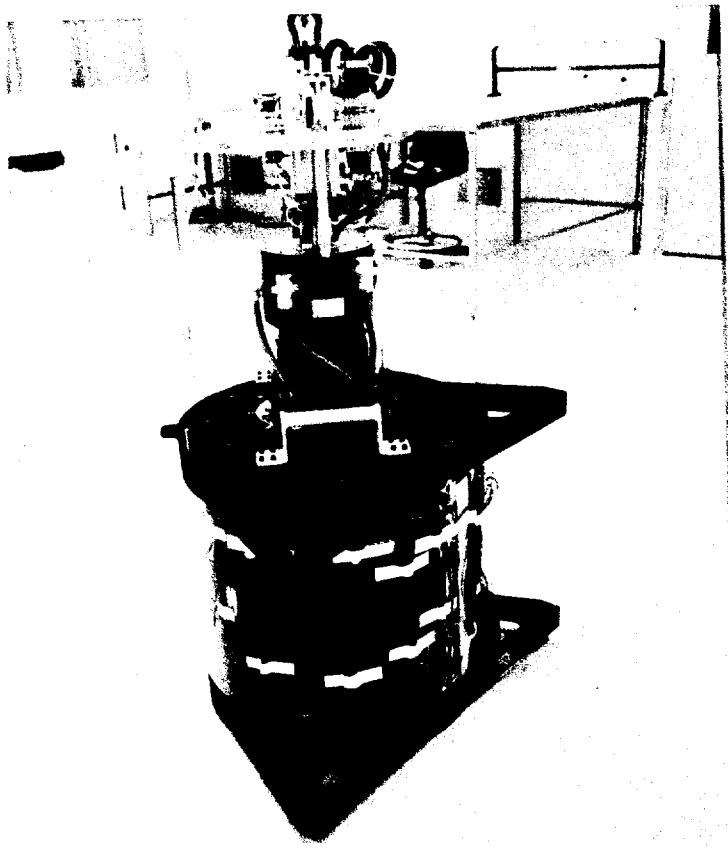

Figure 4. Roll Ring Installation into BMRRM

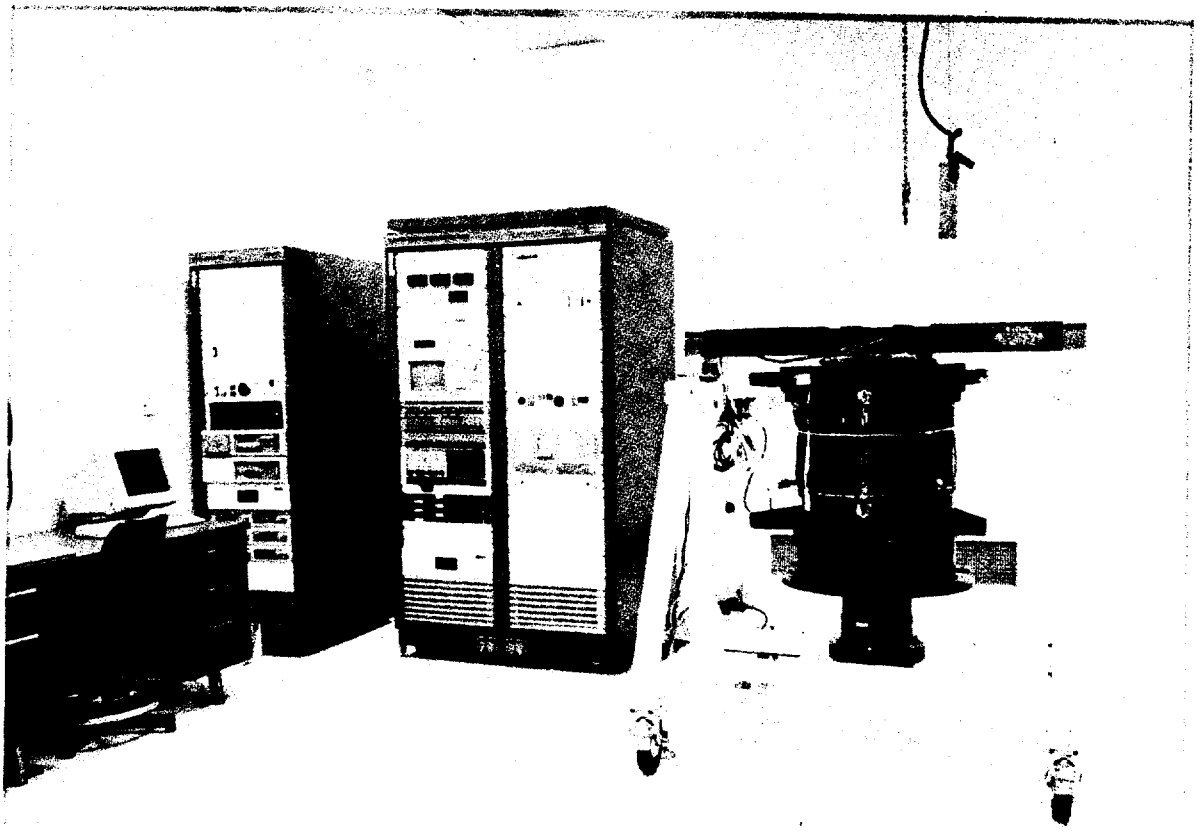

Figure 5. Electrical Functional Test Set

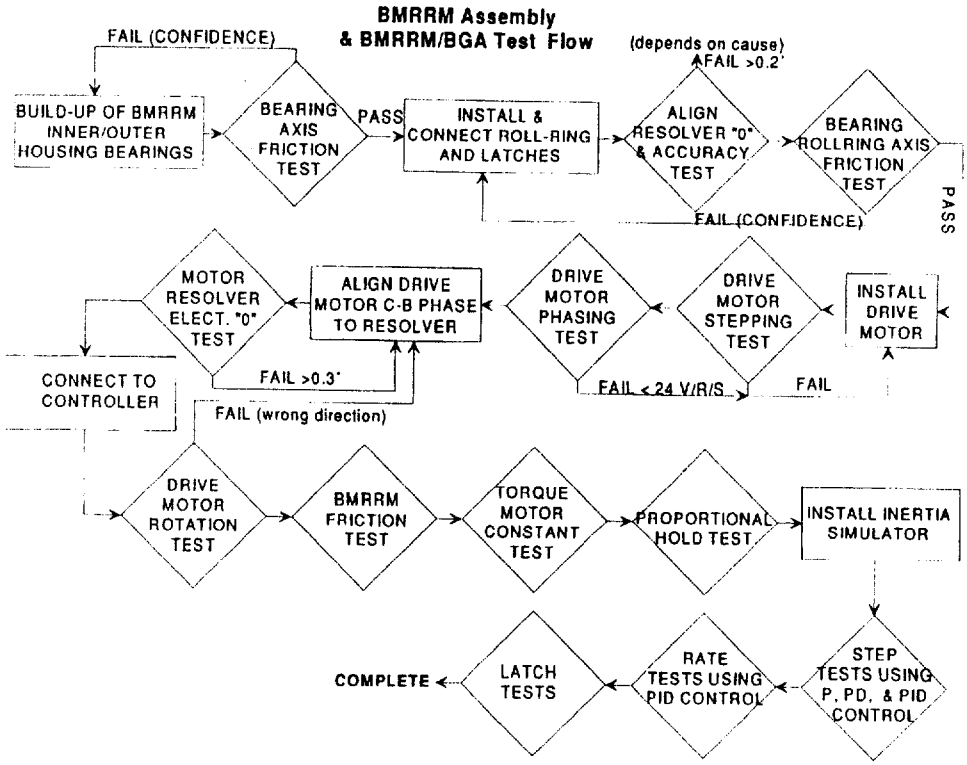

Figure 6. BMRRM Build-up and Test Sequence

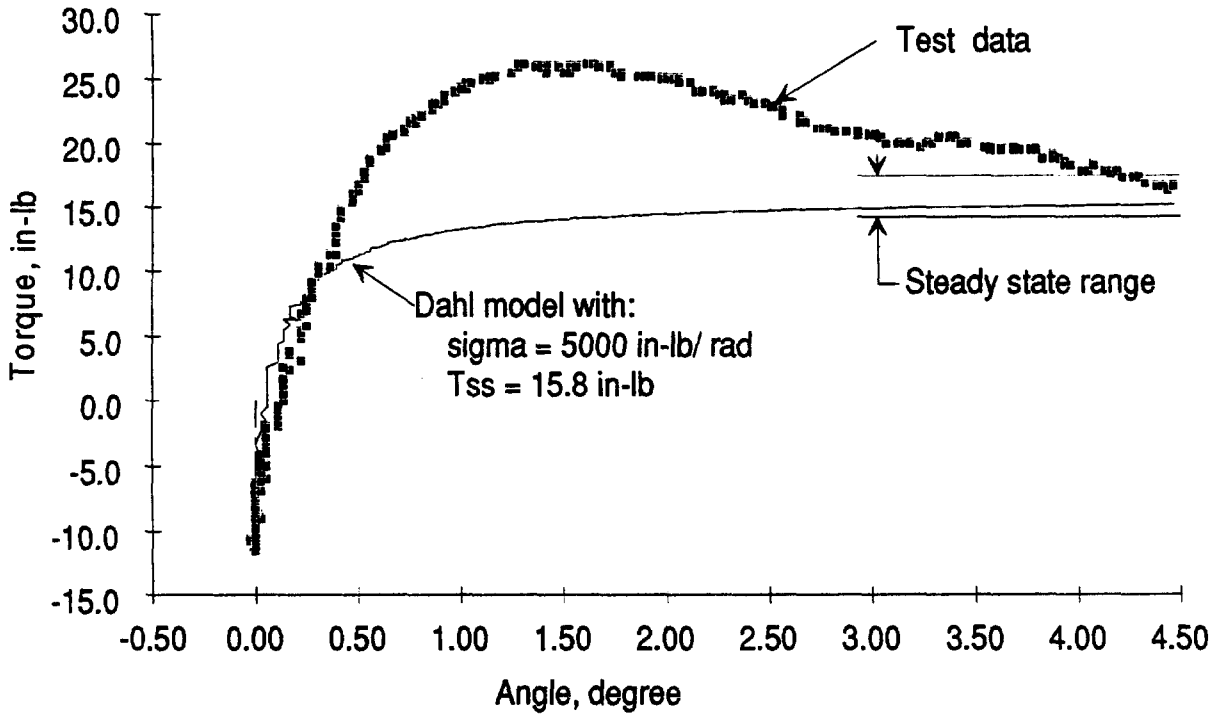

Figure 7. Typical Small Angle Friction Curve. Plot for a 360 degree per minute test.

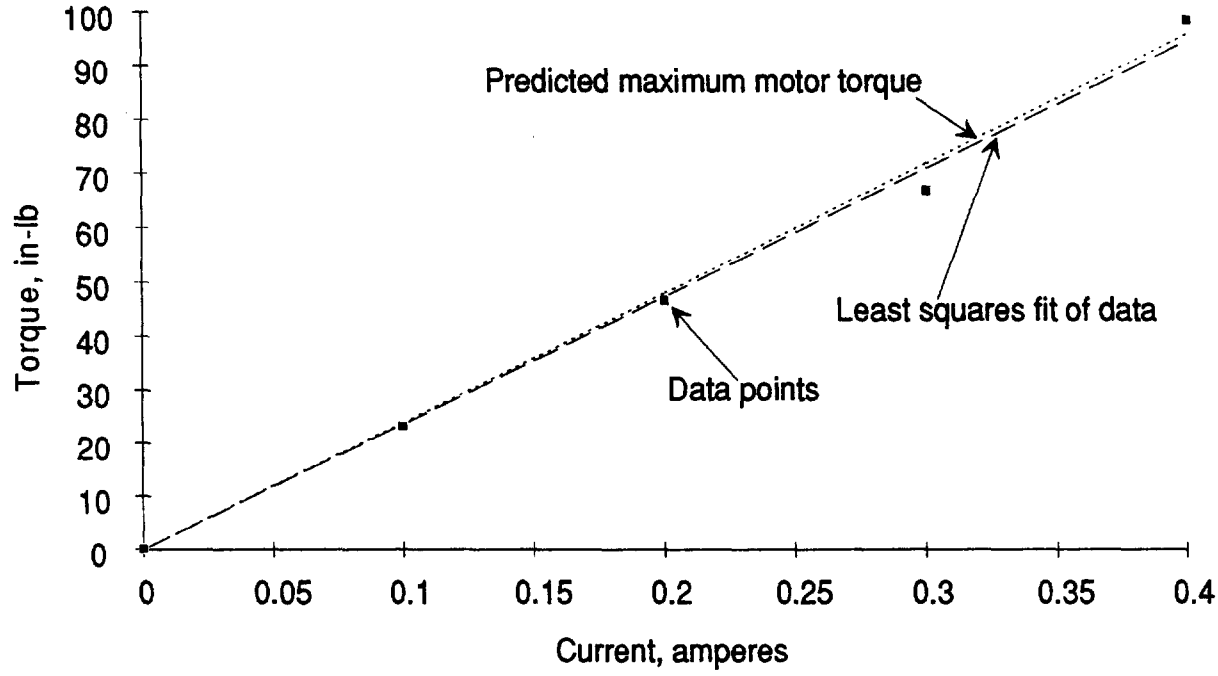

Figure 8. Torque Motor Constant Test

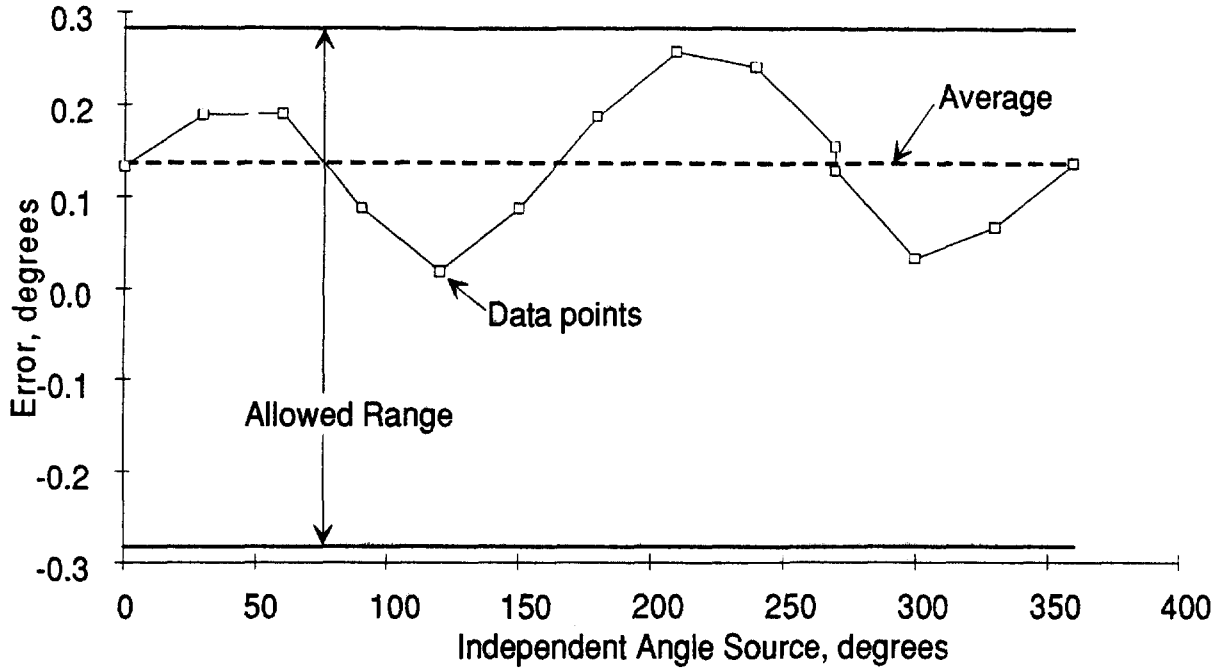

Figure 9. Resolver Accuracy Test

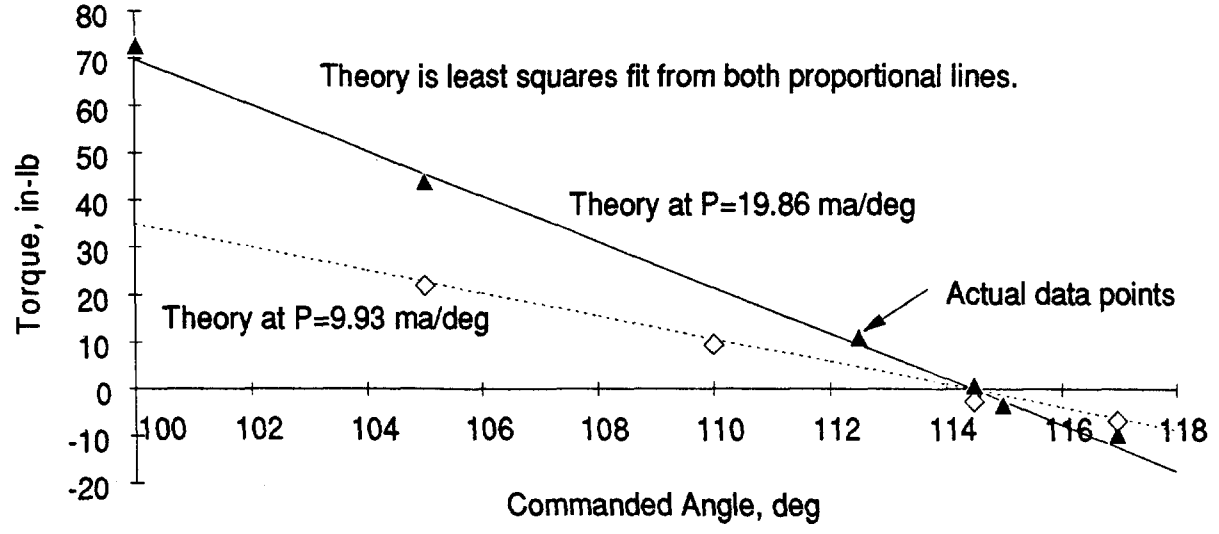

Figure 10. Proportional Hold Test

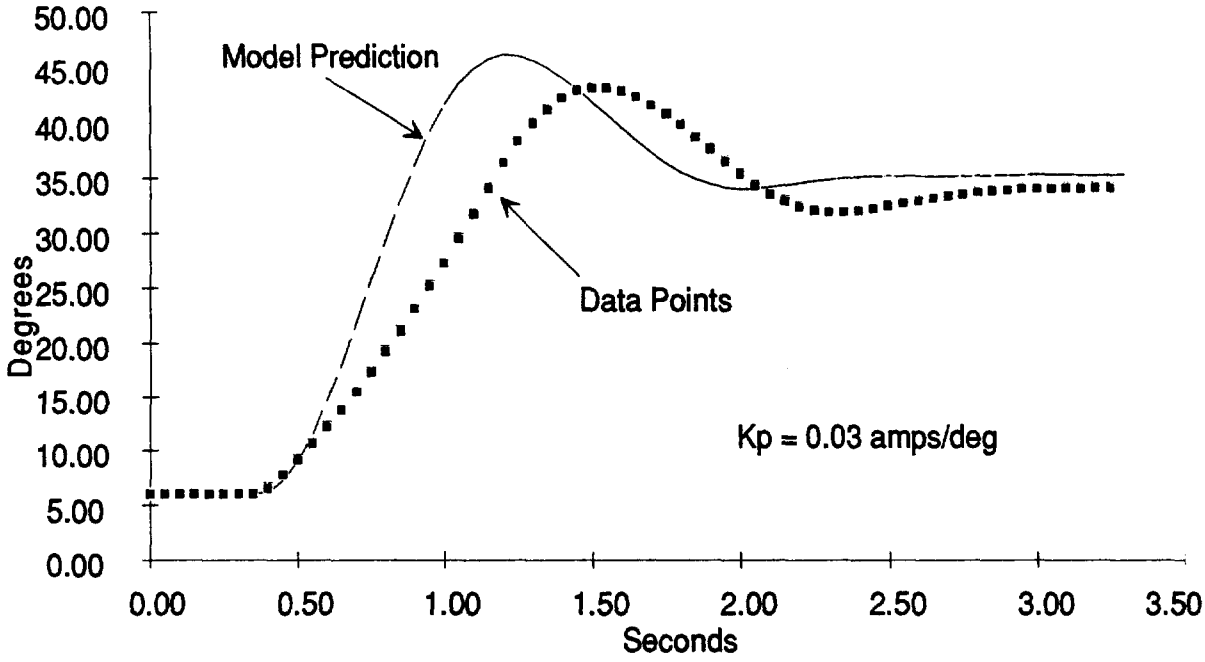

Figure 11. 30 Degree Step Input with Proportional Only Controller

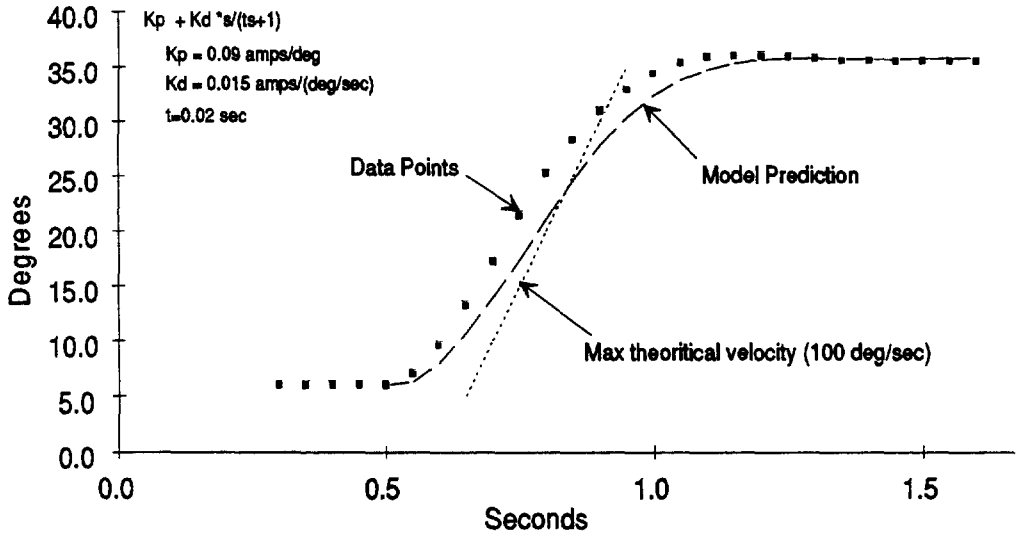

Figure 12. 30 Degree Step Input with Proportional-Derivative Controller

DESIGN, CHARACTERIZATION AND CONTROL OF THE UNIQUE MOBILITY CORPORATION ROBOT

Virgilio B. Velasco, Jr., and Wyatt S. Newman
Case Western Reserve University
Cleveland, Ohio

Bruce Steinetz
NASA Lewis Research Center
Cleveland, Ohio

and

Carlo Kopf and John Malik*
Unique Mobility, Inc.
Golden, Colorado

Abstract

Space and mass are at a premium on any space mission, and thus any machinery designed for space use should be lightweight and compact, without sacrificing strength. It is for this reason that NASA/LeRC contracted Unique Mobility Corporation to exploit their novel actuator designs to build a robot that would advance the present state of technology with respect to these requirements. Custom-designed motors are the key feature of this robot. They are compact, high-performance dc brushless servo motors with a high pole count and low inductance, thus permitting high torque generation and rapid phase commutation. Using a custom-designed digital signal processor-based controller board, the pulse width modulation power amplifiers regulate the fast dynamics of the motor currents. In addition, the programmable digital signal processor (DSP) controller permits implementation of nonlinear compensation algorithms to account for motoring vs regeneration, torque ripple, and back-EMF. As a result, the motors produce a high torque relative to their size and weight, and can do so with good torque regulation and acceptably high velocity saturation limits. This paper presents the Unique Mobility Corporation robot prototype: its actuators, its kinematic design, its control system, and its experimental characterization. Performance results, including saturation torques, saturation velocities and tracking accuracy tests are included.

1 Introduction

The Unique Mobility Corporation (UNIQ) robot is a mechanical arm whose construction was commissioned by the NASA Lewis Research Center, under a small business innovative research contract [1]. It is a compact, powerful, lightweight robot designed for possible use in space applications, where space and mass are at a premium. The purpose of this project

*In memoriam.

was to construct high torque-to-mass density actuators based on the high pole-count Unique Mobility design, compare relative performance of these actuators to competing industrial servomotors, and implement the actuators into a light-weight three-axis robot arm and evaluate their installed performances. This report provides an overview of the project findings and indicates methods by which the robot actuator performances can be improved.

2 General Characteristics of the Robot Arm

The robot has several unique design features.

To save weight without sacrificing stiffness, the links were constructed using a composite of carbon fibers interlaced through an epoxy matrix, instead of using aluminum or steel. This makes it much lighter than aluminum, with much of the strength of steel[2, 3, 4, 5, 6].

The robot uses three compact, high torque-to-mass density three-phase brushless DC motors custom-designed by Unique Mobility Corporation. Wasted space was minimized by fully integrating the sensors, rotor and harmonic drive, resulting in a highly compact design. Each motor has about twice the torque-to-mass ratio of existing servo motors, as will be discussed. They have a high pole count and low phase inductances, which allow high torque generation and rapid commutation [7]. They also have a full complement of sensors: thermal sensors, a motor resolver and two output shaft resolvers (one for coarse angle measurements, one for finer measurements). While the motor resolver reports the angular position of the motor shaft itself (i.e. before the harmonic drive), the output resolvers sense the joint angle, or the position of the shaft after the harmonic drive.

Each motor is connected to a sophisticated controller card which uses surface-mount technology to incorporate features in a compact assembly. Each card has its own microprocessor (an N80C196KC chip), on-board memory and I/O processing devices. The digital signal processor-based cards [8] are responsible not only for motor commutation and current control, but for such tasks as sensor output processing and back-EMF compensation. These features are discussed more thoroughly in Section 3.3.

Output torque is sensed through a custom designed torque sensor that can be used for torque feedback control. The torque sensor consists of a spoked-wheel driven at its hub by the harmonic drive output and connected to the robot link at its outer ring. Calibrated strain gages mounted on the root of the structurally optimized spokes provides the desired torque signal.

3 Hardware Description

3.1 Motor Design and Performance

As explained above, the UNIQ motor was designed to have a high power density and high torque to mass ratio. To demonstrate that these goals were achieved, the UNIQ motor

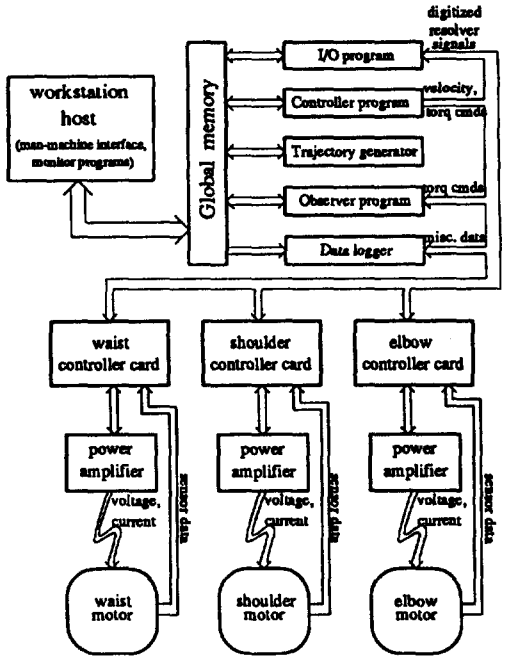

Figure 1: Hardware block diagram

was compared to two similar actuators on the market. The other motors were chosen to have similar torque limits as the UNIQ motor (about 400 $N \cdot m$). However, this is where the similarities end.

The comparison is not a direct one as the UNIQ motor was designed to be used with a harmonic drive which is limited to 2000 rpm and the other motors were not. The other motors will produce much more power for the same amount of torque simply because of the increased speed. In addition, this implies that the other motors have a lower back EMF constant, and thus, a lower torque constant. As a result, the other motors require more current and generate more heat due to I^2R losses.

Another difference is the packaging of the motors. The UNIQ motor has a larger diameter, and has a cavity in the center which is used to house other mechanical components. The other motors, on the other hand, are designed as compact, stand alone units. The UNIQ motor was designed with a specific application in mind, the 3 degree of freedom arm. Therefore a direct comparison shows the UNIQ motor is penalized by the greater diameter and volume as well as the additional weight due to the larger structural components. The additional torque available due to the UNIQ motor's 1:100 harmonic drive ratio is a distinct advantage in the torque density comparison, without the adjustments discussed below.

Yet another difference lies in the environments the motors are designed to work in. The UNIQ motor was designed for a space environment where the heat rejection would

be by radiation only. The other motors were designed for use in the atmosphere, where convection also helps cool the motors. In order to make an equal comparison, the other motors' torque (at 2000 rpm) was derated by the ratio of the temperature rise of the UNIQ motor (60°C) divided by the other motors' temperature rise (90°C).

The torque figures used for the UNIQ motor have not been adjusted to remove the frictional torque from the oversized bearings as well as the friction from the harmonic drive.

Because of these inequities we have shown two comparisons. The first one is a direct system comparison ignoring all of the inconsistencies (Table 1). The second comparison is a motor only comparison using only the torque producing components (TPC) and constraining the other motors to run at 2000 rpm and to run at a derated torque level due to the temperature (Tables 2 & 3). The harmonic drive has been removed from the volume, weight, and torque output of the UNIQ motor.

The motors used in this comparison were the Industrial Drives model #B-104-A-22 (henceforth referred to as the I.D. motor), and the Pacific Scientific model #R32GENC-R2-NS-NV-00 (the Pac Sci motor).

Table 1: Direct motor comparison

	I.D. motor	Pac Sci motor	UNIQ motor
Total Mass (kg)	3.02	3.13	8.62
Total Torque ($N \cdot m$)	0.0467	0.0467	4.92
Total Speed (rad/s)	590.0	470.0	2.09
Total Power (W)	881	707	331
Total Volume (m^3)	0.00118	0.00124	0.00221
Total Power Density (W/m^3)	747,000	570,000	150,000
Total Torque Density (N/m^2)	39.6	37.7	2230
Efficiency (%)	72.0	74.7	?

Table 2: Torque producing components (motor only) comparison

	I.D. motor	Pac Sci motor	UNIQ motor
TPC Mass (kg)	1.45	1.68	1.16
TPC Volume (m^3)	0.000305	0.000331	0.000270

As was expected the direct system comparison of the power density of both the I.D. and Pac Sci motors were much greater than the UNIQ motor, because of the extra power

Table 3: Derated output for temperature and lower speed

	I.D. motor	Pac Sci motor	UNIQ motor
Continuous Power (W)	210	210	331
Continuous Stall Torque ($N \cdot m$)	0.0703	0.0643	0.105
TPC Power Density (W/m^3)	689,000	634,000	1,230,000
TPC Torque Density (N/m^2)	230	194	389
TPC Power/Mass (W/kg)	144	125	285
TPC Torque/Mass ($N \cdot m/kg$)	0.0485	0.0383	0.0905

due to the increased speed and smaller volume due to the compact design. Obviously the UNIQ motors' torque density was much larger due to the harmonic drive.

Once the motors were compared on a more equal, torque producing component basis, we see that the UNIQ motors' power density and torque density are greater than the I. D. and Pac Sci motors. The power to mass ratio of the UNIQ motor is 1.9 times greater than the I.D motor and 2.3 times greater than the Pac Sci motor. The torque to mass ratio of UNIQ's motor is 1.9 times greater than the I.D. motor and 2.4 times greater than the Pac Sci motor.

3.2 Robot Arm Geometry

The arm itself has three degrees of freedom. Each of its three links is driven at the joint by a small but powerful high-performance motor. Joints 1, 2 and 3 are referred to as the "waist," "shoulder," and "elbow," respectively. The robot arm is designed to move payloads of up to 15 Kg at a reach of 1 meter at speeds of up to 2 m/s at the robot wrist.

3.3 Controller Cards

The joint controller cards handle many different tasks. First, the cards are responsible for reading the various sensor signals and converting them to digital form. These sensors comprise the motor shaft (or input) resolver, the coarse and fine output resolvers and temperature sensors on the motors, the strain gages, and the bus voltage and current sensors on the power amplifiers. The digitized readings are stored in a structure on the card's on-board memory, which can be read by programs running on either the host computer or the CPU cards connected to the VME interface (see Section 3.4).

Second, the cards handle motor commutation. That is, they accept torque commands from the controller program support module (see Section 4.1 for details), and control the phase currents based on the resolver signals.

Third, the cards also function as motor current controllers. Using proportional and integral feedback, they make sure that the actual current closely follows the desired current.

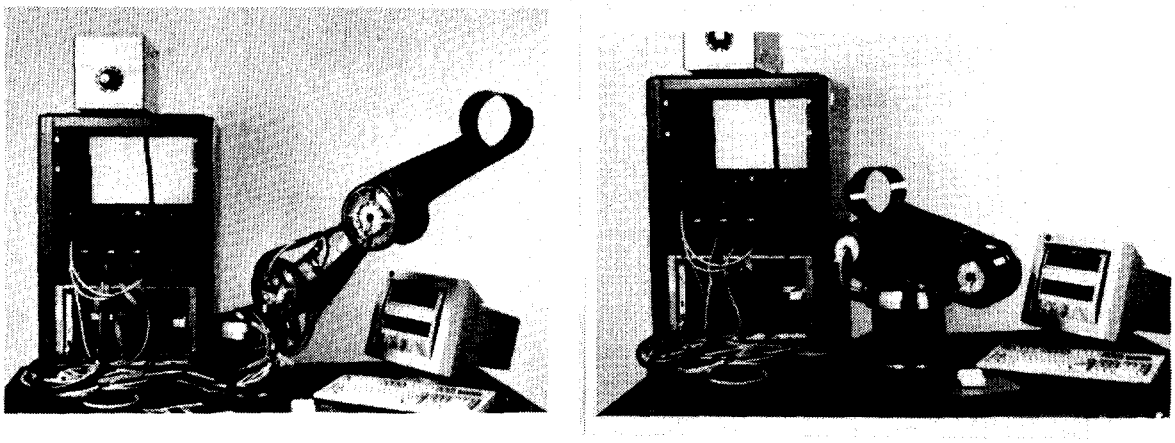

Figure 2: The UNIQ robot arm, controller rack and man-machine interface. Robot fully extended (left) and in stowed position (right)

Their fourth function is to handle switching over from torquing to braking. When the motors are being accelerated, power is delivered from the amplifiers (see Section 3.5) to the motors. During deceleration though, power is regenerated, or transferred back to the amplifiers. To prevent amplifier overload, this power is dumped into several ceramic load resistors instead. The controller cards are responsible for determining when this switching should occur, and for shunting the power into the resistors.

Finally, the cards are responsible for reporting any errors that may occur in torque generation. For instance, if the amount of torque requested exceeds the motor limit, or if a power amplifier appears to be off, the cards report a fault status by setting a variable in their on-board memory. This fault status can thus be detected by other programs on the host or on the VME cage.

3.4 VME interface

To maximize the software's speed and effectiveness, several of the processes must be executed in parallel [9, 10]. The VME interface makes this possible [11, 12].

This interface connects the host computer to a VME card cage. The host is a Sun workstation running UNIX, which serves as the man-machine interface. The card cage, on the other hand, carries several single-board computers (henceforth referred to as "CPU cards") and the aforementioned joint controller cards.

The card cage permits the host, CPU cards and controller cards to communicate with each other. This is done by allowing the host and CPU cards to read and write to the

memory on board both the controller cards and other CPU cards.

The cage uses six CPU cards. Four of these are reserved for the various support modules (see Section 4.1 for details). The fifth is used for the data logging process. The last one functions as a global storage location for variables that are accessed by multiple processes.

3.5 The Power Amplifiers

Each of the three controller cards is connected to a pulse width modulation (PWM) power amplifier, [7, 14, 13] which is in turn connected to one of the motors. These amplifiers are responsible for generating the current which drives the motors. They are also responsible for shorting the motor phases together, when the power is turned off. This effectively acts as a brake, preventing the robot from falling rapidly under gravity loads with the amplifiers off. It is recognized that additional mechanical braking will be required in service.

The controller program support module on one of the CPU cards (Section 4.1) computes the three desired joint torques, and stores these values at designated addresses on the controller cards' dual-port RAM. The cards then perform the motor commutation (as explained earlier in Section 3.3), ordering the amplifiers to produce the proper currents.

4 Software Description

4.1 Support Modules

The software interface to the robot can be divided into five components. The highest-level module, the man-machine interface, runs on the host computer. It is supported by four more modules, which require much more computational speed. These programs run on separate CPU boards in the VME cage.

The I/O program's purpose is to report the motor shaft angles and velocities as quickly and as efficiently as possible. The angles are computed by monitoring the motor resolver readings and the number of rotor revolutions, from which the motor shaft angles can be computed. The velocity can be computed in any of three ways: (1) through raw differentiation of the shaft angle, (2) by digitally filtering the results of this raw differentiaton, to produce a smoother velocity estimate, or (3) by using the velocity estimates returned by the observer program. Under normal operation, the observer-estimated velocity would be used, since it produces the smoothest, most reliable results [17].

The controller program uses a combination of servo control and feedforward torques to make the robot follow its prescribed trajectory. To compute these torques, it uses the actual angles and velocities reported by the I/O program, as well as the desired angles, velocities and accelerations computed by the trajectory generator.

The observer uses the commanded torques and a model of the robot dynamics to estimate the joint velocities. This produces a much smoother velocity estimate than

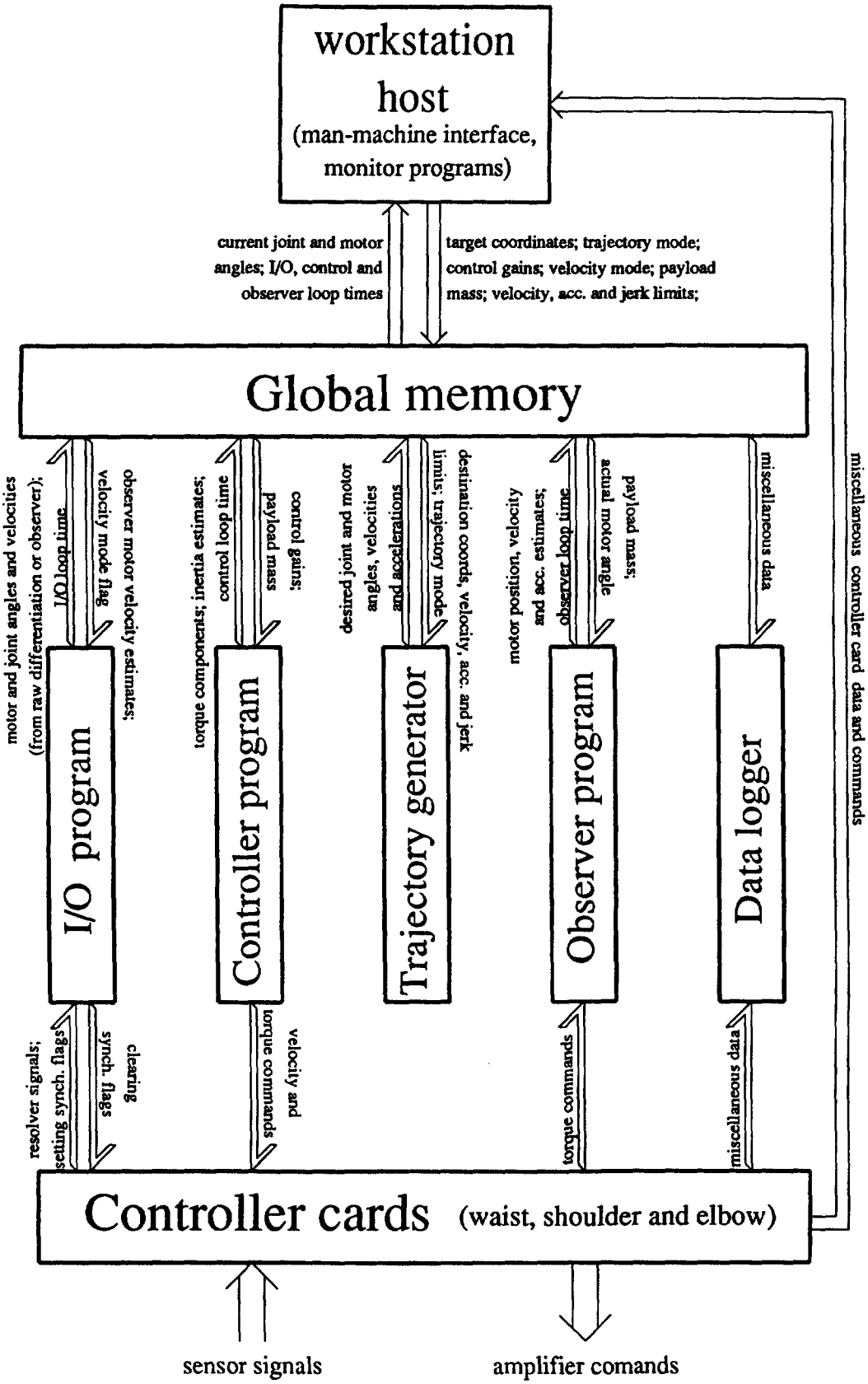

Figure 3: Data flow block diagram

what would be obtained through other means [17].

At present, the observer only works reliably during current control mode (see Section 5.1). It has not yet been fine-tuned for use in voltage control mode. This was partly due to the difficulty of accurately gauging the generated torques in this mode, and partly because velocity feedback is not currently used in voltage control mode.

This trajectory generator computes a smooth trajectory from the robot's current position to some target position. This can be done in either joint space or Cartesian space, subject to user-specified limitations on the velocities, accelerations and jerks. The constraints are imposed to increase the smoothness of the trajectory execution [16]. The computational complexity of the equations used was minimized [19], thus increasing the speed and accuracy of the trajectory generator [18].

4.2 Data logging software

The data logging software is similar to the four support modules in that they also run on a CPU board in the VME cage. They differ in that they are not necessary for operating the robot. However, they are useful for gathering data on various hardware and control variables as the robot is in operation. The logger samples various control-related variables and stores them in a MATLAB data file. This is explained in the report by Velasco [19].

4.3 Interface Programs

The man-machine interface is the program through which all user interaction occurs. Its operation is demonstrated in the report and video by Velasco and Newman [1, 19]. Among other things, it can be used to specify Cartesian or joint-space trajectories and impose jerk, acceleration and velocity limits. It also pre-tests each trajectory, to verify that it is physically permissible (e.g. will not cause collisions or violate joint angle limits).

In addition, the system boasts of a variety of interfaces for monitoring both hardware variables like bus voltage and motor temperature, and control parameters like desired positions and control gains.

5 Control System

5.1 Current Control

The original scheme for driving the motors involved current control. In response to torque commands from the software, the controller boards command the amplifiers to generate the required motor currents. This is done using motor current feedback and a servo control algorithm with proportional and integral gain. Based on this control law, the controller boards command the amplifiers to generate voltage pulses, or pulse width modulation (PWM) signals. These are used to make the motor currents converge to the desired values. In addition, the controller compensates for back-EMF effects by adding

an additional term to the PWM signals. This term is proportional to the motor velocity, and thus serves to counter the back-EMF voltage.

It was discovered, however, that the current sensing scheme led to problems with the current control algorithm. The controller boards sample the current readings at 8.0 kHz, while the PWM frequency is 15.63 kHz. Furthermore, the low phase inductances (79 μH) allow the currents to change quite drastically. (This is discussed further in Section 7.1.) As a result, the current readings are undersampled and do not provide a completely accurate measure of the motor currents. This is shown in Figure 4, where we see that the current sensor reading has strong oscillations. The vigorous current oscillations caused a grinding noise to issue from the motors whenever the robot was in motion.

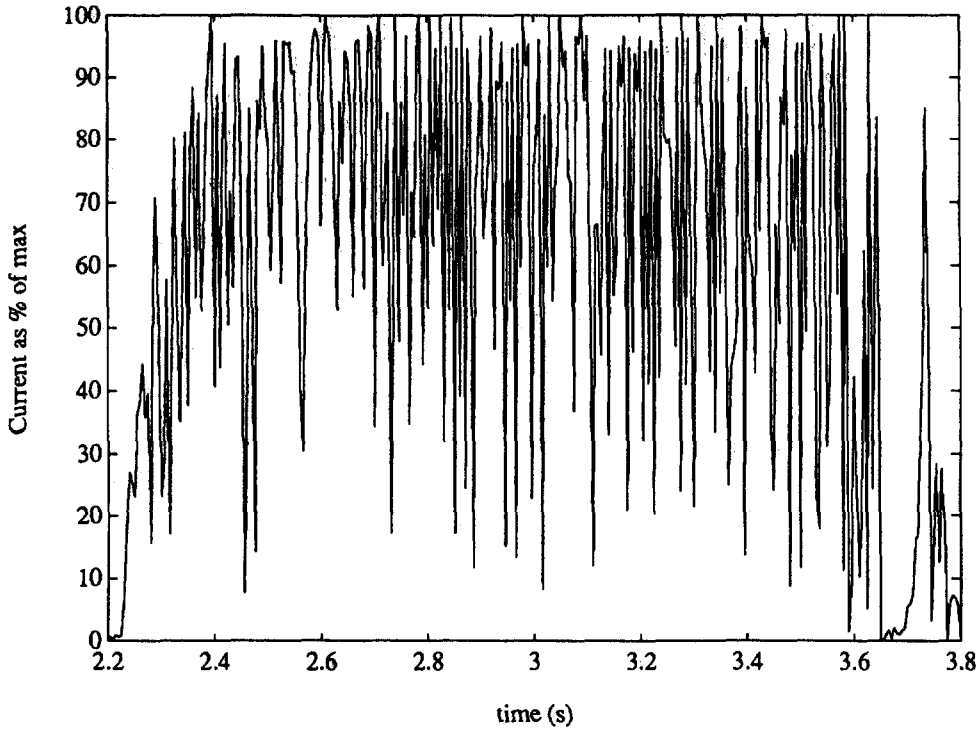

Figure 4: Elbow current readings under current control

5.2 Voltage control

To circumvent this problem, a new scheme was introduced to dispense with current feedback altogether. Instead of controlling the torques by modulating the motor currents, the boards controlled the velocities via the voltage pulses, with inherent back EMF performing equivalent velocity feedback [7, 15].

An additional PWM component is needed to generate a holding torque. This means that even when the arm is at rest, non-zero voltage pulses will be generated to prevent the arm from falling due to gravity. At zero velocity, this PWM component is proportional

to the desired torque. Under this scheme, the net PWM signal is simply the sum of the velocity-dependent and torque-dependent terms and does not rely on current feedback. (As discussed in Section 6 however, it turns out that this is not strictly true during current regeneration. Under certain circumstances, the programs on the DSP-based controller boards actually compute the velocity-dependent terms with some dependence on the torque command. By and large though, the description above is correct.)

5.3 Torque computation

Under current control, the servo control laws used were of the form

$$\begin{aligned} \tau_{n,servo} &= K_{p,n}(\theta_{n,des} - \theta_n) + K_{d,n}(\omega_{n,des} - \omega_n) + \\ & \quad K_{i,n} \int (\theta_{n,des} - \theta_n)\, dt \end{aligned} \tag{1}$$

where saturation limits were placed on the integrated error term on the right. In practice though, the integrator gains $K_{i,n}$ were set to zero because adding integral control caused oscillations in the final position. An explanation of this behavior is given in Section 7.2.

It proved useful to use two sets of control gains: one set of large gains when the joint velocity was greater than some tolerance, and smaller gains when the velocities are below some tolerance. Adjusting these gains on the fly increased the tracking accuracy at high velocities while preventing oscillations at lower speeds.

These servo torques were combined with feedforward torques to produce the net torque commands. These feedforward torques took into account ideal robot dynamics, gravity and friction.

Under voltage control, the net torque commands are simply given by

$$\tau_{n,servo} = K_{p,n}(\theta_{n,des} - \theta_n) \tag{2}$$

As of this writing, neither velocity feedback, integral feedback nor feedforward torques have yet been included. This is because the routines for switching between motor driving and current regeneration will require some fine-tuning before it will work in voltage control mode. This is because the current routines result in occasional amplifier dropouts along the trajectories. Thus, at the moment the desired torques are not accurately generated under voltage control and the observer does not yet produce reliable velocity estimates. The explanation behind these dropouts is given in Section 6.

6 Data and Results

The tracking accuracy was gauged using sinusoidal joint trajectories and straight-line paths in both joint and Cartesian space, for all three trajectory profiles. Due to various malfunctions in the prototype, however, only two working controller cards and two amplifiers were available, so the final tests could only be done on the shoulder and elbow.

In general, trajectory tracking under current control was very accurate, despite the noise and current oscillations. Figure 5 shows the results of a sample move done using

the elbow under current control. The joint angle follows the desired values very closely, with a maximum error of only 0.0104 radians. The precision would be improved if the PWM resolution were increased, as discussed in Section 7.

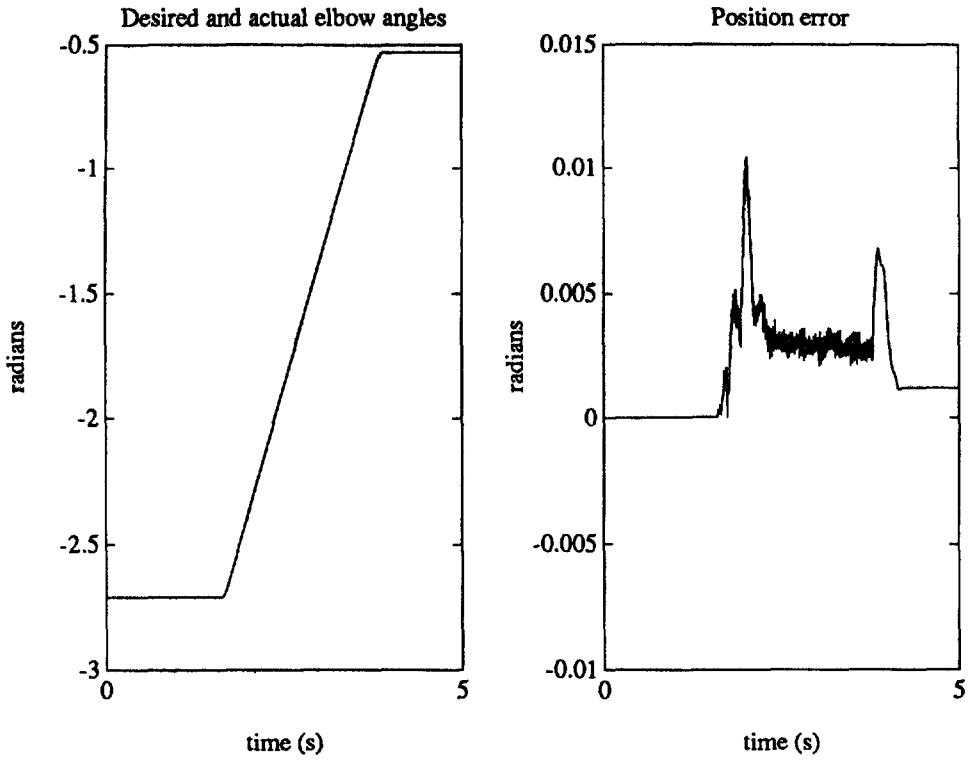

Figure 5: Elbow trajectory tracking under current control

Under voltage control, a bothersome high-speed amplifier switching noise was eliminated. However, Figure 6 shows that the tracking accuracy was not as high. The maximum position error is 0.0424 radians, and the error increases and decreases almost periodically. The decrease in accuracy is partly because of amplifier dropouts, and partly because the servo control gains were decreased to minimize the incidence of these dropouts.

The relationship between the amplifier dropouts and the trajectory tracking is shown in Figure 7. As can be seen from this and the previous plot, the PWM command drops to zero whenever the position error (and thus, the torque command) becomes negative. The cause of this behavior is explained in Section 7.3.

It is believed that when these problems are fixed, the tracking accuracy under voltage control would be comparable to, or greater than, that achieved with current control. It would permit the use of larger control gains, which should greatly increase the tracking accuracy. Tests show that when the position error gain is multiplied by twenty, the number of dropouts increases, but the maximum position error is 0.0234 radians—only about twice that achieved with current control. Without the amplifier dropouts, both the tracking accuracy and the final position error would doubtlessly be much smaller.

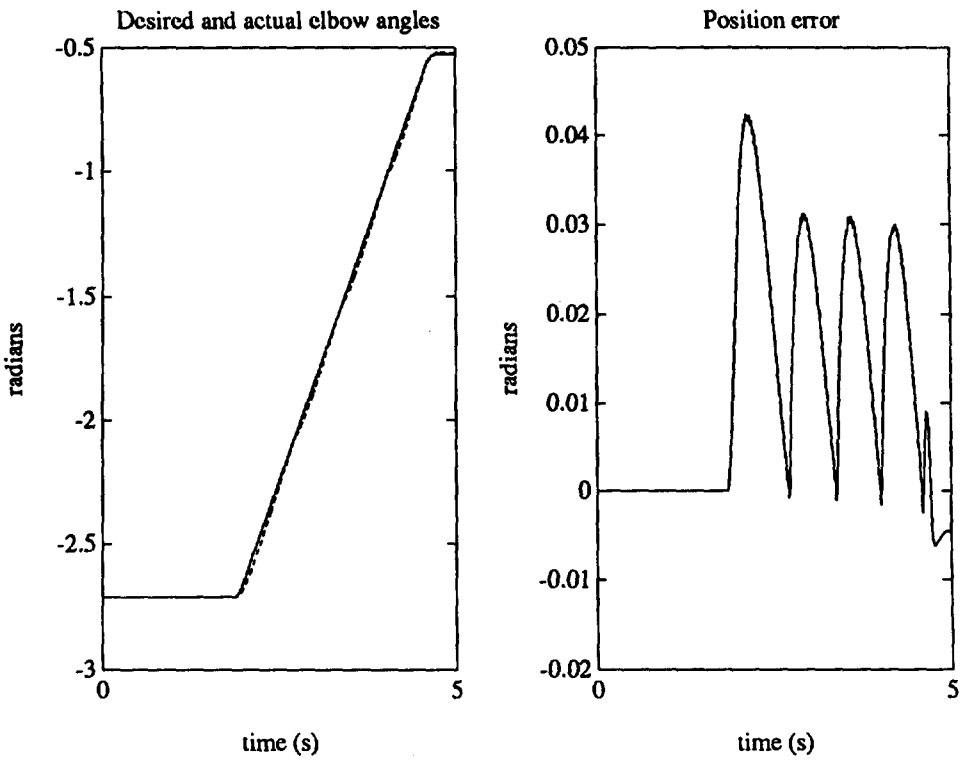

Figure 6: Elbow trajectory tracking under voltage control

7 Analysis

7.1 Current control vs. voltage control

As discussed in Section 6, the low motor inductances, while otherwise desirable, created complications by allowing the currents to change dramatically. At the design PWM frequency, the control hardware could not sample the current readings quickly enough to use them effectively in feedback. Computer simulations show that a single-phase excitation at the PWM frequency of 15.63 kHz and a 50% duty cycle would produce peak-to-peak current swings of up to 16 A. Since the current sensor only samples data at 8 kHz, it obtains a false profile of the actual current. This is aggravated when the profile is used in feedback, resulting in the vigorous high-frequency dynamics in Figure 4. These dynamics manifested themselves as a bothersome grinding noise and rapid position error oscillations [1, 19].

Implementing voltage control eliminated the bothersome noise and error oscillations which resulted from current control. It may be possible, however, to mitigate these effects by increasing the phase inductances. These inductances were kept small in order to achieve high-speed commutation; however, this was done at the expense of accurate current control. To avoid degrading the performance, one would want to maintain an effective stepping rate at the saturation velocity of 200 rad/s and the phase switching rate of 24 times per cycle. Computations show that the inductances can be comfortably

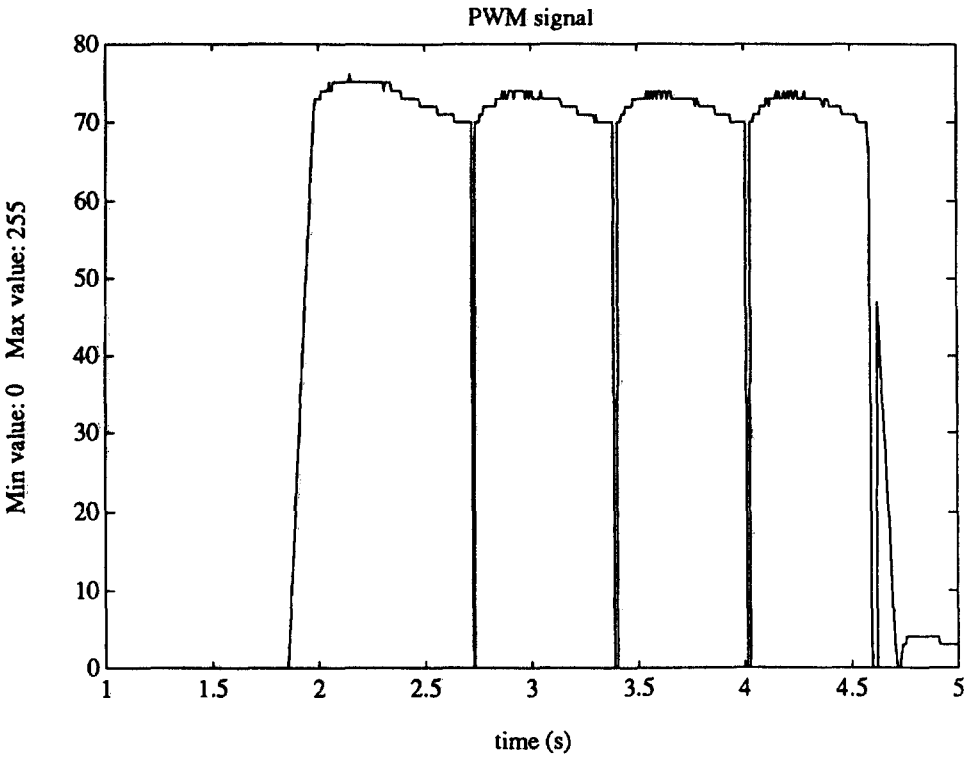

Figure 7: PWM signals for trajectory under voltage control

raised by about 270%. In practice, the inductance may have to be smaller than that, for fine commutation. Nevertheless, this estimate establishes an approximate upper limit to the inductances that can be used.

Increasing the PWM frequency should also reduce the size of the oscillations. In fact, computer modelling shows that by doubling the inductances and increasing the PWM frequency five-fold, the current oscillations can be reduced to one-tenth of their previous value. Similarly, position control error would be reduced as well.

7.2 PWM resolution

The PWM commands are linear combinations of a velocity-dependent term (which counters the back-EMF) and a torque-dependent term. These signals can assume any value from 0 to 255, where zero corresponds to no voltage and 255 corresponds to a duty cycle of 100%.

It was found that at zero velocity, the PWM count which corresponds to maximum torque is about 24. This limits the available torque resolution, and thus, the positioning accuracy. It also accounts for the oscillations that occured with integral error feedback (Section 5.3), and for the difficulties encountered in compensating for the friction. However, this problem can be addressed with some modest modifications to the control hardware.

7.3 Controller board routines

When the system was modified to accomodate voltage control, the resultant arm motion was very smooth, except that the amplifier would drop out on occasion. As shown in Section 6, this is because the PWM signal would drop down to zero whenever the controller board would switch into regeneration mode.

Close examination of the controller board program listing reveals why. Ordinarily, the PWM command is computed based on two terms: one torque-dependent, and one dependent on a velocity command. However during current regeneration, if the torque command is small enough, the second term is computed as being proportional to the commanded torque and inversely proportional to the velocity command. This creates two problems. One is that the PWM command actually decreases as the size of the velocity command increases. The other is that due to discretization errors, a small torque command may make the PWM signal small or even zero. These problems can be readily addressed via some modest changes to the PWM equations used by the controller board firmware.

8 Summary and Conclusions

As expected, the UNIQ motor outperformed other motors in its class. The motor's high power density, high torque to mass ratio and efficient heat dissipation, coupled with the compact, lightweight robot design provides many attractive features for space-based robot applications.

The comprehensive hardware and software developed for the robot permitted accurate trajectory tracking, flexibility and user-friendliness. However, the performance can be improved by modifying the controller board routines and by increasing the PWM frequency, the PWM resolution and the phase inductances.

9 Acknowledgements

This project was supported by a grant from the NASA/Lewis Research Center under contract NAS3-26285.

References

[1] Unique Mobility SBIR Phase II Final Report, Contract NAS3-26285.

[2] Gill, Richard Malcolm. *Carbon fibres in composite materials.* Iliffe Books for the Plastics Institute, London, 1972.

[3] Delmonte, John. *Technology of carbon and graphite fiber composites.* R. E. Krieger Publishing Company, Malabar, Florida, 1987.

[4] Sichel, Enid Keil. *Carbon black-polymer composites: the physics of electrically conducting composites.* M. Dekker, New York, 1982.

[5] Buckley, J. D. and Edie, D. D. *Carbon-carbon materials and composites.* Noyes Publications, Park Ridge, New Jersey, 1993.

[6] Parker, Sybil P., ed. *McGraw-Hill encyclopedia of engineering, second edition.* McGraw-Hill, Willard, Ohio, 1993.

[7] Krause, P. C. and Wasynczuk, O., *Electromechanical Motion Devices.* McGraw-Hill, New York, NY, 1989.

[8] Stanley, W. D., Dougherty, G. R. and Dougherty, R. *Digital Signal Processing.* Reston Pub. Co., Reston, Virginia, 1984.

[9] J. Ish-Shalom and P. Kazanzides. SPARTA: Multiple signal processors for high-performance robot control *IEEE Transactions on Robotics and Automation*, 5(5):628-640, 1989.

[10] Hwang, K. and Briggs, F. A. *Computer Architecture and Parallel Processing.* McGraw-Hill, New York, 1984.

[11] Newman, W. S., "The CAISR Mechatronics Lab Real-Time Multiprocessor System: Theory and Operation," Technical Report TR-89-144, Center for Automation and Intelligent Systems Research, Case Western Reserve University, Cleveland, Ohio, October 1989.

[12] Black, John, ed. *The System Engineer's Handbook: A Guide to Building VMEbus and VXIbus systems.* Academic Press, San Diego, 1992.

[13] H. Sira-Ramirez, M. Zribi and S. Ahmad. Pulse width modulation control of robotic manipulators. *International journal of systems science*, 24(8): 1423, 1993.

[14] Sarjeant, W. J. and Dollinger, R. E., *High-Power Electronics.* TAB Professional and Reference Books, Blue Ridge Summit, Pennsylvania, 1989.

[15] Bose, Bimal K., *Adjustable Speed AC Drive Systems.* IEEE Press, New York, NY, 1980.

[16] Brady, Michael, et al. *Robot Motion: Planning and Control.* The MIT Press, Cambridge, MA, 1984.

[17] Franklin, G. F., Powell, J. D., and Workman, M. L., *Digital Control of Dynamic Systems.* Addison-Wesley, New York, 2nd edition, 1990.

[18] Maron, Melvin J. *Numerical Analysis: A Practical Approach, 3rd ed..* Wadsworth Pub. Co., Belmont, California, 1991.

[19] Velasco, Virgilio B. Jr., "Characterization and Control of the Unique Mobility Corporation Robot Prototype" Technical Report TR-93-142, Center for Automation and Intelligent Systems Research, Case Western Reserve University, Cleveland, Ohio, December 1993.

DEVELOPMENT OF AN INTERCHANGEABLE END EFFECTOR MECHANISM FOR THE RANGER TELEROBOTIC VEHICLE

Robert Cohen and David L. Akin
University of Maryland
College Park, Maryland

Abstract

The Ranger program at the Space Systems Laboratory (SSL) at the University of Maryland is a demonstration of an extremely low cost, space flight experiment. The Ranger vehicle is designed to perform teleoperated spacecraft maintenance. Completing the various tasks included in spacecraft maintenance requires several specific tools. This paper describes the Ranger interchangeable end effector mechanism (IEEM). Its design allows Ranger to change end effectors to utilize the appropriate tool for the various tasks.

The Ranger vehicle is designed with four manipulators. A seven degree-of-freedom (DOF) grappling manipulator securely attaches the vehicle to the work site. A 6 DOF camera positioning manipulator allows the operator to position a stereo pair of video cameras for visual feedback. The two remaining manipulators are the 7 DOF dexterous arms. They are the primary means by which Ranger accomplishes its required tasks. At the end of each of these dexterous manipulators is an IEEM.

This paper begins with a brief overview of the Space Systems Laboratory and the Ranger program. The constraints leading to the requirements for an IEEM are described. The following section then describes the design strategies and the down selection process resulting in two candidate designs, taper and pneumatic connector type. Next, the leading candidate design is described in detail, followed by a preliminary discussion of failure modes and planned testing. The paper concludes with a brief review and a section discussing future work.

Acronym List

EVA	Extra Vehicular Activity
NB	Neutral Buoyancy
NBRF	Neutral Buoyancy Research Facility

NBV	Neutral Buoyancy Vehicle
RSIS	Robotic Systems Integration Standards
SSP	Space Station Program
TFX	Telerobotic Flight Experiment

Introduction

For many years the Space Systems Laboratory has studied how to do useful work in space with a particular emphasis on neutral buoyancy simulation of the micro gravity environment. The primary approaches are to understand how a person performs useful work in weightlessness, how machines operate in weightlessness, and how the two can work together. Neutral buoyancy was chosen as the weightless environment simulation for the Ranger program. This environment allows motion in all 6 DOF, but also introduces some new challenges. For example: the vehicle must be water tight, and the center of mass must coincide with the center of buoyancy to insure rotational neutral buoyancy.

The SSL has developed several telerobotic systems for operations in the neutral buoyancy environment. The Ranger neutral buoyancy vehicle (Ranger NBV) is the newest system to come on-line in the SSL. Ranger NBV, shown in Figure 1, is the development and test unit for the Ranger telerobotic flight experiment (Ranger TFX), shown in Figure 2.

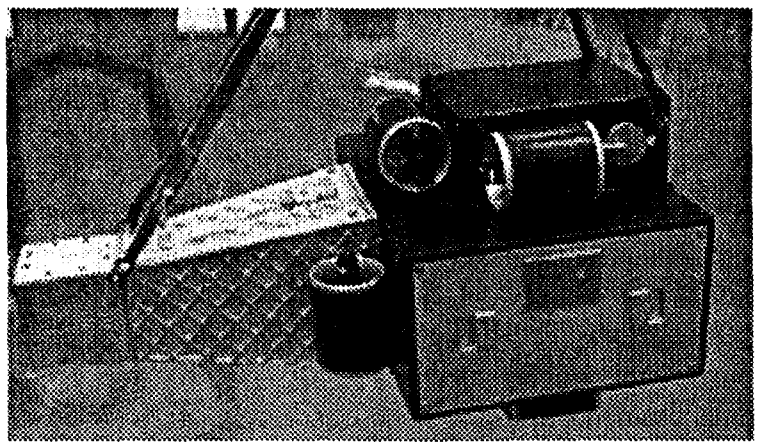

Figure 1. Ranger NBV

Ranger Background

Ranger is a telerobot designed to perform complete, end-to-end spacecraft maintenance operations. These include rendezvous and

docking with a target vehicle, performing a specified task set and departing from the target vehicle. A specified task set includes, but is not limited to, structural assembly, orbital replacement unit (ORU) changeout, battery changeout and satellite refueling. These tasks represent some of the operational research aspects of Ranger. Some of the science and engineering data expected from the Ranger program include: a correlation of the neutral buoyancy environment with the space environment, advanced telerobotics design and control, remote telerobotic maneuvering, human factors of ground based control for space telerobots, and advanced small spacecraft technology (Reference 1).

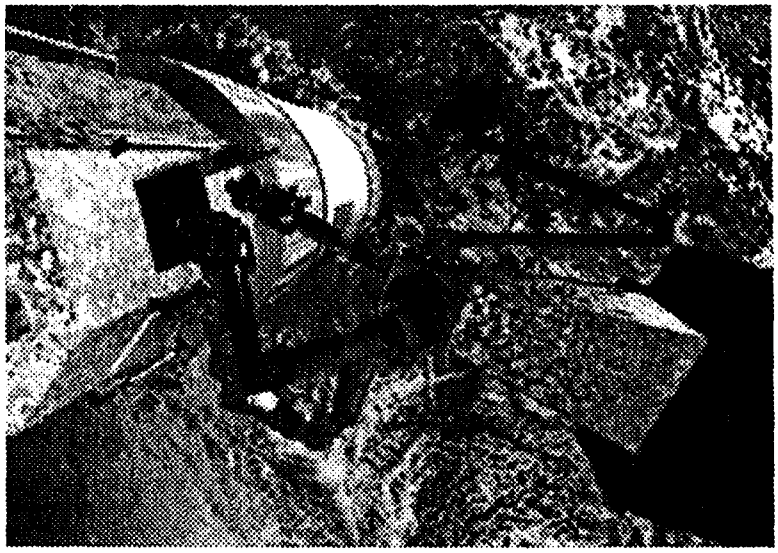

Figure 2. Ranger TFX

The Ranger program's objective to perform spacecraft maintenance operations is realized with the dexterous manipulators. These are 7 DOF, serial, revolute manipulators, designed with a similar work envelope and force exertion capabilities as those of a human. The envelope and force capabilities come from the requirement to operate EVA-type interfaces per NASA STD-3000. See Reference 2 for a more complete discussion of the Ranger manipulators.

In pursuit of the spacecraft maintenance goal, the SSL has accumulated a knowledge base using the Beam Assembly Teleoperator (BAT). BAT has demonstrated the capability to service the extra vehicular activity (EVA) crew training mock-up of the Hubble Space Telescope (HST) at Marshall Space Flight Center's (MSFC) Neutral Buoyancy Simulator (NBS) as shown in Figure 3. During this series of

tests, the limitations of BAT's 5 DOF dexterous arm and a fixed end effector became apparent. These tests contributed to the requirement for an IEEM on Ranger.

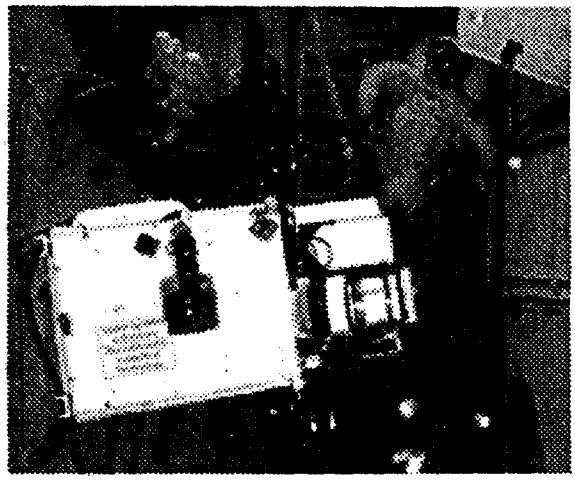

Figure 3. BAT servicing HST

Requirements

During launch, the arms will be configured with the nominal end effector for the initial flight task set installed. This reduces the risk of failure due to a missed end effector exchange early in the mission. The end effectors must be securely stowed in the storage rack for launch. A pyrotechnic or a similar type device will remove the launch restraints allowing the end effectors in the storage rack to engage and release.

The end effector selection for Ranger is based on the accepted robotic interfaces for space hardware as defined in NASA Robotic Systems Integration Standards (RSIS), NASA - SSP 30550 as well as SSL experience. This document requires Ranger to actuate H-handles, micro-conical interfaces, etc. The H-handle interface requires the end effector to have 2 DOF. Therefore, the IEEM shall have two mechanical drives to provide power.

During any kind of exchange, whether an ORU or end effector, there is a possibility of a missed exchange. This is particularly important in space as a missed exchange can easily result in loss of the ORU/end effector. The IEEM requires safeguards such that "no new satellites" are created.

Due to power, size and complexity constraints the latching mechanism shall be passive, requiring no electrical power to latch or

release the end effector. The mechanism for Ranger NBV must be as similar as possible to the mechanism for Ranger TFX. Since the Ranger NBV version of the IEEM will operate in the NB environment, it must be waterproof. Therefore, electrical connectors between the end effector and the wrist are inappropriate.

Design Strategies

A method of identifying options for candidate designs was employed for the down selection process. The method chosen was the development of an options tree (Figure 4).

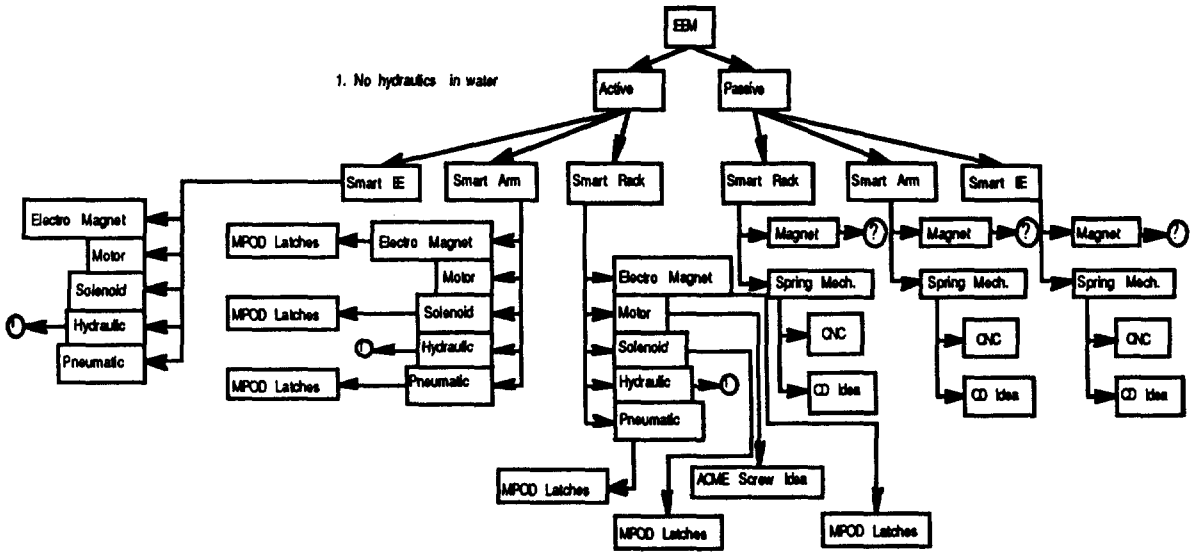

Figure 4. IEEM Options Tree

The options tree started from the general premise of needing a mechanism allowing Ranger to change the current end effector and flowed down to the specific candidates chosen. The process led to the selection of two candidate concepts, a taper design and a pneumatic connector-type design.

The first candidate IEEM is based on a torsional spring providing the force to rotate a cam and pin system (see Figure 5). The outer collar rotates relative to the inner post and the tool post, locking the tool post into the matching taper assembly. This provides the transmission path for the forces and torques to and from the end effector.

When removing the end effector, a set of fingers ride along a cam on the outside of the rotating collar forcing it to turn as the wrist is

pushed forward into the storage rack. This turning action releases the end effector post from the manipulator and it is captured by a similar device on the storage rack side.

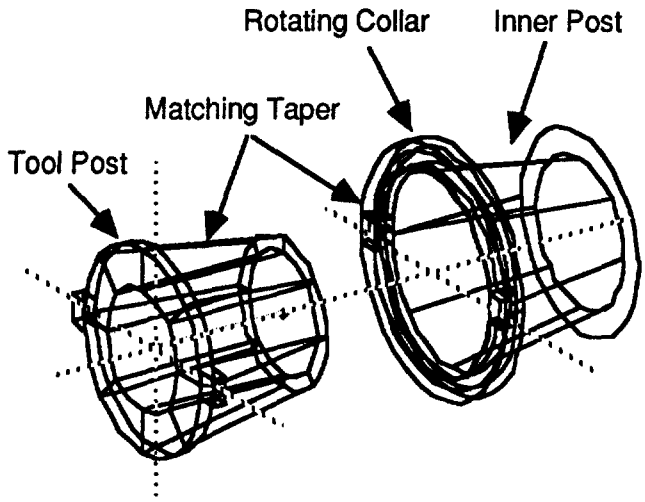

Figure 5. Taper Mechanism Description

The second candidate design is modeled after a pneumatic connector. This design applies a force using a spring loaded device to steel ball bearings in contact with the tool post (Figure 6).

A proof-of-concept article was manufactured demonstrating the functionality of this design. Due to cost considerations and ease of manufacture, some of the materials used were not those of the final design. The entire proof-of-concept article is made of aluminum. The prototype will include parts made from stainless steel for durability.

Figure 6 shows the second candidate IEEM in detail. The spring cavity is where the spring providing the holding force is located. The proof-of-concept version relies on 8, 3.175 mm (0.125 in) diameter springs in parallel to provide the holding force. The prototype version will have a custom-wound wave spring, 111 mm (4.375 in) in diameter. This approach ensures the candidate concept is valid before purchasing the custom wound spring. This provides a simple, low-cost method to evaluate the spring constant.

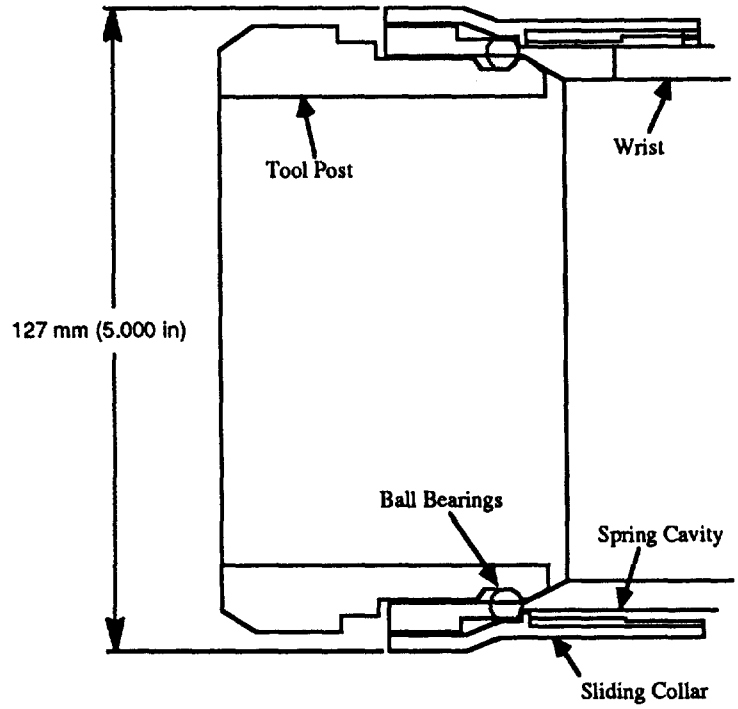

Figure 6. Latching Mechanism

The springs chosen for the proof-of-concept article are 110 kPa (16 psi). The sliding collar compresses 4.76 mm (3/16 in) during attachment and release operations. Applying the equation for a linear spring ($\vec{F} = k \cdot \Delta\vec{x}$) requires the arm to exert a maximum force of 13.3 N (3 lbf). The prototype version will have a spring constant of 55 kPa (8 psi). This softer spring will allow a greater range for the manipulator during the engagement process.

Figures 7 through 11 describe the engagement and release process:

Figure 7 shows the wrist aligned with the tool post and the sliding collar making contact with the retention finger.

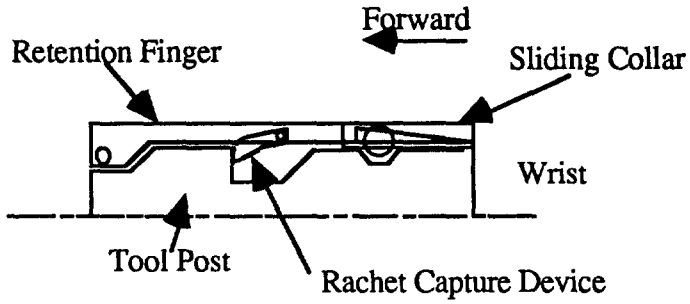

Figure 7. Latching the end effector

In Figure 8, the wrist has moved forward and the retention finger is compressing the spring inside the sliding collar. As the arm continues to push forward, the bevel at the end of the tool post engages the retention finger, pushing the spring loaded finger away. This motion allows the spring force in the sliding collar to move it forward. This wedges the ball bearings against the sliding collar and tool post, locking the end effector in place on the manipulator.

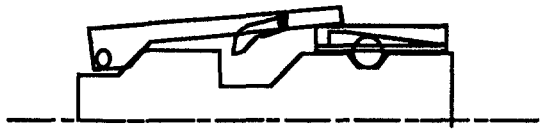

Figure 8. Latching the end effector

Next, the arm moves backward and removes the end effector from the storage rack as shown in Figure 9.

Figure 9. Removing the End effector from the storage rack

Figure 10 shows Ranger's wrist returning the end effector to the storage rack. As the wrist moves forward into the storage rack, the tool deflects a ratcheting capture device. When the arm moves the end effector far enough forward the capture device ratchets down. It now holds the end effector in the storage rack. During the forward motion, the spring in the sliding collar is also compressed by the retention finger. At the point of storage rack capture by the capture device, the spring in the sliding collar is compressed enough to free the wrist from the end effector.

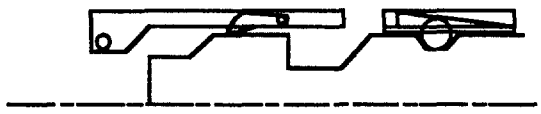

Figure 10. Re-inserting the end effector

At this point the manipulator can leave the end effector in the storage rack or to re-engage it, as shown in Figure 11.

Figure 11. Latching the end effector and withdrawing the arm

Two motors and gear trains provide the required mechanical power to the end effector. The current motor design uses Inland motors attached to pancake harmonic drives to actuate the end effector. The prototype mechanism will include a candidate latching mechanism, as described above, as well as the motors and gear trains for the two tool drives (See Figure 12).

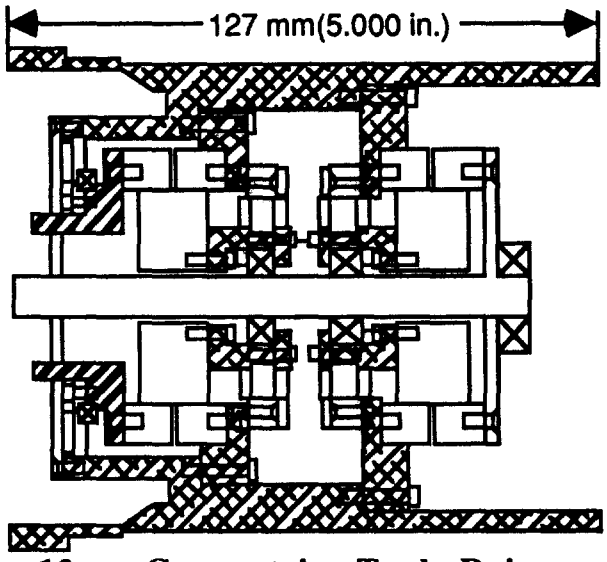

Figure 12. Concentric Tool Drives

Failure Modes

There are several possible modes that may cause complete failure of the candidate IEEM's. In the taper candidate design, the torsional spring performs all the work of engaging and releasing the tool. If the spring binds due to a temperature gradient or another reason, there is virtually nothing the operator can do to fix it.

The pneumatic connector-type candidate IEEM does not suffer from the spring reliability issue. It relies on the dexterous manipulator to provide the energy to make the engagement/release. It does, however, require the operator to maneuver the manipulator very precisely in order to place the end effector in the storage rack. If the wrist moves too far forward during the replacement operation, the

retention fingers would disengage. The end effector would then be recaptured by the sliding collar on the wrist. If this occurs, the end effector replacement process would have to start again. Although not a concern in regards to losing the end effector or jamming the IEEM, the limited time in a single test session makes this a real problem, especially for Ranger TFX. Alleviating this failure mode, requires systems external to the IEEM. A force torque sensor upstream of the IEEM, along with visual cues, will determine when the engagement and release has taken place.

Testing

The testing the IEEM will primarily be accomplished in a fit and function manner. During assembly build up, the device will be thoroughly tested and then tested again during integration. Several load-bearing tests are needed to completely characterize he latching mechanism (Reference 3).

Conclusions

Although not complete, the proof-of-concept IEEM has demonstrated the feasibility of the chosen technology. The pneumatic connector-type candidate has several advantages over the taper candidate. These include: ease of manufacture, better packaging for the tool drives, and less reliance on a single point failure spring for all the engagement/release work. The manipulator provides the force to actuate the IEEM in the pneumatic connector-type design vs. a torsional spring in the taper design.

Future Work

The implementation of the IEEM for Ranger is proceeding rapidly. The schedule for the pneumatic connector-type candidate calls for a completed and integrated prototype on Ranger NBV by the end January, 1994. Results of the testing and integration will be incorporated into the presentation of this paper in May, 1994.

The taper candidate prototype design must be completed by February, 1994. Its fabrication and integration of the proof-of-concept article are scheduled for completion by April, 1994. The testing to determine which is the better mechanism should be completed by August, 1994. Two units of the chosen design should be available in October, 1994.

Acknowledgments

The authors would like to thank Phil Churchill for the original idea for the IEEM and his continued support.

This work is sponsored by NASA Grant NAGW-2245. The enthusiasm and support of grant monitor David Lavery is gratefully appreciated and acknowledged.

References

1. Space Systems Laboratory, "Ranger Flight Experiment Proposal," NASA Telerobotics Intercenter Working Group Flight Experiments Workshop, June 1992

2. D.L. Akin and R.D. Howard, "Manipulator Design and Development for the Ranger Satellite Servicing Vehicle," Twenty Sixth Aerospace Mechanisms Symposium, NASA CP-3147, May 1992

3. Space Systems Laboratory, "Ranger Program Non-Advocate Review," Space Systems Laboratory, December 1993

4. J.C. Parrish et. al., "Ranger Requirements Document," Space Systems Laboratory, SSL-TFX-0005, December 1993

DIAMOND TURNING IN THE PRODUCTION OF X-RAY OPTICS

Steven C. Fawcett
NASA Marshall Space Flight Center
Huntsville, Alabama

ABSTRACT

A demonstration x-ray optic has been produced by diamond turning and replication techniques that could revolutionize the fabrication of advanced mirror assemblies. The prototype optic was developed as part of the Advanced X-ray Astrophysics Facility - Spectrographic project (AXAF-S). The initial part of the project was aimed at developing and testing the replication technique so that it could potentially be used for the production of the entire mirror array comprised of up to 50 individual mirror shells.

INTRODUCTION

The grazing incidence x-ray mirrors for this project are cylindrical shells consisting of parabolic and hyperbolic sections of revolution. Figure 1 is a schematic of the optic, which is designated as a Wolter I, grazing incidence x-ray reflector. The entire mirror assembly is depicted in the drawing of Figure 2. The optical surface resides on the inside of the shells that have a wall thickness on the order of one millimeter. This geometry, and the number of mirrors required, mandates the use of rapid and accurate fabrication techniques. For this project, several aluminum mandrels were diamond turned with the optical profiles on the outside diameter. Diamond turning is a specialized fabrication process that utilizes precision machines and single-crystal diamond cutting tools. The machine is basically a lathe with a stacked X-Z slide and rotary axis configuration. The motion of the precision slides is monitored using laser interferometer feedback to the controller. This system has a linear resolution of 10 nanometers (less than $^1/_2$ microinch). The rotary axis is an oil hydrostatic bearing capable of supporting more than 8900 N with a radial error of approximately 100 nanometers (4 microinch). The surfaces produced by this machine have a roughness less than 30 nanometers (1.25 microinch) RMS. To improve this finish, a tool servo system will be implemented. This system will involve piezoelectric actuation and

capacitance gauge feedback. The piezoelectric will be capable of 25 micrometer (0.001 inch) motion at kilohertz bandwidths. This motion will be utilized to actively compensate for the inherent machine vibrations using inputs from the laser system as well as external sensors. The replication technology for the mirror components and the tool servo implementation has the potential to revolutionize the fabrication of precision components. The extremely high precision required of x-ray optics may lead to advances in the manufacturing techniques that could be utilized in the fabrication of other precision components. The key procedures used in the fabrication process and the tool servo development will be presented with the appropriate testing results.

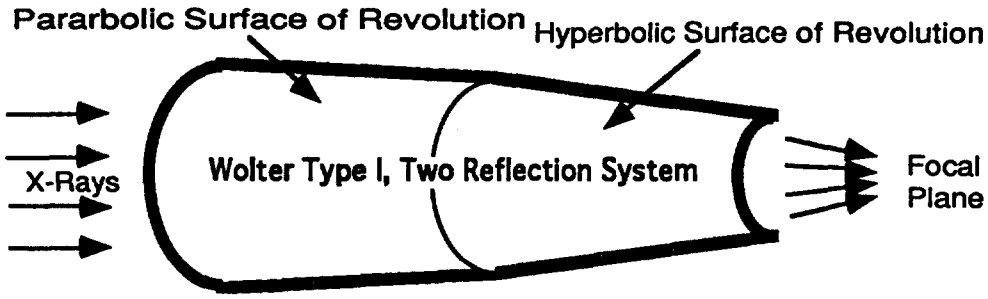

Figure 1 Schematic of the cross section of a Wolter I x-ray optic. The shell is 60 cm long with diameters from 16 to 60 cm. It is formed of 1-mm-thick stress-free nickel with a gold reflecting surface..

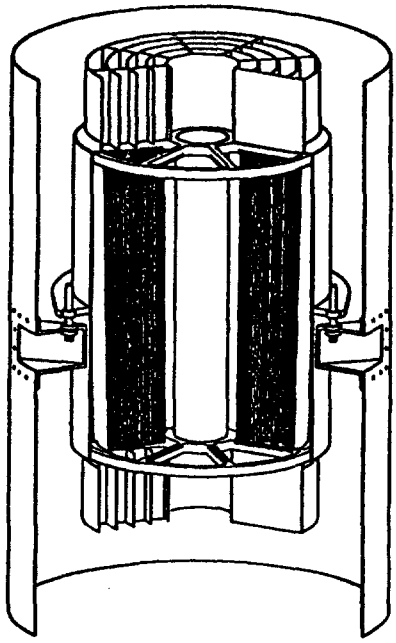

Figure 2 Diagram of the AXAF-S mirror assembly.

DIAMOND TURNING MACHINE

The fabrication process begins with a large aluminum cylinder that will form the core of the replication mandrel. For this project, two aluminum mandrels were formed to the approximate shape on a tracer lathe and then diamond turned with the optical profiles on the outside diameter. The diamond turning machine (DTM) is a Moore Special Tool M-40 Aspheric Generator. This device is capable of turning optical surfaces in ductile materials up to 1.8 meters in diameter. The machine is shown in Figure 3. The linear slide ways are in a stacked configuration with the radial (X) way placed on the axial (Z) way. Both slides ride on precision roller bearings and are driven with DC servo motors and lead screws. The position feedback system is a laser interferometer system with 10 nanometer resolution. The rotary axis typically holds the workpiece and is capable of supporting in excess of 8900 N. The total error motion associated with the oil hydrostatic spindle is less than 100 nanometers.

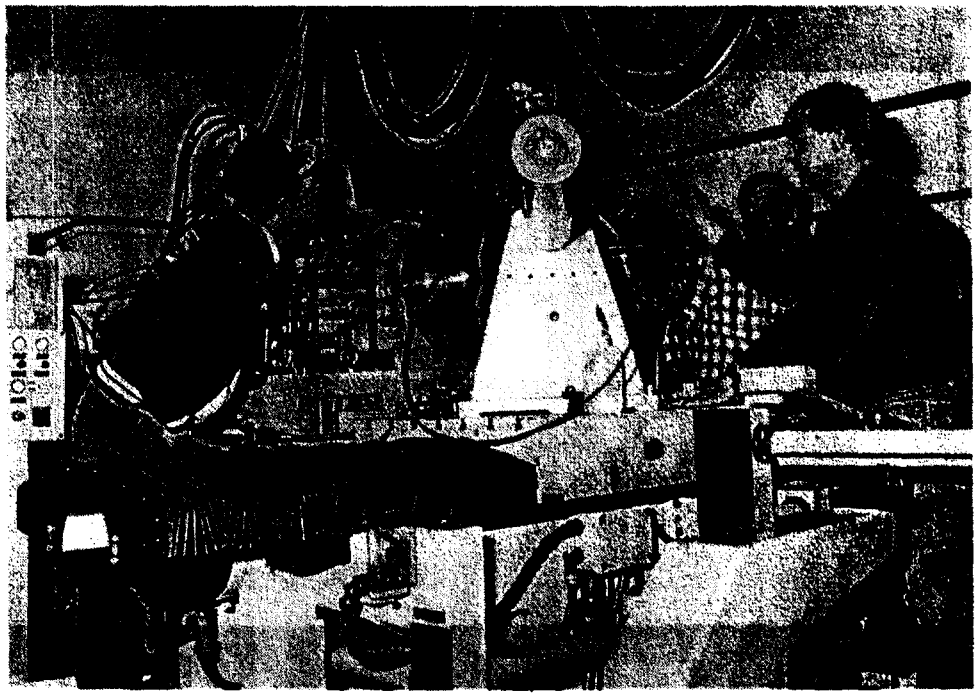

Figure 3 Moore M-40 aspheric generator. The mandrel used to fabricate the full-scale optic is shown attached to the machine spindle. The diamond tool is supported by the large casting in the center of the picture. The radial (X) slide is covered under the bellows in the left part of the picture and the laser interferometer feedback system for the axial (Z) direction is housed in the tube to the right.

The basic components of the mandrel used in the fabrication of the x-ray optic are shown in Figure 4. The body of the mandrel is a hollow aluminum cylinder with approximately 50 mm wall thickness. A tongue and groove mounting system was developed to aid in realignment of the mandrel on the DTM. This system worked well and allowed for centering repeatability to less than 10 micrometers at the end farthest from the spindle. Figure 5 shows a detail of the tongue and groove system. During the initial diamond turning phase, the surface profiles were undercut on the radius by approximately 50 micrometers to allow for the electroless nickel plating. These mandrels were then electroless nickel plated to a thickness of approximately 125 micrometers and re-turned with the aspheric surfaces.

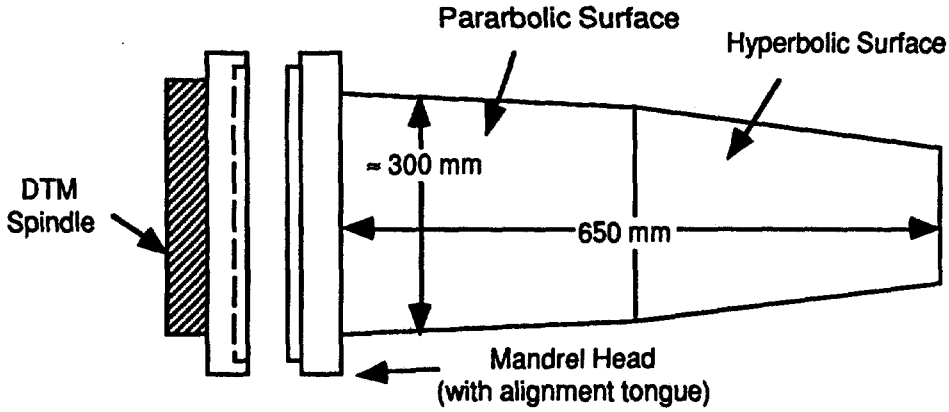

Figure 4 Mandrel for production of Wolter I x-ray reflector.

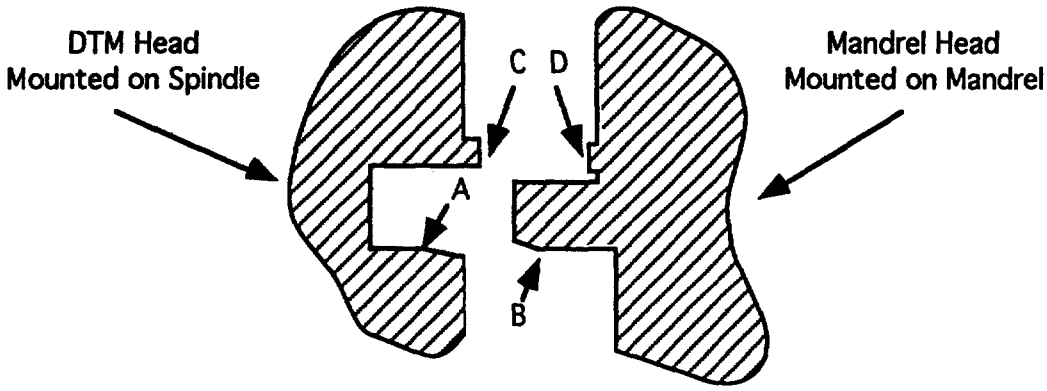

Figure 5 Detail of the tongue and groove used to align the mandrel on the diamond turning machine. The parts mate with a linear contact at points A and B and with a planar contact on surfaces C and D. This system ensured repeatable mounting of the mandrel to the DTM to within 10 micrometers at the far end of the mandrel.

The first mandrel (FS1) had surface finishes after turning that ranged from 30.3 nm (303 Å) RMS on the parabolic surface near the machine spindle to approximately 67.4 nm RMS on the hyperbolic surface at the far end. The average of the measurements was 44.2 nm RMS with a standard deviation of 12.7 nm RMS. Please note that all reported surface finish measurements were made with a Wyko 3D surface finish interferometer at 20X. This corresponds to a measurement area of about 470 by 470 micrometers. An example of this measurement is shown in Figure 6.

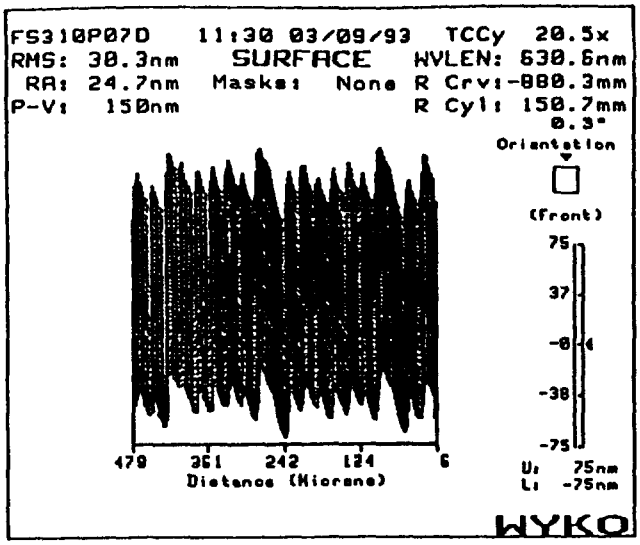

Figure 6 Surface finish measurement of the first mandrel before polishing.

The variation in the surface finish caused significant problems with the subsequent polishing steps. To reduce the finish to the appropriate levels, the hyperbolic surface had to be worked considerably more and the figure accuracy was degraded with the introduction or exaggeration of some mid-spatial frequency errors (10 to 50 mm in length). Also, due to the crossed slide configuration of the DTM, the errors inherent in the axial (Z) slide in the radial (X) direction were not corrected with the laser feedback system. The laser feedback system references the combined axial (Z) motion of both slides back to the metrology frame as was shown in Figure 3. The errors in this direction are therefore measured by the laser system and are corrected for in the controller algorithm. This machine was designed to cut normal incidence optics and only motions in the Z direction are referenced back to the machine's metrology frame with the laser system. Motions in the X direction are referenced as relative motions of the X slide assembly with respect to

the Z slide and are not tied back to the metrology frame. Therefore, the waviness in the X direction of the Z slide remain undetected by the feedback system and are not corrected by the controller. To alleviate this problem, a map of the repeatable waviness error of the Z slide was made using a straight edge reversal technique [1,2]. This error table was subsequently used to correct the cutting path for the second mandrel (FS2). Figure 7 depicts the repeatable way errors for the X direction of the Z slide.

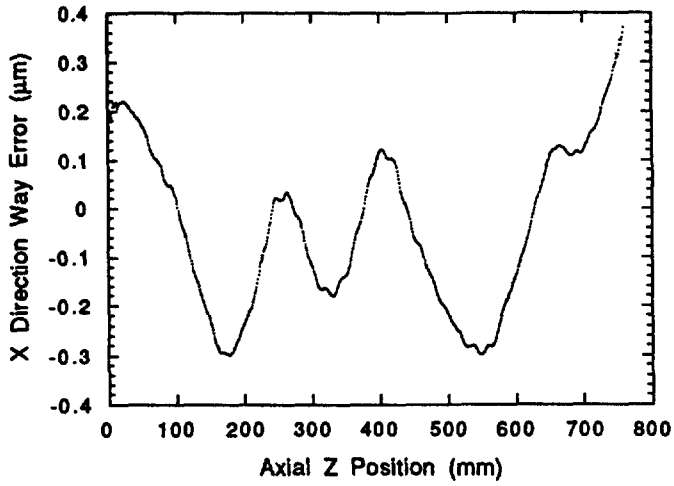

Figure 7 Uncorrected way error in the X direction of the Z slide.

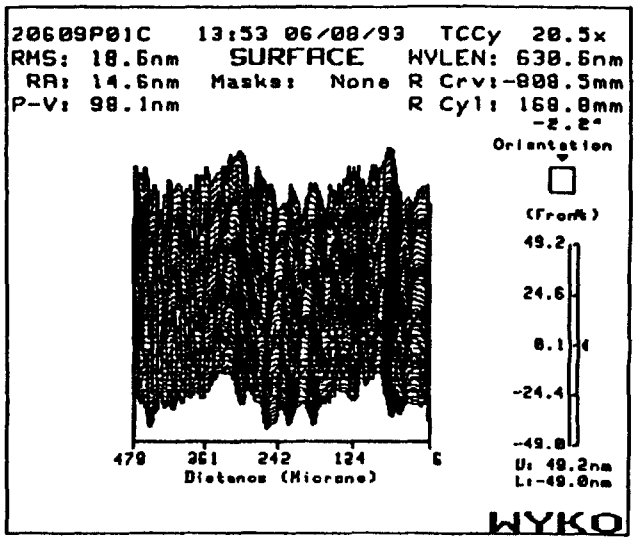

Figure 8 Surface finish measurement of second mandrel after passively limiting the inherent machine vibrations.

Initially, an attempt was made to improve the surface finish by limiting the inherent machine and part vibration for the second mandrel (FS2). This was achieved by altering the spindle speed and using modeling clay as a damping compound inside the mandrel. These changes made a significant improvement in the *as cut* surface finish on FS2. The RMS surface finish readings were much more consistent over the length of the part and ranged from 14.7 nm to 41.3 nm. The average of the measurements was 26.9 nm RMS with a standard deviation of 10.2 nm RMS. An example measurement is shown in Figure 8. This improvement made the polishing operation much easier and resulted in a more accurate overall figure.

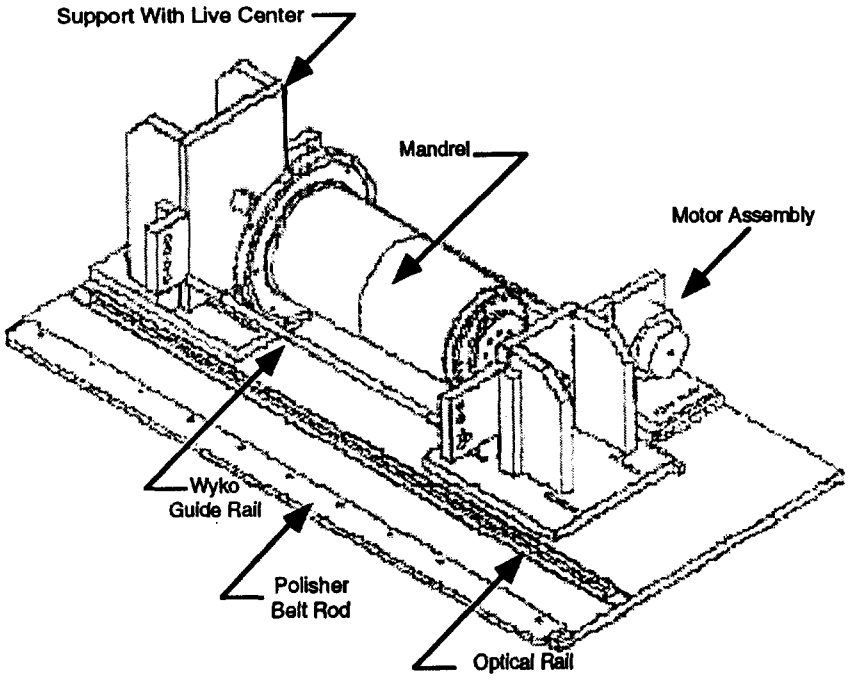

Figure 9 Machine built for polishing the full scale mandrels.

POLISHING

The mandrels are polished to the required surface finish on the specially built polishing machine depicted in Figure 9. The polishing compounds were colloidal silica and aluminum oxide. The surface finish of FS1 after polishing ranged from 1.5 to 2.0 nm RMS. For FS2, the results were much improved and the nominal readings were in the 1.0 to 1.5 nm RMS range. Figure 10 shows a typical surface finish after polishing. Because of the rudimentary design of the polishing arm of

the machine, the automated slide was discarded and the surface was finished by hand. This resulted in a time-consuming process that altered the figure. For future projects, the polishing machine will be upgraded and will include computer control that will systematically polish the mandrel to improve the surface finish. The algorithms for this machine will be developed from empirical polishing data and should be able to reach the desired surface finish characteristics without significantly altering the overall figure of the optical surface. This will be achieved by continuously monitoring the polishing pressure and position to ensure uniform material removal. The optical figure will then be a deterministic function of the accuracy of the diamond turning.

Initially, the figure of the mandrel was measured using a Zeiss coordinate measuring machine (CMM) with a 100-nm resolution. An example measurement is shown in Figure 11. The scatter in the data is apparent and the accuracy of the figure can not be verified to better than a micrometer utilizing this data. Also, the contact nature of the CMM causes defects in the surface of the mandrel after the measurements are made. Figure 12 shows an interferometric scan of the "dimple" left in the surface of the electroless nickel covered aluminum. This defect is about 250 nm deep and is significant when compared to the wavelength of the reflected x-rays. Due to the measurement noise and contact nature, this device proved inadequate and an alternative figure measuring device was considered. The second device chosen for determining the figure of the finished mandrel after polishing was called the Long Trace Profiler (LTP). This instrument was developed by Continental Optical Corporation and uses an optical, non-contact, slope measurement system [3-5]. The second mandrel (FS2) was taken to their facility in Hauppauge, New York, for measurement of the resulting figure after polishing was completed. This device proved quite repeatable and had a much finer resolution (reportedly around 1 nm RMS over the 1-m path). Figure 13 shows the five measurements made on the parabolic end of FS2 with the global curvature and slope removed. This plot is a map of the mid-spatial frequency errors left on the mandrel. These mid-frequency errors are a problem when the optic is used to focus x-ray. Errors of this type tend to scatter the x-rays and blur the focus. The goal of the project is to produce an optic that exhibits 100 arc second resolution at x-ray energies to 10 keV. The mid-frequency deviations shown in Figure 13 may circumvent the attainment of that goal. To eliminate these errors, the inherent machine vibrations must be significantly reduced by either passive or active damping methods.

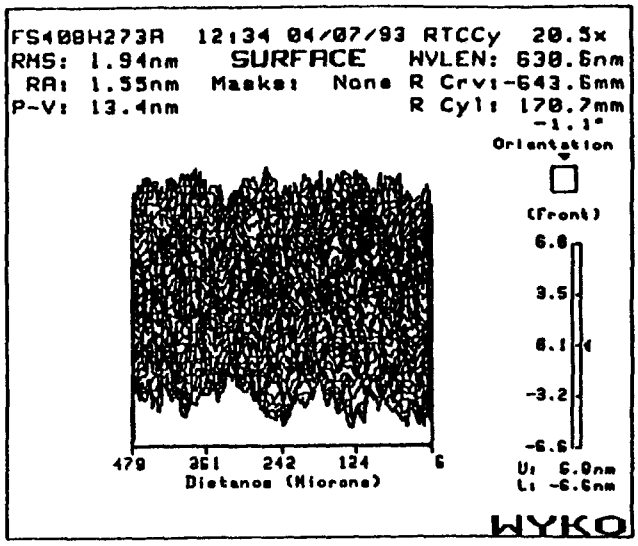

Figure 10 Surface finish measurement of mandrel after polishing.

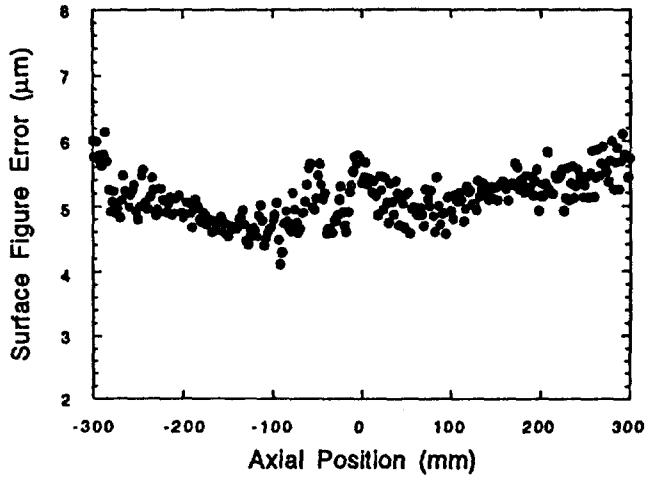

Figure 11 Surface figure measurement of mandrel from the CMM.

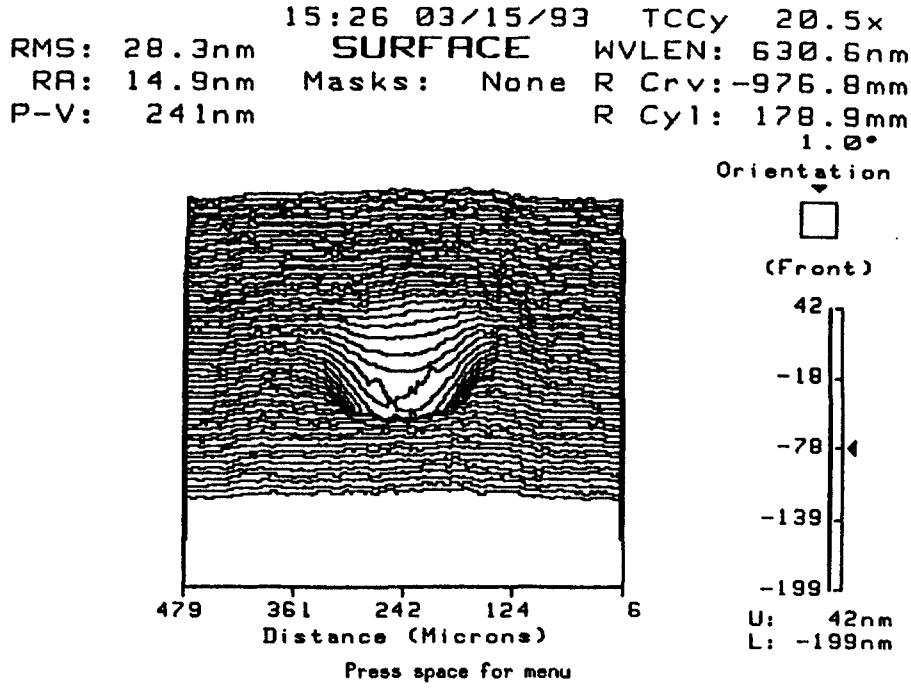

Figure 12 Residual surface defect left in mandrel after measurement with the CMM.

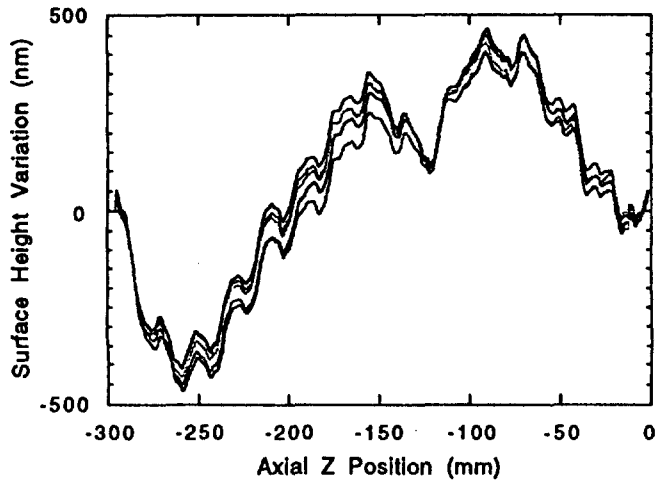

Figure 13 Surface height variation for the parabolic end of FS2 as measured with the LTP.

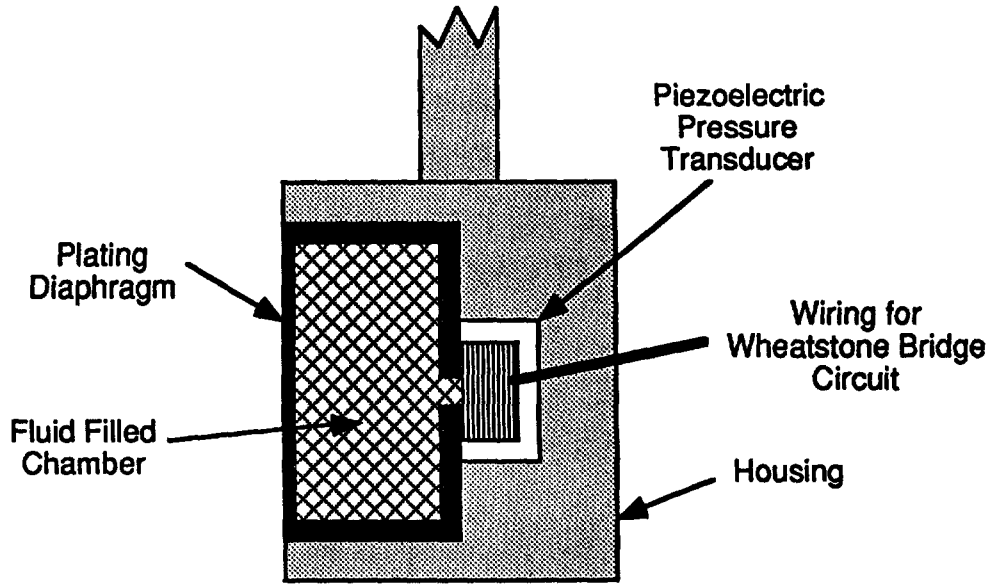

Figure 14 Stress monitor for the electroforming process.

REPLICATION PROCESS

After the mandrel is polished to the required finish and thoroughly cleaned, the electroless nickel is passivated by actively inducing the growth of a thin nickel oxide on the surface. This passivation is an electrolytic process and is controlled in such a manner to produce the desired stoichiometry. The mandrel is subsequently plated with an approximately 100-nm-thick layer of gold by either vapor or electrochemical deposition. This gold layer ultimately replicates the optical profile and is the reflection surface. Over the gold layer, a special stress-free nickel shell is electroplated to approximately 1 mm thick. The stress of the electroformed nickel is monitored with a custom stress monitor that measures the plating stress with a diaphragm and a piezoelectric transducer. The stress monitor is shown schematically in Figure 14. As the nickel is simultaneously deposited on the mandrel and the diaphragm, the slight deformation of the diaphragm due to stress is magnified by the fluid chamber and is sensed by the transducer. The output from the piezoelectric is converted to a voltage with a bridge circuit and then input to a computer for process monitoring. The algorithm uses the plating current as the control variable and forces the plating to proceed in a state of zero stress. This ensures that the formed mirror shell will not deform when it is removed from the mandrel. To eliminate the edge effects from the polishing phase (the substrate is removed at a faster rate when the

polishing pad encounters a discontinuity in the surface), the mandrel is formed longer than the required optical surfaces. Therefore, the electroformed optic must be cut to the desired length before separation from the mandrel. The cutting process is performed with a thin diamond blade on a grinder attached to the DTM. When the length cuts are complete, the shell is removed from the mandrel with a cryogenic separation procedure. The differential expansion of the shell with respect to the mandrel allows for a small gap to form between the two when the inside of the mandrel is filled with liquid nitrogen. Once removed, the Wolter I x-ray optic is complete and ready for mounting and testing in a 100-meter-long vacuum tunnel retrofitted with an x-ray source and detector.

ACTIVE VIBRATION COMPENSATION

To improve the surface finish characteristics of the diamond-turned mandrel, active vibration compensation methods are being considered. In one scenario, the vibration of the mandrel is monitored in real time and this error signal is used to move the cutting tool to compensate [6]. The amplitude of the vibration that occurs during the precision diamond turning of optical components is typically small (less than 10 micrometers) and occurs at frequencies below 100 hertz. This type of motion can easily be compensated for by using a piezoelectrically driven tool servo [7,8]. The basic design of the servo is shown in Figure 15. The diamond turning process requires a significant stiffness for all components in the metrology loop (between the part and the cutting tool). Therefore, a ceramic piezoelectric actuator is the ideal choice for providing the tool motion. In Figure 15, the cutting tool is intimately mated to the piezoelectric ceramic stack with a preload provided by the spring steel flexures. This preload serves dual purposes. First, it provides the required mating force to ensure the closed loop stiffness. Also, the preload ensures that the operation of the servo will occur with the ceramic consistently in compression. This is to counteract the inertial forces encountered when the servo is operating at the higher bandwidths. These forces result from the relatively small, but significant, mass associated with the tool and the mounting flange. The ceramic material is very strong in compression but will only permit a small amount of tension before failure. Therefore, for longevity and repeatability of the servo mechanism, the compression preload is required.

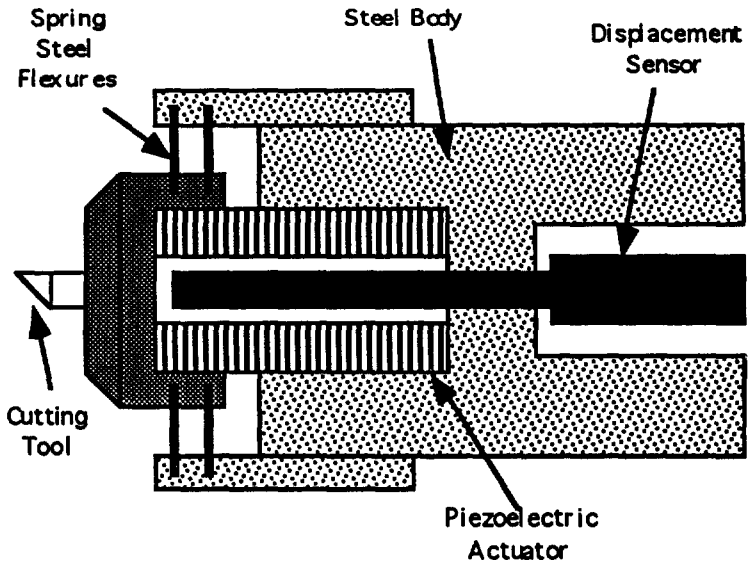

Figure 15 Cross section of a piezoelectric tool servo.

To compensate for the inherent machine vibration that occurs in the cutting process, a closed-loop control system must be utilized. This system consists of a real-time vibration sensor that feeds back to the tool servo. This sensor can be either an accelerometer or a displacement sensor, such as a capacitance gage. In this application, a non-contact capacitance gage will be required. The vibration of the mandrel will need to be monitored at both ends and the actual radial displacement at the cutting point will then be interpolated. This configuration is shown schematically in Figure 16. The sensors are placed at the ends of the mandrel and are referenced to the metrology frame (machine base). These signals are then processed in a control algorithm through a data acquisition system based on a personal computer. The other input to the system will be the current axial location of the cutting tool. The actual radial displacement at the cutting position can then be calculated, inverted and the output sent to the tool servo amplifier. This signal then provides tool motion that is equal and opposite of the vibration and negates its effect. The geometry of this particular application and the presence of cutting fluids and debris will make the implementation of this approach somewhat difficult. It is felt that the technique can be successfully utilized with proper engineering.

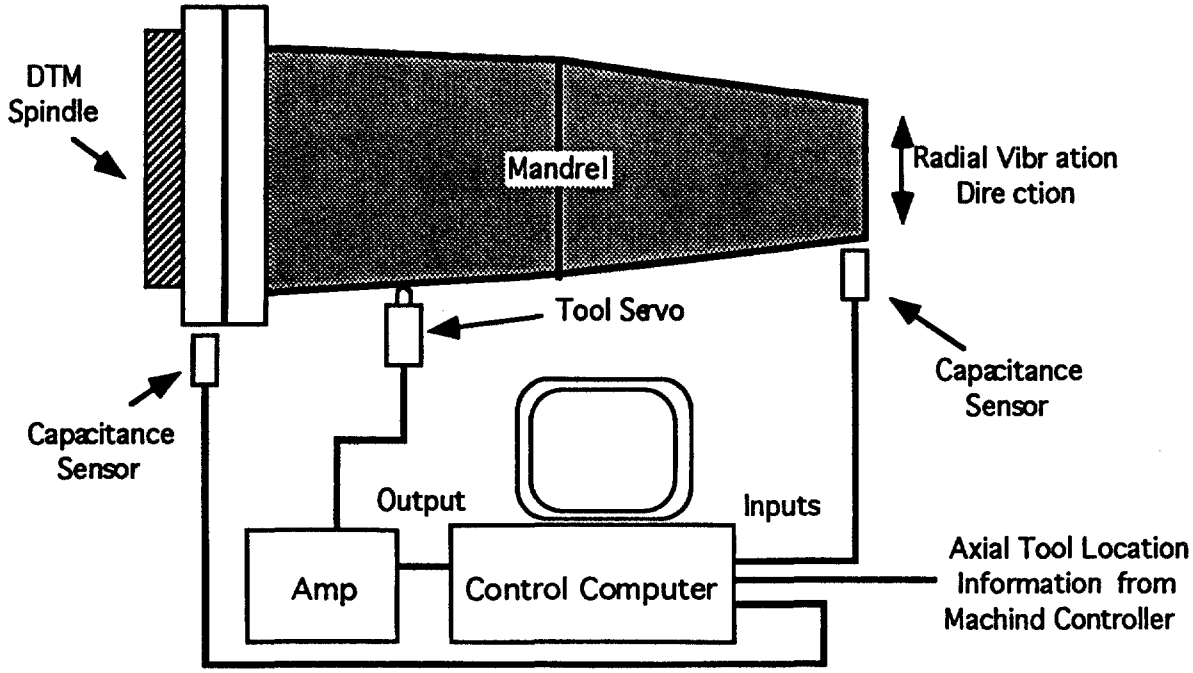

Figure 16 Schematic of the closed loop vibration control system.

CONCLUSION

The diamond turning and polishing operation to form the replication mandrels for the AXAF-S x-ray optics were quite successful. The program produced four full-scale mirror shells with dramatically improved results for each subsequent iteration. The final shell was successfully tested with x-rays and demonstrated 120 arc second resolution at the higher energies. The development program is considered a complete success and proved the technique as viable. However, several problems still exist in the processes and may be correctable for future mandrels. The primary areas of concern are the lack of a suitable thermal environment for the DTM and the inherent machine/part vibration during turning. The thermal environment is probably the main cause of the longer spatial frequency errors and will be corrected when the machine is moved to a new facility. The machine vibration will be corrected with passive damping and active compensation. The errors shown in Figure 13 with a wavelength of approximately 20 mm are related to the vibration problems and may be corrected with the vibration control measures and the closed-loop tool servo system.

ACKNOWLEDGEMENTS

This program was completed with the assistance of numerous individuals at Marshall Space Flight Center. The sheer number of people involved precludes giving individual recognition to all involved. The author in no way claims the results of this program as an individual achievement. However, several individuals whose work is reported here in detail should be recognized. The mandrel design and fabrication was facilitated by Bruce Weddendorf, Scott Hill, Janet Washington and John Redmon, Sr. The diamond turning was completed with the assistance of Caroll Black. The polishing and metrology was done in collaboration with Dave Lehner, Charlie Griffith, Raj Khanijow, Darryl Evans and Tom Kester. The mirror development program was managed by Robert Rood, James Bilbro and Charles Jones. The primary contributor to the development of the replication process was Darell Engelhaupt of the University of Alabama in Huntsville.

REFERENCES

1) Bryan, J.B. and D.L. Carter. "How Straight is Straight?" American Machinist, p. 61, December 1989.
2) Estler, W.T. "Calibration and Use of Optical Straightedges in the Metrology of Precision Machines," Optical Engineering, p. 372, Vol. 24, No. 3, May/June 1985.
3) Takacs, P.Z. and S. Qian. "Surface Profiling Interferometer," United States Patent #4884697.
4) Takacs, P.Z., E. L. Church, S. Qian and W. Liu. "Long Trace Profile Measurements on Cylindrical Aspheres," 32nd Annual International Technology Symposium on Optical and Optoelectronic Applied Science and Engineering, Proc, SPIE, 966, San Diego, CA, p. 354, August 14 - 19, 1988.
5) Irick, S.C. "Determining Surface Profile from Sequential Interference Patterns from a Long Trace Profiler," Review of Scientific Instruments, 63, No. 1 (Part IIB), p. 1432, January 1992.
6) Fawcett, S.C. "Small Amplitude Vibration Compensation for Precision Diamond Turning," Precision Engineering, Vol. 12, No. 2, p. 91, 1990.
7) Patterson, S.R. and E.B. Magrab. "Design and Testing of a Fast Tool Servo for Diamond Turning," Precision Engineering, Vol 298, p123.
8) Falter, P.J. and T.A. Dow. "The Development of a Fast Low Amplitude Tool Servo," Precision Engineering Center Annual Report, North Carolina State University, 1986.

INNOVATIVE MECHANISM FOR MEASURING THE MASS PROPERTIES OF AN OBJECT

Kedron R. Wolcott
I-NET Inc.
NASA John F. Kennedy Space Center
Kennedy Space Center, Florida

Todd A. Graham
NASA Kennedy Space Center
Kennedy Space Center, Florida

and

Keith L. Doty
University of Florida
Gainesville, Florida

Abstract

The Kennedy Space Center Robotics Group recently completed development and testing on a novel approach to measure the mass properties of a rigid body. This unique design can measure the payload's weight, mass center location, and moments of inertia about three orthogonal axes. Furthermore, these measurements only require a single torque sensor and a single angular position sensor.

1. Introduction

This paper describes the results of KSC's development and testing efforts. First, a description of the mechanism will be given along with its principle of operation. Next, experimental results will be discussed, and a description of the analytic studies will follow. The paper will conclude with a summary of the results and recommendations for future study.

2. System Description

The actual mechanism developed and tested by the Robotics and Automation Group is shown in Figure 1. A schematic representation of the device is shown in Figures 2-4. **U** is a shaft whose orientation is parallel to the hypotenuse of a cube. **U** can be rotated to any angle Θ from an initial position and fixed. **A** is a shaft rigidly attached to **U** at an angle α = 0.9553 rad (54.7°). When Θ = 0 rad (0°), **A** is vertically oriented. **B** is a circular platter with a center B^*. **B** can be rotated relative to **A** about the line OB^* to any angle δ from an initial position

and fixed. **E** is the payload and it is rigidly attached to **B**. The mass center of **E** is E^*.

The weight of the payload can be calculated by holding Θ fixed and first measuring the static torque in **U**. Then, after moving **E** with respect to **B** a known amount and direction, the static torque in **U** is again read. The weight is calculated from the difference in the static torque readings.

The first mass moment vector of the system is mgr, where mg is the weight of the payload and **r** is a position vector from O to E^*, as depicted in Figure 5. This vector can be calculated from three sets of measurements, where each measurement set consists of samples of the static torque in **U** and samples of the static angular position Θ of the system. Furthermore, each set of data is taken when the system is in a different orientation, where a particular orientation of the system is described by a value of Θ and δ. Three different orientations, and hence three data sets, are required to calculate mgr. The position vector **r** can be calculated by normalizing mgr with the weight of the test specimen.

The system's total moments of inertia I_{tz1}, I_{tz2}, and I_{tz3}, about three orthogonal axes parallel to z_1, z_2, and z_3, respectively, can be calculated by taking three sets of dynamic torque and dynamic position measurements, one set per axis. The total moment of inertia I_{tzn} includes: the central moment of inertia of the test specimen **E** about an axis parallel to z_n, the tare central moment of inertia about an axis parallel to z_n, and the parallel axis term md^2, where m is the combined mass of **E** and **B** and d is the minimum distance between the **B** and system mass center combination and the axis of rotation.

Figures 6-11 provide an illustration of the three dextral, orthogonal axes z_1, z_2, and z_3. The first set of dynamic measurements is made by rotating **U** in a sinusoidal motion, with $\delta = 0$ rad (0°), as shown in Figures 6 and 7. Dynamics measurements are taken for Θ and for the torque in **U**. From this data, the system's total moment of inertia I_{tz1} about z_1, an axis parallel to **U**, can be calculated. **B** and the system are next rotated to $\delta = {}^{2\pi}/_{3}$ rad (120°), and the process is repeated. I_{tz3}, the total moment of inertia about z_3, can then be determined, as indicated in Figures 8 and 9. This is again an axis parallel to **U** as before, but z_3 is perpendicular to z_1. Finally, **B** and the system are turned to $\delta = {}^{4\pi}/_{3}$ rad

(240°), and the total moment of inertia I_{tz2} about z_2, the third orthogonal axis, is calculated, as shown in Figures 10 and 11.

The payload's central moments of inertia about the orthogonal axes can be determined by simple subtraction of the tare terms (system inertia) from the respective total moments of inertia.

3. System Testing and Results

Extensive testing was done on the prototype shown in the attached photograph. The test object was an aluminum block, 0.302 x 0.203 x 0.140 m (11.9 x 8.0 x 5.5 in) and weighed 221.5 N (49.8 lb). The torque sensor was a JR3 3-axis Force Torque Sensor with a full scale (FS) torque reading of 211.9 N•m (1875 in•lb) and an accuracy of ±1% FS about the axis of concern. The angle Θ was measured by a Rotary Variable Differential Transducer.

The results of the testing are given in Table 1. The determination of the weight and mass center location was conducted with static measurements, and the determination of the moments of inertia was done through dynamics measurements.

Table 1: Experimental Results

Measurement Type	Accuracy	Repeatability
Weight	4.9%	not measured
mgr	not measured	±3.5%
I_{tz1}	not measured	±10%

The prototype was not configured to easily measure the weight of the payload, as per the procedure outlined in the System Description. However, one weight measurement was conducted to experimentally verify the procedure. The system was held at a fixed $\Theta = 0$ rad (0°), and the static torque in **U** was measured with the payload in an initial position. Next, the payload was moved 0.076 ± 0.0016 m (3.0 ± $^1/_{16}$ in) in a known direction and the torque in **U** was again determined. From there, the weight of the specimen was calculated, and that value compared to the known weight. Since only one experiment was conducted, the repeatability issue was not addressed.

The second row of Table 1 provides the repeatability results for the first mass moment vector mgr. The numerical value for mgr was calculated in 30 experiments, and the minimum-norm, least-squares result of those experiments was used as the standard for comparison.

As mentioned above in the System Description, each experimental calculation of mgr takes three sets of measurements. Consequently, 30 experiments would normally require 90 data sets. For the sake of efficiency, the 30 experiments were constructed using permutations of 30 measurement sets--10 sets taken at each of three different orientations of the mechanism. The three orientations were:
$(\Theta, \delta) = [\ (+35°, 0°)\ ,\ (-35°, 120°),\ (-35°, 240°)]$

Each set of data was made from 3000 samples of the static torque in U and 3000 samples of the position Θ. The result listed in Table 1 is the largest difference between the 30 calculated values of mgr and the standard value. The accuracy issue was not addressed since it was believed that benefits-to-effort ratio would not be favorable for this first-generation prototype.

The third row of Table 1 lists the repeatability results for the total moment of inertia, I_{tz1}. The repeatability result was resolved from repeating the same experiment 10 times. In all cases, $\delta = 0$ rad (0°). For each experiment, the system was first tilted at an angle Θ such that the effects of gravity were minimized. Next, the system was manually oscillated about U at a frequency of approximately 8 Hz and 5000 samples of the dynamic torque in U and 5000 samples of the dynamic angular position Θ were taken. From that data, I_{tz1} was calculated. The minimum-norm, least-squares fit to the results of the 10 experiments was used as the standard. The repeatability value was the largest of the differences between each of the experiments and the standard value. Again, the accuracy was not addressed for the reason given above.

4. Analytic Studies

Analytic studies were made to model the mechanism's static and rigid body dynamic characteristics, and these studies were used to develop techniques for data analysis. The initial study was performed using *Kane's Method of Dynamic Analysis.* A redundant analysis was conducted with a Lagrangian Formulation.

The dynamics for determining the payload's moments of inertia are

$$\tau = \tau_g + I_{tzn}\ddot{\Theta} \qquad (1)$$

where τ is the dynamic torque measured in U, τ_g is the gravity torque -- which results from the payload's mass center being offset from the axis of rotation, and I_{tzn} is the total moment of inertia. To determine I_{tzn}, the following equation was used:

$$Itzn = \frac{\frac{1}{X}\sum_{n=1}^{X}\left|\tau_n - (\tau_g)_n\right|}{\frac{1}{X}\sum_{n=1}^{X}\left|\ddot{\Theta}_n\right|} \qquad (2)$$

where X = 5000 represents the number of samples taken.

The numerical attributes of this approach made it necessary to simultaneously minimize τ_g and maximize Θ. By initially tilting the system to a particular value of Θ such that the system was "balanced", i.e., $\tau_g \approx 0$ N•m, and oscillating the system about that point with only small displacements, the effects of τ_g could be kept at a minimum. Furthermore, since the amplitude of the oscillation was small, the frequency had to be very high in order to maximize Θ. Thus, the system was jogged as fast as possible by hand, which was at a frequency of approximately 8 Hz.

The analytic studies also provided a very important insight into the measurement of mgr: a system configuration was determined that optimized the numerical characteristics of the mgr calculation. If this calculation is made with the system in the optimum configuration, *the accuracy of the mgr measurement is equal to the accuracy of the torque sensor used to collect the data.* Consequently, this system is capable of measuring mgr to an accuracy of $\pm 0.1\%$, the accuracy of many commercially available torque sensors. The optimum configuration follows a function of δ, Θ, and α. The optimal selections for δ are at u rad., u + $2\pi/3$ rad, and u + $4\pi/3$ rad, where u is an arbitrary initial angle. These selections for δ are independent of Θ and α. The optimal values

for Θ and α, however, are not independent of each other; rather, they are related by the equation

$$3 \sin^2(\Theta) \sin^2(\alpha) = 1 \qquad (3)$$

For example, in the model presented in the System Description, α = 0.9553 rad (54.7°), so the optimum value for Θ is $\pm\pi/4$ rad ($\pm$45°). Therefore, for optimum numerical characteristics in the calculation of mgr, the orientation of the payload must be at $\Theta = \pm\pi/4$ rad ($\pm$45°), and δ=u, δ=u+$2\pi/3$, and δ=u+$4\pi/3$.

The model was also used to study the merits of alternate configurations of the geometry, such as that shown in Figure 12. This configuration, in particular, minimizes the amount of tilt, i.e. Θ, at which the payload must be positioned. In this concept, $\alpha = \pi/2$ rad (90°), so from the equation, the optimum value for Θ = 0.6155 rad (35.26°).

5. Lessons Learned

The results emphasize the difficulty in determining the moments of inertia. While it is theoretically possible to measure the moments of inertia with this design, steps were necessary to achieve even repeatability results of $\pm$10%, such as the extreme care taken to minimize the effects of gravity: tilting the system until it was "balanced" about U and shaking it at ≈8 Hz. A torque sensor that matched the measured torque more closely would substantially improve the results, since the maximum torque read during the testing was $\pm$33.9 N•m ($\pm$300 in-lb), only 16% of the FS torque.

Friction was also more of a problem than anticipated. Originally, it was believed that the friction forces would not affect results appreciable since they would induce negligible torques when compared with the torques necessary to drive the system. However, friction and stiction significantly influenced the "balance point" of the system. Instead of a true point, there was a balance range of $\pm$0.0873 rad ($\pm$ 5°). Consequently, the effects of τ_g were not minimized to the greatest extent possible. Replacement of the roller bearings with air bearings would be one possible solution to this problem.

Measuring an object's weight with this approach has not been rigorously tested but only basic feasibility determined. The results listed above in Table 1 could likewise be greatly improved with a more

appropriate torque sensor, but mechanically simpler and more accurate methods may prove to be more practical.

This project has demonstrated the ease with which modern prototyping can be done. The mechanical design of the actual mechanism was carried out using Intergraph, so blueprints could be generated from an initial concept in a matter of minutes instead of days. The data acquisition system was developed with the National Instruments LabVIEW, which allowed for the necessary acquisition software to be written in 2 days--by an engineer, not a programmer--and the electrical hardware setup to be finished in a single day. Finally, the analysis was done with the numerical package MATLAB, a program that readily allowed for the manipulation of literally over hundreds of thousands points of data. Essentially, the power and the ease-of-use of commercially available equipment now allows for the physical testing of a concept in a remarkably short period of time.

6. Conclusions & Recommendations

The mechanism holds significant promise for the measurement of the mass center location of an object. As delineated earlier, an optimal combination of payload orientation exists that allows for the calculation of the mass center to an accuracy equivalent to the accuracy of the torque sensor used in the implementation. Consequently, a mechanically simpler configuration, like that shown in Figure 12, could be built that would measure the mass center location of a payload with an accuracy of 0.1%, the accuracy of many commercially available torque sensors.

Additional work needs to be done to refine torque measurement techniques and the mechanism design to enable accurate measurements of the mass moments of inertia of an object. The challenge experienced with the prototype device was that the dynamic torque was roughly an order of magnitude less than the gravity torque. Innovative methods for correcting this problem need to be developed in order for measurement of mass moments of inertia to be pursued any further. Additionally, mechanism design changes should be made to eliminate all aspects and effects of friction (e.g., air bearings).

In conclusion, the testing done on the prototype confirmed: 1) the feasibility of accurately measuring an object's center of mass, and 2) the difficulty in measuring moments of inertia of a payload. A derivative of the prototype design, used in conjunction with a device that can

accurately measure the weight of the payload, could yield a system that has the capability of accurately and easily measuring the mass center of a payload.

7. Acknowledgments

The authors would like to thank William Jones, James Spencer, Richard Bennett, Rhonda McNulty, and Ronald Remus for their engineering support, leadership and contributions. Thanks are also given to the NASA Summer Faculty Program and I-Net, the Engineering Support Contract.

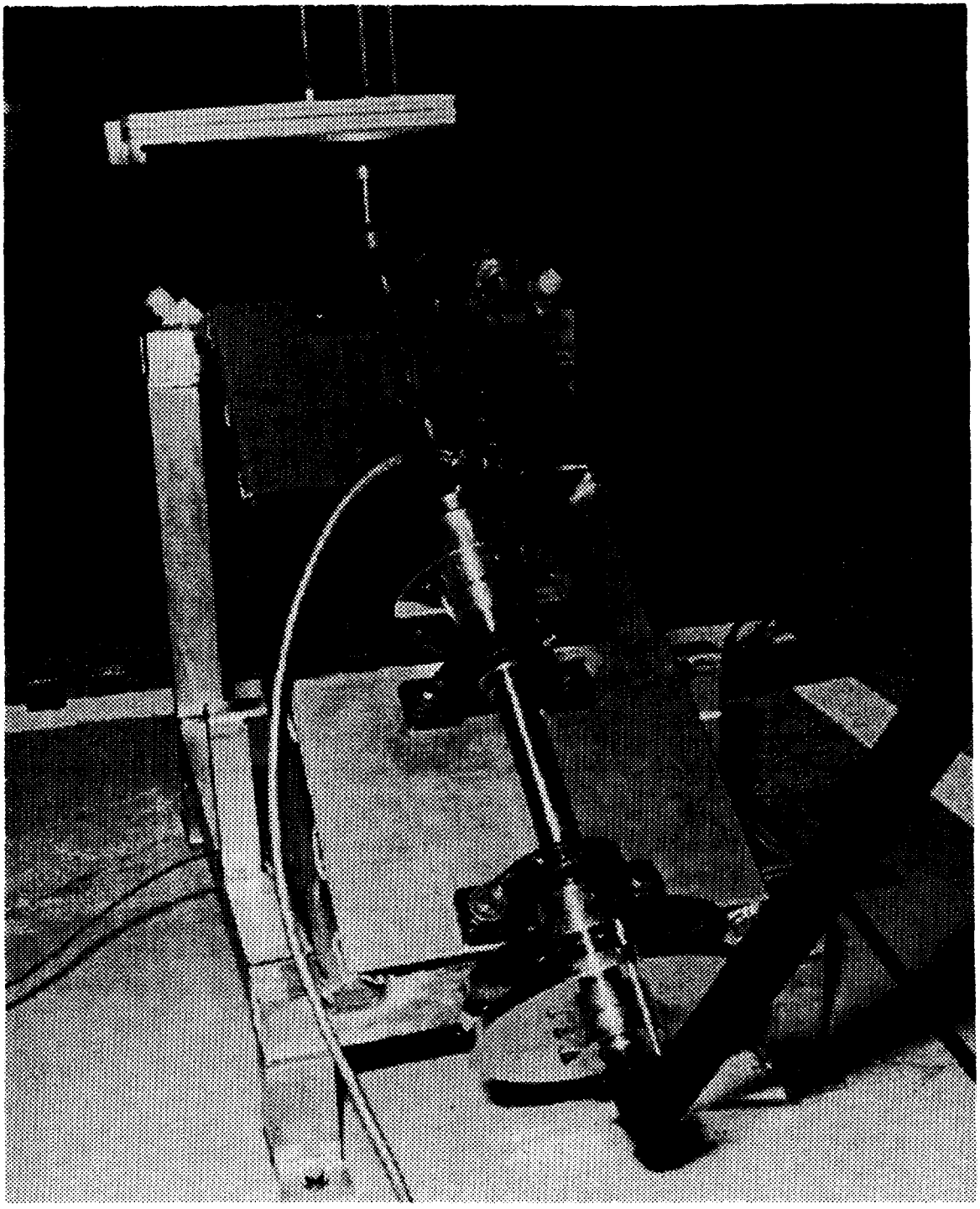

Figure 1. Prototype Mechanism

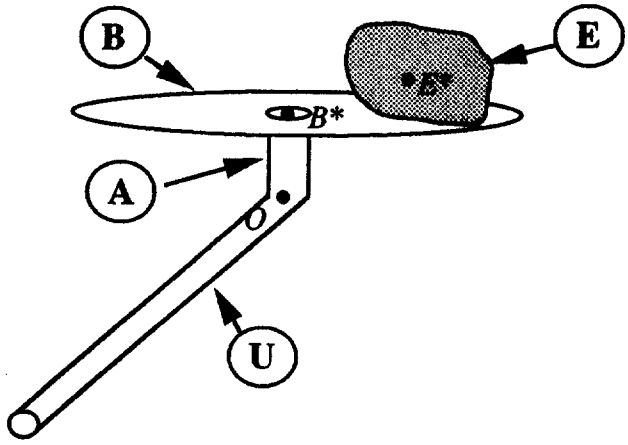

Figure 2

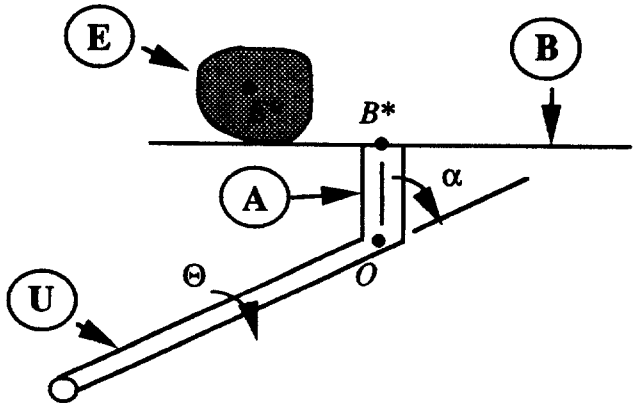

Figure 3

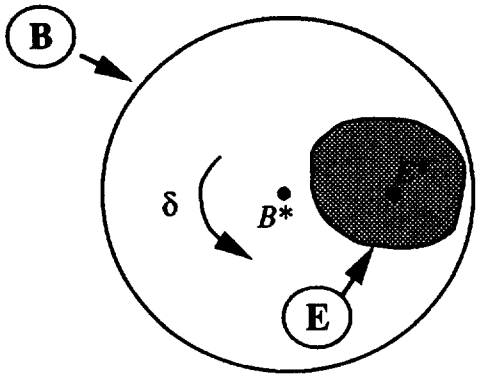

Figure 4

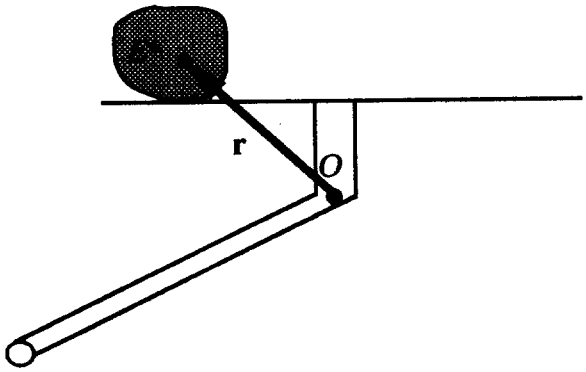

Figure 5

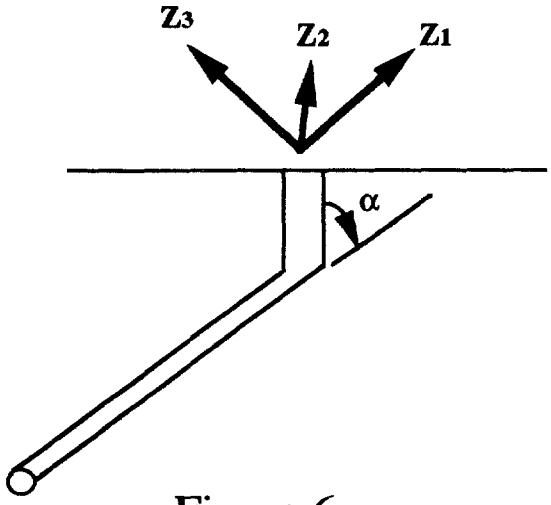

Figure 6

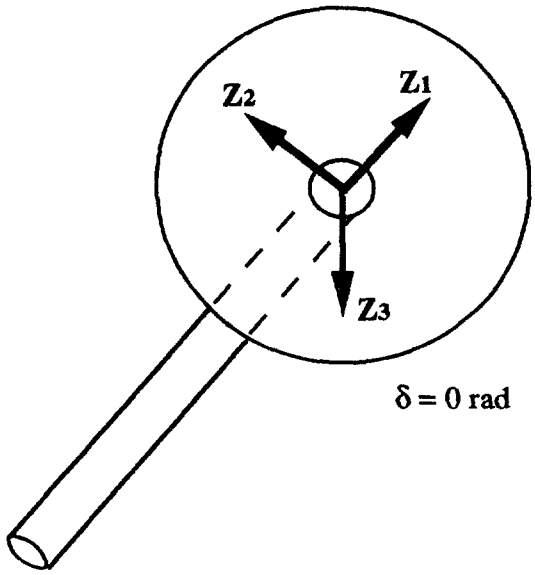

Figure 7

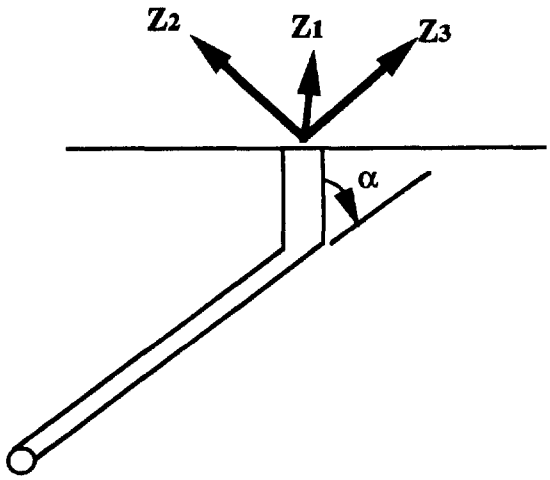

Figure 8

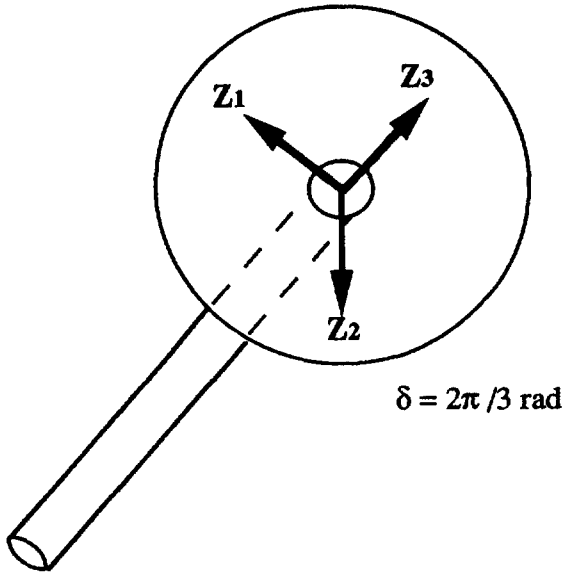

Figure 9

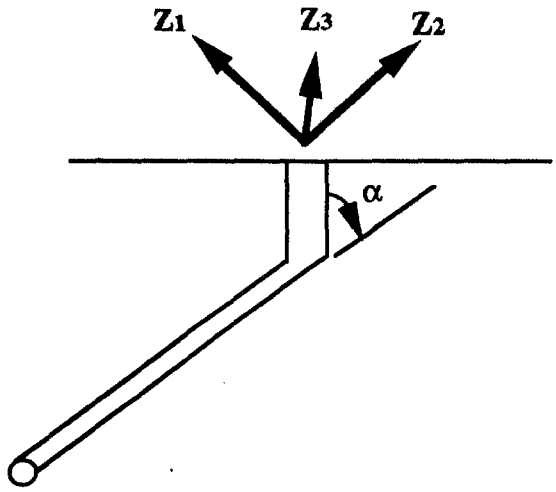

Figure 10

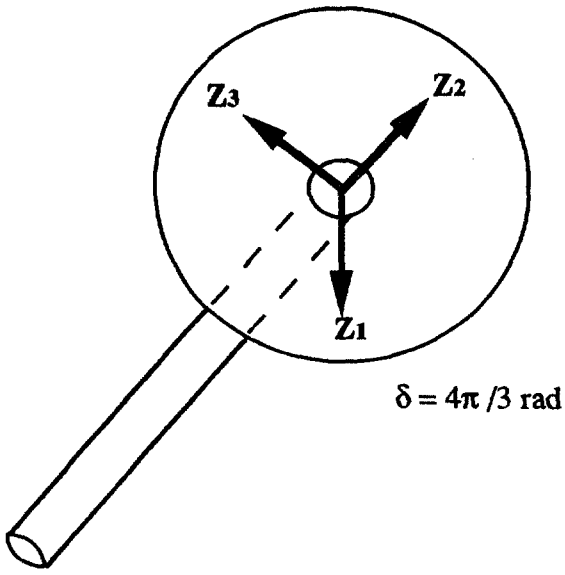

Figure 11

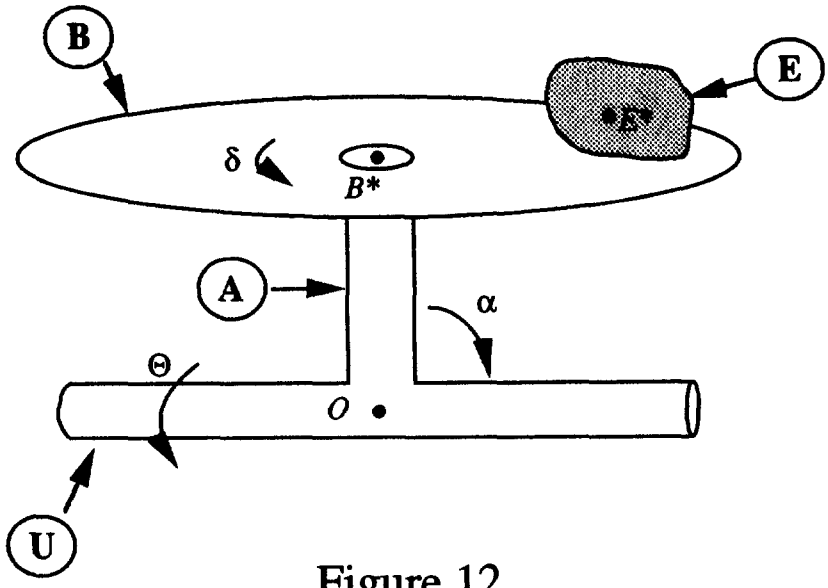

Figure 12

SPACE STATION FREEDOM SOLAR ARRAY TENSION MECHANISM DEVELOPMENT

Curtis Allmon and Bert Haugen
Lockheed Missiles & Space Company
Sunnyvale, California

Abstract

The tension mechanism is used to apply a tension force to the Space Station *Freedom* Solar Array Blanket. This tension is necessary to meet the deployed frequency requirement of the array as well as maintain flatness of the flexible substrate solar cell blanket. The mechanism underwent a series of design iterations before arriving at the final design. This paper discusses the design and testing of the mechanism.

Introduction and Requirements

Tension mechanisms are mounted to the containment box base of the Space Station solar array in two locations. The internal torque developed by two power springs as they wrap around an arbor is transferred to a cable which is wound on a spiral reel (Figure 1). The cable is attached to a tension distribution bar, which in turn transfers the tension to the solar cell blanket. In order to meet the overall system frequency requirement, the tension mechanism is required to provide an output force of 166.8+/- 44.5 N (37.5 +/- 10 lbs). This force range must be maintained over a 71 cm (28 in.) stroke for 35 blanket deployment cycles and over a 15.2 cm (6 in.) stroke for 88,000 thermally induced cycles . Qualification testing required additional margin for twice the life cycles plus acceptance test cycles.

Design History

Negator Spring

The original design used negator springs to obtain the required force. Three springs were connected to a central hub which rotated during cable pay-out, reeling in the springs and producing the required force. The advantage of this design over others was that it produced a near constant force without requiring a spiral cable reel to compensate for variations in torque. This design was capable of meeting the output force requirements based on analysis and test; however, once the large number of cycles required to meet thermal cycling over 15 years of operational life was identified, this design was not capable of meeting fatigue requirements within the existing weight and envelope constraints.

Power Spring

The next design considered was a power spring design. The power spring used a strip of Elgiloy 3.8 cm (1.5 in.) wide, and .08 cm (0.032 in.) thick . The spring was wrapped inside a 15.2 cm (6 in.) diameter housing with one end attached to the housing and the other end to an arbor. The housing was attached to a helical reel and rotated on a bushing with respect to the arbor. The helical reel offset the spring rate as the cable payed-out in an effort to maintain a

near constant force. Development testing showed the average force to be within the acceptable range; however, with hysteresis, the force exceeded the specified range. This hysteresis caused the torque developed during cable pay-out to be significantly greater than the torque developed during cable pay-in. Some hysteresis was expected but not to the magnitude found during testing.

Power Spring (Bearings)

At this point, analysis and test suggested a major contributor to the hysteresis was the friction produced from the bushings. It was expected that by replacing the bushings with ball bearings the friction, thus hysteresis, would be reduced. This change, along with several other changes made to meet revised force and stroke requirements, were then incorporated into the design. The spring material, as well, was changed from Elgiloy to stainless steel. This was done originally to reduce cost and improve material availability; however, testing performed by Vulcan Spring showed that the stainless steel also out performed Elgiloy in cycles to failure.

A new unit was then built and tested. The results from testing showed that the hysteresis had not been significantly reduced and the loads still exceeded the specified range. This led to the conclusion that the power spring itself was the main source of hysteresis overwhelming all other sources. At this point an effort to reduce spring hysteresis, by providing oil lubrication or by co-wrapping Teflon material with the springs, was attempted with only very minor improvements. In parallel, the deployed frequency requirement was revisited. It was found that using an "average" force from the hysteresis curve was acceptable and that the tension mechanism output was within acceptable limits.

A life-cycle test was then initiated on the mechanism. As cycling continued through the first several thousand cycles, the hysteresis gradually began to increase. At the same time, a pile of metallic powder began to form beneath the mechanism. The cycling continued through 26,000 cycles at which point it was stopped due to the increased hysteresis. Examination of the mechanism revealed that the springs had large patterns of wear which had produced the debris. These wear patterns on the springs were a result of the spring rubbing on itself as it was cycled (many layers are formed as the springs are wrapped inside the 19 cm (7.5 in.) diameter housing).

The solution to this problem was to add lubrication to the springs. All springs previously tested had been unlubricated. A separate wear test was initiated with the purpose of selecting the most appropriate lubrication for the spring.

Power Spring (Lubricated)

As a result of the wear test, it was decided that the springs would be coated with an unburnished impinged Molydisulfide (MoS_2) and a light coat of Braycote 815Z oil. This combination was added to two new springs which were inserted into the existing mechanism for further testing. Testing showed that the output force was within the acceptable range and the hysteresis remained constant throughout the required 176,000 cycles with no signs of adverse wear.

Special Testing

Wear Test

A coupon wear test fixture was designed to test spring coupons coated with various lubricants by simulating the load and motion seen by the actual spring. These coupons were cut

out of the actual mechanism spring material and were stacked three high with the top and bottom coupons fixed and the middle coupon attached to a linear motion device. To simulate the force that occurs between spring layers in the actual mechanism, compression springs were used to apply a normal force to each coupon stack. A load cell was part of the driving arm of the linear motion device and was used to measure the force required to pull the middle coupons. Preliminary testing was performed to calibrate the normal force by reproducing the wear that occurred during life cycling. Two test runs, six coupon sets each, were made for over 200,000 cycles each.

The selection of coatings or lubricants to be tested were based on the coating/lubricant's successful history in space applications, its ability to be applied to the 6.1 m (20 ft) spring, and its availability. In addition, the following considerations applied to specific coupons:

-Bare 301 was tested as a baseline to which other samples could be compared.
-Bare Elgiloy was tested to investigate if the composition of the base metal significantly effected the performance.
-Braycote 815Z oil was used on various coupons due to its extremely low volatility, easily controlled application, and successful history on bearings.
-A black oxide coating was investigated primarily as a controlled surface finish that would potentially provide better adhesion for the oil.
-Various forms of MoS_2 were tested due to the potential advantages of a dry lubricant.
-Braycote 815Z oil in conjunction with impinged MoS_2 was investigated for their combined effect.
-Braycote 600 was tested as a grease alternative.

Each coupon set was cycled under both ambient conditions and a nitrogen purge. The nitrogen purge was used to minimize humidity effects on the MoS_2. All coupons were life cycled; after which, a select few underwent a cold test to demonstrate the oil's performance in a cold environment. Figure 2 shows a plot of load vs. cycles for 6 sets of coupons.

It became evident after cycling all the coupons that those coated with even small amounts of oil performed the best. Further testing revealed that the coupons coated with oil and the unburnished impinged MoS_2 performed the best of any combination tested. Other interesting points observed from the test include:

-The unburnished MoS_2 coupons outperformed those that had been burnished.
-The heat cured MoS_2 coupons outperformed those that had been air dried.

The cold test was performed by cooling the coupons with liquid nitrogen. Thermocouples were strategically placed on the coupons to monitor the temperature. The low end of the temperature range of the tension mechanism in its operational environment was predicted to be -56.7°C (-70° F); however, the detailed thermal model of the mechanism predicted the low extreme of the spring to be -26.1°C (-15°F).

In order to get a conservative range of data, the temperature of the spring was taken below -73.3°C (-100°F) during the test runs. Results from the tests were recorded on a strip chart, plotting force and temperature as a function of time (Figure 3). These plots revealed that the force necessary to pull the middle coupon remained constant until the temperature had reached -28.9°C (-20°F), at which time the force began to increase slightly. The force didn't increase significantly until the temperature had dropped to approximately -51.1°C (-60°F). The data also indicated that the force returns to its initial range after exposure to extreme temperatures. This test confirmed that the lubricated spring would not be affected by the cold temperatures of the Space Station environment.

Life Test

The life test was performed by placing the mechanism on the fixture shown in Figure 4 and cycling it for 176,000 cycles. The output force of the mechanism was monitored continuously using a strip chart, and after every 5,000 cycles, a full functional test was run. The results showed that, after an initial break-in of several hundred cycles, the mechanisms output force remained relatively constant for the entire 176,000 cycles without showing signs of wear. Figure 5 shows an example of a test run made late in the life cycle test. The top line is the force during cable pay-out over a 71 cm (28 in.) stroke and the bottom line is cable pay-in over a 71 cm (28 in.) stroke.

This test proved that the tension mechanism will adequately meet all output force requirements. It also revealed that each mechanism will need to be broken in by cycling it several hundred times and that the amount of oil applied to each spring needs to be held to a minimum to prevent oil migration out of the mechanism housing.

Conclusion

The development of the Space Station Solar Array Tension Mechanism has been completed revealing the following lessons: 1) A power spring design provided the best weight and envelope for the required tension range, 2) Inherent hysteresis in the power springs is significant and only marginally affected by lubrication, 3) Wear in the power springs requires the use of a lubricant, and 4) A combination of MoS_2 and Braycote 815 Z oil provided the best performance of the options tested for this design. The Tension Mechanism now awaits qualification testing (including 176,000 cycles under full thermal vacuum conditions) scheduled for the second quarter of 1994.

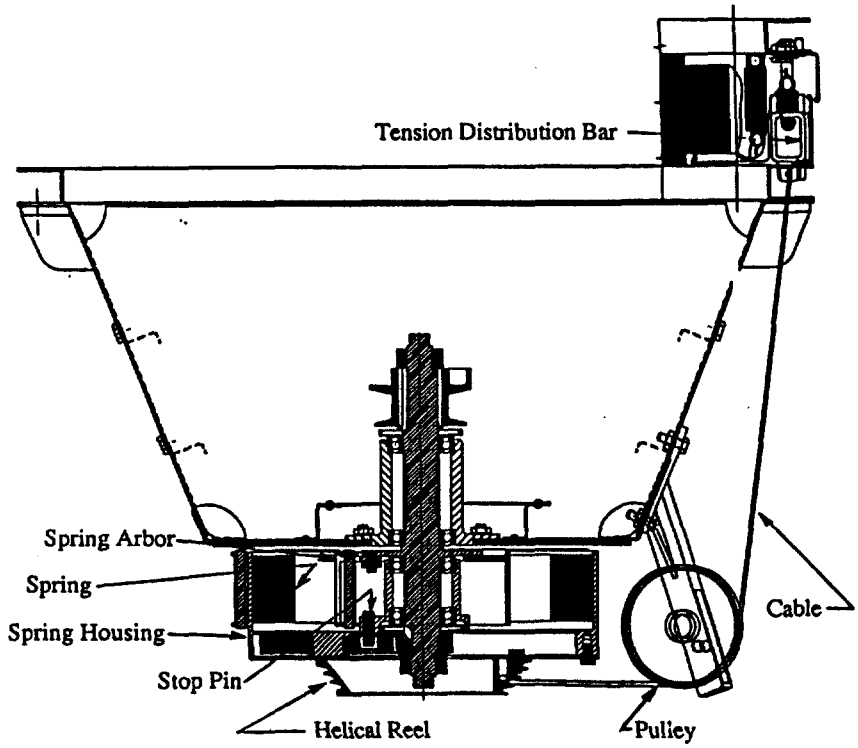

Figure 1: Cross-Sectional View of Tension Mechanism

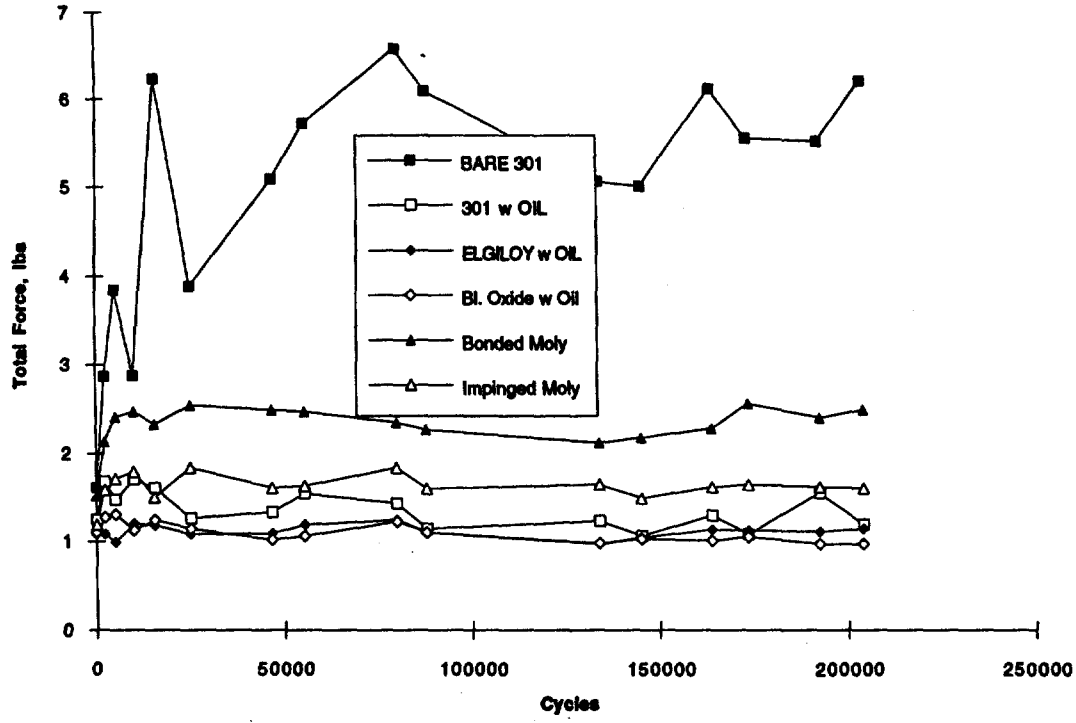

Figure 2: Representative Plot of Force vs Time for 6 coupon sets.

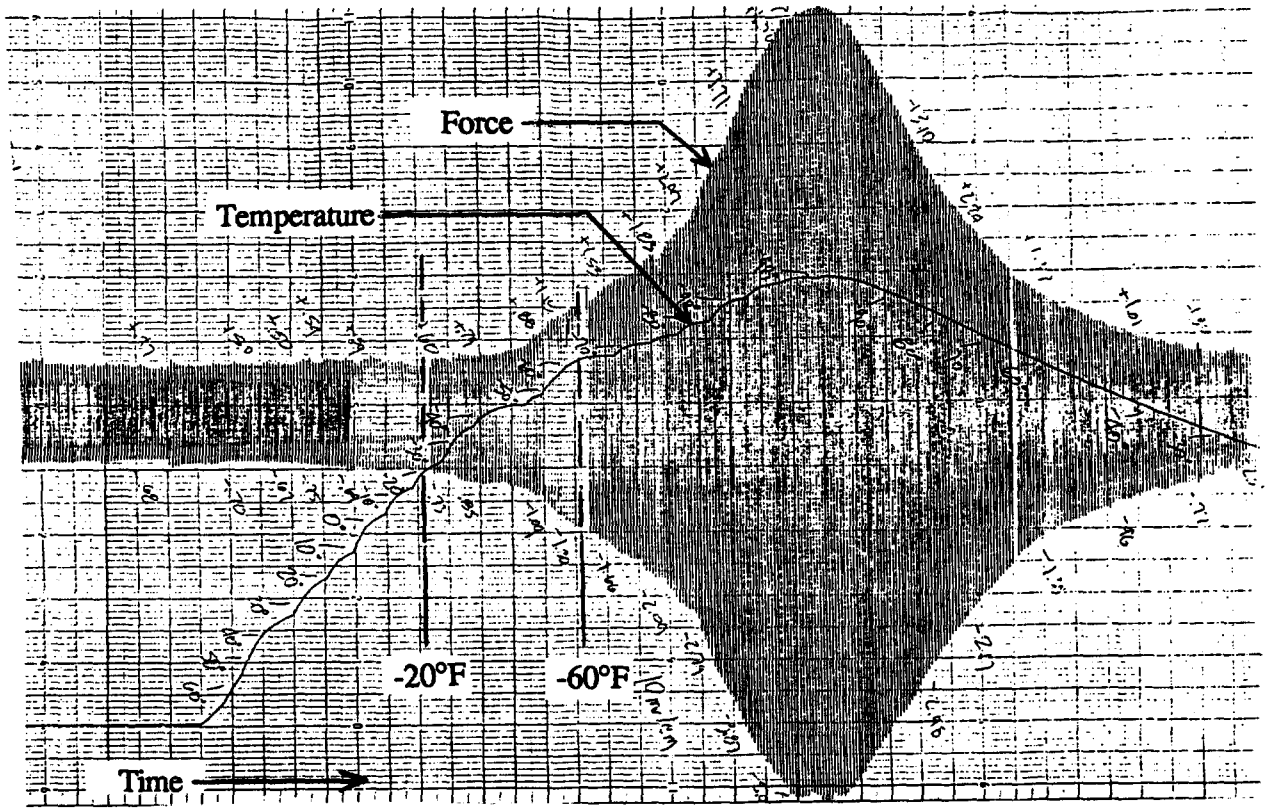

Figure 3: Cold Test Data

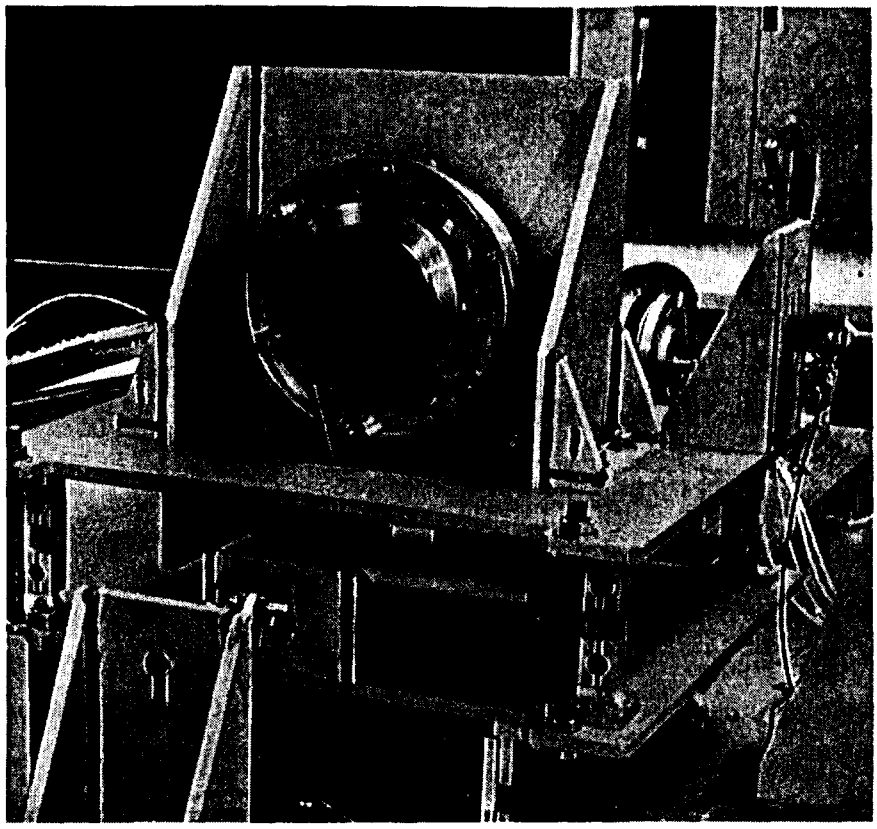

Figure 4: Life-Cycle Test Fixture

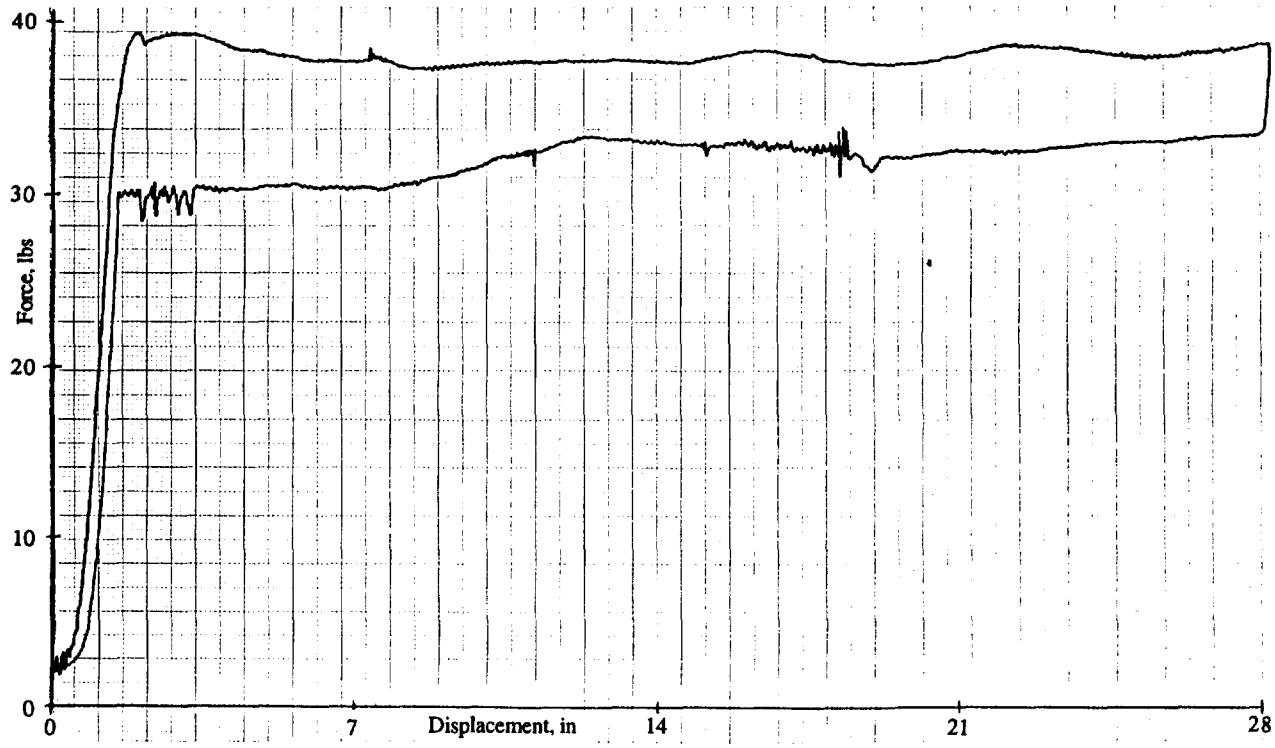

Figure 5: Force vs. Displacement Plot Over Full 28 in. Tension Mechanism Stroke

LEVERAGING METAL MATRIX COMPOSITES TO REDUCE COSTS IN SPACE MECHANISMS

Ted Nye, Rex Claridge, and Jim Walker
TRW Space and Electronics Group
Redondo Beach, California

ABSTRACT

Advanced metal matrix composites may be one of the most promising technologies for reducing cost in structural components without compromise to strength or stiffness. A microlight 12.50 N (2.81 lb), two-axis, solar array drive assembly (SADA) was made for the Advanced Materials Applications to Space Structures (AMASS) Program flight experiment. This SADA, as shown in Figure 1, had both its inner and outer axis housings fabricated from silicon carbide particulate reinforced aluminum. Two versions of the housings were made. The first was machined from a solid billet of material. The second was plaster cast to a near net shape that required minimal finish machining. Both manufacturing methods were compared upon completion. Results showed a cost savings with the cast housing was possible for quantities greater than one and probable for quantities greater than two. For quantities approaching ten, casting resulted in a reduction factor of almost three in the cost per part.

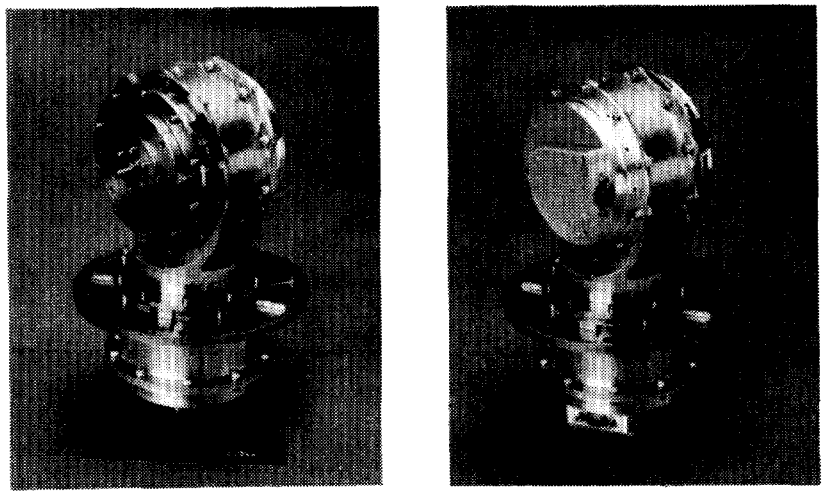

Figure 1. Metal Matrix Composite Solar Array Drive Assembly

INTRODUCTION

Changes in the spacecraft business have motivated a re-evaluation of low cost fabrication methods. Satellite metallic structures are typically machined from an oversized billet of raw stock. It is common in this industry to remark how a seemingly small, intricate part originated from a huge billet of material. This approach to fabrication yields a component with one appreciable value added feature: it is truly homogenous and monolithic. Problems from structural discontinuities are minimized. Nonetheless, the sheer number of cutting operations

and potential of scrapping a part from machining errors makes this approach inefficient and risky, particularly in light of current customer production expectations.

Casting, injection molding, and forging are all viable alternate fabrication processes that we evaluated for this study. High reliability satellite manufacturers have historically shunned these approaches due to structure non-homogeneity, poor property predictability, poor mechanical strength repeatability, or because very small quantities were required. Advances in the last decade have resulted in the maturity of fabrication processes, especially motivated by commercial-world pressures to drive defects to zero. A recent trend prompting spacecraft builders to give a fresh look at alternative fabrication methods is government customer insistence that the cost of spacecraft hardware be dramatically reduced with no compromise in performance.

Advanced structural materials combined with a low cost fabrication approach can result in a significant cost efficiency improvement. One method for evaluating materials is to rank them based upon their *specific* strength and stiffness. Figure 2 shows these comparisons. Spacecraft mechanism structures tend to be located in regions of high elastic strain energy, such as at the root of appendages or in assemblies where bending is inevitable, but undesirable. Therefore, materials that exhibit high specific strength and stiffness are preferred.

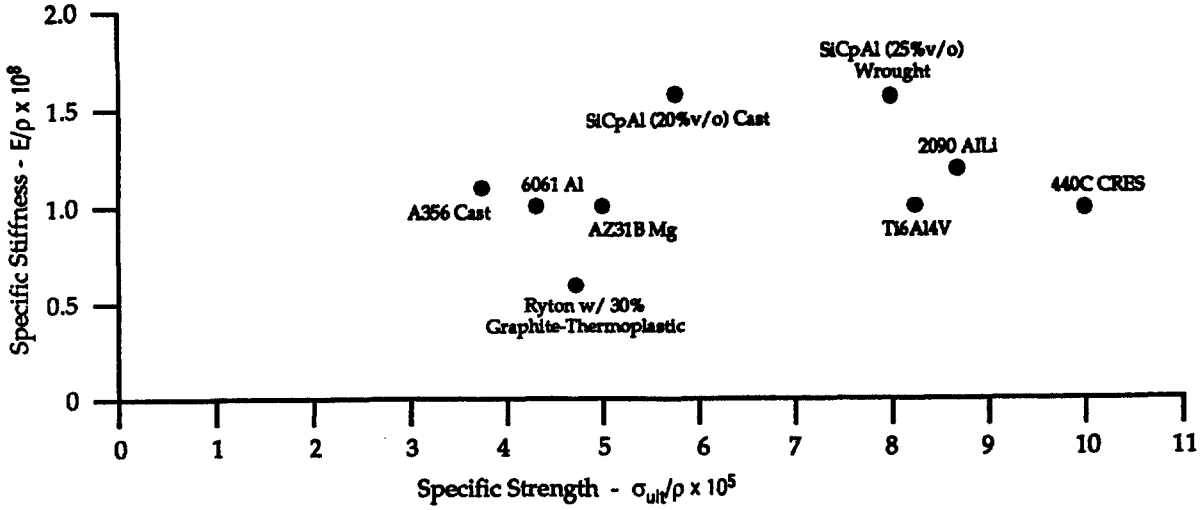

Figure 2. Comparison of Specific Strength of Aerospace Materials

Table 1 shows that when comparing metal matrix composites (MMCs) to metallic or plastic based systems, MMCs exhibit a low strain to failure and fracture toughness, but superior strength and stiffness. This failure strain and toughness issue was a reasonable concern because a design could be sensitive to inclusions acting as crack initiation sites, leading to ultimate, sudden failures. We addressed these problems by employing standard NDE methods of surface dye penetrant, and X radiography inspection (MIL-STD 2175, Class 2, Grade C), followed by static proof testing in three axes. If one looks closely at our cast MMC housings illustrated in Figure 3, generous radii and smooth load path transitions were intentionally included in the design. Inserts, although effective to distribute point concentrated fastener

loads, were avoided altogether in favor of through-holes for bolted joints. Liberal tolerances and machinist drawing reviews were used to create a tolerant, forgiving design that minimized the number of secondary cutting operations.

Table 1. Mechanical Property Comparison for Aerospace Materials

	Density (kg/m^3)	Ultimate Strength (kPa)	Yield Strength (kPa)	Youngs Modulus (MPa)	Strain to Failure (%)	Thermal Expansion ($10^{-6}/°C$)	Thermal Conductivity (W/m·K)	Fracture Toughness ($MN/m^{-3/2}$)
SiCp/Al (20% v/o)								
Duralcan F3D-F Die Cast	2823	296-352	290-303	113.8	0.1-0.4	5.2	147	unknown
Duralcan F3S-20S Plaster Cast	2765	317-359	310-338	98.6	0.4	5.5	145	16
SiCp/Al (25% v/o)								
DWA 6013-T6 Machined Billet	2851	552	421	115.8	3.8	4.7	138	21
Reinforced Thermoplastic								
Ryton, 30% Chopped Gr Injection Molded	1412	163	N/A	24.8	0.6	4.4	0.36	unknown
Al-Li Alloy								
2090-T8 Machined Billet	2602	552	517	75.8	4-8	7.3	87	27
Aluminum								
6061-T6 Machined Billet	2713	310	276	68.9	12	7.3	166	29
A356 Plaster Cast	2685	255-276	200	75.1	6	6.6	151	17
Titanium								
6Al-4V Annealed and Machined	4429	896-1000	827-931	113.8	14	2.7	6.7	55
6Al-4V Cast and Annealed	4429	931	827	113.8	12	2.7	6.7	55

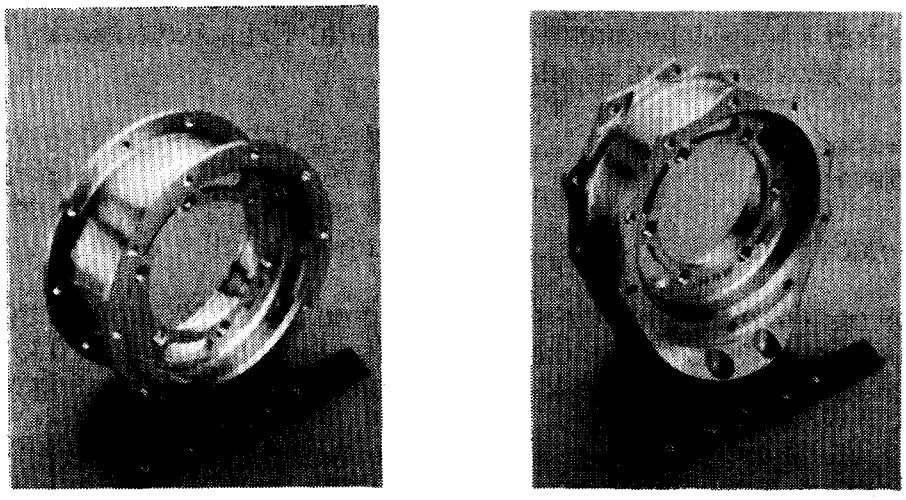

Figure 3. Cast MMC Inboard and Outboard SADA Housings

METHODS OF MANUFACTURING

When beginning the design of this SADA, we embarked on a technology survey to not only arrive at a low cost fabrication approach, but to conclude with a material system exhibiting superior yield and modulus properties. A third aspect under consideration was to take advantage of low volume or medium volume mass production: quantities of 10 to 100 units. This objective enabled the potential for an assembly line operation in contrast to a one-of-a-kind craftsman type assembly. Candidate approaches for fabrication included die and plaster casting, injection

molding, forging and stamping of an aluminum or thermoplastic based composite material system.

The results of our survey concluded with choosing a SiCpAl/FDS-20S plaster cast aluminum fabrication process. We found there was a comparable cost to both injected molded graphite thermoplastic and plaster cast aluminum. Previous experience on other TRW programs showed MMC aluminum castings would likely achieve a superior design to injection molded thermoplastic. This was due to expected higher toughness, lower part attrition, higher attainable stiffness (independent of temperature), and less sensitivity to on-orbit thermal threat issues and atomic oxygen. Fabrication methods of forging and stamping involved an initial large capital expenditure (to develop dies and processes) which could only be recovered for production quantities approaching hundreds of units. These processes also resulted in parts more deviant from final dimensions, which would require significant finish machining.

Several casting approaches were considered. For large volumes, die casting the housing, as shown in Figure 4, resulted in the most economy and highest fabrication speed (approximately 50 seconds per unit). This approach would result with components containing exceptional part to part repeatability, low void density, excellent surface detail, and as a result of the high casting pressures, reduced structural shrinkage. Die casting would result in superior mechanical properties from quickly chilled, fine grained metallurgical structure. Expected accuracy in geometrical dimension were as follows:

Thinnest Sections	0.102 to 0.152 cm (0.040 to 0.060 in)
Tolerances	± 0.0016 cm (± 0.004 in) linear 0.025 cm (0.010 in) concentricity
Surface Finish	127 μm (50 μ in)

Steel casting dies, although sufficient to produce 20,000 units without wear, proved too expensive in cost and schedule to be recouped over a 10 to 100 unit production run. Thus, we decided to investigate and alternate casting methods.

Rubber plaster mold casting was discovered to be ideal for our needs. Typical for quantities of 10 to 100, this process could readily produce units without the need of expensive dies. The compromise, however, would be in final surface dimensions and tolerances, which would require a minor finish machining operation. Comparing with die casting, accuracies were as follows:

Thinnest Sections	0.152 to 0.203 cm (0.060 to 0.080 in)
Tolerances	± 0.0127 cm (± 0.005 in) linear 0.025 cm (0.010 in) concentricity
Surface Finish	318 μm (125 μin) typical for sand castings

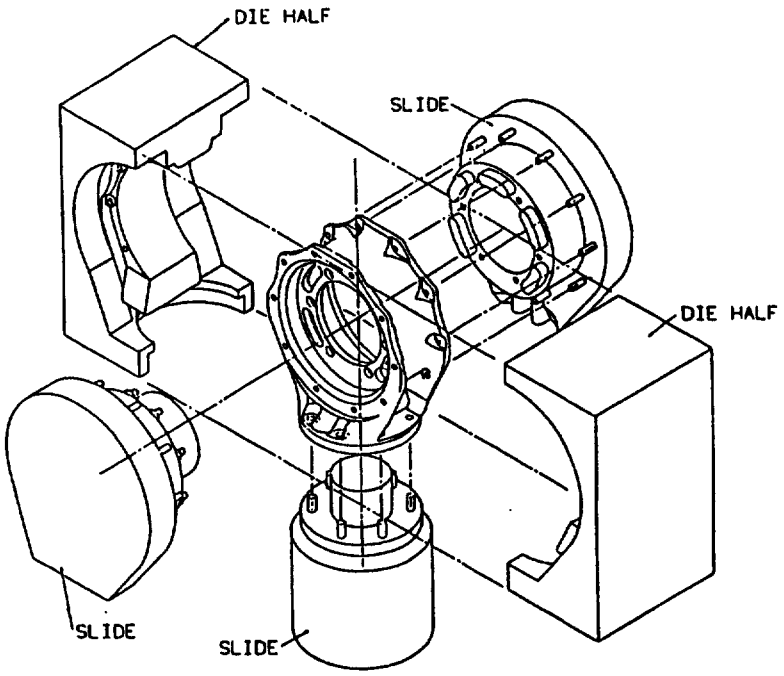

Figure 4. Conceptual Drawing of Outer Housing Die Assembly

To make a one-for-one cost/complexity evaluation with traditional fabrication methods, one set of SADA housings was machined from solid billets of SiCpAl and another set was plaster cast. Table 2 shows the cost results from these two approaches with actuals indicated. Unit costs for lots of one, ten, and one hundred are shown. From this table, two machined outboard units would have cost $12,136. This is approximately the same price as 10 cast units at $12,420. It became apparent that the cost effectiveness of casting would be realized at a quantity of approximately two or greater, with a cost avoidance of approximately 50% for a quantity of ten. This cost savings was realized with overall improved mechanical properties!

Table 2. Cost Comparison of Conventional Machining versus Casting

	Unit Cost for Lot of 1-9	Unit Cost for Lot of 10-99	Unit Cost for 100 or Greater
Outboard Solar Array Drive Assembly Housing:			
Machined Part Total	$6068.00†	$3138.00	$1979.00
Plaster Cast Part Total	$6510.00	$1242.00†	$374.00
Inboard Solar Array Drive Assembly Housing:			
Machined Part Total	$3925.00†	$1904.00	$905.00
Plaster Cast Part Total	$4571.00	$1021.00†	$284.00

† Costs taken from paid invoices, other costs quoted

SADA OVERVIEW

The two-axis SADA was the result of an effort to reduce size and weight of spacecraft mechanisms without sacrificing performance. This SADA uses two-phase, bipolar, 15-degree stepper motors with non-redundant windings coupled to 100:1 harmonic drive gear reducers in an extremely compact arrangement. Each

axis contains potentiometer position feedback and uses preloaded duplex bearings for reaction loads. Hard mechanical stops were used on each axis to limit rotation range. Each housing had bonded strip heaters and individual thermostats for temperature control. Lubricant used was Penzane X2000 with a lead additive, that was previously life tested on other TRW programs. This SADA was originally designed for gimballing 48.9 N (11.0 lb) thin-film solar arrays on a micro-satellite. Minimum pull-out running torques of 2.94 N•m (26 in•lb) and unenergized holding torques of 4.97 N•m (44 in•lb) were measured for each axis. Drive voltage can vary, but is nominally approximately 26 volts for each axis, with potentiometer excitation of 10 volts DC.

LESSONS LEARNED

Inclusions in the cast MMC parts were the only significant fabrication problem encountered. These were discovered during X-ray NDE and were the cause of remaking one batch of castings. A quantity of 10 of each housing were initially requested. When inspected to the Mil standard, only 5 of 20 outboard housings passed within the grade C allowable. For the inboard housings, 2 of 10 housings were conditionally accepted. All housings contained small gas holes, but rejected ones had these near free surfaces, in violation of the specification. Conditionally accepted housings had near-surface gas holes, but in benign stress regions. Vast experience was claimed by vendors of standard cast aluminum. However, casting MMC's systems introduced unique problems due to silicon carbide particulate dispersion, flow characteristics, mold moisture, and humidity conditions during casting. Experience for MMC systems is improving. It was not a factor for the enthusiasm and cooperation of the vendor to resolve these difficulties.

ACKNOWLEDGMENTS

This work was sponsored under the AMASS Program, Contract No. F33615-90-C-3200 and under the Moderate Strength Particulate Reinforced Aluminum Composites Program, Contract No. F33733-89-C-1011, both from Wright Laboratory, Wright Patterson AFB. We are grateful to Paul Lindquist, the AMASS Contract Officer, and to Lt. Col. Mike Obal of BMDO for his sponsorship.

DESIGN, DEVELOPMENT, AND TESTING OF A LIGHTWEIGHT OPTICAL SENSOR COVER SYSTEM

Mike Hurley
Naval Research Lab
Washington, DC

and

Scott Christiansen
Starsys Research Corporation
Boulder, Colorado

ABSTRACT

This paper discusses aspects of the design, development and testing of the sensor cover on the Clementine (DSPSE) spacecraft. Particular attention is given to defining the typically ambiguous issue of cleanliness (i.e. how clean is clean?). To characterize performance with respect to these requirements, a simple and effective method for testing prototype seals was developed. This testing was useful for comparing various types of seals as well as for providing information about achievable cleanliness levels. The results were invaluable input for defining a realistic final cleanliness requirement that satisfied everyone from mechanisms to sensor engineers.

Balancing torque margins (reliability) versus cost and/or weight of the system can be significantly influenced by choice of seal type. Several seal types are discussed in terms of both cleanliness and ease of implementation. These design issues influence actuator selection and structural integrity of the door.

The cover system designed and fabricated as described above was thoroughly tested both on a component level and on the Clementine system level. Testing included characterization, vibration, pyro-shock, life, and thermal/vacuum. The extensive testing identified problems early enough that they could be resolved prior to integration and launch.

INTRODUCTION

As more and more sensors are being flown, sensor covers are becoming a standard mechanisms subsystem on most satellites today. The two primary functions of a sensor cover are to protect the optics from debris and from exposure to excessive radiation. These cover functions lead to some level of sealing requirement and, often, a repeatable use requirement.

The Clementine spacecraft carries a cluster of five optical instruments to be used for imaging and ranging. The instruments were arranged in a relatively tight cluster to utilize a single optical bench and allow use of a single cover.

WHAT IS CLEAN?

A primary driver for design of a protective cover is defining what types of contaminants must be kept away from the optics. Considering the various environments (and what is known about them) encountered from integration through flight operation, establishing a realistic definition can be difficult. Over-specifying can lead to an over-complex design and threaten the reliability of the cover system. Under-specifying can lead to inadequate protection and allow contamination that could degrade instrument performance.

Ground handling and launch environments are relatively well understood. The primary contaminants to control are air born particles stirred up and/or carried by air currents. Covers also protect from inadvertent contact by hands or tools during integration and handling. Conditions during flight are more difficult to evaluate. During instrument operation the cover must be open, of course, and the optics are exposed to any contamination that may be present. Design engineers must determine whether protection is necessary during periods when increased contamination is expected (delta-V burns, maneuvering with thrusters, passage through zones of "space dust", etc.). Determining whether to add the complexity of a cover versus no cover at all is a difficult problem which must be solved considering the instrument and flight requirements specific to the given mission.

The requirements for the optics on Clementine were evaluated based on mission requirements and events. It was determined that protection for the optics was required during a solid rocket burn during flight as well as during ground operations and launch. It was also desirable to be able to close the cover if higher levels of contamination were encountered or if maneuvers caused extended exposure to solar radiation. The primary concern was to avoid particulate contamination on the optics surfaces. Sealing requirements for the cover were established such that the optics would be protected against particles larger than 0.1 mm diameter while the cover was closed.

SEAL DEVELOPMENT TESTS

The requirements for particulate protection established that a hermetic seal was not required. In considering the design of the cover and seal two basic approaches were compared. The choice of seal would have a significant influence on the drive system design. The first approach was to use an "energized" seal such as an O-ring or a wipe type contact seal (similar to weather stripping on a door). The second

was to use a non-energized seal such as a labyrinth seal. During the initial design stages it was thought that an energized seal would probably provide better sealing, but would also require much higher torques to open and then to re-close and re-seal. The non-energized seal would be preferred from a drive mechanism point of view, but might not provide adequate sealing. Because of potential problems with sticking an O-ring/elastomeric seal was not considered.

In order to obtain additional information on seal effectiveness and related torque requirements a quick and dirty seal test was conceived. Two cover mock-ups were fabricated. One was made with a wipe seal made from Kapton strip and the other with a labyrinth seal. The covers were made from a clear plastic so that the interior space could be inspected without opening the cover. Each cover was then placed in a chamber and subjected to a dust-filled environment. Figure 1 shows the chamber with a cover/seal mock-up.

Several substances were investigated as particle sources for the desired particle distribution. Of the easily obtained sources, flour provided the best distribution with particles ranging from approximately 0.05mm to 0.5mm diameter. The flour was introduced into the chamber using a high speed air stream. During the tests the covers were held closed under several different conditions to simulate environments expected during flight. The air currents swirled the flour forcefully throughout the chamber, coating all surfaces with dust. The mock-up cover was then removed, the exterior was carefully cleaned, and the protected area was inspected for particles that may have intruded past the seal.

The test results indicated that the labyrinth seal tested provided better protection than the Kapton wipe seal. This approach was approved and the labyrinth seal was incorporated into the design. A cross section of the cover system showing the drive components and a portion of the seal area is shown in Figure 2. The seal geometry is shown in Figure 3. Figure 4 is a photograph of the competed cover system.

SUMMARY

The success of the labyrinth seal allowed the use of a very lightweight cover and drive system. The non-energized seal did not require a heavy cover structure to establish adequate sealing. The system could also operate with lower torques, allowing al lightweight, reliable drive system. The total mass of the drive system, cover, and mating seal was 1.38 kg.

The flight cover system was delivered to the Naval Research Laboratory in August, 1993. Acceptance testing, including system characterization, vibration, pyro-shock, life and thermal/vacuum, was completed. Several anomalies were identified and resolved by mid-November, 1993. The spacecraft was successfully launched on January 25, 1994.

LESSONS LEARNED

1. Defining realistic cleanliness requirements for an instrument requires a balance between the actual needs of the optics, the anticipated environmental conditions, and the practicality of designing and using an adequate cover system.

2. Very simple, easily interpreted tests can provide information critical for comparing different, but apparently equivalent, design approaches.

3. The "flour test" is a rigorous development test invaluable for characterizing a seal system.

4. Extensive acceptance testing of the flight system can identify anomalies that can then be quickly resolved prior to integration and launch

TABLES AND FIGURES

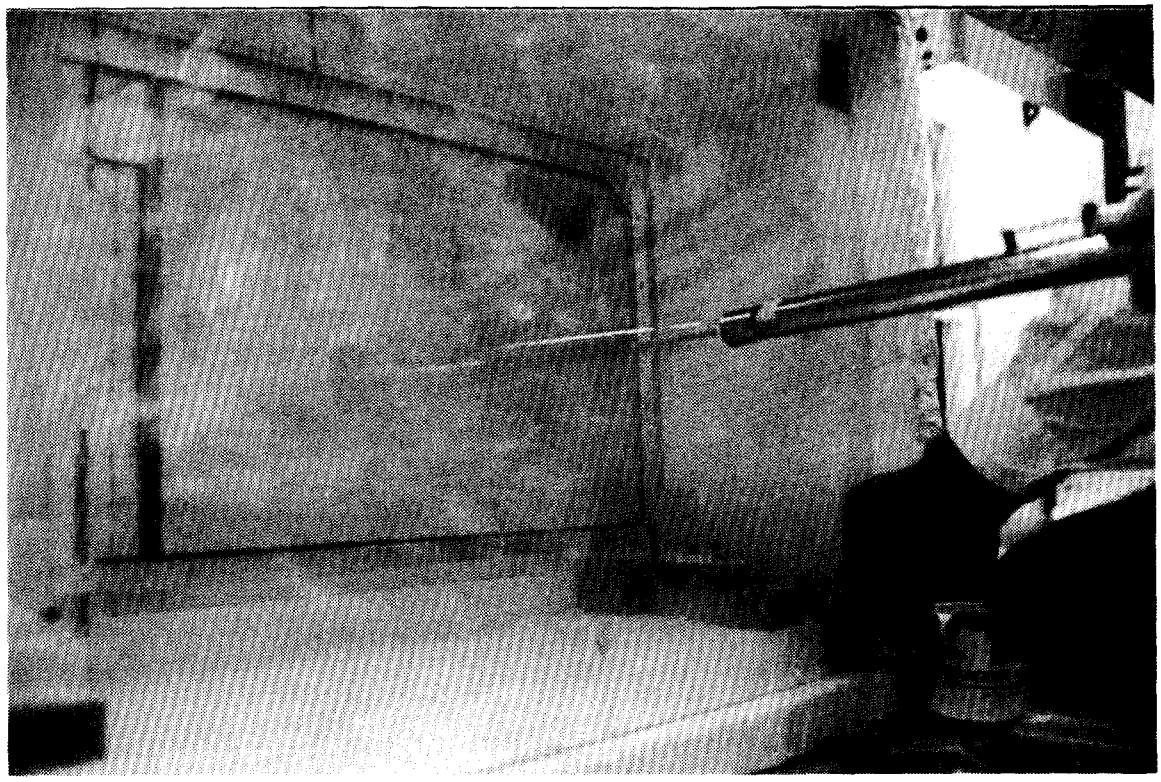

Figure 1. Seal mock-up and test chamber during flour test.

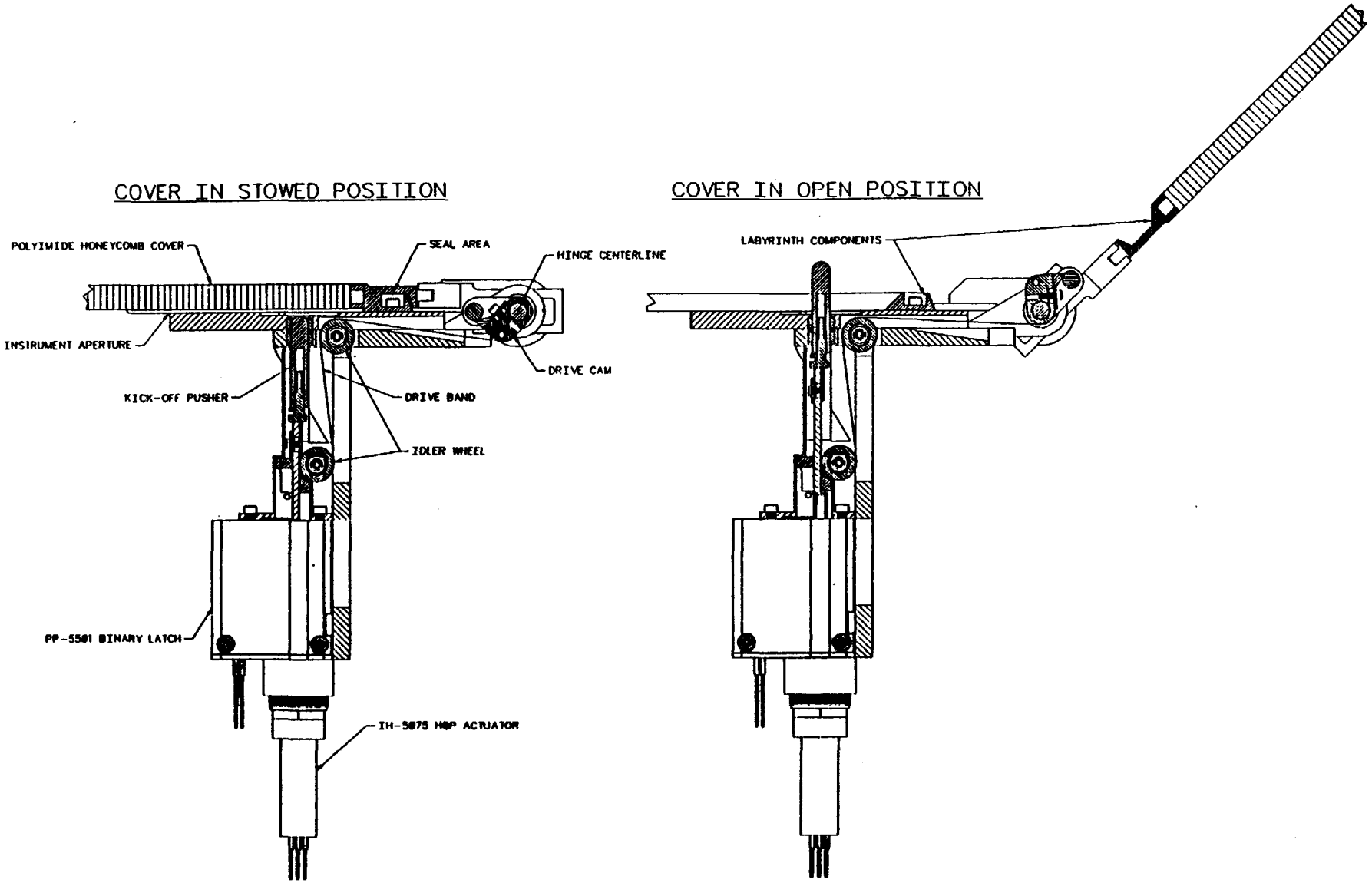

Figure 2. Partial cross section of cover, seal, and drive mechanism for Clementine sensor cover system.

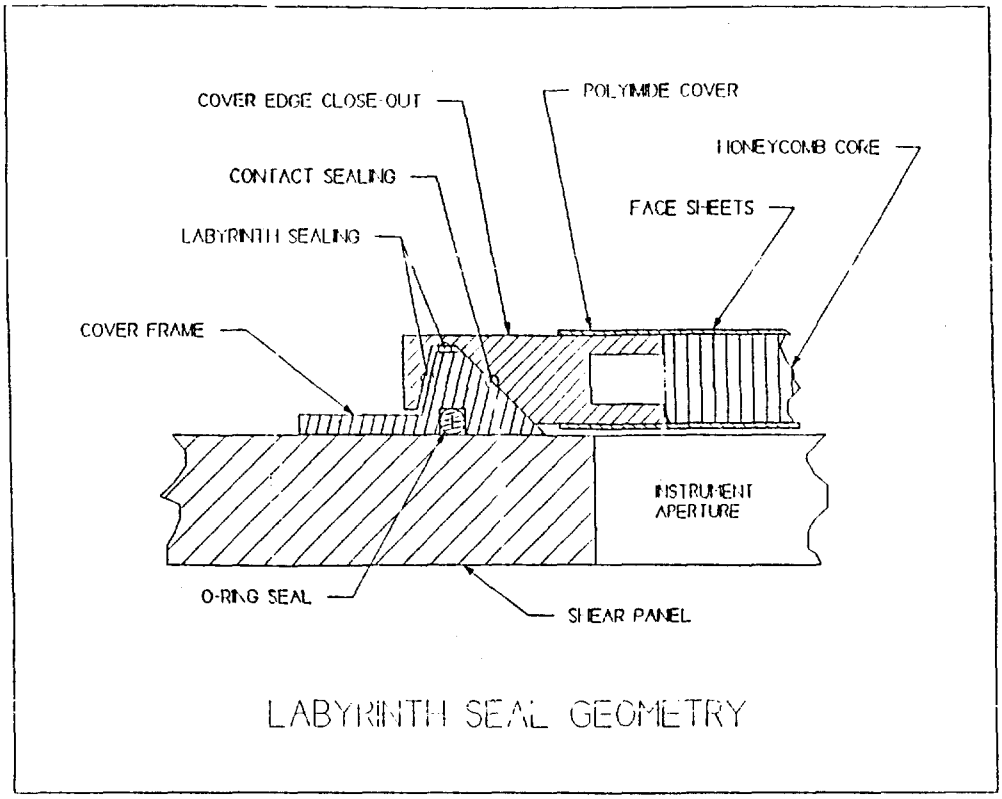

Figure 3. Labyrinth seal geometry.

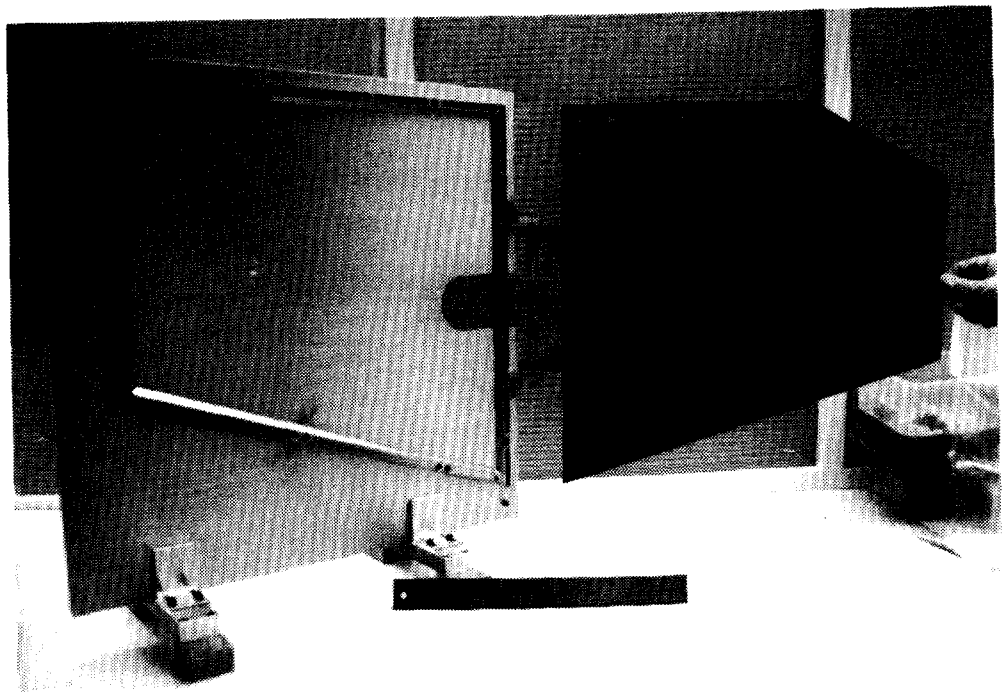

Figure 4. Compete cover system mounted to test plate.

ENERGY ABSORBER FOR THE CETA

Clarence J. Wesselski
Lockheed Engineering and Sciences Co.
Houston, Texas

ABSTRACT

The energy absorber that has been developed for the CETA (Crew Equipment and Translation Aid) on Space Station Freedom is a metal on metal frictional type and has a load regulating feature that prevents excessive stroking loads from occurring while in operation. This paper highlights some of the design and operating aspects and the testing of this energy absorber.

INTRODUCTION

EVA systems offer many challenges for developing mechanisms that will function properly for a 10 year or longer life span. The design challenges arise because of these numerous factors of which the following three are considered key design drivers:

1. Requirement to operate over a temperature range of approximately 110 deg. C,
2. Long non-operating storage under hard vacuum, and
3. Atomic oxygen and micro meteorite effects on exposed surfaces.

One such case in point is the development of energy absorbers that will be used on the CETA carts. These devices will be used for dissipating the kinetic energy if the CETA cart brakes fail without imposing excessive G's on other space station hardware, structure, or EVA crew member.

Common methods of dissipating energy such as forcing fluids through an orifice or crushing some deformable material have some serious disadvantages. The combined effects of space environments render most solutions developed for ground, air, or even marine operations unacceptable. For example, changes in fluid viscosity with temperature, lack of long term stability of most elastomers, creep of Teflon and other classic sealing materials under load render most pneumatic or hydraulic solutions inappropriate. Using crushable or deformable material is also undesirable because of the necessity of refurbishment each time the energy absorber is used. A frictional energy absorber design offers the best solution to the problem. However, using the current design for frictional energy absorbers has known drawbacks such as; lubricated surfaces subjected to wear and exposed to vacuum are currently at the limits of certified

materials, and because of uncertainty of the friction coefficient of sliding surfaces, the stroking load is unpredictable.

DEVELOPMENT TEST ARTICLE

EVA Systems has developed a frictional energy absorber that will meet the stringent requirements of long orbital life and yet have a stroking load that is predictable within reasonable bounds. In principle, this energy absorber uses a hardened Inconel 718 shaft sliding through several beryllium copper diaphragm elements as shown in Figure 1. As noted in Figures 2 and 3, there is a significant interference fit between the shaft diameter and the inside diameter of the diaphragm elements so that a high friction drag load occurs in the compression direction. A return spring resets the absorber after each stroke. Most important in the advancement of this art is that this absorber uses a force sensing and regulating (in principle a force feedback mechanism) device. The operating principle is shown in Figure 4. In stroking, the friction diaphragms are reacted by one or more Belleville springs. If the friction load becomes too high, the Belleville springs deflect more, which in turn reduces the normal pressure acting against the friction rod, thus lowering the stroking load. This novel feature will serve to keep the stroking load at a reasonable level even if the friction coefficient increases greatly. The force feedback device also serves to desensitize the singular and combined effects of manufacturing tolerances, sliding surface wear, temperature changes, dynamic effects, and lubricity. Analysis suggests that the stroking force will increase only 30% if the coefficient of friction should happen to increase from 0.10 to 0.30. This 30% variation is an acceptable level of predictability for the energy absorber to assure that the space station is protected from high structural loads. With conventional friction energy absorbers, the stroking force is nearly directly proportional to the friction coefficient. This means that a friction coefficient change from 0.10 to 0.30 would result in the stroking load increasing by a factor of 3.0 if a conventionally designed energy absorber were used. Such an uncertain performance would offer the possibility of very high loads on the space station structure.

TESTING HIGHLIGHTS

A prototype of the EVA Systems' energy absorber has been fabricated and tests have been conducted that prove the concept. Eight (8) diaphragms were used in the test article for each test that was performed. Using the Instron machine, stroking loads have been measured for various conditions and compare favorably to predicted values. The tests also indicate that the force regulating feature of this absorber works according to analytical predictions. As shown in Figure 5, for instance, a test was run with dry unlubricated surfaces. With no force regulation, the stroking load

reached a maximum of 180 N. When the force regulating Belleville springs were put back in, the stroking load reached 84 N.

A new set of eight diaphragms was then installed in the test article. Then repetitive cycling tests at ambient conditions were run in an Instron machine to compare the merits of two candidate lubricants. Five hundred load cycles were run using Krytox LVP grease as the lubricant. The stroking force gradually increased from 61 N to 83 N at the end of the 500 cycles. The diaphragm ID wear was measured at 0.01mm. Next, the unit was degreased and refurbished with a new set of eight diaphragms. It was re-lubricated with a thin, wipe-off film of Braycote 815Z oil. Then 500 load cycles were run again. The stroking load started at 63 N and had a slight decline of load to 61 N at the end of the 500 cycles. The diaphragm inner diameter (ID) wear was almost negligible at 0.005 mm. Since the wear limit is .05 mm, both of these lubricants performed quite well. It was also obvious that Braycote 815Z lubricant was the better choice of lubricants under ambient test conditions.

In addition to cycling tests that were run under ambient conditions, cycling tests were also performed in an environmental thermal vacuum chamber. Because of negligible wear from the previous test, the same test article was used in the "as is" condition and Braycote 815Z lubricant was used for these tests. Six runs of 100 load cycles each were performed. Run #1 was performed at room temperature; run #2 at -51 deg C and the rest of the runs were alternated in this manner. All of these tests were performed under vacuum conditions. Fig. 6 shows the results of these tests. Note that at ambient temperatures, the load held steady at about 55 N. At -51 deg C, the load had a small increase up to about 75 N. The wear for these tests was 0.03 mm from the diaphragm ID, which was also below the wear limit.

CONCLUSIONS

The design goal of having an energy absorber that will function predictably over a long orbital life can be achieved with the EVA Systems design. On the basis of the tests that have been performed, the energy absorber has low sensitivity to manufacturing tolerances, lubricity, and other variables. Test results indicate that it will fulfill all of the requirements in the expected environments in a very satisfactory way. By choosing the appropriate design parameters, this energy absorber can find many uses for commercial, marine, military, and aerospace applications.

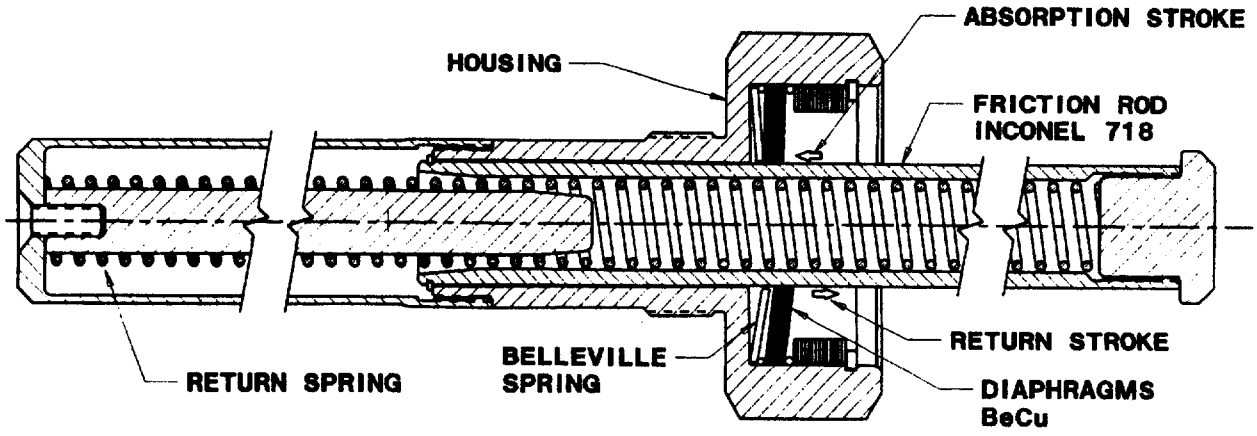

Fig. 1. Energy Absorber Cross Section.

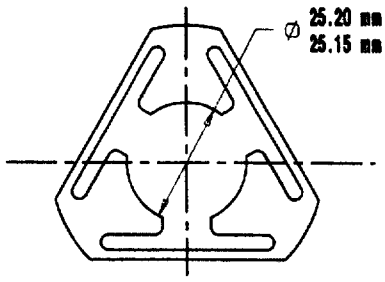

Fig. 2. Friction Diaphragm.

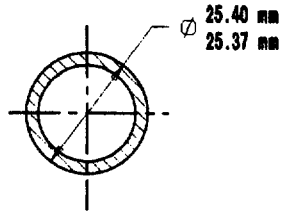

Fig. 3. Friction Rod Cross Section.

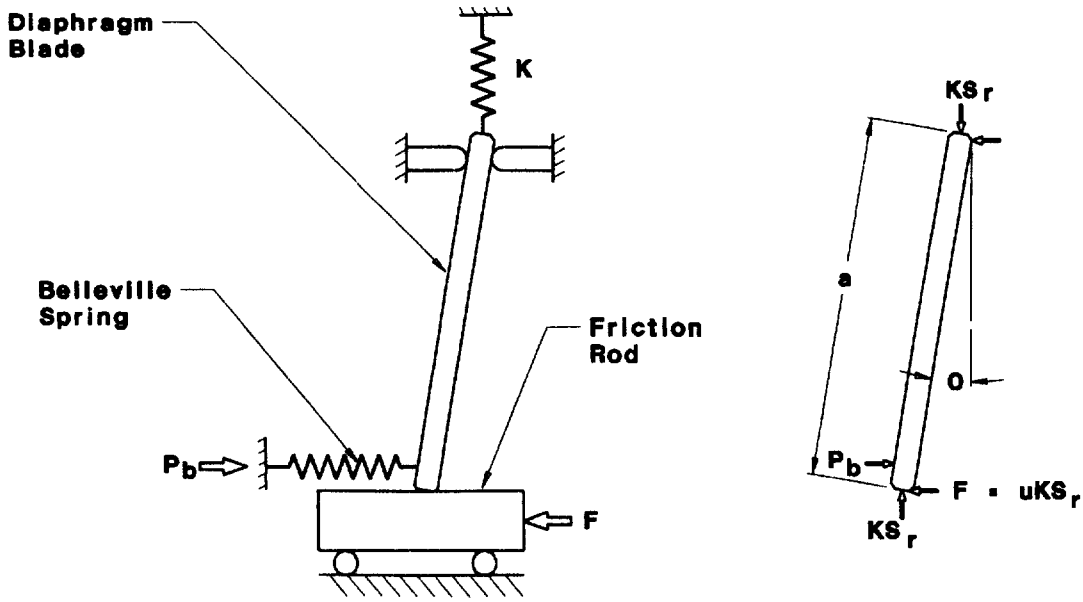

Fig. 4. Schematic of Operating Principle.

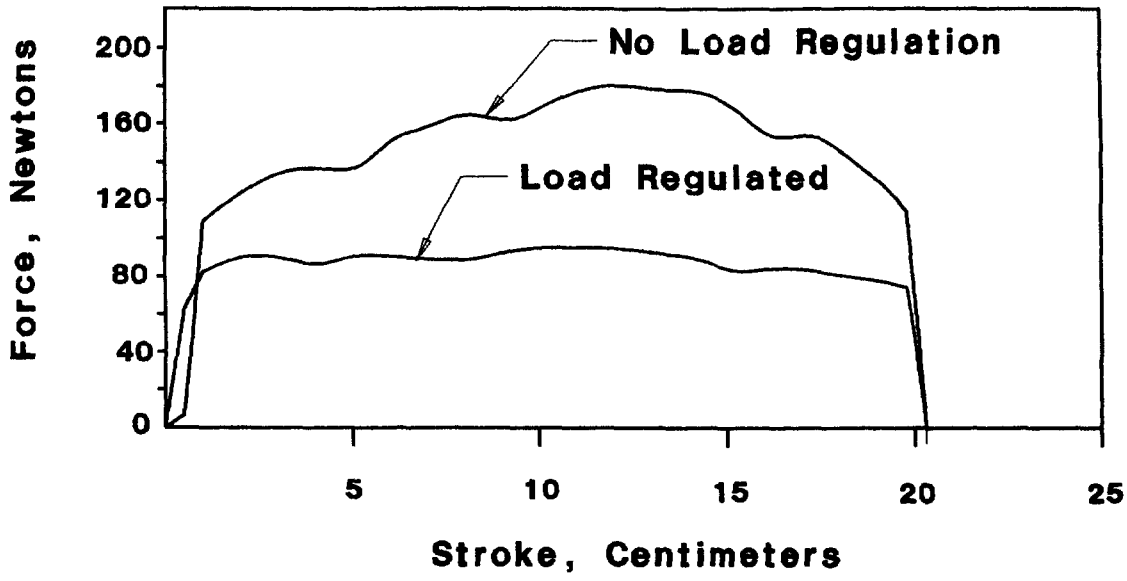

Fig. 5. Load vs Stroke for Unlubricated Conditions.

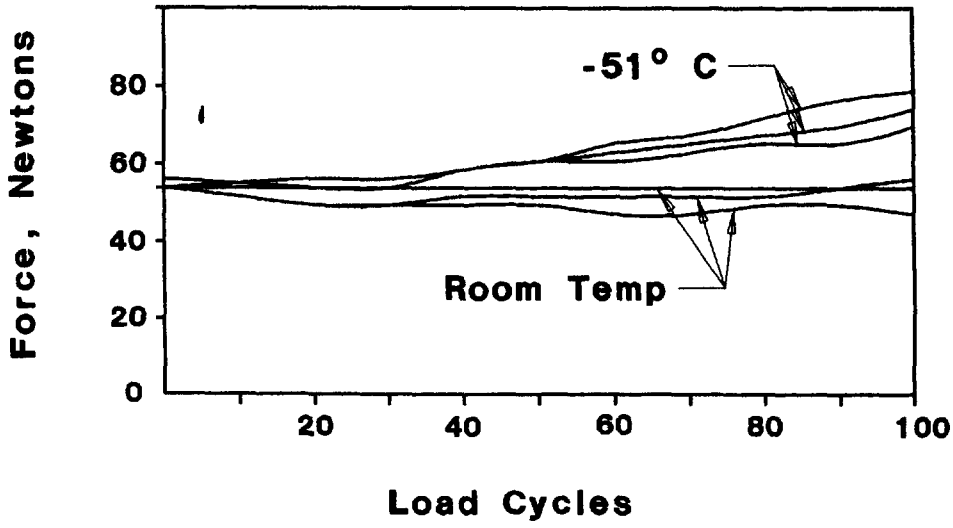

Fig. 6. Environmental Tests in Vacuum Chamber.

DESIGN, CHARACTERIZATION, AND CONTROL OF THE NASA THREE DEGREE OF FREEDOM REACTION COMPENSATION PLATFORM

Craig Birkhimer and Wyatt Newman
Case Western Reserve University
Cleveland, Ohio

and

Benjamin Choi and Charles Lawrence
NASA Lewis Research Center
Cleveland, Ohio

Introduction

Increasing research is being done into industrial uses for the microgravity environment aboard orbiting space vehicles. However, there is some concern over the effects of reaction forces produced by moving objects, especially motors, robotic actuators, and astronauts. Reaction forces produced by movement of these objects may manifest themselves as undesirable accelerations in the space vehicle, making the vehicle unusable for microgravity applications. It is desirable to provide compensation for such forces using active means.

This paper presents the design and experimental evaluation of the NASA three degree of freedom reaction compensation platform, a system designed to be a testbed for the feasibility of active attenuation of reaction forces caused by moving objects in a microgravity environment. Unique "linear motors", which convert electrical current directly into rectilinear force, are used in the platform design. The linear motors induce accelerations of the displacer inertias. These accelerations create reaction forces that may be controlled to counteract disturbance forces introduced to the platform. The stated project goal is to reduce reaction forces by 90%, or -20 dB. Description of the system hardware, characterization of the actuators and the composite system, and design of the software safety system and control software are included.

System Hardware

Figure 1 shows the design of the platform system. The platform system consists of a passive spring-mass-damper with added active components and sensors. The passive system attenuates forces at frequencies greater than the resonance, and passes forces at frequencies below the resonance. Figure 2 shows a Bode plot of the transfer function from the disturbance force applied to the platform to the residual force felt at the mechanical ground. Since the passive system provides at least -20 dB disturbance attenuation for frequencies above 88 $^{rad}/_{s}$, the active system design should be most concerned with disturbance rejection below that frequency. The resonant frequency could be lowered by decreasing the spring constant, at the expense of larger platform excursion, or by increasing the system mass, which may not be desirable in a space-going system. Also, damping could be added to reduce the effect of the resonance, but this may spread the phase transition over an unacceptably large frequency range.

The displacers of the linear motors are constrained to vertical motions with respect to the platform, and can thus react to vertical disturbance forces (along the

z-axis) and moments about the x- and y-axes. The motors are each capable of 712 N maximum force. All have a displacer mass of 5.6 kg, and a stroke of 0.3 m. Some insight can be gained by using the maximum force rating of the motors and the stroke limit to plot force and position attainable as a function of frequency, as shown in Figure 3. Below 4.8 Hz, the force available is limited by the position constraint; above that frequency, the position amplitude is limited by the maximum force constraint. Therefore, it is safe to attempt control at high frequencies, while commanding a large-amplitude control signal at low frequencies may be unsafe or ineffective. The switch frequency could be decreased by increasing the mass of the motor displacer, which may be undesirable, or by increasing the displacement limit, which would require replacing the motors. Increasing the motor mass would have the added effect of decreasing the maximum velocity, which would decrease forces due to friction and back-EMF.

All of the motors are equipped with optical incremental encoders accurate to 10 μm, home switches, and limit overrun switches. In addition, each motor is equipped with a compressed air "spring" support system to counteract forces due to gravity on the displacers. Maximum velocity of the motor displacers for sinusoidal force inputs is 4.2 $^{m}/_{s}$.

The force sensors and accelerometers are piezoelectric and are effectively high-pass filtered with a time constant of 2.5 s due to their design, making control of low frequencies using these sensors impossible. The force sensors have a maximum rating of 2670 N, and the accelerometers have a maximum rating of 98 $^{m}/_{s2}$.

Communication between the control program and the motors and sensors takes place through a Programmable Multi-Axis Controller (PMAC) board. This board does encoder interpretation and velocity estimation for the motors, receives information from the sensors, performs commutation for the three-phase motors, and sends current commands generated to the motors. Motor force commands are sent out at 2.3 kHz. The board also performs auto-shutdown of the motors in case of a position limit fault. The PMAC board has a built in high-level motion control language, which is interpreted in real time rather than being compiled; this makes program execution very slow, and unsuitable for running extensive control programs.

The actual control takes place on a 80486-based PC running at 33 MHz. The control program is written in C, and compilation is optimized for speed by using some of the features of the 80486 microprocessor. The control loop runs at 1.1 kHz.

Characterization

Without accurate modeling of motor and composite system behavior, high-performance control is not possible. In particular, information on the force constant, mass, friction, maximum force and velocity, and bandwidth of each motor are needed before any active compensation using the motors can be attempted. Although the motors have electrical and mechanical characteristics very similar to

three-phase rotary motors, the mechanical stops prevent the use of rotary motor characterization techniques. Instead, techniques similar to those utilized in robotics were used to prevent motor damage[1]. These methods use small cyclical forces or motions to obtain data on motor parameters.

During the characterization, it became apparent that there were some dynamics in the motor and/or the air spring that had not been accounted for. Further examination revealed the presence of a position-dependent force offset. This offset requires that, at a certain position, the motors must exert a constant force to prevent the motor displacers from accelerating. The offset is probably the result of a "detent force," an attraction of the motor displacers to certain positions along their tracks, plus position-dependent air spring dynamics. The data taken for one of the motors, and the function used to model this phenomenon, are shown in Figure 4. The modeling function takes the form of a sinusoid-plus-slope-plus-constant.

Control

The control consists of three discrete parts: the force feed-forward controller, which directly responds to incoming forces read from the force sensors; the acceleration feedback controller, which responds to accelerations of the platform mass; and the motor position controller, which attracts the motors to equilibrium position, provides software damping for the motors, and also acts as a primary safety system.

The feedforward force control is a very straight-forward design, similar in principle to methods used in audio noise reduction. The disturbance forces are obtained by the force sensors; the signals are then negated (phase inverted) and reapplied using the actuators. Performance is limited by the design of the force sensors, motor modeling errors, and the digital delay inherent in all digital systems. Although only preliminary data has been collected on this control scheme, simulations have shown that 20 dB attenuation is achievable for frequencies between 55 $^{rad}/_{s}$ and 150 $^{rad}/_{s}$.

Control of the platform using feedback of the acceleration data proved to be a difficult problem. Phase shifts due to the platform itself, the piezoelectric nature of the sensors, and the time delay inherent in digital systems combined to cause problems with stability and control bandwidth. Classical control methods would produce the desired disturbance attenuation at high frequencies only at the expense of disturbance amplification at low frequencies, and state-space control seemed encouraging in simulation, but was too sensitive to partly measured or unmeasured values.

It is necessary to have a motor position controller to attract the motors toward zero position, so that disturbances caused by the motor triggering the safety system are kept to a minimum; it is also desirable to have velocity control to provide damping. The proportional-derivative (PD) control scheme is well documented and seems suitable for this task, but closer examination reveals limitations in this scheme. In order to insure that the limits are never overrun, a PD-controller would

have to have a resonant frequency of about 36 $^{rad}/_{s}$, significantly degrading the lower frequency response of the combined controller.

To alleviate this problem, higher-order functions of position and velocity are used to achieve a bumper-like effect. These types of functions tend to have small effect at high frequencies or small amplitude motions, but large effect at low frequencies or high amplitude motions. This has the effect of allowing high frequencies, but attenuating low frequencies where the motor cannot exert full force safely. Careful selection of the gain parameters allows only slight degradation in frequency response of the force and acceleration controllers, while providing another level of safety for the motors and attracting motor displacers toward equilibrium position.

Unfortunately, operation of the nonlinear "bumper" is directly opposed to operation of the acceleration controller. Any control effort from the bumper shows up at the platform as an acceleration; if the acceleration controller is working properly, it will then attempt to cancel this acceleration by applying an opposing force, defeating the purpose of the bumper controller. This problem can be solved by including a reference term before the acceleration controller, that is a result of the bumper control effort filtered through the plant model to give an acceleration. See Figure 5.

In addition, superimposing the desired forces from all the controllers may result in a condition where the desired bumper force is defeated, leading to a motor collision and possible damage. To avoid this, the desired forces from the force sensor and accelerometer loops are filtered through a nonlinear function that is dependent on the desired bumper force. The forces are superimposed only if the sign of the combined force is the same as that of the bumper force; if the signs are opposite, the combined force is multiplied by a gain of between zero and one, depending on the magnitude of the bumper force. Lower gain is applied for higher bumper force, so that the bumper force takes higher precedence. This policy is summed up in the following equation: $F_{out} = F_b + f(F_b)F_c$, where F_b is the desired bumper force, F_c is the desired control force, and $f(F_b)$ is a continuous function which equals 0 for F_b greater than an upper threshold value, 1 for F_b less than a lower threshold value, and decreases linearly from 1 to 0 for values of F_b between the two threshold values.

Conclusions

The force and stroke limits of the motors both serve as actuator saturation limits. The force limit sets the saturation at high frequencies, while the stroke limit sets the saturation at low frequencies.

Classical control proved to be ineffective for control in the acceleration feedback loop. Control using classical methods yielded either small attenuation of forces or attenuation at high frequencies only at the expense of amplification at low frequencies. Also, the use of state-space methods in the acceleration controller proved to be ineffective due to oversensitivity to partly measured or unmeasured

quantities, and the inability of state-space controllers to accept reference inputs in the case of the platform system [2].

The nonlinear "bumper" position and velocity controller proved to be more desirable than the commonly-used PD controller due to the bumper's lower force commands for high frequency/low amplitude motor motion. This allowed greater bandwidth of the combined controller.

The anticipated force disturbance rejection for the combined system is at least -20 dB attenuation for frequencies greater than 55 $^{rad}/_{s}$, which will extend the lower bandwidth by 33 $^{rad}/_{s}$ below that of the passive system alone, without an increase in platform mass or decrease in spring stiffness.

References

1. Velasco, Vergilio B., Jr. "Characterization and Control of the Unique Mobility Corporation Robot Prototype." Case Western Reserve University thesis, December, 1990, pp. 53-56
2. Franklin,Gene F., J. David Powell and Michael L. Workman. *Digital Control of Dynamic Systems.* New York: Addison-Wesley, ©1990, pp. 654-720

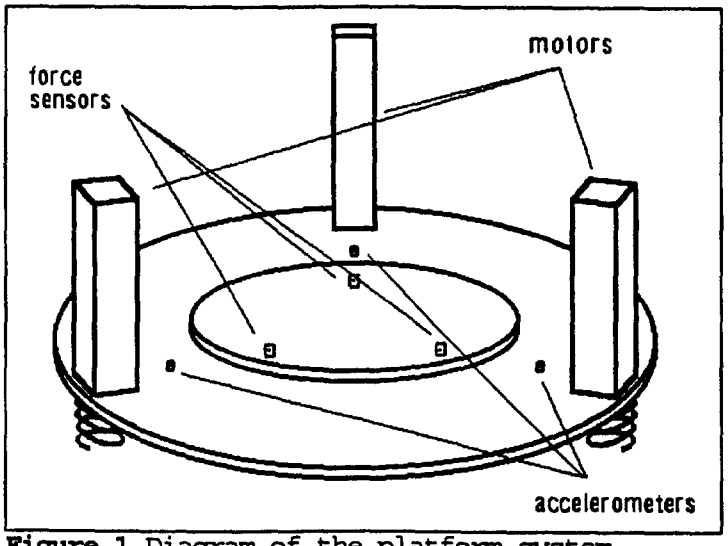

Figure 1 Diagram of the platform system.

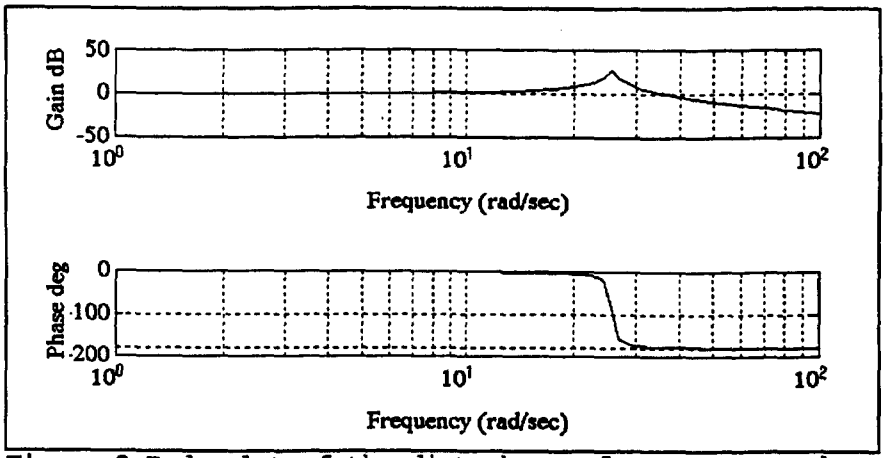

Figure 2 Bode plot of the disturbance force to ground transfer function for the passive platform system.

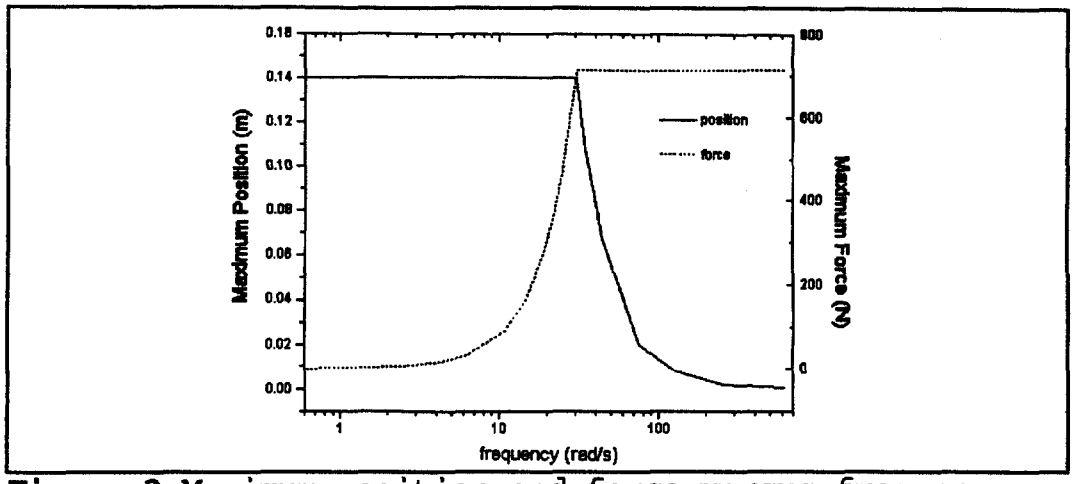

Figure 3 Maximum position and force versus frequency.

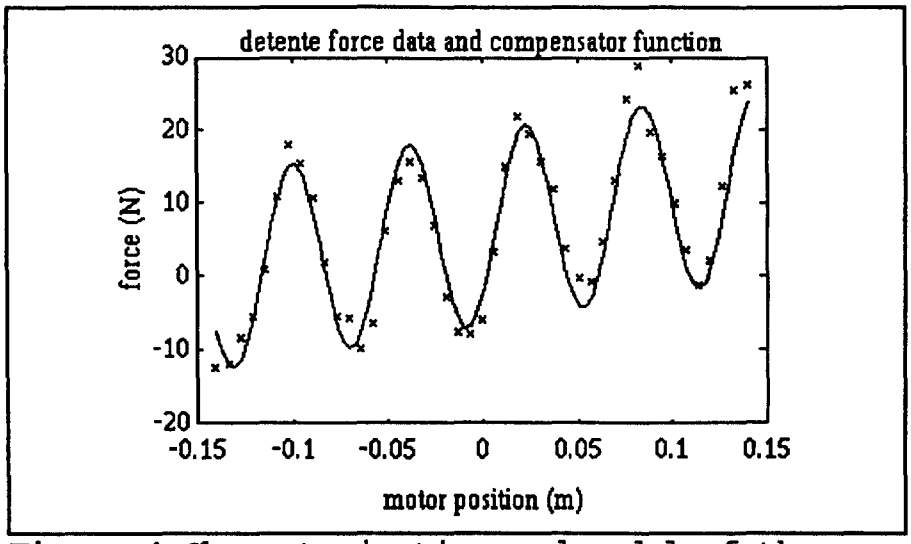

Figure 4 Characterization and model of the detente force for one of the motors.

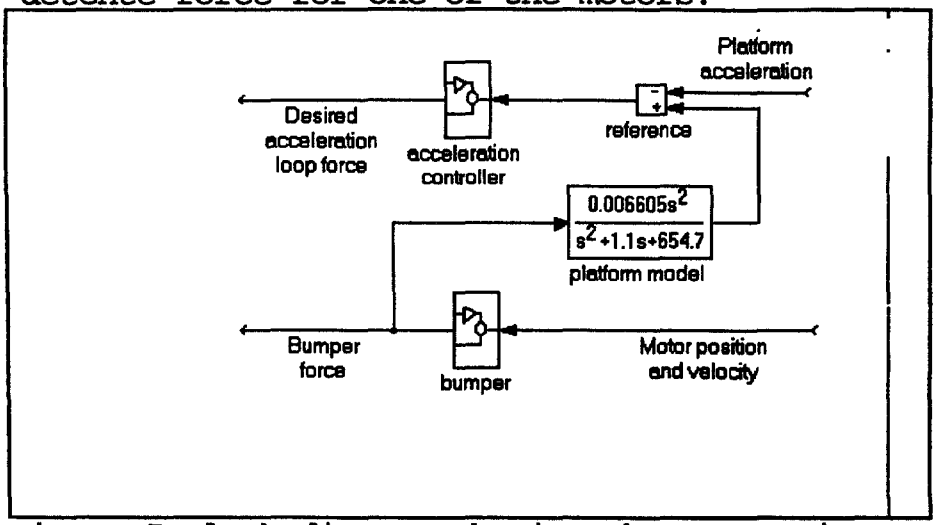

Figure 5 Block diagram showing the correction for opposing acceleration and position control.

PIP PIN RELIABILITY AND DESIGN

Lane P. Skyles
Lockheed Engineering & Sciences Company
Houston, Texas

ABSTRACT

Pip pins are used in many engineering applications. Of particular interest to the aerospace industry is their use in various mechanism designs. Many payloads that fly aboard our nation's Space Shuttle have at least one actuated mechanism. Often these mechanisms incorporate pip pins in their design in order to fasten interfacing parts or joints. Pip pins are most often used when an astronaut will have a direct interface with the mechanism. This interfacing can be done during Space Shuttle mission EVAs (Extra Vehicular Activities). The main reason for incorporating pip pins is convenience and their ability to provide quick release of interfacing parts. However, there are some issues that must be taken into account when using them in a design. These issues include documented failures and quality control problems when using substandard pip pins. A history of pip pins as they relate to the aerospace industry as well as general reliable design features is discussed.

INTRODUCTION

Pip pins are a logical choice in a design that requires expedient release of joints of interfacing parts. Shear loads are most often present in these interfacing joints, however, pip pins can be designed to react tensile loads. Although they are efficient and effective in utilization, there are several aspects to consider when incorporating a pip pin into a design. Several failures have occurred during NASA vibration and thermal/vacuum testing of past flight projects. Due to these failures, general design considerations of pip pins have been scrutinized and reconsidered to alleviate inherent problems with previous designs. As a result, new techniques in the design and fabrication of pip pins have been developed to create a more reliable pip pin.

HISTORY

The name pip pin is a short abbreviation of "push in and pull" pin.

Although several documented inadvertent releases of pip pins have been noted, no serious documented failures occurred in our nation's space program until 1990. During this year, NASA began environmental testing of the EVA Development Flight Experiments (EDFE) payload. During vibration testing, several locking balls in the pip pins vibrated out of their sockets. In addition, the lubricant inside of the pins froze and seized the pins during cold temperature vacuum testing. NASA solved these problems by using Military Standard pip pins that were quality controlled and removed all lubrication from the pip pins. Since the EDFE pip pins would be used for only one mission, and lubrication was mainly provided for corrosion protection, it was decided that the lubrication was not needed.

Although NASA/JSC had previously proposed improvements in pip pin designs, as a result of the EDFE project, JSC began working on additional design solutions to make all pip pins more reliable. Several design changes were made to existing pip pins as a result of this process in order to generate "space" quality products.

DESIGNS

It should be noted that the improvements made to the general design of pip pins were dictated by NASA to create more reliable pip pins for our nation's space program. Design changes were made specifically for space applications. There are no other designs (vendor or Military Specification) known that are specifically for space applications. Design improvements made are as follows (Figure 1 details these design features):

Four Locking Balls

Four locking balls are utilized in all of the new designs. Incorporating four balls provides redundancy if one of the balls falls out of its socket. Designs with two locking balls are not redundant, if one ball falls out, the inner shaft becomes loose and the remaining ball may no longer be in contact with the internal shaft. This loose fit may then vibrate to the point causing the remaining ball to fall into the inner

shaft ball groove or fall out of the barrel end of the pin. With the four ball design, if one ball falls out of its socket, the inner shaft will be retained by the remaining three balls.

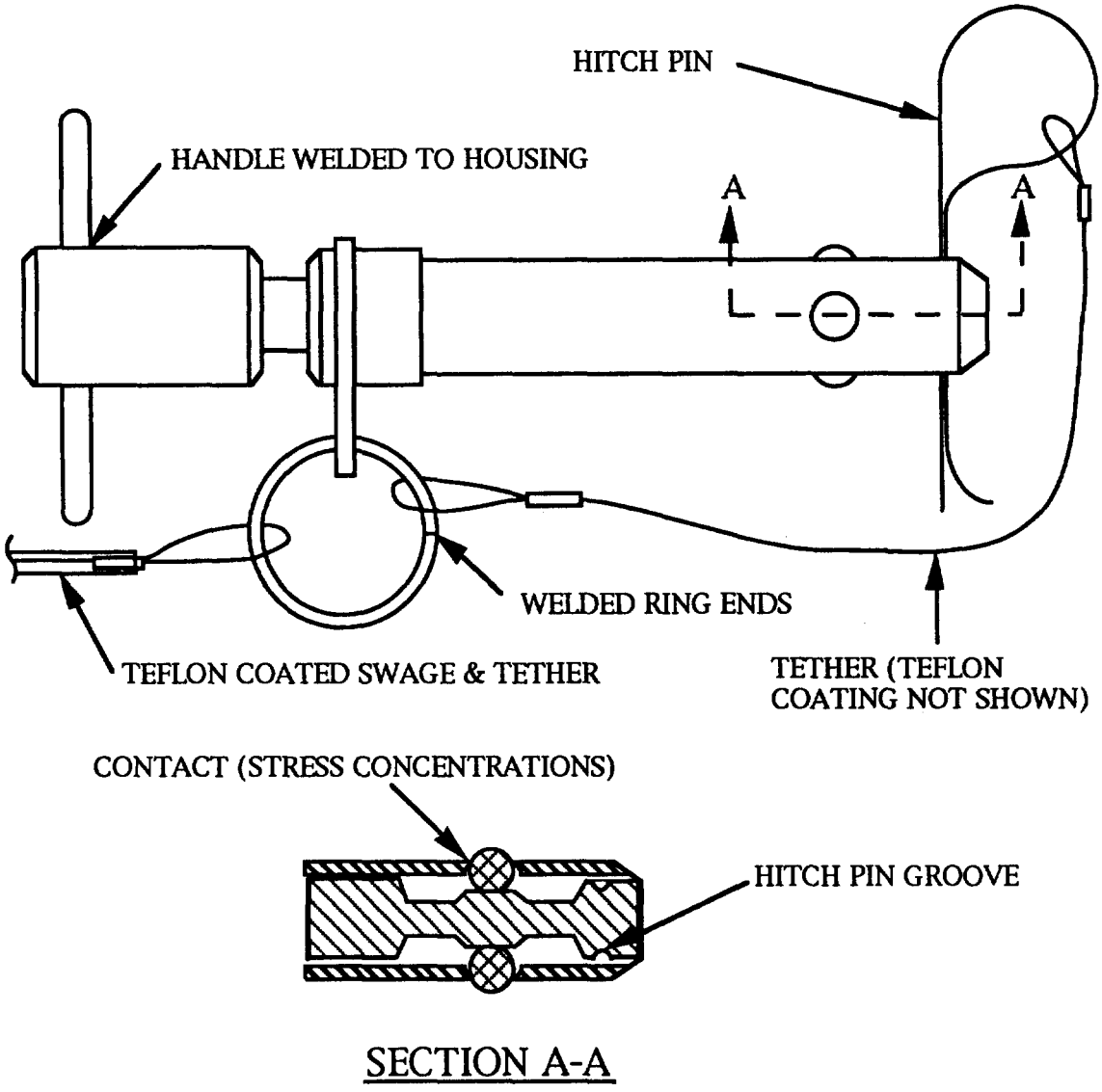

Figure 1. Pip Pin Schematic (T-Handle, Double Acting)

Double Acting

Most single acting pip pins only provide release capability when a spring loaded release button on the handle is pushed. Referring to

Section A-A of Figure 1, the double acting pip pins provide release capability when the handle is either pushed or pulled. Grooves are cut in the inner shaft on both sides of the locking balls to provide this capability. The benefit from providing this capability is that the pin is more ergonomically compatible. It provides more efficient and effective removal from and insertion into mating pip pin holes.

Teflon Coated Tethers

When wire tethers are swaged onto tether rings, the possibility exists that the wire end may protrude beyond the swaged fitting. This would create a tear hazard for an astronaut's pressure suit. Therefore, a Teflon sleeve was added to cover the swage fitting & cable termination. A Teflon coating on the cable provides a smooth surface on the outside of the tether thereby preventing the possibility that the astronaut's suit will come into contact with any frayed or broken cable strands.

Welded Handle and Tether Ring

In many pip pin designs, handles are pinned into place with a dowel pin. This oversized fit between the dowel pin and dowel hole provides fastening of the handle onto the head of the pip pin. This presents failure scenarios of the dowel pin shearing or working out of the hole due to vibration or thermal effects. These failure scenarios were corrected by welding a one piece handle to the head of the pip pins, providing assurance that the handle will not easily separate from the pip pin head.

Tether rings are critical in preventing the pip pin from floating away in a zero gravity environment. Therefore, a reliable tether attachment is essential. In order to provide the most dependable tether arrangement, all tether rings are either solid or have welded ends. When a ring is not created as a one piece solid, there will be two ends of the ring that will come together. These ends are welded to increase reliability. Split rings (such as a key chain ring) were considered hazardous because of two reasons: 1) an accidental release could occur due to the tether working itself between the ring splits, and 2) because an astronaut could tear a glove on the sharp tip edges where the splits begin and end.

Ball Staking

Present fabrication techniques for installing locking balls into their respective sockets involves a method called staking. This technique consists of first dropping the ball into its socket. Then a punch is used to deform the virgin material at the top edge of the hole. In doing this, the material deforms around the ball to reduce the diameter of the opening which should keep the ball in its socket.

There are several problems with this method. The actual staking is a crude operation. There is a large amount of room for error when a technician conducts this operation. Inspections have shown that, on several occasions, all of the expected material was not staked into the hole. This results in the ball not being completely retained in the socket, allowing it to fall out during certain loading applications. Another problem with staking appeared during vibration testing. Tests have shown that, occasionally, the staked material is relatively thin & that stress concentrations can be created at the tip of the staked material. During vibration these thin areas may fracture as a result of high stress concentrations. Once the material fails, the locking ball could fall out creating a hazard.

On-going research and development techniques are being studied on how to alleviate the problem of staking. Techniques to create the ball socket without staking are being considered. One possibility includes creating a tapered socket from the inside of the pin barrel by the use of Electronic Discharge Machining (EDM). If the proper socket can be created, the balls could be installed from the barrel end of the pin with no staking or deforming operations required.

Lubrication

Dry film lubricants are now being used to lubricate all internal parts of the pip pins. The problem of an organic grease or oil freezing, which can seize a pin, is corrected by using a dry film lube. In addition, the dry film lube will not collect and trap contaminants like a grease or oil would. Trapping contaminants creates another possibility that the pip pin will seize.

Hitch Pins

One area of pip pin design that has created some controversy is the use of hitch pins to ensure the pip pins are not inadvertently removed or disengaged. Hitch pins are a highly reliable design feature to incorporate into a pip pin design. The hitch pins manually secure the ball activation spindle, locking the balls into the locked position. Even if all locking balls are lost from the pip pin, the pin will remain installed until the hitch pin is removed.

Hitch pins are ideal for secure or high reliability applications where the pip pin only has to be removed and not re-installed. Re-installation of a hitch pin is difficult due to the small diameter hole the hitch pin has to be inserted into. The possibility also exists that hitch pins present a snag hazard for the astronauts' pressure suit. Any snag condition to a space suit could result in a catastrophic hazard.

Summary

Pip pins are very useful in many aerospace mechanism applications. When they are utilized, several design and fabrication features should be considered in selecting a proper pin. If the pin is in a critical location and a substandard pin is selected, a catastrophic failure of the mechanism could result. Several design features to be considered when selecting or designing the pins are; 1) the use of four locking balls, 2) providing a double acting engagement/disengagement feature, 3) provision of Teflon coated tethers, 4) welded handles and tether rings, 5) locking ball installation procedures, 6) choosing the correct lubrication, and 7) the use of hitch pins. The selection of the proper pip pin could be the difference between a successful mission and a catastrophic hazard.

ACKNOWLEDGEMENTS

The author would like to thank W. B. Wood (NASA/JSC), Gary Krch (ILC/JSC), and Robert Stondell (Space-Lok Inc./Burbank, CA) for their input on the design process of the new techniques developed for pip pins. He would also like to thank John Zipay (NASA/JSC) for providing a history of pip pins as they relate to our nation's space program. Carolyn Ricaldi (Lockheed/JSC) should also be acknowledged for her help in putting this paper together.

INTELLIGENT CONTROL OF A MULTI-DEGREE-OF-FREEDOM REACTION COMPENSATING PLATFORM SYSTEM USING FUZZY LOGIC

Benjamin B. Choi and Charles Lawrence
NASA Lewis Research Center
Cleveland, Ohio

and

Yueh-Jaw Lin
University of Akron
Akron, Ohio

ABSTRACT

This paper presents the development of a general-purpose fuzzy logic (FL) control methodology for isolating external vibratory disturbances of space-based devices. According to the desired performance specifications, a full investigation regarding the development of an FL controller was done using different scenarios, such as variances of passive reaction-compensating components and external disturbance load. It was shown that the proposed FL controller is robust in that the FL-controlled system closely follows the prespecified ideal reference model. The comparative study also reveals that the FL-controlled system achieves significant improvement in reducing vibrations over passive systems.

INTRODUCTION

Passive systems may perform effectively in reducing vibration caused by the vibration object when the operating frequency of the object is high. However, their performance is serious degraded in the low frequency range. Hence, active vibration isolation systems may appear to be the only means to overcome vibration isolation problems in the low frequency range. Although the benefits of using active vibration compensating systems are obvious, it requires a high-performance control system that is capable of handling all undesirable dynamic disturbances in an extremely short period of time. In particular, a robust control system that provides a wide range of dynamic disturbance compensating capability, is the key to a vibration-free dynamic environment. Toward this end, some recent advancements in active vibration control schemes [1-5] have been evident. They have been able to reduce the level of vibration to a certain extent, their limitations and performances are still far from being satisfactory. Therefore, there is a need of developing a new control system with good intelligence and robustness such that it can cope with rapid varying vibratory disturbances in a real-time manner.

To accomplish this, a fuzzy logic algorithm that possesses the nature of mimicking human thinking, is proposed for the desired intelligent control system. Due to the fuzzy nature of the proposed control system, potential dynamic disturbances are identified and classified into distinct groups. For each group of identified disturbances a unique control action will be taken to compensate for the undesirable disturbances. The control actions may be adjusted from time to time based on a set of adaptive fuzzy rules designed specifically for a particular application, such as the control of the platform system under study.

DYNAMIC FORMULATIONS

The configuration of the two-plate platform system is shown in Figure 1. In the first stage of the study, comprehensive dynamic formulations of the six-degree-of-freedom platform system were formulated by applying Lagrange's and Newton-Euler methods. Since Newton-Euler formulation is more structured and hence easier to be manipulated, it was further linearized and utilized for system dynamics and control investigation. Detailed derivations of dynamic formulations are omitted due to space limitation.

PASSIVE DYNAMIC RESPONSES

Passive responses in terms of the bottom plate acceleration and displacement occurred at four different locations of interest on the top and bottom plates, namely, the center and the three actuator locations, are studied. The translational responses of the three actuator positions are shown in Figure 2. In this study, it is simulated to be an impulsive force of 445 N (100 lb) for 0.5 second.

FUZZY LOGIC CONTROLLER DESIGN

Referring to Figure 3, the measured accelerations of the bottom plate at the three actuator positions are used as the control feedback signals. After they are compared with the desired zero acceleration the resultant error signals are then used to fire the fuzzy engine residing in the fuzzy logic controller. The desired performance of the fuzzy-logic controller will be achieved when the detected accelerations reach the prespecified tolerances. The three actuators are controlled by three different fuzzy-logic controllers whose fuzzy logic rule bases are set up independently, according to the passive dynamic responses at their respective locations.

The basic architecture of the designed fuzzy-logic controller is depicted in Figure 4. Basically, it consists of four principal components: scaling, fuzzification, decision making process, and defuzzification. The scaling factors map the controller inputs $e(t)$, $\Delta e(t)$ and controller output $\Delta u(t)$ to and from the normalized intervals in which the fuzzification and defuzzification processes take place. The controller inputs $e(t)$ and $\Delta e(t)$ are chosen to be the bottom plate acceleration error and its variation, respectively. The controller output $\Delta u(t)$, however, represents the resultant actuation force.

The universe of discourses for the two inputs are determined by using the passive dynamic acceleration responses of the bottom plate shown in Figure 2. More specifically, the maximum/minimum amplitudes and slopes are utilized. However, the universe of discourses of the output $\Delta u(t)$ are determined based on the actuator's capability. In addition, they are further discretized into seven quantization levels. Then, a fuzzy set is defined by assigning grade membership values to each discretized segment.

Seven linguistic variables are used and correspond to the peaks of the seven triangular membership functions. The overlaps of two adjacent membership functions are uniformly determined to be 45°. This is then followed by the fuzzy decision-making process, which is performed by an interface engine that matches the conditions of all the rules and determines the partial degree of matching of each rule. Finally, it aggregates the weighted output of the rules, generating a possibility distribution of the values on the output universe of discourse.

The resultant fuzzy output set are listed in Table 1, as a look-up table, which defines the output of the controller for all possible combinations of the input signals.

CONTROLLER PERFORMANCE EVALUATION

A comparative study of the dynamic responses of the passive and active fuzzy logic controlled platform system is carried out. Figure 5 shows the time domain acceleration responses of the passive and the controlled systems. Responses at actuator positions 2 and 3 are similar. It is clear that the fuzzy logic controller reduces the accelerations at each actuator position of the bottom plate by about 90% over the passive system. Figure 6 shows the dynamic behavior of the center of the bottom plate.

The simulation results reveal that the acceleration of the center of the bottom plate, which is a critical measure of the performance of the entire platform system, only sightly off against the desired zero acceleration line through the entire simulation history due to the compensation of the fuzzy logic controller. This verifies that the developed fuzzy logic controller is effective for the reduction of undesirable vibratory accelerations.

Moreover, comparisons of the displacement responses of the platform bottom plate between the passive and active controlled systems are made. They also show that with the fuzzy logic active control, all four displacement responses stay around the zero displacement line through the entire simulation period, only with some ignorable offsets.

CONCLUSION

In the first stage of the study, comprehensive dynamic formulations of the six-degree-of-freedom platform system were formulated by applying Lagrange's and Newton-Euler methods. Since Newton-Euler formulation is more structured and hence easier to be manipulated, it was further linearized and utilized for system dynamics and control investigation. Based on the compensation requirement with a desired (reference) zero acceleration of the platform bottom plate, a fuzzy logic controller was designed. Dynamic and control motion simulations were performed in terms of comparative study of the passive uncontrolled and the active controlled platform system. The results showed that the designed fuzzy logic controller possesses the following features: a) it is robust and hence less sensitive to the disturbance input variations; b) it is easy to design and hence eliminating the tedious gain selection process required in conventional

controller design; c) its speed of response is rapid; d) it is adaptive in that the fuzzy rule-base is adjustable; and e) it is readily implementable by microelectronic devices since it uses logical operations.

In light of the comparative study shown in the simulation results, it was demonstrated that the designed fuzzy logic controller could almost completely eliminate undesirable vibratory accelerations of the bottom plate induced by the specific impulsive disturbance. The effectiveness of the fuzzy logic controller was further confirmed by viewing the significant reductions of bottom plate's displacements shown in the comparative study.

REFERENCES

[1] Ross, C.F. 1991. "Active Isolation of Ship Machinery Platform," *27th IEEE Conf. Decision and Control 3:2045-2046.*

[2] Owen, R.G. and Jones, D.I. 1986. "Multivariable Control of an Active Anti-vibration Platform," *IEEE Trans. Magnetics* 22(5):523-525.

[3] Sommerfeldt, S.D. 1991. "Multi-channel Adaptive Control of Structural Vibration," *Noise Control Engineering Journal* 37(2):77-89.

[4] White, A.D. and Cooper D.G. 1984. "Adaptive Controller for Multivariable Active Noise Control," *Applied Acoustics* 17:99-109.

[5] Sommerfeldt, S.D. and Tichy, J. 1991. "Adaptive Control of a Two-stage Vibration Mount, " *27th IEEE Conf. Decision and Control* 3:2039-2044.

[6] Crouch, T. 1981 *Matrix method Applied to Engineering Rigid Body Mechanics 1st Ed.*, Oxford: Pergamon Press Ltd.

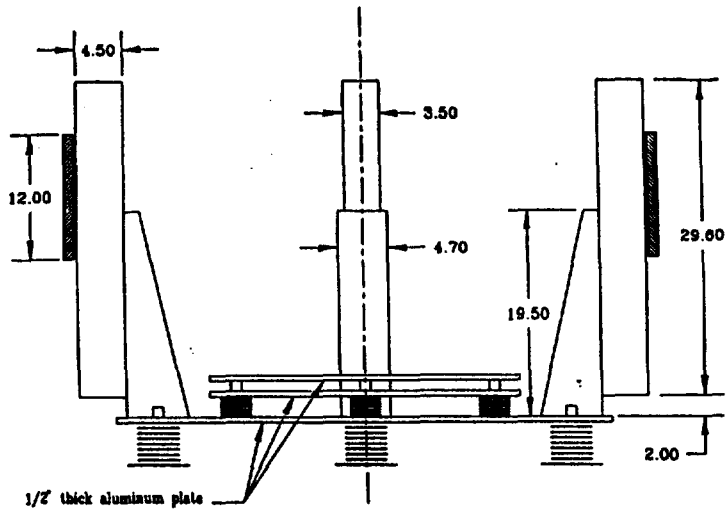

Figure 1. Configuration of the platform system.

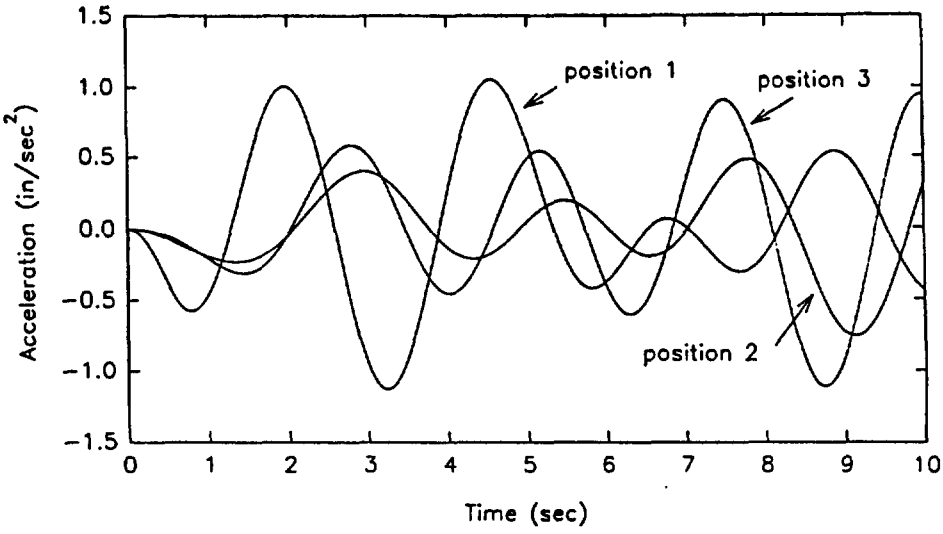

Figure 2. Passive acceleration response at actuator locations.

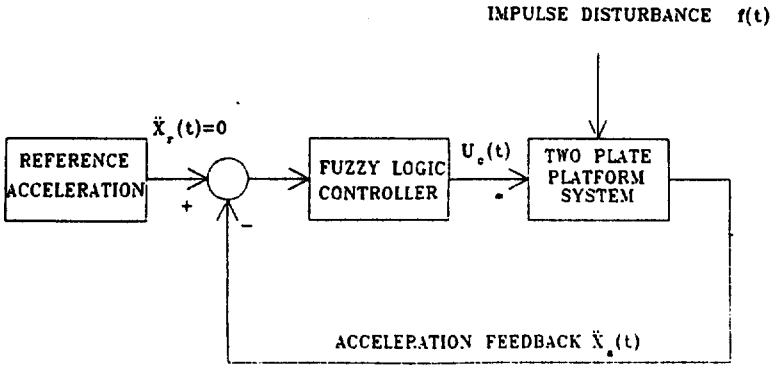

Figure 3. Block diagram of the entire control system.

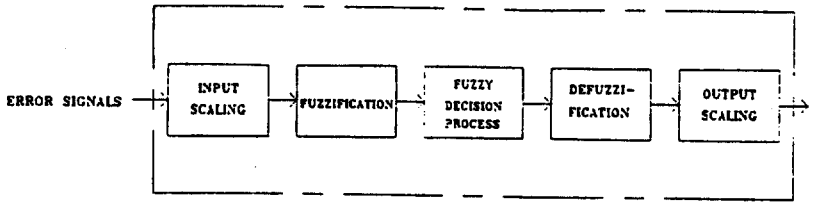

Figure 4. Basic architecture of a fuzzy logic controller.

Table 1. Designed fuzzy logic rule base.

Δe \ $\dot{e}$	NL	NM	NS	ZE	PS	PM	PL
NL	-3	-3	-2	-1	0	1	2
NM	-3	-2	-2	-1	1	1	2
NS	-3	-2	-2	0	1	2	3
ZE	-3	-2	-1	0	1	2	3
PS	-3	-2	-1	0	2	2	3
PM	-2	-1	-1	1	2	2	3
PL	-2	-1	0	1	2	3	3

-3	NL
-2	NM
-1	NS
0	ZE
1	PS
2	PM
3	PL

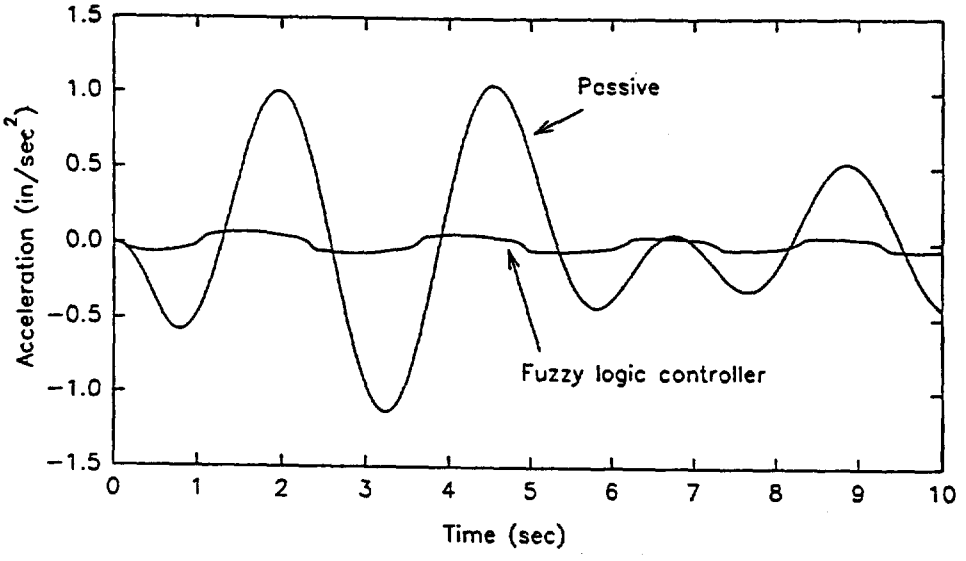

Figure 5. Comparison of acceleration response at actuator 1.

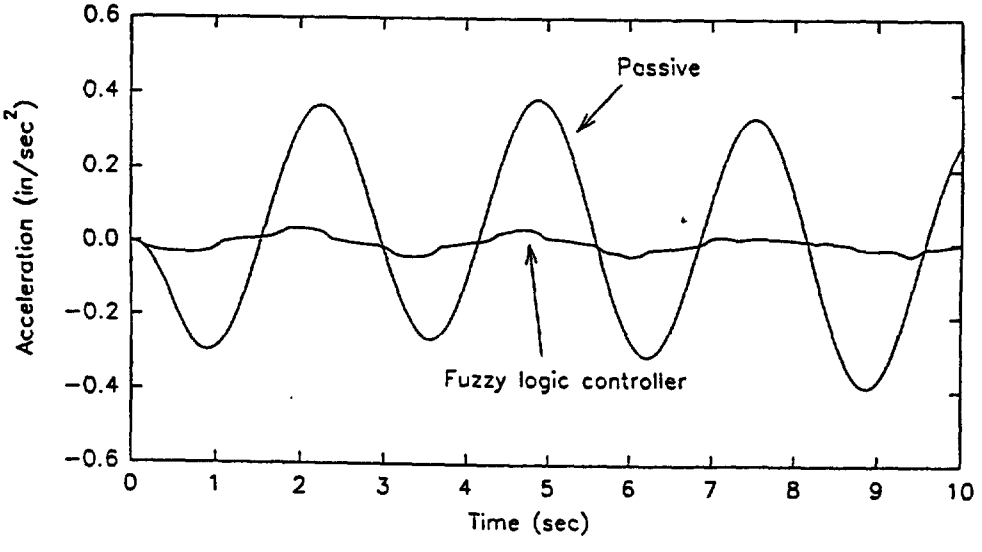

Figure 6. Comparison of acceleration response at the center.

HIGH PRECISION MOVING MAGNET CHOPPER FOR VARIABLE OPERATION CONDITIONS

Winfried Aicher and Manfred Schmid
Dornier GmbH
Friedrichshafen, Germany

Abstract

In the frame work of an ESTEC technology contract a Chopping Mechanism was developed and built with FIRST (Far Infrared and Submillimeter Telescope) astronomy mission as a reference. The task of the mechanism is to tilt the subreflector of the telescope with an assumed mass of 2.5 kg about one chopping axis at nominal frequencies of up to 5 Hz and chopping angles of up to +/- 11.25 mrad with high efficiency (minimum time for position change). The chopping axis is required to run through the subreflector vertex.

After performing a concept trade-off also considering the low operational temperatures in the 130 K range, a design using moving magnet actuators was found to be the favorite one. In addition, a bearing concept using flexible pivots was chosen to meet the high chopping accuracy required.

With this general concept approach a very reliable design could be realized since the actuators work without any mechanical contact between its moving and fixed parts and the only bearings used are two flexible pivots supporting the subreflector mounting interface.

The mechanism was completely built in titanium in a lightweight and stiff design, the moving magnet actuators were designed to meet the stringent requirements for minimum risetime (time necessary to move from one angular position to a new one) in the 20 msec range. The angular position and the corresponding chopping frequency as well can be arbitrarily selected by the user.

The mechanism is equipped with two linear sensors of high resolution. One of them is used to control the exact working position, the second one is used for position readout. The linearity of the sensors were calibrated under low temperature environment so that it is possible to compensate for the temperature drift.

After complete integration, the mechanism was functionally tested under ambient and thermal-vacuum conditions as well. It was found that the mechanism works perfectly under all temperature conditions and the most of the performance requirements were achieved.

Only the risetime which was specified to be within 20 msec for an angle of 3,75 mrad, was exeeded by about 30%.
The reason for this behaviour was found in a lower actuator force than expected, caused by magnetic effects and cross flux influences in the actuator.

Fig. 1 depicts an overview of the mechanism hardware.

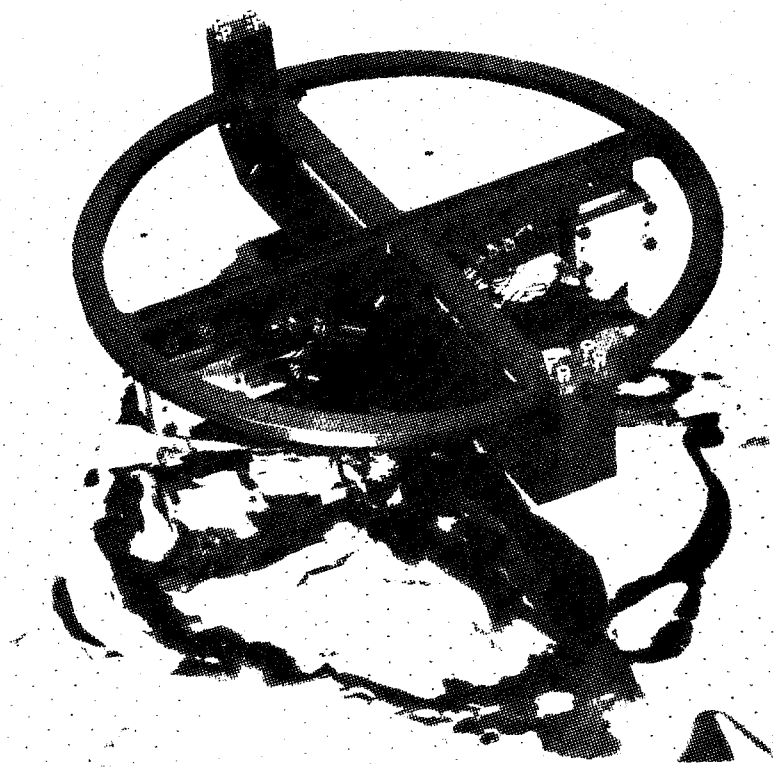

Fig. 1: Chopping Mechanism Hardware

Introduction

Based on an ESTEC technology study a Focus and Chopping Mechanism (FCM) was developed on the example of the FIRST telescope requirements. The FCM can physically be subdivided in two mechanisms, namely the Focusing Mechanism and the Chopping Mechanism.

The function of the Focusing Mechanism is to axially refocus the subreflector of the telescope at a stroke of up to 5 mm with a resolution in the 10 micrometer range. This is performed by means of a linear actuator composed of stepper motor, nut and spindle. Due to the very restrictive requirements concerning resolution and backlash at temperatures in the 130 K range, the axial displacement is supported by flexible suspension elements.

The purpose of the Chopping Mechanism is to calibrate the thermal background emission of the FIRST telescope. This task can be performed with maximum efficiency by wobbling the subreflector about its vertex, in order to alternatively observe two pointing directions in the sky, symmetrical with regard to the mean direction of the main reflector thermal gradient. Fig. 2 shows an overall view of the location of FCM on the FIRST telescope as well as the detailed FCM configuration.

In order to provide applicability to applications other than FIRST, the functions of the FCM, namely refocusing and chopping, were clearly separated during the trade-off phase. In this way, the dedicated application of each separate function becomes possible.

This paper describes the technology development of the chopping function for which very challenging requirements were established.

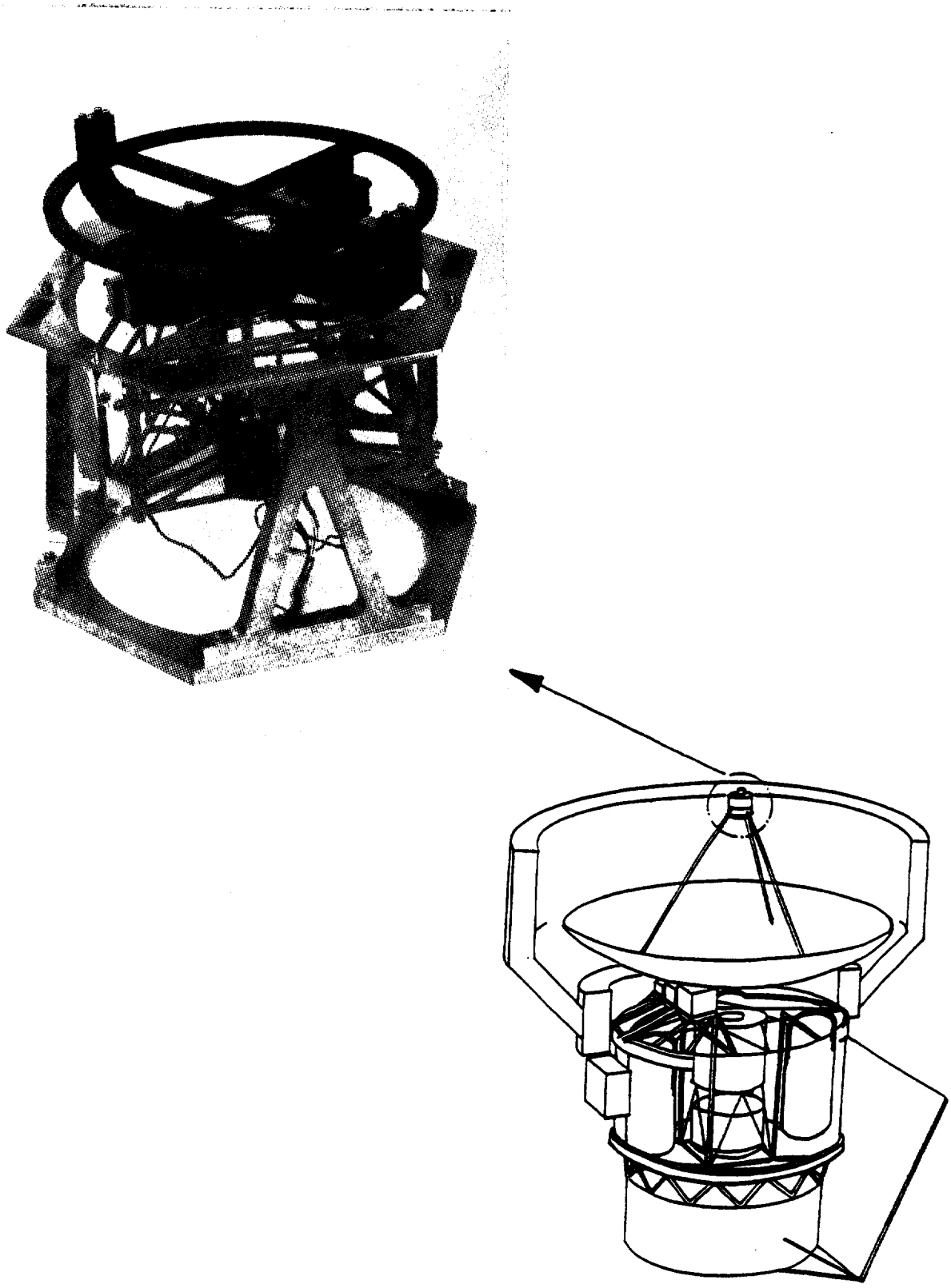

Fig. 2: FCM Configuration on FIRST Telescope

Requirements

The main requirements for the design of the Chopping Mechanism are

- a mechanism mass of 4 kg overall including the subreflector with a mass of 2.5 kg and
- an in-orbit lifetime of 3.6 years, which results in about 8 million chopping cycles.

The environmental conditions valid for the Chopping Mechanism are

- an operational temperature range of 130 to 150 K,
- additional ambient temperature for test purposes,
- vacuum conditions and
- quasi static launch loads assumed in the 20 g range.

The main performance requirements of the mechanism are

- a mass of 2.5 kg of the subreflector to be moved
- with a chopping angle of up to +/- 11.25 mrad,
- a chopping frequency between 0.01 and 5 Hz and
- an efficiency of 80%.

  (Efficiency is defined as the relation between the time necessary to move the subreflector from one extreme position to the other and the complete chopping time based on the chopping frequency. This results in the requirement to move the subreflector in the maximum time of 20 msec from one extreme position to the other within a range of 3.75 mrad at a frequency of 5 Hz.)

An important performance requirement is the accuracy of the Chopping Mechanism, namely

- a position accuracy and reproducibility below 2%, that means e.g. 0.04 mrad at a chopping angle of 2 mrad,
- a tilt angle stability of 0.1% of the chopping angle, that means e.g. 0.002 mrad at a chopping angle of 2 mrad.

  (Position accuracy describes the capability of the Chopping Mechanism to reach a specified position whereas tilt angle stability describes the capability of the Chopping Mechanism to hold a specified position.)

The defocusing of the vertex during the chopping motion must not exceed 10 microns and the decentering of the vertex is limited to 0.5 microns for an angle of 2 mrad.

Design Description

The Chopping Mechanism has to perform a lateral chopping motion of the subreflector about an axis vertical to the refocusing axis. This motion has to be performed reliable within the specified limits namely at a small chopping angle of maximum +/- 11.25 mrad with a very high position accuracy of better than 2%, a tilt angle stability of better than 0.1% and at high acceleration values required to move the subreflector within a minimum risetime. Additionally this performance data have to be achieved over a wide temperature range from ambient conditions down to 130 K.

Based on the set of performance requirements, a trade-off was established in the beginning of the study in order to determine the most suitable Chopping Mechanism design principle with the outcome to use magnetic actuators (moving magnet principle) attached to a fixed support yoke. The actuator induces the oscillating chopping motion of the movable subreflector support structure. The main advantages of this principle are its simple and reliable design, its very good dynamic behavior and its low interface complexity.

The design principle of the Chopping Mechanism is realized with two main elements - the structural yoke with the linear actuators attached and the subreflector support structure. Both elements are connected by the chopping rotational axis which is realized by a set of flexural pivots.

The structural yoke consists of a u-shaped support with two cross beams mounted rectangularly to the support by screws and set pins. The moving magnet linear actuators are fixed to the cross beams. The moving parts of the linear actuators are directly attached to the subreflector support structure. Additionally two non-contact inductive sensors are mounted to the cross beams. One sensor is used as position sensor for the control electronics, the other one for position monitoring during the motion.

The subreflector support structure is used in this design as a mounting base for the permanent magnets of the linear actuators, for the moving part of the position sensors and it allows to fix a dummy mass representative for the subreflector. Additional plates can be attached to verify different masses and moments of inertia for different subreflector configurations.

The design of the Chopping Mechanism is presented in detail in figures 3a and 3 b:

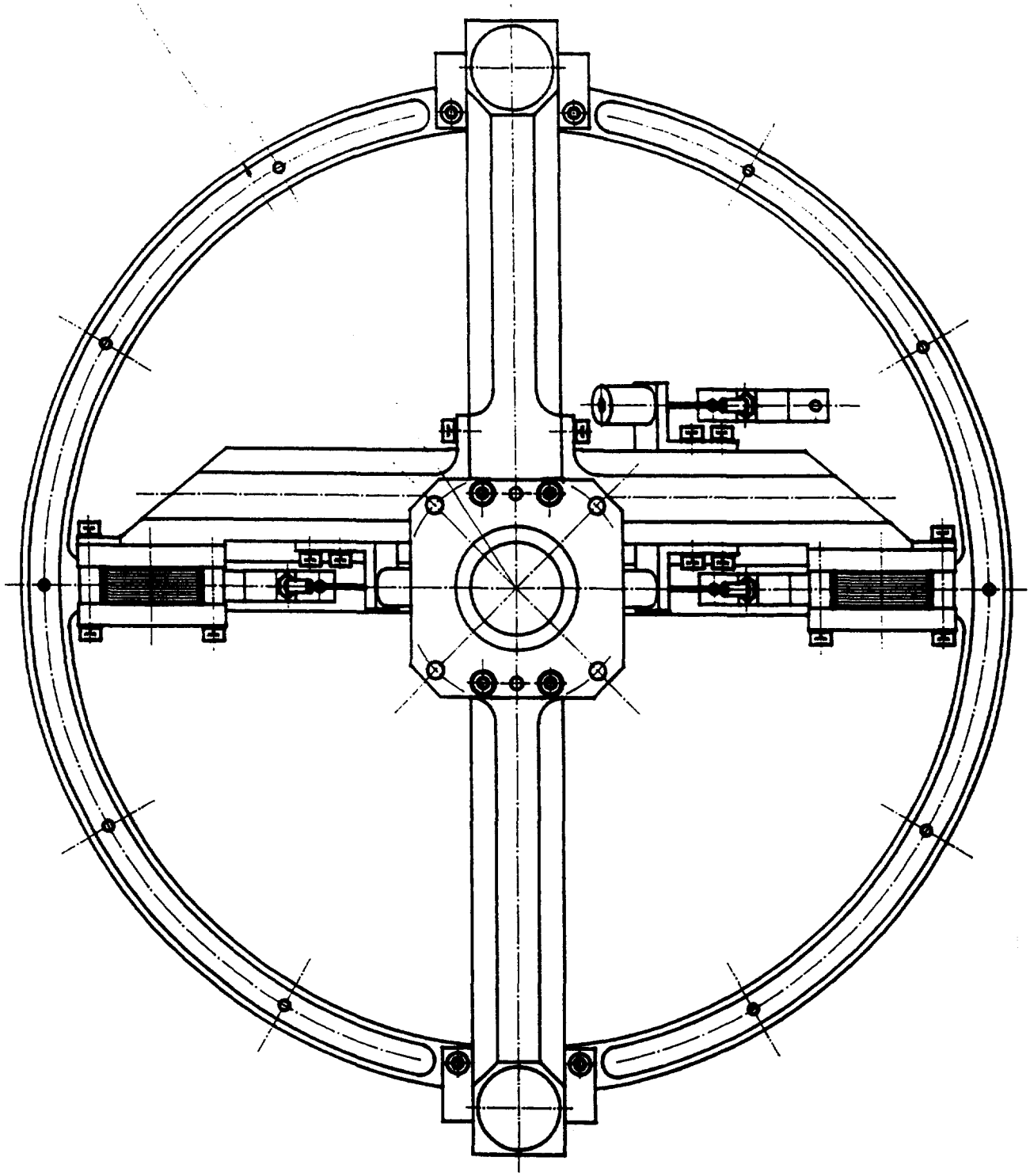

Fig. 3a: Design of the Chopping Mechanism - Top View

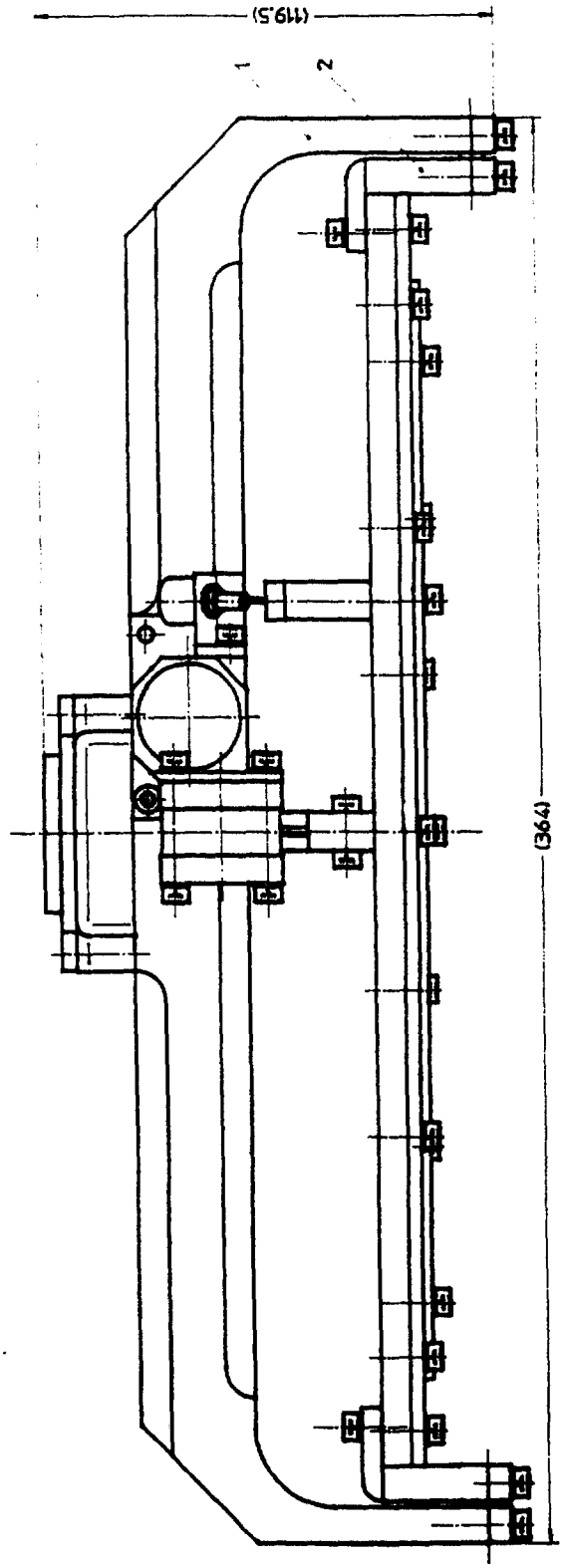

Fig. 3b: Design of the Chopping Mechanism - Side View

Linear Actuator

A magnetic linear actuator with moving magnet is used to perform the chopping motion of the mechanism according to the specified requirements.

In principle the linear actuator is composed of two symmetrical stator parts with a moving permanent magnet in the common air gap. The actuator force is induced by the interaction of the magnetic fields of the permanent magnet and the stator coil. The coils are powered in a way that the moving permanent magnet is pushed out of one stator part and at the same time pulled in the other stator part. The principle is independent from tilting of the permanent magnet in his plane as induced by the chopping motion of the FCM subreflector, that means there is no change of air gap between the magnet and the stator part during the chopping motion.

The principle of the linear actuator is presented in fig. 4.

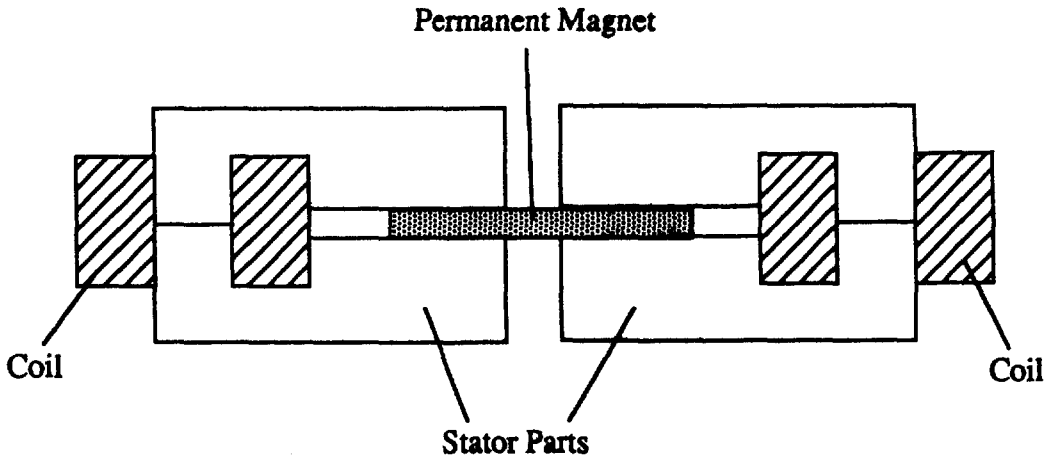

Fig. 4: Design Principle of Linear Actuator

The principle of the linear actuator described, allows for wide design variations which leads to simple and reliable solutions for the required chopping motion.

For the Chopping Mechanism discussed in this paper, the two stator parts were separated to obtain two independent actuators. These actuators was placed on both sides of the cross beam as shown in Fig. 3. This leads to a very simple design without additional levers required to transfer the output forces. Furthermore, due to the symmetrical arrangement, lateral forces acting on the flexural pivots during chopping motion are minimized.

The linear actuator was designed to achieve the requirements concerning chopping angle and acceleration. The required acceleration rate results in an actuator force of about 15 N (including margins).

The motion of the linear actuator is controlled by the control electronics. The interface between mechanism and electronics is formed by a contactless inductive sensor fixed on the cross beam. To obtain an optimal dynamic behavior of the Chopping Mechanism, three control loops with different tasks are inserted into one another.

The inner loop with the servo amplifier generates a current through the motor coils proportional to the control signal. It represents a fast integral-action controller (I-controller) with a time constant of 0.5 msec. The middle loop represents a velocity controller designed as proportional-action controller (P-controller). The outer loop represents the position controller designed as proportional-integral-action controller (PI-controller).

Tests Performed

To verify the functional requirements of the Chopping Mechanism, the following test steps were performed at ambient as well as at low temperature vacuum conditions with temperatures down to the 130 K range:

- Chopping Frequency
  Measurement of the subreflector response in relation to the commanded chopping frequency by means of a linear sensor

- Position Accuracy
  Measurement of the actual position of the subreflector in relation to the commanded chopping frequency by means of a linear sensor

- Angle Stability
  Measurement of the stability of a commanded subreflector position over a time period of up to 50 sec.

- Efficiency and Risetime
  Measurement of the time required to achieve a new commanded subreflector position

Test Results

- Chopping Frequency

The chopping frequency test was performed with different representative frequencies and at a maximum chopping angle of +/- 11.25 mrad. The frequencies chosen were the 0.1 Hz, representative of a slow chopping motion, the 1.4 Hz representing the mechanical rotational eigenfrequency of the moving mechanism and the 5 Hz representative of a fast chopping motion.

The Chopping Mechanism followed all required frequencies in ambient as well as low temperature conditions well.

- Position Accuracy

The position accuracy test was performed at different representative chopping angles namely the 0.25 mrad as representative of a very small chopping angle, the 2 mrad as representative of the nominal chopping angle and the 7.5 mrad as representative for a great chopping angle.

To verify the position reproducibility, each of the specified chopping angles was measured five times. The Chopping Mechanism fulfilled the required position accuracy at all angles well.

- Angle Stability

The angle stability test was performed by measuring the chopping angles 0.25 mrad, 2 mrad and 7.5 mrad over a time period of 50 sec at ambient as well as thermal conditions.

The output signal of the sensor during stability measurement was superimposed by the noise signal caused by the electrical test setup (0.017 mrad) which was higher than the required stability value.

- Efficiency and Risetime

The efficiency test was performed by measuring the risetime for a chopping angle of +/- 3.75 mrad at different chopping frequencies. The risetime represents the time passed for the change from the subreflector position -3.75 mrad to the subreflector position +3.75 mrad. To realize the required efficiency of 80%, this risetime has to be 20 msec for a chopping frequency of 5 Hz up to 100 msec for a chopping frequency of 1 Hz.

The test shows a dependency of the risetime on test temperature and vacuum conditions. For low temperature vacuum operation, the specified efficiency can be fulfilled for chopping frequencies of up to 1 Hz only whereas for ambient conditions an efficiency of 80% can be reached for chopping angles up to 2.3 Hz. This means that the specified requirement concerning the efficiency was not fulfilled with the actual design.

One reason for this result was given by the changed transient behavior of the linear actuator at low temperature vacuum conditions. The change in the transient behavior was found to be a reaction on eliminated air damping and of a change in the spring stiffness of the flexural pivots at low temperatures.

Another reason for not fulfilling the efficiency and risetime requirements is caused by the design of the linear actuator. The reasons for this fact will be considered next.

To summarize the functional testing, the following table shows the results of all tests performed:

Item	Predicted Values	Actual Values	+	-
Mass of Chopping Mechanism	< 1500 g	1418 g	x	
Mass of Subreflector	2500 g	2494 g	x	
Maximum chopping angle overall	22.5 mrad	22.8 mrad	x	
Chopping frequency	0...5 Hz	0...5 Hz	x	
Efficiency	> 80 %	80 % up to 2,3 Hz	x	x
Risetime for +/- 3.75 mrad	20 msec	43...90 msec		x
Position accuracy (< 1.875 mrad)	+/- 0.0375 mrad	+/- 0.011 mrad	x	
Position accuracy (> 1.875 mrad)	< +/- 2 %	+/- 0.03 mrad	x	
Angle stability	< 0.1 %	Noise Level		

Optimization of the Linear Actuator

As indicated in the previous section "Test Results", one main reason for the lack of performance concerning the efficiency specification is caused by the design of the linear actuator. Additional tests showed that the linear actuator generated a force in the 5 N range instead of the required 15 N. The tests also showed that this force is approximately dependent on the depth of insertion of the permanent magnet into the stator part.

This leads to the conclusion that the loss of actuator force was basically caused by the separation of the linear actuator in two different independent stator parts with two separate permanent magnets. By performing this separation the actual coil flux is reduced to only half of the expected theoretical coil flux. Thus the actual actuator force is also reduced to the half of the theoretical actuator force. Furthermore, saturation effects on the stator parts material caused an additional loss in actuator force.

To compensate for these problems, an upgraded new linear actuator with optimized design parameters was developed for inclusion into the Chopping Mechanism. The new actuator was manufactured with sheet iron cores instead of massive iron in order to reduce the saturation effects of the material and more windings on his coil were established to enlarge the actuator force.

The principal intent in choosing the separated actuator concept instead of the integrated one was to optimize the performance of the overall FCM system with the advantages of:

- Simple interface between the actuator magnets and subreflector moving parts
- Avoidance of lateral forces on the flexural pivots due to symmetric design
- Reduction of mass

The chosen concept which subdivides the integral actuator into two separate independent actuators however has the consequence that the electrical performance (actuator force) is reduced by the reasons described above.

Through the chosen measures and design changes, the actuator output forces were increased to a higher level compared to the original design. Thus an improvement of the overall chopping concept resulted.

The functional test results performed at ambient conditions for the improved design are listed as follows:

	Actuator Force	**Risetime for +/- 3.75 mrad**	**Efficiency of 80 % up to**
Original Design	5 N	43 msec	2.3 Hz
Improved Design	12 N	30 msec	3.5 Hz

Conclusions

The chosen design of the Chopping Mechanism provides an optimal solution from the mechanical point of view especially concerning:

- Symmetry of the design
- Only moments (no shear loads) are transferred via the flexural pivots (important for vertex shift during chopping motion)
- Simple actuator interfaces due to direct connection of the moving magnet to the movable structure of the Chopping Mechanism become possible.
- Low mass due to simple actuator concept
- Low thermal distortions at high temperature changes (low temperature conditions)

The chosen solution was found to be not optimal concerning the output actuator forces which would have been higher for an integrated actuator solution (double iron stator with one common magnet).

By introducing the improvements described above, the output force values and thus the performance values, particularly risetime, could be significantly increased. In this way, an optimal combination of the design advantages of the chosen concept together with improved actuator performance could be achieved.

TWO-AXIS ANTENNA POSITIONING MECHANISM

Michelle Herald
Space Systems/Loral
Palo Alto, California

and

Leilani C. Wai
INTELSAT
Palo Alto, California

ABSTRACT

The Two-Axis Antenna Positioning Mechanism (TAAPM) is used to position three Ku- and one C-band spot antennas on the INTELSAT VII (I-VII) spacecraft, which is a commercial telecommunications satellite purchased and operated by INTELSAT, an international consortium. The first I-VII was successfully launched on 22 October 1993 from French Guiana on an Ariane launch vehicle. All TAAPMs on the first I-VII satellite successfully completed their in-orbit functional testing.

The TAAPM was an entirely new design for Space Systems/ Loral. This paper will describe the spacecraft/ system requirements and application of the TAAPM, and present the technical findings of TAAPM qualification and protoflight testing.

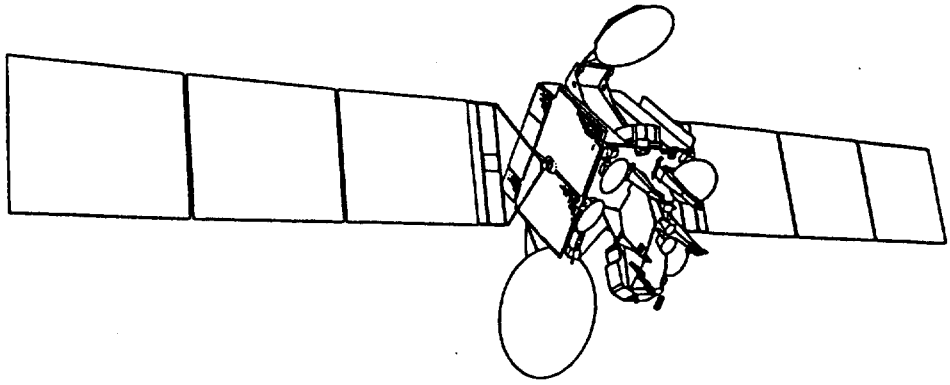

1.0 DESCRIPTION

The TAAPM is used to position the spot antennas in two axes. The following describes the spot antenna subsystem and the TAAPM.

1.1 SUBSYSTEM DESCRIPTION

The antenna sub-system consists of (see Figure 1):

a) Antenna: spot beam reflector, feeds, antenna structure
b) Spot holddown
c) TAAPM
d) Waveguides
e) Thermal blanketing (not shown for clarity)

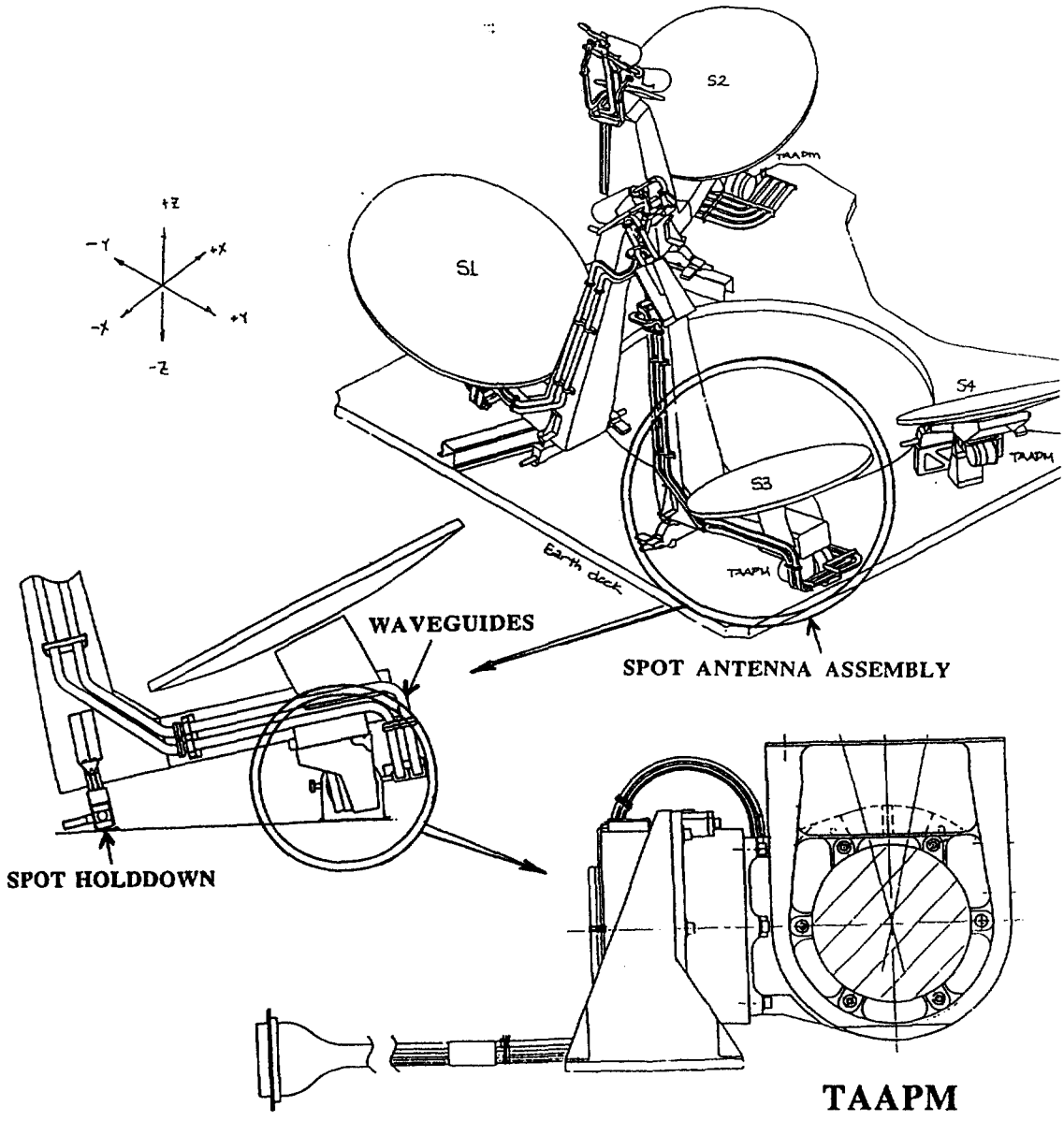

Figure 1. Spot antenna sub-system and TAAPM

During launch, the antenna is held securely in two places with the spot holddown, which absorbs the majority of the launch loads. When geosynchronous orbit has been achieved, the holddowns are released and the antenna is positioned by the TAAPM.

This configuration of TAAPM, antenna, and holddown is used during dynamic testing to verify the structural integrity of the TAAPM under simulated launch loads.

Each axis of the TAAPM is independently controlled by the Spacecraft Control Electronics (SCE) to position the antenna to point anywhere on the earth disk. The first axis (nearest the earthdeck) is the elevation actuator for antenna pitch (S1 and S3 antennas). The second axis is the azimuth actuator for antenna roll. The S2 and C-spot antennas are not aligned with spacecraft axis and therefore require conversion from pitch and roll to azimuth and elevation.

1.2 TAAPM DESCRIPTION

The TAAPM consists of two orthogonal rotary actuators and three brackets. Position telemetry is provided by redundant potentiometers in the rotary actuators.

1.3 ROTARY ACTUATOR DESCRIPTION

The rotary actuators are procured from an outside vendor and are integrated into a TAAPM assembly at Space System/ Loral. The rotary actuators are extensively tested at the vendor and at the TAAPM assembly level.

Each rotary actuator consists of a redundant three-phase 1.5-degree stepper motor, a 160:1-ratio harmonic drive gear reducer, a duplex bearing pair at the output, one coarse and two fine potentiometers. This configuration provides an output of 0.009375 degree/ step.

The fine potentiometers are coupled to the stepper motor through a 1.5:1 ratio such that each step can be resolved. The coarse potentiometer is coupled to the output to determine the cycle of the fine potentiometers so that the antenna position is given unambiguously.

2.0 SYSTEM REQUIREMENTS/ APPLICATION

The TAAPM performance requirements are derived from:

- System pointing requirements
- System pointing error budget
- Torque Margin
- Structural loads during launch
- Thermal environment on-orbit
- Modal analysis (frequency and stiffness)
- Telemetry requirements

2.1 Pointing requirements

Pointing requirements are essential to providing accurate and timely coverage for INTELSAT customers. All spot antenna TAAPMs are

commanded from the space control center at INTELSAT headquarters in Washington, D.C. Customers depend on the spacecraft's ability to give instant accurate coverage, especially in remote locations around the world. The Ku- and C-band spot antenna TAAPMs provide a significant part of that capability.

2.2 Pointing Error Budget

The pointing error budget consists of various spacecraft characteristics which include the pointing capabilities of the TAAPM. The following is a breakdown of the mechanism contributions. Unit and system level ground testing have proved the TAAPM parameters fall well within this allocation.

Pointing Error Source (degrees)	Budget	Actual
Fine potentiometer backlash/ hysteresis	0.005	0.002
TAAPM backlash/ hysteresis	0.028	0.026
Potentiometer voltage accuracy	0.015	0.004
Potentiometer voltage (SCE)	0.000	0.005
TOTAL	0.048	0.037

2.3 Torque Margin

The TAAPM must provide sufficient torque to move the antennas, waveguides, and thermal blanketing at any temperature within the predicted temperature extremes. The torque provided must exceed the resistances by a ratio of 3 to 1.

2.4 Structural Requirements

The structural requirements are derived from the coupled loads analysis which determined the worst-case accelerations on both the Ariane and Atlas launch vehicles. The TAAPM was designed to withstand loads greater than 1.3 times the predicted flight loads.

The protoflight and qualification TAAPMs were proof load tested to the appropriate static loads without failure. All units are vibration tested to levels which meet or exceed the launch environment. Sine vibration levels are based on the quasi-static accelerations; random vibration levels are based on acoustic noise levels measured during acoustic testing performed on the protoflight units. These tests have verified the TAAPM meets the structural requirements.

2.5 Thermal Requirements

The temperatures predicted for the TAAPMs were derived from the thermal model of the spacecraft, which yielded the maximum and minimum temperatures expected during the operating lifetime. Margins have been added to the predicted temperatures to obtain test limits.

Temperature limits are:

- Operating: -50°C to +80°C
- Non-Operating: -60°C to +85°C

2.6 Frequency/ Stiffness Requirements

To avoid dynamic coupling with the spacecraft control system during launch, a structural frequency goal of 50 Hz was established. This frequency was used to design the TAAPM brackets for sufficient stiffness, and to obtain minimum axial, radial and moment stiffnesses of the rotary actuator, which governs overall TAAPM stiffness.

Dynamics testing performed on the first three flight sets has demonstrated that the antenna/ holddown/ TAAPM system has a primary mode between 50 and 55 Hz. This mode is primarily due to the antenna structure and holddown, independent of the TAAPM. The structural model predicted 51 Hz, giving good correlation to test results.

2.7 Telemetry

Position telemetry is provided by the output of the redundant fine potentiometers, which vary from 0 to 5 volts, repeating every 150 steps. The cycle number of the fine potentiometer is determined by the coarse potentiometer which spans the whole range (~26°) in less than 5 volts. The voltage/ angle calibration is performed during final functional testing performed at the TAAPM level. Temperature telemetry is provided by thermistors.

3.0 TESTING

The overall test program consists of qualification, protoflight, and flight acceptance testing. Qualification testing was the most extensive, including testing for stiffness, strength, detent torque, running torque, and stall torque to verify structural models and to confirm vendor data taken at the rotary actuator level. Due to schedule constraints, the protoflight units were required before the qualification unit could be fully tested. As a result, the protoflight units underwent extensive testing, approximately equivalent to qualification. The data gathered during protoflight testing was evaluated to determine which tests were appropriate for the acceptance units.

3.1 TEST METHODS

To characterize TAAPM performance, unique test methods were required. These test methods allowed testing to be performed in two axes without reconfiguring.

3.1.1 Tiltsensor

To accurately meet the TAAPM pointing requirements, a precise calibration of potentiometer voltage to angle is required. Several alternatives were investigated: optical encoders, laser interferometers, and tiltsensors. The tiltsensor was chosen for the following reasons:

- The ability to accurately (<.005°) measure angles in two axes with one unit
- Alternatives could not be used under thermal-vacuum conditions without costly modifications
- Low technical skill level required to use (no alignments)
- Lowest cost

The tiltsensor is an electrolytic device that uses a conductive fluid contained in a glass tube similar to a bubble level. The tiltsensor used for testing TAAPMs is a biaxial device: one unit contains two independent, orthogonal tubes. When the tube is tilted the bubble movement causes a resistance change that changes a voltage output which is read by a processor. The output voltage of the processor is correlated to an independent angle measurement device (such as a laser interferometer) to obtain a voltage vs. angle calibration of the unit (in the form of a data file, a.k.a. conversion file). In use (after calibration), the processor voltages are translated into angular data through the conversion file.

The accuracy of the tiltsensor is primarily affected by two variables: temperature and settling time.

TEMPERATURE: Since the tiltsensor consists of liquid metal that has a high coefficient of thermal expansion, the temperature must be tightly controlled to achieve consistent results. To maximize accuracy at ambient conditions, the temperature must be controlled within 26.00 ± 0.005 °C. To achieve temperature control, a heating/ cooling system utilizing a thermo-electric device (Peltier effect) was added to the tiltsensor.

Tests performed on the first four TAAPMs under thermal-vacuum conditions indicated that the temperature could not be controlled well enough to consistently obtain meaningful data. Also, exposure to temperature permanently damaged several tiltsensors.

At this point, it was decided to eliminate the use of tiltsensors under thermal-vacuum conditions. This decision was partially validated by comparing the step count vs. potentiometer voltages at ambient and temperature conditions: the differences were insignificant. Also, ambient and thermal-vacuum data taken with one particularly robust tiltsensor indicated no significant angular differences under temperature.

SETTLING TIME: When the tiltsensor is tilted, the liquid metal moves to become level. The momentum of the liquid particles causes "sloshing" about the true-level position. Eventually, the damping of the liquid allows equilibrium near the true-level position. The amount of time required to obtain measurements within a certain error band is called the tiltsensor "settling time".

An experiment was performed using a TAAPM, a laser (to measure angle precisely) and a tiltsensor set at various settling times. The results indicate that:

- Optimum settling time was unique to each unit
- Units possessed repeatable error that was location dependent
- Settling time was sufficient at approximately 2.5 $^{seconds}/_{step}$.

The location-dependent error was determined to be related to the tiltsensor hysteresis. This error is caused by slight imperfections in the glass tube or electrodes, which react to the surface tension of the liquid. The tiltsensor hysteresis has been fairly repeatable to less than 0.03 degree. This number is greater than the accuracy required of the measurement, which is 0.005 degree. However, the tiltsensor hysteresis only effects the data when comparing data from two different directions. The tiltsensor has shown to be repeatable when coming consistently from the same direction.

3.1.2 Inertia:

There are three loads the TAAPM must drive: the bending resistance of the flexible waveguide, the resistance of thermal blankets, and the inertial load induced by the mass of the antenna. To correctly simulate loads, testing was performed with waveguide simulators and an inertia simulator. Thermal blanket resistances were determined to be insignificant and were not simulated.

To simulate inertia without inducing gravity effects for a two-axis unit is not straightforward. To obtain the correct inertia, a lumped mass is used with a moment-arm. It is desirable to minimize the required weight of the lumped mass to minimize the reaction force on the unit, which is not present in zero g. However, due to limited volume available in vacuum chambers, a large mass with a small moment-arm was necessary. This required that the mass be off-loaded with a three dimensional off-loader (see Figure 2).

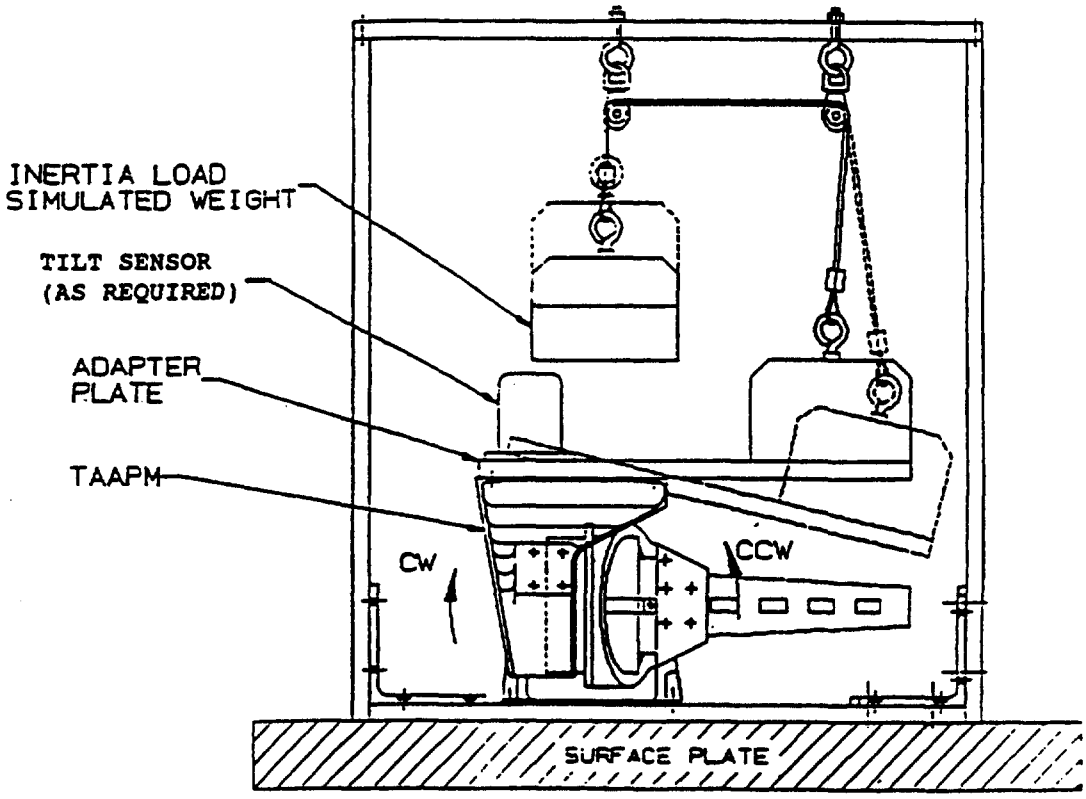

Figure 2. TAAPM Inertia Load Test Setup

Testing performed on the first four units showed much higher hysteresis (friction) than expected. The test set-up was evaluated, and as often is the case, the test fixturing was the culprit. The inertia simulator off-loader was fabricated using commonly available sleeve pulleys. When the pulleys were changed to high quality ball bearings the friction dropped nearly 80%, to levels which were acceptable.

Even with the modification mentioned above, there were consistent differences in measured torque according to direction of travel. Tests performed without inertia simulators showed no directional bias, indicating that the raising and lowering of the weight was affecting the measured data.

The approximate magnitude of the inertially induced torque (in zero g) was calculated, and was very small, less than 0.1 N•m. Since the inertia simulator was clouding the data, and the inertia effect in-orbit is very small, the use of inertia simulators has been abandoned.

3.1.3 Torque Margin

The torque margin[1] of the TAAPM is required to be greater than 3.0 for any operating condition. Measuring the torque margin (torque output/resistance torque) of a single-axis rotational device is simple to do with a torque transducer; however, with a two-axis device a direct torque measurement is not possible.

An indirect method of determining the torque margin was developed: for each rotary actuator, the torque versus voltage relationship was measured (see Figure 3). During testing, the minimum voltage required to drive the load without skipping steps was determined (threshold voltage). Using the torque vs voltage plot, the torque corresponding to the threshold voltage is determined; this torque is compared to the torque available at the nominal operating voltage, derated to correspond to spacecraft end-of-life voltage (23V). The ratio of the torque at 23V to the torque at the threshold voltage is the torque margin.

Example: $$\text{Torque Margin} = \frac{\text{26 N•m (at 23V, end-of-life)}}{\text{2.8 N•m (at ~11V, threshold)}} = 9.2$$

3.2 TEST RESULTS

3.2.1 Potentiometers

ROTARY ACTUATOR TESTS

During rotary actuator level testing, two significant potentiometer anomalies were revealed. The first was a coarse potentiometer voltage shift

---

[1] Torque margin is a misnomer. In this case, the torque margin is defined to be a ratio of available torque to resistance torque, which is not the same as "margin".

at neutral position (center of travel). The second pertained to voltage dropouts seen after random vibration testing.

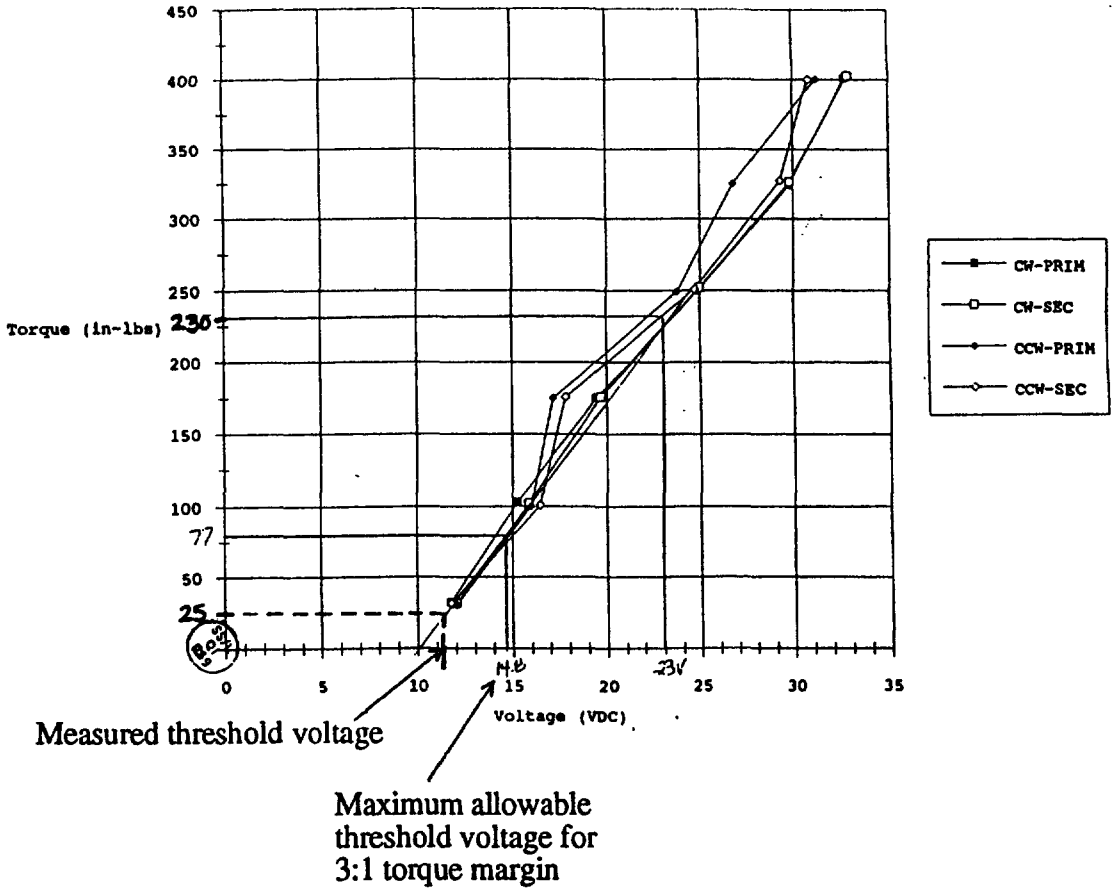

Figure 3. Rotary Actuator Torque versus Voltage Curve

Coarse potentiometer voltage shift

The rotary actuator is "calibrated" during assembly to obtain a potentiometer voltage corresponding to the neutral position. The test specification required the coarse potentiometer voltage to be 2.5 ± 0.025 VDC at neutral. During testing, the coarse potentiometer voltage varied from the calibrated neutral position as much as 0.046 VDC.

An extensive design and statistical data analysis was performed, as well as a physical inspection and some investigative testing. The following possible sources for the coarse potentiometer voltage variations were considered:

- shaft to front housing interface
- shaft to coupler interface
- coupler to potentiometer shaft interface
- mechanism internal to potentiometer
- potentiometer housing to motor housing interface

- motor housing to retainer interface
- harmonic drive hysteresis
- fine potentiometer gear mesh
- harmonic drive flexcup to front housing interface
- external equipment error

The analysis pinpointed the source to the potentiometer coupler to shaft interface, which allowed the greatest amount of relative motion. Because this interface was difficult to redesign, the voltage tolerance requirement was revisited.

One revolution of the fine potentiometer is equivalent to a 0.21 VDC change in the coarse potentiometer voltage. The neutral position coarse potentiometer tolerance was opened to ± 0.100 VDC, which still accurately determines the fine potentiometer revolution and provides an acceptable test limit that all actuators can meet.

Voltage dropouts

After three axes of random vibration, the qualification rotary actuator exhibited coarse potentiometer voltage dropouts (seen on strip chart recordings). The dropouts were attributed to the dithering between the potentiometer wiper and element caused by the shaft to coupler interface movement during vibration testing. It is believed that the dropouts are a discontinuity caused by debris generated during the vibration dithering. These dropouts were diminished and eventually "wiped" away with subsequent operation of the rotary actuator.

The vibration levels were re-evaluated and lowered based on recently acquired spacecraft test data. Subsequent testing at the lower levels was successfully completed without any dropouts.

TAAPM TESTS

At TAAPM-level testing, potentiometer voltage dropouts resurfaced. There were dropouts noted after vibration as well as during cold thermal-vacuum testing. In both cases, the dropouts were eliminated by continued operation of the TAAPM through the regions affected.

During vibration in the antenna subsystem configuration, the coarse potentiometer receives the worst loading since it is tied to the output of the TAAPM while the fine potentiometers are geared to the motor input and see less "free play".

After vibration testing, the TAAPM goes through non-operational and operational thermal cycles to simulate the space environment. During operational testing, the potentiometers are monitored by a strip chart recorder. Dropouts were seen on these strip charts and detected by test software problems due to inconsistent voltage readings. The worst dropouts were seen during the qualification life testing at cold temperature.

A combination of vibration exposure and difference in the coefficient of thermal expansion between debris and/or the materials of the potentiometers appears to cause the dropouts. At cold temperature there seems to be a greater mismatch. Once the TAAPM is returned to ambient or hot temperatures, the dropouts disappear.

3.2.2 Resolution Step Size/ Repeatability

Step size is defined as the angular movement of one step. Repeatablilty is the angular difference between two measurements of the same step location. The rotary actuator step size varies cyclically throughout the range of motion due to the design of the harmonic drive (see Figure 4). The rotary actuator vendor maximizes the accuracy of the step size by positioning the harmonic drive to have the range of motion in the best area of the harmonic drive accuracy curve.

For on-orbit pointing, the angular repeatability of the step position over the range of motion is more important than the size of each individual step. Test results indicate very good repeatability, typically less than the magnitude of one step (~0.010 degree).

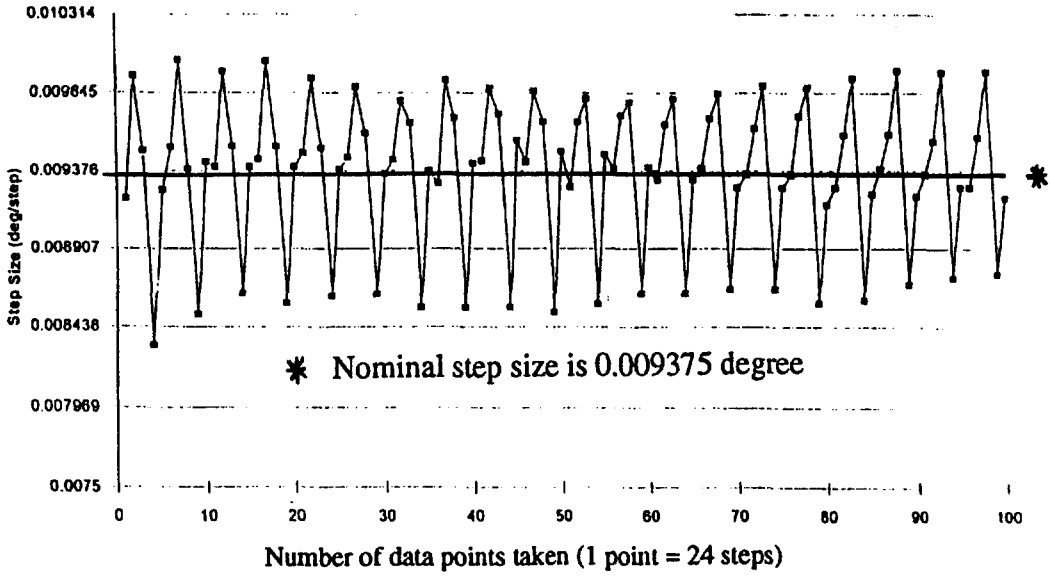

Figure 4. Typical cyclic step size variation over Rotary Actuator range of motion

3.2.3 Hysteresis

TAAPM hysteresis is measured as the total difference in step readings when approaching a given position from opposing directions. Tiltsensor hysteresis made quantifying actual mechanism hysteresis very difficult (see paragraph 3.1.1 Tiltsensor). The TAAPM hysteresis is primarily comprised of the harmonic drive flexibilty, potentiometer and waveguide effects.

Although the harmonic drive design offers essentially zero backlash, a disadvantage arises in positional hysteresis. The flex spline of the harmonic drive acts as a spring and tends to wind up when driven into a stop. This wind up causes a step versus position error. Since antenna positioning is estimated by step counting, whenever a stop is hit, this error must be taken into account. Tests show this error to be ~0.026 degree. Potentiometer error is ~0.002 degree, while the waveguide hysteresis is ~0.01 degree.

3.2.4 Vibration

The antenna subsystem, consisting of antenna, holddown and TAAPM has a resonance near 50 Hz. To obtain realistic vibration loads, the TAAPM is vibration tested using an antenna simulator and a flight holddown.

Sine vibration testing attempts to simulate quasi-static launch loads. The quasi-static loads (for example 10.0 g lateral) are basically achieved in the low frequency region of the vibration test, near 20 Hz. Above 20 Hz, the sine input excites resonances, which are not necessarily part of the launch environment being simulated. To address this shortcoming of the test, the input can be limited such that the flight expected loads are not exceeded.

During the TAAPM vibration testing curious behavior occurred while limiting the input. The system resonance was so abrupt that the input could not be controlled. This behavior was characterized as being very non-linear: the resonance did not normally drop off with increasing frequency, but dropped off abruptly, as shown in Figure 5. This type of behavior is associated with the dynamic behavior of mechanical gaps or dead-bands.

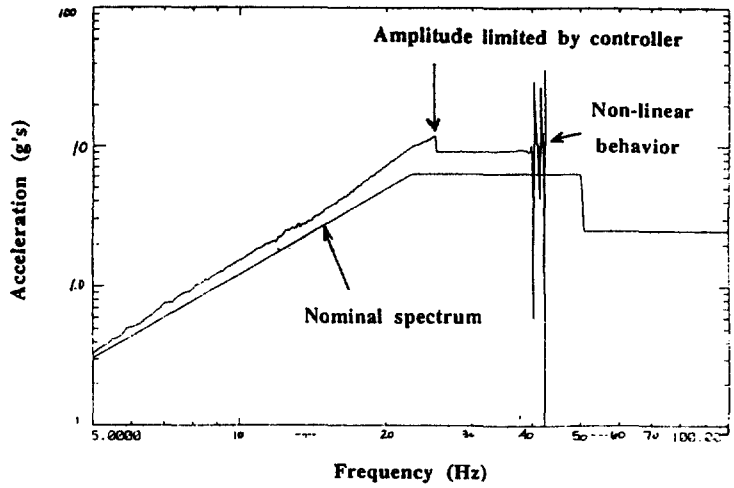

Figure 5. Spot Antenna Feed Response During Sine Vibration

The design of the holddown was thoroughly evaluated: there were several areas which contained excess free-play (slop). The design was

revised to eliminate the free-play, and vibration testing was repeated without further anomaly. The system still has a 50 Hz resonance; however, the magnitude of amplification is greatly reduced.

As a result of testing in the "subsystem" configuration, this design oversight was able to be corrected early in the test program, before the components were integrated to the spacecraft. The interactions of various elements of a system can not always be predicted, which necessitates a thorough system/subsystem test plan.

3.2.5 Torque margin

Torque margin was highest at cold temperatures. Even though the waveguide stiffness and internal frictions increase with cold temperature, the motor develops more torque due to the decrease in winding resistance and resulting increase in current.

Duty cycle has a pronounced effect on output torque of the unit: full rated torque can only be developed at 100% duty cycle. The TAAPM is normally operated at 57% duty cycle for power and thermal reasons. Full torque is not realized at 57% duty cycle because the motor reverts to detent torque during the 43% off portion of the pulse. The result is that above a certain voltage, torque does not linearily increase with increasing voltage. This result is shown in Figure 6.

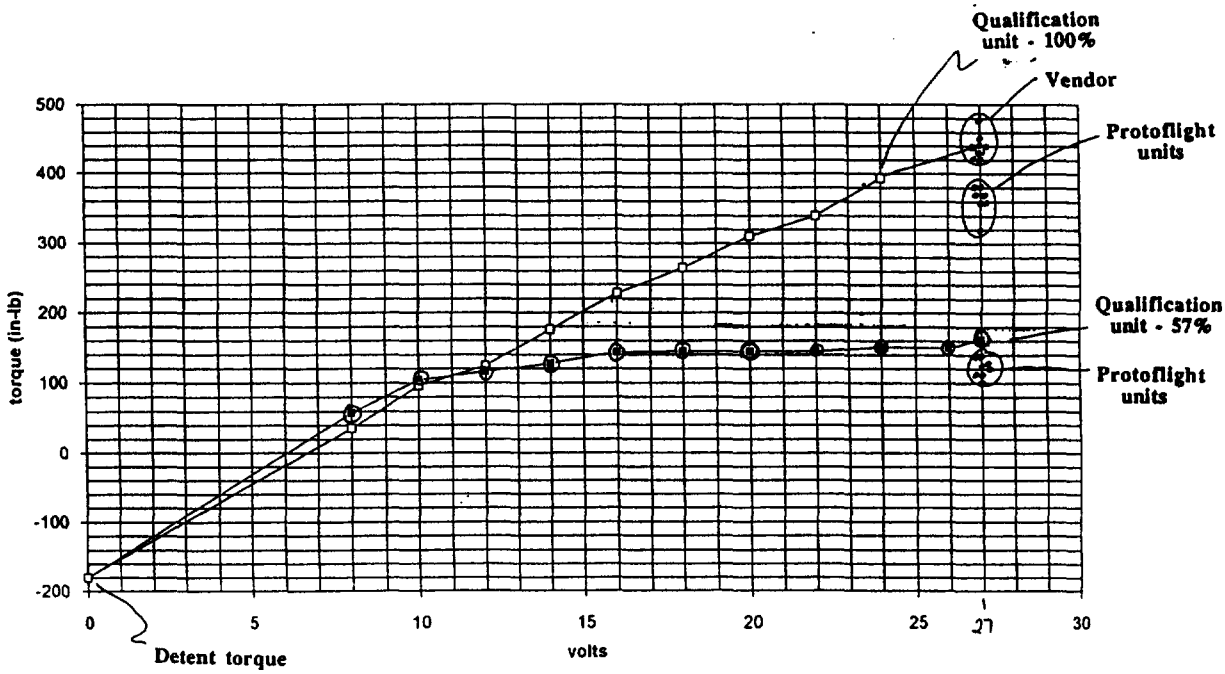

Figure 6. Torque versus Voltage at 57 % and 100% duty cycle

3.3 SPACECRAFT TESTING ISSUES

At system level, antenna pointing, TAAPM range of motion and torque margin are verified at ambient and worst-case thermal-vacuum conditions. In order to verify the spot antenna/ TAAPM performance, an off-loader is required to react the large gravity moments induced by the antenna. Since the center of gravity of the spot antenna is not located on the structure but at a point in space (see Figure 7), an off-loader was difficult to design. On the S2 spot antenna, off-loader design was compounded by the requirement for movement at an odd angle to the gravity vector.

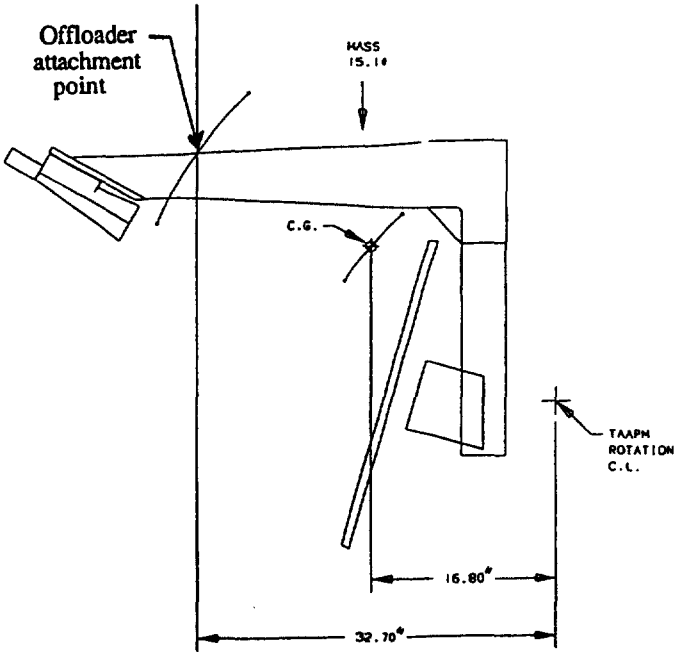

Figure 7. Location of center of gravity (c.g.) on spot antenna assembly

3.3.1 Two off-loader designs

Two different off-loaders were required for system level testing: one for the Compact Antenna Test Range (CATR) testing where pointing telemetry and RF antenna pattern are correlated, and one for the spacecraft thermal-vacuum test where TAAPM range of motion and torque margin are verified at temperature extremes.

The CATR off-loader utilized a calibrated constant force spring assembly while the spacecraft thermal-vacuum off-loader consisted of a pulley and counterweight system. The CATR offloader proved to be a better design.

3.3.2 Effects of the off-loader on spacecraft thermal-vacuum test results

The primary factor that adversely affected the range of motion and torque margin during spacecraft thermal-vacuum testing was hysteresis due to gravity torques and friction in the pulley system. With this system, the uncompensated gravity torques vary throughout the TAAPM range of motion, and with the addition of friction in the pulleys, it was very difficult to determine an accurate torque margin. The friction was of significant magnitude to prohibit TAAPM motion. Since off-loader effects obscure the data, it was decided to use unit-level data to prove design torque margin.

4.0 ON-ORBIT OPERATION/ CONCLUSION

On-orbit range of motion tests were successfully completed on all spot antennas during the period of 31 October thru 2 November 1993. The on-orbit test results were very consistent with the unit and spacecraft ground-level testing at Space Systems/ Loral.

4.1 On orbit test results

During these tests, all TAAPM potentiometers were continuously monitored. The following observations were made:

1. During the range of motion tests, the S2 spot antenna coarse potentiometer exhibited "glitches" or dropouts in the location of the stowed/ launch configuration; this same location was anomalous during ground testing.

2. On-orbit data was taken at specific positions through the range of motion, at zero and near the TAAPM stops (approximately 1000 to 1300 steps from the zero position). In general, the on-orbit telemetry agreed with the final spacecraft (prior to launch) test data to within 1 step.

4.2 Conclusion

The most significant "lesson learned" during the TAAPM test program was that subsystem application must be seriously considered in developing test methods and setups for unit-level qualification. Although the TAAPM could easily meet unit requirements, unexpected problems arose during subsystem (flight configuration) testing.

Secondly, proper design of equipment used during ground testing is fundamentally important for obtaining meaningful test results on flight hardware. As evidenced by this paper, subsystem configuration and test setups proved to make TAAPM testing much more challenging than anticipated.

DESIGN AND PERFORMANCE OF THE TELESCOPE AND DETECTOR COVERS ON THE EXTREME ULTRAVIOLET EXPLORER SATELLITE

James L. Tom
Space Sciences Laboratory
University of California
Berkeley, California

ABSTRACT

Two cover mechanisms were designed and developed for the Extreme Ultraviolet Explorer (EUVE) science payload to keep the EUVE telescope mirrors and detectors sealed from the atmospheric environment until the spacecraft was placed into orbit. There were four telescope front covers and seven motorized detector covers on the EUVE science payload. The EUVE satellite was launched into orbit in June 1992 and all the covers operated successfully after launch. This success can be attributed to high design margins and extensive testing at each level of assembly. This paper describes the design of the telescope front covers and the motorized detector covers. This paper also discusses some of the many design considerations and modifications made as performance and reliability problems became apparent from each phase of testing.

INTRODUCTION

The EUVE science payload consists of three scanning telescopes and a deep survey spectrometer (DS/S) telescope. Figure 1 is an artist's sketch of the EUVE science payload shown with the telescope front covers in the open position. Within each telescope are microchannel plate imaging detectors each housed in a vacuum chamber. There is a detector in each scanning telescope and four detectors in the DS/S telescope. Each telescope contains Wolter-Schwarzchild type grazing incident mirrors which focus onto the microchannel plate detectors. The mirror and optical elements in each telescope are extremely sensitive to particulate and molecular contamination which would degrade the optical transmissivity. The microchannel plate detectors contain various types of filters for imaging at various wavelengths and in addition to being sensitive to contamination, are also sensitive to degradation by atmospheric oxygen. Figure 2 is a cross-sectional view of the scanning telescope and Figure 3 is a cross-sectional view of the DS/S telescope. To prevent contamination of the optics, the telescopes were designed to be contained within a sealed cylindrical housing, as shown in Figures 2 and 3, where the optics cavity was maintained at a positive pressure with high purity dry nitrogen until deployed into orbit. The detectors were designed to be contained within a vacuum chamber that is continuously maintained at a vacuum below 10^{-5} torr. Each detector vacuum chamber contains a motorized cover, as shown in Figures 2 and 3, which provides a vacuum seal around the opening to the detector imaging area. While on the ground, the optical cavity of each telescope was periodically repressurized through a valve on each of the front covers. Each front cover also contains a breather assembly to allow the pressure within the

telescope to vent during launch or be backfilled with atmospheric air should the spacecraft be retrieved from space to Earth.

THE TELESCOPE FRONT COVERS

Each of the three scanning telescopes and the DS/S telescope were designed with identical front cover plates where one front cover design could be used to seal the 41-cm-diameter opening on each telescope. Figure 4 shows the configuration of the front cover assembly. The basic design concept for the front covers was based on using stored energy of springs to power the cover into the open position. Such a mechanical energy system was considered simpler and more reliable than an electrically-powered motor-driven system, especially where there were no requirements to operate the cover after being opened in orbit. The front cover is pivoted about two support arms and contains a captive o-ring seal around the perimeter of the cover. Two types of springs were used to open the cover. One was a pair of compression springs with a high spring constant (580 $^{kg}/_{cm}$ each) and with a linear travel of 2.5 cm. The second type was a pair of torsion springs each with a torsional spring constant of 98 $^{kg \cdot cm}/_{radian}$ and with an angular travel of 180 degrees. Figure 5 shows the front cover in various positions from the fully closed position. The high force compression spring was designed to ensure the unsealing of the o-ring sealed cover, especially should the seal force become large, as a result of stiction from the o-ring being in a sealed condition for a long (2 year) period of time. The torsion springs were designed to swing the cover into the fully open position. To prevent the cover from stopping with a large impact force at the end of travel, a honeycomb crush pad was designed to absorb the residual energy in the spring-driven system. The development of the telescope front covers entailed refinements and changes made to meet several requirements of the front cover. Some of these requirements were to achieve a reliable long-term front cover seal, to have a reliable mechanism to release the sealed front cover, and to have a positive means to retain the cover in the fully open position. The force to operate this mechanism was designed with a margin of 5. This margin was intended to provide adequate force in the event of potential inadvertent obstructions from spacecraft wiring or thermal blanketing. The following paragraphs describe and discuss some areas of development and testing to verify and qualify the front cover design for flight.

The Front Cover Seal

The front cover seal was designed with the capability of maintaining a positive gauge pressure over 14 kPa within the optics cavity of the telescopes without the need for frequent repressurization. There were a total of 16 o-ring seals in the optics cavity of the scanning telescope including seals around the focal plane plate, detector chamber, motorized cover, structural interfaces, electrical feedthrus, and a number of devices on the front cover. An initial source of leakage found in the front cover o-ring seal was attributed to deflection in the cover resulting from the large single point bolting force required for an 18% o-ring compression. The amount of deflection of the cover was reduced by increasing the depth of the o-

ring groove to lower the o-ring compression force without losing o-ring contact for a pressure-tight seal.

Additional distortion of the front cover was caused by the excessive clamping force of the single retention bolt acting on the cantilevered tongue of the cover. To reduce this distortion, a procedure was implemented to prevent over-tightening of the clamping bolt once the front cover o-ring and springs were fully compressed.

Pyro-actuated Release of the Front Cover

The front cover was held in the closed position by a single 0.8-cm-diameter bolt that passes through the opening of two pyro actuated bolt cutters as shown in Figure 4. The bolt cutter farthest from the front cover was the prime cutter, and the bolt cutter closer to the front cover was the back-up cutter. From extreme temperature testing, the pyros were found to leak small amounts of explosive (gun) powder at low (-50° C) temperatures. This was a concern for contamination of the telescope mirrors. As a result, an enclosure was designed around the pyro bolt cutters to contain possible particulates from the cutters. In addition, the thickness of a captive plate for the severed bolt and nut was increased to prevent the plate from being bent by the high velocity impact of the severed parts.

Positive Front Cover Latching Mechanism

The front cover opens in about 0.3 second and stops against a honeycomb crush pad. As the cover engages the crush pad, ratchets on each side of the cantilevered tongue of the cover engage pawls to provide positive retention of the front cover in the fully open position. Although the residual torsion spring force was adequate to keep the front cover in the fully open position against the crush pad, a two fault tolerate mechanism to retain the front cover was a shuttle safety requirement. During vibration testing, the adequacy of the two latching mechanisms was verified. It was found that the vibration of the front cover mass between the latch and honeycomb crush pad resulted in repetitive impact on the crush pad to eventually crush the residual amount of honeycomb. However, it was found that with the latching mechanism disabled during vibration testing, the front cover was able to gradually swing against the torsion spring force and return against the crush pad without large impact forces. The latch retention mechanism was retained in the flight design to comply with the two-fault tolerant requirements. Figure 6 is a photo of the front cover assembly on the DS/S with the honeycomb crush pad and latching pawls installed.

THE MOTORIZED DETECTOR COVERS

Each of the seven detectors on the science payload was enclosed within a vacuum chamber. Figure 7 shows the configuration of the motorized door assembly which was designed as a self-contained modular unit. The motorized door assembly fits onto the focal plane adjacent to the detector vacuum chamber and seals the 8.6-cm-diameter opening of the vacuum chamber as shown on the

telescope cross-sectional views in Figures 2 and 3. The motorized door assembly uses a four-bar linkage with an over-center position to provide positive locking of the cover in the sealed position. Each motorized door assembly has a pyro-actuated opening mechanism that would be used in the event of a failure in the mechanical, electrical, or command/control system. The pyro-actuated mechanism severs a bolt to allow compressed bevel springs to disengage miter gears to the drive motor and also moves the detector cover to the fully open position. The following paragraphs will discuss the design changes implemented after a number of vibration and thermal cycle tests. Changes were made in the detector cover adjustment mechanism, bearings, and brushes on the DC motors, and refinements were made to the support housing to alleviate failure from fatigue stresses.

Detector Cover Adjustment Provision

The detector cover was initially designed with a compression spring between the cover and actuating arm to achieve a more constant sealing force from variations in the travel of the actuating arm as shown in Figure 8, which is an assembly drawing of the motorized door. This spring loading turned out to be undesirable because the fundamental frequency of the spring was very close to the resonant frequency of the focal plane plate on which the detector mounts. Attempts were made to shift the frequency with a vibration damper but a tuned damper was sensitive to mounting accuracy and it was difficult to achieve repeatable results. Testing showed that without a spring interconnection, the detector cover o-ring sealed satisfactorily under random vibration loads. The compression spring was replaced by a threaded attachment to the actuating arm where each cover was individually adjusted for the proper O-ring seal compression and a locking screw was used to prevent movement from the adjusted position.

Because of contamination concerns, the use of lubricants for a good vacuum seal was limited to a few possibilities. Braycote 601 was an acceptable lubricant for use in preventing stiction but was not a good vacuum seal grease between the viton o-ring and the stainless steel flange. Repeated testing revealed that a good vacuum seal between a viton o-ring and stainless steel could be achieved without the use of any lubricants.

The housing for the motorized door was of a cylindrical shape with a cutout for the actuating mechanisms as shown in Figure 9. This cutout finally resulted in a fatigue failure from repeated vibration testing. Although the design loads were not extremely high, the failure was analyzed as fatigue and stress concentration caused by the small radii of the cutouts. This was modified by a using a thicker cylinder wall and enlarging the radii around the cutout in the cylinder. There were no failures after the modification.

Modifications to the DC Motors

The detector doors were operated by DC motors retrofitted with Bartemp bearings; Braycote 601 lubricant was applied with a hypodermic needle directly onto the ball bearings to minimize potential contamination; conventional motor

brushes were replaced with silver impregnated brushes; and stiffer brush springs were used for more reliable contact pressure. These modifications were made to prevent stalling of the motor and erratic (arcing) motor currents at low temperatures. Figure 10 is a photo of the motorized cover assembly during testing.

SUMMARY

The EUVE science payload contained eleven mechanical devices (four telescope covers and seven detector covers). A failure in any one of them would have resulted in the functional loss of an instrument. Repetitive functional and environmental testing at the component level helped to provide early identification of problems in design, manufacturing, materials, and assembly. However, the possibility of a malfunction or failure of the mechanisms after a long dormant state was difficult to assess as there were no trivial tests for time degradation in lubrication effectiveness, stiction in o-ring seals, and potential increases in static friction from handling and shipping loads. Assembly of all the telescopes was completed in January 1990 at which point the mechanisms on the telescopes were last operated in a vacuum during calibration. After launch of the EUVE satellite in June 1992, all four telescope front covers opened successfully with the prime pyro actuating system. Additionally the motorized covers continue to operate successfully to date after 19 months in orbit. The successful operation of all the mechanisms on the EUVE payload can finally be attributed to adequate testing and design margins.

ACKNOWLEDGMENTS

The author wishes to thank Roger Malina for his advice and encouragement on this project. This work has been supported by NASA contract NAS5-29298.

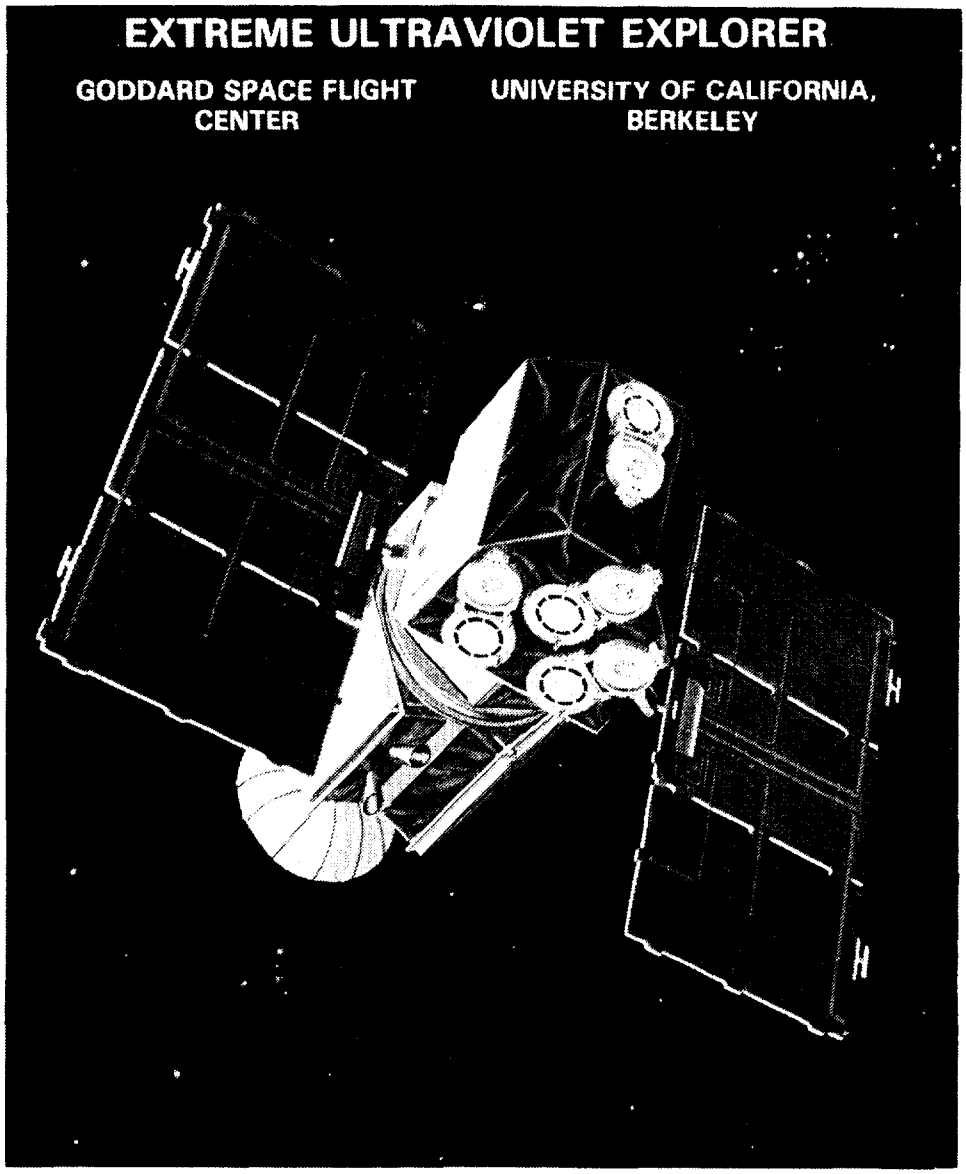

Figure 1. Artist rendition of the Extreme Ultraviolet Explorer with the front covers on the 3 Scanning Telescopes and the Deep Survey Spectrometer shown in the **OPEN** position

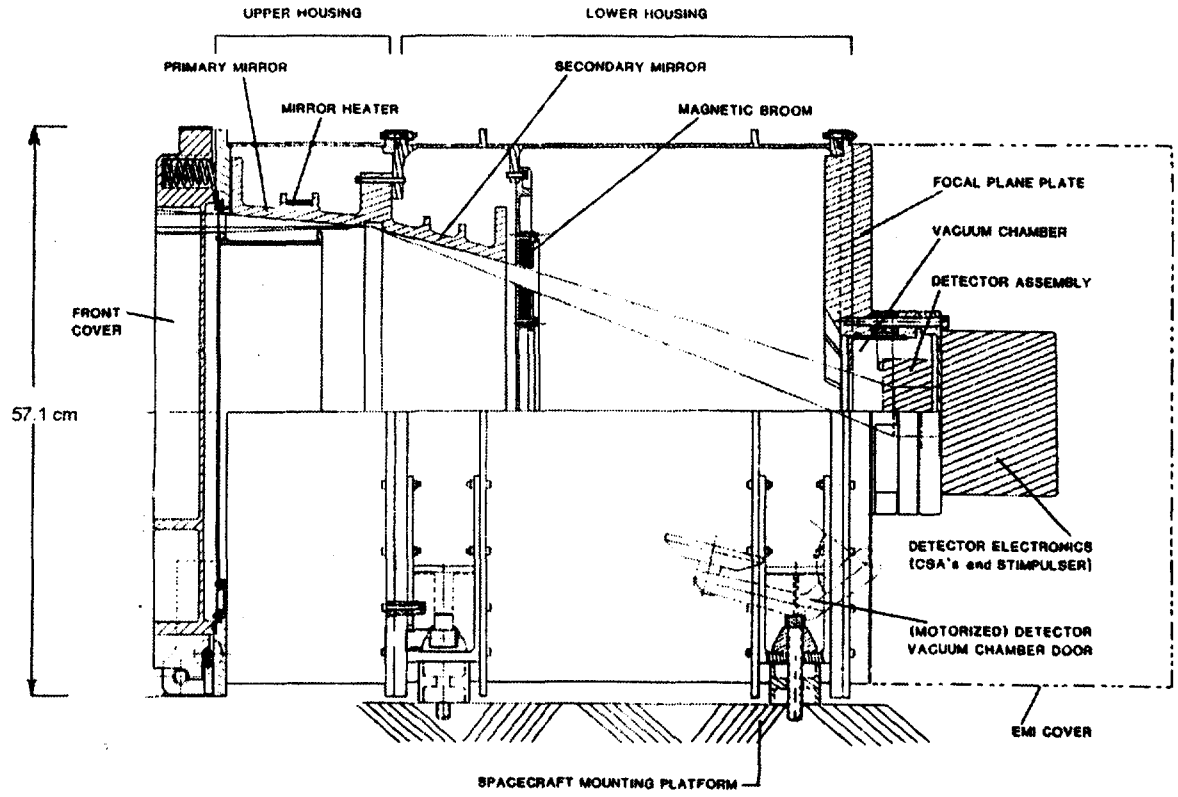

Figure 2. Cross-sectional View of Scanning Telescope

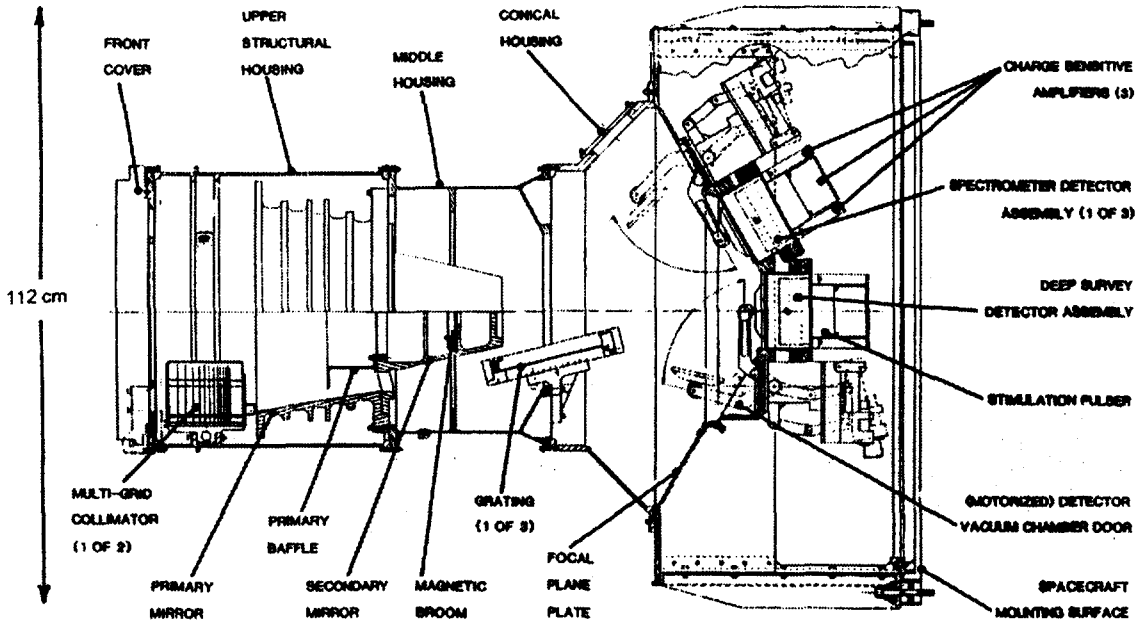

Figure 3. Cross-sectional View of Deep Survey/Spectrometer Telescope

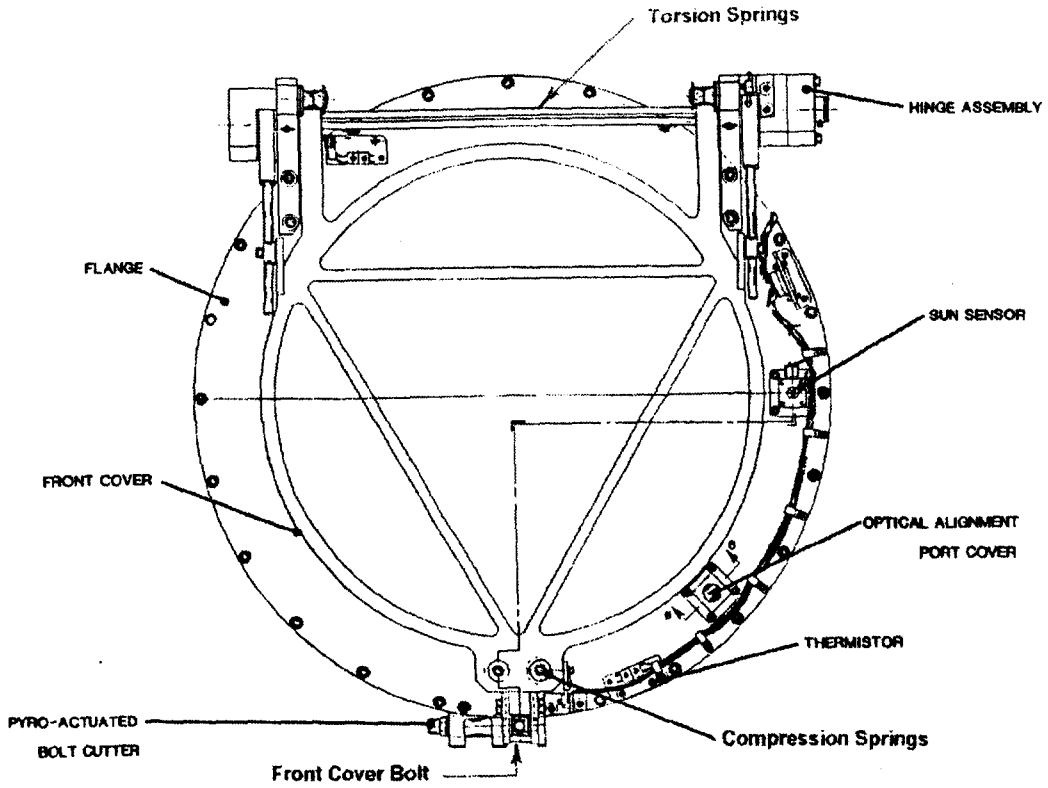

Figure 4. Telescope Front Cover Assembly

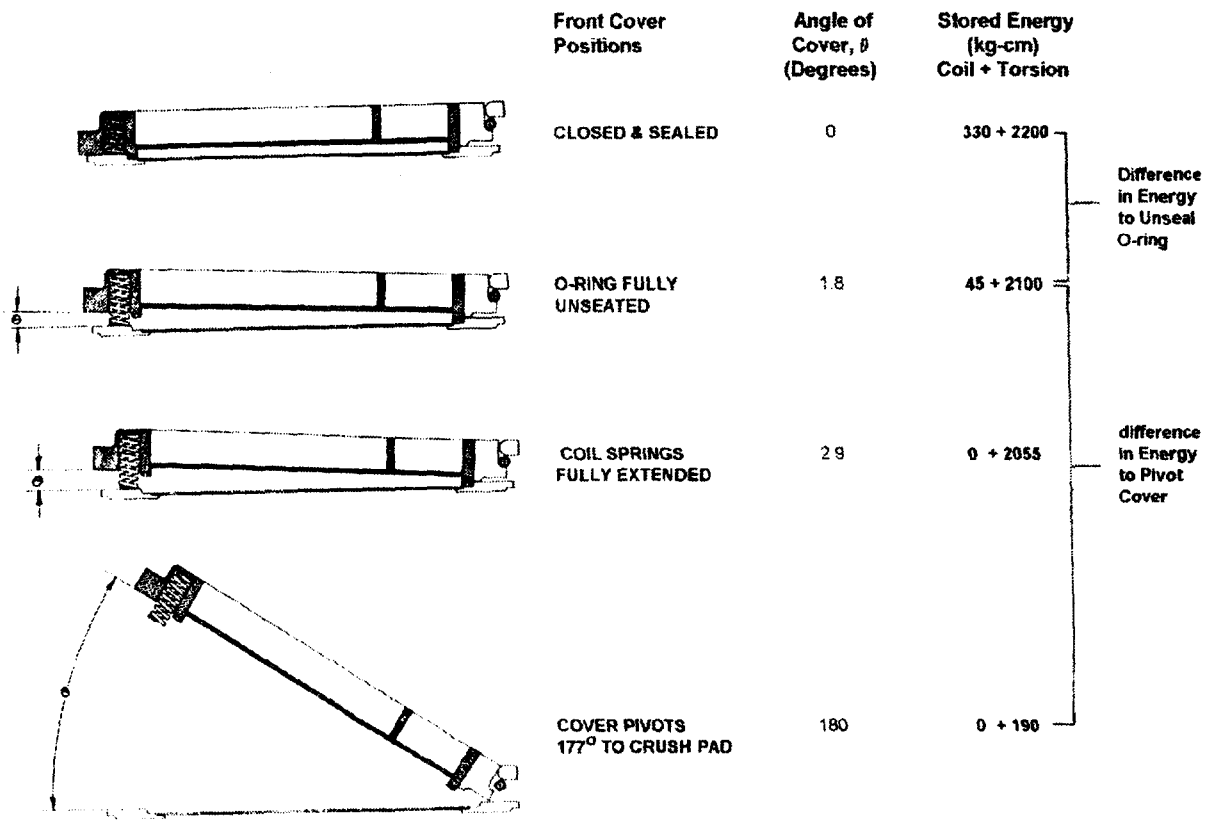

Figure 5. Front Cover Positions and Stored Energy of Springs

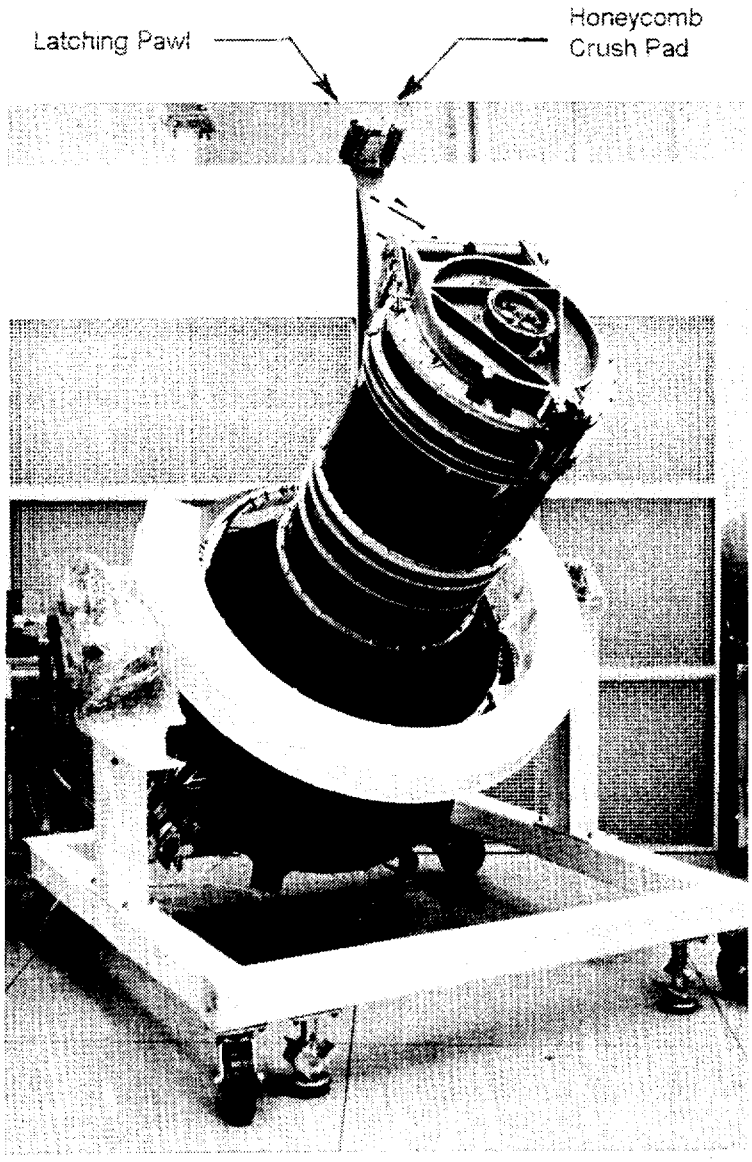

Figure 6.
Front Cover Assembly on the
Deep Survey Spectrometer

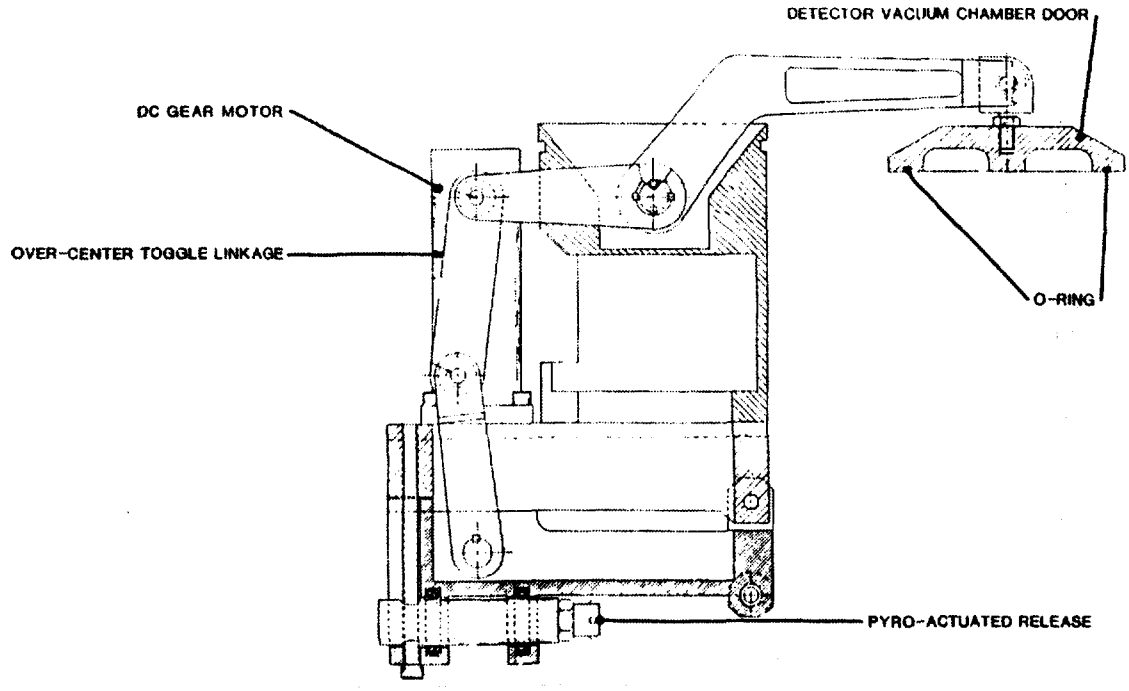

Figure 7. Motorized Detector Door Assembly

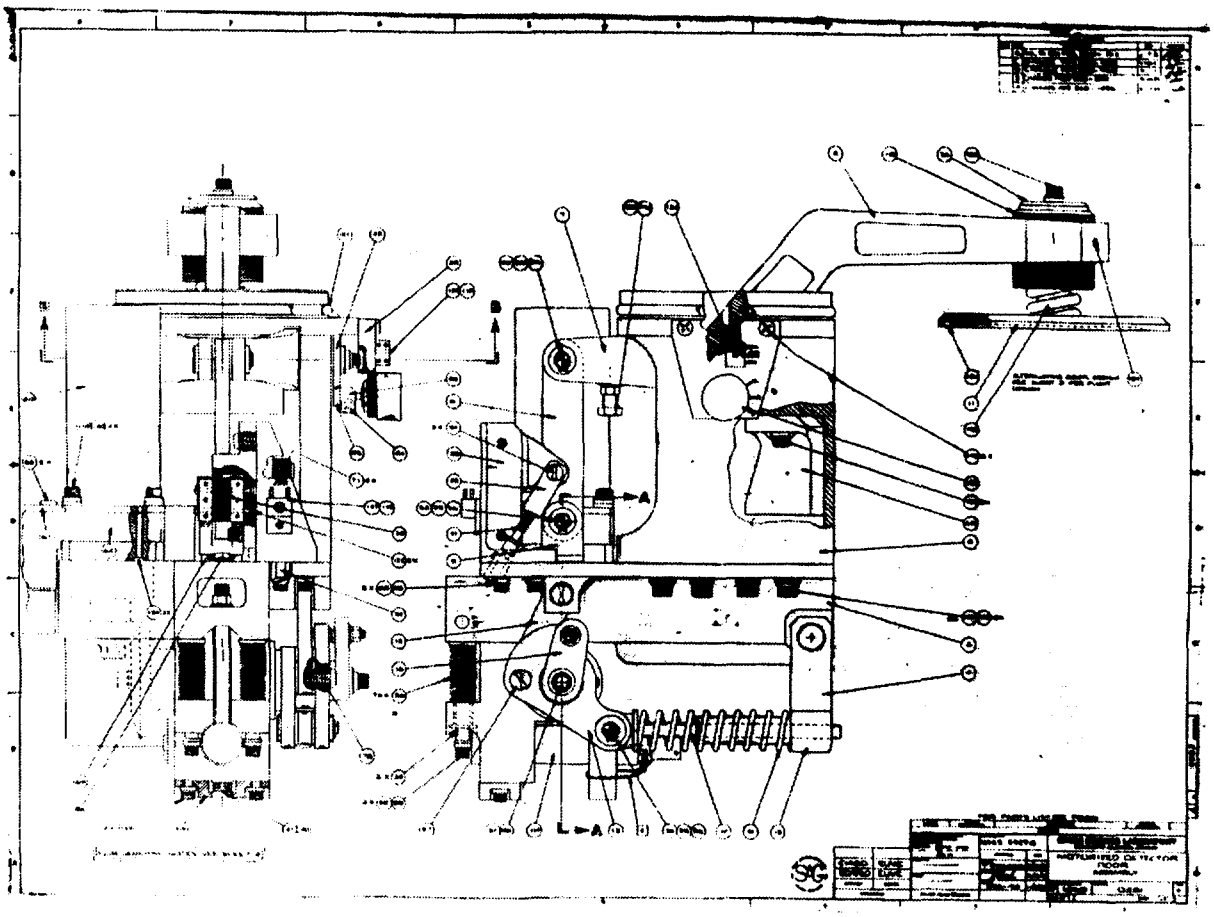

Figure 8. Drawing of the Motorized Detector Door Assembly

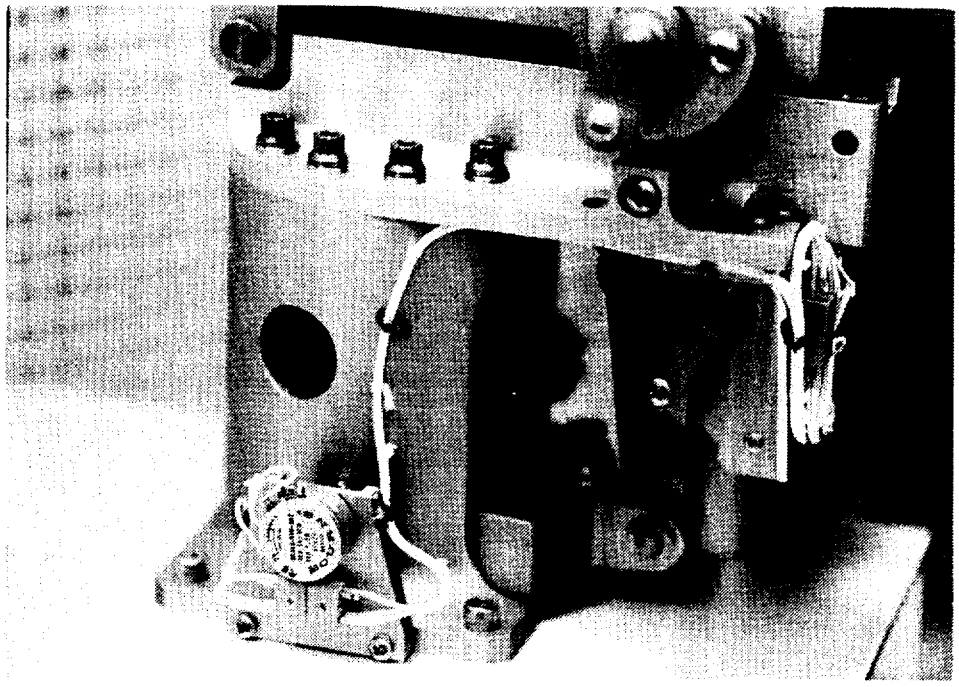

Figure 9. Cylindrical Housing of the Motorized Cover Assembly

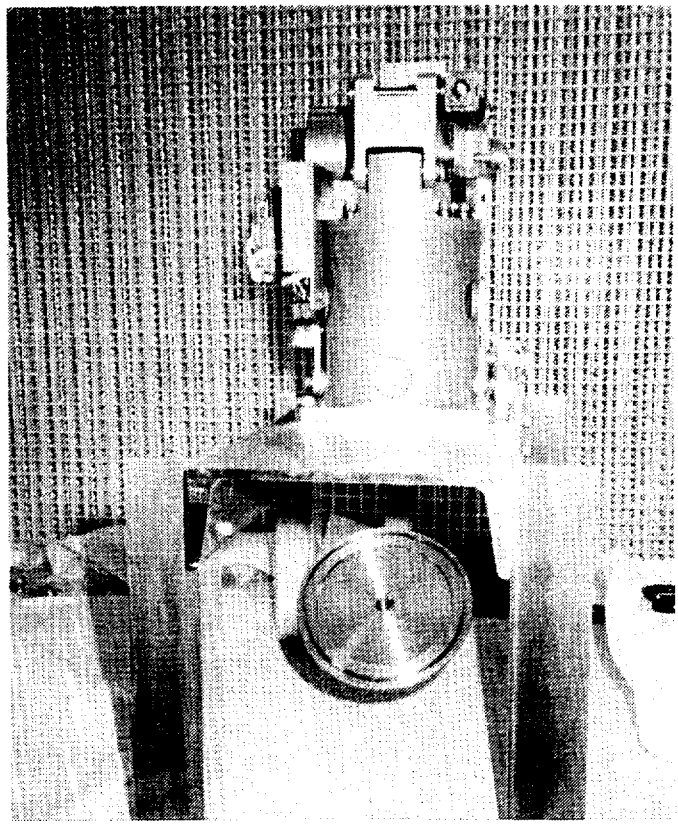

Figure 10. Testing of the Motorized Cover Assembly on a Clean Bench

POINTING AND TRACKING SPACE MECHANISM FOR LASER COMMUNICATION

A. Brunschvig and M. de Boisanger
Automatic Control Systems & Propulsion Division
Matra Marconi Space
Toulouse, France

ABSTRACT

Space optical communication is considered a promising technology regarding its high data rate and confidentiality capabilities. However, it requires today complex satellite systems involving highly accurate mechanisms.

This paper aims to highlight the stringent requirements which had to be fulfilled for such a mechanism, the way an existing design has been adapted to meet these requirements and the main technical difficulties which have been overcome thanks to extensive development tests throughout the C/D phase initiated in 1991. The expected on-orbit performance of this mechanism is also presented.

INTRODUCTION

The "Coarse Pointing Assembly" (CPA) is a two-axis gimbals mechanism developed by MMS in the frame of the SILEX (Semiconductor Intersatellite Link EXperiment) ESA program dedicated to optical space communications between Low Earth Orbit and Geostationary Orbit satellites. The first SILEX Terminal is to be flown on SPOT4 LEO spacecraft and its GEO counterpart will be installed on ARTEMIS platform from Alenia. These two Terminals should thus enable the first inter-orbit communication link to be demonstrated in 1997.

To date, a complete flight-representative CPA has been manufactured and qualification of the design has been started. As part of the Pointing, Acquisition and Tracking sub-system, the main function of the CPA is to perform the pointing of the SILEX telescope over wide angles in order to compensate for the satellite ephemerids (see Figure 1).

The SILEX CPA design concept is derived from the IOC (Inter-Orbit Communication) experiment which proved to work satisfactorily on-orbit during the one year flight of the EURECA (EUropean REtrievable CArrier) mission. However, the IOC design which was intended for RF communications has had to be largely adapted to the SILEX specific and more demanding laser communication application.

SYSTEM REQUIREMENTS

The on-orbit mission of the CPA can be split in two distinct phases. The first one corresponds to the "acquisition" of the laser communication beam between the two Terminals each time the LEO satellite comes "in-sight" of the GEO spacecraft.

During this phase, the overall SILEX system operates in open-loop and the CPA must guarantee very accurate and stable pointing of the two telescopes towards each other until the "fine" stage of each Terminal acquires the narrow laser beam. The acquisition procedure involves a particular scanning pattern of the laser beam generated by the GEO satellite beacon over the "uncertainty cone" of the LEO satellite relative position. Because of its open-loop nature, the acquisition phase is the most critical period of the SILEX mission. In particular, the CPA performance (bias and short-term stability) is a major contributor to the probability of acquisition success between the two Terminals.

When the "acquisition" procedure is completed and the communication link is established, the overall system is operating in closed-loop, using the laser beam itself as a pointing error signal. During this second phase, the CPA remains commanded in open-loop and must insure tracking of the two Terminals. The CPA performance requirements are somewhat less critical in this mode regarding pointing accuracy, but a major constraint remains on the torque disturbances induced by the CPA on the host spacecraft. Indeed, these disturbances must be reduced to a minimum in order not to corrupt the satellite payload operations.

The CPA main performance requirements are summarized hereafter :

• Terminal mobile part characteristics :	
- mass	75 kg
- inertia	5 m^2.kg
- mass unbalance	60 mm
• kinematics requirements (2 axes) :	
- angular coverage	< 200 °
- angular rates	< 0.2 °/s
- angular accelerations	< 0.02 °/s^2
• pointing requirements :	
- two-axis bias	< 0.02 °
- two-axis random (f > 0.01 Hz)	< 0.02 ° (3 sigma)
- stability over 1 s (one axis)	< 0.003 °
- stability over 70 ms (one axis)	< 0.001 °
• torque disturbances :	
- torque noise (one axis)	< 2.10^{-8} $(N.m)^2$/Hz (PSD)

DESIGN HERITAGE AND ADAPTATIONS

The CPA is composed of the mechanism itself (CPM) and a dedicated electronic unit (CPDE) as shown on Figure 2. The CPM consists of two articulations (CPMA) linked by a carbon fibre reinforced plastic (CFRP) L-shaped bracket and corresponds to a 800 mm large sub-assembly, weighing 21 kg and dissipating approximately 20 W.

Each CPMA (see Figure 3) features a high resolution hybrid stepper motor mounted on a large annular pre-loaded ball-bearing pair, a direct drive transmission, a 10-bit optical encoder for "coarse" position telemetry, a friction-type blocking device which guarantees stable unpowered position of the telescope, electrical limit stops and a cable-wrap which routes all signals from the Terminal mobile part to the

satellite fixed part with minimum torque disturbances. The CPDE is a fully redundant unit which contains 11 double-Europe size PCB's and two DC/DC converters directly bolted to the box structure. It weighs 12 kg and dissipates a maximum of 30 W.

The motor command is of the open-loop type and uses high resolution micro-stepping technique associated to a high performance current-controlled drive electronics. In order to minimize torque disturbances and pointing errors, models of the main articulation "parasitic" torque (motor, ball-bearings, cable-wrap) are implemented in the electronics processor unit, thus enabling open-loop compensations specific to each CPMA.

Since a significant improvement in performance was required for SILEX with respect to IOC application, the CPA early design phase was mainly devoted to optimizing the original IOC concept. Potential improvements have been investigated in three directions : the articulation design itself, the open-loop compensations and the drive electronics.

In order to reduce the torque noise of the CPMA which cannot be compensated for, it was decided to modify the motor/bearing assembly so that only one bearing pair would be implemented instead of two, as for IOC. This modification was compatible with the SILEX specified launch loads. The other major design change which was identified to reduce further the bearing torque noise was a change in lubrication. The CPMA design was adapted to accommodate wet lubricant which was felt to induce smoother motion capability than solid MoS_2 used on IOC mechanism. Finally, the teflon individual ball separators were replaced by phenolic retainers which were also considered a better solution for torque regularity, especially during transitions at change of motion direction.

Based on IOC experience, the articulation model was reviewed and the open-loop compensations of the CPMA "parasitic" torque have been refined and adapted to match more closely the specific SILEX needs.

Regarding the motor driver electronics, the topology of the IOC power amplifiers (PWM type) has been largely modified in order to improve the motor current accuracy and the related harmonic distortion which generates torque disturbances.

PERFORMANCE-DESIGN RELATIONSHIP

The overall CPA pointing performance stems from one axis performance which is combined at the two-axis level, taking into account the L-bracket influence.

The one axis bias is directly influenced by the mean resistive torque of the CPMA which is composed of :

- bearing/motor overall solid friction torque (hysteresis),
- bearing/motor equivalent viscous friction torque,
- cable-wrap stiffness and hysteresis.

The final pointing bias performance is determined by the on-ground compensation residuals of these resistive torques and by their on-orbit environmental and aging effects which are not compensated for (see Figure 4).

L-bracket contributions to the two-axis pointing bias are mainly related to the on-ground misalignment measurement uncertainties, the launch effects (micro-displacements) and to the on-orbit thermoelastic and desorption behavior.

One axis short term stability, random pointing performance and torque disturbances are essentially determined by :

- torque harmonics (motor, electronics),
- overall torque noise (motor, bearings, electronics) over the relevant frequency range,
- motor transfer function.

The torque harmonics and noise spectra, which are frequency-related to the angular rate of the CPMA, are filtered by the motor transfer function. They are amplified at motor resonance (1.8 Hz, + 20 dB typical). It is of the utmost importance that their initial amplitude be as small as possible. For this reason, initial compensation of the motor harmonics is required. Nevertheless, the motor harmonic compensation residuals will be largely influenced by the CPMA remaining bias error. Indeed, this uncompensated error induces a phase shift in all harmonic compensations, equivalent to an increase of the harmonic residuals (see Figure 5) which, in turns, degrades all dynamic performance.

The LEO dynamic performance (pointing and torque) is more critical, since the LEO kinematics requirements (< 0.2 °/s) are more stringent than the GEO ones (< 0.02 °/s).

Because the final CPA performance would be so closely dependent on the various design adaptations and modifications made after IOC, it was decided to begin validation through extensive development tests on dedicated flight-representative bread-board and engineering models. These tests have involved 3 successive articulations and one electronic unit. They have been mainly oriented towards the following :

- compensation architecture validation,
- bearing assembly performance,
- cable-wrap torque behavior,
- motor harmonics identification,
- drive electronics performance.

COMPENSATION ARCHITECTURE

The CPA overall compensation architecture involves both one axis and two-axis error compensations. The two-axis compensation being purely geometrical (e.g. L-bracket non perpendicularity), it is directly performed by the On-Board-Processor (OBP) which sends the commands to the CPA : actual positions of the rotation axes with respect to the CPA mechanical interfaces are identified on-ground at CPA level and fed to the OBP which can then compute the relevant corrections on each single axis command.

The CPA one axis compensation architecture is described in Figure 6. The OBP angular relative commands are received and processed by the CPDE at 50 Hz. Four initial corrections are computed in parallel and applied to these commands so that the various "parasitic" torques of the articulation can be compensated:

- the motor torque harmonics H_4 (fourth harmonic of the electrical period) which corresponds mainly to the motor detent torque :

$$C_{H4} = C_0 \sin 4p\theta$$

- the articulation overall torque hysteresis Cd represented by a solid friction Dahl model of the form :

$$dC_d = -K_d \left(1 + \text{sign } (d\theta) \frac{C_d}{C_{d_{max}}} \right) d\theta$$

Although this model was known to specifically represent bearing friction behavior [1], its application was extended to include the combination of all CPMA hysteresis sources including the motor and possibly the cable-wrap. For small amplitude alternate angular displacements, this model superimposes an additional equivalent stiffness (K_d) to the motor stiffness. For higher amplitude displacements, torque saturation is reached and the influence on motor stiffness disappears. This behavior was well observed and correlated with the model throughout the development tests.

- the articulation overall viscous resistive torque, proportional to the angular rate :

$$C_v = -F_v * \frac{d\theta}{dt}$$

- the cable-wrap resistive torque induced by its average stiffness :

$$C_{cw} = K_{cw}(\theta - \theta_0)$$

This correction uses the absolute angular position information θ delivered by the 10-bit optical encoder.

The corrected relative angular commands are then used to read the sine and cosine PROM tables which contains 2048 current values over the motor electrical period (1.2 °). These PROM's also incorporate the motor first (H1) and second (H2) torque harmonic compensations.

Final interpolations are made by the CPDE processor to extend the number of micro-steps over one motor period up to 32 768 and to generate commands at 100 Hz in order to minimize the effect of command harmonics generated by the command quantization. Commands are eventually sent to the 12-bit DAC of the motor drive electronics. The torque harmonic disturbance induced by the 100 Hz command rate is then reduced by an analog second order Butterworth filter. Its simple structure allows stable performance and the induced command phase shift can thus be open-loop compensated at OBP level.

For each articulation, these compensation parameters are derived from a specific characterization test procedure which is being carried-out on a dedicated test bench (see Figure 7). This characterization procedure involves specific angular profiles at

different rates and accelerations which are automatically generated and commanded to the articulation.

The test set-up features Kistler piezo sensors for torque measurement and a 24-bit Heidenhain optical encoder for position error determination (static and dynamic). The performance of the motor driver implemented in the test bench are such that the contribution of the electronics to the CPMA pointing errors and torque disturbances is negligible. The same test bench is also used for articulation fine performance verification after compensation.

The above described compensation architecture was successfully tested on the articulation bread-board both without and with cable-wrap.

BEARING ASSEMBLY

The CPA bearing assembly is made of two ball-bearings mounted 40 mm apart on beryllium spacers. Ball-bearings themselves are 200 mm large annular high precision (ABEC 7T) bearings from ADR with phenolic retainers lubricated with Pennzane SHF 2000.

Given the size constraint on the bearing assembly, the main concern is to minimize the ball-bearing mean torque and torque noise. The mean torque induces direct bias on the CPMA pointing accuracy and the torque noise impacts the random budget, the short term stability and torque disturbances.

To reduce the initial bias, the ball-bearing mean torque is characterized on ground for each CPMA at various angular rates in both CW and CCW directions. Its behavior is represented by a viscous friction torque coefficient and a solid friction torque (Dahl model) which is part of the CPDE open-loop compensations. It is then crucial that all variations of this average torque (including torque noise) which cannot be compensated for, be reduced to minimize the on-orbit pointing degradation.

Assuming the bearing torque variations are somewhat proportional to the initial average torque, it was decided to minimize this mean torque in the first place. For that purpose, the initial pre-load adjustment was specified to a minimum (300 N) for this type of bearing and the tolerance on this value was not to exceed ± 30 N. The first development tests made on a representative motor/bearing assembly showed an unexpectedly high bearing mean torque which was also not consistent with the test results obtained by the bearing manufacturer. Investigation revealed that the initial pre-load was largely modified after integration of the bearing in the CPMA housing. Machining tolerances would not allow the radial bearing expansion during the clamping operation. After detailed calculation and measurements (see Figure 8) of the typical expansion of the inner and outer rings, each CPMA housing has been matched to the bearing actual dimensions to accommodate this expansion effect and to minimize the residual clearance after clamping which could generate transverse bias of the CPMA rotation axis.

A major source of on-orbit pre-load variation is the thermal environment of the mechanism which can induce temperature gradients between inner and outer rings

of the bearing. Based on IOC bearing conductance data, preliminary thermal analysis showed that the maximum expected temperature gradient on the bearing would be such that the initial small pre-load could be entirely lost, thus leading to unacceptable transverse bias of the CPMA rotation axis. Yet, it was felt that the change in lubrication could have a significant impact on this result for SILEX. Additional tests confirmed that the bearing conductance was indeed significantly improved by the presence of wet lubrication and was very little affected by the pre-load itself or the lubricant exact quantity. The refined thermal analyses predicted temperature gradients of less than -2 °C/+1.5 °C.

Under such circumstances, theoretical bearing analyses showed that the worst case pre-load variations induced by thermoelastic effects (see Figure 9) would be acceptable.

After the initial bearing pre-load and its variations had been validated, the relationship between the mean torque and these pre-load variations were measured (see Figure 10). It was thus demonstrated that the bearing mean torque would remain below 0.03 Nm for the CPA application (rates < 0.2°/s). Torque noise itself was not precisely measured during these tests but it was considered not to exceed 0.003 Nm over the entire pre-load range. This hypothesis would be confirmed later-on during CPMA performance tests.

Considering the stringent CPA two-axis bias and random specifications, it is also very important that the transverse articulation pointing errors be minimized. These errors, known as the wobble (mean value and noise), are essentially determined by the bearing, spacer and housing geometrical imperfections after assembly. Because of significant volume constraints, the CPA bearing assembly overall implementation was not optimized with respect to such errors. Indeed, the small distance imposed between the two large annular bearings make the design very sensitive to these geometrical imperfections. In order to minimize this effect, most parts involved in the bearing assembly have been machined with an accuracy down to 3 µm. Resulting wobble figures on the order of 10 arcsec for average values and of 5 arcsec for noise have been consistently measured.

CABLE-WRAP

The cable-wrap resistive torque behavior over the CPMA angular coverage would induce both pointing errors and torque disturbances. Indeed, the overall cable-wrap stiffness and hysteresis would generate a variable pointing bias of the CPMA which in turns would degrade the motor harmonic compensations and therefore the dynamic performance. For that reason, the compensation architecture within the CPDE foresees the compensation of the cable-wrap stiffness and hysteresis on the basis of on-ground characterization.

The exact behavior of the cable-wrap resistive torque is closely dependent on the actual technology used for the sheet manufacturing, the definition and the number of cables implemented, the detailed design of the attachment points and the sheet geometry. Final performance of the cable-wrap were therefore difficult to predict and

it was decided that the main design trade-offs should be shortly followed by development tests on a flight-representative cable-wrap bread-board.

The overall cable-wrap behavior was characterized both at ambient and extreme temperatures. It appeared that the stiffness variation over the temperature range was small enough (<35%) that no compensation versus temperature was needed. The hysteresis behavior however was significantly different than what was anticipated. The absolute value of the hysteresis was higher than expected and the hysteresis pattern was also such that the transitions at change of direction were fairly "slow" (over 20 ° typical), thus reducing the linear portions of the cycle (see Figure 11) and making the average stiffness estimation less accurate.

The origin of this observation could be two-fold : the sheet plastic deformation itself and the friction of the sheets on the bottom of the cable-wrap structure under the influence of gravity. A new test simulating "0G" on-orbit conditions showed that the friction phenomenon contributed to only 10 % of the overall hysteresis. On-ground characterization of the cable-wrap hysteresis was therefore not questioned. Identification of the bearing/motor solid friction torque for compensation purposes would not be corrupted by the parasitic friction of the cable-wrap ("0G" test not practical on flight hardware).

Nevertheless, the "soft" transitions observed on the hysteresis cycle were no longer compatible with the compensation pattern foreseen in the CPDE (single Dahl model for all hysteresis sources). It was shown that the actual behavior of the cable-wrap torque hysteresis could be well described by a specific Dahl model with reduced equivalent stiffness (K_d). However, implementation of a second Dahl model in the compensation architecture has not been decided yet.

The CPA pointing budget has been consolidated assuming no specific compensation of the cable-wrap hysteresis and assuming its origin is pure plastic behavior of the sheets. Additional aging and thermal uncompensated effects (±50 %) are therefore applied to the total measured hysteresis in order to derive worst case end-of-life figures.

MOTOR HARMONICS

Based on IOC experience, it was known that, for this type of motor (SAGEM 57PPP60), the torque harmonics H_1, H_2 and H_4 of the electrical period were the most significant in amplitude and could be well identified and compensated for. Higher harmonics were shown to be also highly unstable, both in amplitude and phase, over a complete motor revolution. Compensation efficiency of these harmonics would therefore be rather poor.

Nevertheless, motor harmonics are identified for each articulation up to the 12th harmonic. Amplitudes and phases are determined from the pointing error measured under quasi-static conditions (no dynamic effects involved) over 15 ° coverage selected around the cable-wrap mid-point, using a least square identification algorithm. The compensation efficiency is then verified over the complete CPMA

angular coverage and iterations can be made to optimize the final parameters. Figures better than 70% have been achieved on-ground for H_1, H_2 and H_4 compensation efficiency. Worst-case on-orbit performance should be better than 50%.

As the highest contributor to dynamic pointing errors and torque disturbances, the compensation of H_4 harmonic is very critical and requires particular attention. For that purpose, the phase of H_4 is identified specifically for each direction of the motor rotation whereas a single phase (average value) is determined for each harmonic H_1 and H_2, regardless of the direction of motion. It was further verified that H_4 amplitude before compensation was almost not affected (< 5 %) by the temperature variations of the motor itself or the maximum amplitude of the current driven into the motor phases. The compensation of H_4 would therefore be fairly robust to the motor direct environment.

DRIVE ELECTRONICS

Particular attention has been paid to the drive electronics imperfections so that their impacts on the overall CPA performance be minimized. The main end-of-life requirements applicable to the CPDE are the following :

- amplifier gain asymmetry: < 0.4 %
- current offset asymmetry : < 0.4 % of max amplitude
- current settling time asymmetry : $< \pm 3$ ms
- current noise : $< 50\ \mu A/\sqrt{Hz}$ (PSD)
- harmonic distortion : > 74 dB

Development test results have been successfully correlated with the theoretical analyses which showed that the CPDE current offset asymmetry between phases directly generates H_1 harmonic and that amplifier gain error as well as settling time asymmetry actually create H_2 harmonic.

CPDE specifications were established in such a way that H_1 and H_2 harmonics generated end-of-life by the electronics would be of similar amplitude to H_1 and H_2 motor harmonics, after compensation. Current noise and harmonic distortion stringent requirements would also guarantee that the beginning-of-life CPDE contribution to the CPA random and stability budgets be less important than the motor/bearing effect.

Compatibility tests with a CPMA bread-board have confirmed that the beginning-of-life CPDE performance were much better than the specifications and that the CPMA compensations were not affected by the electronics. This result justified a posteriori that the identification of the compensation parameters for each CPMA model could be performed without the associated CPDE. The resulting programmatic flexibility would be exploited.

CPA PERFORMANCE

Because of the high pointing accuracy and stability required from the CPA, verification of the two-axis performance by test was rapidly found not to be practical. Indeed, the influence of gravity would induce pointing errors one order of magnitude higher than those to be measured. Furthermore, these errors would vary significantly over the specified CPA wide angular coverage and their compensation would be very complex (e.g. anti-gravity device).

The selected approach for performance verification was therefore to extensively focus on the one axis performance measurements at the CPMA level and to rely on a detailed one axis functional simulation model and a theoretical pointing budget in order to extrapolate the two-axis worst case CPA performance.

The detailed CPA one axis simulation model which has been developed includes non linear dynamic models of the motor, the bearings, the cable-wrap, the CPDE processor unit with all CPMA compensations and the motor drive electronics. This simulation model was refined and validated throughout the various development tests referred to above. It was then extensively used for test prediction and interpretation, sub-assembly specification analyses, performance assessment during transitions (change of motion direction) and correlation with the linear mathematical model used for the overall CPA pointing budget calculations.

Worst case predictions of one axis performance are then obtained from the mathematical model under steady-state conditions, assuming combined environmental and aging effects (see Figure 12 for results). Torque noise performance was directly derived from bread-board measurements which typically exhibited low-frequency noise spectra (<1 Hz) at an angular rate of 0.2 °/s. Computation of the equivalent PSD ($5\ 10^{-5}$ $(Nm)^2/Hz$) from the total variance shows that it remains a very critical performance with respect to the requirements.

The individual azimuth and elevation pointing errors are then combined at two-axis level, taking into account their probability distributions. L-bracket contributions such as initial misalignment measurement uncertainties, thermoelastic and desorption effects (calculated) are also superimposed to extrapolate the final two-axis CPA performance. Only the structural dynamic behavior of the L-bracket is not taken into account in the CPA two-axis performance presented in Figure 13. This contribution is analyzed and consolidated at system level within the overall SILEX Terminal pointing budget.

CONCLUSION

The CPA illustrates the ability of a large open-loop mechanism to meet high dynamic pointing accuracy and reduced torque disturbances. This performance have been achieved thanks to detailed characterization and fine tuning of the design, thus enabling the definition of efficient open-loop torque compensations. The importance of development tests on flight-representative hardware in this context has been emphasized.

It should be considered, however, that the ultimate performance has been reached for this type of mechanism using open-loop technology. Closed-loop design would be recommended to meet even more stringent requirements or to provide better evolution potentials.

REFERENCES

[1] Models for steady & non steady Coulomb Torque in Ball-bearings, M.J. Todd, ESTL Northern Research Lab., Risley, England

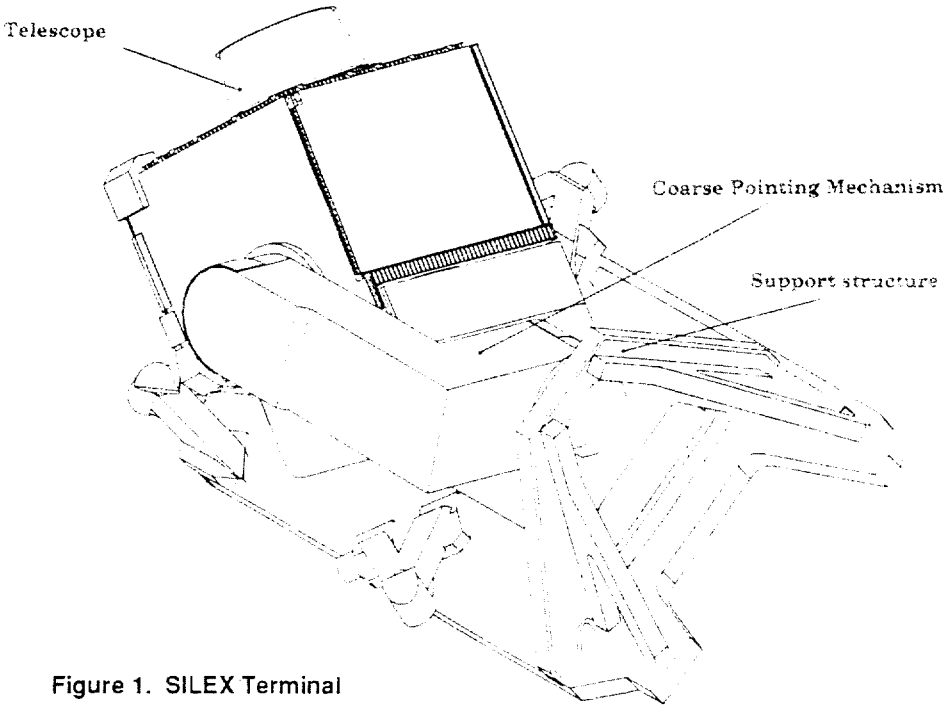

Figure 1. SILEX Terminal

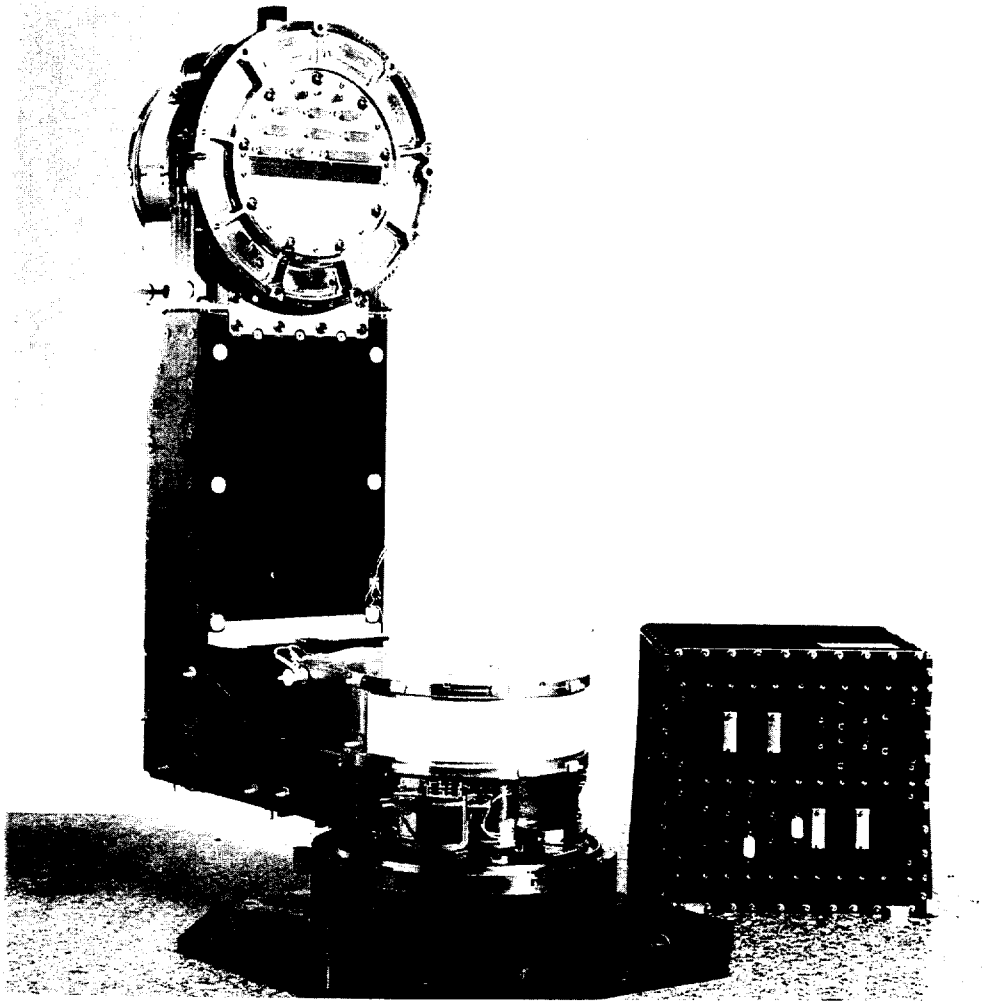

Figure 2. CPA (flight representative)

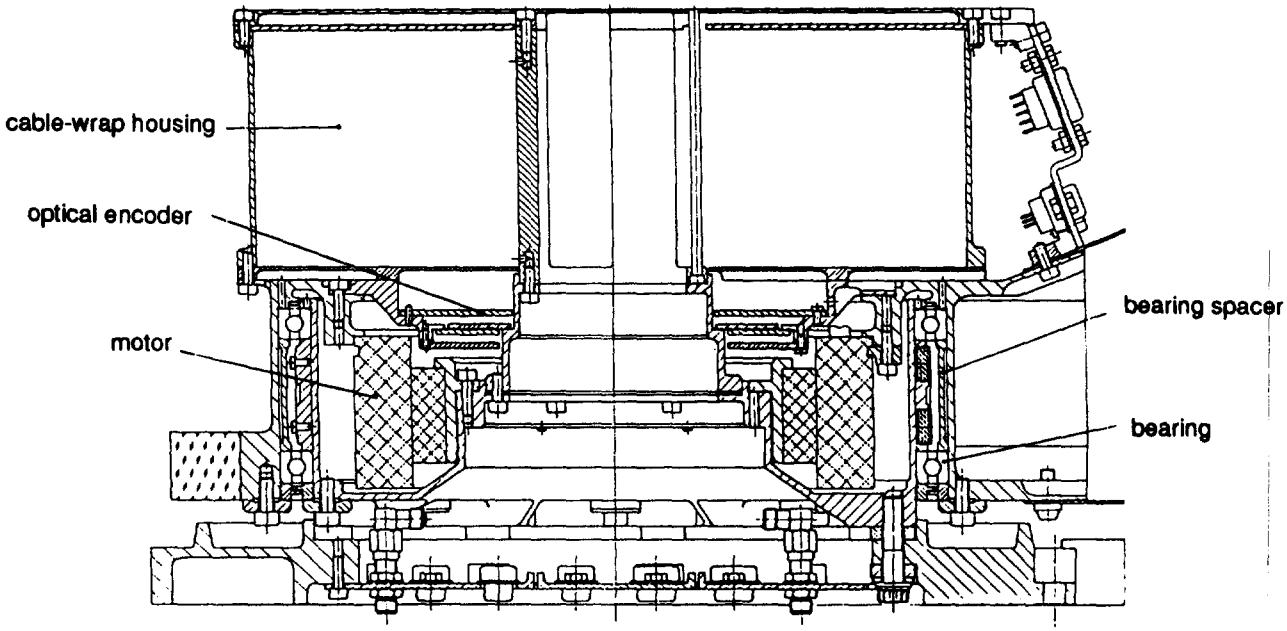

Figure 3. CPMA cross-section

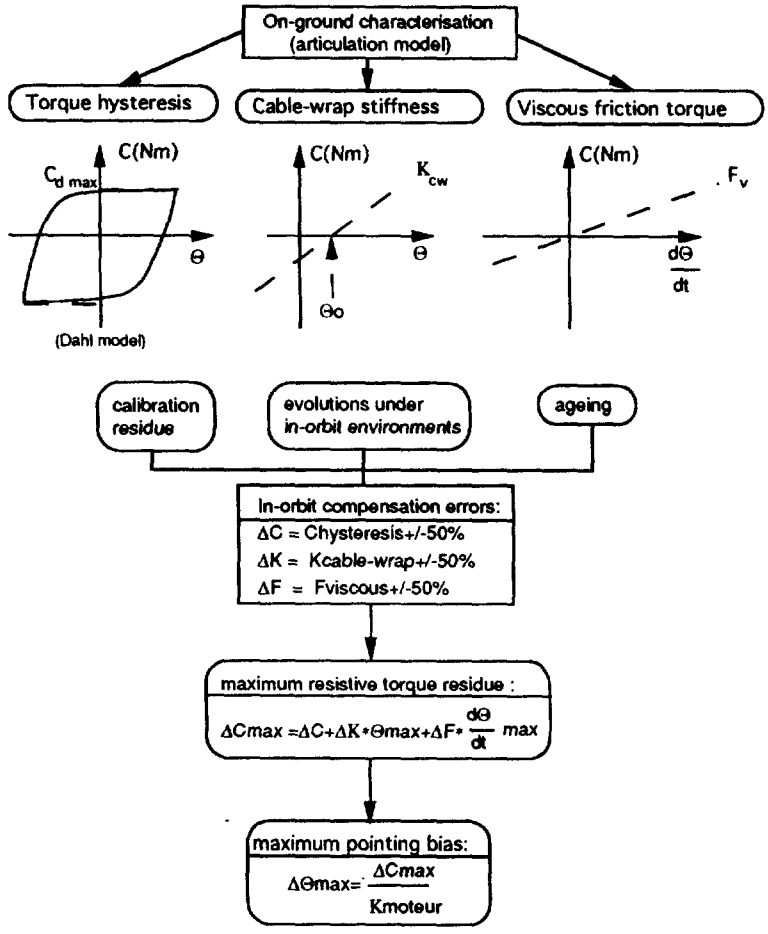

Figure 4. Estimation of maximum in-orbit pointing bias (one axis)

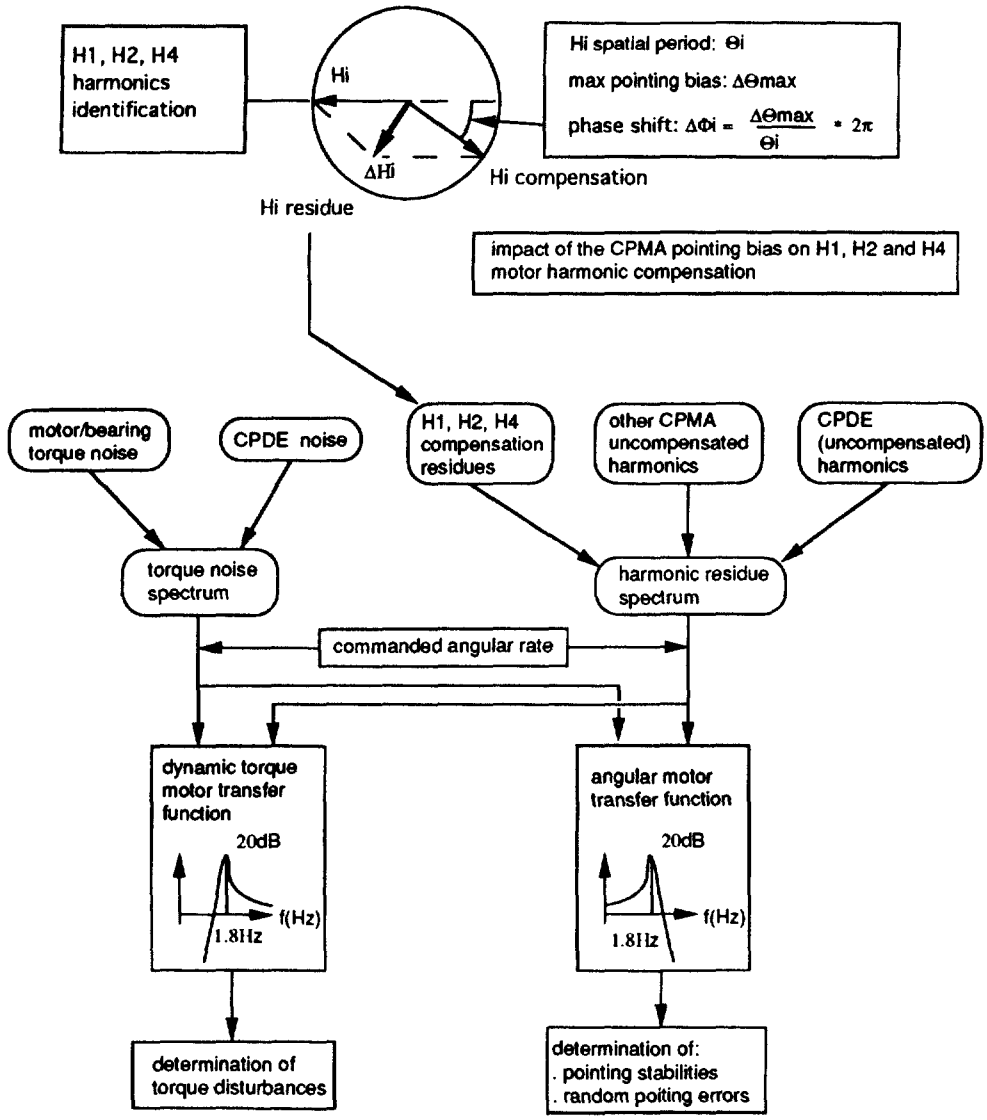

Figure 5. Torque harmonics and torque noise impacts on dynamic performances (one-axis)

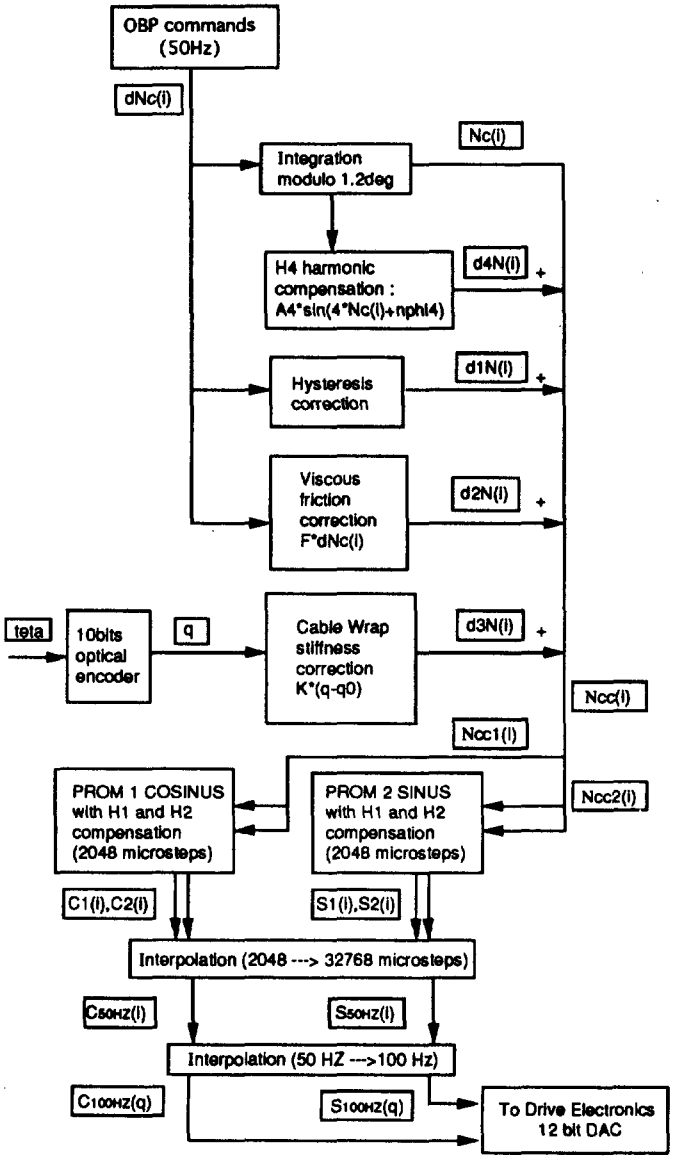

Figure 6. Compensation architecture

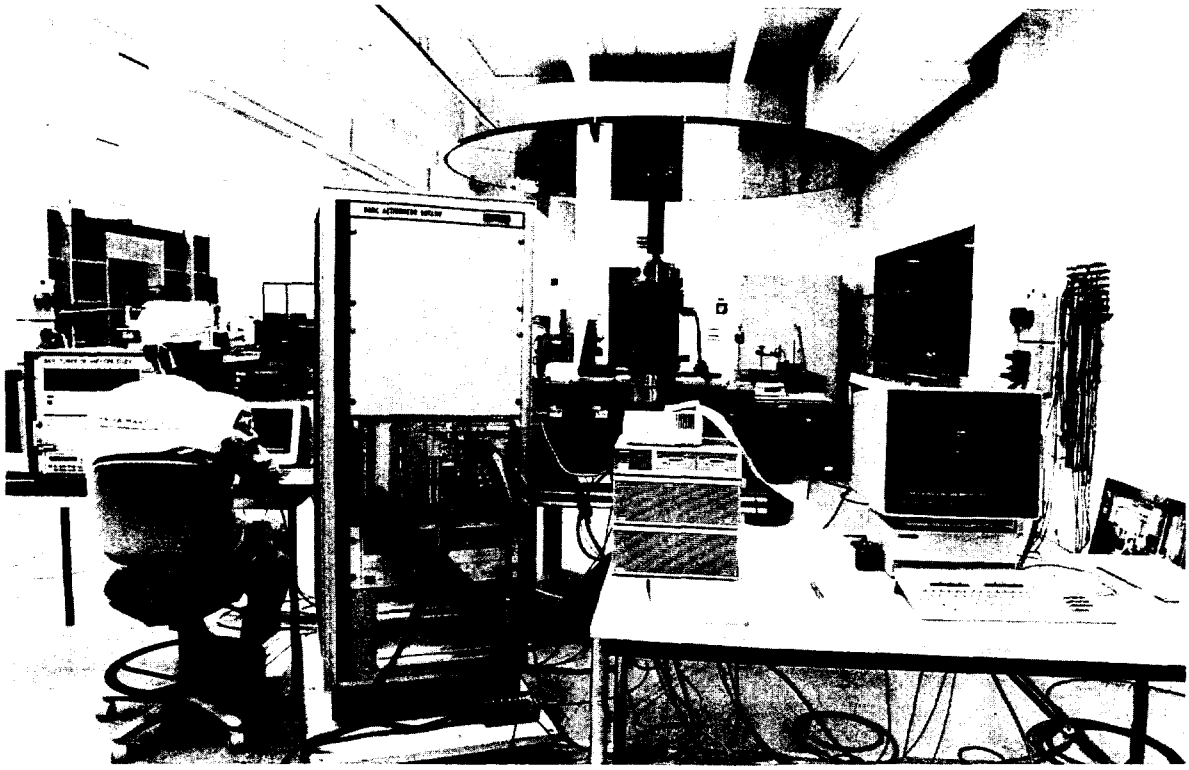

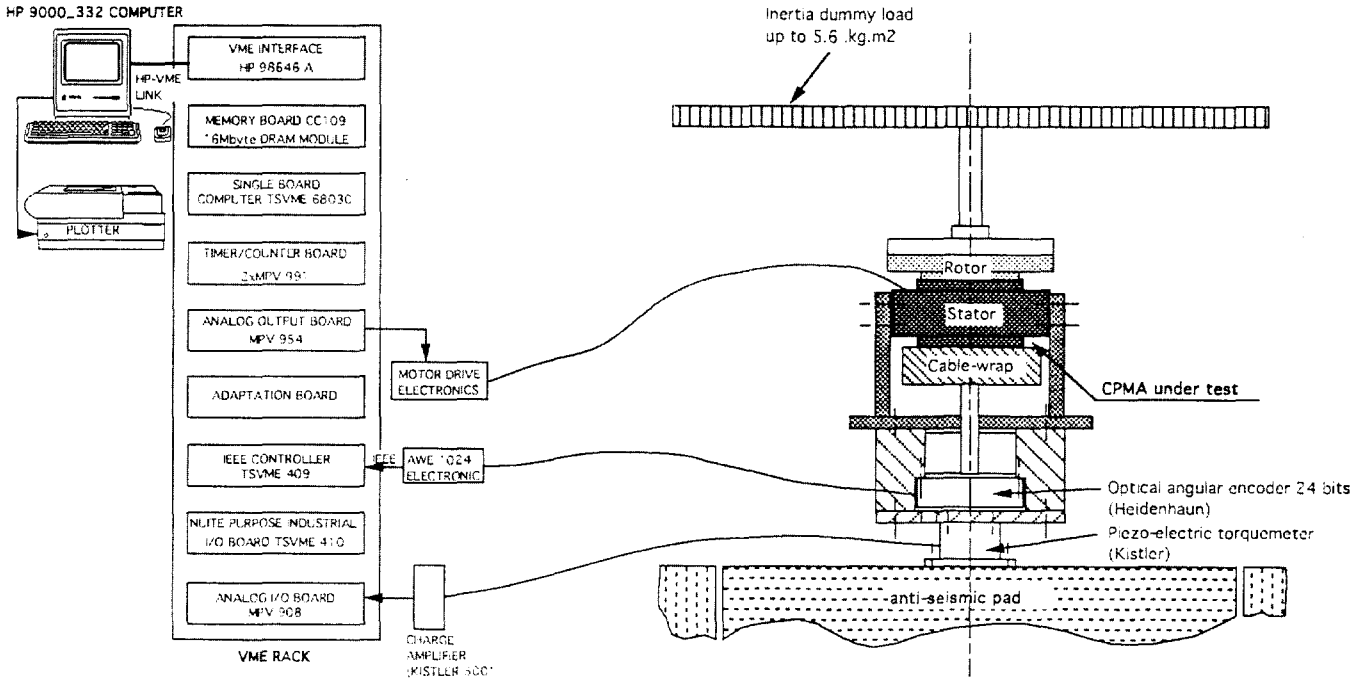

Figure 7. CPMA Test bench

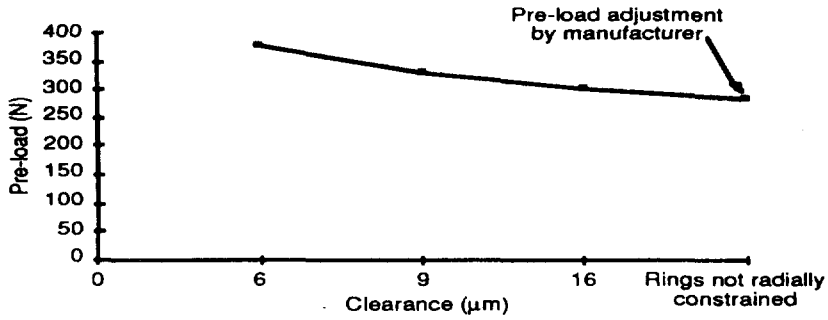

Figure 8. Bearing pre-load vs outer-ring/housing clearance (measured)

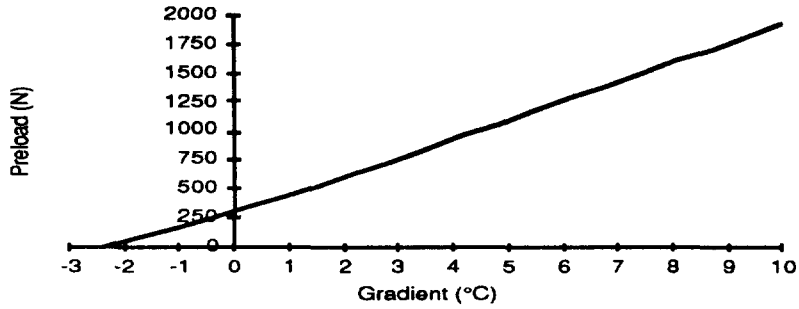

Figure 9. Bearing pre-load vs temperature gradient (calculated)

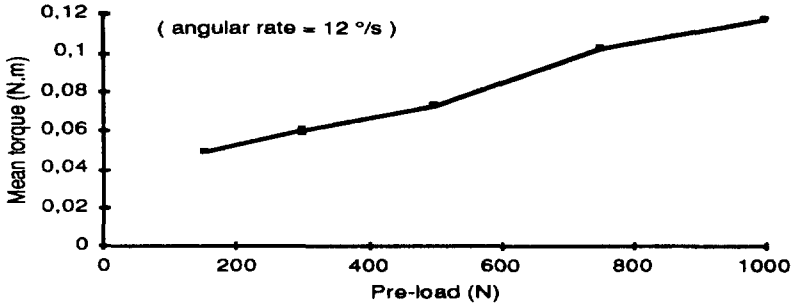

Figure 10. Bearing mean torque vs pre-load (measured)

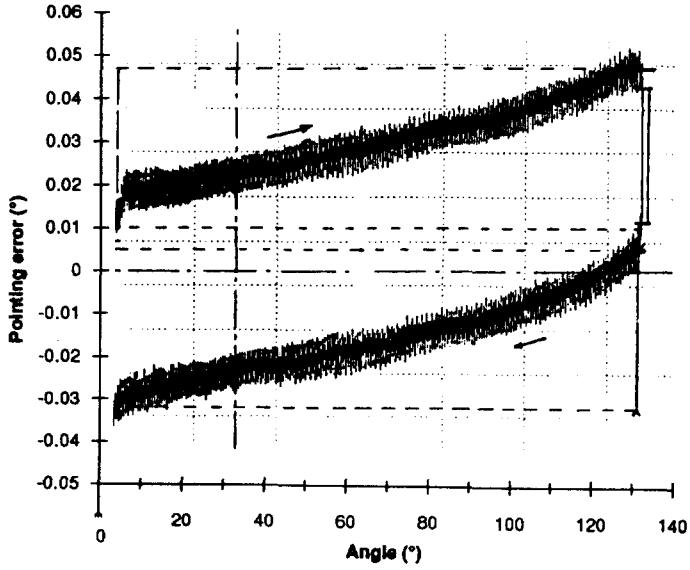

Figure 11. Typical CPMA pointing error hysteresis

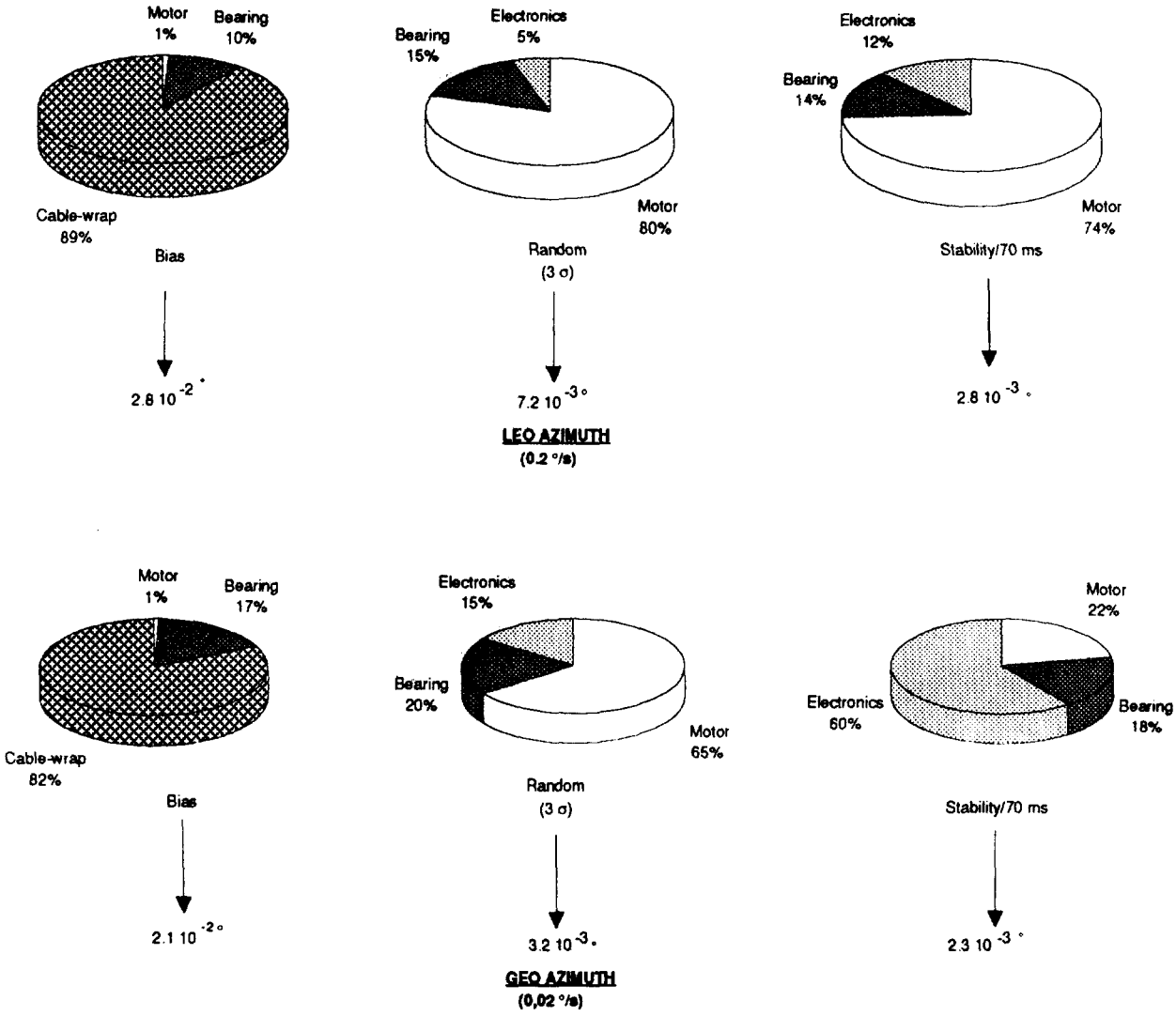

Figure 12. One axis worst-case pointing performances with contributors identification

	LEO (0,2 °/s)	GEO (0,02 °/s)
Bias	$3{,}2\ 10^{-2}$ °	$2{,}8\ 10^{-2}$ °
Random (3 σ)	$8{,}0\ 10^{-3}$ °	$4{,}0\ 10^{-3}$ °

Figure 13. Two-axis worst-case pointing performances

A COMPARISON OF THE PERFORMANCE OF SOLID AND LIQUID LUBRICANTS IN OSCILLATING SPACECRAFT BALL BEARINGS

Steve
S. Gill
European Space Tribology Lab
AEA Technology
Risley, Warrington, United Kingdom

ABSTRACT

The European Space Tribology Laboratory (ESTL) has been engaged in a programme to compare the performance of oscillating ball bearings when lubricated by a number of space lubricants, both liquid and solid. The results have shown that mean torque levels are increased by up to a factor of five above the normal running torque, and that often torque peaks of even greater magnitudes are present at the ends of travel. It is believed that these effects are caused by a build-up of compacted debris in the contact zone, thus reducing the ball/race conformity ratio.

INTRODUCTION

The increasing use of scanner systems on earth observation spacecraft demands reliable and predictable behaviour from oscillating ball bearings. ESTL is increasingly being asked about this aspect of bearing behaviour, both when utilising dry lubrication techniques and liquid lubricants. This paper describes tests performed by ESTL to provide baseline data for comparing these different lubrication techniques. In order to perform this testwork, ESTL has designed and built an in-vacuo test facility which oscillates three pairs of preloaded bearings simultaneously

ESTL TEST FACILITY

A schematic diagram of the rig is shown in Figure 1. The rig incorporates three test stations, allowing different angles of oscillation to be tested concurrently. The test bearings (1) are mounted in a housing at the lower end of the rig. They are preloaded by a pair of belleville washers (2), and the stationary inner shaft is held by the shaft of a Teldix DG1.3 inductive torque transducer (3). The torque transducer is supported by a thin sheet of shim, to allow for small misalignments whilst ensuring torsional rigidity.

The oscillatory motion is induced by a stepper motor (4). Two of the test stations have 25,000 step per revolution microstepping motors fitted, whilst the third has a 400 step per revolution motor. Control is open loop, and the required motion profiles are generated by a PC based indexer control board. The adequacy of the open loop system has been subsequently proved by the post test bearing inspections. The system is very flexible, and relatively easy to programme.

The oscillatory motion is transmitted into the chamber via ferrofluidic rotary feedthroughs (5). The test bearing outer housing is fastened to one end of a main support shaft which has its own housing and bearing system (6). The support bearings were lubricated with KG80 oil. Two high torsional stiffness bellows couplings are used to cater for small misalignments.

MATERIAL COMBINATIONS

To date eight different lubricant/cage combinations have been tested as shown below in Table 1.

TABLE 1

Table of Lubricant/Cage Combinations Tested

	Lubricant	Cage Type
i)	Sputter Coated MoS_2	Duroid 5813
ii)	Ion Plated Lead	Lead Bronze
iii)	Race uncoated	Duroid 5813
iv)	"	Vespel SP3
v)	"	Salox M
vi)	Fomblin Z25	Phenolic
vii)	Braycote 601	Phenolic
viii)	Pennzane SHFX2000	Phenolic

For the coated bearings (i-ii), 0.2-0.5 μm of lubricant film was applied to each race, and in addition the MoS_2 coating was also applied to the balls. For the wet lubricated bearings (vi-viii), the phenolic cages were vacuum impregnated with oil prior to fitting (using Fomblin Z25 in the case of the grease, vii).

TESTED MOTION PROFILE

For each of the cage material and lubricant combinations, measurements were taken of the torque behaviour for a pair of angular contact bearings oscillating over three different angles:

± 0.5° before equilibrium rolling is fully established.

± 5° corresponding to limited rolling.

± 20° large amplitude rolling, but insufficient to cause cage to race material transfer.

Tests were performed over ten million surface passes (2 passes per complete oscillation) under a vacuum of 10^{-5} torr or better. The testing was performed at fairly high rotational speed, which was reduced by a factor of 4 when making torque measurements. This was necessary due to rig torsional natural frequency effects, caused by the relatively low stiffness of the transducer, swamping the real torque signals. Even having restricted the speed, in the case of the ± 20° test it was still necessary for the signal to be electronically low-pass filtered, although this was shown to have no effect on the DC measured levels.

The speed motion profile was trapezoidal with a period of constant speed motion. The chosen motion profile parameters are shown below in Table 2. These parameters were chosen such that the elapsed time for testing at each of the three angles of oscillation would be nominally the same.

Table 2

Motion Profile Parameters

Test Station	1	2	3
Distance	0.99	9.99	40.5 degrees
During Measurements:			
Velocity	0.01	0.1	0.41 revs/sec
Acceleration	0.108	1.08	4.41 revs/sec^2
During Running:			
Velocity	0.04	0.4	1.64 revs/sec
Acceleration	1.337	13.37	54.5 revs/sec^2

The tests were performed at a nominal preload of 60-70 N; unfortunately however, a load-setting problem led to the tests with Duroid cages alone (iii) being performed at higher preloads (100-150 N). All bearings were subjected to a limited run-in prior to testing, with the exception of those coated with MoS_2 (i). These bearings were not run-in in order that there should be no transfer of PTFE from the cages to the races prior to starting the test.

On completion of the tests, the bearings were disassembled and examined optically. Selected components were also examined by scanning electron microscopy (SEM).

BEARING DETAILS

The test bearings were standard 20mm bore profile (conformity 1.14) ED20 ball bearings to ABEC 7 specification manufactured from 52100 steel by SNFA. Further details are shown in Table 3:-

Table 3

ED20 Bearing Size Parameters

Outer Diameter	42 mm
Inner Diameter	20 mm
Bearing Width	12 mm
Ball Size	7.14 mm
Ball Complement	10
Contact Angle	15°

THEORETICAL PERFORMANCE

A number of calculations based on the geometry of the bearings under test can be performed in order to give an idea of the expected torque performance behaviour and the likely scar dimensions. Firstly, for a ball bearing the ball spin frequency per rotation is given by the following equation:-

$$F = [P/(2B)] \times [1-(B/P)^2 \times \cos^2 A]$$

where F = Ball Spin Frequency
P = Pitch Diameter
B = Ball Diameter
A = Contact Angle

Assuming a ball pitch diameter of 31mm and taking other data from Table 3, the ball spin frequency is 2.06 revs per revolution of the bearing.

For a dry lubrication system relying on lubricant replenishment from the cage, then the theoretically required angle of oscillation will be ± 21.8° before the balls will perform the 90° rotation required for cage material transfer to the raceways.

The lengths of the expected wear scars on the races for the three angles of oscillation tested can also be generated from this ball spin frequency assuming that there is no slip at the ball to race interfaces. The scar length will be given by the following equation:-

$$L = \text{Angle} / 360 \times F \times \pi \times B$$

and the results are tabulated in Table 4:-

Table 4

Scar Length Predictions for Tested Bearings

Oscillation deg	Angle deg	Scar Length mm
± 0.5	1	0.13
± 5	10	1.29
± 20	40	5.14

It is also possible to calculate the expected torque performance and the contact stresses of the test bearings. Calculations have been performed using BAPTISM, the ESTL in-house coding, which has been verified against the results of many bearing tests over the years since its conception. The torques calculated by BAPTISM are those expected for bearings under continuous rotation due to the Coulombic torque contribution.

Table 5 shows the BAPTISM-calculated torque predictions for a pair of ED20 bearings, which is the configuration used in these tests. The table shows the effect on the expected running torque both by increasing the preload and also by reducing the number of balls in contact. The friction level

of 0.15 was used as a typical value for lead lubricated bearings (ii).

Table 5

Coulombic Torque Predictions

Preload N	Balls	Friction Coeff.	Torque Nm x 10^{-4}	Mean Hertzian Contact Stress MPa
65	10	0.15	20	679
150	10	0.15	60	890
65	5	0.15	25	850
65	3	0.15	30	1001
65	10	0.2	25	679
65	10	0.05	10	679
65	10	0.5	60	679

In addition the effects of changing friction levels on the bearings can also be ascertained. The value of 0.05 is about the lowest to be reasonably expected and represents a typical value for MoS_2 lubricated bearings (i), whereas 0.2 is the average value for Duroid lubrication alone (iii) and represents the highest expected figure. The Hertzian contact stress figures quoted for each load case are the mean contact stress on the inner race. The Hertzian contact ellipse will be of major axis 0.22mm and minor axis 0.06mm for the standard 65N preloaded pair with ten balls in contact. BAPTISM also predicts that the full rolling torque will not be attained until the angle of oscillation is greater than about ± 2°

As a further exercise BAPTISM has been used to generate a curve of torque versus the conformity ratio of the bearing (raceway diameter ÷ ball diameter) for the nominal test conditions, and this data is shown in Figure 2. It can be seen that this ratio causes a dramatic increase in the expected torque levels as it is reduced.

TEST RESULTS

The material combinations will be split into three groupings to allow the data to be presented in a comparable manner : the dry coated bearings (i-ii); the cage dry-lubricated only bearings (iii-v); and the wet lubricated bearings (vi-viii). Torque levels quoted throughout are those

measured for a pair of bearings and are either zero-to-mean or zero-to-peak as quoted. The values have been taken as spot readings at regular intervals on a digital storage oscilloscope, with a hard copy produced on a plotter.

Figures 3-5 relate to the results taken from the sets of bearings oscillated through ±0.5°. These bearings all gave similar outputs which resembled a sine-wave. The coated bearings (i,ii) performed with lower torques than the cage lubricated bearings (iii-v), although the MoS_2 coated bearings had reached torque levels of 100 × 10^{-4} Nm by the end of the tested 10^7 oscillatory passes. The cage dry-lubricated bearings (iii-v) quickly registered torques of 100-130 × 10^{-4} Nm. For the oil lubricated bearings, the Fomblin Z25 (vi) showed a rapid increase to 100 × 10^{-4} Nm before settling back to 80 × 10^{-4} Nm, whereas the Pennzane lubricated bearings (viii) only showed a gradual increase from 20 up to 40 × 10^{-4} Nm over the duration of the test. The Braycote 601 grease lubricated bearings (vii) showed a rapid increase over the first million passes to around 60 × 10^{-4} Nm and then stayed stable for the rest of the test.

The bearings tested at ±5° and ±20° displayed a different torque behaviour, in that they exhibited a square wave profile on start-up which in many cases was modified by a peak on reversal which grew in size during the test. For this reason graphs relating to these angles of oscillation show both a zero-to-mean value for the running zone and a zero-to-peak value relating to the reversal point.

Figures 6-8 relate to the test results taken from the bearings oscillated through ±5°. The MoS_2 coated bearings (i) performed better than the lead (ii) in this instance. The lead mean level increased to 150-200 × 10^{-4} Nm over the first 3 million passes, whilst the MoS_2 mean level remained low at 20 × 10^{-4} Nm throughout. Both types suffered a reversal peak torque, 300-400 × 10^{-4} Nm for the lead and 100 × 10^{-4} Nm for the MoS_2 by the end of the test. Turning to the cage lubricated bearings (iii-v), the torque of the Duroid caged bearings rapidly rose to 200 × 10^{-4} Nm and continued to increase to 600 × 10^{-4} Nm by 6 million oscillatory passes. At the same time a reversal peak level of 1200 × 10^{-4} Nm was attained and so the test was stopped to protect the torque transducer. The torque of the Vespel caged bearings (iv) also rose quickly to a mean level of 200 × 10^{-4} Nm for the duration of the test. The peak level on reversal reached a maximum value of nearly 600 × 10^{-4} Nm at 3 million oscillatory passes, but in this case fell back to 300 × 10^{-4} Nm by the end of the test. The Salox M caged

bearings (v) performed the best in this category and held a mean torque level of 20 × 10^{-4} Nm with a peak of 50-60 × 10^{-4} Nm after an initial short stabilising period. The wet lubricants (vi-viii) performed in a very similar manner throughout this test, with mean torque levels around 20 × 10^{-4} Nm and peak torque levels up to 40 × 10^{-4} Nm.

Figures 9-11 relate to the test results taken from the bearings oscillated through ±20°. The MoS_2 and lead coated bearings (i-ii) performed similarly for over half of the test duration, although the lead bearings were noisier on reversal and ran at higher mean torque levels. By the end of the test however, starting at around 7 million oscillatory passes, the mean torque levels for both types had risen to 100 × 10^{-4} Nm, with peak levels on reversal as high as 200 × 10^{-4} Nm for the lead. The cage dry-lubricated bearings (iii-v) showed no major variations after the initial settling period. The Salox M (v) caged bearings again performed the best of the trio with mean levels of around 50 × 10^{-4} Nm compared with 100 × 10^{-4} Nm for the Vespel (iv) and 150 × 10^{-4} Nm for the Duroid (iii). Again the wet lubricants (vi-viii) performed in a very similar manner throughout this test, with mean torque levels around 15-20 × 10^{-4} Nm and peak torque levels up to 30 × 10^{-4} Nm for the Braycote grease and Pennzane oil (vii,viii). The Fomblin Z25 (vi) recorded higher mean levels, 30 × 10^{-4} Nm, with peak torque levels up to 60 × 10^{-4} Nm during the second half of the test.

POST TEST INSPECTION & DISCUSSION

Inspection of the bearing condition post testing has revealed very obvious contact zones in most cases, especially in the case of the dry lubricants (i-v), which are of sizes in agreement with the predictions in Table 4. In the case of the coated bearings (i,ii) the motion has worn a groove into the lubricant with a build up of debris around the edge. In the case of the cage dry-lubricated bearings (iii-v) compacted zones of material have been generated on the bearing surface during the motion. These details have been confirmed by a small number of Talyrond measurements, and also by removing the debris in the latter case. The wet lubricated bearings also show obvious contact zones of sizes similar to those in the dry lubricated bearings, however the height of these features has not been measured at this time. However it is not believed that any steel bearing surface material wear has occurred in any of these tests.

In a number of cases balls have more than one pair of corresponding contact zone markings indicating that some balls were not in contact at all times. This observation helps to explain the manner in which material can be transferred from the cage to the ball-race interface despite the fact that theoretically the balls do not rotate over a large enough angle.

Figure 12 shows two of the SEM photographs taken of the contact zones post testing. The upper photograph shows the whole of a ±5° contact zone from the MoS_2 test (i). The debris around the edge of the contact zone can be clearly seen. The lower photograph shows the end of a contact zone from the Salox M cage test (v). The end-of-travel debris is visible in the centre, with the contact zone going to the right. To the left is the running-in transfer film. Similar marks have been visible on all the bearings, although not quite so distinct on the wet lubricated bearings (vi-viii).

By reference to Table 5 it is clear that increases in the friction coefficient or the preload setting, or alternatively a reduction in the number of contacting balls within the bearing cannot induce the high levels of torque which have been recorded in these tests. However, changes in the conformity ratio can produce such dramatic changes, as shown in Figure 2. The Talyrond measurements have confirmed that the build-up of debris on both the raceways and the balls is sufficient to close the gap between ball and race, thus allowing such close conformities to be achieved.

CONCLUSIONS

The measurement of torques in oscillating bearings has revealed levels many times higher than would be expected from continuously rotating bearings. Factors of five on mean torque levels are common, and in addition torque peaks on reversal of even higher magnitude have been recorded. This should be taken into account when calculating mechanism drive torque requirements.

It is obvious from the test results that there is no one ideal lubricant technique to cater for all the angles of oscillation, and ESTL will be continuing to investigate this aspect further in the future. It has been shown that it is difficult to explain the torque increases seen in oscillating bearings purely by a change in friction or preload levels or by a reduction in the number of balls in contact, and ESTL therefore proposes that the change in conformance at the

contact due to compacted debris build up is the cause of the increased torque levels.

ACKNOWLEDGEMENTS

This programme of work has been sponsored by the European Space Agency.

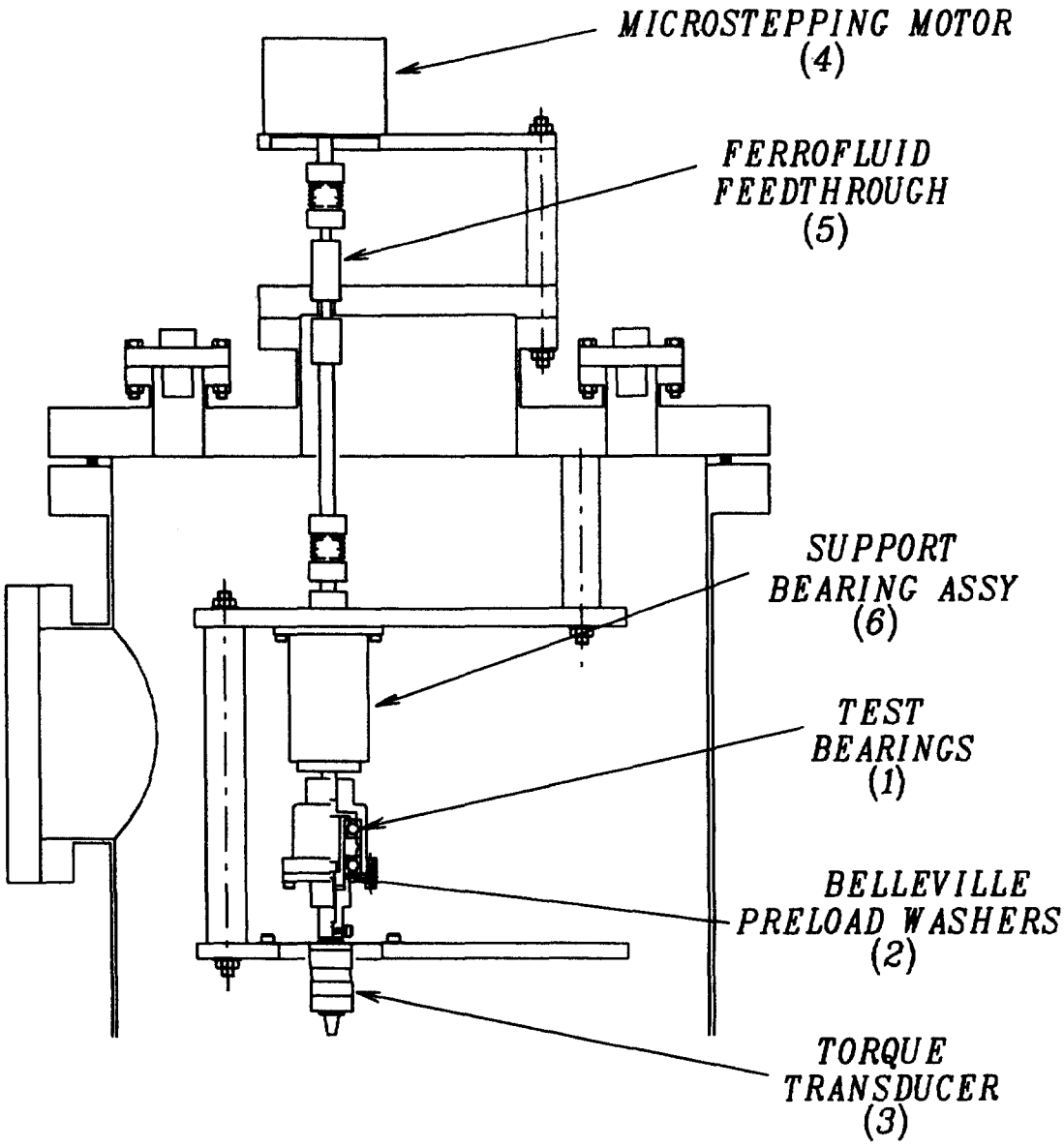

FIGURE 1 OSCILLATING BEARING RIG SCHEMATIC

Figure 2
Calculated Torque versus Conformity for a Pair of Test Bearings

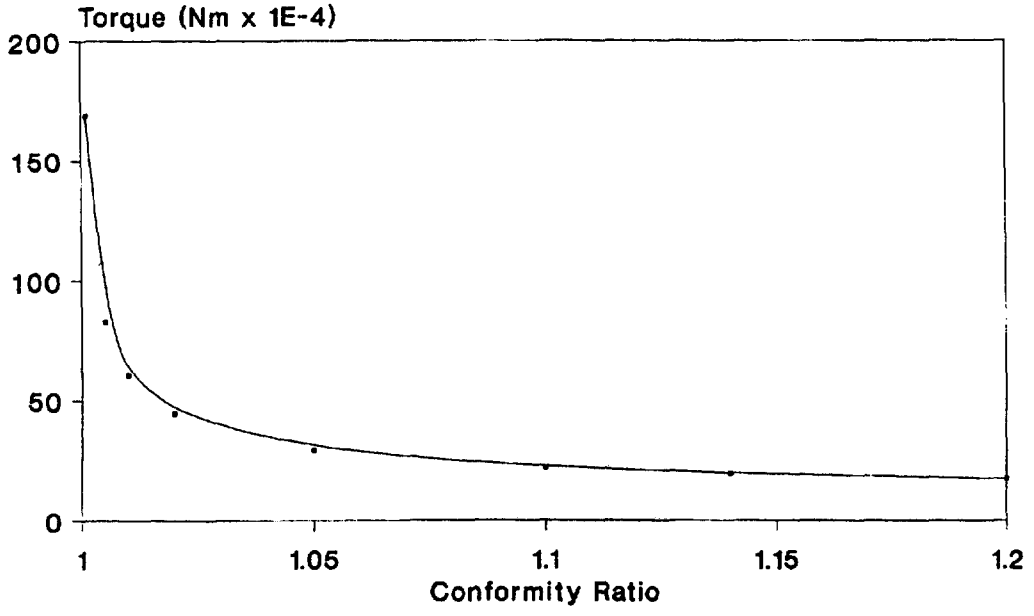

Friction Coefficient 0.15
Preload 65N

Figure 3
Torque versus Number of Oscillations Angle of Oscillation +/- 0.5 degrees

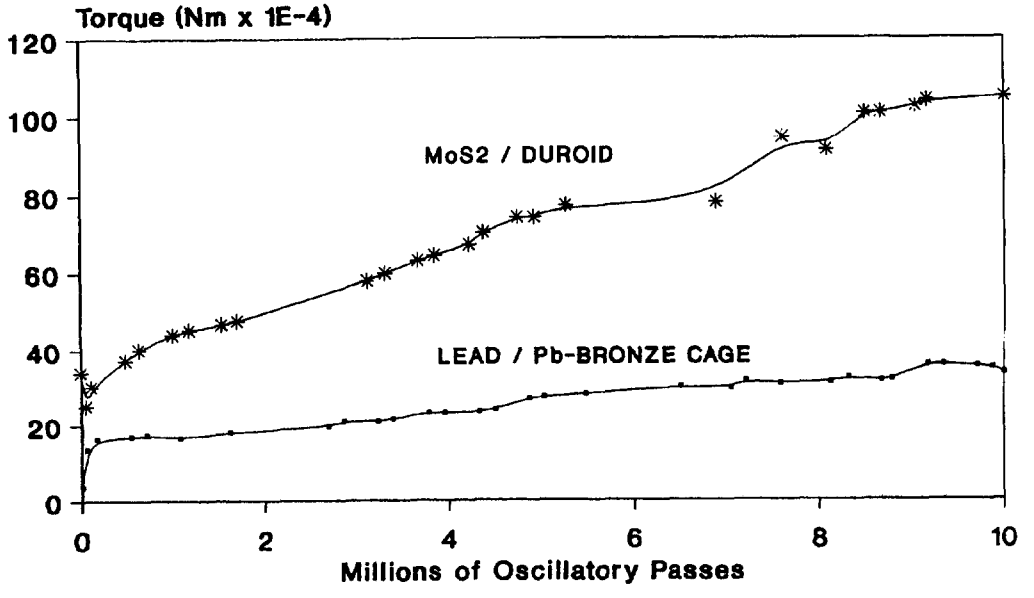

MoS2 with Duroid Cage
Preload 65N

Lead with Lead/Bronze Cage
Preload 68N

Figure 4
Torque versus Number of Oscillations
Angle of Oscillation +/- 0.5 degrees

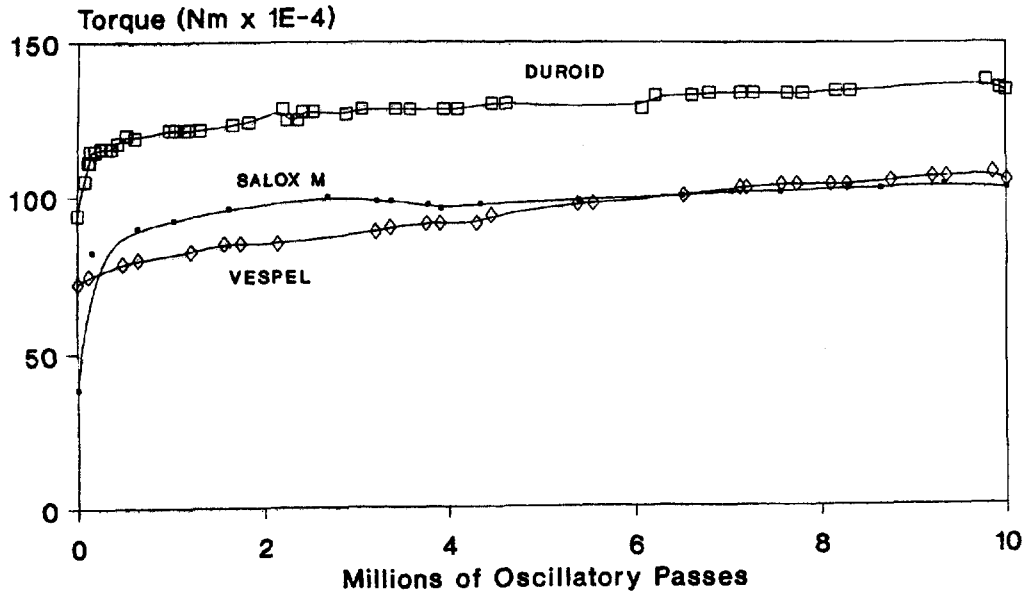

Salox M Cage
Preload 65N

Duroid Cage
Preload 150N

Vespel Cage
Preload 75N

Figure 5
Torque versus Number of Oscillations
Angle of Oscillation +/- 0.5 degrees

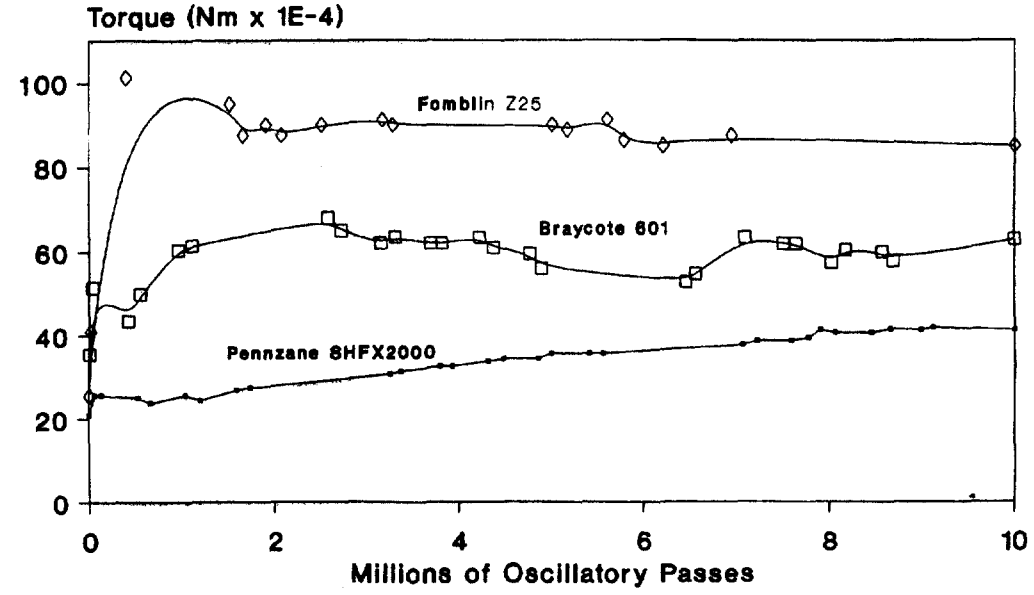

Fomblin Z25
Preload 65N

Braycote 601
Preload 65N

Pennzane SHFX2000
Preload 65N

Figure 6
Torque versus Number of Oscillations
Angle of Oscillation +/- 5 degrees

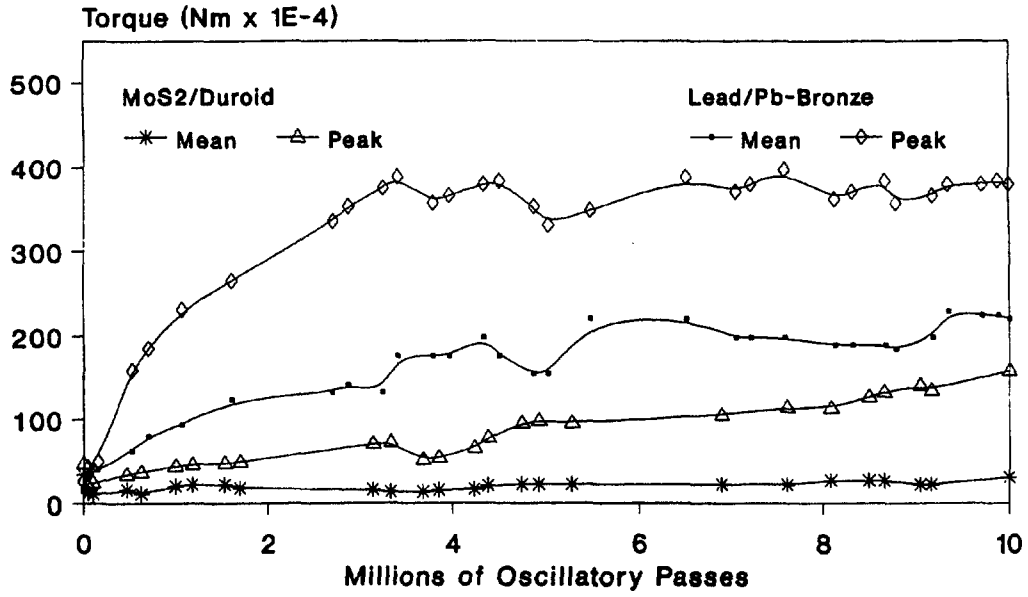

MoS2 with Duroid Cage
Preload 68N

Lead with Lead/Bronze Cage
Preload 62N

Figure 7
Torque versus Number of Oscillations
Angle of Oscillation +/- 5 degrees

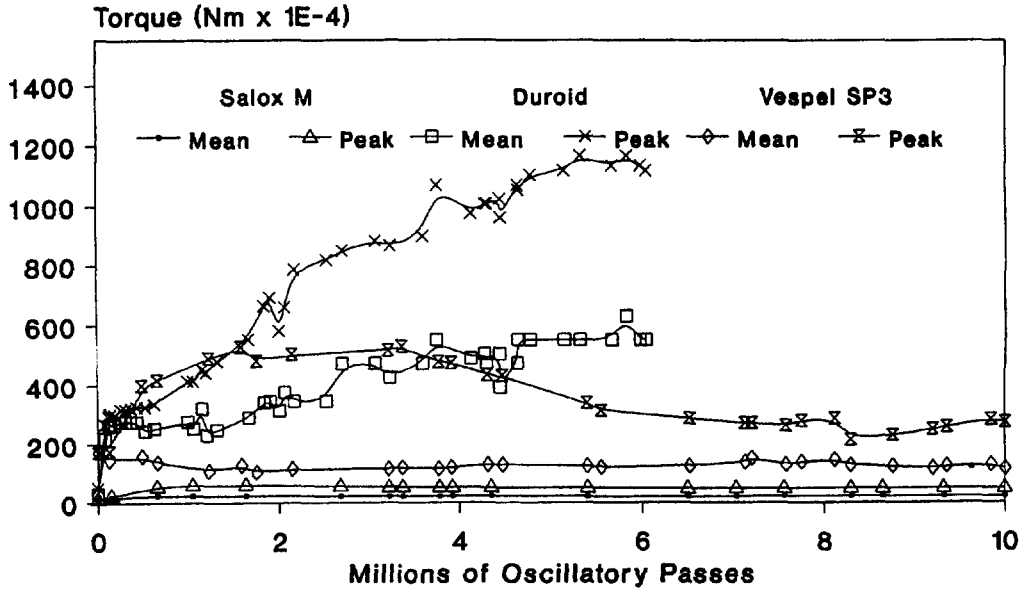

Salox M Cage
Preload 66N

Duroid Cage
Preload 132N

Vespel Cage
Preload 66N

Figure 8
Torque versus Number of Oscillations
Angle of Oscillation +/- 5 degrees

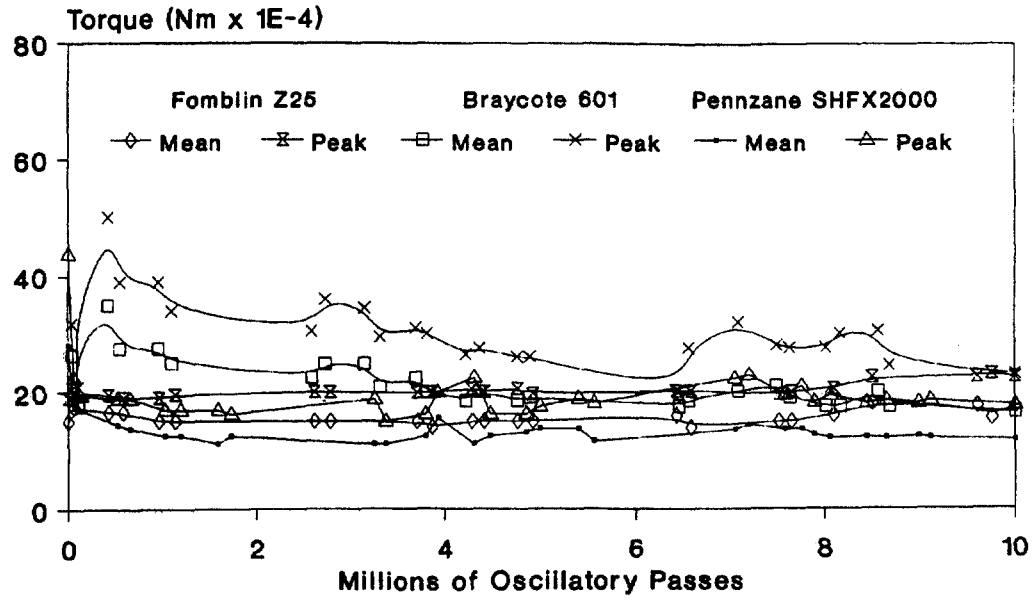

Fomblin Z25
Preload 65N

Braycote 601
Preload 60N

Pennzane SHFX2000
Preload 64N

Figure 9
Torque versus Number of Oscillations
Angle of Oscillation +/- 20 degrees

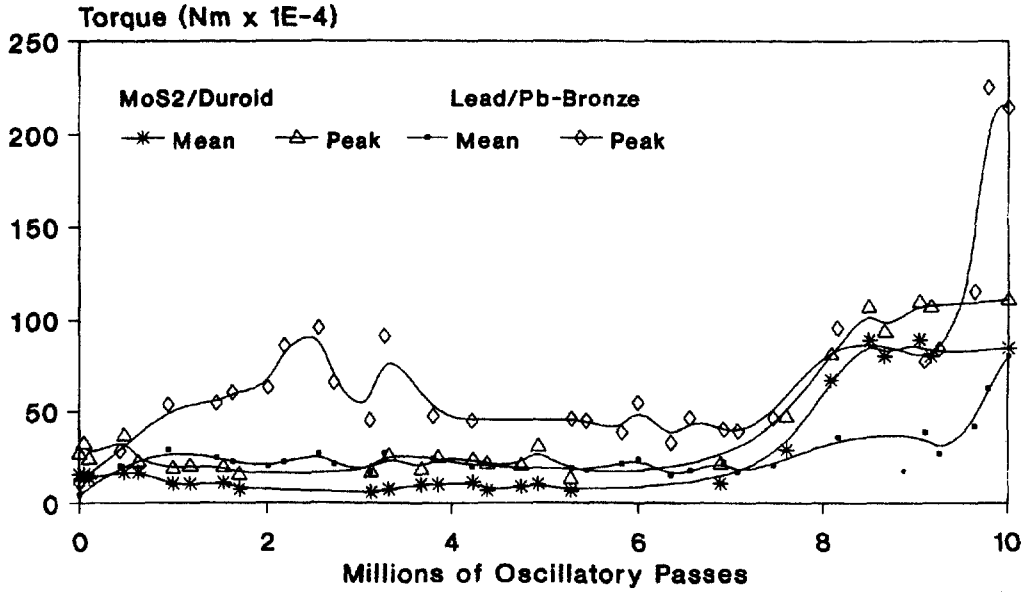

MoS2 with Duroid Cage
Preload 70N

Lead with Lead/Bronze Cage
Preload 75N

Figure 10
Torque versus Number of Oscillations
Angle of Oscillation +/- 20 degrees

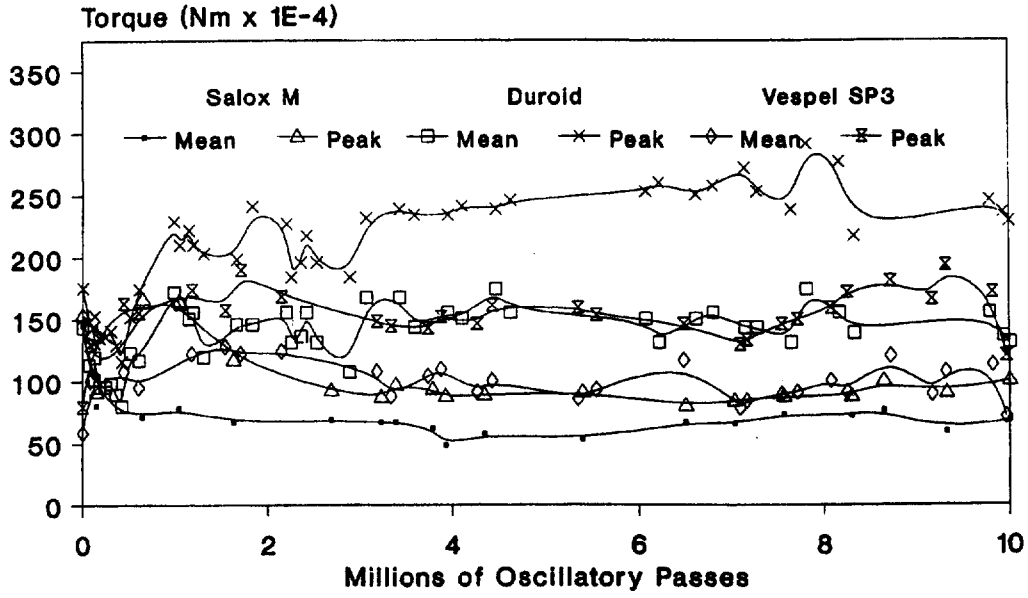

Salox M Cage
Preload 66N

Duroid Cage
Preload 94N

Vespel Cage
Preload 66N

Figure 11
Torque versus Number of Oscillations
Angle of Oscillation +/- 20 degrees

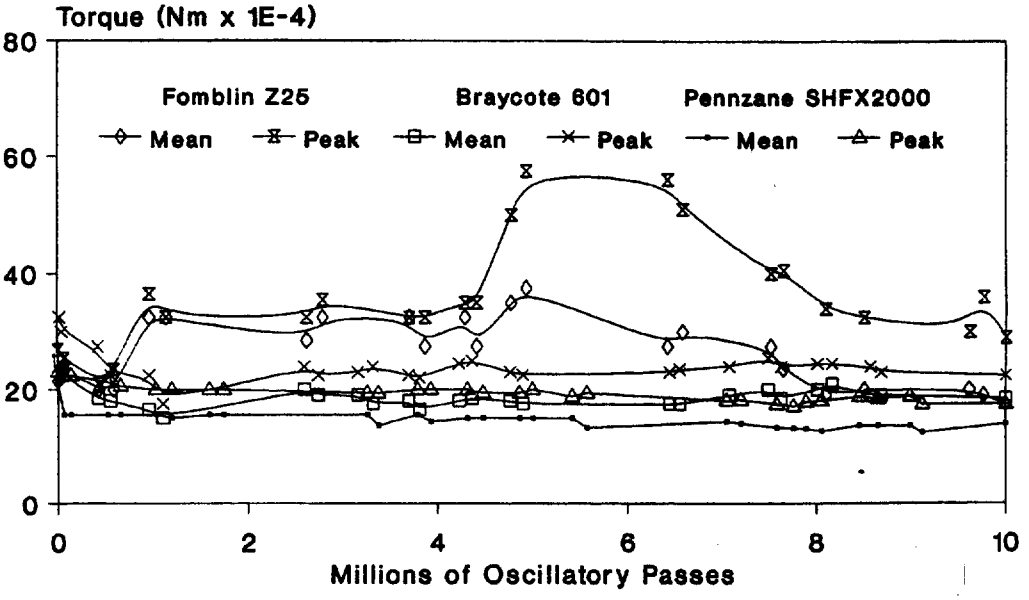

Fomblin Z25
Preload 66N

Braycote 601
Preload 60N

Pennzane SHFX2000
Preload 63N

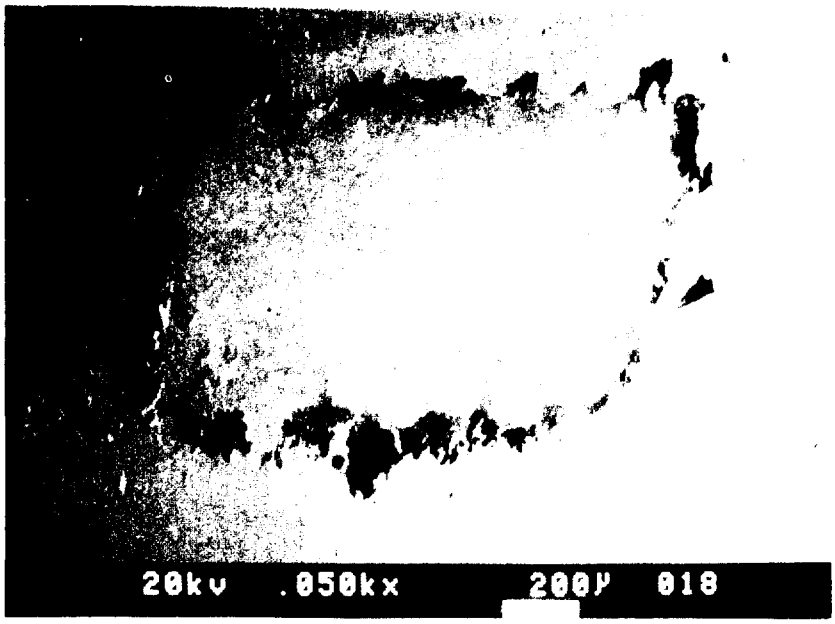

MoS_2 Lubrication (i), ±5° Test
Secondary electron image of inner race contact zone

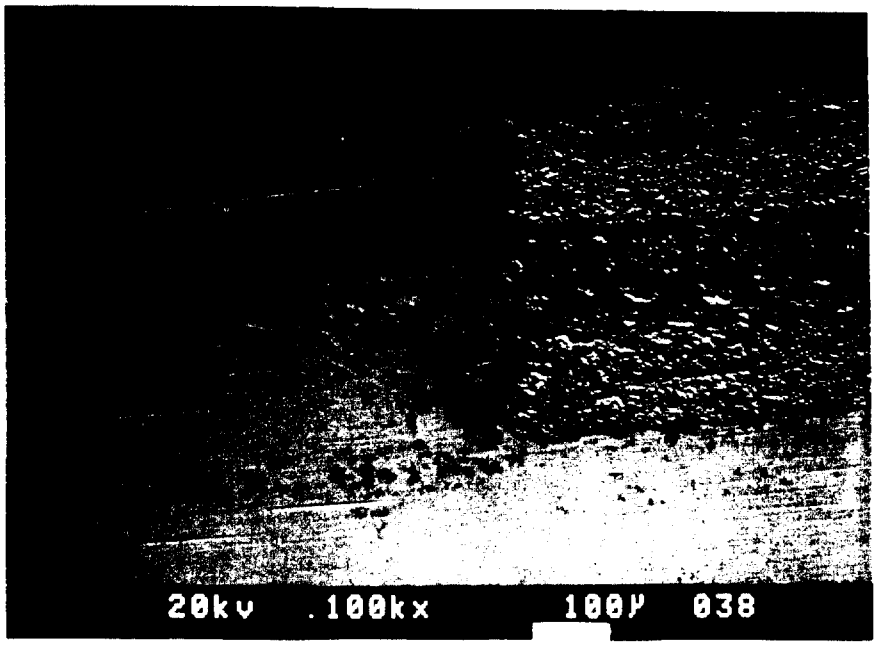

Salox M Lubrication (v), ±20° Test
Backscattered electron image of inner race contact zone

Figure 12 SEM Photographs of Contact Zones Post Testing

DEVELOPMENT OF LONG-LIFE, LOW-NOISE LINEAR BEARINGS FOR ATMOSPHERIC INTERFEROMETRY

E.W. Roberts, R.B. Watters, and S. Gill
European Space Tribology Laboratory
AEA Technology
Risley, Warrington, United Kingdom

and

R. Birner, G. Lange, and W. Posselt
Deustche Aerospace AG
Ottobrun, Germany

ABSTRACT

This paper describes the development of dry-lubricated linear bearings for use on the Michelson Interferometer for Passive Atmospheric Sounding (MIPAS). Two candidate bearing systems were developed and tested. In the first, use was made of linear roller (needle) bearings equipped with a pulley-and-cable arrangement to prevent cage drift and to minimise roller slip. The second design was of a roller-guided bearing system in which guidance was provided by ball bearings rolling along guide rods.

The paper focuses on the development of these linear bearing systems and describes the approach taken in terms of bearing design, lubrication methods, screening programmes and thermal-vacuum testing. Development difficulties are highlighted and the solutions ultimately adopted are described.

INTRODUCTION

The Michelson Interferometer for Passive Atmospheric Sounding (MIPAS) is an ESA-developed instrument for use on the first European Polar Platform, ENVISAT-1, which is planned for launch in 1998. The design calls for very high precision linear bearings for the two interferometer slides. These slides carry corner cube reflectors which describe a back-and-forth motion, this motion being in countermovement so as to cancel disturbing forces. The bearings should be capable of maintaining a low-noise performance whilst operating continuously at low temperature (-70 deg.C) over four years.

The requirement to operate at low temperature and the need for zero contamination of the optical components, precludes oil lubrication. However, the requirements of long duty and low frictional noise combine so to push the capability of solid lubrication systems to their limits. The work reported here is principally concerned with assessing the ability of MoS_2-based solid lubricants to meet these system requirements.

Accelerated life tests were undertaken on two candidate bearing systems. The first comprised a pair of linear roller (needle) bearings lubricated with sputter deposited molybdenum disulphide. The second test was carried out on a roller guide system which utilised conventional rotary ball bearings loaded against two parallel rods. This system was also lubricated with sputtered MoS_2.

Additionally, supplementary tests were carried out - simultaneously with the life tests - with the aim of assessing alternative lubricants and material combinations.

MECHANISM REQUIREMENTS

The task of the bearings is to carry and guide a corner cube slide of mass 1.7kg over a stroke of 110mm. The nominal cycling motion requires a trapezoidal speed versus time profile. The absolute speed of the corner cubes is 25 mm/sec and must be controlled to achieve a relative velocity (w.r.t the speed of the second slide) error of < 1.2% (3σ).

The main requirements, crucial to the successful performance of the instrument, are:

- low and stable friction, so as to maintain a drive force of <1N

- linear motion over 110mm with a velocity of 25mm/sec

- long lifetime: four years life on-orbit under continuous operation (9 secs per cycle)

- operation at -70 deg.C

- low vibration and play (< 10 μm)

- no release of contamination

DEVELOPMENT OF THE TWO CANDIDATE BEARING SYSTEMS

a) Design 1: linear roller bearing guided slide

Initial screening tests on candidate linear bearings

In order to select the most suitable type of linear bearing for this design, screening tests were undertaken at the start of the programme on four types of linear bearing. The bearing types and their specifications are given in Table 1. The types examined were a slide bearing; a roller bearing; and two types of ball bearing. In each case, lubrication was provided by applying a 1-micron thick coating of magnetron sputtered MoS_2 (according to ESTL procedure ESTL/QP/073) to the races. Bearings were tested in pairs and operated until completion of 370,000 cycles at a stroke length of 90 mm. The tests were undertaken under high vacuum at a temperature of -50 deg.C, the drive force being monitored throughout the test period.

Table 1 Types of linear bearing assessed in screening tests

MAKE	TYPE	SPECIFICATION	COATINGS	CAGE	SCHEMATIC
Schneeberger	Ball	R9200 R9150 AK 9 x 6 Balls: 6mm diam	Sputtered MoS2 on balls & races	MoS2-coated steel	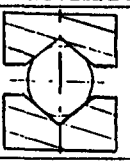
Hydrel	Roller	ML 5020/15Lx200 M 4020/x200 V 4020/15x150 MW 15 x 83.5	Sputtered MoS2 on raceways	PTFE-coated	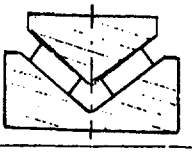
Hydrel	Ball	ML 5020/15Lx200 M 4020/ x200 V 4020/15 x150 MBW 2X15X83.5 Balls: 2mm diam	Sputtered MoS2 on raceways. Ball: TiC-coated	PTFE-coated	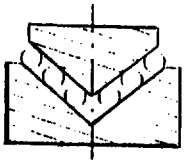
Hydrel	Slide	ML 5020/15Lx200 M 4020/ x200 V 4020/15 x 100	Sputtered MoS2 on raceways: Precoated with Me-CH	No cage	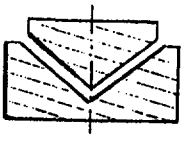

A major finding of these screening tests was that those bearings which utilised rolling elements (ie. all the bearings except the slide bearing) were adversely affected by creep of the rolling elements and cages. In all cases this led to high force spikes at one or both ends of travel. These high forces were generated as the cages were driven into contact with the bearing end-stops at which point any further movement of the non-stationary races resulted in sliding motion between races and rolling elements. In addition to causing higher friction forces this effect also resulted in more rapid wear of the MoS_2 film.

The best overall performance was given by the roller bearing which lasted the planned test duration, maintained its low friction and exhibited the squarest drive force profile. Furthermore, theoretical analysis indicated that, under identical operating conditions, frictional losses would be lower in the roller bearing than in the linear ball bearings and the slide bearing. For these reasons it was decided to select the linear roller bearing for accelerated life testing.

Design details

The linear roller bearing guided slide (Fig.1) consisted of 2 sets of Hydrel V- and M-shaped raceways (Fig.2a). The bearings were preloaded by a compliant suspension (achieved using flat springs) of one stationary raceway. This compliant suspension provided a constant preload, insensitive to thermal changes, wear-out and residual misalignment. Preloading was adjustable using four compression springs, housed in special set screws (Fig.2b).

Each bearing (Fig.2a) was fitted with a PTFE-coated (ALTEF coating 40-50μm) aluminium cage of length 165mm, the length of the races being 230mm. Each bearing contained 12 steel rollers (of length 4.5mm and diameter 2mm), with six rollers arranged symmetrically at each end of the cage. The roller groups at each end were separated at a distance greater than the travel of the rollers so as to prevent overlapping of the wear tracks. The bearing races and rollers were lubricated with sputtered MoS_2 (thickness 1 μm).

In order to prevent roller and cage creep, and thus eradicate high end forces, a pulley-guide system was devised which ensured that the cages were driven at half the speed of the linear carriage. This was achieved as follows. Each end of the

cage was fitted with a Vespel SP1 pulley which ran on an MoS_2-coated steel axle. A thin stranded steel cable looped around each pulley and was solidly clamped to the end of the carriage mounted raceway, whilst being flexibly loaded via a spring to the end of the static raceway. A schematic diagram illustrating the principle of the pulley guide system is shown in Fig.2c.

b) Design 2: ball bearing roller guide

A second design of bearing system was devised in which guidance was provided by ball bearings rolling against guide rods. This design was chosen as it was expected to yield inherently low friction and, since no conventional linear bearings were employed, problems associated with cage wandering and its control were eliminated.

The roller guide system is depicted schematically in Figs.3a and 3b. The carriage is supported by radial ball bearings which run on a pair of parallel guide rods (precision ground shafts). The guide rods were manufactured from hardened steel and coated with thin dense chrome (TDC, an Armoloy Technology Coating) prior to being sputter coated with molybdenum disulphide (to ESTL process ESTL/QP/073). The bearings used throughout were of standard 440C material fitted with TiC-coated balls and Duroid (PTFE/MoS_2/glass fibre) cage. The raceways were coated with sputtered MoS_2.

The slide utilised a total of eight ball bearing pairs. Of these, five pairs were used for guiding purposes and the remaining three pairs were used to preload the system. Two sets of triple bearing pairs (spaced 120 degrees apart on the circumference of the guide rod) ran on the upper guide rod. This bearing arrangement is tolerant of misalignment and thermal- or load-induced deflections. Zero play was achieved by means of springs which provided radial preloading of each roller. Each ball bearing pair was axially soft preloaded (by means of wavy washers) - again with the aim of achieving high running precision. The nominal radial preload of the triple bearing set was 3 to 5N. The nominal preload of the lower ball bearing pair was 9 to 15N. This difference in bearing loads was chosen, following calculation of frictional losses, so as to achieve equal friction forces on both the upper and lower guide rod, thus minimising torque disturbances on the slide.

TEST CONDITIONS

Tests on candidate bearings systems

Each bearing system was subjected to oscillatory motion over stroke lengths of up to 110mm. All tests were undertaken in high vacuum (< 10^{-6} torr) at a temperature of -70 deg.C. The tests were accelerated by running the bearings at speeds which were three times higher than their design speed.

In the case of the Hydrel needle bearings, further acceleration of the test was achieved by increasing the bearing preload above its design value. The aim was to accelerate the life by a factor five through increases in load. This was achieved in the following manner. First, the variation of contact stress (per roller) as a function of bearing load was calculated (Fig.4). The nominal design preload for the Hydrel bearing is 10N. This corresponds to a mean contact stress of about 50MPa (Fig.4). Secondly, it is known from empirical data for (angular contact) bearings lubricated with sputtered MoS_2 that the low-torque life is inversely proportional to (contact stress)$^{3.8}$. Using this relationship as a guide we calculated how the MoS_2 life on linear roller bearings would be reduced for values of contact stress in excess of 50MPa. This reduction, which we term the acceleration factor, is plotted in Fig.5. as a function of contact stress and load. It follows from these plots that in order to reduce film life at a bearing load of 10N by factor five, the load should be increased to 23N.

Acceleration of the life test of the ball bearing roller guide system was limited to a threefold increase in slide velocity. Accelerating the life test by other means (such as increasing the radial load between bearings and guide rod) was rejected since it was difficult to predict with confidence the relationship between lifetime and load. However, by accelerating the test using a higher speed (x3) the desired number of cycles could not be achieved on the programme timescale. Nevertheless, this approach gave the option of continuing testing if this was considered appropriate at a later stage.

Initially, tests on the roller guide system were made with a stroke of 100mm. Following completion of 2 x 10^6 cycles it was decided to introduce short stroke cycling into the test so at to (a) increase the total number of cycles that would otherwise be achieved and (b) more accurately simulate the operation of the

MIPAS bearings which, in practice, undergo short strokes during calibration periods. Thus following the first 2 x 10^6 cycles, testing comprised cycling alternately over short and long strokes. The shortened stroke had a length of 20mm and in fact was too short to allow a period of constant velocity at the values of acceleration used (250 mm/sec^2). All force measurements were made over the longer stroke length of 100mm.

Supplementary tests on alternative material combinations

The lubricants and materials used in both the linear roller bearing and ball-bearing roller guides were chosen following a survey and trade-off of promising candidates. It was, however, considered worthwhile to undertake supplementary tests in which alternative methods of lubrication for the critical design areas could be assessed. These critical areas were deemed to be the bearing/guide rod interface, the ball bearings and the pulley wheel/axle interface.

To this end a simple rig was designed in which ball bearings could be rolled under load against a guide rod and pulley wheels could be made to rotate under the action of a loaded cable. In this way the material combinations shown in Tables 2 and 3 were tested and compared. Conditions of testing (ie loads, speeds, vacuum environment etc.) were representative of those occurring within the candidate bearing systems under life test. The supplementary tests were continued until completion of 2.5x 10^6 cycles.

Table 2 Material Combinations in Pulley/Cable Tests

Pulley Material	Cable Coating	Axle Lubrication
Vespel SP1	MoS2	Sputtered MoS2
Vespel SP3	Nylon	Sputtered MoS2
Vespel SP3	MoS2	Sputtered MoS2
Lead Bronze	MoS2	Ion-plated Lead

Table 3 Material combinations in bearing/rod tests

Race	Balls	Cage	Outer Race (outer surface)	Guide Rod
MoS2	TiC	Duroid	-	TDC/MoS2
Lead	440C	Lead bronze	Lead	TDC
Lead	440C	Lead bronze	-	TDC/MoS2

THERMAL-VACUUM TEST RIG

The test rig employed for the accelerated life tests is depicted schematically in Fig.6. Each bearing system was mounted in a housing which was itself attached to a heat exchanger which controlled the specimen temperature (assisted by an enclosing thermal shroud). The heat exchanger support was bolted to an annular support plate which was carried by three piezoelectric force transducers which monitored the bearing drive force. The transducer bodies were supported in a further annular support plate attached to the vacuum chamber lid by three support pillars.

Drive was applied from a crosshead to the linear carriage through a link arm, which comprised a pair of spherical rod-end bearings. The crosshead was connected to a Roh'lix linear drive mechanism. The Roh'lix is a proprietary component which incorporates six ball bearings mounted in two sets of three on a block around a central shaft. The bearings are angled relative to the drive shaft such that shaft rotation induces linear motion of the Roh'lix block. The drive shaft was supported at both ends by support bearings and was rotated, via a rotary vacuum feedthrough, by a high-resolution microstepping motor (25,000 steps per revolution).

A linear position encoder (Sony Magnescale) was fitted to provide feedback on the position of the crosshead/test bearings. The required motion profile was programmed via a computer terminal. The motion profile was then generated by a microprocessor indexer card whilst monitoring the feedback from the encoder and thus ensuring that the bearings underwent consistent reciprocating motion over the same length of stroke.

The Roh'lix bearings, shaft support bearings and linear encoder were all lubricated with Braycote 601 grease. It was found necessary to refurbish these components on a regular basis (every 1.5 million cycles) due to severe degradation of the grease.

TEST RESULTS

Linear roller bearing guided slide (Design 1)

Prior to the vacuum life test, measurements were made (in dry nitrogen gas) of drive force versus bearing load. These measurements were undertaken so as to gain a measure of the contribution of the pulley-guide system to the overall drive force. Fig.7 shows the resulting plot of drive force versus preload. Clearly there is a residual drive force at zero preload which is attributable to frictional losses within the pulley system (and, to a degree, to friction at the cage/roller interfaces). Thus for the intended operational preload of 10N (and indeed the test preload of 23N), this residual component represents a significant contribution to the overall drive force.

Following the above tests, the preload springs were adjusted to give a bearing preload of 23N and the test rig mounted in the vacuum chamber. Prior to evacuation of the chamber, the bearings were run over a few cycles in nitrogen to confirm satisfactory operation.

The chamber was then evacuated to a pressure of better than 10^{-6} torr and the temperature of the bearings reduced (by passing refrigerated alcohol through the heat exchanger) until the outer bearing temperature reached -75 deg.C (the inner races attaining a temperature of -58 deg.C). These temperatures were then maintained for the duration of the accelerated life test which proceeded until completion of 3.5×10^6 cycles.

Fig. 8 shows the variation in mean drive force and peak drive force as a function of cycles over this period.

The behaviour of the bearing pair can be summarised as follows. During the first 10^5 cycles there occurs a sharp decrease in drive force (this, we believe, is principally attributable to the running-in of the pulley/cable system). Thereafter there is a more steady decrease in force until

approximately 1.2 x 10^6 cycles are completed, after which the force does not change greatly with number of cycles. In this region, the mean force has a value of 0.3N.

Examination of the curve of peak force shows that there is a sharp decrease initially corresponding to the decrease observed in the mean force. Between 10^5 and 2.5 x 10^6 cycles the peak force does not show any great variation and lies in the range 0.6N to 1.0N. Cycles undertaken thereafter, however, show a distinct trend - the peak force increasing almost monotonically, reaching values of 1.7N at the end of test.

Ball bearing roller guide (Design 2)

Fig.9 shows the variation in mean force and peak force as a function of number of cycles. In general, the mean force has remained in the range 0.05N to 0.1N with no evidence of degradation. Likewise, no distinct trend is observed with the peak force, this lying in the range 0.15N to 0.24N.

Supplementary tests on alternative lubricants/material combinations

The results of the supplementary tests may be summarised as follows:

- wear of the pulley wheels (at axle interface) was least for the leaded bronze combination, followed by SP3 and SP1

- the highest and most variable drive forces were observed for the combination of lead-bronze pulley and lead-coated axle

- consistently low drive forces were observed for the combinations of Vespel pulleys (both SP1 and SP3) in conjunction with MoS_2-lubricated axles

- wear of ball bearing/guide rod interface was less with lead lubrication than with MoS_2 lubrication.

- lead lubrication of the ball bearings yielded torques which were approximately twice that generated by the MoS_2-lubricated bearings and thus gave a higher drive force.

DISCUSSION

Linear roller bearing guided slide

The use of a pulley/cable arrangement was successful in controlling the stroke and speed of cages within the Hydrel bearing, but its presence made a significant contribution to the drive force, and it is believed that wear debris from the pulley wheel generated additional frictional noise.

The decrease in mean force seen in the early stages of testing is, we believe, attributable to the running-in of the pulley cable system. Preliminary testing had demonstrated that, prior to life testing, approximately 80% of the drive force was attributable to frictional losses within the pulley-cable system (Fig.7). Thus any decrease in these losses would result in a significant decrease in drive force. That such decreases in frictional losses did occur is supported by evidence from the supplementary tests. In these, the mean force needed to rotate an SP1 pulley wheel decreased by a factor four during the first 10^5 cycles.

Whilst the mean drive force of the Hydrel bearings showed little change after the running-in phase, the peak force exhibited larger variations. Up to 2.5×10^6 cycles, and after running-in, the peak force remained within the range 0.5 - 1 N. However, as the cycles increased beyond this point, the peak became larger, its value at the end of testing being 1.7N, the highest force observed. These peak forces tended to occur near the end of the stroke. Examination of the race wear tracks formed by the rollers indicate that MoS_2 lubricant is still present in these regions, thus precluding lubricant loss as the reason for the high forces. However, there was a second much narrower wear track observed running parallel to some of the wear tracks. These additional tracks which extended beyond the ends of the roller tracks are lined by wear debris. From their position, it is clear that these tracks were caused either by rubbing of the cage on the raceway or by abrasive action of debris entrapped between cage and race. The latter effect is the more likely since there was little sign of heavy wear on the cages themselves. The most likely sources of debris are wear particles (Vespel SP1) from the pulley wheel whose path to the raceways would be via the relief holes in the pulley slots. It seems plausible therefore that the higher forces observed near the end of strokes are due to this entrapped debris rubbing against the raceways. Effects such as

these could be reduced by having larger clearances in the bearings eg by having larger diameter rollers or thinner cages.

Another method of minimising this effect would be to manufacture the pulley wheel from Vespel SP3 since measurements of the wear of the different pulley wheel materials indicated that SP3 yielded lower wear whilst still providing low friction.

The use of sputtered MoS_2 on the raceways can be considered successful in that the coatings withstood 3.5×10^6 cycles under enhanced load. Our calculations show that this number of cycles is equivalent to 17.5×10^6 cycles at the operational load of 10N. This number is similar to that required in the lifetime of MIPAS.

Ball bearing roller guide

The roller guide system completed a total of 5×10^6 cycles under operational bearing loads. For most of the test period the mean drive force remained in the range 0.05 to 0.1N, the overall trend being one of a slow increase in mean force. The peak force varied between 0.15N and 0.25N but no trend was discernible. Force peaks were uniformly distributed across the force profiles with no particularly strong peaks occurring at the end of stroke. At completion of the test period there was no indication of bearing distress or that degradation was imminent.

Since the test bearings were not disassembled it was not possible to examine the component parts in detail. There were well defined wear tracks on the guide rods but the amount of MoS_2 coating remaining could not be assessed. However, our supplementary tests clearly show that lead coatings on the outer surfaces of the ball bearings are more effective than the sputtered MoS_2 in reducing wear at the interface between the ball bearing and the TDC-coated guide rod interface. It should be noted however that a depletion of lubricant on the guide rods would not necessarily lead to a higher drive force since the major contribution to frictional losses in the roller guide occurs within the ball bearings.

CONCLUSIONS

The use of sputtered MoS_2 on the raceways of the Hydrel bearings maintained effective lubrication between rollers and races over the equivalent of 17.5 million cycles (consistent with life requirements). The pulley/cable arrangement proved successful in controlling the stroke and speed of cages and the extremely high end-forces observed with uncontrolled cages were not seen. However, the pulley/cable system made a significant contribution to the drive force, and wear debris generated from the pulley wheel gave rise to additional frictional noise.

The ball bearing roller guide system generated low consistent friction forces throughout the test duration. The use of MoS_2 lubrication within the bearings was demonstrated to be the best choice, but supplementary tests indicated that thin lead films were more effective (than MoS_2) in preventing wear of the guide rods.

ACKNOWLEDGEMENTS

This programme was funded by the European Space Agency.

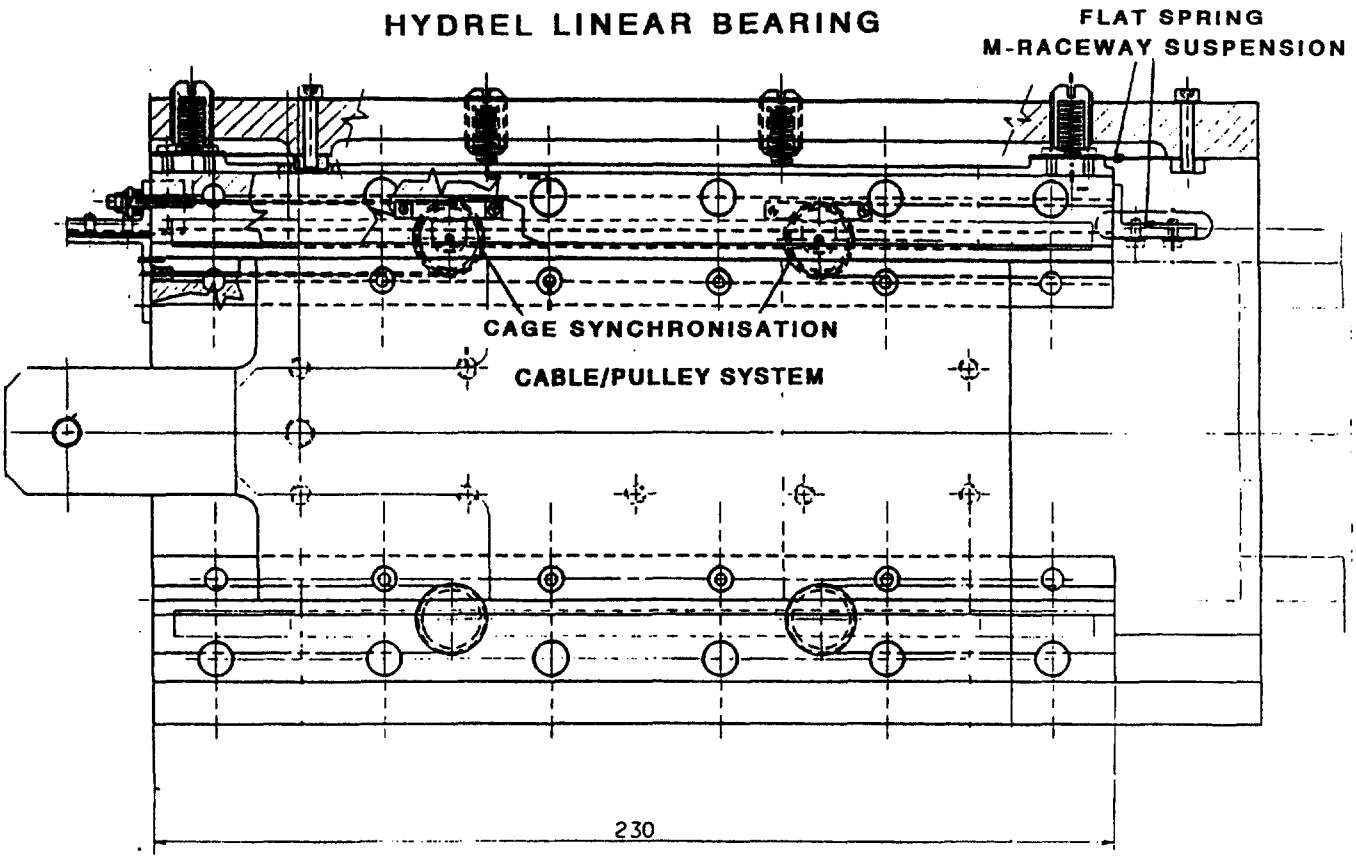

FIG.1 THE LINEAR ROLLER-BEARING GUIDED SLIDE

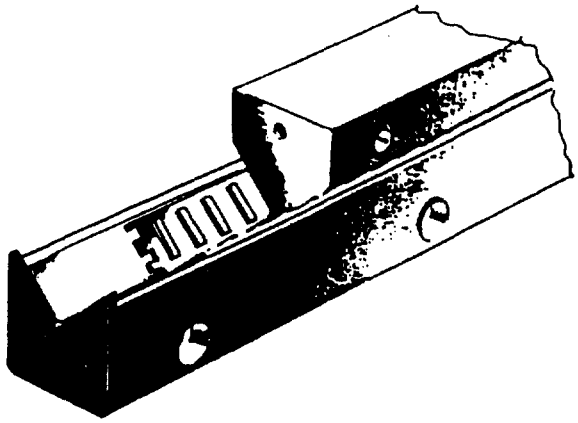

(a) HYDREL ROLLER BEARING

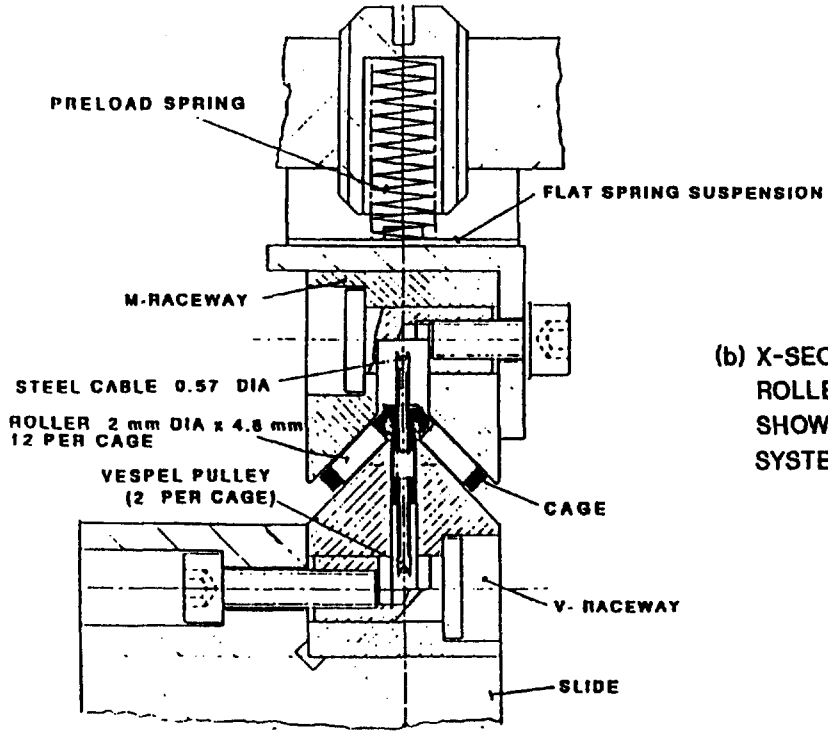

(b) X-SECTION OF HYDREL ROLLER BEARING SHOWING PRELOADING SYSTEM

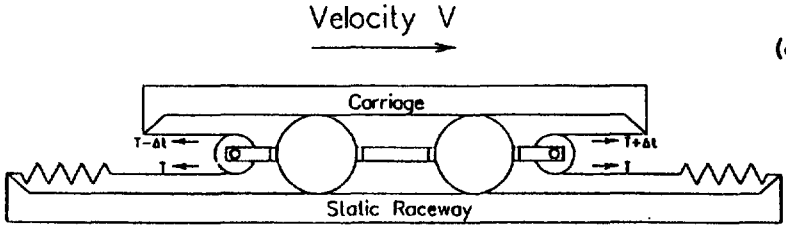

(c) SHOWING PRINCIPLE OF PULLEY/CABLE SYSTEM FOR CONTROLLING CAGE SPEED

FIG.2

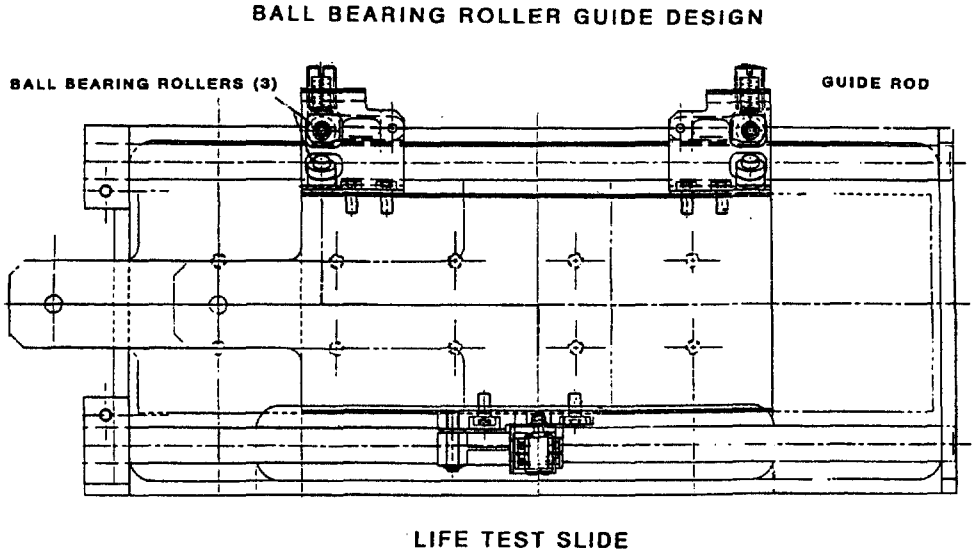

(a)

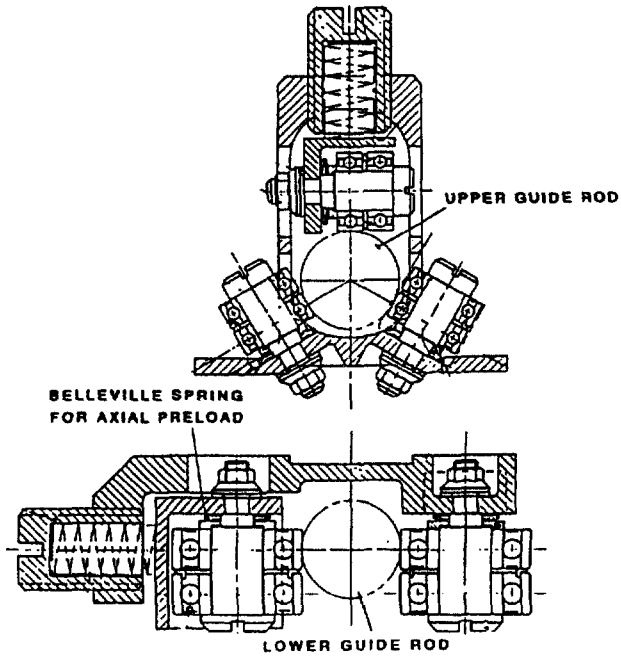

(b)

FIG.3 TWO VIEWS OF THE BALL-BEARING ROLLER GUIDE SYSTEM

FIG.4 HYDREL ROLLER BEARING
COMPUTED MEAN CONTACT STRESS PER ROLLER

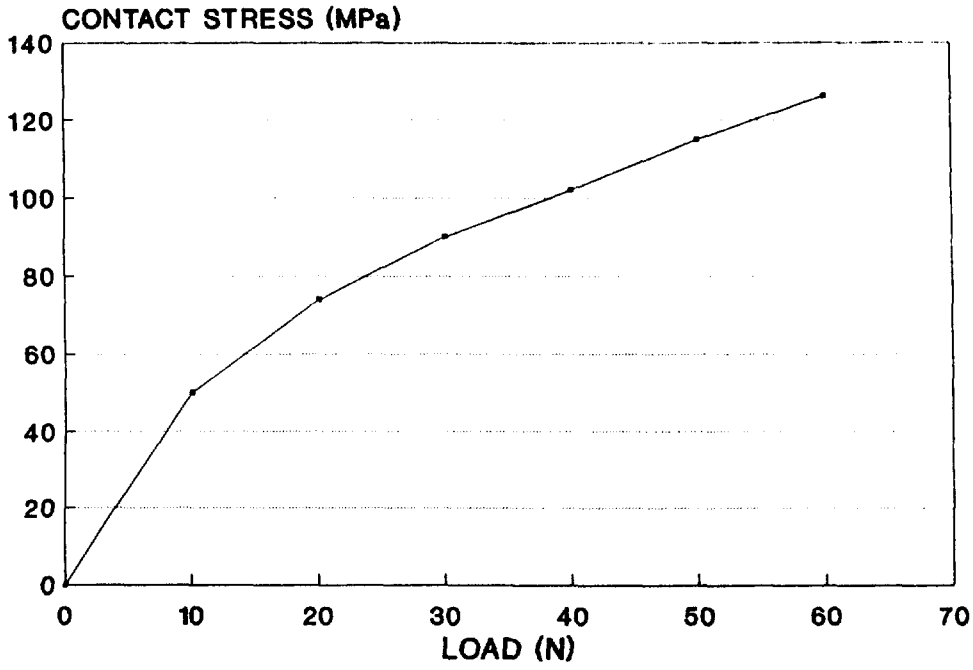

Film Life Acceleration Factor
Hydrel Roller Bearing

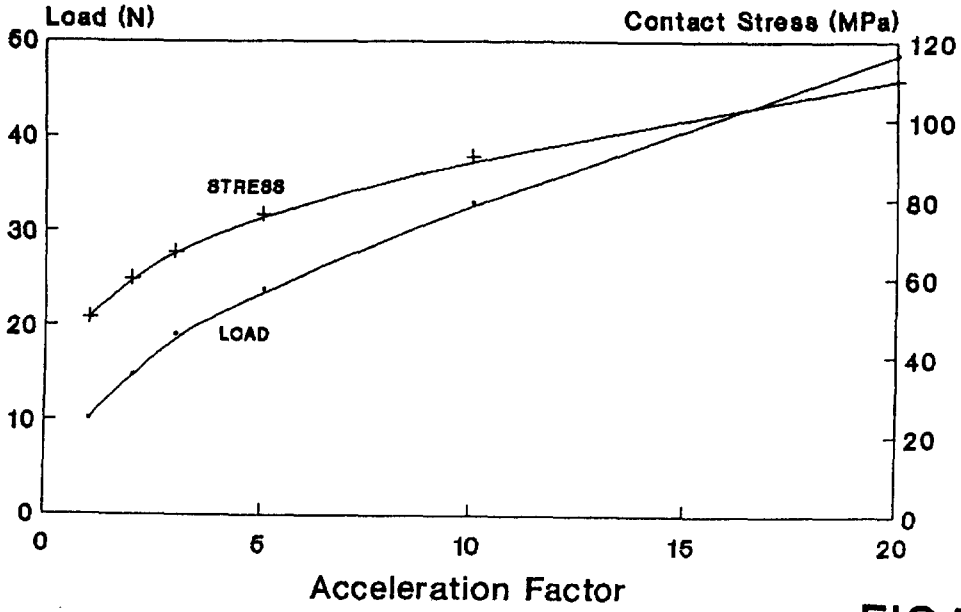

(relative to design load of 10N)

FIG.5

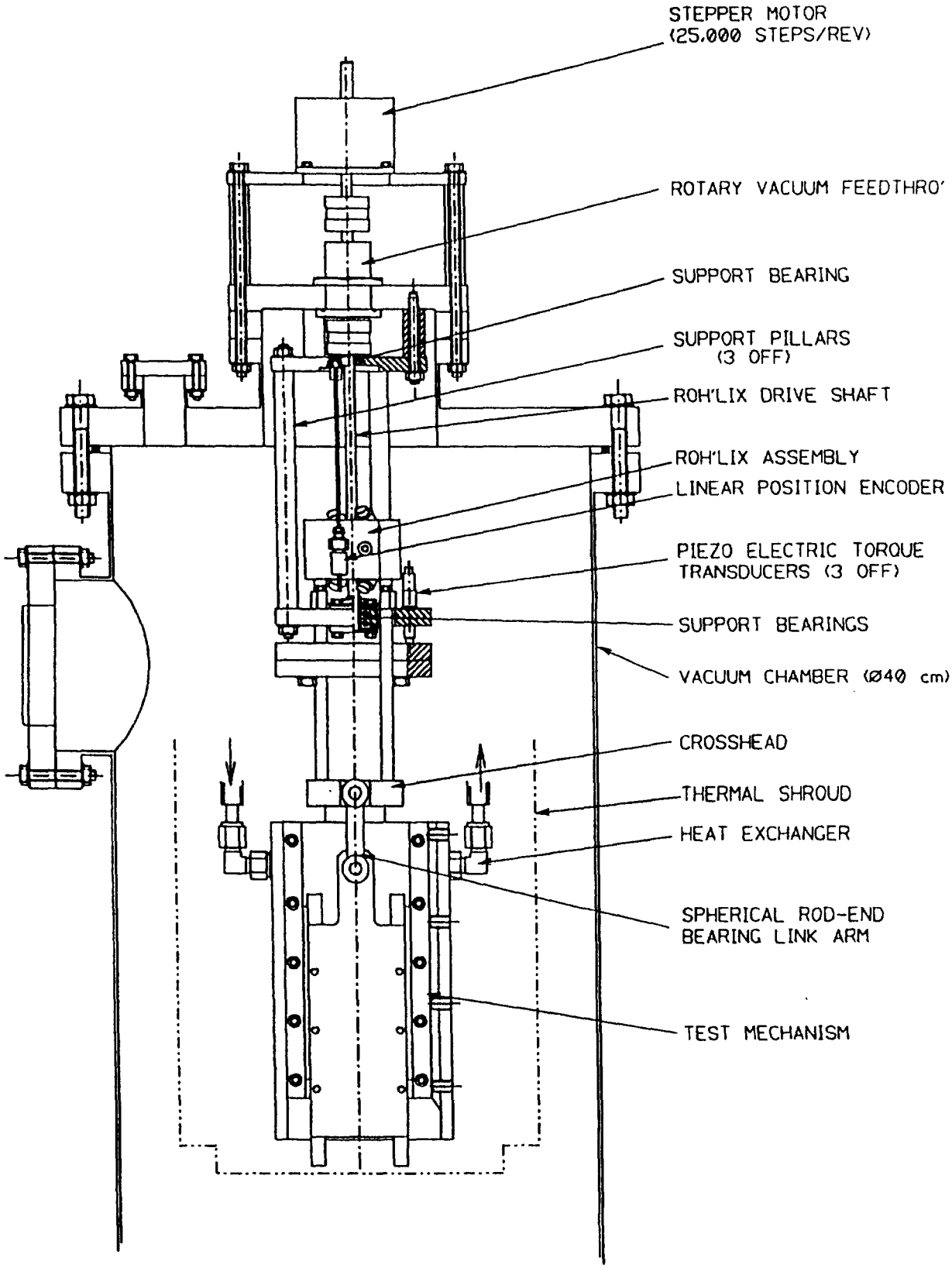

FIG.6 RIG FOR TESTING HYDREL BEARINGS UNDER THERMAL VACUUM CONDITIONS

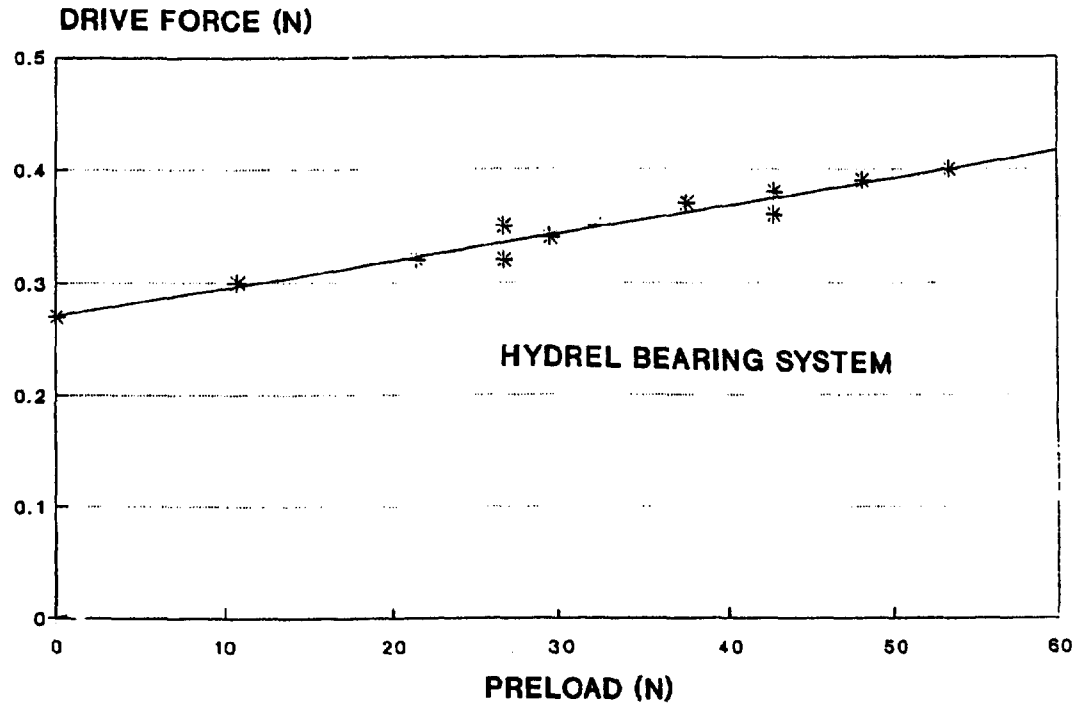

FIG.7 MEAN DRIVE FORCE VS PRELOAD (IN NITROGEN)

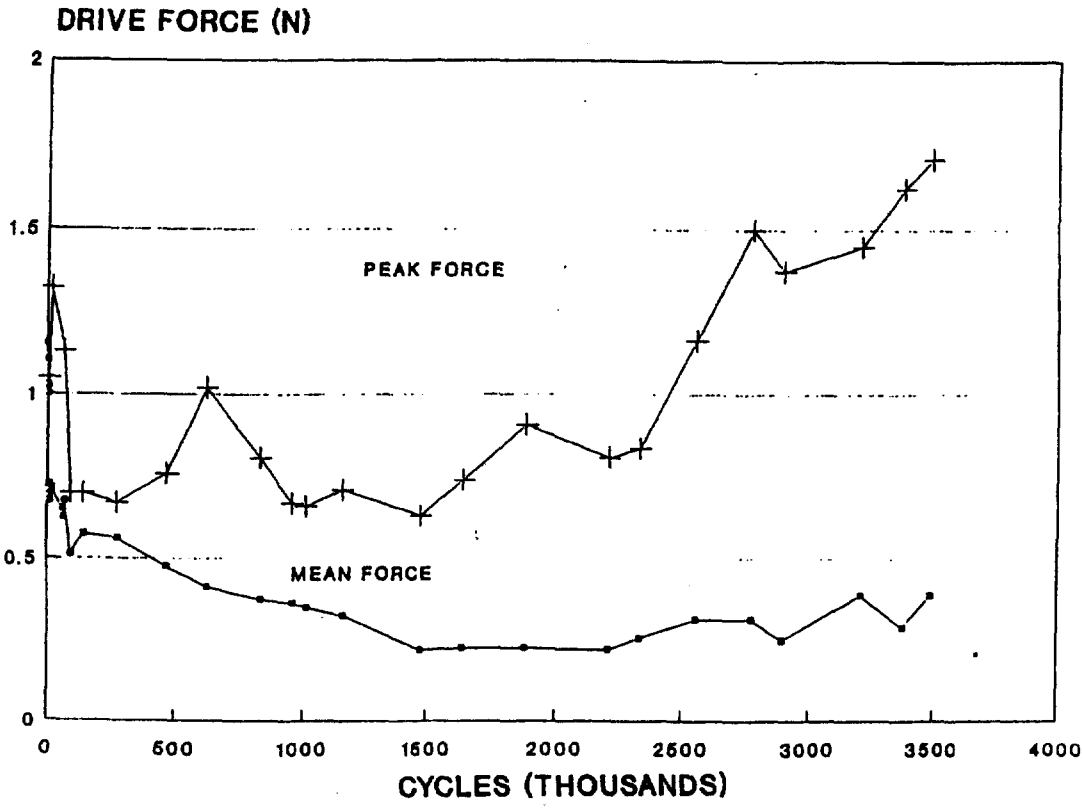

FIG.8 DRIVE FORCE VS. CYCLES OF HYDREL BEARING SYSTEM

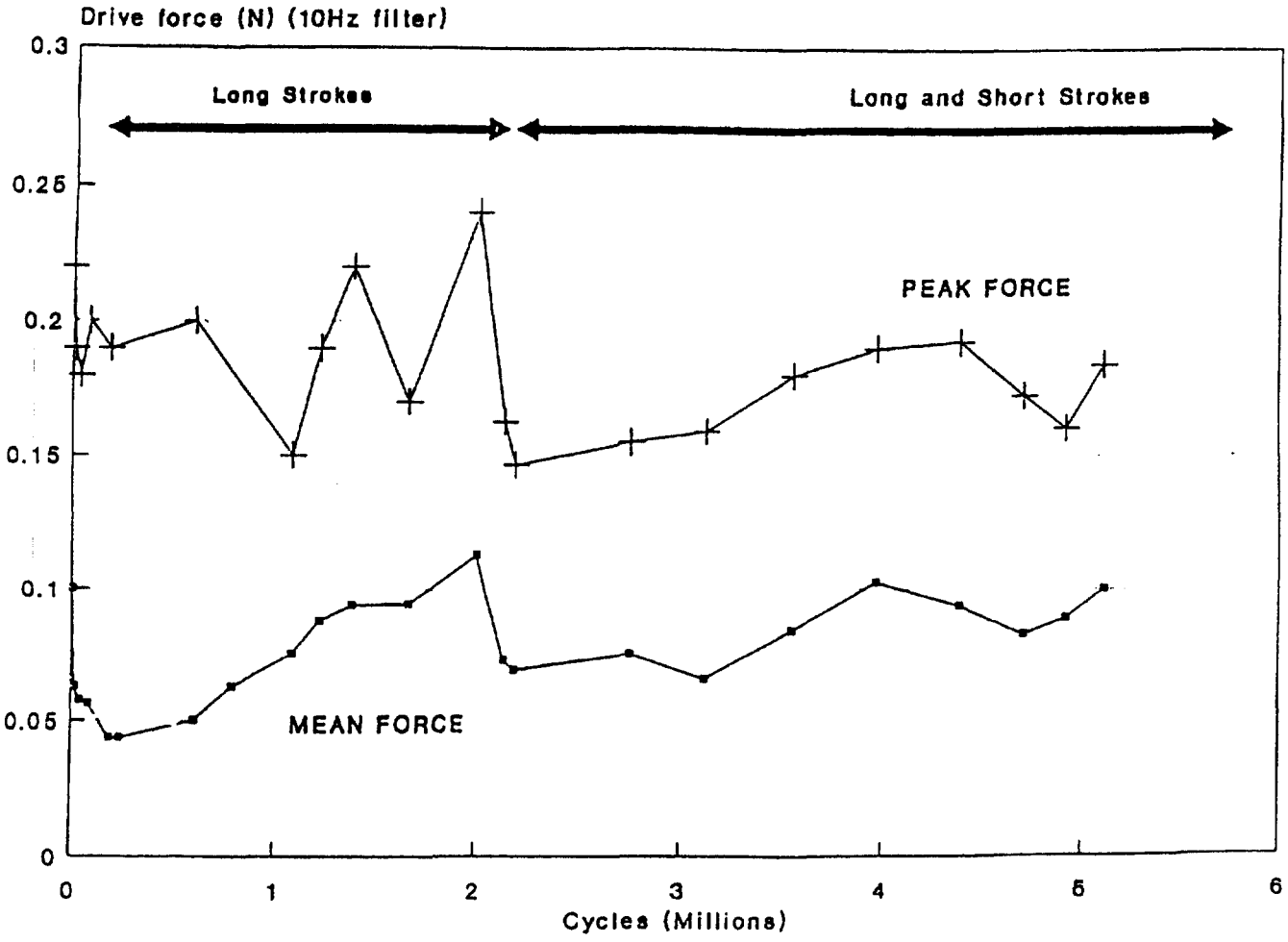

FIG.9 Roller Guide System - MIPAS
Drive force vs. no. of cycles

THE PRELIMINARY EVALUATION OF LIQUID LUBRICANTS FOR SPACE APPLICATIONS BY VACUUM TRIBOMETRY

W.R. Jones, Jr., S.V. Pepper, P. Herrera-Fierro, D. Feuchter,
T.J. Toddy, D.T. Jayne, D.R. Wheeler, P.B. Abel,
E. Kingsbury, W. Morales, R. Jansen, and B. Ebihara
NASA Lewis Research Center
Cleveland, Ohio

L.S. Helmick
Cedarville College
Cedarville, Ohio

and

M. Masuko
Tokyo Institute of Technology
Tokyo, Japan

Abstract

Four different vacuum tribometers for the evaluation of liquid lubricants for space applications are described. These range from simple ball-on-flat sliders with maximum in-situ control and surface characterization to an instrument bearing apparatus having no in-situ characterization. Thus, the former provide an abundance of surface chemical information but is not particularly simulative of most triboelements. On the other hand, the instrument bearing apparatus is completely simulative, but only allows post-mortem surface chemical information. Two other devices, a four-ball apparatus and a ball-on-plate tribometer, provide varying degrees of surface chemical information and tribo-simulation. Examples of data from each device are presented.

Introduction

The development of new satellite, spacecraft, and space station components will place increased burdens on the tribological systems for the many mechanical moving assemblies (Ref. 1). These assemblies include: momentum/reaction wheels, solar array drives, pointing mechanisms, filter wheels, de-spin mechanisms, slip rings, gears, etc. (Ref. 2). Improved lubrication systems are not only required because of increased mission lifetimes but also to insure greater reliability. In the past,

other components (e.g., batteries, electronics, thermal and optical systems) caused premature spacecraft failure (Ref. 3). It is now apparent, that advances in these areas have now exposed tribology as the primary roadback in achieving mission requirements.

Liquid lubricants (or greases) are often used in space mechanisms for a variety of reasons. These include: no wear in the elastohydrodynamic (EHL) regime, low mechanical noise, ease of replenishment, relatively insensitive to environment, and ability to scavenge wear debris. A number of different chemical base stocks have been used. These include: mineral oils, esters, polyalphaolefins, perfluoropolyethers (PFPE) and more recently, synthetic hydrocarbons (Ref. 4) and silahydrocarbons (Ref. 5).

Based on the speed, load, temperature, type of motion and type of contact, these lubricants are required to operate in either the EHL, mixed, or boundary lubrication regimes. For a more detailed discussion of these regimes, see Reference 6. Spacecraft designers are in constant need of tribological data for various material/lubricant combinations. These data include: lubricant degradation and outgassing characteristics, friction, torque, and wear characteristics.

Short term characteristics can easily be measured using conventional techniques. However, long term performance of liquid lubricated components poses some difficult problems. Mission lifetimes are typically five to thirty years. This obviously precludes real time testing in most cases. Usually, some form of accelerated test is required. Tests can be accelerated by increasing temperature, load, speed, and duty cycle.

For unlubricated or solid lubricated components, these accelerating methods are usually valid. However, liquid lubricated systems are much more difficult to accelerate. If one is trying to simulate the boundary or mixed film regimes, speed increases may well drive the contact into EHL regime resulting in surface separation. Obviously, this situation is not simulative. In some cases, speed increases are combined with temperature increases. Increasing temperature decreases viscosity and, if carefully controlled, can negate the film forming speed effect. However, high temperatures can initiate chemical reactions and also increase volatility. Stepper motor tests are often accelerated by increasing the duty cycle by removing dead time. This may also cause partial EHL film formation.

Vacuum Tribometers

There are four tribometers available at the NASA Lewis Research Center for evaluation of liquid lubricants under vacuum conditions. These are: (1) UHV rubbing apparatus, (2) four-ball apparatus, (3) ball-on-plate apparatus and (4) instrument bearing apparatus.

These devices range from a simple slider with maximum in-situ control and characterization of the flat rubbed surface to a complete rolling contact ball bearing with no in-situ characterization. Since friction and wear is affected by and also alters surface chemistry, in-situ control and characterization are obviously advantageous. However, there are trade-offs in that control and characterization usually require flat geometries that are not simulative of real components. Thus, the greatest degree of control and characterization requires triboelements unrealistically simple and realistic simulation precludes effective in-situ surface analysis. Therefore, our suite of tribometers spans these trade-offs from the simple planar slider with x-ray photoelectron spectroscopy (XPS) providing in-situ analysis but poor simulation to the instrument bearing apparatus providing no in-situ analysis but complete tribo-simulation

UHV Rubbing Apparatus

The UHV rubbing apparatus is depicted in Figure 1. The device consists of a 6 mm diameter bearing ball which is placed in pure sliding contact with a flat disk. The disk is positioned below the ball and remains stationary during the test. The ball is held in a chuck which is attached to a long rod through a flex pivot assembly. The rod is attached to an XYZ manipulator which is motorized in the Y axis. The entire apparatus is mounted on a 6 inch flange which attaches directly to the preparation chamber of an XPS spectrometer. The virtue of this arrangement is that the flat which is to be rubbed may be subjected to surface analysis and surface treatment (ion bombardment cleaning or in-situ lubricant deposition) without exposure to air either before or after rubbing. Loading is effected by a spring attached to the flex pivot assembly which is extended when the ball contacts the disk surface. Specifications for this tribometer appear in Table 1.

Four-Ball Apparatus

The overall apparatus is shown in Figure 2. The specimen configuration is the same as the conventional four-ball apparatus, except for the use of 9.5 mm (3/8 in.) diameter precision bearing balls (grade 10). The apparatus is mounted in a vacuum chamber. The chamber is evacuated using a turbomolecular pump (140 l/s) and a mechanical backing pump to achieve a vacuum of approximately 10^{-4} to 10^{-6}Pa. The chamber is equipped with a hot filament ioization gage for chamber pressure and mass spectrometer (residual gas analyzer).

The rotating upper ball is mounted on a spindle which is connected to a ferrofluidic rotary feedthrough. The lower three stationary balls are fixed in a ball holder (lubricant cup) which is mounted on the stage. The stage can be moved upward from outside the chamber with a pneumatic cylinder through a linear motion feedthrough sealed with a welded metallic bellows.

The shaft of the linear motion feedthrough is supported under the "flex pivot" inside the chamber with a linear ball bearing. The lower end of the shaft of the feedthrough is mounted on a plate outside the chamber which is supported with four linear ball bearings. A load cell is mounted between the plate and the pneumatic cylinder to measure the applied load.

The "flex-pivot" shown in Figure 2, which is stiff toward axial thrust but elastic for angular displacement around its center axis is used to mount the stage, where the lubricant cup is fixed, on the top of the shaft of the linear motion feedthrough. Torque is obtained by measuring the angular displacement of the cup holding the three balls. A set of Hall-effect position sensors and a magnet are used to measure the angular displacement. The capability of this tribometer is summarized in Table 1.

Ball-on-Plate Apparatus

This apparatus is a planar simulation of the rolling contact in a ball bearing. The ball-on-plate geometry is shown schematically in Figure 3. The device consists of a ball set rolling between a stationary bottom plate and a spinning top plate. The apparatus is contained in a turbomolecularly pumped cubical vacuum chamber (typical pressure, 10^{-6}Pa). The top plate is driven by an external motor through a ferrofluidic feedthrough. Load is applied upward on the bottom plate with a deadweight through a lever system located below the apparatus. Typically, for 12.5 mm diameter ball specimens, a total of three balls are used. These are grade 10 precision bearing balls.

These balls are placed between the plates with a positioning device which locates them 120° apart azimuthally and at the same radial distance from the center of the plates. After loading and the start of rotation, the balls will spiral out to the disk periphery. Their spiral path is eventually stopped by a bumper (shown in Figure 3). Each ball in turn is nudged back to its original track once each orbit. This causes a repositioning scrub mark on the bottom plate track, made as the rolling balls are pushed back to their original radius by the bumper. The bumper assembly contains a transducer to determine the force on the bumper. The length of the scrub and the bumper force indicates the degree of boundary lubrication. A cold cathode ionization pressure gauge and a quadrupole mass spectrometer are used to detech species released into the ambient during the rolling and bumping process. The plate to plate electrical resistance determines any separation between ball and plate caused by insulating lubricant films.

The balls are lubricated by a dip coating process by submerging in a dilute solution of the lubricants. Upon removal from this solution, the solvent evaporates, leaving a thin residue of lubricant. The plates are not lubricated but lubricant is transferred during the rolling process. More details about the kinematics of this device appear in Reference 7. Other specifications appear in Table 1.

Instrument Bearing Apparatus

The final vacuum tribometer is shown in Figure 4. As in the other tribometers, the apparatus is contained in a cubical vacuum chamber and driven by an external motor through a ferrofluidic feedthrough. In this case, the motor is a micro-stepper which is computer controlled to effect either continuous rotation or precise dither motion. Loading is effected by a precision screw mechanism below the apparatus. Provision has been made for either hard or soft loading.

The test component is an instrument angular contact bearing. This bearing has the following specifications: O.D. 30.16 mm, bore 19.05, 18-3.175 mm balls and a porous polyimide retainer. Bearing torque is measured with a flex pivot assembly which is instrumented with micro-strain gages. The vacuum cube is also instrumented with a mass spectrometer. The test bearing is also electrically isolated so that contact resistance can be measured. Other specifications are tabulated in Table 1.

Examples of Test Data

UHV Rubbing Apparatus

This apparatus is generally used to generate tribological surfaces for fundamental surface chemistry studies. Typically a flat surface is cleaned and characterized by X-ray photoelectron spectroscopy (XPS). Then it is placed on a collimator and a thin (~40 Å) lubricant film is deposited by evaporation. An in-situ rubbing experiment can then take place. An example is shown in Figure 5 from Reference 8.

Figure 5 is a micrograph of a rubbed area on a 440 C disk lubricated with a perfluoropolyether (PFPE). The area was generated by loading a 440 C bearing ball against the flat translating it linearly in reciprocating motion with a velocity of 0.3 mm/s. A lateral translation of 50 μm at the end of each stroke produced a rectangular patch 5 mm X 8 mm. XPS analysis of this rubbed area indicated that, even under this mild sliding, single pass conditions, surface fluoride was formed. This indicated that the PFPE had been degraded at room temperature. Its chemical signature was similar to that observed during static high temperature experiments. Therefore, this device is very useful in studying the effects of surface pretreatments, such as ion implantation, on the tribological process.

Four-Ball Apparatus

Because of the high loads and pure sliding conditions employed in this device, a great amount of energy is dissipated in the contact regions. This accentuates chemical reactions and therefore results in a highly accelerated test. Steady state wear rates are generated with this device which yield qualitative rankings of the boundary lubrication performance of liquid lubricant basestocks and formulations.

Figure 6 contains a comparison of wear rates for three aerospace lubricants in air and vacuum (Ref. 9). Test conditions were: 25°C, 200N load, and a 100 rpm rotational speed. The three lubricants were (1) an unbranched PFPE (Z-25), (2) a branched PFPE (143 AB) and (3) a formulated synthetic hydrocarbon (2001). Results in air and vacuum clearly discriminate between the more reactive unbranched PFPE (Z-25) compared to the less reactive branched fluid (143 AB). This trend correlated with other vacuum four-ball results (Ref. 10) and vacuum sliding experiments (Ref. 11). In addition, the better performance of formulated hydrocarbons compared to unformulated PFPE fluids correlated with oscillating gimbal tests (ref. 12) and boundary lubricant screening tests (ref. 13).

Ball-on-Plate Apparatus

Figure 7a shows bumper force and mass spectrometer data obtained with a PFPE boundary lubricant at room temperature, 6 rpm and 10^{-6}Pa. In this test the bumper force reached a maximum of 28N and lasted 1.2 seconds. The ball load was 140N, for a sliding friction coefficient of 0.2. Figure 7b shows the corresponding mass spectrometer data for evolution of mass 69 (CF_3) lubricant fragments: background, no rotation, level I; rotation, no bump, level II; and during a series of bumps, level III.

Instrument Bearing Apparatus

Performance data for an MPB 1219 size bearing operating in a retainerless mode and lubricated with a synthetic hydrocarbon (Nye 2001) are shown is Figure 8. Figure 8 illustrates the effect of speed on torque and contact resistance at room temperature, a hard load of 44.5 N and a vacuum level of approximately 10^{-4}Pa. A gradual increase in torque with increasing speed is observed. Contact resistance as a function of speed shows the transition from the boundary regime to mixed and finally to full EHL.

References

1. Fusaro, R.L.: "Tribology Needs for Future Space and Aeronautics Systems," NASA TM-10425, 1991.
2. Fusaro, R.L. and Khonsari, M.M.: "Liquid Lubrication for Space Applications," NASA TM-105198, 1992.
3. Fleischauer, P.D. and Hilton, M.R.: "Assessment of the Tribological Requirements of Advanced Spacecraft Mechanisms," Aerospace Corporation, Report No. TOF-0090 (5064)-1, Sept. 1991.
4. Vernier, C.G.: "Multiply-Alkylated Cyclopentanes (MACS): A New Class of Synthesized Hydrocarbon Fluids," Lubr. Engr. 47, 7, pp. 586-591, July 1991.

5. Tamborski, C.; Chen, G.J.; Anderson, D.R.; and Snyder, C.E., Jr.: "Synthesis and Properties of Silahdrocarbons, A Class of Thermally Stable, Wide-Liquid-Range Fluids," Ind. Eng. Chem. Prod. Res. Deve. 22, p. 172, 1983.
6. Jones, W.R., Jr.: "The Properties of Perfluoropolyethers Used for Space Applications," NASA TM-106275, 1993.
7. Kingsbury, E.: "Kinematics of an Elastic Sphere Rolling on a Plane and Between Two Planes," Trans. ASME 115, pp. 476-480, July, 1993.
8. Herrera-Fierro, P.; Jones, W.R., Jr.; and Pepper, S.V.: "Interfacial Chemistry of a Perfluoropolyether Lubricant Studied by XPS and TDS," NASA TM-105840, 1992.
9. Masuko, M.; Jansen R.; Ebihara, B.; and Pepper, S.V.: "A Vacuum Four-Ball Tribometer to Evaluate Liquid Lubricatns for Space Applications," NASA TM-106264, 1993.
10. Masuko, M.; Fujinami, I.; and Okabe, H.: "Lubrication Performance of Perfluoropolyalkylethers Under High Vacuum," Wear, 159, pp. 249-256, 1992.
11. Mori, S. and Morales, W.: "Tribological Reactions of Perfluoroalkyl Polyether Oils with Stainless Steel under Ultrahigh Vacuum Conditions at Room Temperature," Wear, 132, pp. 11-121, 1989.
12. Conley, P.L. and Bohner, J. J.: "Experience with Synthetic Fluorinated Fluid Lubricants," Twenty-fourth Aerospace Mechanism Symposium, NASA CP-3062, pp. 213-230, Apr. 18-20, 1990.
13. Hilton, M.R. and Fleischauer, P.D.: "Lubricants for High-vacuum Applications,: Aerospace Report No. TR-0091 (6945-03)-6, Mar. 1993.

Table 1. Specifications of Vacuum Tribometers

Apparatus	UHV Rubbing	Four-Ball	Ball-on-Plate	Instrument Bearing
Initial Mean Hertz Stress, GPa	0.43	2-4	1-2	1-1.5
Motion	pure sliding/ reciprocating	pure sliding	rolling/ sliding/ pivoting	rolling/ sliding/ dither
Atmosphere	air, N_2, or vacuum	air, N_2, or vacuum	air, N_2, or vacuum	air, N_2, or vacuum
Load Range, N	~1N	50-1000	45-450	25-200
Speed Range, rpm	0.02-0.2 (linear speed)	10-500	1-100	1-1200 (1Hz dither)
Environmental Pressure, Pa Temperature Specimens (440C Steel)	10^{-7} room 6 mm diameter bearing ball	10^{-6} room to 50°C 9.5 mm diameter bearing balls	10^{-6} room to 50°C 12.7 mm diameter bearing balls 50.8 mm diameter disks	10^{-6} room to 50°C angular contact instrument bearing (1219 size)

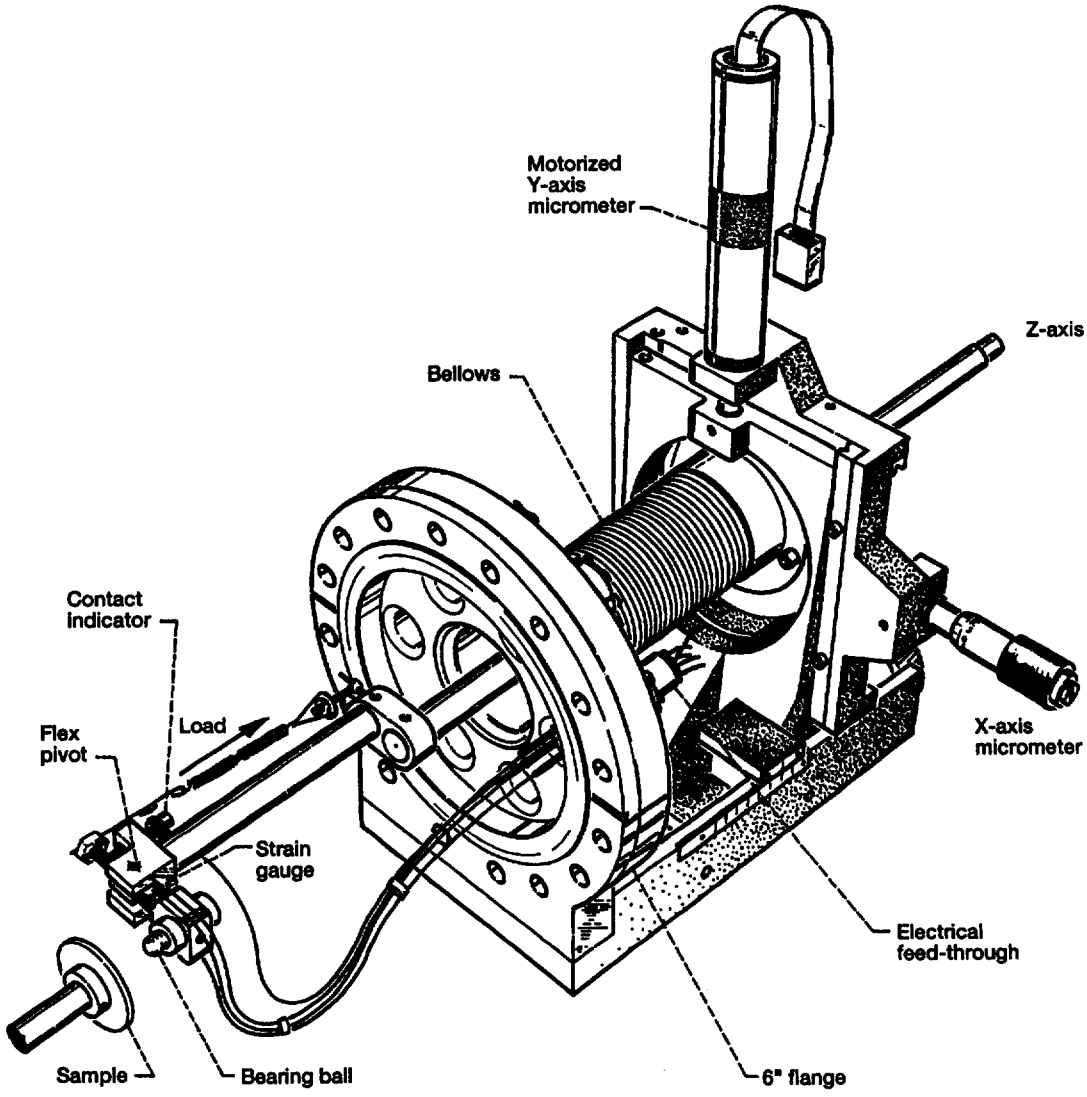

Figure 1.—UHV tribometer.

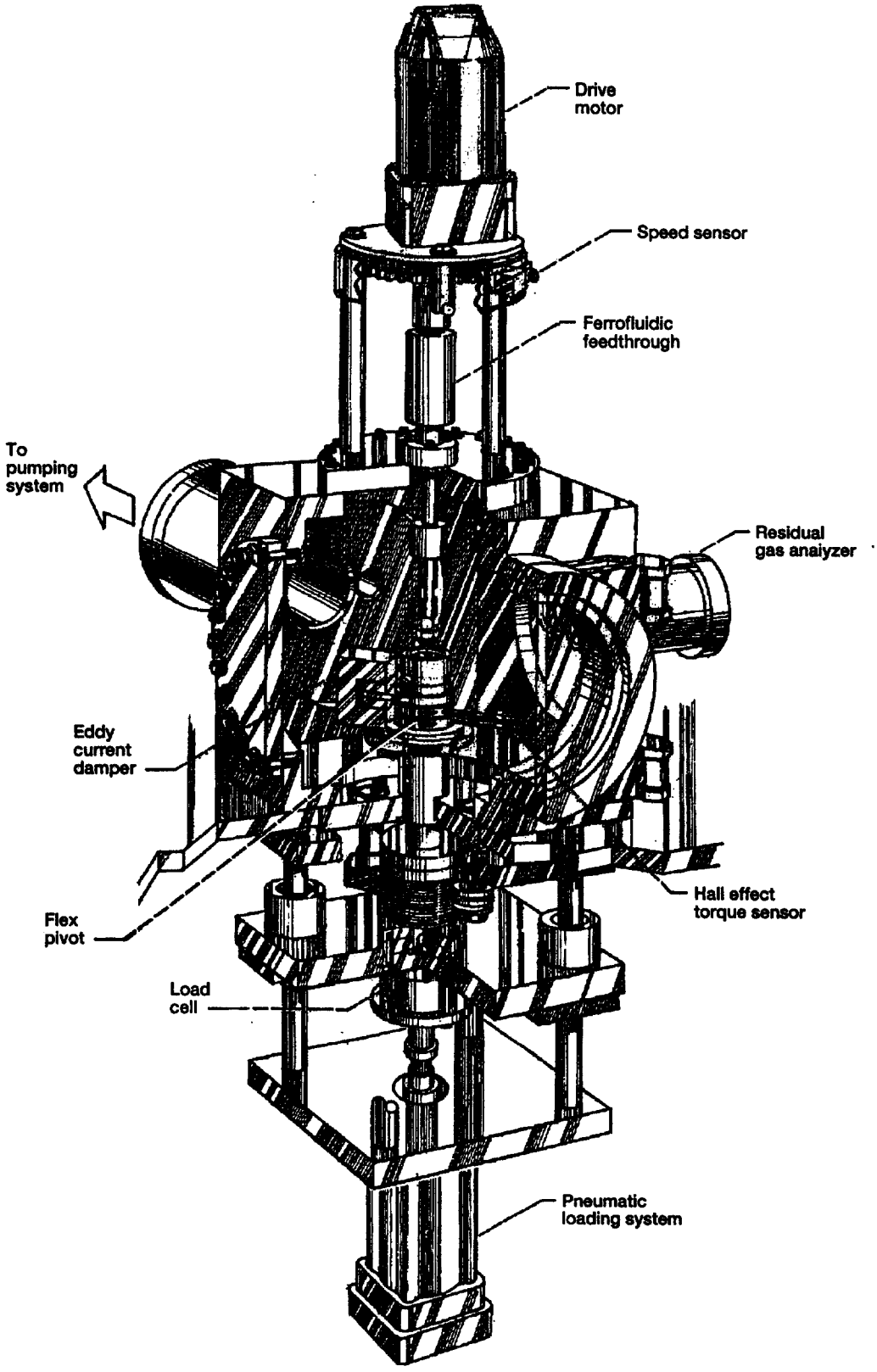

Figure 2.—Four-ball apparatus.

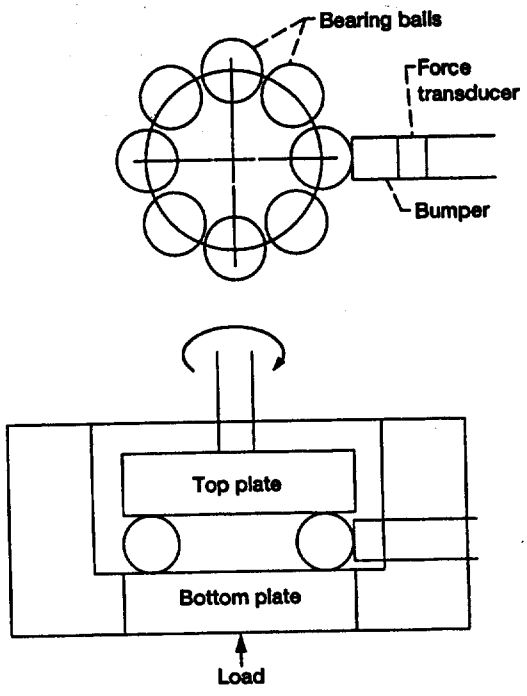

Figure 3.—Ball-on-plate geometry.

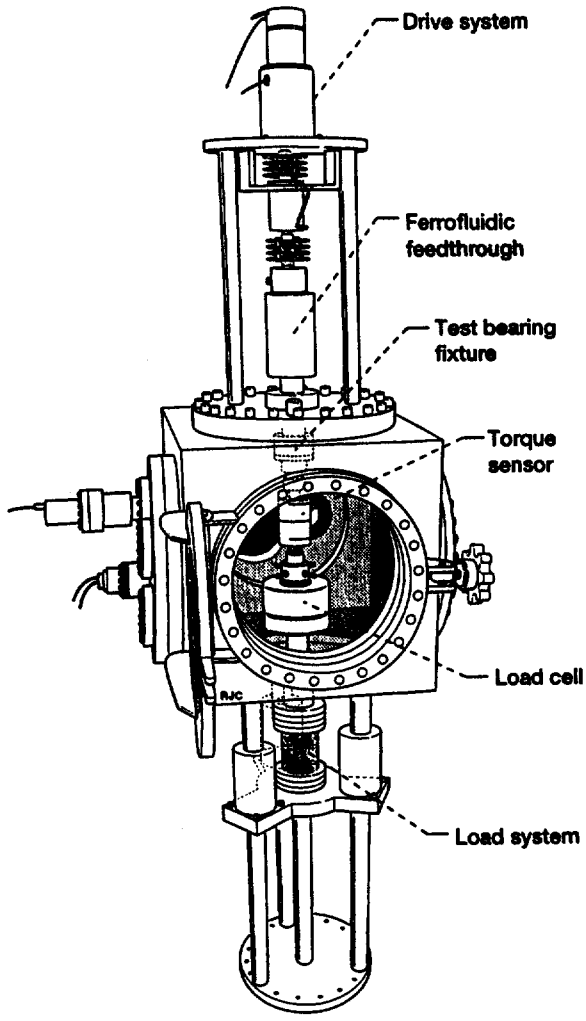

Figure 4.—Instrument bearing test rig.

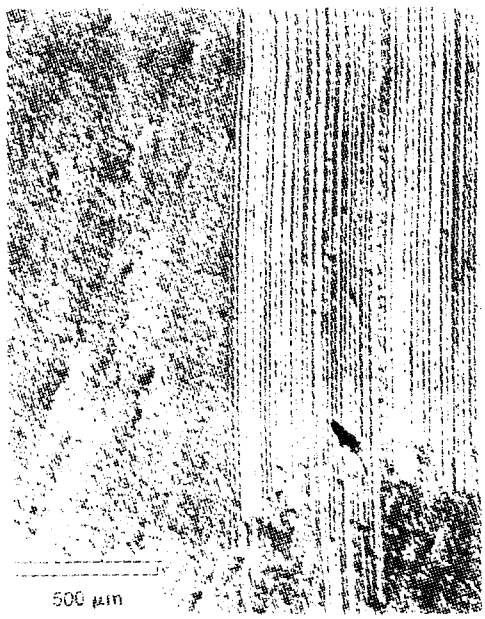

Figure 5.—Optical micrograph of soft 440C steel surface after rubbing with a 440C bearing ball. Lubricant: 50Å Fomblin Z-25.

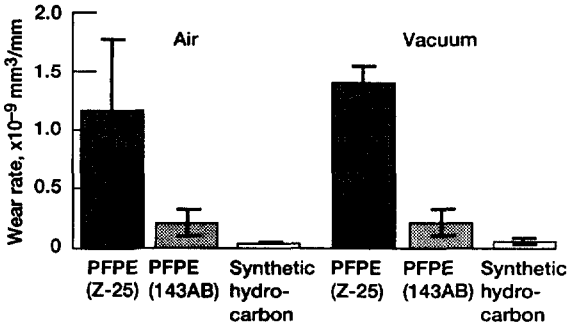

Figure 6.—Wear rates for three commercial aerospace lubricants in air and vacuum (25 °C, 200N load, 100 RPM).

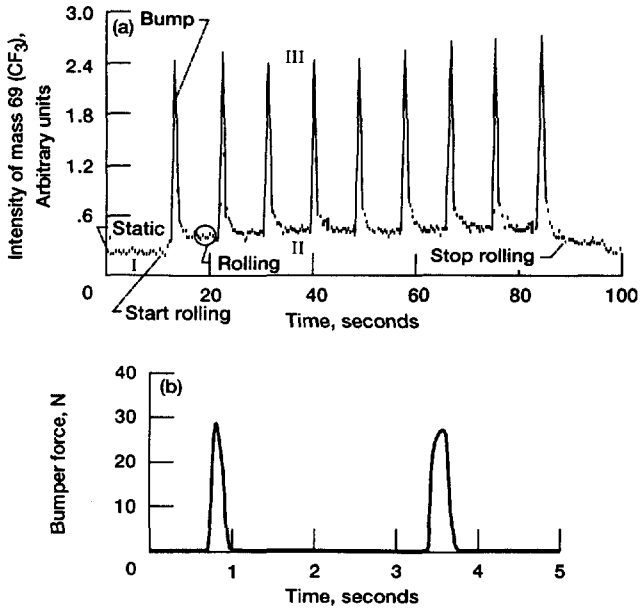

Figure 7.—(a) Intensity of mass 69 (CF_3) from residual gas analyser as a function of time. (b) Bumper force as a function of time (lubricant, Krytox 16256; load, 140N; vacuum, 10^{-6}Pa; speed, 6 RPM).

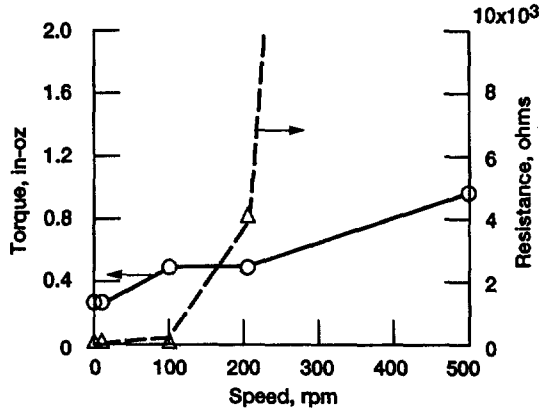

Figure 8.—Bearing torque and contact resistance as a function of speed (44.5N hard load).

DESIGN OF A HIGH-SPEED RELIABLE BALL BEARING

Herbert B. Singer and Erik Gelotte
The Charles Stark Draper Laboratory
Cambridge, Massachusetts

SUMMARY

A high-speed, reliable ball bearing has been designed for at least fifteen years of operation in space effectors, MWAs, and RWAs. Advance bearing concepts have been used in this design, such as: no ball retainer, which eliminates all retainer-related problems; an external lubricating system that will supply the lubricant at a specified flow rate; and a cartridge assembly that will allow the instrument user to purchase a ready-to-use bearing assembly, with lubricator. Currently, two assemblies are on life test at 12,000 RPM and have accumulated over 20,000 hours, each, with consistent low-torque losses. The paper will describe each of the salient features.

SALIENT FEATURES

Retainerless Design

The ball retainer has been eliminated to ensure no retainer-related problems, such as retainer instability (squeal). Dr. Kingsbury has shown that contrary to current theory there is a lubricant film between the balls to ensure no ball damage during operation. These tests will be described.

External Lubricator

An external lubricator, named an *oozing flow lubricator*, has been designed to give a specified flow rate of lubricant to the ball contacts. The oozing flow lubricator is shown schematically in Figure 1. The lubricant is driven through the interface by the centrifugal pressure head caused by the rotation of the lubricator. Thus, at storage conditions, no oil is lost from the lubricator.

The flow rate of the oil is controlled by the properties of the interface; for high interfacial pressures, the flow is only proportional to the cube of the flow channels' dimension. These channels can be controlled either through surface finish controls or other means. The flow is also controlled by the oil viscosity.

As the oil is lost from the lubricator, the head and the flow rate change exponentionally with running time.

Screening tests will be described to measure the flow rates from four oozing flow lubricators. See Figure 2. A correlation of flow rate with surface finish will be established.

Optimum Flow Rate Determination

Parched EHD theory was used to determine the optimum flow rate for the bearing size, a basic 100-size design, preload (10 pounds), and speed, 12,000 RPM. The tests on the counter-rotating rig will be described to show that a flow of at least 0.2 micro-grams per hour would be needed to maintain a parched EHD film.

Cartridge Bearing Design

A cartridge bearing design was selected for this bearing assembly. See Figure 1. Based on the expected loads and environment, the bearing was designed to have a pitch diameter of a 100-size bearing. There are fourteen (14) 0.1875-inch diameter balls in each bearing row. The reservoir and the ID of the outer races comprise the oozing flow lubricator. Nye 176A oil, a PAO with a kinematic viscosity of 437 CS at 100°F, is the lubricant of choice. This cartridge design with the lubricator and shaft is configured so that a competent bearing manufacturer can produce and screen the assembly. This will relieve the instrument manufacturer from handling the ball bearing.

Life Tests

Two bearing assemblies, one with a wheel and one as a cartridge only, is running at 12,000 RPM for over 20,000 hours. Torque and oil flow rates are periodically measured. The change of oil flow rate with time follows the prediction. See Figure 3. The torque losses at 12,000 RPM are around 0.4 in-oz and are consistent with time for both bearings. See Figure 4.

Figure 1.

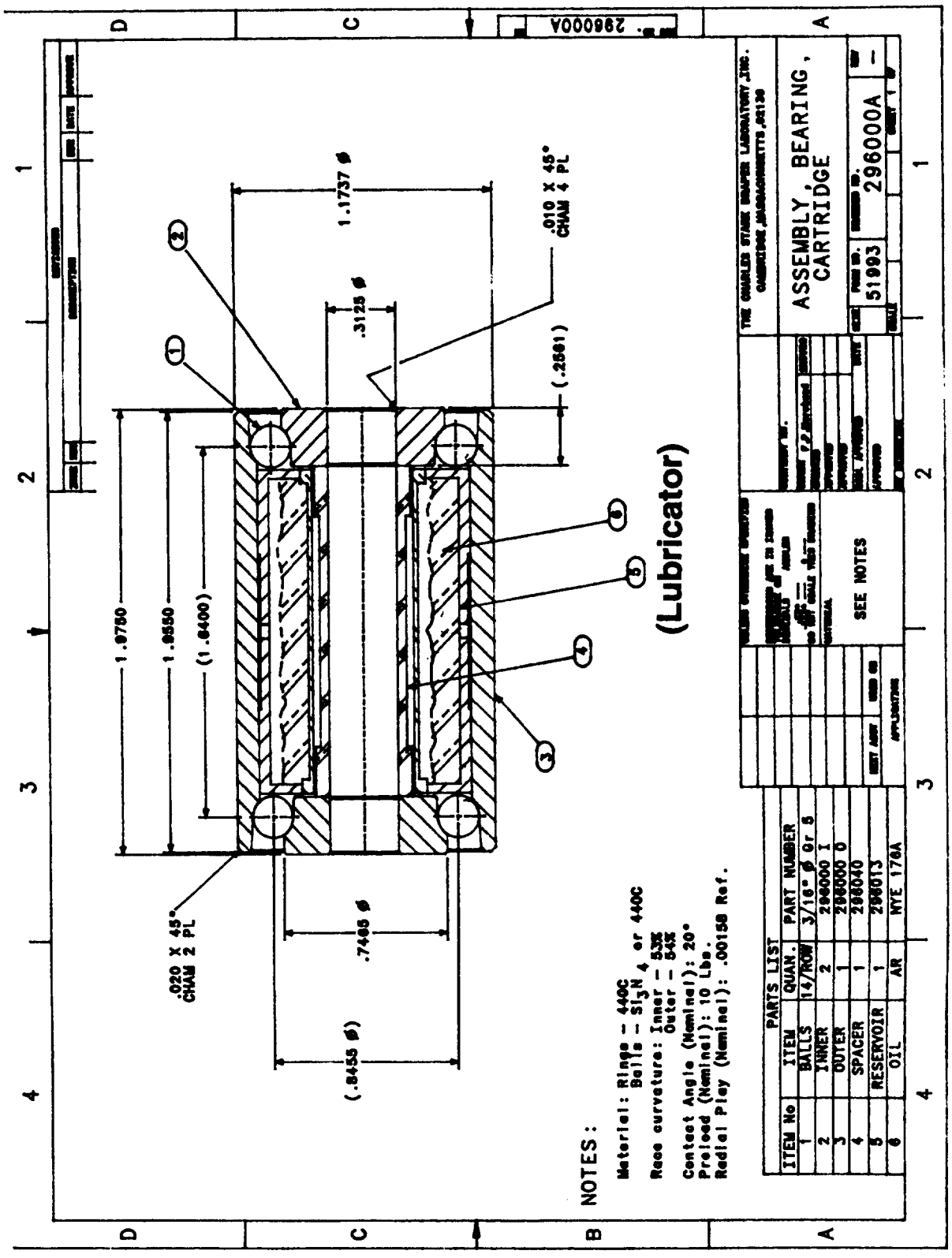
ASSEMBLY, BEARING, CARTRIDGE
296000A
51993
SEE NOTES
(Lubricator)
1.1737 ø
.3125 ø
.010 X 45° CHAM 4 PL
(.2501)
1.9750
1.9550
(1.8400)
.020 X 45° CHAM 2 PL
.7465 ø
(.8455 ø)
NOTES:
Material: Rings - 440C
Balls - Si_3N_4 or 440C
Race curvature: Inner - 53%
Outer - 54%
Contact Angle (Nominal): 20°
Preload (Nominal): 10 Lbs.
Radial Play (Nominal): .00158 Ref.
PARTS LIST
ITEM No | ITEM | QUAN. | PART NUMBER
1 | BALLS | 14/ROW | 3/16" ø or 5
2 | INNER | 2 | 296000 I
3 | OUTER | 1 | 296000 O
4 | SPACER | 1 | 296040
5 | RESERVOIR | 1 | 296015
6 | OIL | AR | NYE 178A

Figure 2.

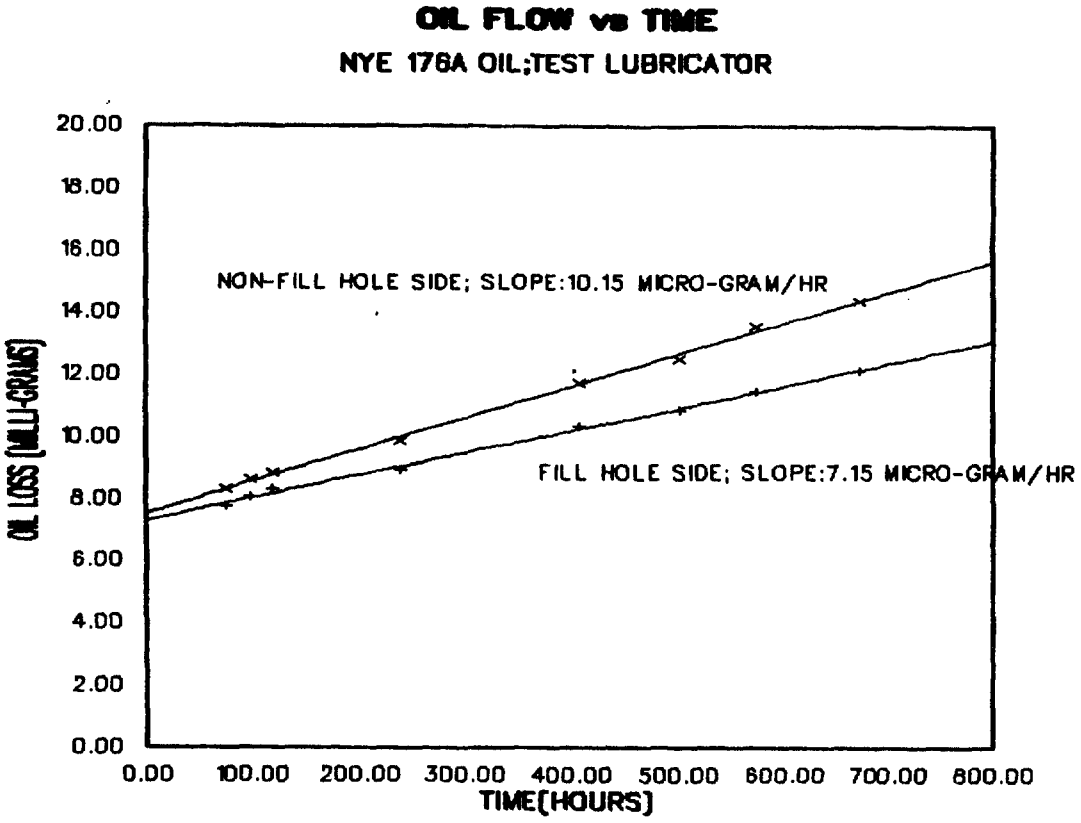

Figure 3a. Flow Rates for S/N 005

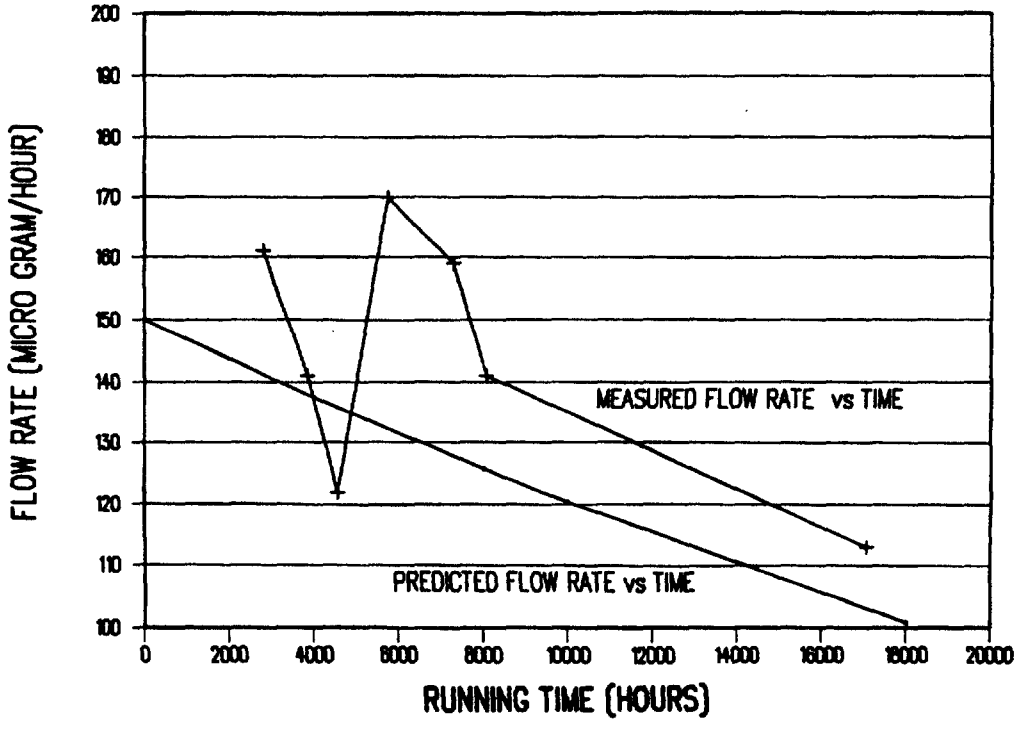

Figure 3b. Flow Rates for S/N 007

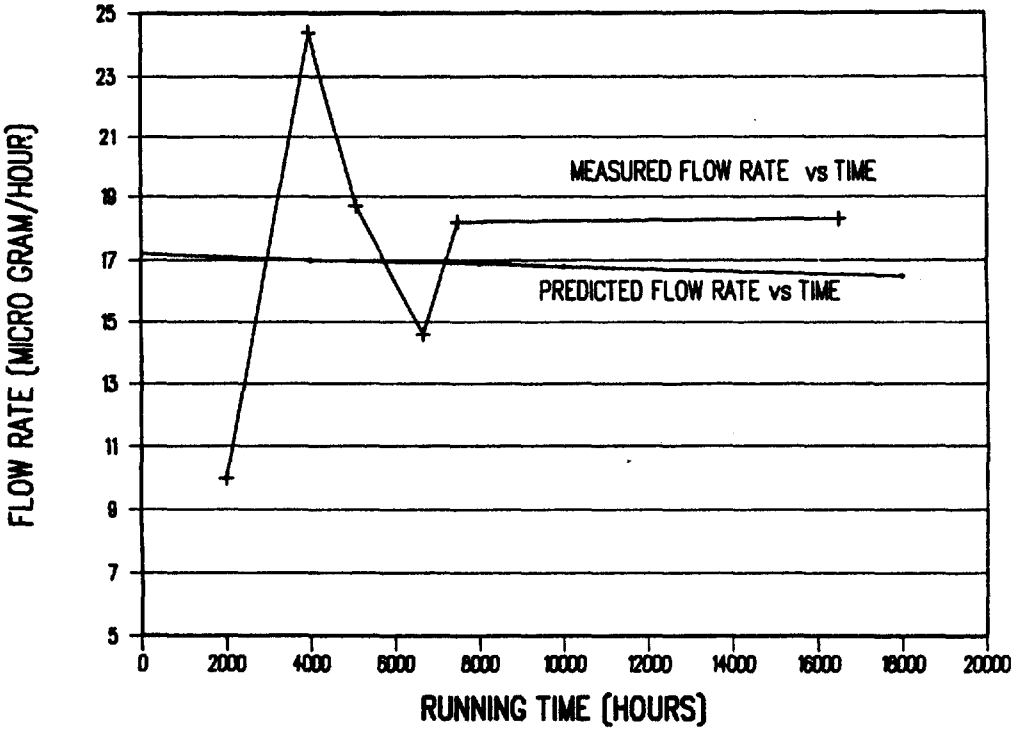

FIGURE 4. CARTRDGE BEARING LIFE TEST

TORQUE vs RUNNING TIME

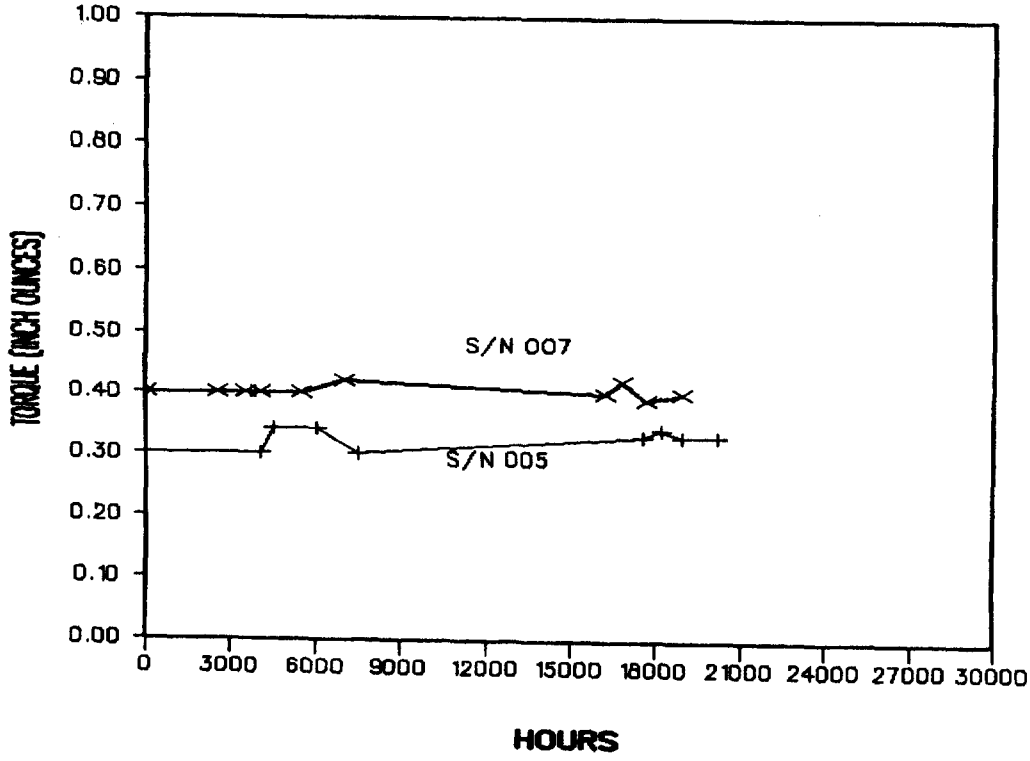

MSAT BOOM JOINT TESTING AND LOAD ABSORBER DESIGN

D.H. Klinker, K. Shuey, and D.R. St. Clair
Lockheed Missiles and Space Co.
Sunnyvale, California

ABSTRACT

Through a series of component and system-level tests, the torque margin for the MSAT booms is being determined. The verification process has yielded a number of results and lessons that can be applied to many other types of deployable spacecraft mechanisms.

The MSAT Load Absorber has proven to be an effective way to provide high energy dissipation using crushable honeycomb. Using two stages of crushable honeycomb and a fusible link, a complex crush load profile has been designed and implemented. The design features of the Load Absorber lend themselves to use in other spacecraft applications.

INTRODUCTION

MSAT is a commercial project developing a satellite-based cellular telephone, data, and fax network that will provide coverage throughout North America. When the system is fully operational, MSAT will have two satellites, each having two large Wrap-Rib™ reflectors used to transmit and receive data. The reflectors are positioned on the satellites by graphite epoxy booms as shown in Figure 1. The MSAT booms offer a number of lessons and design solutions that can be applied to many types of deployable spacecraft mechanisms. This paper will provide an overall description of the MSAT booms and focus on two specific aspects: torque margin verification testing, and design and testing of an energy dissipating mechanism.

SECTION 1: BOOM DESCRIPTION

MSAT Wrap-Rib™ reflectors, designed and manufactured by Lockheed Missiles and Space Co. (LMSC), will be used to transmit and receive communications data on the MSAT satellites. The reflectors are parabolic with a maximum distance from rib tip to rib tip of 5.7 meters. Each reflector consists of a reflective mesh material supported by 16 flexible aluminum ribs attached to a 81-cm-diameter hub. The ribs are designed such that they can be tightly wound around the hub when the reflector is stowed. During deployment the ribs unwind to form a parabolic shape.

The reflectors are supported on the the spacecraft by graphite epoxy booms. Each boom has three joints ("Shoulder", "Elbow", and "Wrist"), connecting three graphite epoxy tubes, with a "Load Absorber" and "Reflector Positioning Mechanism" (RPM) at the end of the boom (See Figure 1). The Load Absorber is

used to dissipate energy from the reflector deployment and reduce the loads on the boom and spacecraft. The RPM (provided by Hughes Space and Communications) is used to provide fine pointing adjustments.

All three of the boom joints have essentially the same mechanism components: an eddy-current damper, two constant-torque laminated springs, two sets of duplex-pair angular-contact bearings, and a latch. Figure 2 shows the typical cross-section of each joint. The size and shape of each joint is different (see Figure 3), however they all share a common mechanism core.

The Load Absorber mechanism is shown in Figure 4. When the reflector ribs "lock-up", the Load Absorber interface plate rotates about the Load Absorber bearings. As it rotates, honeycomb in the Load Absorber Megatube is crushed, limiting the torque applied by the reflector and absorbing some of the energy of the deployment. Two stages of honeycomb are used in order to give two levels of crush force. After the honeycomb has been crushed and rotation about the Load Absorber bearing is stopped, the Load Absorber spring returns the Load Absorber interface plate back to its original position.

Over 95% of all boom surfaces are shielded from Passive Intermodulation (PIM) by PIM blankets, which also provide thermal protection. PIM is an electromagnetic phenomenon that is caused by energy being radiated off of PIM sources and interfering with incoming signals. PIM sources include such things as junctions of dissimilar metals, bolted interfaces, sharp corners, etc. The PIM shields have become quite complex and produce significant drag during deployment.

Power to the RPM is provided by a command and telemetry cable that runs the length of the boom. Also running the length of the boom are two pyro harnesses used to fire pinpullers at the joints and the reflector release mechanism. All of these harnesses cross the joints and Load Absorber producing significant drag at low temperatures.

SECTION 2: JOINT TORQUE MARGIN VERIFICATION

This next section will focus on the MSAT boom mechanism testing used in the torque margin verification process. Torque margin testing of the MSAT Reflector Boom joints produced a number insights on what tests should be performed on mechanisms and how to improve the efficiency of mechanisms testing. This section will give an outline of the torque margin verification method, a description of each component test, and present highlights from the test results.

TORQUE MARGIN DEFINITION

Torque margin is calculated using the following formula:

$$\text{Torque Margin} = \frac{\text{Deploying Torque} - \text{Dynamic Torque}}{\text{Resistive Torque}} - 1$$

For the boom joints, "Deploying Torque" is provided by the two constant-torque laminated springs. "Resistive Torques" are from harness bending, blanket bending, bearing friction, latching friction as well as less obvious sources such as spring losses due to interlaminate friction, and damper drag due to internal gear friction within the dampers. "Dynamic Torque" is resistance to deployment caused by spinning of the spacecraft. Due to the relatively low spin rate of the MSAT spacecraft during deployment (1 rpm), the dynamic torque does not significantly affect torque margin.

TEST PLAN

Torque margin verification testing was divided into three phases. Phase 1 involved testing the components that went into the joints separately prior to installation in the joints. Phase 2 involved testing the assembled joints prior to being bonded with the graphite epoxy tubes and Phase 3 tests are currently being performed on the assembled booms. Table 1 shows which parameters were measured during each phase of testing.

Table 1
Torque Margin Test Plan

	Phase 1 (Component)	**Phase 2** (Joints)	**Phase 3** (Booms)
Spring Torque	Ambient	Ambient	
Spring Friction	Ambient	Ambient	
Damper Drag	Ambient Cold Temp		
Damping Rate	Ambient Cold Temp		
Latch Friction (Protoflight only)		Ambient	Ambient (Hot & Cold Vac.)
Bearing Friction (Protoflight only)		Ambient	Ambient (Hot & Cold Vac.)
Harness Bending Torque (Protoflight only)			Ambient (Hot & Cold Vac.)
Blanket Bending Torque (Protoflight only)			Ambient (Hot & Cold Vac.)

As shown in Table 1, the spring torques and frictions are not measured at high or low temperatures. This was done primarily to save on testing time but also because it was assumed that no significant changes in the spring torque or the spring friction are likely to occur over the protoflight temperature range of -22°C to +46°C. The springs are stainless steel that have stiffness properties that do not change significantly at the MSAT protoflight temperatures, making it unlikely that the torque available will change significantly. The properties of the dry-film lubrication used on the springs also do not change significantly at the protoflight temperatures.

Early on in the program, testing of the joints was given high priority by the design team. Designers working on the test equipment worked closely with the mechanisms designers to assure that the joints could be tested thoroughly and efficiently. Strong emphasis was placed on automating testing as much as possible in order to speed up the testing of all twelve joints. Most of the component and joint tests were run with motor-driven fixtures controlled by the same computer used for data acquisition. A MacIntosh-based data acquisition program called LabView[1] provided flexible data acquisition options with very little programming time. Test fixtures were designed specifically for the MSAT joints making it very easy to set up and conduct tests. While these steps required a sizeable initial investment, they proved to provide significant reductions in testing time.

PHASE 1: COMPONENT TESTING

Spring Torque and Friction Tests

All of the joint deployment springs were component tested at ambient conditions by mounting them on a motor-driven fixture that cycled the springs three times and plotted the torque vs. angle hysteresis loops as shown in Figure 5. The torque available from the spring is the average between the stowing and deploying torques and the spring friction is half the difference between the stowing and deploying torques.

Springs were ordered with 6, 7, and 8 laminates in order to provide a range of torques from which to choose from. After all the springs were tested, the combination of springs that provided the desired torque was selected. For example, at the elbow one 7-laminate spring and one 8-laminate spring are used, while at the shoulder and wrist two 8-laminate springs are used. Having the flexibility to change torques by simply changing springs proved to be very valuable when additional torque was required in the development program.

Damper Component Testing

Each joint has an eddy-current damper installed along the axis of the joint as shown in Figure 2. The principles of the Honeywell-built eddy-current dampers are discussed in some detail in Reference 1. Basically, an eddy-current damper

[1] LABView, National Instruments Inc.

consists of a copper disk spinning between samarian-cobalt magnets, and a 4-stage planetary gear train. The damping rate at room temperature can be varied from 1100 $^{N\text{-}m\text{-}s}/_{rad}$ to 2200 $^{N\text{-}m\text{-}s}/_{rad}$, by rotating a plate on the back of the damper that changes the alignment of the magnets.

Extensive component tests were run on each eddy-current damper to determine damper drag and damping rate over temperature. Damper drag is defined as the minimum torque necessary to cause the damper to rotate 360° without stopping.

Damper drag was tested to be on the order of 4.5 to 5.6 N-m, which was one of the primary sources of resistance in the joints. This was an important factor in the torque margin calculation because the damper friction largely drove the spring requirements, which in turn drove the damping requirements. In other words, selection of the eddy-current damper led to the requirement for larger springs, which led to the requirement for higher damping rates to accommodate the larger springs. Unfortunately, the higher damping rate and spring torques led to higher loads on the damper which is limited to 79.1 N-m. Meeting all the requirements required very careful balancing of these factors.

Damping rate was determined by applying a known torque on the damper and measuring the rotation vs. time. Figure 6 shows how the damping rates over temperature varied for two different dampers. Tests run over temperature demonstrated that damping rates vary widely from damper to damper. The temperature variation for each damper is most likely caused by changes in lubrication fluid viscosities, and changes in internal tolerances of the dampers at low temperatures. The variation in damping rate between different dampers is most likely caused by manufacturing tolerances.

Note, most of the testing done on the dampers over temperature was done to satisfy a requirement for simultaneity of the boom deployments. This requirement was canceled after the testing was complete, making most of the testing unnecessary. While the information obtained during these tests is interesting, it would have been much more economical to test at only the minimum, maximum, and room temperature, rather than over the range of temperatures.

Cable Harness Bending Tests

As part of the development test program, harness bending torques were measured at ambient and cold temperatures. The information gained from these tests helped in sizing of the deployment springs as well as being used in the final torque margin verification. Harness bending torque is the third largest cause of resistance after damper drag and spring friction.

PHASE 2: JOINT COMPONENT TESTING

Most of the extensive joint tests were run on the joint test stand shown in Figure 7. The joint test stand uses a stepper motor to open and close the joints, while load cells and a potentiometer monitor torque and angle. The stand also has an inertial simulator which approximates the inertial load the joints will see during deployment on the spacecraft. The inertial simulator consists of a bar with weights on the ends connected to the joint through a 20:1 gear box. The 20:1 gear box magnifies the effective inertia of the bar and weights by a factor of 20 squared.

Cold tests were run on the joint test stand by enclosing the inner portion of the stand with foam and spraying liquid and gaseous nitrogen into the enclosed region. The joint test stand proved to be extremely valuable by allowing the joints to be thoroughly tested before installation with the boom tubes, both at room temperature and cold temperature.

The first tests run on the joint test stand were bearing and latch friction tests. During these tests, the joints were opened and closed with no springs or damper installed. The primary purpose of these tests was to determine the latching torque and detect any problems with the bearings. The bearing torque was measured during these test to determine if the correct preload was on the bearings, and to determine if there was excessive drag on the bearings.

Next, the springs were installed and the joints were cycled with the springs to determine spring torque, and spring and bearing friction. Torque curves similar to Figure 5 were obtained, however, during these tests both springs were tested together and the friction value included friction from the fully loaded bearings. The torque information from these tests was used directly in the torque margin calculation as "Deploying Torque".

The last step in the joint acceptance sequence was to install the damper and run a series of deployment tests at both ambient and cold temperatures. During the deployments, the joints were stowed with the motor and then allowed to deploy, rotating the inertial simulator at the same time. These tests were used to determine deployment times and demonstrate that the joints would deploy at cold temperatures.

PHASE 3: BOOM ASSEMBLY TESTING

Deployment testing of the booms provides the remaining information necessary for the torque margin verification. Specifically, it is used to determine the cable harness bending torque, blanket bending torque, and bearing friction torque with all components in flight configuration. As explained earlier, a total of four booms and four reflectors have been built. All four booms will go through at least five deployments at ambient conditions. In addition, one boom will go through a series of protoflight tests, which include one cold and one hot thermal-vacuum deployment. Information obtained at temperature on the protoflight unit will be applied to the other units by similarity.

Boom deployment tests are run on a large aluminum frame that holds the inner boom arm fixed (Figure 8). A spacecraft simulator is attached to the shoulder and is supported by a cable running from a point on the ceiling directly above the shoulder pivot axis to a point on the spacecraft simulator. This cable forms a conical pendulum that offloads the weight of the spacecraft simulator as it deploys about the shoulder axis. The spacecraft simulator has the same inertia about the shoulder axis as the boom and reflector assembly and it also has all of the spacecraft interface attachment points.

A second cable goes from the wrist to a point on the ceiling directly above the elbow. This cable forms a conical pendulum which allows the outer arm to deploy about the elbow axis. The wrist axis is perpendicular to the shoulder and elbow axes. Deployment about the wrist axis requires a counterweight that places the mass center of all parts outboard of the wrist on the wrist axis. Both offload cables have load cells in-line that monitor the loads in the cables during deployment. Having these loads cells proved to be very valuable when diagnosing an alignment problem that will be discussed later.

Strain gages, mounted on a shaft coupled to the damper, are used to measure torque input to the dampers during deployment. Assuming that the joints deploy at a relatively constant rate, the torque input to the damper is equal to the spring torque minus any losses. Therefore losses due to cable harnesses, blanket bending and other non-damper-related losses can be determined by taking the difference between the spring drive torque determined during joint component testing, and the damper drive torque determined during boom deployment tests.

Figure 9 shows a typical damper torque vs. angle curve obtained during deployment testing. Superimposed on the graph are the spring torque results from the joint component test for the particular joint. The difference between the spring torque and the torque from the boom deployment test can be determined as shown in Figure 9. This difference is the total frictional loss of the joint during ambient deployment. It includes blanket friction, cable harness drag, bearing friction, latch friction, as well as test equipment influences. Damper friction and spring friction torques from component testing are added to this resistance to get the total resistive torque.

Three of the booms have completed pre-environmental deployment testing. One more boom will be tested pre-environmental and then all four will be re-tested after vibration and thermal cycling tests. Thermal-vacuum testing of the protoflight boom is scheduled for March, 1994. After the thermal-vacuum tests are conducted, a new total resistive torque value will be determined at cold temperature for one of the booms. This resistive torque will be compared with the ambient torques for that boom to determine what increase in torque was caused by the cold temperature. The resistive torques for the other three booms will then be increased by the same amount to determine their worst case torque margins by similarity.

Boom deployment tests are run on a large aluminum frame that holds the inner boom arm fixed (Figure 8). A spacecraft simulator is attached to the shoulder and is supported by a cable running from a point on the ceiling directly above the shoulder pivot axis to a point on the spacecraft simulator. This cable forms a conical pendulum that offloads the weight of the spacecraft simulator as it deploys about the shoulder axis. The spacecraft simulator has the same inertia about the shoulder axis as the boom and reflector assembly and it also has all of the spacecraft interface attachment points.

A second cable goes from the wrist to a point on the ceiling directly above the elbow. This cable forms a conical pendulum which allows the outer arm to deploy about the elbow axis. The wrist axis is perpendicular to the shoulder and elbow axes. Deployment about the wrist axis requires a counterweight that places the mass center of all parts outboard of the wrist on the wrist axis. Both offload cables have load cells in-line that monitor the loads in the cables during deployment. Having these loads cells proved to be very valuable when diagnosing an alignment problem that will be discussed later.

Strain gages, mounted on a shaft coupled to the damper, are used to measure torque input to the dampers during deployment. Assuming that the joints deploy at a relatively constant rate, the torque input to the damper is equal to the spring torque minus any losses. Therefore losses due to cable harnesses, blanket bending and other non-damper-related losses can be determined by taking the difference between the spring drive torque determined during joint component testing, and the damper drive torque determined during boom deployment tests.

Figure 9 shows a typical damper torque vs. angle curve obtained during deployment testing. Superimposed on the graph are the spring torque results from the joint component test for the particular joint. The difference between the spring torque and the torque from the boom deployment test can be determined as shown in Figure 9. This difference is the total frictional loss of the joint during ambient deployment. It includes blanket friction, cable harness drag, bearing friction, latch friction, as well as test equipment influences. Damper friction and spring friction torques from component testing are added to this resistance to get the total resistive torque.

Three of the booms have completed pre-environmental deployment testing. One more boom will be tested pre-environmental and then all four will be re-tested after vibration and thermal cycling tests. Thermal-vacuum testing of the protoflight boom is scheduled for March, 1994. After the thermal-vacuum tests are conducted, a new total resistive torque value will be determined at cold temperature for one of the booms. This resistive torque will be compared with the ambient torques for that boom to determine what increase in torque was caused by the cold temperature. The resistive torques for the other three booms will then be increased by the same amount to determine their worst case torque margins by similarity.

SECTION 3: LOAD ABSORBER DESIGN DEVELOPMENT

The MSAT Load Absorber has proven to be an effective way to dissipate unfurling energy for the MSAT reflectors. It is a non-viscous energy dissipating mechanism with potential applications in other systems requiring low-weight, non-velocity dependent, and high energy dissipating capability. The next section of this paper will discuss the design characteristics of the Load Absorber, describe the key Load Absorber lessons learned, and present the current acceptance and qualification test status of the Load Absorbers.

LOAD ABSORBER DESIGN

The need for the Load Absorber arose after a development boom and reflector had already been built and the four end-items units were in assembly. During testing of the development reflector, it was determined that the reflector would need to be redesigned to stiffen the ribs allowing the reflector to maintain shape after deployment in 1 g. Stiffening the ribs resulted in increased predicted deployment energy, producing lock-up loads on the spacecraft and boom which were much higher than allowed. It was the need to reduce the loads that led to the implementation of the Load Absorber in parallel with the redesign of the reflector.

The following were the key design drivers for the load absorber:

1) Implementation late in the program required quick development, incorporation within existing envelopes, and mating to existing hardware.
2) Complicated force coupling required that the force profile be well defined, weight be minimized, and variability in force be minimized.
3) Maximum reflector unfurling energy must be known to avoid bottoming out against the boom structure and the resulting high forces.
4) To ensure reflector rib lockup, the force reaction had to exceed 17 N-m for a minimum of 1 second.
5) All boom mechanism requirements were to be met, including 175% torque margin for the return springs.
6) Alignment and positional repeatability errors had to be minimized so as not to significantly increase the overall pointing error for the assembly.

These requirements were met by adding an energy-absorbing mechanism called a Load Absorber at the end of the boom near the reflector hub. A key aspect of the Load Absorber is how the reflector rotational motion is converted to axial motion. During unfurling of the reflector, a torsional loading is applied to the the Load Absorber interface plate (See Figure 4). The interface plate is connected to the boom through a duplex-ball-bearing interface that allows the plate to pivot about the bearing axis. As the interface plate rotates, the torsional load is converted to axial loading on the Megatube honeycomb assembly through a high-strength stainless steel band operating on a constant radius cam. The kinetic energy associated with the unfurling is dissipated by the linear crushing of the honeycomb. After the honeycomb has been crushed, a constant-torque spring returns the Load Absorber to its original configuration. The return spring also

provides sufficient preload of the load absorber to maintain pointing accuracy, even with the specified on-orbit spacecraft excitations.

Initially, the Load Absorber had only one cylinder of honeycomb producing a single reaction load level during reflector deployment. The honeycomb crush strength and stroke were sized to absorb the estimated deployment energy from the stiffened end-item reflector. Because of the uncertainty in the estimates of the reflector energy, the initial end-item reflector deployment was performed with a stronger crush strength honeycomb. This was allowable since the test was not performed on the end-item boom. The energy absorbed by the stronger honeycomb in this test indicated that the reflector deployment energy would significantly exceed the energy absorption capability of the honeycomb intended for flight use.

In order to absorb the additional energy and still keep the loads transmitted to the boom and spacecraft acceptable, a longer, softer honeycomb was required. However, this conflicted with the minimum torque required to ensure reflector lockup. Therefore, the Load Absorber was redesigned to incorporate a two-stage honeycomb system. During the first approximately 15 degrees of Load Absorber rotation, (approximately 1 second of reflector unfurling), the crush strength was sufficient to lockup the reflector ribs. Following rib lockup, a low torque, long duration, energy dissipation phase was implemented. See Figure 10 for the design configuration and Figure 11 for the two-stage force profile. Note Figure 11 shows both a minimum and maximum crush force profile, the actual profile will lie in the working domain depending on the deployment energy.

In the two-stage design, the honeycomb is stacked in series such that initially both pieces of honeycomb are being crushed at the same time. A mechanical fuse is used to allow the two honeycomb phases to function together. Each piece of honeycomb is grounded to the Megatube, passing loads directly from the honeycomb to the support boom tube. When the phase I honeycomb (2.5 cm) reaches solid crush height, a fusible link is fractured and the phase II honeycomb continues crushing at its lower load level.

Both phases of honeycomb are contained within the Megatube assembly. This assembly is comprised of two tubular frames supported by a "T" bracket and an "L" bracket. The "T" bracket is the primary load path to the boom mating bolt interface. The "L" bracket has an axial degree of freedom along the tube to allow for thermal expansion and contraction of the aluminum tube on the graphite boom.

KEY LESSONS LEARNED

Development testing also indicated that the friction between the piston and the guide tube played a critical role in the repeatability of the load absorber assembly crush force. It was initially anticipated that the honeycomb would crush straight, with little tendency to deform in a bending mode. In actuality, the minor variation in position of the honeycomb relative to the band force caused a

significant side force between the piston and the tube. Several different lubricants were employed including dry films (moly-disulfide and Anotef) as well as moly grease, however, the magnitude and variability in the friction properties were not satisfactory. Therefore, low friction wheels employing ball bearings were incorporated into the piston assemblies for each phase of the honeycomb.

The mechanical fuse was selected as the simplest concept to connect the two honeycomb cylinders and provide the desired two-stage crush force profile. The fuse is a tensile specimen designed for ultimate failure; it is an aluminum part with a functional diameter of 0.318 cm and a working length of approximately 1.27 cm polished to an 8 micro-finish. Development testing of the fusible links demonstrated that by pretesting all fusible links to 2% yield prior to installation the ultimate failure load could be accurately predicted within 5%. The fusible links have 2335 N yield strength and an additional +98 N force is required for fracture.

Knowledge of the actual loads being reacted by the Load Absorber was critical in the development of the final design. To gain this information, the bands were instrumented with strain gages and calibrated to 5338 N. This calibration also served as a proof test of each band.

The need to implement the two-stage Load Absorber, with the associated schedule and weight impacts, indicate the criticality of having the design requirements accurately defined early. The fact that the Load Absorber design and reflector redesign were proceeding in parallel made it difficult to accurately determine the reflector unfurling energy. In this situation, more conservatism in the design of the initial Load Absorber would have been helpful.

LOAD ABSORBER STATUS

At this time, the Load Absorber design has been qualified; four end-item units have been built, acceptance tested, and are installed on the end-item booms. This process included a series of torque margin tests very similar to those described previously for the boom as well as functional tests (both ambient and thermal) to validate each Load Absorber meets the force profile shown in Figure 11.

In addition to these four flight units, a fifth flight-quality Load Absorber has been built and acceptance tested to support the deployment tests of the end-item reflectors. This unit has been tested during actual deployments of the flight reflectors in ambient and thermal-vacuum environments.

CONCLUSION AND SUMMARY

The plan behind the MSAT boom torque margin verification can be summarized by the following guidelines:

1. Identify and understand all parameters that will affect the torque margin as early as possible.

2. Involve test personnel early in the design process to ensure testability of the hardware.

3. When testing several units, emphasize making test equipment automated and data acquisition systems easy to program and use.

4. Thoroughly test all components before installation in assemblies to detect problems early. However, test in environmental conditions only the parameters that are expected to have significant impact.

5. Thoroughly analyze test fixtures to identify test equipment influences.

Each of these guidelines is intended to discover potential problems as early and make the testing as efficient as possible. For the most part these guidelines were successfully followed on the MSAT booms, with the most notable exception being the problems that occurred during boom deployment testing. These guidelines along with the lessons learned from the actual testing provide a good example that can be applied to many other types of spacecraft mechanisms.

The MSAT Load Absorber has proven to be an effective way to dissipate unfurling energy for the MSAT reflectors. The ability to create a complex load profile, using two stages of honeycomb and fusible link, has been effectively demonstrated. The lessons learned from the load absorber design and testing can be applied to other types of spacecraft mechanism requiring low weight, high energy dissipation.

ACKNOWLEDGMENTS

The authors would like to acknowledge Dave Putnam who was responsible for coordinating the design of the booms, as well as developing the testing strategy, and Darrell Shen whose effort made the Load Absorber possible. We would also like to thank Ed Boesiger for his editorial assistance.

REFERENCES

1. Ellis, R.C., Fink, R.A., Rich, R.W., "Eddy Current Damper", Proceedings of the 23rd Aerospace Mechanisms Symposium, May 1989, NASA Conference Publication 3032.

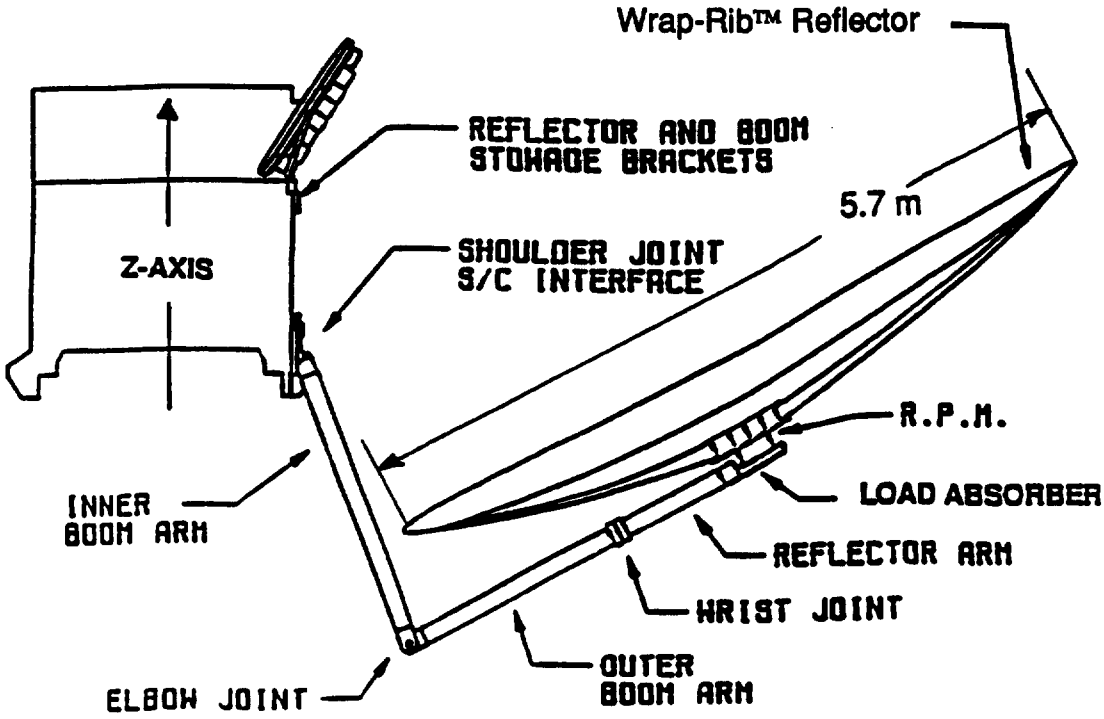

Figure 1. MSAT Reflector and Boom Deployed Configuration

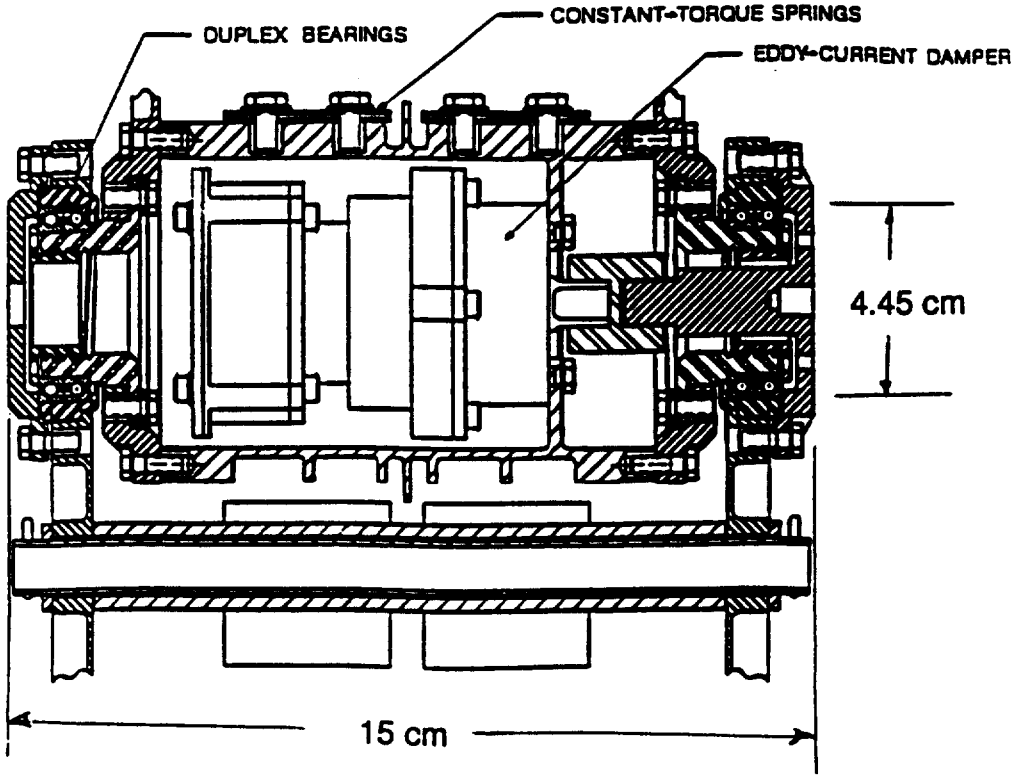

Figure 2. Wrist Joint Cross-section

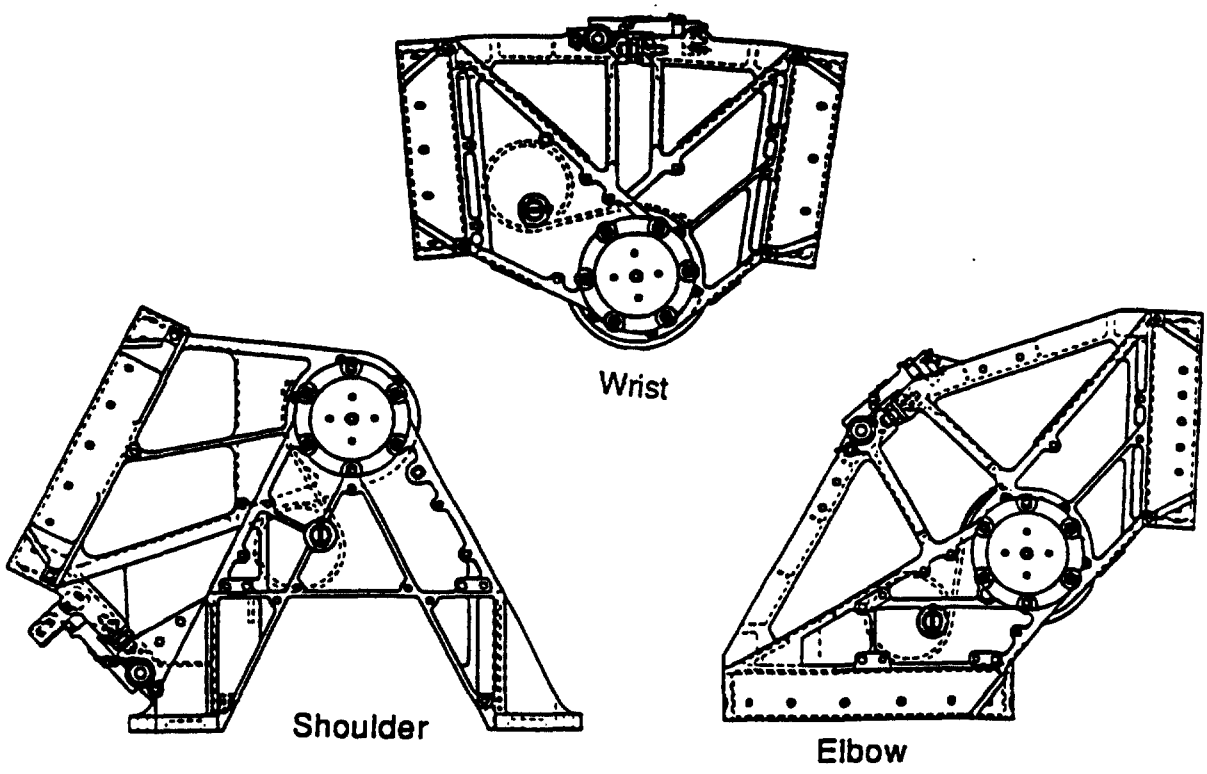

Figure 3. MSAT Boom Joints Deployed Configuration

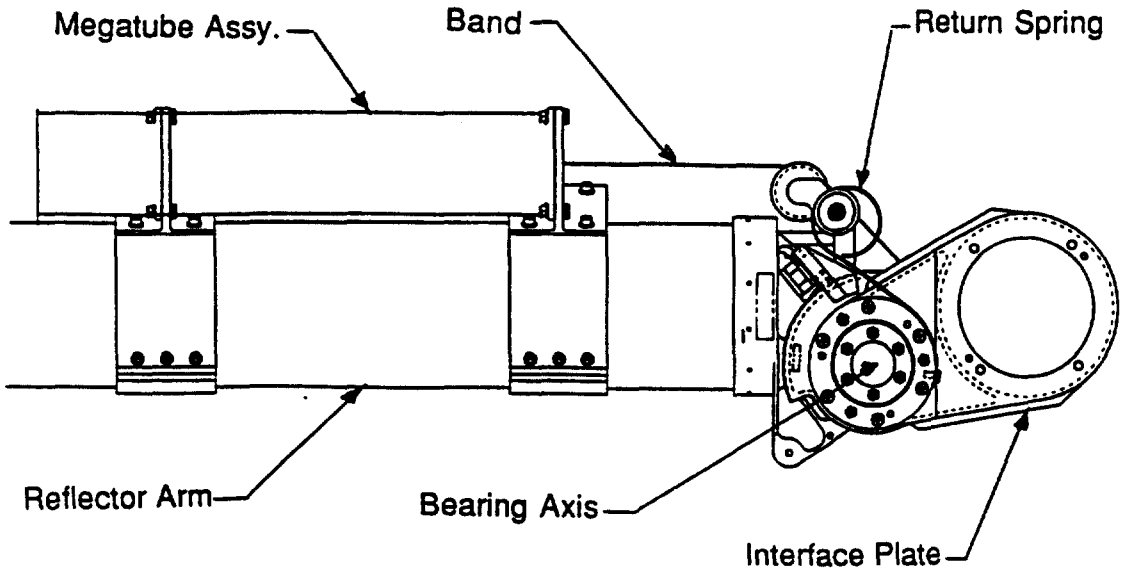

Figure 4. MSAT Load Absorber

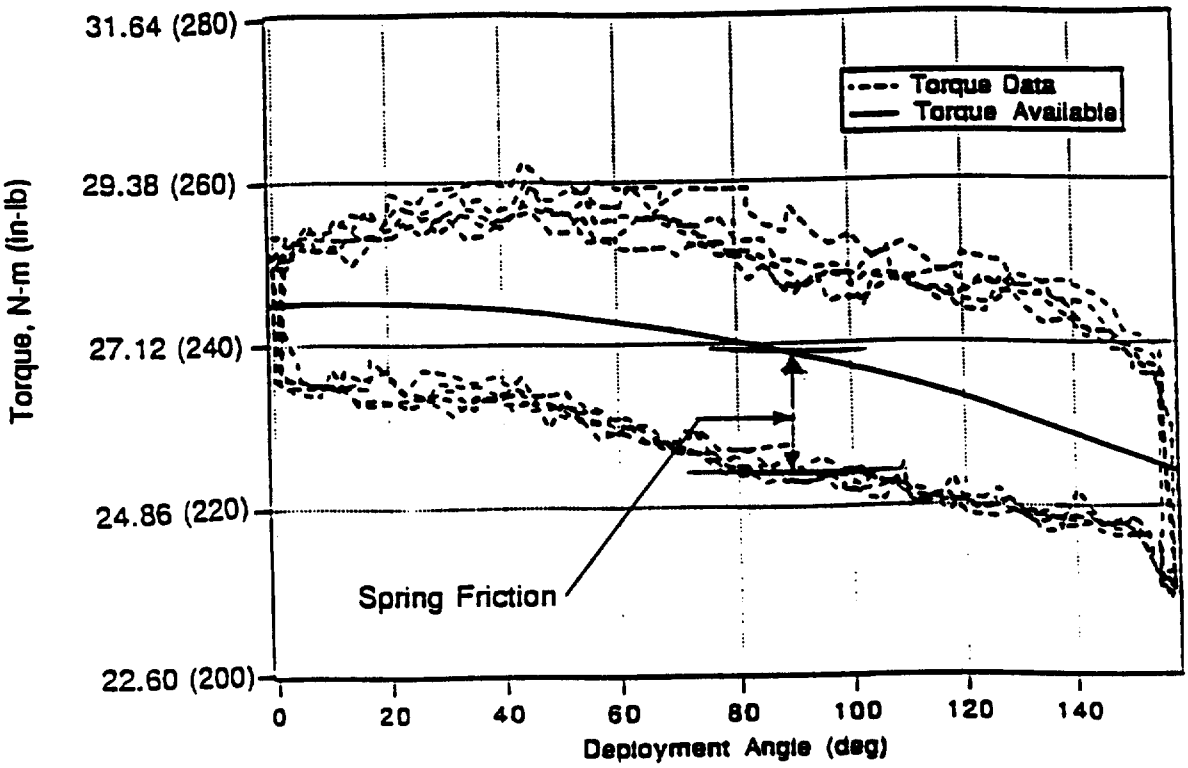

Figure 5. Shoulder Spring Torque vs. Deployment Angle
Data from spring component testing

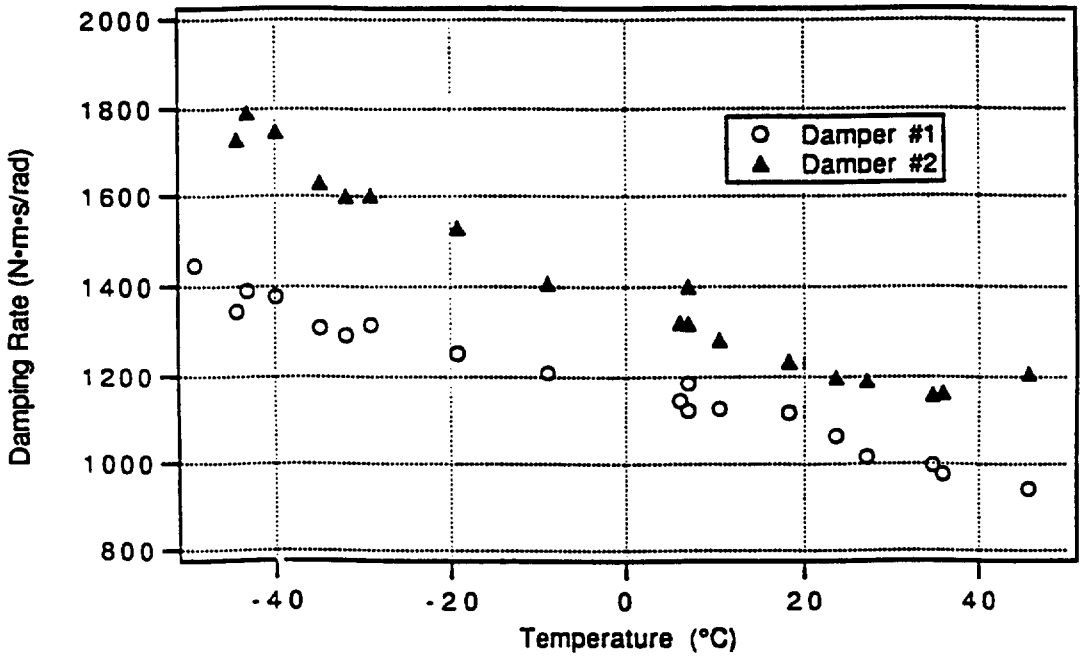

Figure 6. Damping Rate vs. Temperature for 2 Dampers
Data from damper component testing.

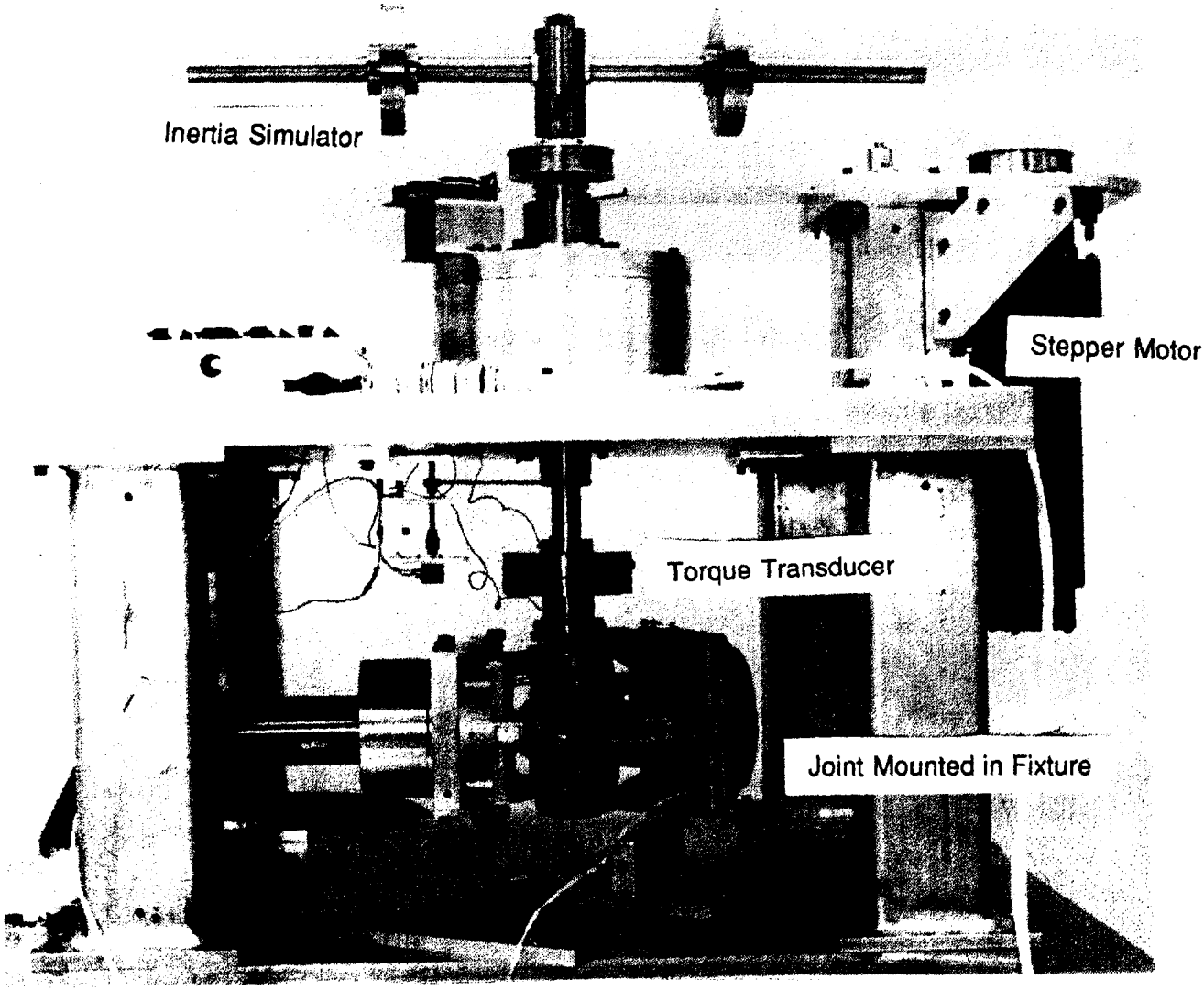

Figure 7. Joint Test Stand with Joint Installed

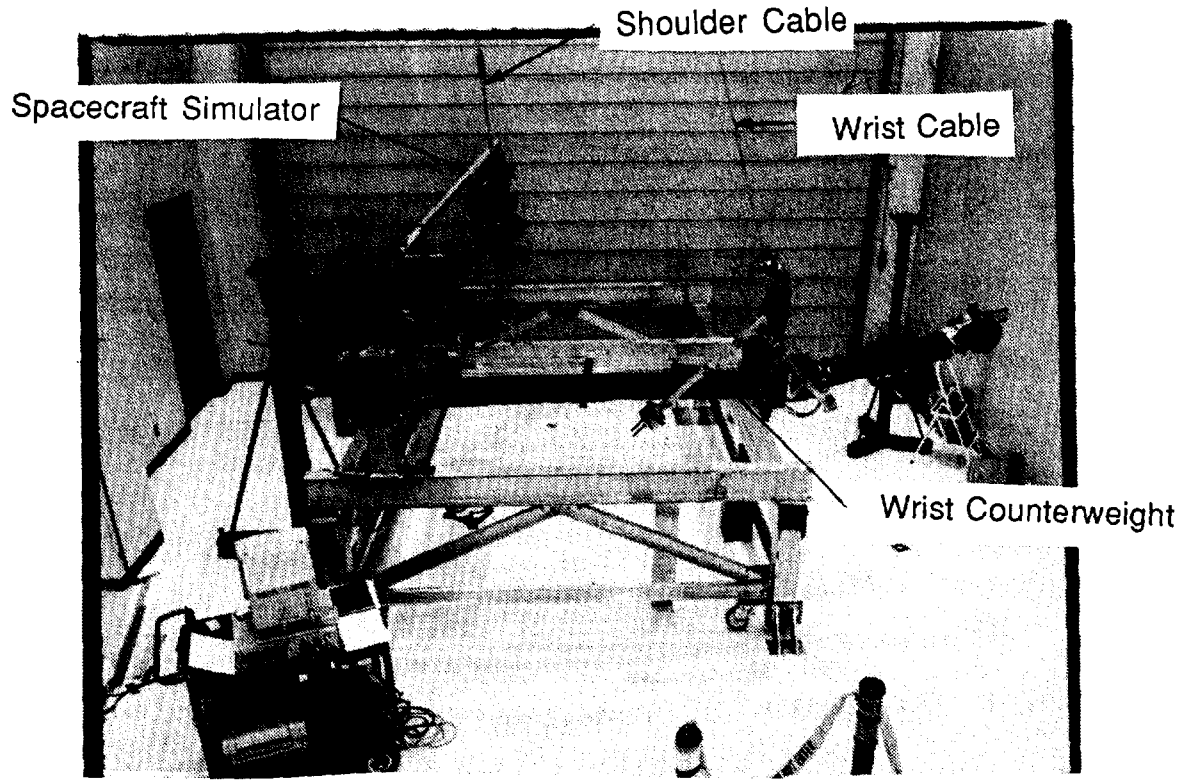

Figure 8. Boom Deployment Stand with Development Boom Installed

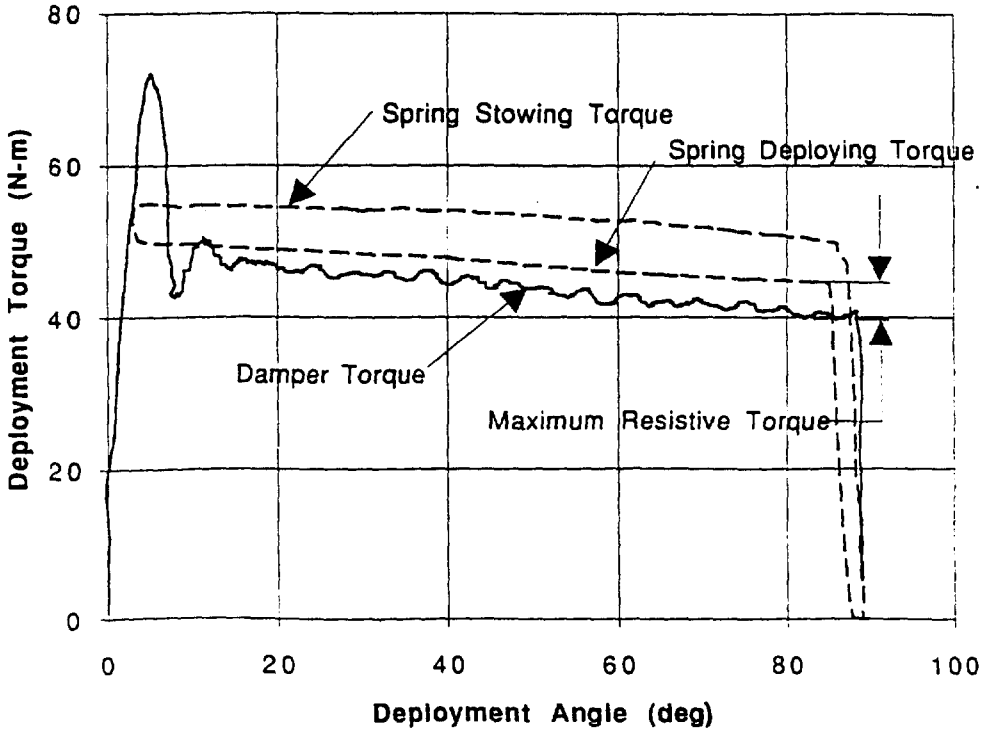

Figure 9. Damper and Spring Torque vs. Angle
(Damper torque determined during boom deployment testing, spring torque determined during joint component testing)

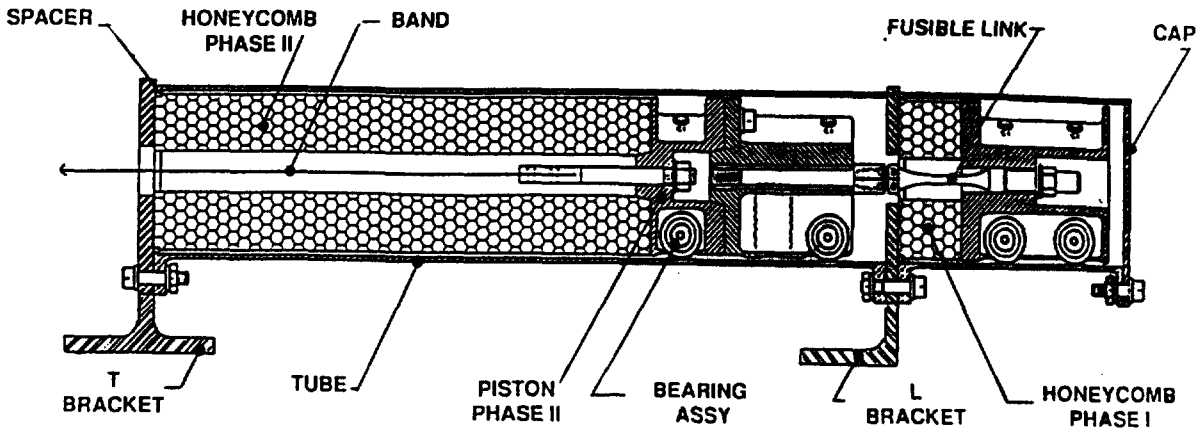

Figure 10. Load Absorber Megatube Assembly

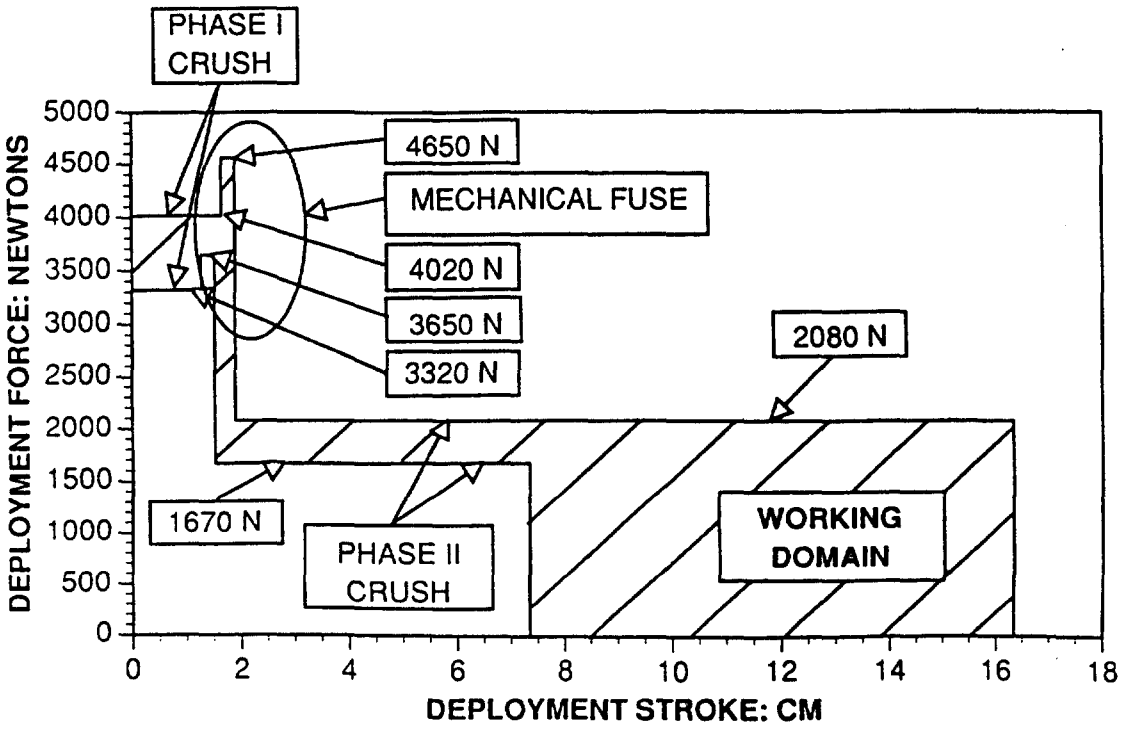

Figure 11. Load Absorber Force Profile
(Maximum and minimum profiles shown. Actual profile in working domain.)

SPECIAL TEST EQUIPMENT AND FIXTURING FOR MSAT REFLECTOR ASSEMBLY ALIGNMENT

Jeffrey A. Young, Michael R. Zinn, and David R. McCarten
Lockheed Missiles and Space Co.
Sunnyvale, California

ABSTRACT

The MSAT Reflector Assembly is a state of the art subsystem for Mobile Satellite (MSAT), a geosynchronous-based commercial mobile telecommunication satellite program serving North America. The Reflector Assembly consisted of a deployable, three-hinge, folding-segment Boom, deployable 5.7 x 5.3-meter 16-rib Wrap-Rib™ Reflector, and a Reflector Pointing Mechanism (RPM). The MSAT spacecraft was based on a Hughes HS601 spacecraft bus carrying two Reflector Assemblies independently dedicated for L-band transmit and receive operations. Lockheed Missiles and Space Company (LMSC) designed and built the Reflector Assembly for MSAT under contract to SPAR Aerospace Ltd. Two MSAT satellites were built jointly by SPAR Aerospace Ltd. and Hughes Space and Communications Co. for this program, the first scheduled for launch in 1994.

When scaled for wavelength, the assembly and alignment requirements for the Reflector Assembly were in many instances equivalent to or exceeded that of a diffraction-limited visible light optical system. Combined with logistical constraints inherent to large, compliant, lightweight structures; "bolt-on" alignment; and remote, indirect spacecraft access; the technical challenges were formidable. This document describes the alignment methods, the special test equipment, and fixturing for Reflector Assembly assembly and alignment.

INTRODUCTION

The MSAT Spacecraft Bus and Reflector Assemblies are illustrated in Figure 1. In operation, the MSAT Satellite consisted of the MSAT Bus with deployed Transmit and Receive Reflector Assemblies. From spacecraft interface to outboard end, the Boom Assembly consisted of 3 hinges, Shoulder, Elbow and Wrist, a Load Absorber Mechanism, and 3 interconnecting graphite-epoxy tubes. Deployed Interface Shims were used in-between the Shoulder Hinge Base and Spacecraft. The Reflector was mounted on the Load Absorber, attached to it by the Reflector Pointing mechanism (RPM), RPM Shim and Spider. The RPM, built and furnished by Hughes, was a two-axis gimbal mechanism for on-orbit reflector-to-spacecraft tip and tilt alignment correction. The Deployed Interface and RPM shims were plane-parallel and for contingency use only.

The Spider was the critical structural element by which Reflector attachment to the Boom Assembly and ground alignment to the Spacecraft were simultaneously achieved. Integrated Alignment was the operation which established and manufactured the Spider to its requisite form: wedge, axial separation, and shear

(decenter and clocking) relationship of the Reflector Hub and RPM interfaces. Spider manufacture, free-state characterization of the Boom Assembly and remote site transfer of the spacecraft interface and coordinate system were the challenging aspects of Reflector Assembly alignment and verification. All of these technical challenges were resolved by precision special test equipment (STE) and fixturing.

Reflector Assembly Alignment Overview

The baseline methodology for MSAT Spacecraft alignment required that Reflector Assembly alignments be performed independent of the Spacecraft Bus. Bolt-on alignment interfacing of the Reflector Assembly to the Spacecraft Bus at the end of the project was to be relied upon to 1) accurately orient and position the deployed reflector relative to the spacecraft-mounted reflector feeds, and 2) achieve a less critical stowed fit.

In response, the Reflector Assembly alignment and verification (A&V) was architectured with heavy reliance upon master & slave drill tool pairs; precision templates to establish and transfer spacecraft interface hole patterns. Two sets of master/slave drill tools were used, one set for the Transmit Reflector Assembly and a second for the Receive Reflector Assembly. Each set consisted of two master/slave tool pairs, one for the deployed interface and the other for the stowed interface. Both spacecraft were serviced by these two sets of master/slave tools. For the alignment-critical spacecraft deployed interface, the master/slave tooling was also relied upon to transfer spacecraft coordinate system knowledge from the Spacecraft Bus A&V site to the remote Reflector Assembly A&V site. Reflector Assembly A&V would follow, coordinated to the Spacecraft Coordinate System as-represented by the drill tools.

Master/slave drill tool use was adopted because it was a simple, low tech, low cost, high reliability manufacturing technique for establishing and transferring precision interfaces. Its practicality drove the decision to use master/slave tools for all alignment-sensitive pinned interfaces on the Reflector assembly: LMSC-Hughes interfaces involving the Hughes-supplied RPM and Reflector Assembly (RPM-Spider and RPM-Load Absorber interfaces), and LMSC intrafaces (Reflector Hub-Spider). All STE and fixturing that attached to any master/slave drill tool-controlled interface had their interfaces similarly generated.

An alignment plan and alignment error budgets were generated in accordance with this philosophy, which accommodated constraints associated with offloading large, compliant, lightweight structures; remote spacecraft access; and no practical means to perform end-to-end alignment verification tests. The fundamental elements of the Reflector Assembly alignment plan are detailed in Figure 2. The alignment plan relied upon subassembly-level testing, alignment-repeatable interfaces, high performance STE and fixturing. Stringent attention to manufacturing and test workmanship was required, especially when alignment-critical interfaces were involved. The RSSed error budgets were the principle means of evaluating error propagation, suballocating requirements and incorporating interface "bolt-on" alignment repeatability and other manufacturing

tolerances. Two methods of estimating "bolt-on" alignment repeatability were used. The first was by RSS-based hand calculation and the second was computerized variation simulation analysis (VSA). Both methods took into account the geometric tolerancing of component interface features for the two mating parts comprising the interface. Tests on STE, breadboard mock-ups and flight hardware, verified these modeling techniques.

Boom Assembly Alignment And Verification

The Boom Assembly was constructed on the Boom Assembly and Retention Tool (BART), a dual purpose assembly and alignment fixture. Initially, BART was used to mechanically fixture boom components during Boom assembly. Afterward, during Integrated Alignment, it was reconfigured to fixture the Boom Assembly in its free-state condition. BART, detailed in Figure 3, consisted of a three-legged/two-sided 90° "fence" weldment that supported 5 vertical "Smart Plates". Each "Smart Plate" featured a boom component tooling interface and 3 tooling balls that were used to establishing plate manufacturing and alignment datums. BART design was based on modular fixturing concepts, to coordinate and simplify BART manufacturing, assembly and alignment. Boom assembly and alignment consisted of 1) interfacing the 3 hinges, Load Absorber Mechanism and boom stow fitting upon their BART tooling interfaces to establish their required alignment, and 2) installing and attaching the 3 interconnecting graphite epoxy Boom Tubes. Two BART fixtures were made, one for the assembly of Transmit Boom Assemblies, the other for the Receive Boom Assemblies. For Integrated Alignment, the Load Absorber Mechanism, Wrist Hinge and Elbow Hinge interfaces were reconfigured with adjustable boom retention clamps. The Shoulder Hinge tooling interface was not reconfigured.

Measuring and verifying BART alignment stability was a major concern, in particular the flexible 90° sidewall-sidewall configuration. The solution was to kinematically interface BART to the floor and establish accurate and redundant BART coordinate system references. The BART-facility floor interface: The corner column leveling foot was bolted directly bolted to the floor. The 2 end column leveling foot locations rested upon identical single degree-of-freedom translation stages, "soft" axes oriented parallel to the BART walls. BART coordinate system references: Three tooling balls mounted on top of the BART columns in a precise, level, 90° arrangement defined the local BART Coordinate System. The 3 axis-adjustable BART Cube Module cube was accurately oriented orthogonal to this coordinate system. The smart plate balls and Spacecraft Cube Module cube served as redundant coordinate system references. The 3 axis-adjustable Spacecraft Cube Module was used to define nominal spacecraft orientation and was a back-up reference for the Spacecraft Coordinate System cube on the Shoulder Drill Tool. Over the duration of the program (approx. 1 year) no alignment changes could be measured for BART and co-aligned optical cubes. Angular measurement accuracy was ± 3.4 μrad (7 arc sec/0.005 in over 120 in). Position measurement accuracy was ± 0.13 mm (0.005 in) or better.

Reflector Assembly And Verification

The fundamental elements of Reflector assembly and alignment are detailed in Figure 2. Reflector assembly (Figure 4) consisted of attachment and alignment of 16 ribs to the Reflector Hub, surface mesh integration, and concluded with surface contour adjustment to obtain the desired shape and shape alignment. A coordinate measuring theodolite system was used for this final task, measuring approximately 600 surface-mounted targets. All of these assembly and alignment operations, plus Integrated Alignment, were coordinated to optical and mechanical references on the Reflector Reference Tool (RRT). The RRT, shown in Figure 6, was used to establish the Reflector Hub Coordinate System, a local coordinate system orthogonal to the Reflector Hub geometry. Its functional requirements were: Accurate and stable coordinate system references, accurate recalibration and realignment of these references, and repeatable interfacing onto the Reflector Hub Strongback. Each reflector had a dedicated RRT and Reflector Hub Strongback.

RRT references consisted of 4 equally-spaced retro-reflective button targets, 4 equally-spaced tooling balls, a fifth "ambiguity" retro-reflective target (to prevent photographic misinterpretation of targets) and an optical octagon with 3 axis-adjustable mount. The octagon mount consisted of a box flexure stage (tip and tilt) topped by a rocker hinge flexure (clocking) that supported the octagon. Granite table metrology was used to determine the local (X, Y, Z) position of all four (4) balls and five (5) targets. Optical and mechanical runout techniques (air bearing rotary table and granite table metrology) were used to align the octagon orthogonal to the target-defined coordinate system. The octagon was aligned to the to 4.8 μrad (10 arc sec) or better in each degree of freedom and this alignment was maintained for the duration of the program (> 1 year). Alignment repeatability of the RRT on the strongback was 1.5 μrad /0.05 mm (4 arc sec/0.002 in) or better.

Spacecraft Interfaces and Spacecraft Coordinate System Transfer

Master and slave drill tools established the Reflector Assembly-to-Spacecraft deployed and stowed interfaces. The master tool generated the interface on both the Spacecraft Bus and the slave tool. The slave tool generated the interface on the Reflector Assembly. All interfaces were "flange-style": flat and coplanar mating surfaces, fastener clearance holes and shear pin holes. Only the shear pin holes required accurate drilling and reaming, the only precision required of the transfer process. Flat and coplanar mating surfaces were essential on the flight hardware and master/slave tooling, especially where high accuracy bolt-on alignment was expected. Hand lapping was frequently performed to establish flatness and coplanarity better than 0.013 mm over 250 mm (0.0005 in over 10 in).

Spacecraft Interface Transfer: The deployed interface slave tool was mechanically aligned to 'nominal position" relative to the Shoulder Hinge, see Figure 7, and the hole pattern transfer drilled and reamed into the hinge base. The stowed interface slave tool relied upon its deployed interface features (generated using the deployed interface master tool) to mechanically align the stowed

Reflector Assembly. Transfer drilling of holes typically held true-position accuracy of ±0.008 mm (0.0003 in) and diameter accuracy of ±0.005 mm (0.0002 in).

Spacecraft Coordinate System Transfer: The deployed interface master/slave tools were also used to transfer spacecraft coordinate system knowledge to the Reflector Assembly A&V site. At LMSC, the slave tool, the Shoulder Drill Tool (SDT), functioned as a spacecraft simulator. The SDT was calibrated in conjunction with the spacecraft-calibrated master tool, the HAC Tool. The calibration process, shown in Figure 7, was performed with the two tools interfaced to each other. Calibration was always performed horizontally, resting on a foam pad to obtain the "free-state" condition. Both tools had alignment references that consisted of 3 tooling balls and an optical cube. The SDT cube, mounted on a 3 axis-adjustable flexured gimbal stage, was aligned "dead-on" to the Spacecraft Coordinate System. Using a coordinate measuring machine, the SDT tooling balls positions were measured in relation to the HAC Tool tooling balls and transformed into spacecraft coordinates. The measured interfacing repeatability of the HAC Tool and SDT was 4.8-7.3 μrad (10-15 arc sec) and 0.018-.038 mm (0.0007-0.0015 in). Tooling ball calibration measurement accuracy was 0.013-0.018 mm (0.0005-0.0007 in) and 2.4-3.4 μrad (5-7 arc sec) for theodolite-based cube alignments. Cube alignment granularity was approximately 1.5-2.4 μrad (3-5 arc sec) and alignment to the Hac Tool/theodolite-defined Spacecraft Coordinate System was under 4.8 μrad (10 arc sec).

Integrated Alignment: Strain-Free Boom Assembly Operations

Three separate tests were conducted to measure and verify strain-free fixturing of the Boom Assembly on the BART Fixture, the necessary precondition for Reflector-to-Spacecraft Bus alignment. A fourth, independent, test was performed to verify Boom Assembly alignment stability. The STE and fixtures used in these tests, and their relationship to the Boom Assembly are detailed in Figures 8 through 12. The basic procedures for these tests were cube-to-cube angular measurements using optical theodolites and target-target (or tooling ball) position measurements using a coordinate measuring theodolite system. All measurements were made relative to coordinate system established by STE attached to the Shoulder Hinge Base, a Spacecraft Bus structural "ground".

Strain-Free Test #1: Boom Assembly, suspended on cables by the 3 BART-mounted boom offloaders, was "floated-in" relative to BART to mate the Shoulder Hinge Base to the Bart Shoulder Hinge tooling interface and the offloaded SDT. Shoulder Hinge Cube Module (SCM; see Figure 9) cube elevation measurements relative to gravity were made to obtain the free-state attitude of the BART-fixtured Shoulder Hinge Base.

Strain-Free Test #2: The floating "free-state" Boom was characterized by this test. Suspended by 3 boom offloaders, the Boom Assembly was leveled to the exact Strain-Free #1 SCM cube attitude. Orientation measurements of the Load Absorber Cube Module (LACM; see Figure 10) and RPM Cube Module (RPMCM; see Figure 11) cubes relative to the SCM cube were then performed. Position

measurements of the RPMCM target and LACM Keel Ball were made relative to the Shoulder Hinge Base tooling balls.

Boom Segment Alignment: The outermost boom segment, Wrist Hinge-to-Load Absorber Mechanism, was "3-1-1-1" kinematically fixtured to BART and aligned to the BART-fixtured Shoulder Hinge per the Strain-Free Test #2 characterization. The Load Absorber Mechanism and Wrist Hinge were constrained by the Load Absorber Clamp (LAC) and the Wrist Clamp Assembly (WCA) respectively. Both tools are detailed in Figure 12. First, Strain-Free Test #1 was repeated to re-attach the Shoulder Hinge to the BART tooling interface and offloaded SDT. SCM cube and Shoulder Base tooling ball coordinate systems were then re-established. A tooling ball was then interfaced to the LAC bushing and the LAC was adjusted to position this ball to the LACM Keel Ball position measured during Strain-Free Test #2. The boom was then adjusted to engage the LACM Keel Ball into the LAC bushing, which kinematically functioned as a cone, to mechanically establish position alignment of the boom outboard end in 3 degrees of freedom. WCA screw adjustments, quantity 3 adjusters, oriented the RPMCM and LACM cubes relative to the SCM cube in 3 angular degrees of freedom; the outermost boom segment pivoting about the Keel Ball/LAC bushing interface. In parallel, the BART-mounted Elbow Hinge jackscrew support point was adjusted until a slight change in LACM and RPMCM cube alignment was detected.

Pre- and Post-Environmental Tests: After completion of Integrated Alignment, Pre- and Post-Environmental Alignment tests were performed on the Boom Assembly to measure boom alignment stability after thermal-vacuum testing. These tests were conducted in a manner identical to Strain-Free Test #2 and included the Spacecraft Interface Cube Module (SICM). The SICM, see Figure 13, was used to establish a local coordinate system at the Deployed Spacecraft Interface. For these tests interface alignment repeatability for the SICM, SCM, LACM and RPMCM was required. The measured angular repeatability for these tools were: SICM ± 2.4 μrad (5 arc sec); SCM and RPMCM ± 4.8 μrad (10 arc sec); LACM ±14.4 μrad (30 arc sec). Position repeatability was less than 0.05 mm (0.002 in) for these tools. SDT-SCM measurements during Strain Free Test # 2 establish Spacecraft Coordinate System traceability to the STE.

Integrated Alignment: Reflector-Spacecraft/Boom Assembly Alignment Operations

Reflector-Spacecraft/Boom Assembly Alignment was conducted in 3 separate operations. The end-item objective of these operations was a completed Spider. The STE and fixtures used in these tests, and their relationship to the Boom Assembly are detailed in Figures 14 through 17. The basic measurement techniques used were cube-to-cube angular measurements using optical theodolites and target-target position measurements using a coordinate measuring theodolite system. Granite table-based mechanical metrology, epoxy replication and jig & fixture machining were used for Spider manufacturing.

Reflector-Spacecraft/Boom Assembly Alignment: The Reflector, supported by the Integrated Alignment Stand (IAS), was first aligned to the Spacecraft

Coordinate System and relative to the free-state fixtured Boom Assembly. The Integrated Alignment Stand (IAS), detailed in Figure 14, was used to support and precisely align the stowed Reflector to the Spacecraft Coordinate System in six degrees of freedom. An adjustable "3-2-1" kinematic platform, the IAS aligned the Reflector Assembly with ±0.5 μrad (1 arc sec) and ±0.025 mm (0.001 in) precision relative to the test equipment and maintained alignment better than 2.4 μrad (5 arc sec) and 0.01 mm (0.004 in. over a 24-hour period. The Spacecraft Coordinate System was defined by the SDT cube (orientation) and tooling balls (position). The RRT octagon, targets and tooling balls similarly defined the Reflector Hub Coordinate System. This alignment operation is shown in Figure 5. Alignment was maintained during strain-free, precision mechanical replication of the RPM-side of the Load Absorber/RPM Interface and the Spider-side of the Reflector Hub/Spider Interface. A secondary mechanical replication operation, performed off-line on a granite table, established mechanical simulation of the Load Absorber-side of the Load Absorber/RPM Interface and the Spider-side of the Reflector Hub/Spider Interface. These two replication operations, and STE, are detailed in Figure 15.

Tooling Spider Fabrication: In this operation, presented in Figure 16, the tooling spider was epoxy-generated using the mechanical simulator. Here the Aft Tooling Spider, RPM and RPM Shim were integrated into the simulator, mechanically aligning the Aft Tooling Spider (RPM-Spider Interface) relative to the Forward Tooling Spider (Reflector Hub-Spider Interface). The Forward Tooling Spider, an integral part of the mechanical simulator, was then epoxied to the Aft Tooling Spider to create the Tooling Spider. The Tooling Spider mechanically represented the required flight Spider in form and feature.

Flight Spider Fabrication: The flight Spider was "cloned" from the Tooling Spider by conventional machining techniques detailed in Figure 17. Forward versus rear interface wedge and clocking, the mechanical form and features that governed Reflector angular alignment, were duplicated to ±0.013 mm over 406 mm (0.0005 in over 16 in) or better. Decenter and axial thickness were duplicated to 0.051 and 0.178 mm (0.002 and 0.007 in) or better, respectively.

CONCLUSION

The STE, fixtures, test equipment and procedures described in this paper were used to successfully ground-align 4 Reflector Assemblies. The budgeted ground alignment requirement for Reflector-to-Spacecraft alignment, as-defined by the Reflector Reference Tool and Shoulder Drill Tool respectively, was ± 29 μrad (1 arc min) in orientation, and ± 1 mm (0.04 in) in position, each degree of freedom. To confirm ground alignment accuracy, Integrated Alignment for the MSAT 1 Transmit Reflector Assembly was independently repeated, including complete Shoulder Drill Tool recalibration to the HAC Tool to re-establish the Spacecraft Coordinate System. The first-replication mechanical simulators generated by these tests were compared and agreed to 87 μrad (3 arc min) and 2 mm (0.080 in) or better. In between these tests the Boom Assembly was subjected to static load testing, which measured Boom Assembly alignment hysteresis of approximately ± 58 μrad (2 arc min) and ± 2 mm (0.08 in).

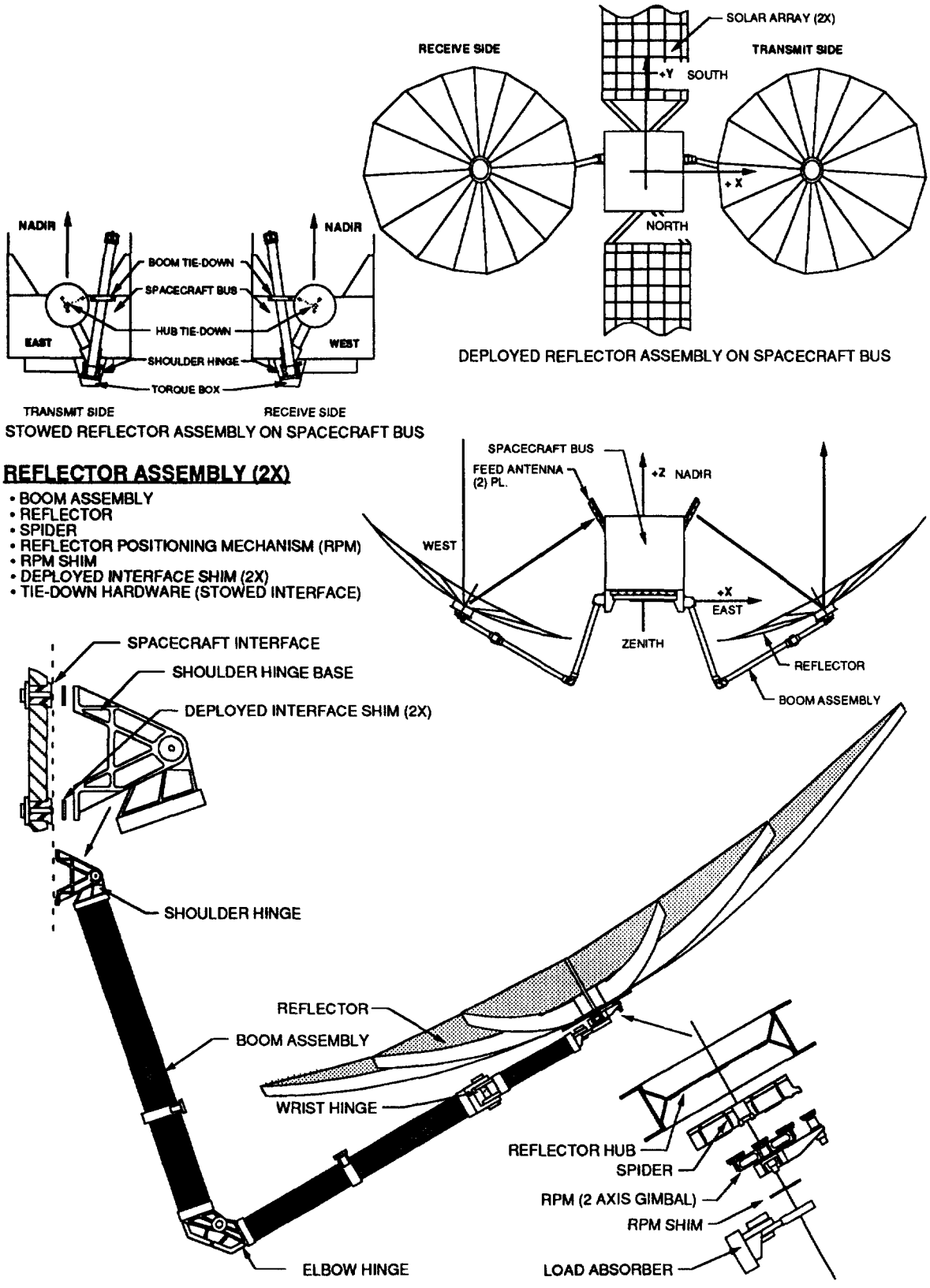

Figure 1 MSAT Reflector Assembly

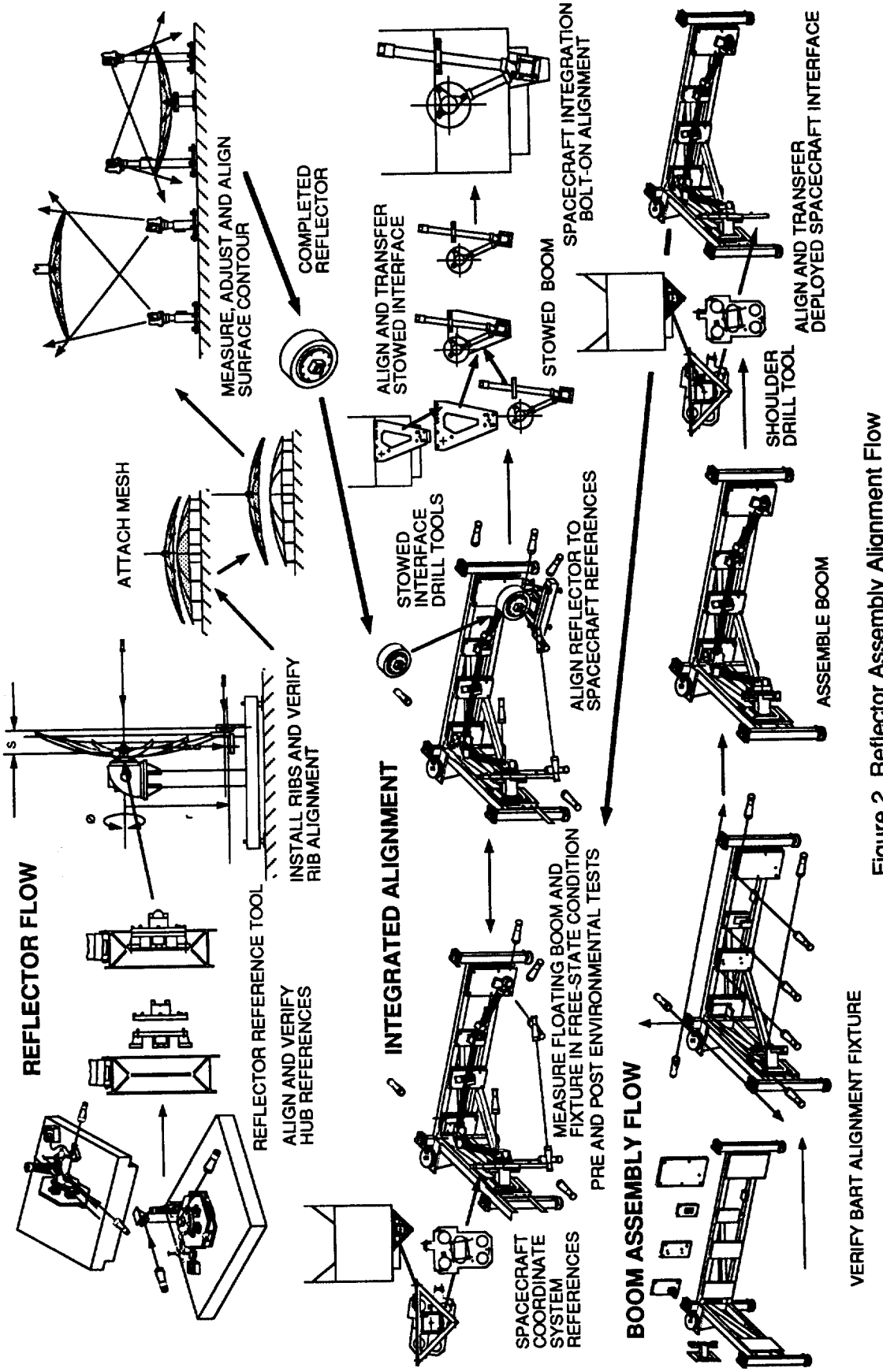

Figure 2 Reflector Assembly Alignment Flow

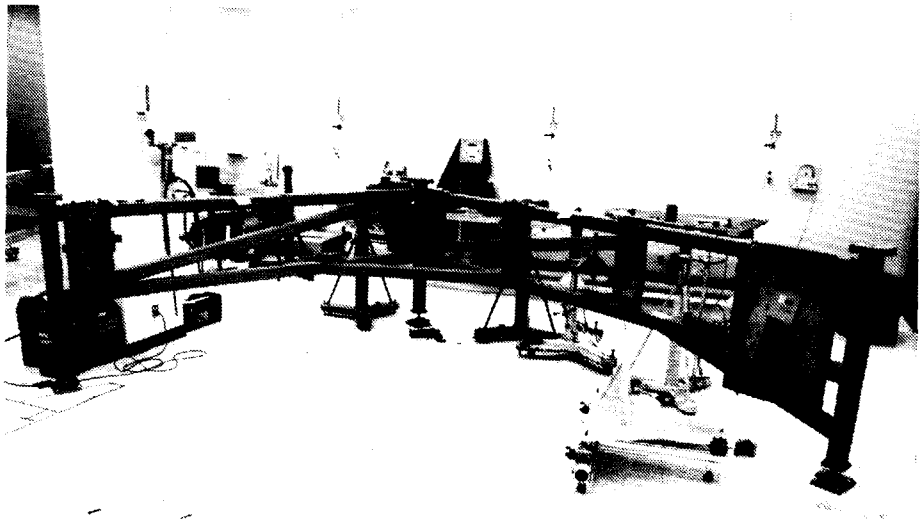

BART FIXTURE FOR TRANSMIT BOOM ASSEMBLY

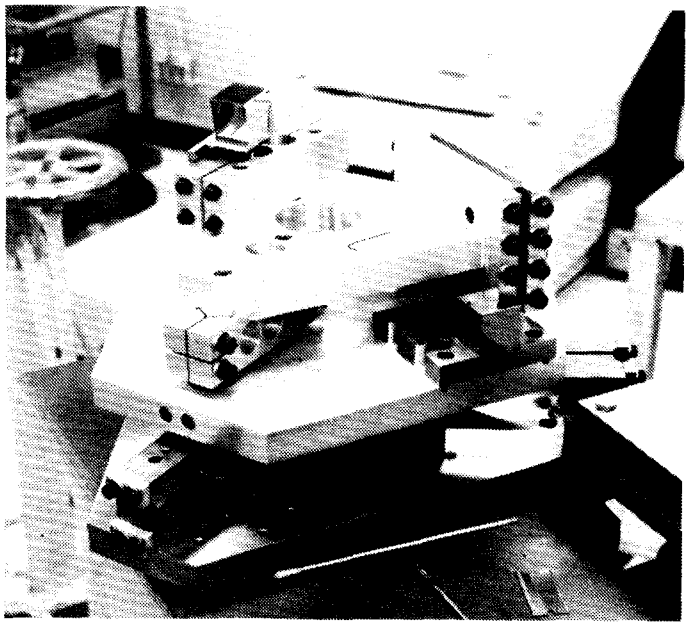

BART FIXTURE AND SPACECRAFT CUBE MODULES

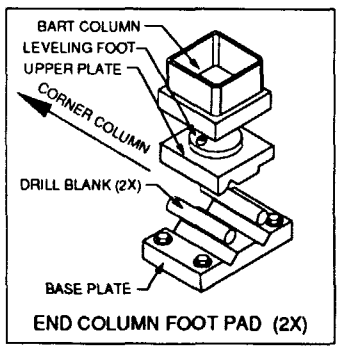

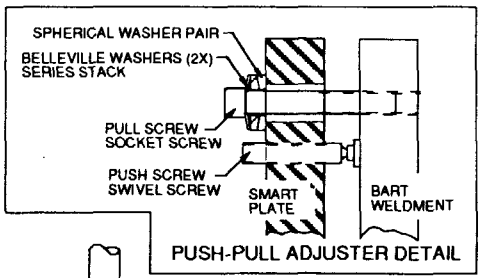

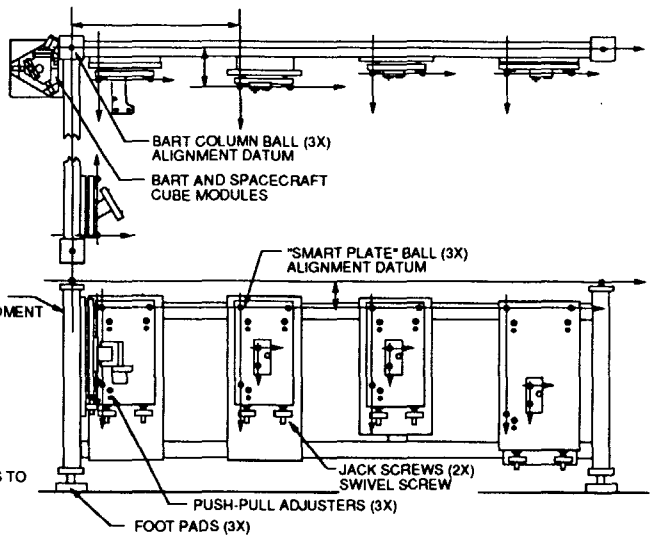

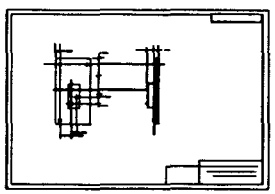

COMPONENT DESIGN COORDINATES TOOLING BALLS AS MFG. DATUMS AND ALIGNMENT REFERENCES

1

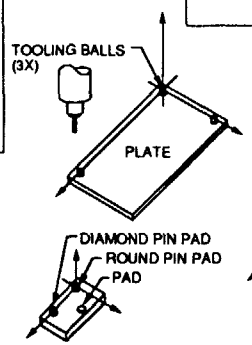

MANUFACTURE COMPONENTS

2

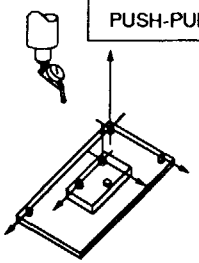

ALIGN AND ATTACH COMPONENT INTERFACE BLOCK TO PLATE ON NC MACHINE

"SMART PLATE" ASSEMBLED

3

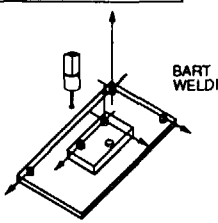

MEASURE COMPONENT INTERFACE BLOCK FEATURES TO PLATE TOOLING BALLS WITH COORDINATE MEASURING MACHINE (CMM)

"SMART PLATE" VERIFIED

4

SMART PLATES ALIGNED ON BART

5

Figure 3 BART Assembly Details

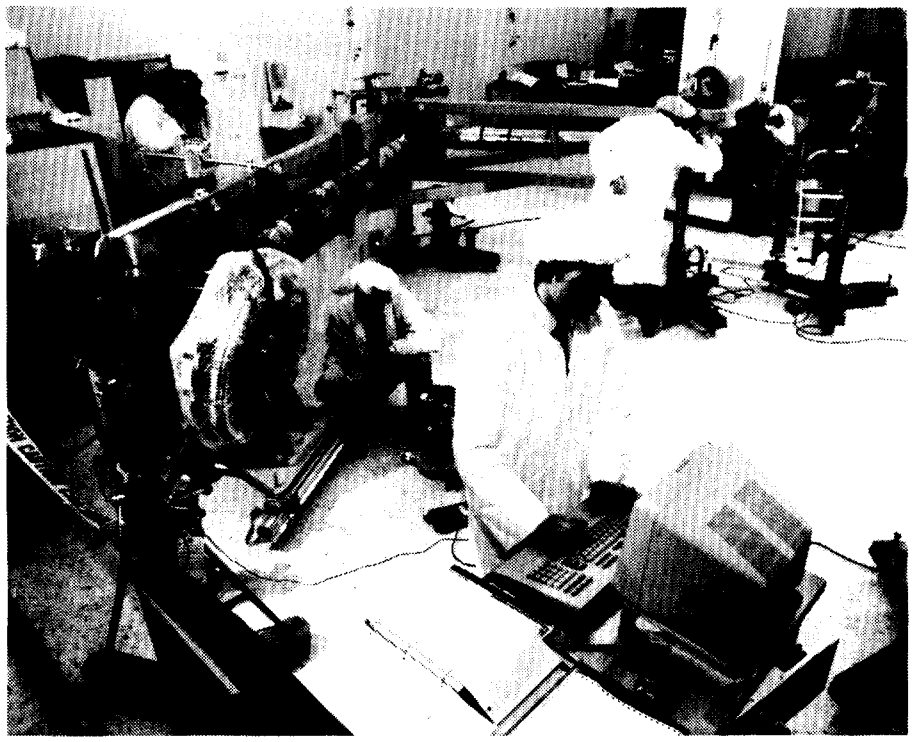

Figure 5 Integrated Alignment, MSAT Receive Reflector Assembly

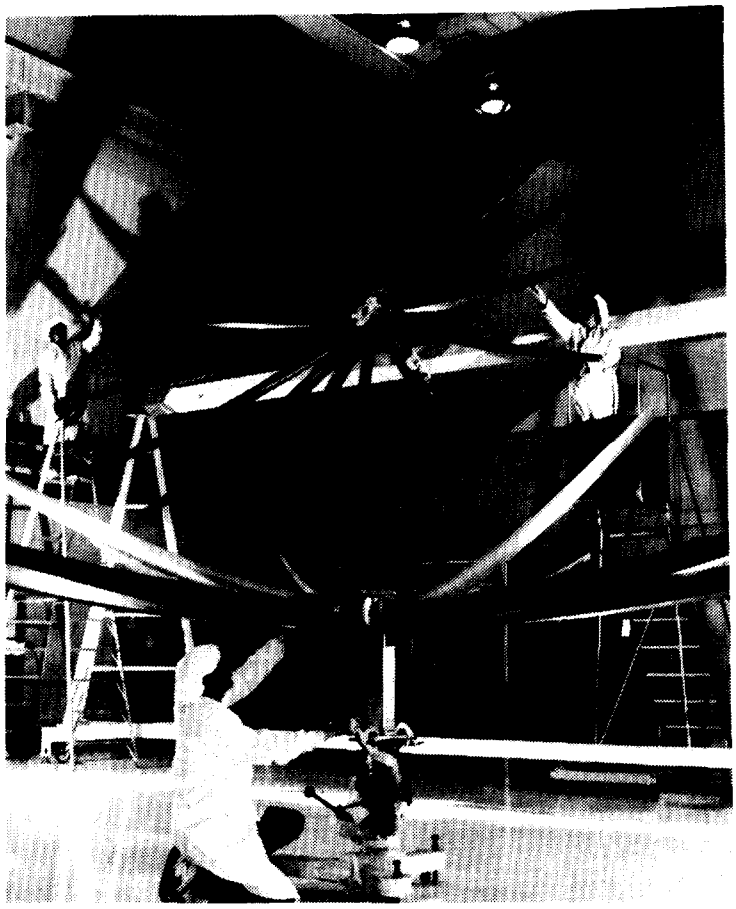

Figure 4 MSAT Reflector During Assembly

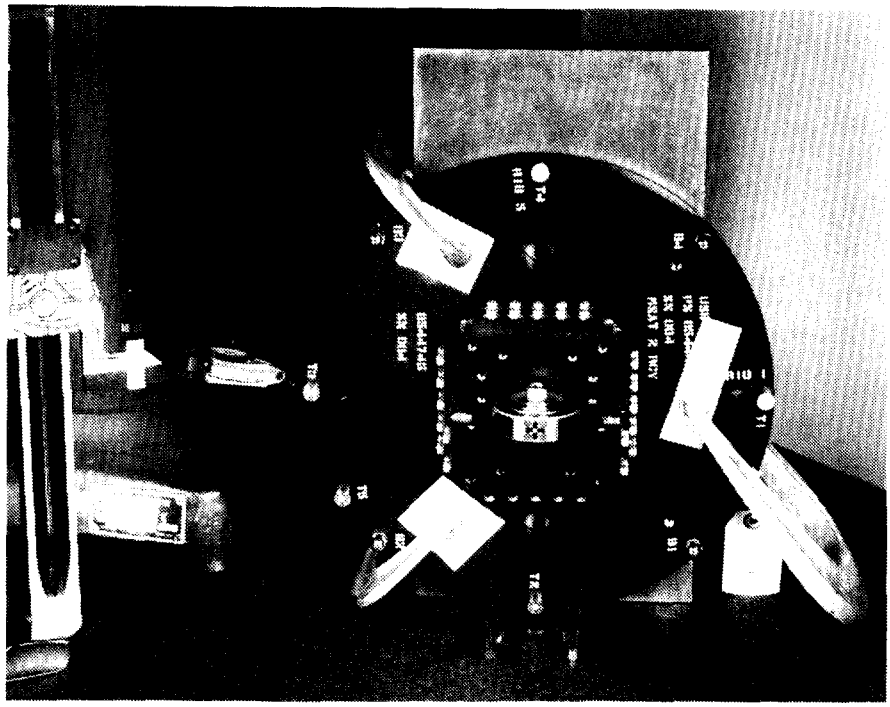

Reflector Reference Tool During Calibration

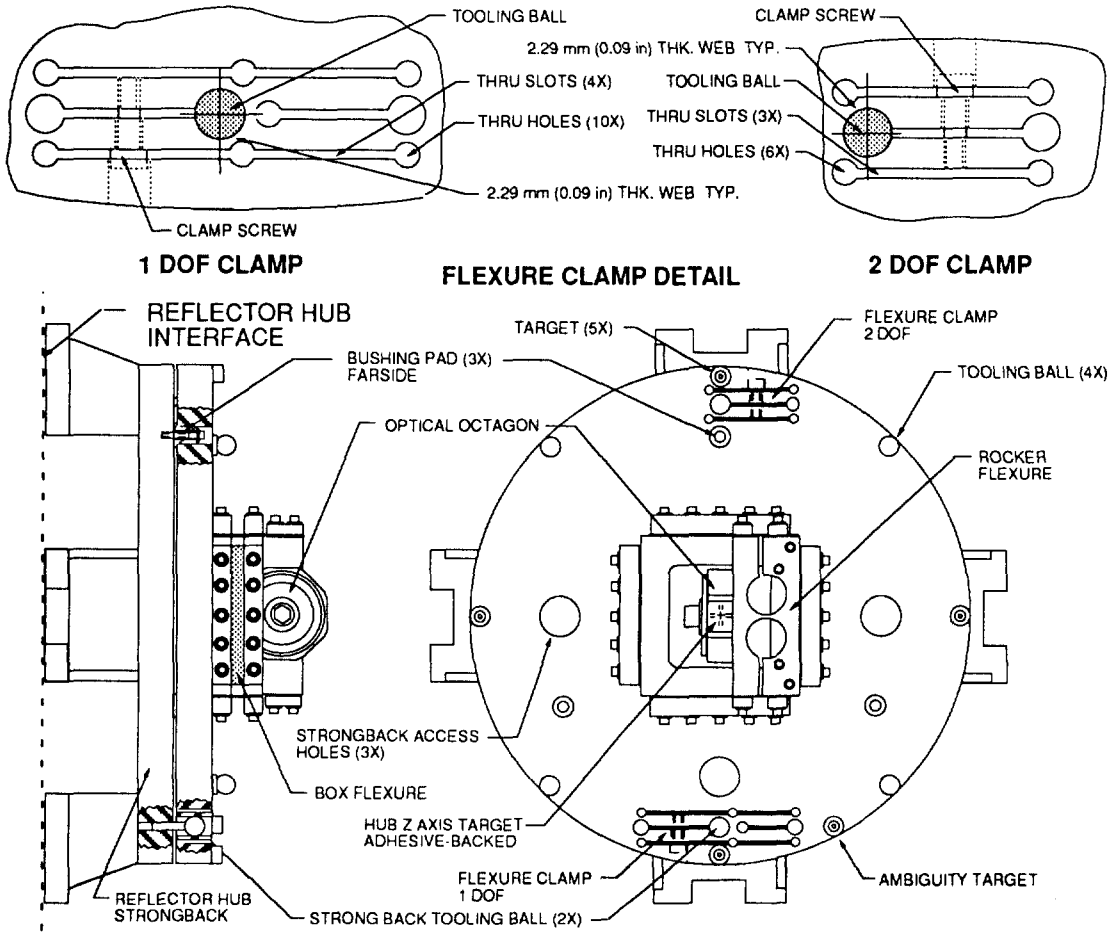

Figure 6 Reflector Reference Tool

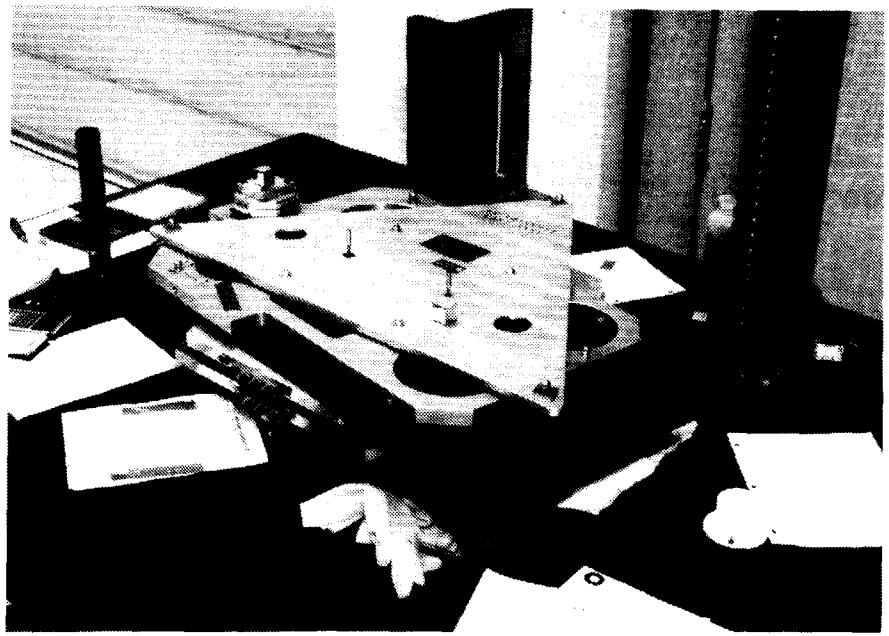

SPACECRAFT COORDINATE SYSTEM TRANSFER FROM HAC TOOL

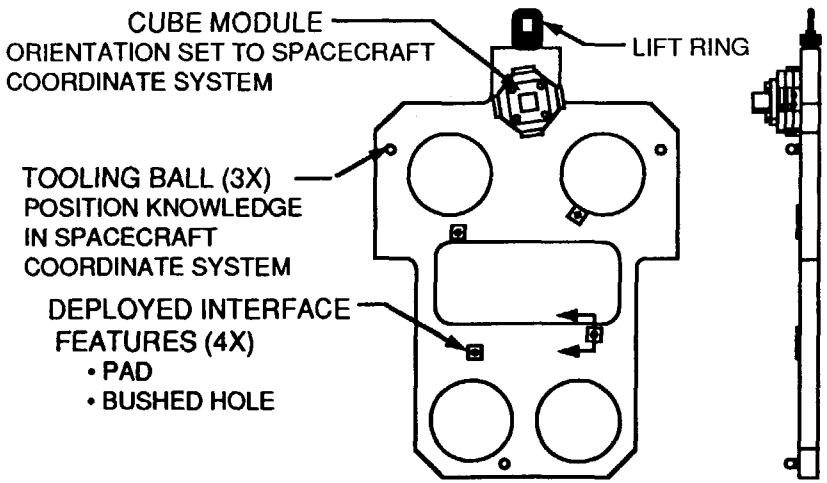

SHOULDER DRILL TOOL ATTACHED TO BOOM ASSEMBLY

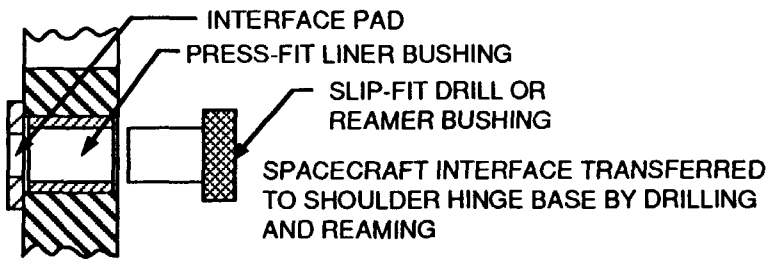

INTERFACE FEATURE DETAIL

Figure 7 Shoulder Drill Tool

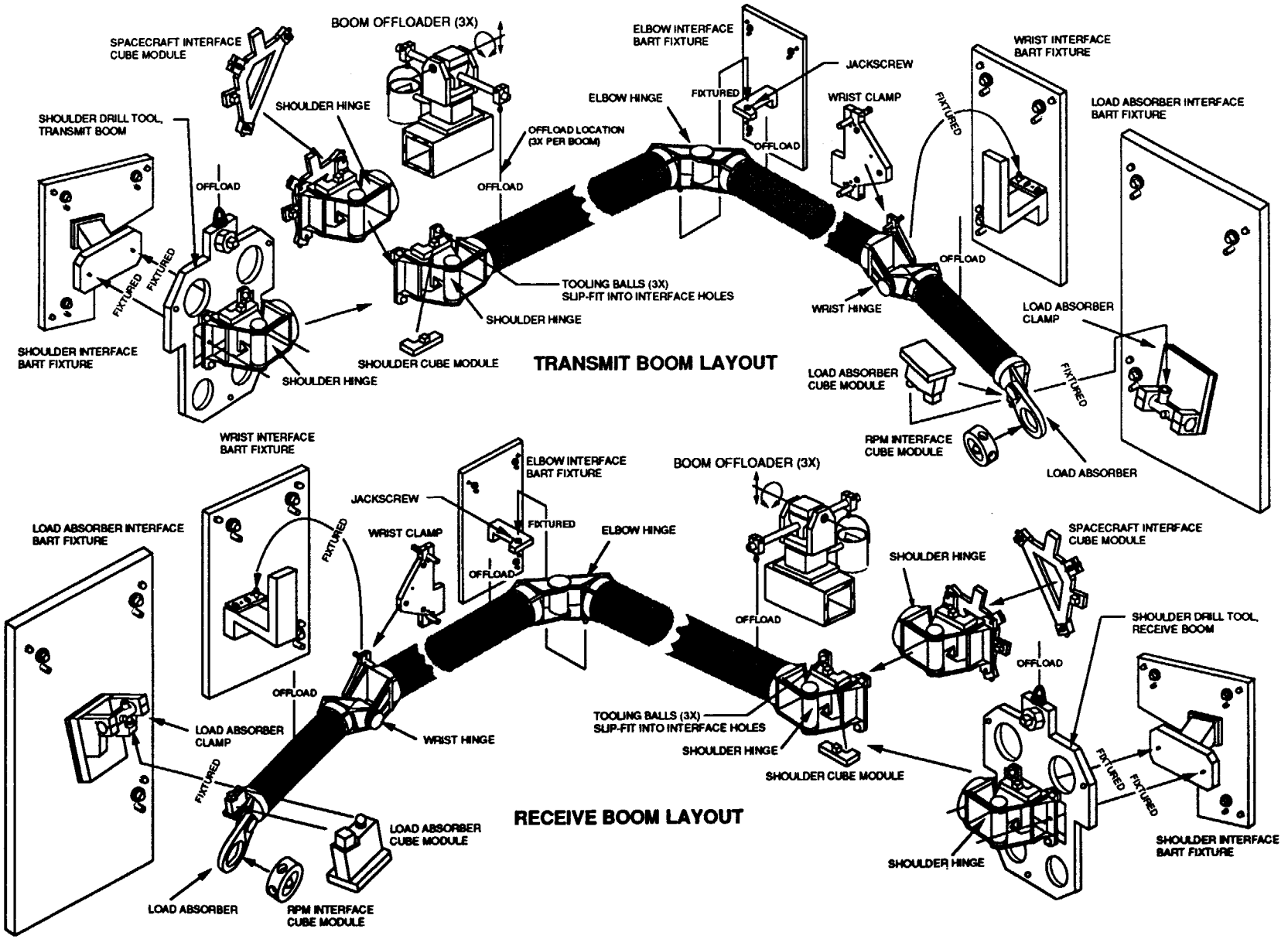

Figure 8 Boom Assembly And Special Test Equipment (STE)

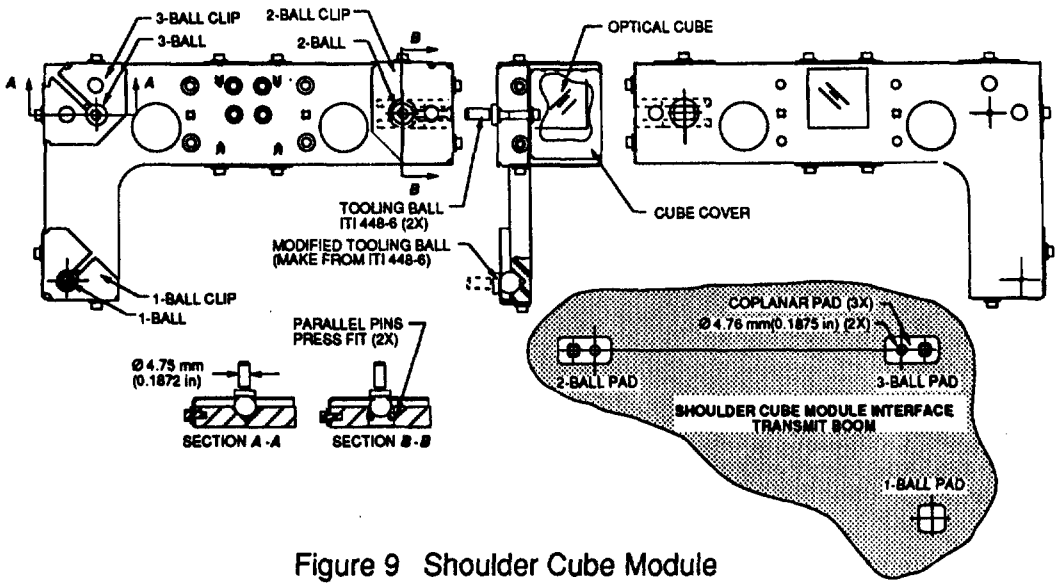

Figure 9 Shoulder Cube Module

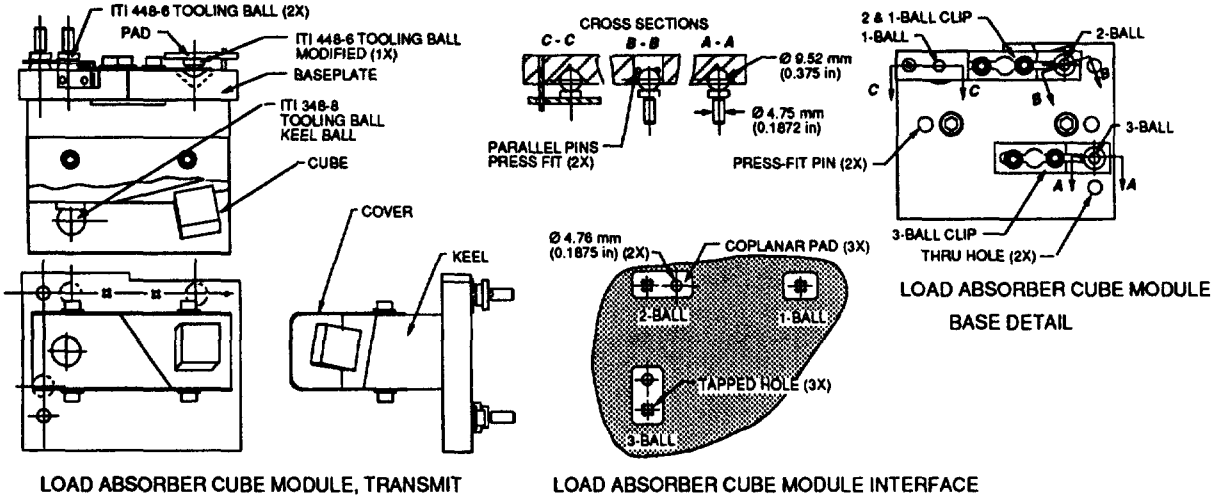

Figure 10 Load Absorber Cube Module

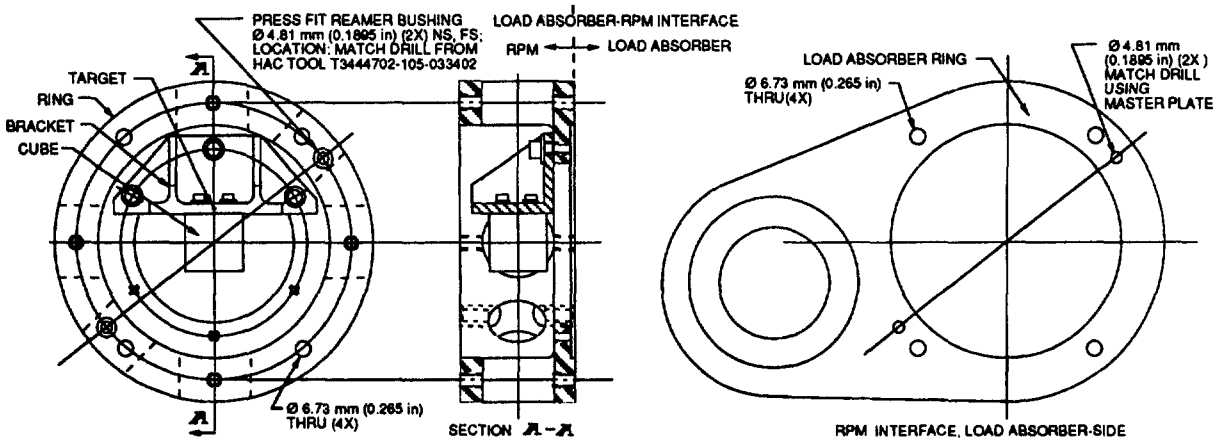

Figure 11 RPM Interface Cube Module

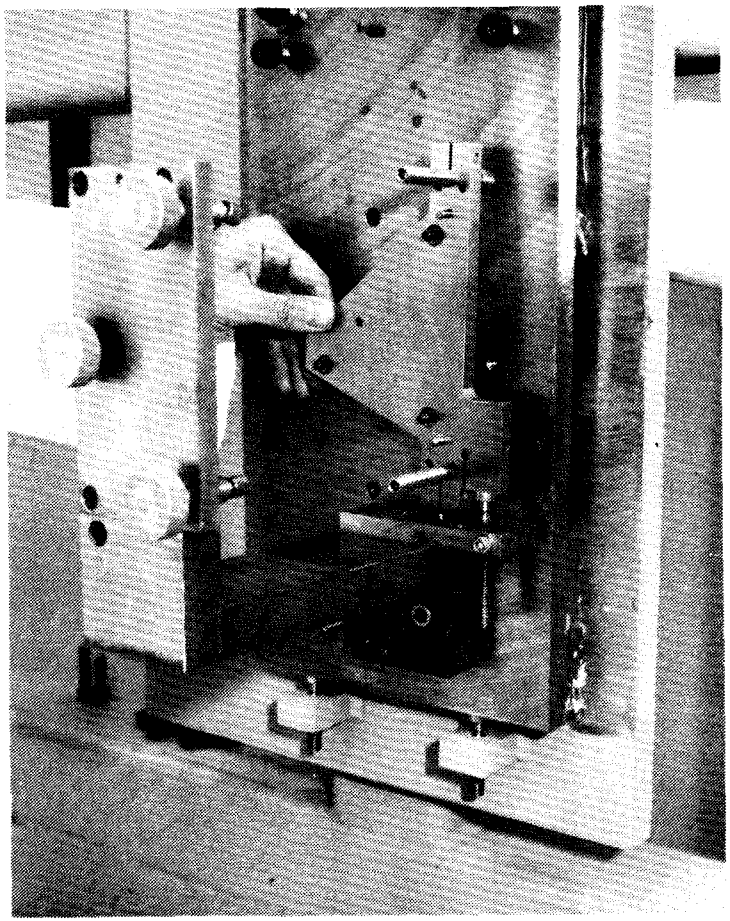

RECEIVE BOOM WRIST CLAMP ASSEMBLY ON BART

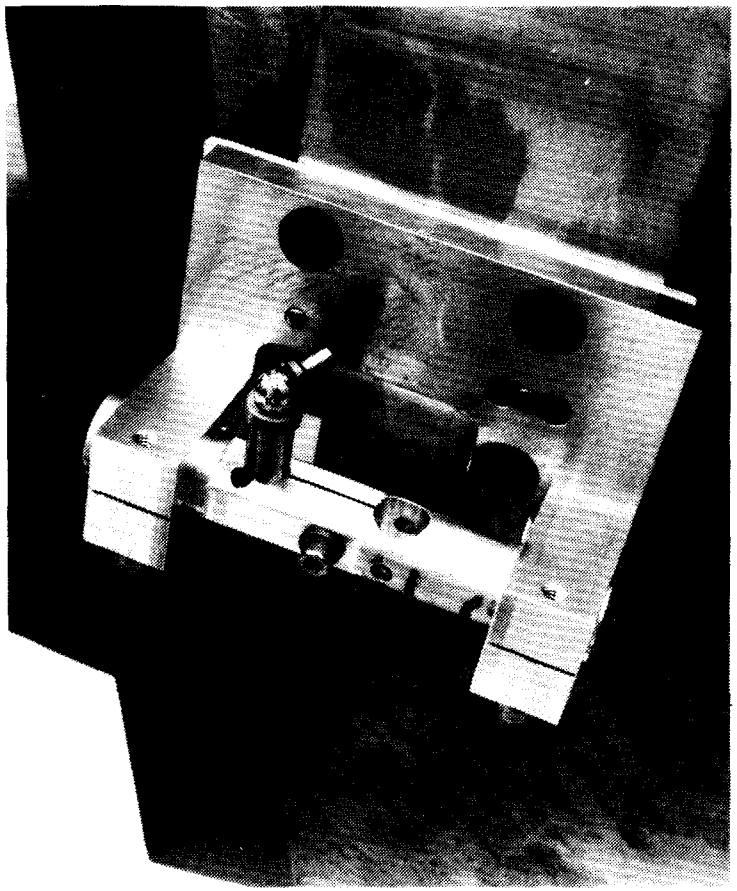

TRANSMIT BOOM LOAD ABSORBER CLAMP ON BART

FIGURE 12 ADJUSTABLE BOOM RETENTION CLAMPS

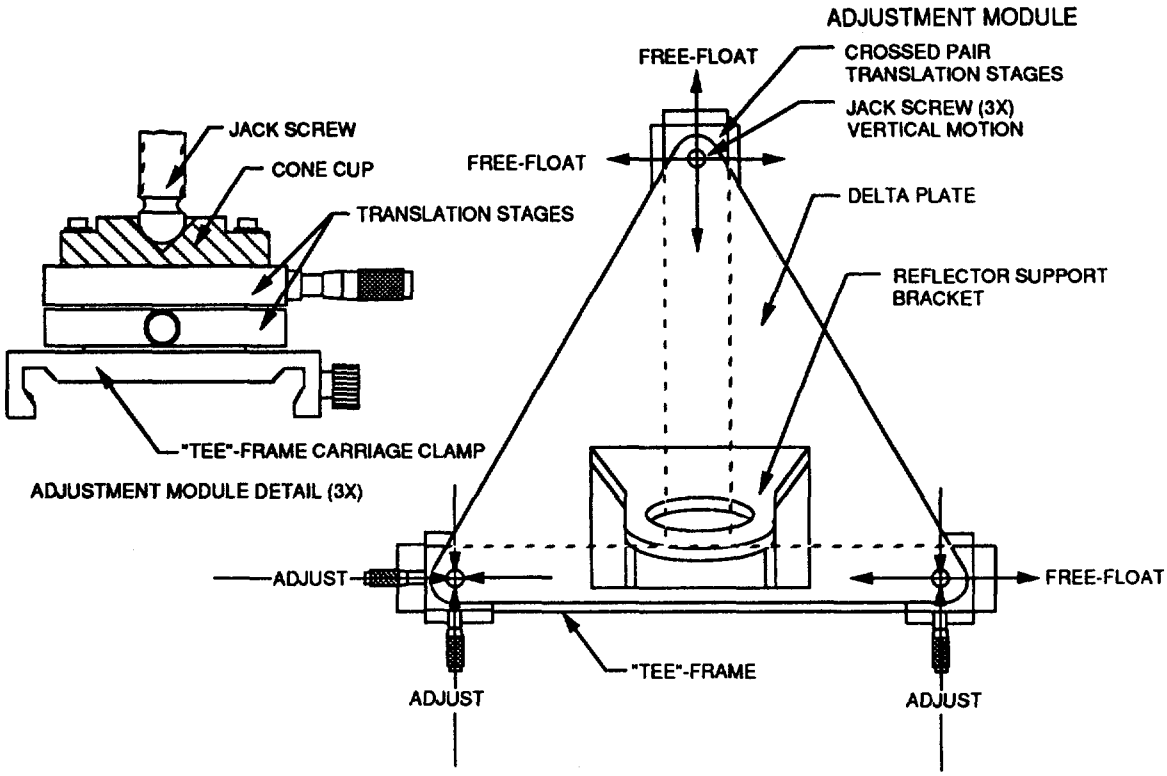

Figure 14 Integrated Alignment Stand

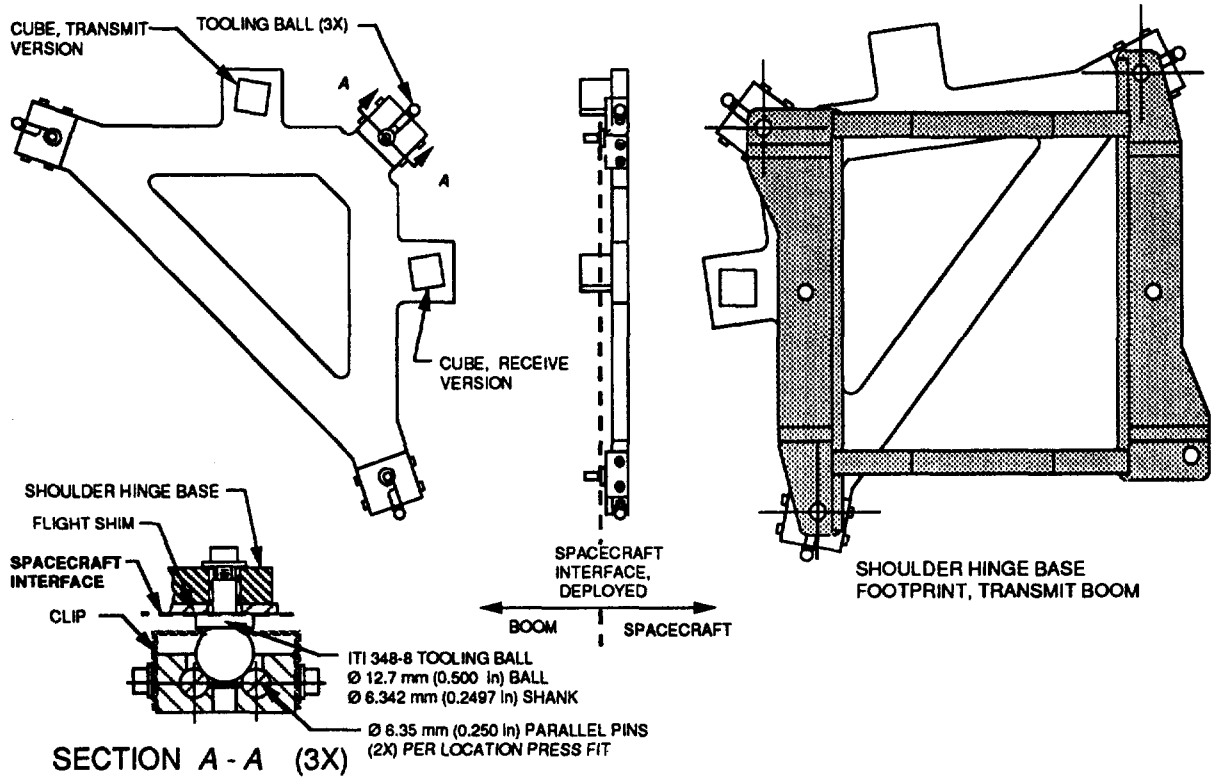

Figure 13 Spacecraft Interface Cube Module

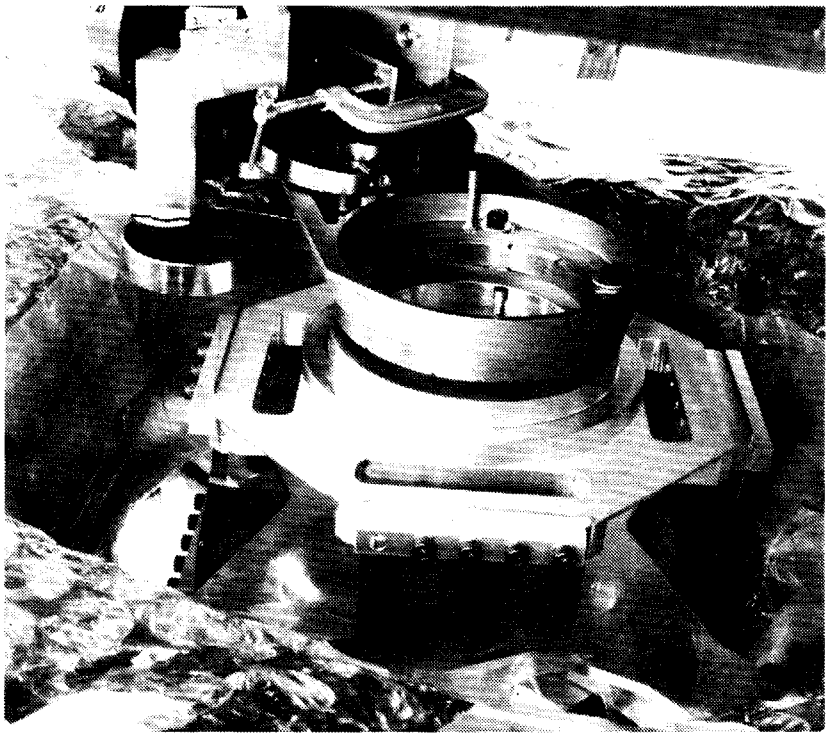

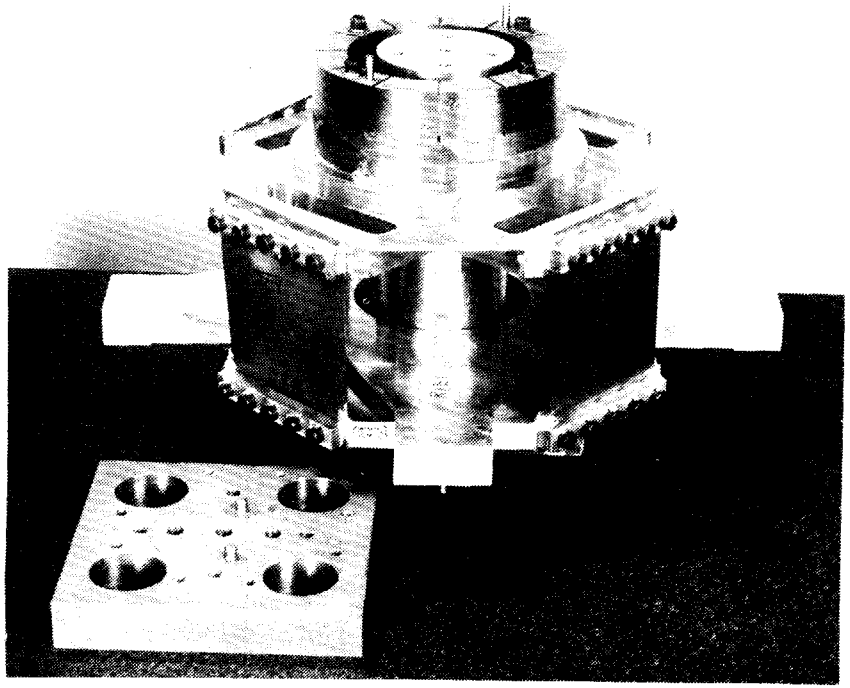

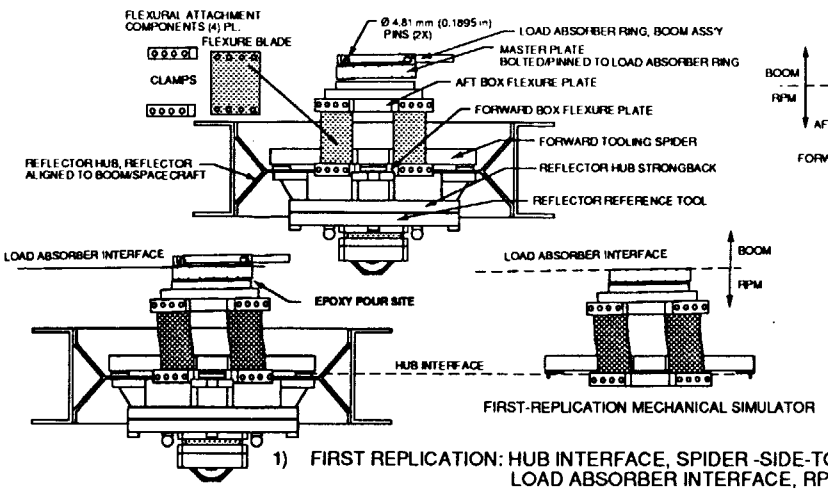

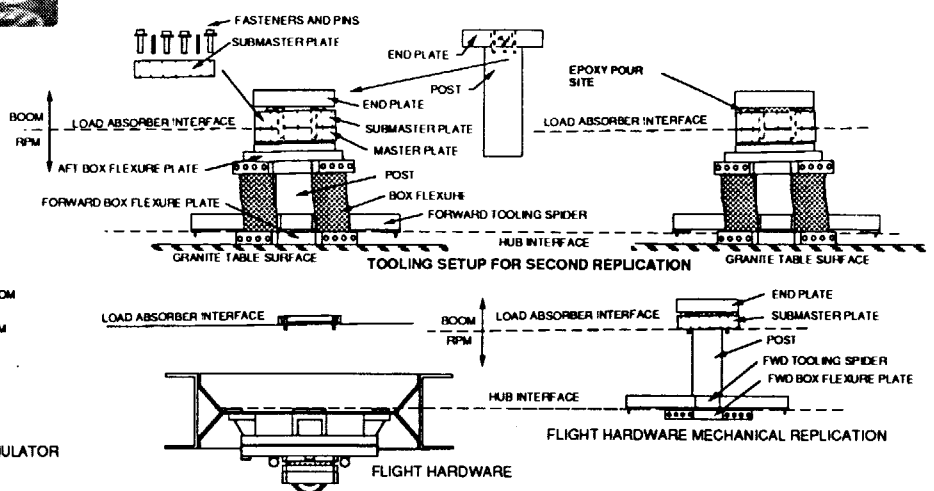

1) FIRST REPLICATION: HUB INTERFACE, SPIDER -SIDE-TO-LOAD ABSORBER INTERFACE, RPM-SIDE

2) SECOND REPLICATION: HUB INTERFACE, SPIDER-SIDE-TO-LOAD ABSORBER INTERFACE, BOOM-SIDE

Figure 15 Reflector-Boom Alignment: Reflector Hub-To-Load Absorber Interface Replication

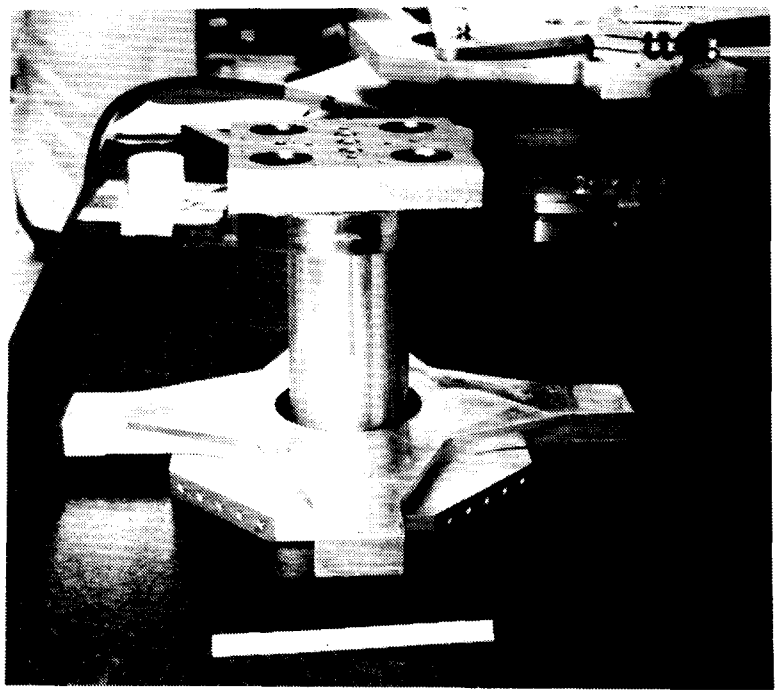

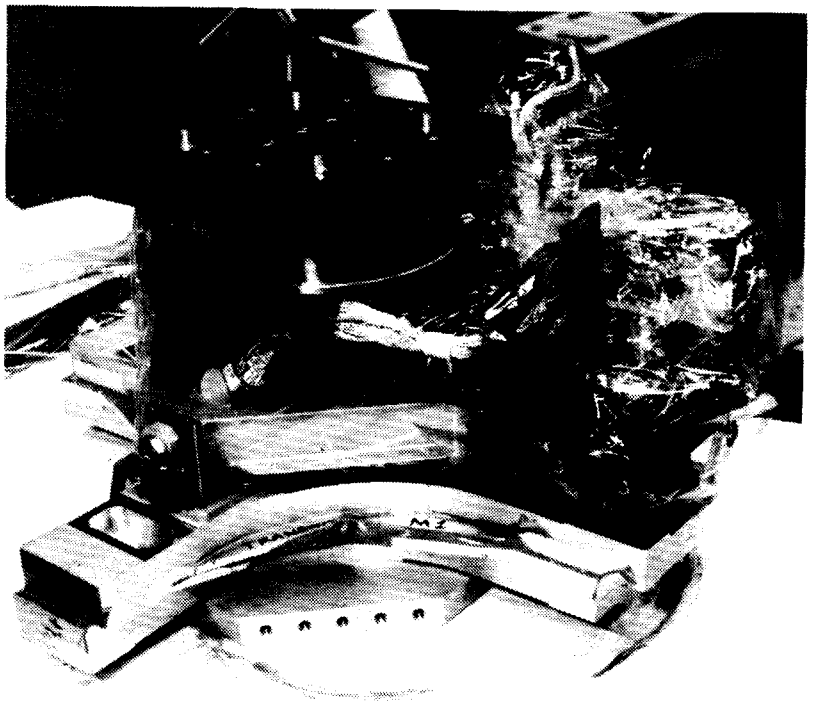

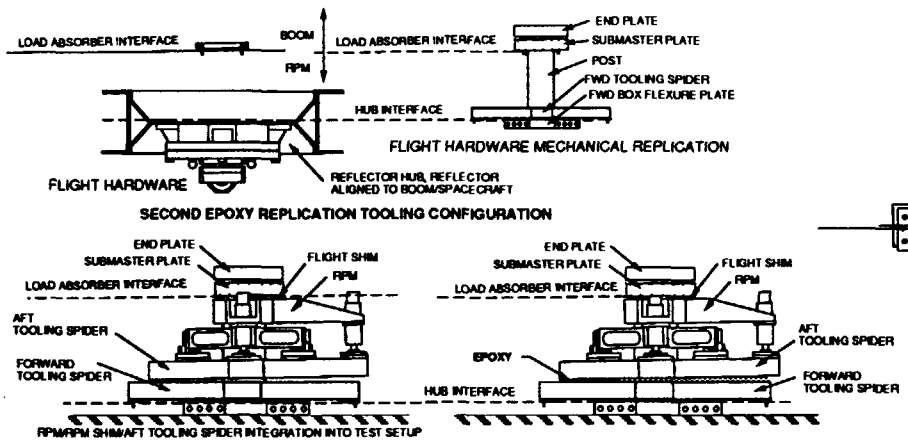

3) THIRD AND FINAL EPOXY REPLICATION: TOOLING SPIDER GENERATION

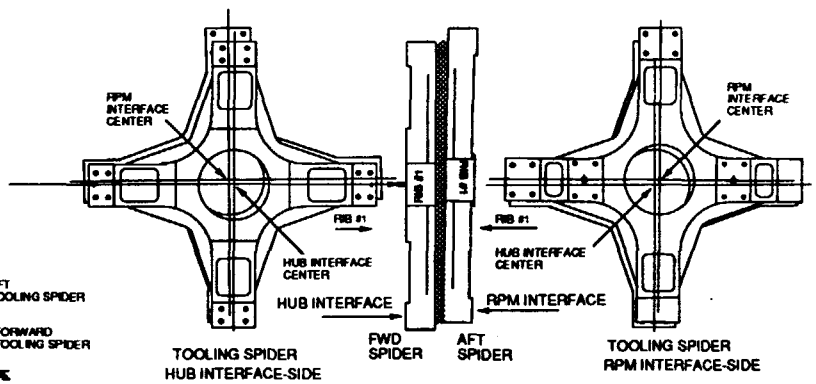

4) COMPLETED TOOLING SPIDER

Figure 16 Reflector-Boom Alignment: Tooling Spider Generated From Replication Tooling

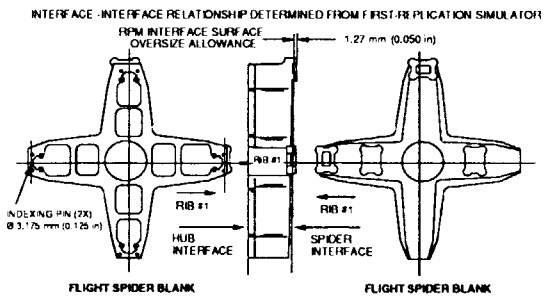

FIGURE A MSAT FLIGHT SPIDER BLANK FABRICATION

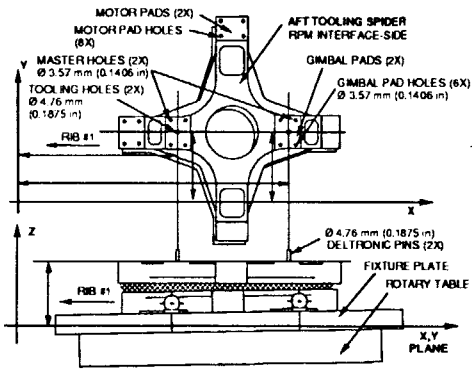

FIGURE B TOOLING SPIDER RPM INTERFACE BASELINE

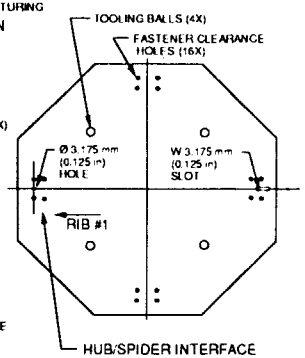

INTERFACE GENERATED USING HUB/SPIDER MASTER DRILL TOOL

FIXTURE PLATE

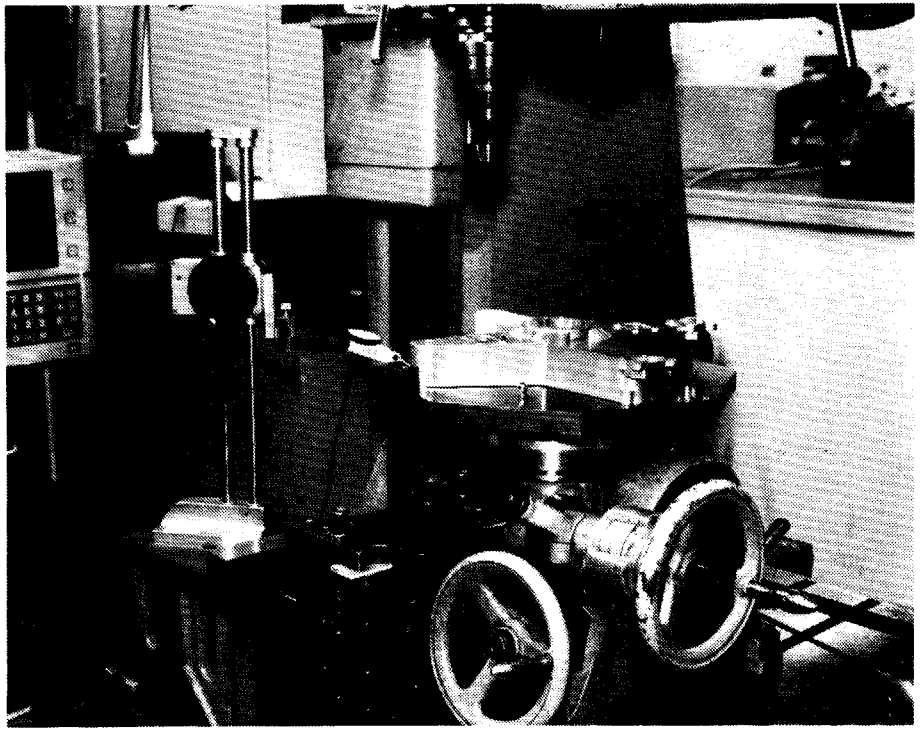

SPIDER MACHINING SETUP: JIG BORER WITH Ø 33 CM (13 IN) ROTARY TABLE AND FIXTURE PLATE

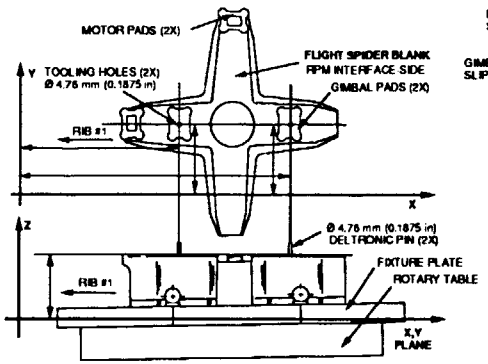

FIGURE C CUT RPM-SPIDER INTERFACE PADS AND BORE TOOLING HOLES TO TOOLING SPIDER BASELINE

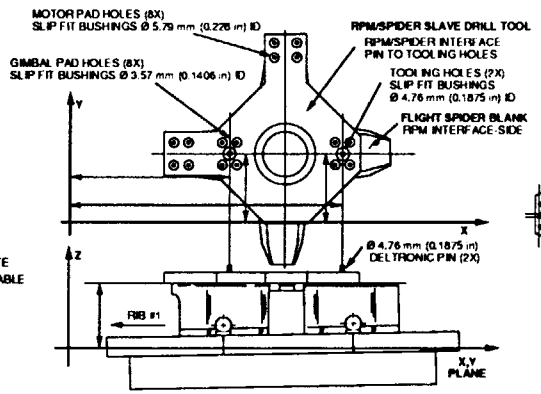

FIGURE D GENERATE FLIGHT SPIDER-RPM INTERFACE HOLE PATTERN

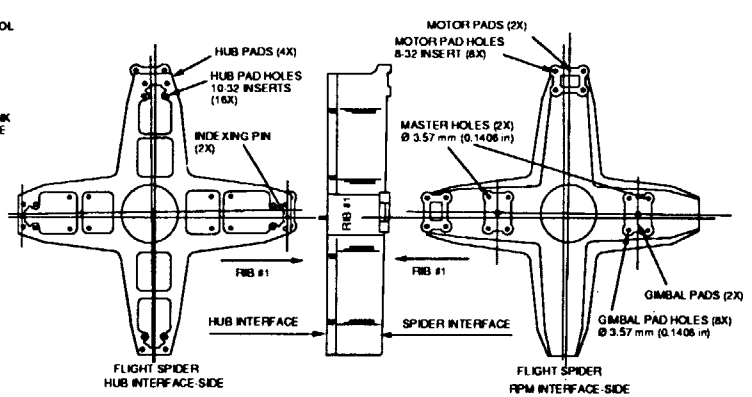

FIGURE E COMPLETED MSAT FLIGHT SPIDER

Figure 17 Flight Spider Manufacturing Process

DEPLOYABLE AND RETRACTABLE TELESCOPING TUBULAR STRUCTURE DEVELOPMENT

M.W. Thomson
Astro Aerospace Corporation
Carpinteria, California

ABSTRACT

A new deployable and retractable telescoping boom capable of high deployed stiffness and strength is described. Deployment and retraction functions are controlled by simple, reliable, and fail-safe latches between the tubular segments. The latch and a BI-STEM (Storable Tubular Extendible Member) actuator work together to eliminate the need for the segments to overlap when deployed. This yields an unusually lightweight boom and compact launch configuration.

An aluminum space-flight prototype with three joints displays zero structural deadband, low hysteresis, and high damping. The development approach and difficulties are discussed. Test results provide a joint model for sizing flight booms of any diameter and length.

INTRODUCTION

The new telescoping boom was developed to service recent spacecraft requirements for lightweight, high strength and stiffness deployable and retractable boom structures. An example of the new design is shown stowed and cutaway in Figure 1.

Telescoping booms have tapered section properties, which makes them ideal for most cantilevered boom systems, and thin wall tube segments can be stowed very compactly. Telescoping booms have few parts and simple deployment kinematics and are therefore intrinsically reliable [Ref. 1]. They are also exceptionally resistant to structural failure from micrometeoroid or other bombardment. The nested tubes of a telescoping boom can be fabricated from metallic or composite materials depending on the structural performance that is required, and they may be perforated to minimize weight and thermal gradients.

BACKGROUND

One problem that must be addressed in the design of compact telescoping booms is the need for stabilization during deployment and retraction. Tube segments that are in relative motion can easily bind inside one another, particularly during retraction.

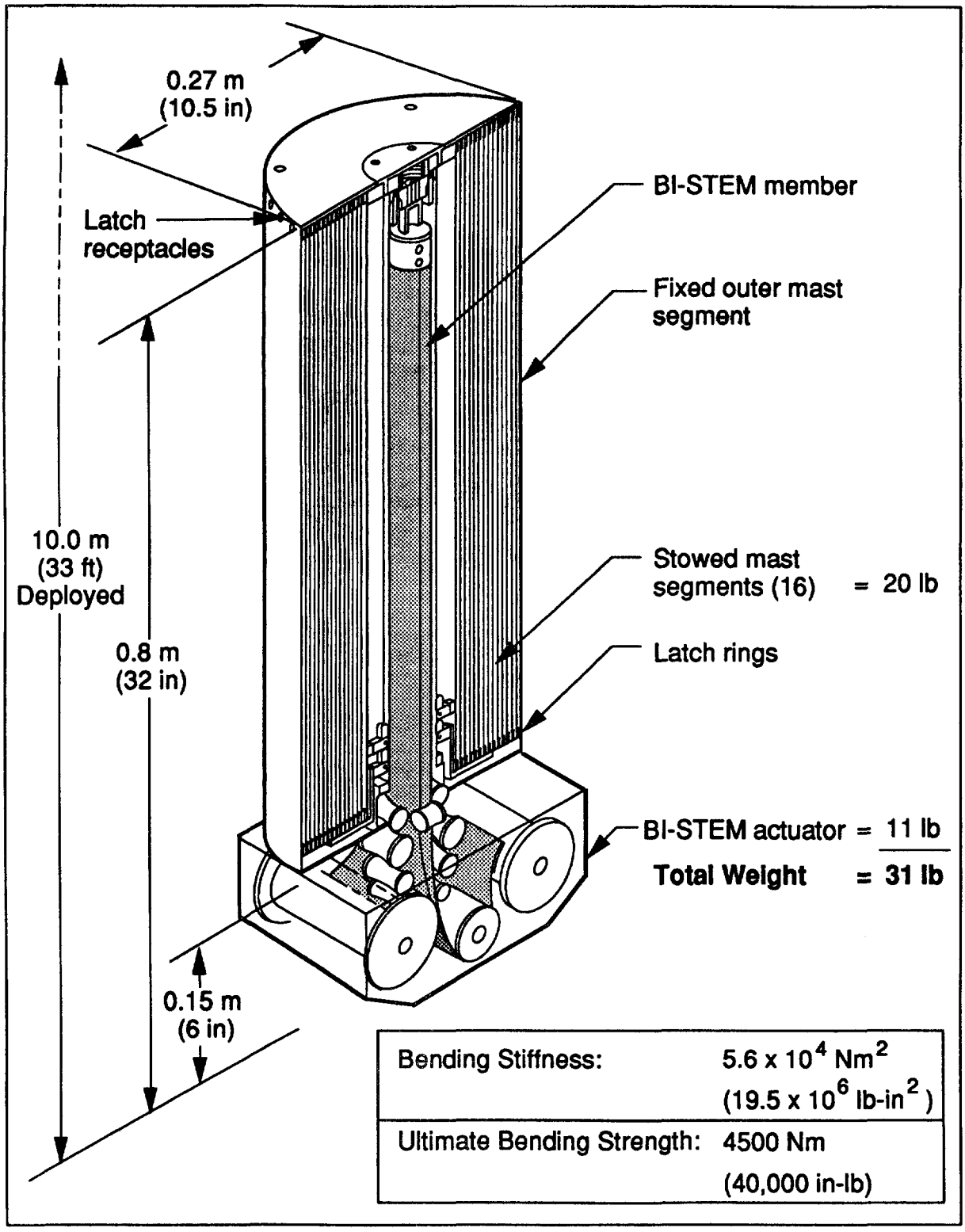

Figure 1. Telescopic Boom Unit—Stowed.

A compact boom that is deployed from the root needs a high degree of stabilization. The forces required to stabilize root deployment are proportional to the ratio of boom length to deployer length, which may be as high as 20, so stabilization is an important issue. Furthermore, any play between the deploying boom and the stabilizer is exaggerated at the boom tip by the same ratio. This intensifies dynamic nonlinearities and the loads thereof.

Stabilization is usually provided by overlapping adjacent deployed tube segments. More overlap is needed if the tube walls are thin or have surface irregularities or relatively soft coatings. Designs that depend upon precisely nesting diameters to reduce overlap are prone to jam from elastic or thermal deformations. The amount of overlap needed can be as much as three tube diameters [Ref. 1]. Overlap increases not only the deployed nonstructural weight, but also the number of tube segments required to fit the total boom length into a given launch envelope. The loss of structural efficiency can be significant for designs with many segments, particularly if the ratio of stowed length to maximum tube diameter is less than about eight.

Play in the latches between deployed tubes is a common problem with telescoping booms, particularly those with numerous joints [Ref. 1]. Latch designs that have both high stiffness and autonomous retractability can be complex and heavy. It is essential that the latches be lightweight and of simple design if high structural efficiency and reliability are to be achieved.

Finally, the axial thickness of the latches at the joints of telescoping booms often end up stacked when stowed. This staggers the tube lengths and reduces the potential length of the boom. The amount of lost boom length is magnified by the number of tube segments. For instance, a stack of 20 tubes successively staggered by 1 centimeter loses 2 meters of potential deployed length.

DESIGN GOALS

The primary goal was to design new deployment and latching mechanisms that eliminate the compromises that can detract from the structural efficiency of telescoping booms. The new design should be able to sequentially deploy and retract from the tip, instead of from the root, to minimize the stabilization needed and to maximize the stiffness of the system at all extended lengths. All functions should be achieved with minimum complexity so that the design can be readily and cost-effectively scaled to a variety of sizes. Some reduction of stiffness due to latch compliance will be inevitable, but the goal is to keep the joint knockdown factor below 25 percent and to eliminate structural deadband.

An additional goal was a well-rounded design that is easily adapted to a wide range of applications. The design of the tubes should be simple and compatible with metallic and composite materials. Deployment and retraction should be tolerant of dynamic loads and the loads exerted by payloads such as flexible solar array blankets. The boom should be capable of precise positioning and of deployment and retraction forces up to 450 N (100 lb). The ability to retract autonomously in 1 g would reduce the expense of qualification whether or not retraction is required in orbit.

GENERAL DESIGN APPROACH

It was decided that the BI-STEM, (a pair of Storable Tubular Extendible Members) would actuate and stabilize sequential tip deployment to eliminate the need for the tubes to overlap. A veteran of space flight, the BI-STEM consists of two "C" sections of thin formed metal that are flattened so they can be rolled onto separate spools for launch, as shown in Figure 2. Deployable booms in the STEM family are simple and extremely lightweight; they have been successfully deployed over 300 times in space without any known failures.

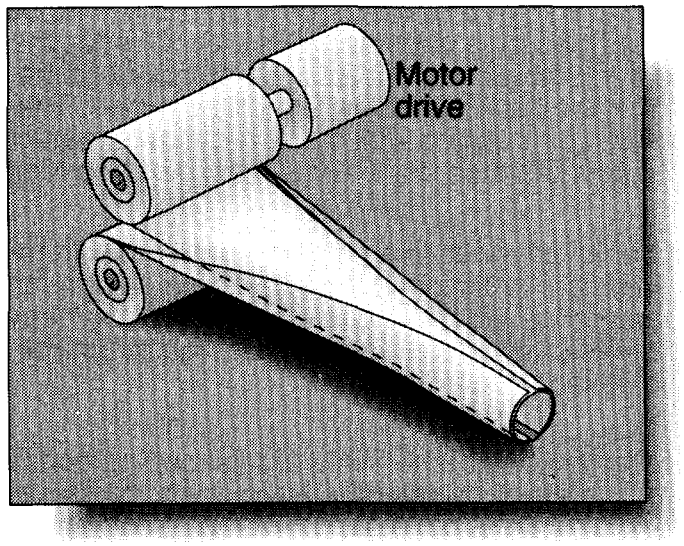

Figure 2. BI-STEM.

The payload and package of stowed tube segments are pushed from the inside of the fixed external root segment by the BI-STEM. When the package reaches the end of the fixed segment, the outer tube in the package latches to it, as shown in Figure 3. This tip deployment process repeats sequentially until all tubes are latched into place. The same sequence is reversed to retract.

The innermost of the undeployed tubes is fixed to the tip of the BI-STEM in order to stabilize the moving package of tubes. An ample diametral clearance is provided between the tubes and their neighbors so that the BI-STEM can deflect moderately without the tubes binding. Because the BI-STEM actuator does not need to be exceptionally stiff, its diameter and weight can be low. The clearance between tubes reduces the impact of any thermal distortions or imperfections in the walls so that larger tubes can be made at a lower cost than previously thought possible [Ref. 2].

BI-STEMs can exert 450 N (100 lb) of compressive deployment force in the largest common diameter of 51 mm (2 inches) and can be accurately positioned. Tubes that have been latched into structure behind the deploying tip of the boom can brace the BI-STEM element laterally to enhance its ability to react tip loads or to reduce the size of the element. Lightweight annular supports can be deployed periodically as shown in Figure 3. The supports can be spaced as close as one tube length apart, which may be necessary so that the BI-STEM can exert high deployment forces without buckling the element.

To minimize the number of tubes, they are all the same length and are stowed coincident with each other, as shown in Figure 1. Larger booms can further minimize stowed volume if the BI-STEM can be placed inside the smallest tube, as shown in Figure 4. The latches fit in the annular gap between adjacent tubes in a stiffening

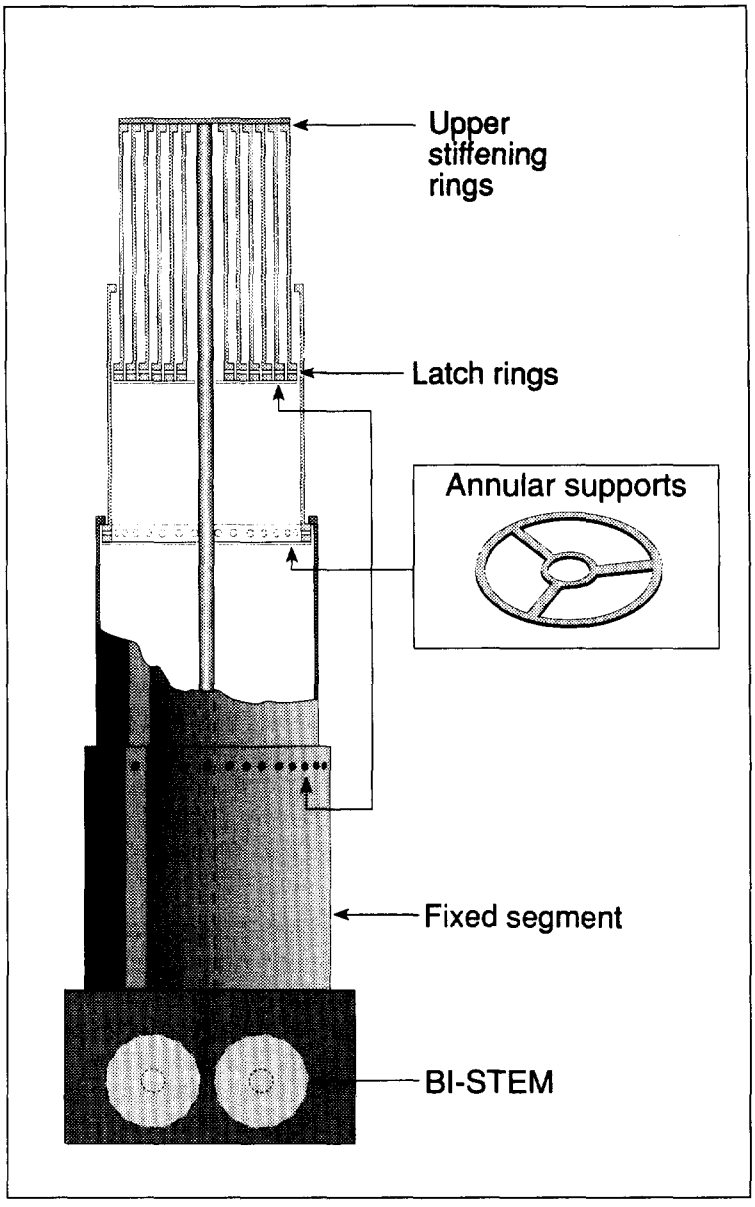

Figure 3. Telescopic Boom Unit Tip Deployment.

ring at the lower end of each tube. The adjacent larger tube in turn necks down to a thin stiffening ring at the upper end. The stiffening ring helps to center and align the adjacent smaller tube and to lessen local deformations between the latched segments in bending. The consequent step in successive tube diameters creates a moderate taper that can be tailored to optimize structural performance.

The ultimate success of the boom is centrally reliant upon a simple, lightweight and structurally linear latch between the tube segments. Although the BI-STEM offers a novel option for deployment, it is designed to push, pull, and position the boom tip. The latch must, therefore, provide fail-safe control of the deployment and retraction sequence without—as a goal—any additional components.

LATCH DESIGN

To eliminate structural deadband, there must be a preloaded latch at the joints between segments. It was decided that small tapered pins would be distributed circumferentially in the stiffening ring at the lower end of each tube. The pins are loaded radially outward by short springs to engage with tapered holes at the upper end of each larger adjacent tube, as shown in Figure 5. When stowed, the springs and pins are compressed by the interior surface of the adjacent larger tube. During deployment, the tips of the pins slide on the surface until they pop into the tapered seats to latch.

The included angle of the taper avoids a locking taper geometry that would make retraction difficult. The preload is sufficient to prevent the pin from squeezing out of the seat as a result of boom bending. It was reasoned that numerous smaller pins would increase redundancy, stiffness, strength, and linearity by evenly loading

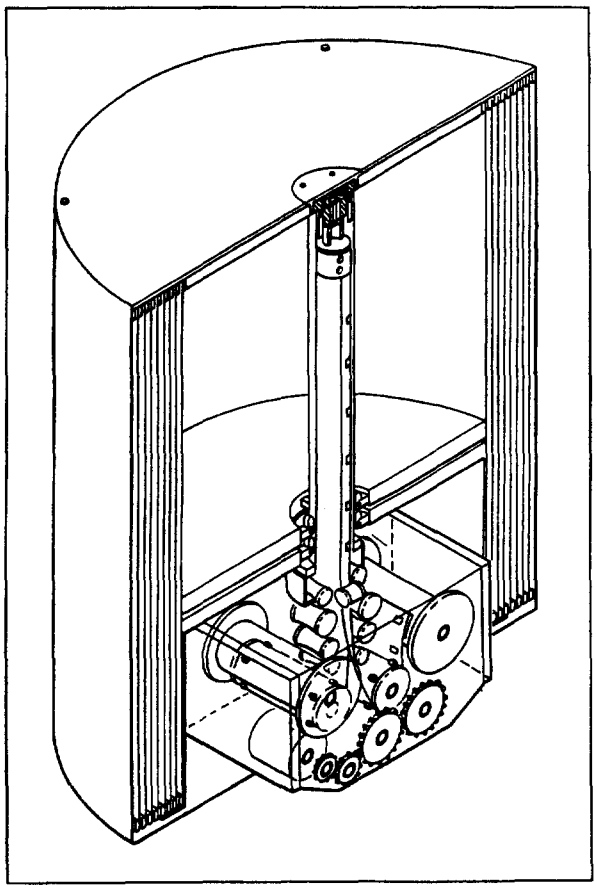

Figure 4. Large Diameter Compact Telescoping Boom.

the thin tubular walls. The taper of the pins also makes it easy for them to "find" the seats during deployment despite any mismatch between pins and receptacles. Coarse torsional alignment up to the point of latching is maintained by a key or "clocking strip" that is affixed to the exterior of each tube. The clocking strip engages a notch on the inner diameter of the upper stiffening rings.

Getting to this stage of the concept during the design process was relatively easy. Satisfactory solutions to the remainder of the design goals, sequencing and autonomous retractability, were not as easily achieved.

SEQUENCING

Numerous complex variations of the basic tapered pin latch were conceived to cause it to sequence and retract the boom. The designs did not seem sufficiently robust and would have been costly to manufacture.

After repeated trial and error, an elegant solution emerged. It was realized that because the tubes are stowed coincident to each other, each ring of compressed latch pins can engage the adjacent smaller ring with simple detents as shown in Figure 5. All the nested tubes are thus locked together so that they can be pushed as a package during deployment. When the latch ring in the outermost tube of the package locks it into deployed structure, the detents retaining that tube to the moving package of tubes are released. The now smaller package of moving tubes continues without interruption.

The male component of the detent on the interior end of the latch pin is conically shaped to make the latching function fail-safe. If one or more springs fail, the affected pin is forced out of the way by the female side of the detent, which acts as a ramp, as shown in Figure 5. Without the spring to preload the pin in the tapered receptacle that pin cannot contribute to the deployed stiffness of the boom, however, deployment will not be impeded.

RETRACTION

The sequencing concept provides a direct means for coordinating the movement of each tube with its neighbors. To retract a given tube, its latch pins are pulled

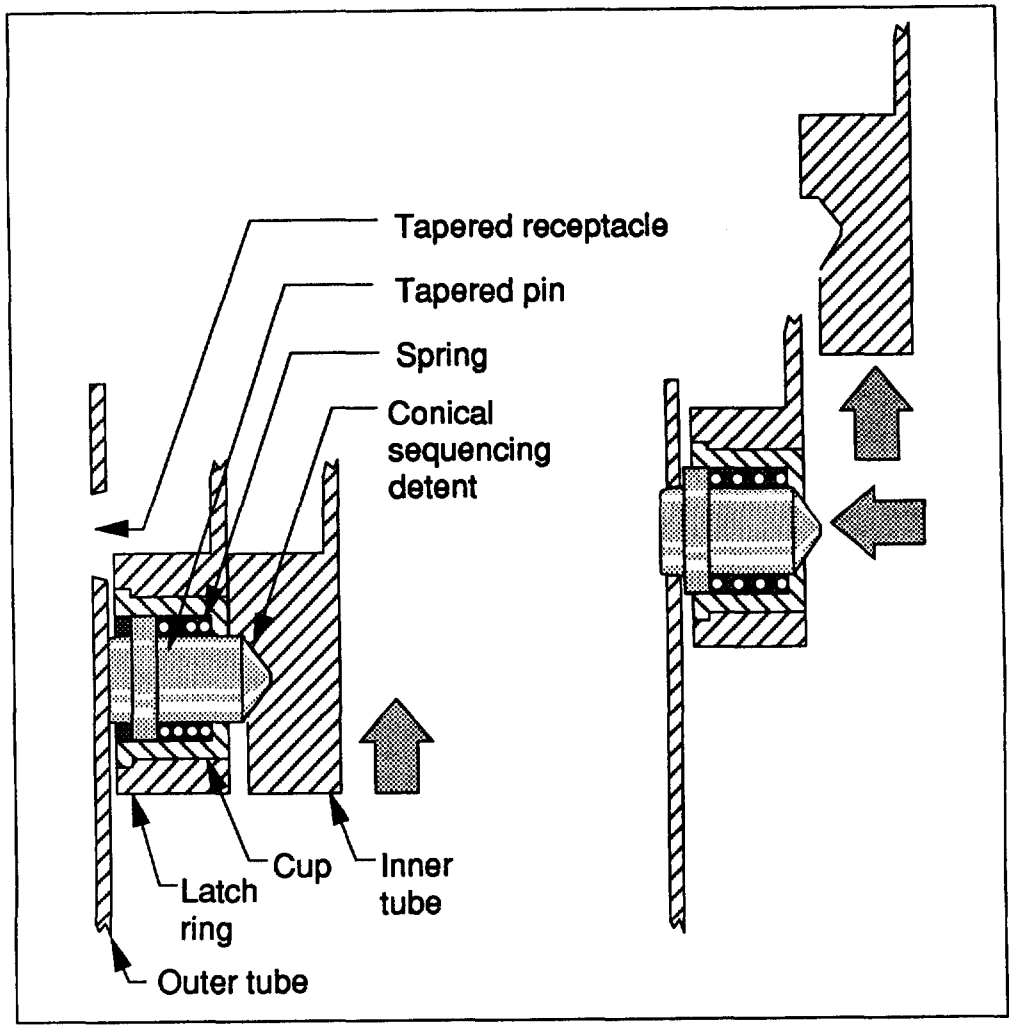

Figure 5. Tapered Pin.

from engagement with the next larger tube by ramps in the next smaller tube. The ramps are hollowed out of the latch rings to engage conical rims at the male detent end of the latch pins, as shown in Figure 6.

The BI-STEM is attached to a short piston located in the smallest tube segment at the boom tip. The piston provides end fixity in bending for the deployment stabilization function yet affords axial motion. The lower end of the piston has retraction ramps and female sequencing detents but no latch pins. The BI-STEM is reversed to pull the piston toward the latch ring of the tip tube to release it, which initiates retraction. Retraction continues until the retraction ramps in the latch ring of the tip tube releases the next larger tube, and so forth, as the sequencing detents bind the package of stowed tubes together in reverse.

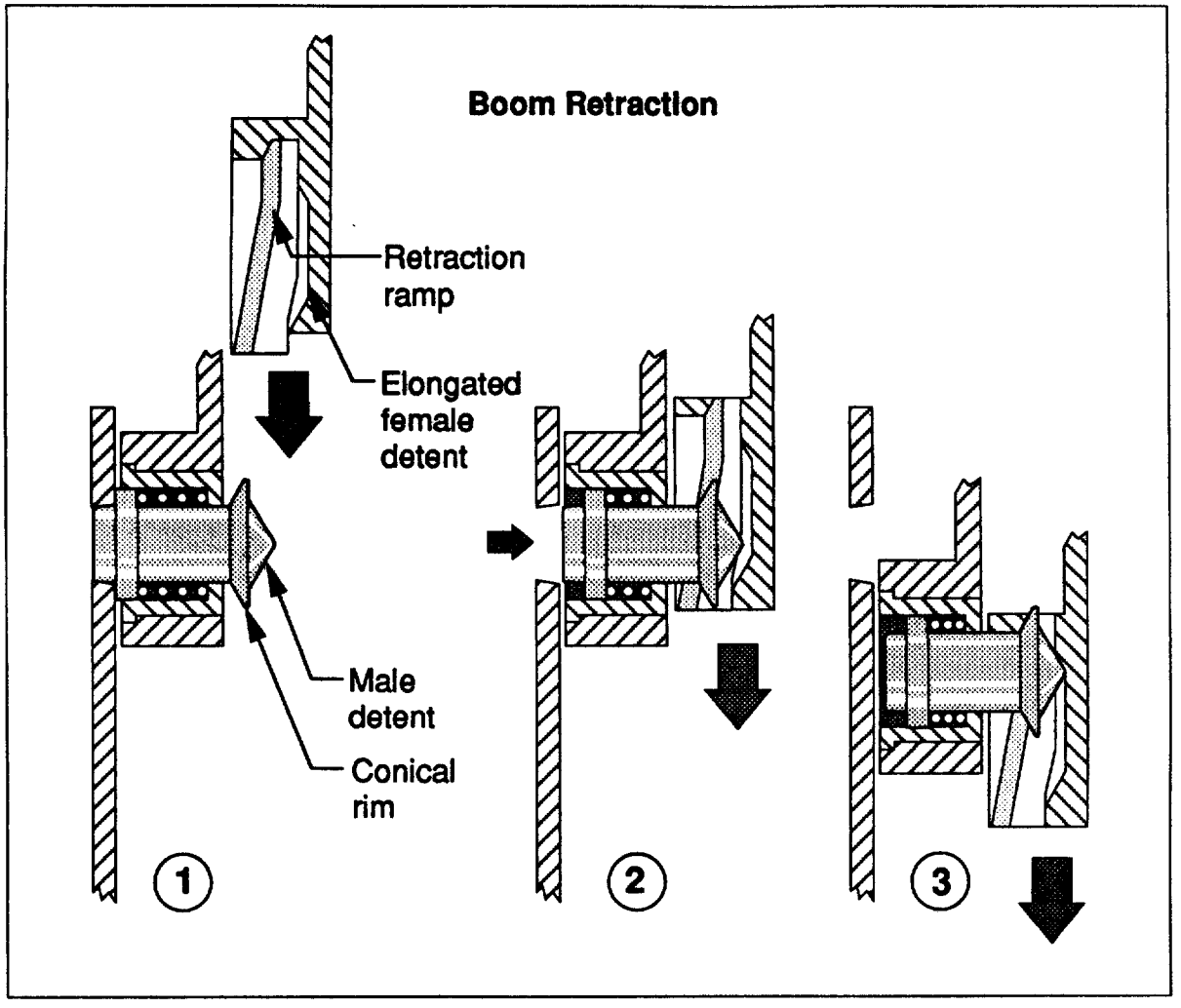

Figure 6. Boom Retraction.

Latch pins are alternated with retraction ramps and detents in increments around the circumference of each ring. Each successive tube in the assembly is indexed by one such increment relative to its neighbors so that everything meshes properly, as shown in Figure 7. Figure 7 also shows the clocking strips that maintain precise rotational alignment between adjacent tubes.

The sequencing function of the detents is not affected by retraction if the female portion of the detent is elongated into a trough, as shown by the first inset of Figure 6. This accommodates the axial motion between the latch and the adjacent smaller ring as the pins are pulled. The length of the trough is controlled so that the detents will engage before the deployed tube is unlatched, as shown in the second inset of Figure 6. The failure of one or more latch springs will not impede retraction so that fail-safe functionality is retained.

LAUNCH RESTRAINT

A launch restraint mechanism is shown in Figure 8. A cap plate is preloaded over the end of the stowed boom by a ball detent latch. The latch engages a tube that is fixed to the BI-STEM housing on the inside of the stowed boom. The cap plate is released when the BI-STEM begins to deploy. This feature eliminates the need for pyrotechnic or other active devices to unstow the boom.

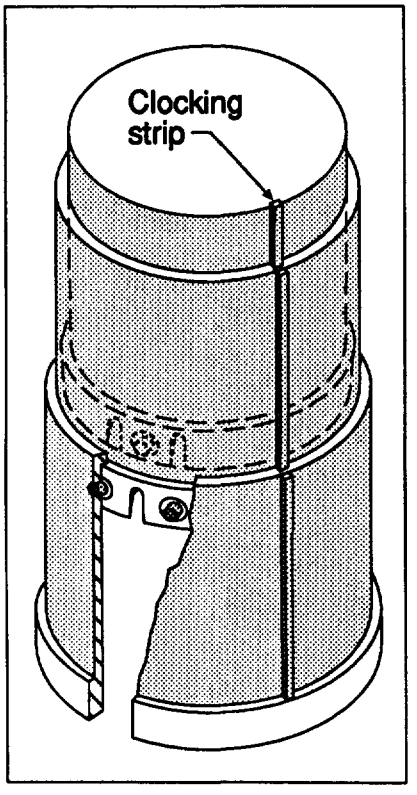

Figure 7. Latch Pins and Retraction Ramp.

FLIGHT PROTOTYPE DESIGN

A flight quality aluminum prototype, shown deployed in Figure 9, was built to prove the feasibility of the boom concept. The model has a length of 2.3 m (91 inches) with a 12 cm (4.7 inch) average diameter. The four segments range in diameter from 14 to 10 cm (5.5 to 4.0 inches) and all have wall thicknesses of 0.64 mm (0.025 inch). The boom is actuated by a 3.4 cm (1.34 inch) diameter BI-STEM actuator.

The diametral pitch between tube segments was set at 1.27 cm (0.5 inch) to provide a moderately tapered configuration. A larger pitch

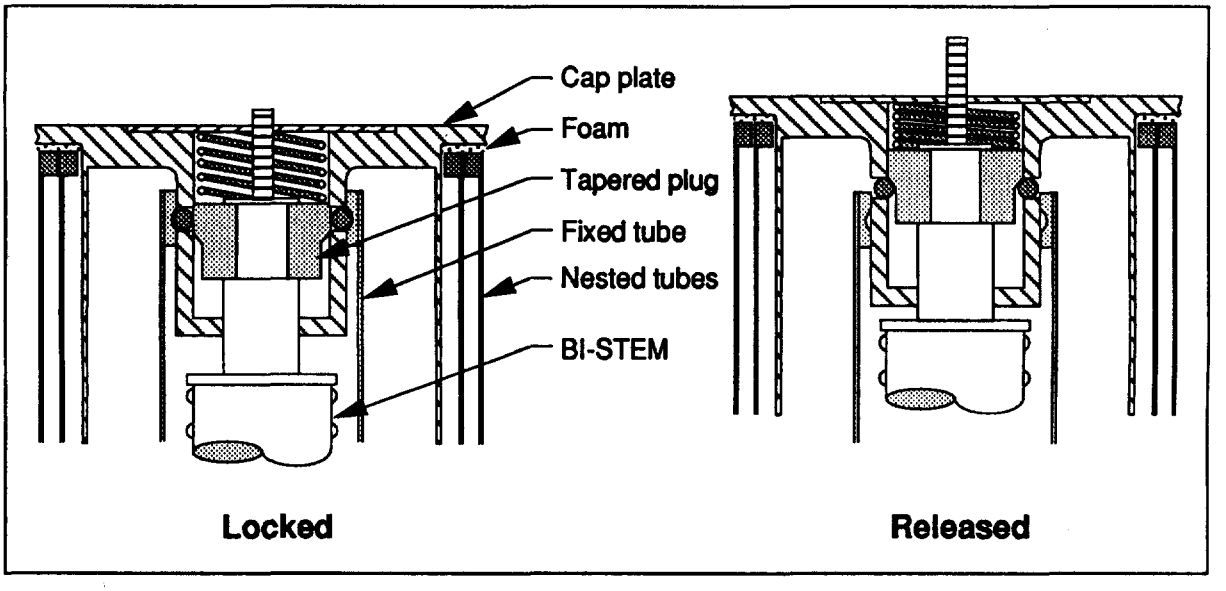

Figure 8. Launch Restraint.

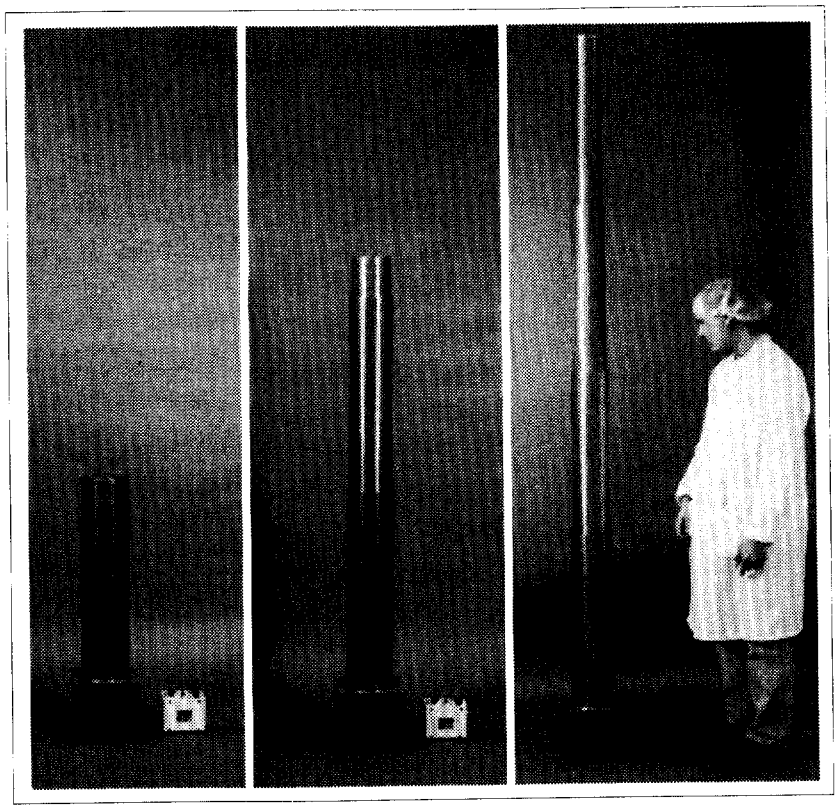

Figure 9. Telescopic Boom Aluminum Prototype.

would have resulted in a relatively bulky latch ring and stowed configuration with the boom diameter selected for the model. The maximum thickness of the latch and stiffening rings is therefore limited to a maximum of 0.61 cm (0.24 inch).

The pins and springs are set in cups, as shown in Figure 10, and the assembly is retained by the conical detent and retraction rim which is threaded into the pin and staked. The pin and cup units can be inexpensively produced in quantity with precisely mated pin and bore diameters. There are 12 identical pin assemblies in each latch ring. The springs used during structural tests provide a preload of approximately 9 N (2 lb). This can be increased to a maximum of about 16 N (3.5 lb) within the envelope available for the springs. The pin assemblies are installed in bores in the latch rings of each tube. Figure 11 shows a sample ring that is detached from the tube. Once the latch pins have been installed, the tube assembly stands alone and requires no additional fabrication.

The axial height of the lower ring along the tube length was set at 1.3 cm (0.5 inch). This height permits a shallow retraction ramp angle and ample tolerances for initial and final engagement with the retraction rims on the latch pins. The ramps have a shallow slope, as shown in the lower right-hand inset of Figure 11, which minimizes the force the BI-STEM must exert to withdraw the pins, thus ensuring smooth retraction.

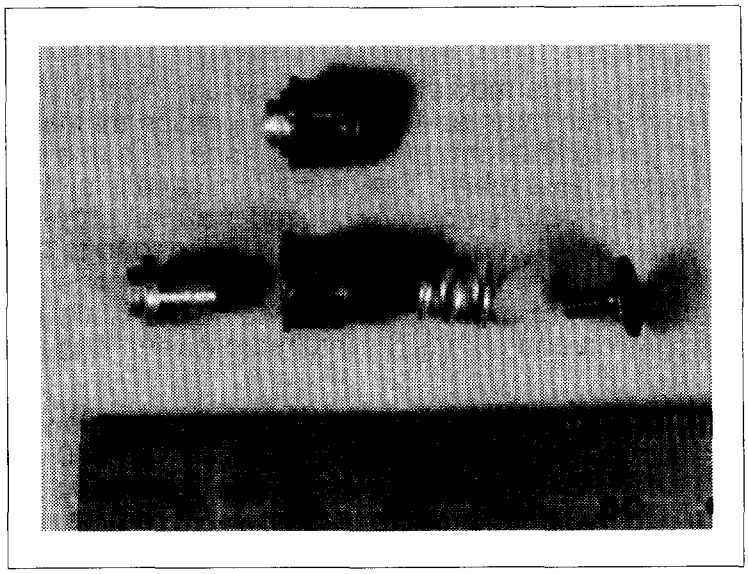

Figure 10. Development Model Latch Pin Assembly.

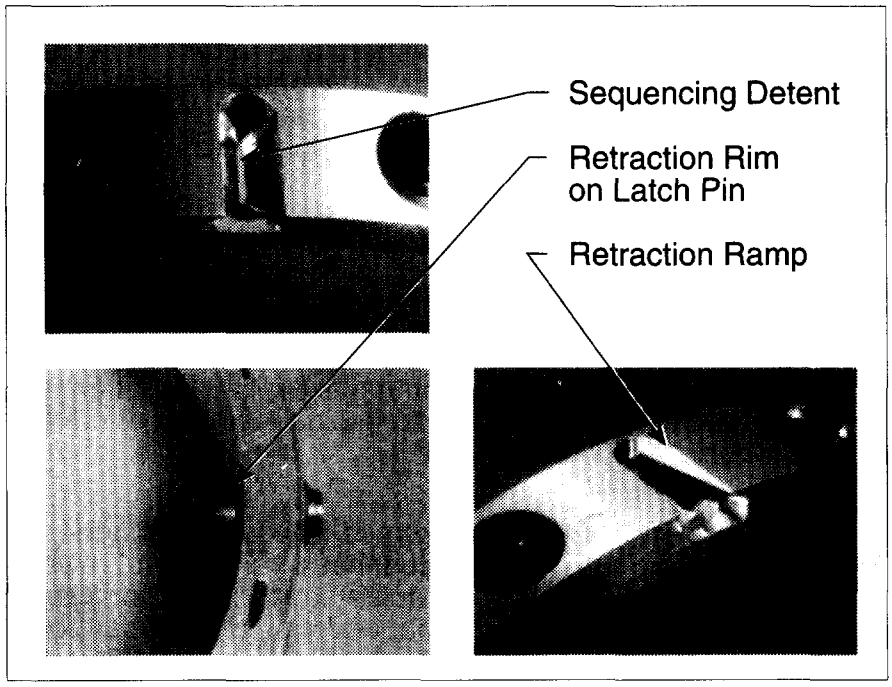

Figure 11. Latch Ring.

The tube manufacturing process is a key technology for the production of low cost telescoping boom systems. The prototype tubes were machined from heavy wall aluminum extrusions. This approach provides tubes with highly consistent dimensions and can be cost effective for smaller diameters.

Development work performed at Astro subsequent to the prototype has resulted in methods for making large and adequately precise thin-wall tubes from sheet metals that are joined to separate stiffening rings. The use of sheet stock results in relatively inexpensive tubes. The cost effectiveness of metallic tubes can be increased if sheet metals that display enhanced material properties from the forming process are utilized. Composite tubes can be bonded to separate metallic rings for further improved boom performance. Because the rings are axially short and the greatest percentage of composite fibers would be axially aligned, the coefficients of thermal expansion can be easily matched between ring and tube.

Depending upon the material, tube wall thicknesses as low as 0.25 mm (0.010 inch) are practical up to diameters of 20 to 25 cm (8 to 10 inches) without sacrificing essential durability or necessary buckling strength. Tubes of around 60 cm (24 inches) diameter in metal or composite would require minimum wall thicknesses of approximately 1 mm (0.040 inch).

The interiors of the prototype tubes are coated with a Teflon-impregnated electroless nickel plating. The plating lowers friction and prevents the aluminum from being galled by the tips of the pins as they slide along the length of the tube during deployment. The pin tips are radiused to provide a significant patch of contact area at their interface with the tube wall. Burnished tracks were left on the interior of the prototype tubes after several hundred deployment and retraction cycles, but wear was low and evidence of galling absent. In the environment of space, the high emissivity of the nickel-Teflon coating would decrease solar-induced thermal gradients across the diameter of the boom, particularly if the tube walls are not perforated.

The diametral clearance between the latch rings and adjacent larger tube walls is 0.8 to 1 mm. This allows the BI-STEM to deflect under moderate loads without binding the moving package of tubes in the deployed segments. The prototype is capable of deploying and retracting with a constant tip moment of 22 Nm (200 in-lb). This tip moment exceeds what is typically induced by the deployment tension of a large flexible solar array blanket that is cantilevered from the boom tip. The clearance between the latch rings and the inside diameter of the adjacent larger tube prevents them from touching when latched.

Detailed tolerance studies were performed while designing the tubes and latch components. The design phase revealed that a very careful review of tolerances is crucial if the latch is to display adequate structural performance, be able to sequence fail-safe deployment and retraction, and be tolerant of a moderate amount of random fabrication errors in the tubes.

PROTOTYPE BOOM PERFORMANCE

Tip load versus deflection for the 2.3-m-long prototype is given in Figure 12. The boom displays linear structural behavior, which confirms that the joints are preloaded. The data was taken after several hundred deployment and retraction cycles. The performance of the boom when new, with a latch pin preload of 9 N (2 lb), was equal to the values reported to within experimental error. Other tests were performed with a latch pin preload of 13 to 16 N (3 to 3.5 lb) which yielded somewhat higher stiffness and lower hysteresis [Ref. 2]. The preload was returned to the lower value to ensure the longevity of the boom for multiple deployment cycles.

The load-deflection curve is characterized by a region of reduced stiffness within approximately ±5 N of zero tip load that is flanked by regions of fully developed stiffness at larger tip loads. Beam theory was used to estimate the stiffness of an idealized conical aluminum boom having the same root diameter, tip diameter and wall thickness as the prototype, but without joints. The idealized boom has a tip stiffness of 9.37 N/mm (53.4 lb/in) which is about 16 percent higher than the fully developed 8 N/mm (46 lb/in) tip stiffness of the prototype.

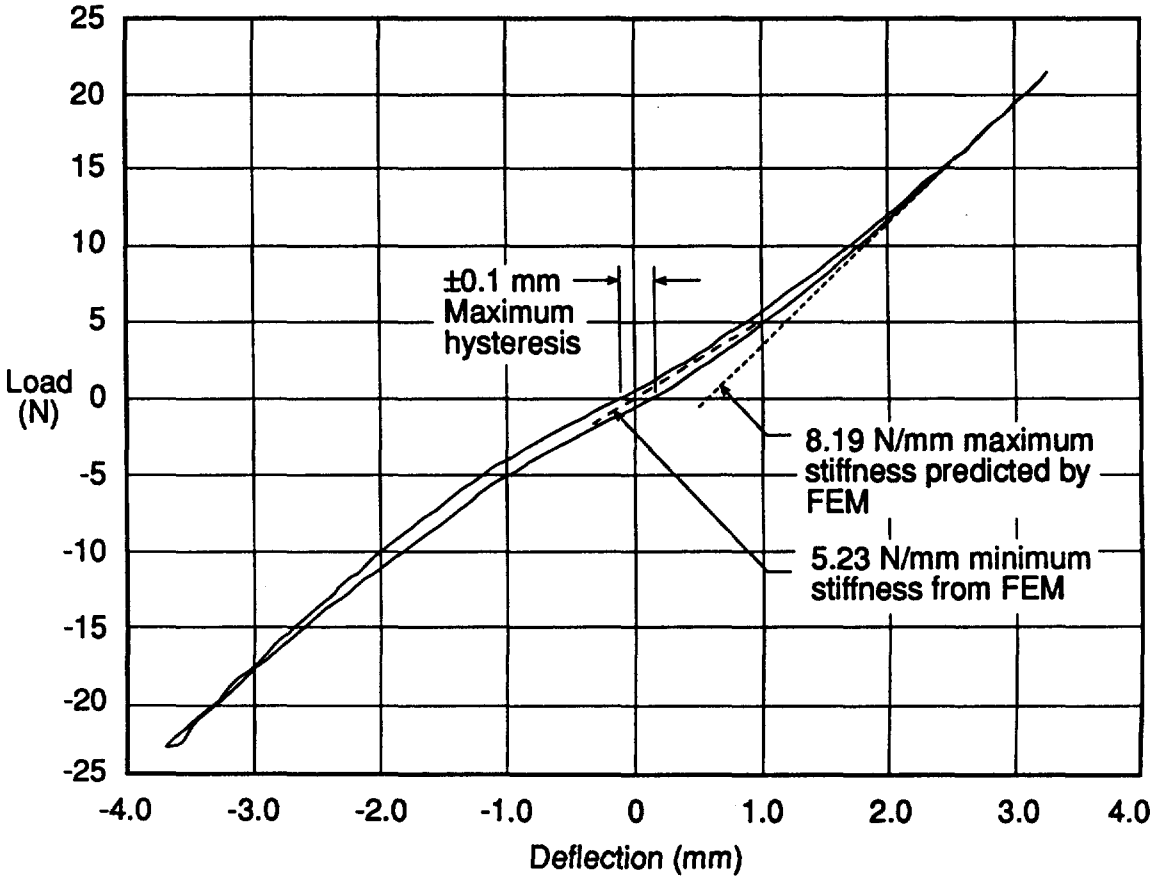

Figure 12. Prototype Boom: Tip Load Vs. Deflection.

A finite element model was constructed using COSMOS/M™ to simulate the actual geometry of the prototype boom. The FEM includes local deformations of the latch ring and tube walls that arise from the discontinuous load path between the stepped tube diameters, as shown in Figure 13. The FEM predicts a tip stiffness of 8.19 N/mm (46.7 lb/in), which correlates well with the fully developed stiffness of the prototype, as shown by the dotted line in Figure 12.

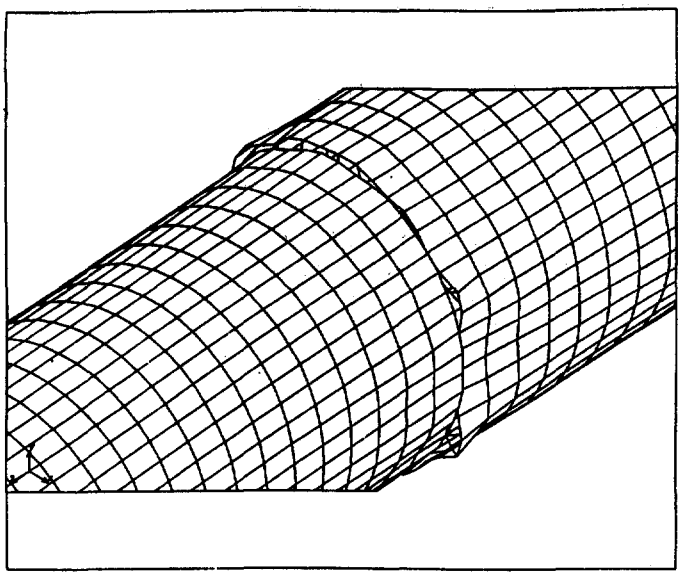

Figure 13. Finite Element Model.

The latch reduces the stiffness of the prototype to 5.1 N/mm (29 lb/inch) for small deflections, a knockdown of 39 percent. It is presumed that the diametral gap between the latch pins and the bores in the cups (Figure 5) prevents most of them from developing high local stiffnesses near zero load. As the beam is progressively loaded, all the latch pins eventually develop fully preloaded contact at the twelve latch points. To model this conjecture it was postulated that only the pins near the bending plane develop full stiffness at zero load. An FEM case was run with four pins engaged, two on each side of the boom. The four-pin case yielded a tip stiffness of 5.23 N/mm (29.8 lb/inch), as noted by the dashed line in Figure 12, which correlates well with the actual stiffness of the boom at zero load.

Hysteresis loops were repeatable to within the resolution of the LVDT used in the test, approximately ±0.02 mm (±0.001 inch). Maximum hysteresis at the boom tip is ±0.1 mm for alternating tip loads of 22 N and higher. For alternating tip loads of up to 4 N, the maximum hysteresis goes down to ±0.05 mm or less.

Dynamic damping was measured between 2 and 5 percent, depending upon amplitude, as shown in Figure 14. The data shown was initiated with a single impulse of 3 mm in the X direction. The fundamental vibration mode in the X direction differs from that in the Y direction by a small amount, probably due to the non-isotropic distribution of latch pins in orthogonal planes. At 17.5 and 17 Hz, the X and Y modes are significantly coupled, as evidenced by the modal cross-talk. For amplitudes over about 0.25 mm (0.010 inch) the damping ratio is 5 percent. Under 0.25 mm amplitude, the damping ratio is reduced to about 2 percent. The reduction of damping correlates well with the relative reduction of hysteresis that was observed at low deflections.

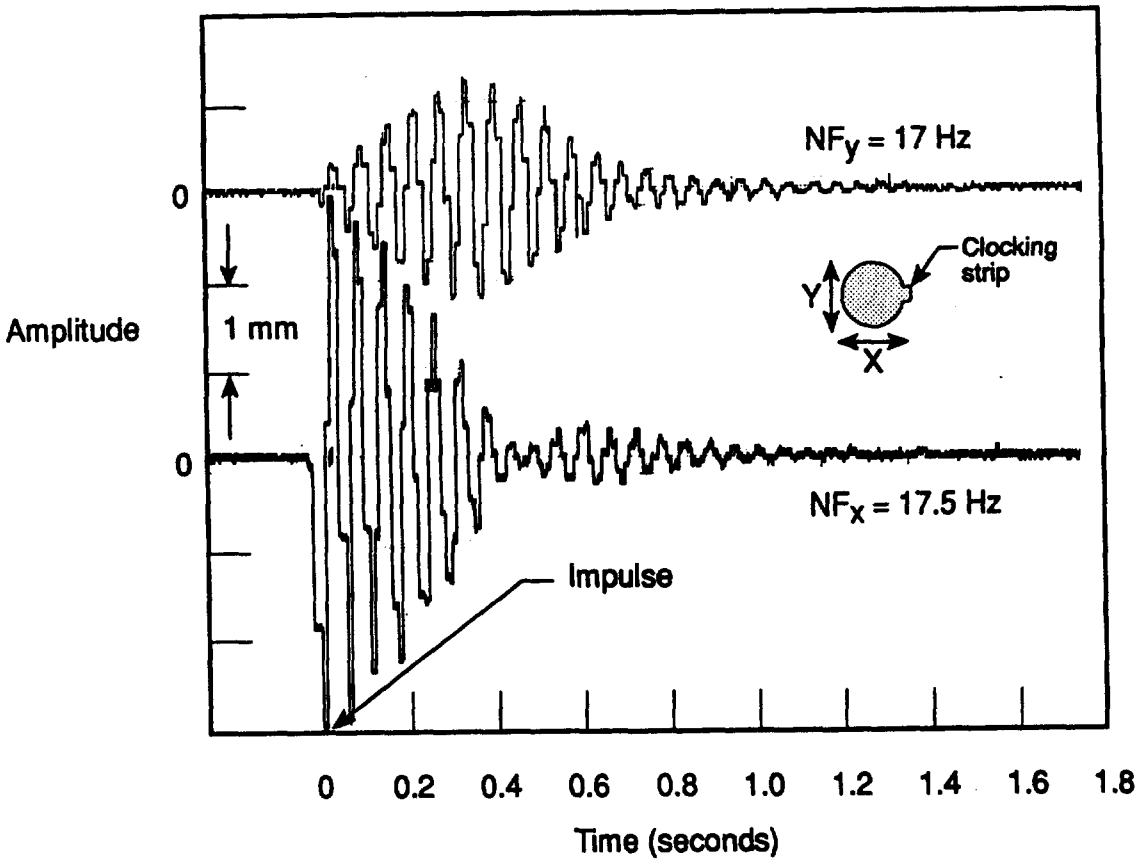

Figure 14. Damping Test Results.

DISCUSSION OF RESULTS

The 39 percent knockdown factor of the prototype latch is higher than desirable, the goal being 25 percent or less. To reduce the knockdown factor for small deflections, several things can be done. The preload can be increased, but the associated gain in stiffness would be difficult to predict. Replacement of the latch springs is very easy to accomplish, so increasing the preload is better left as an optional post-fabrication enhancement if required. Another alternative would be to increase the number of pin latches. This would reduce local deformations and increase the number of pins adjacent to the bending plane. The performance gains can be readily predicted using finite element analysis.

The preferred method of reducing structural knockdown for small deflections, however, is a matter of balancing the tube and latch ring stiffnesses. The prototype latches actually produced much greater stiffness than expected, so the thought of "improving" them leads us to review the relative stiffness of the tubes. The 0.64 mm (0.025 inch) wall thickness of the tubes in the prototype provide more stiffness than

would probably be required of a boom that size for a flight program. The knockdown factor using the prototype joint as-is would be in the vicinity of 25 percent if the tubes had a 0.4 mm (0.016 inch) wall thickness, or if 40 percent of the wall material was removed by perforations for high solar thermal stability.

SUMMARY AND CONCLUSION

The new telescoping boom achieves a unique level of performance, reliability and cost effectiveness as a high performance deployable and retractable boom structure. The design of the latch, in concert with the use of the BI-STEM as an actuator, has made this stride in deployable structure design possible.

The performance of the prototype validates the potential of the boom design to position payloads with high accuracy and without structural deadband. The high stiffness and dynamic damping of the boom are advantageous for spacecraft control purposes. Finally, the strength and efficiency of tapered tubular section properties are useful for deploying large payloads and for resisting high on-orbit loads while minimizing mass and stowed volume.

Future designs will benefit from the effort expended to understand the performance of the prototype boom. The design of the latch and the tubes can be balanced to achieve the goal of 25 percent joint knockdown by utilizing the analytical techniques described herein.

REFERENCES

1. "Evaluation of Space Station Solar Array Technology," First Topical Report No. A981486, LMSC, 1970 and 1972.

2. M.W. Thomson, "Deployable and Retractable Telescoping Tubular Structure Development," AIAA No. 93-0976, Aerospace Design Conference, Irvine, CA, 16-19 February 1993.

LESSONS LEARNED FROM SELECTING AND TESTING SPACEFLIGHT POTENTIOMETERS

T. Iskenderian
California Institute of Technology
Jet Propulsion Laboratory
Pasadena, California

ABSTRACT

A solar array drive (SAD) was designed for operation on the TOPEX/POSEIDON spacecraft that was launched in August, 1992. The experience gained in selecting, specifying, testing to failure, and redesigning its position sensor produced valuable lessons for future component selection and qualification. Issues of spaceflight heritage, cost/benefit/risk assessment, and component specification are addressed. It was found that costly schedule and budget overruns may have been avoided if the capability of the candidate sensors to meet requirements had been more critically examined prior to freezing the design. The use of engineering models and early qualification tests is also recommended.

INTRODUCTION

Uncommon rotational axis pointing accuracy, for a SAD, is required due to the precision orbit determination (POD) requirements on the TOPEX/POSEIDON spacecraft. This information is vital to the primary mission of the spacecraft, which is to survey the variation in ocean elevation to an accuracy of a few centimeters over the period of at least three years. TOPEX/POSEIDON uses a single, very large solar array that acts as a sail in the solar wind. The solar pressure and aerodynamic forces acting on the array cause much of the total non-gravitational forces which must be accounted for in the POD process; if orientation of the array with respect to the satellite body is in error, the solar pressure and aerodynamic force models will be in error. The total error allocation from POD for the pitch, or rotational axis of the SAD, is 5.6 mrad (0.32°), 1 sigma, for all error sources, including thermally induced and structural misalignments. That amount of error corresponds to a worst-case altitude error of about 1 cm. A 3-sigma accuracy requirement of 0.1% absolute linearity was assigned to the position sensor in the process of allocating the pitch axis error to all sources of uncertainty.

Besides high accuracy, continuous rotation in either direction is necessary, with no interruption of signal. Operating rate in flight could range from zero to 110 mrad (6.3°) per minute, but could go much higher in ground test. Life, in terms of total number of revolutions, was not a

major design challenge for any of the options we studied. An electronic means of switching between potentiometer (pot) elements to maintain continuous function over 360° was proposed, which removed the reliability concern of mechanical switchover.

Pots, optical encoders, resolvers, and induction-based technologies were considered. However, pressure to minimize cost led to selection of a pot, with its low component and electronics costs. When one pot vendor was found who could meet the requirements and demonstrate spaceflight experience, a pot-based scheme was chosen for its substantially lower estimated total cost. JPL contracted with Schaeffer Magnetics, Inc. to design and produce the SAD assembly, and to integrate the vendor-supplied pots with the SAD upon final assembly.

Problems with electrical noise and poor mechanical integrity of the pots began to show up as soon as environmental tests began. After four design cycles and three rounds of failure analysis, all problems except for electrical noise were completely corrected. Although the noise was reduced to a large extent, development problems halfway through the effort prompted the project management to seek risk reduction by asking for an additional means of position feedback. Thus an electronic motor-step counting circuit, named the SAD Incremental Counting Mode (SICM), was designed and built concurrently with the pot rework efforts. The final configuration of the SAD mechanism is shown in Figure 1. Figure 2 shows the general layout of the pot mounting and surrounding structure.

As a result of the failures and efforts to eliminate them, the SAD delivery was delayed by one year, and the cost overran the maximum estimate by approximately 50%.

The spacecraft was launched successfully on August 10, 1992. Since then, the pot position signal has been nominally in agreement with the position calculated from the step counting electronics. While the SICM is used most often in the SAD's position control loop for reasons of signal processing convenience, the pot has not displayed any noise in the spacecraft's telemetry.

REQUIREMENTS AND TRADE STUDY

Early in the design process, a study team was chartered to perform a cost-vs-performance trade and determine the best means of position sensing. The following overview describes the main issues which the study team considered; Table 1 summarizes the most significant requirements in that study.

Table 1
Position Sensor Requirements

Position Knowledge Accuracy, 3 Sigma	7.22 mrad (±0.414°), ±0.115% absolute linearity
Mechanical Range of Motion	± 360° continuous rotation
Electrical Range	± 360° continuous rotation and signal output
Signal Output	12 bit digital
Reliability	Electrically redundant
Life	30,000 revolutions
Environmental:	
Thermal	-30° C to + 85° C design limits
Dynamic	19.6 g rms, 20 — 2000 Hz random 5 g peak, 11—100 Hz sine
Radiation	100 krad

An industry survey identified the candidate sensor options. After considering several vendors, the characteristics of the best representative of each type were compared. Table 2 summarizes these findings.

We initially chose a resolver as the solution that would meet the accuracy requirement with acceptable cost and power. We selected three units as representative, each advertised with 1.2 mrad or better accuracy.

As the project's requirements and scope matured, however, the relatively high cost and mass of the resolver-based system caused much attention to be focused on the potentiometer option. At just under 1 kg per redundant unit, resolvers made the 0.24 kg pots look attractive. Sensor electronics mass is not considered in this estimate; the difference would be exaggerated further if it were. The resolver mass would likely have been even higher, if rotary transformers were included in the package to preserve its clean signal. Furthermore, existing resolver-to-digital (R/D) electronics were not available with class S radiation-hardened parts. The most promising specification indicated a 20-krad demonstrated capability with local shielding, so a qualification test program would have had to be undertaken.

The estimated cost for this effort was $450,000, and success was not assured. Pots, seductively priced at 17% of their competition, appeared to be a reasonable choice.

Table 2
Position Sensor Trade Options

Characteristic	Pot	Optical Encoder	Resolver	Inductively Coupled
Accuracy, 3 sigma	±6.8 mrad	±1.5 mrad (12-bit A/D) or better	±1.5 mrad (12-bit A/D) or better	±1.5 mrad (12-bit A/D) or better
1988 Estimated Cost (electronics & sensor), normalized to pot	1.0	8.7	5.8	6.7
Reliability concerns	Electrical noise in vacuum, wiper lubrication	High parts count	Requires qual program for discrete 16-bit R/D, also slip rings or rotary transformer	High parts count
Other concerns			Mass	Mass and power

The primary focus of the trade study was to contrast the cost and likelihood of success of qualifying the 16-bit resolver electronics on the one hand, against the accuracy and vacuum reliability of pots on the other hand. The risks of using a resolver were investigated more thoroughly than those of the pot. In fact, we assumed that the pots would not require a development effort. We surveyed resolver vendors for quality and drafted a qualification plan for the R/D converter. Little scrutiny was applied to components' ability to survive the temperature and vibration environments. Because accuracy requirements were relaxed just enough to allow the pot to be competitive, reliability and overall mass became the determining qualities of merit.

The study team investigated reports of poor pot reliability in a literature search.[1] Their findings warned that electrical noise could occur

in pressures below 1E-5 Torr, particularly if the sliding electrical contacts were not lubricated. There were also reports of failed internal mechanical switches used to alternate between pot elements and avoid the deadband of each element. This concern was obviated, however, because our switching would be done by digital electronics inverting the most significant bit of one pot element in a pair.[2] The technique of switching between these elements, designated "primary" and "secondary", is illustrated in Figure 3. Wear did not appear to be a significant problem for this application; our requirement for total revolutions was about 1/10 to 1/20 of the value where electrical noise was observed to commence in life tests of other pots.

We had set successful spaceflight heritage as an important criterion for sensor selection. This was not a problem for the resolver, but our choice of pots was limited to those offered by only one pot vendor who could demonstrate the capability to manufacture a multi-element pot with the required accuracy. A large outside diameter of 7.6 cm (3 in) would be necessary to achieve the linearity requirement. Although it was believed that this particular design was sufficiently similar to other flight-qualified units, we failed to thoroughly research the heritage of these pots. When failures in test occurred, it was determined that this design had not actually been used in a spaceflight or vacuum application. The pot vendor had built similar, although smaller, pots for spaceflight use; unfortunately, important design differences and unfavorable scaling of their response to a dynamic environment rendered those units inapplicable to qualify the large pots by similarity.

Under pressure to choose in a constrained-cost environment, the team committed to using pots.

SPECIFICATION

A general cross section view of the pot is shown in Figure 4. The resistive and conductive tracks are two annular rings on each element, co-molded into the Diallyl Phthalate (DAP) disk substrate during fabrication. Each pot element is manually trimmed to specified linearity by grinding away small fractions of these co-molded resistive tracks by removing material from an annular channel that is cut adjacent to the track for this purpose. A thin electrical wiper contact, whose contact force is controlled to approximately 15 cN, sweeps over each track. As seen in Figure 5, two wipers per element, originally made of beryllium copper alloy, are resistance welded to their wiper arm. The wiper arm grips an insulating ring on its respective hub by friction generated through spring force when the arm is sprung open, much like a retaining ring, to install it on the hub.

As is common with aerospace procurements, there was schedule pressure to release a specification for the potentiometer Request For Proposal at the earliest possible time because of the lengthy procurement lead time. This left some important areas incompletely or inadequately defined. This discussion details aspects of the specification that received insufficient attention or suffered from lack of mature analysis at the time of contract start.

The specification was written at least 6 months before a preliminary structural analysis of the SAD design was completed. Without conservative interpretation of a preliminary analysis, the designer was forced to guess at the vibration levels that the pot may experience at its mounting surface. The value chosen was 19.6 grms, or 1.24 times the level of 15.7 grms input to the SAD mounting points during protoflight test. Also, while the specification called for a safety factor of 2.0 yield and 3.0 ultimate throughout the pot design, no analysis was done to verify these margins. We relied entirely on the pot vendor's past experience in similar dynamic environments.

Some features of the "inherited" units departed from well-known, good design practice. While any change from inheritance should be considered with great caution, some design changes are appropriate risks. For example, the hub of each pot element was fastened to the common shaft by one cone point set screw in the proposed design. This shortcoming was noted at the pot's design review, but a non-standard solution was effected: the single fastener interface to the shaft was retained, but that fastener was backed up by another set screw to lock it in.

Absolute linearity was defined and limited to within ±0.1% for each element per Variable Resistive Components Institute Industry Standard VRCI-P-100A[3]. Thereafter, the four elements had to be aligned so that the signal from either of the two redundant element pairs would deviate less than ±0.115% from absolute over a full revolution.

The initial release of the specification required that units assembly take place in FED-STD-209 class 10,000 or better conditions. We later found that, in practice, this was difficult or impossible to achieve with the limited clean room equipment available to the pot vendor. To preclude contamination in shipping, a packaging method which seals the pots into individual nylon bags was called for.

FAILURE, INVESTIGATION, AND REDESIGN

Problems began to surface prior to manufacturing the units. JPL's Quality Assurance representatives surveyed the manufacturer's facility and found its cleanliness and process controls to be typical of most commercial houses, i.e., inadequate. However, the pot vendor did correct these discrepancies, as verified by a follow-up QA report.

Packaging

The first lot of units was received with incorrect packaging. They were externally contaminated with fibrous debris from the packing material, the vent filter screens were held loosely by their retaining rings, and shaft torque measurements displayed noticeable torque variations over a full revolution. We convened a Material Review Board to disposition these concerns. The pot vendor explained that the torque variations are normal for this type of pot, with multiple elements and friction sources. The Board decided to use the pots as is, with the belief that any access path of a particle to the resistive elements within was sufficiently serpentine to preclude harm to those sensitive areas. The serial numbers of these first units were 001 through 004.

Loosened Hubs

Further problems with this first lot surfaced when protoflight tests began on the assembled mechanism. Random vibration tests developed calibration shifts of up to 40 mrad in the pots. We traced this phenomenon to internal looseness of the wiper hubs on the shaft, caused by failure of the set screw joint which, as mentioned, was the subject of concern at the initial design review. We implemented a successful solution on all subsequent lots: each steel hub was first mechanically fastened to the shaft with two set screw joints (one cone point, one cup point) at 90° to each other, then bonded with a bead of epoxy at the shaft/hub interface. The set screws themselves were blocked from backing out by a drop of epoxy. Absolute position error was measured by automated sampling of thousands of data points in a revolution. Subsequent vibration testing proved that these design changes successfully kept the pot elements within calibration.

Electrical Signal Noise

Electrical signal noise was experienced on many occasions. The noise most often occurred after vibration tests, but would sometimes be manifest before exposure to any flight environment. It was often of a very dramatic nature, sometimes opening the pot circuit altogether. A sample chart record of pot noise is shown in Figure 6. The noise signature could vary

considerably for each pot over extended running, from occasional blips to gross open circuits.

The effect that the noise would have on the SAD controller was not known. To justify expending the effort to correct this problem, controller behavior in response to typical pot noise had to be quantified. An electronic noise source was designed to inject varying voltages and pulse durations into the pot signal line. Two kinds of noise were generated: single-pulse and multiple-pulse. The single pulses were set at 200 ms, 400 ms, and 1 sec, and from 1.0 to 3.5 volts amplitude. Multiple pulses were timed at 1 Hz and 2.44 Hz intervals, 2 volts in amplitude, and pulse-width set at either 35 or 200 ms. These tests demonstrated that the controller was indeed sensitive to noise that approximated what we saw in pot testing, and that we needed to pursue efforts to eliminate the problem.[4]

For each of the first three lots, at least one representative unit was completely disassembled and subjected to failure analysis with the hope of finding a solution to pot noise and the other problems. This was a troublesome process, because the pot was designed such that epoxy bonds had to be chiseled loose, which generated debris. This debris interfered with the investigator's search for particulate contamination, sometimes yielding ambiguous results.

The failure analysis comprised the following minimum set of activities:

- Radiographic (X-ray) inspection of the units before disassembly
- Scanning Electron Microscope (SEM) visual and chemical analysis of internal surfaces
- Wiper force measurements
- Macroscopic video records of the pot elements as they were exposed, one by one, in disassembly

Serial numbers 001 and 004 from the first lot displayed a high degree of internal contamination, both metallic and fibers of DAP. The investigator judged that most of these did indeed result from the assembly and final calibration trimming process. Several particles were found clinging to the wipers. SEM photos of the wiper contacts showed some wear, even through the gold plating on some surfaces. Some of the tracks, both resistive and conductive, displayed discrete markings where their respective wiper was known to have rested during vibration. A SEM photo of a typical vibration mark is shown in Figure 7. We concluded that the electrical noise was due to loose particles interfering with the electrical contact, and vibration damage to the contact surface. Although the contact's gold plating wore

through in places, this probably was not a contributing factor, because noise also occurred before significant wear was experienced.

It is a common practice to apply lubricant to electrical contact surfaces. In an effort to smooth out resistance at the contacts and minimize surface damage during vibration, we built the next lot of pots, numbers 005 through 007, to the same specification, except that Bray 815 Z oil was applied to each track during assembly. We chose 815 Z oil for its compatibility with the same oil in the pot bearings. The pot vendor was cautioned to use the class 100 laminar flow bench more effectively for assembly operations.

We were rewarded with severe noise starting less than two revolutions into a run-in test of No. 006 pot in <1E-3 vacuum. Numbers 005 and 007 also displayed similar noise signatures, even before exposure to vibration.

Number 006 pot was dismantled and analyzed. The oil on most tracks had beaded into a dew-like appearance, and was clearly mixed with varying amounts of wear debris and other particles. DAP and cotton fibers were trapped on the wetted surfaces. A long cotton fiber was found intertwined in the noisy element No. 1 wiper, among a number of DAP particles in a matrix of black, tarry oil. A photo of one wiper, encrusted with these particles, is shown in Figure 8. Although the tarry mixture contained conductive carbon wear debris, resistance measurements of the substance indicated >20 MΩ with micrometer probes. Concerns were raised about traces of epoxy found to have outgassed onto internal metal surfaces, and of a varnish with volatile constituents used to seal the calibration trim groove. Nevertheless, no trace of either material could be found on the element tracks or wipers.

Our findings, and the pot vendor's opinion, convinced us that the contact lubricant was not helpful, and could actually be trapping debris and exacerbating the noise problem. In fact, most of the wiper contacts displayed more wear in SEM photos, as shown in Figure 9, than did the unlubricated contacts with the same normal force.

It was also clear that much stricter cleanliness measures had to be taken. However, our failure analysis of specific elements showed only a fair correlation between particulate contamination and electrical noise. To vanquish the noise, both the pot vendor and the mechanism design engineers agreed that it would be beneficial to increase the wiper contact force. The first two lots were built with the pot vendor's standard 10 to 11 cN contact force specification; this low force was desirable to minimize friction torque. Any increase in torque would proportionately increase the error of the SAD's rotational axis signal due to the torsional wind-up of the

pot drive coupling. The risk was assessed, and it was agreed that the contact force could be increased to 18 ± 4 cN. This was accomplished by re-forming the Be-Cu alloy wipers to increase their preload when assembled to the same geometry as the previous pots.

Wiper Contact Fracture

The new lot of pots, numbers 008 - 012, entered vibration test with acceptable characteristics. Unfortunately, we found that the wipers had not been adequately re-engineered; the wipers fractured halfway through the random vibration test at regions of high stress. The fracture was observed as the pot signal was monitored in vibration; a sudden step change in the position signal occurred as a new contact point was established with the stub of the remaining wiper.

Metallurgical analysis of the failed wipers showed they had broken due to crack propagation from fatigue loading, followed by ductile failure. Failure analysis photos of a representative broken wiper are shown in Figures 10 and 11. It turned out that Be-Cu alloy No. 25, in the half hard condition and fully heat treated after forming, was among the least fatigue-resistant of Be-Cu alloys.

We turned to the J. M. Ney Company, a firm that specializes in the design, test, and manufacture of sliding electrical contacts, for a solution. Ney recommended its Paliney-7, a precious metal alloy primarily comprising palladium, silver, gold, copper, and platinum. This material was developed for use in sliding electrical contacts, and has been applied in other manufacturers' pot designs. The available fatigue property data for this alloy suggested that it would be fair to expect excellent performance in vibration. New wiper contacts of Paliney-7 were fabricated to a contact force specification of 20 ± 4 cN, and assembled into the final lot, serial numbers 013 through 018.

The Engineering Model SAD was used as an instrumented test-bed to determine the actual dynamic environment at the pot. We found accelerations of up to twice the specified 19.6 grms pot capability. To mitigate the structure's amplification, the vibration spectrum input to the SAD was notched.

This fourth design lot successfully passed all screening and qualification tests. We employed advanced, real-time x-ray technology to perform Non-Destructive Evaluation (NDE) of pot internal parts after they were subjected to the qualification tests. This approach yielded objective, convincing evidence of unit integrity when optical inspection was impossible.

We proceeded to perform a life test to verify that the performance did not degrade within the 30,000 revolution requirement.[5] Because the SAD often operates in an oscillating mode, a motion controller was designed to emulate flight-like operation with a substantial number of oscillating cycles. The total number of test cycles was 188,907. These comprised approximately 30% continuous rotation and 70% oscillating mode. Prior to the life test, the subject pot was vibrated at three specific shaft positions, with different levels of random input at each level. Temperatures of 24°, 40°, and 75° C were applied in a bell jar evacuated to <5 E-5 Torr. The rate was generally accelerated 60x the flight rate to achieve enough wear in the limited time available. The test was periodically stopped to check for pot calibration shifts and friction torque. Signal voltage was continuously monitored; we observed wiper contact behavior by recording, alternately, the actual contact resistance or rapidly changing anomalies in the signal voltage.

Table 3
Potentiometer Design History

	Potentiometer Serial Number			
	001–004	005–007	008–012	013–018
Wiper Track Lubricant	None	Bray 815 Z	None	None
Wiper Force	10 to 11 cN	10 to 11 cN	18 ± 4 cN	20 ± 4 cN
Wiper Material	Be-Cu	Be-Cu	Be-Cu	Paliney 7
Hub Fastening	Single set screw joint	Two set screw joints + hub bond	Two set screw joints + hub bond	Two set screw joints + hub bond

Results from life testing were favorable. Element number three tended to have more noise than the others, but within acceptable bounds. By comparing the noise amplitude and location with the vibration level at that shaft dwell position, a clear correlation between vibration damage (Figure 9) and noise was observed. Noise behavior at rates ranging from 1x to 120x flight showed no significant rate dependence. A trend towards increased shaft friction torque was noted; average values at the start of the test were 0.0105 N•m, increasing to 0.0199 N•m at the end. Average error

remained within specification for the duration of the test, although a worsening trend is clear (Fig. 12).

LESSONS LEARNED

1) Seek out and consult with established industry experts when persistent problems arise; don't try to save money and time with repeated efforts within your own organization.

The final design embodiment includes changes in wiper contact material, contact force, process and cleanliness controls, and improved fastening of internal parts. Of these, we attribute the critical enabling technology to the J. M. Ney Company, which advised on wiper material selection. Any engineer who is embarking on a design and development effort for a new electrical contact application would be well advised to consult with this company, and refer to its excellent textbook on the topic.[6] We also recommend the use of real-time radiographic services as a fast, cost-effective tool for NDE.[7]

2) There can be a high risk in buying custom-designed components which are based on qualification by similarity. If a good match of flight pedigree to requirements is not possible, a careful design analysis and/or early component qualification program should be planned. The use of engineering models is strongly recommended.

We developed screening and qualification tests which provided rapid, clear indication of pot flightworthiness. The engineering model SAD was an invaluable test-bed for instrumented vibration tests and early performance measurements.

The risks associated with the original SAD design using the resolver were investigated more extensively, including a QA survey of the vendor and a qualification plan for the Resolver-to-Digital converter. The probable cost of development for a resolver was estimated. As part of the apparent cost savings for the pots, it was assumed that development would not be required. It is wise to fully understand the qualification and the flight history of the custom component progenitors.

4) It is not always practical to develop a complete flow-down of requirements for components at the time that they need to be specified and procured. Under these circumstances, the specifications developed for the components must drive assembly design.

Sufficient analyses or special tests need to be performed to make the assembly design and performance compatible with the component specifications.

5) There is a real benefit in having QA residents at contractor facilities.

We may have avoided certain quality problems this way, or at least, could have made earlier decisions to disposition the questionable parts and avoid delays.

6) When faced with a development program, build and test as many solutions, in one iteration, as can be reasonably foreseen .

When problems do occur, pause long enough to plot out a course of action. Brainstorm all the possible fixes to the problem, and implement as many as possible at an early date. The added cost of building many design variations at once may be dwarfed by the cost of maintaining an organization through several cycles of redesign and retest. For example, the second lot of pots could have been built with the four permutations of high and low wiper force, coupled with lubricated and non-lubricated contacts.

7) Design assemblies for ease of disassembly as well as assembly.

The pace of failure analysis was slowed due to the great caution required to disassemble the pots. Moreover, confidence in the meaning of the analyst's findings was diminished. Redesign and rebuild cycles could have been faster if new flight pots did not have to be fabricated from scratch at each design iteration.

The work described in this publication was carried out by the Jet Propulsion Laboratory, California Institute of Technology, under contract with the National Aeronautics and Space Administration.

REFERENCES

1 JPL internal IOM 343-88-146, M. L. Agronin to G. R. Lane, Potentiometer Failures in Hughes Environmental Tests

2 NASA Tech Briefs, Vol. 16 No. 2, "Eliminating Deadbands in Resistive Angle Sensors," February 1992

3 VRC-P-100A, Industry Standard for Wirewound and Nonwirewound Precision Potentiometers, Terms and Definitions, Inspection and Test Procedures, Variable Resistive Components Institute, Lincolnwood, Illinois, 1988

4 JPL internal IOM 343-91-451, R. O. Allen to R. F. Williamson, TOPEX Noise Pulse Test Using a Flight SADE at SMI on 5/09/91

5 JPL internal document EM 343-92-1272, R. O. Allen to R. F. Williamson, TOPEX SADA Life Test Pot SN 016

6 Pitney, Kenneth E., Ney Contact Manual, The J. M. Ney Company, Bloomfield, Connecticut, 1973

7 Real-time microfocus radioscopy services provided by Fein Focus USA, Inc., Agoura Hills, Ca.

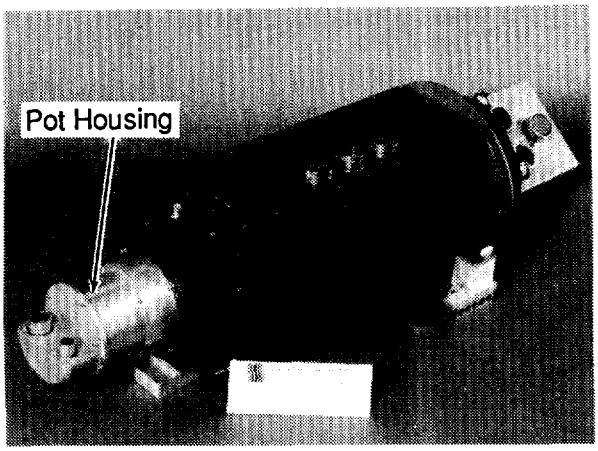

TOPEX/POSEIDON SAD

Figure 1

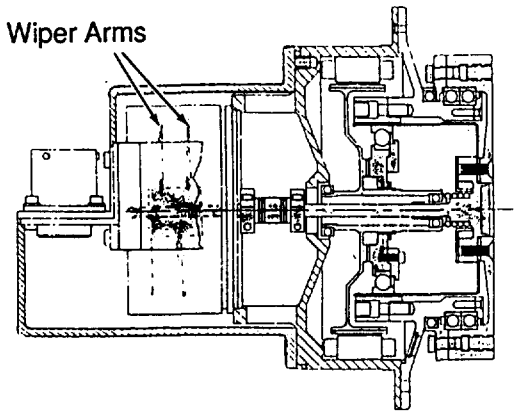

Potentiometer/Actuator Module

Figure 2

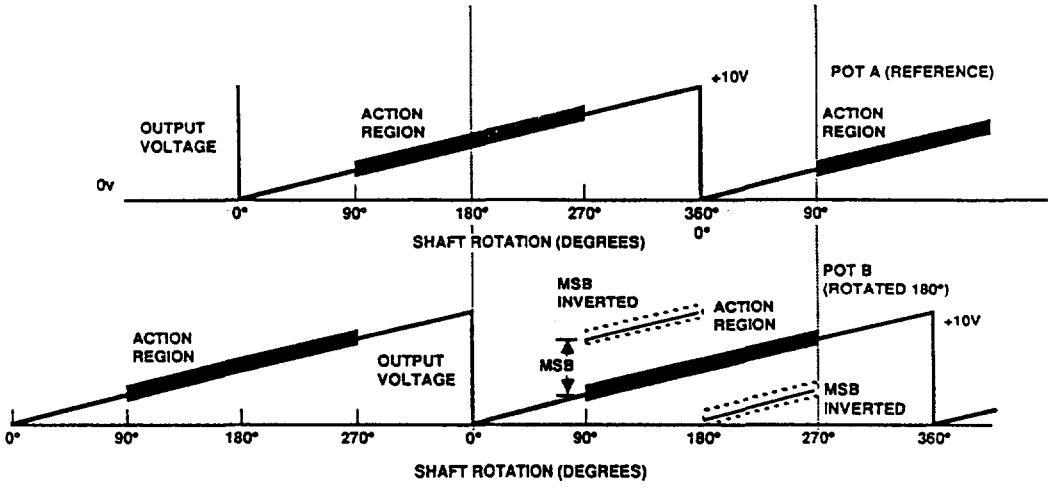

ALGORITHM

(1) WHEN IN ACTIVE AREA OF POT A, USE DIGITIZED OUTPUT UNMODIFIED
(2) WHEN IN ACTIVE AREA OF POT B, INVERT MSB OF DIGITIZED OUTPUT

Digital Method of Selecting Active Potentiometer Element

Figure 3

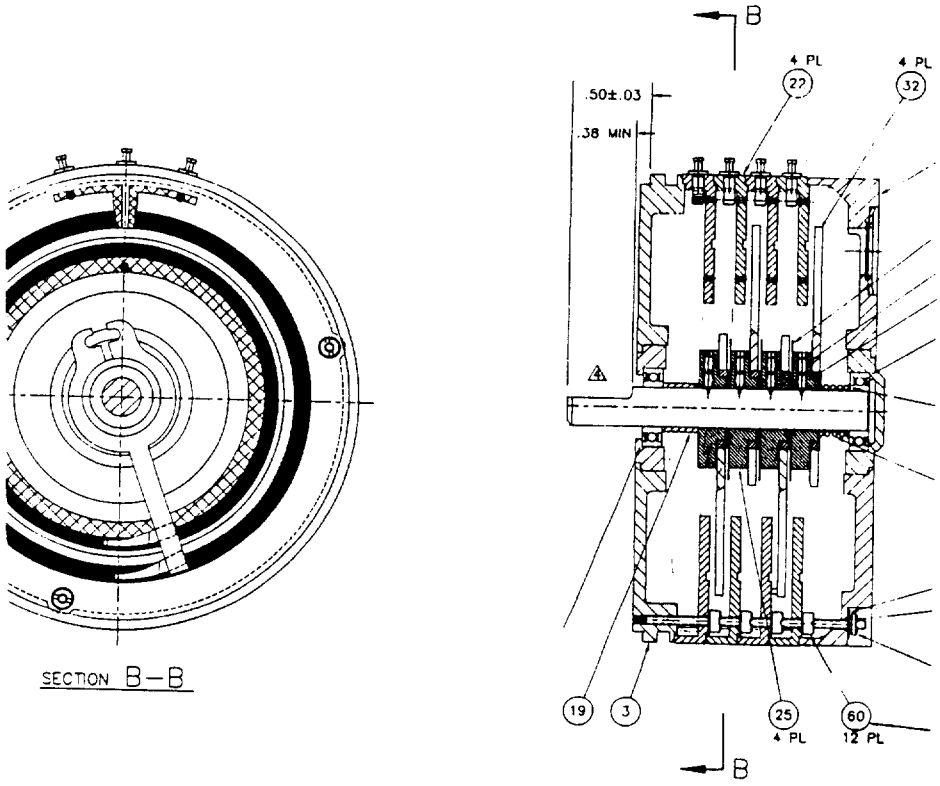

Potentiometer Cross Sections

Figure 4

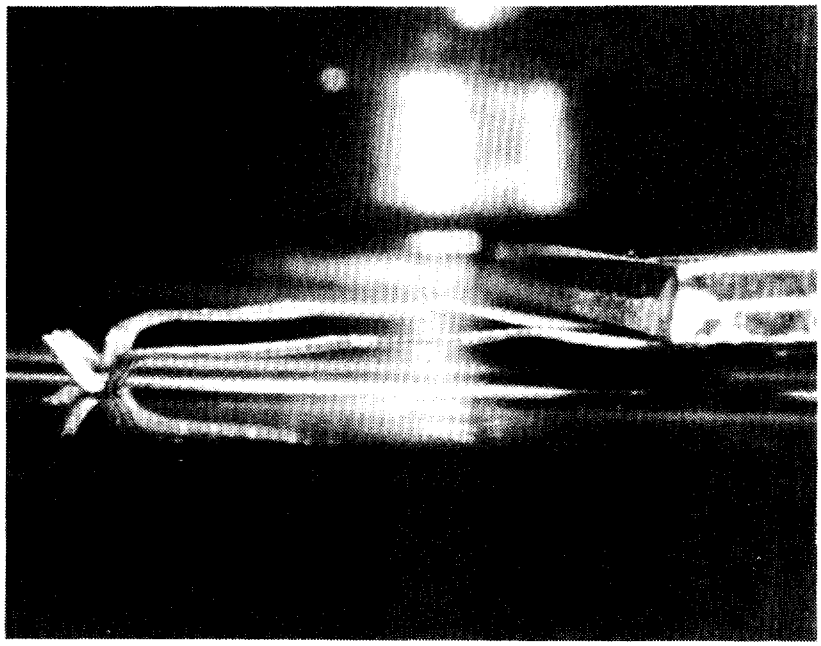

Photo of Typical Wiper Contact Pair

Figure 5

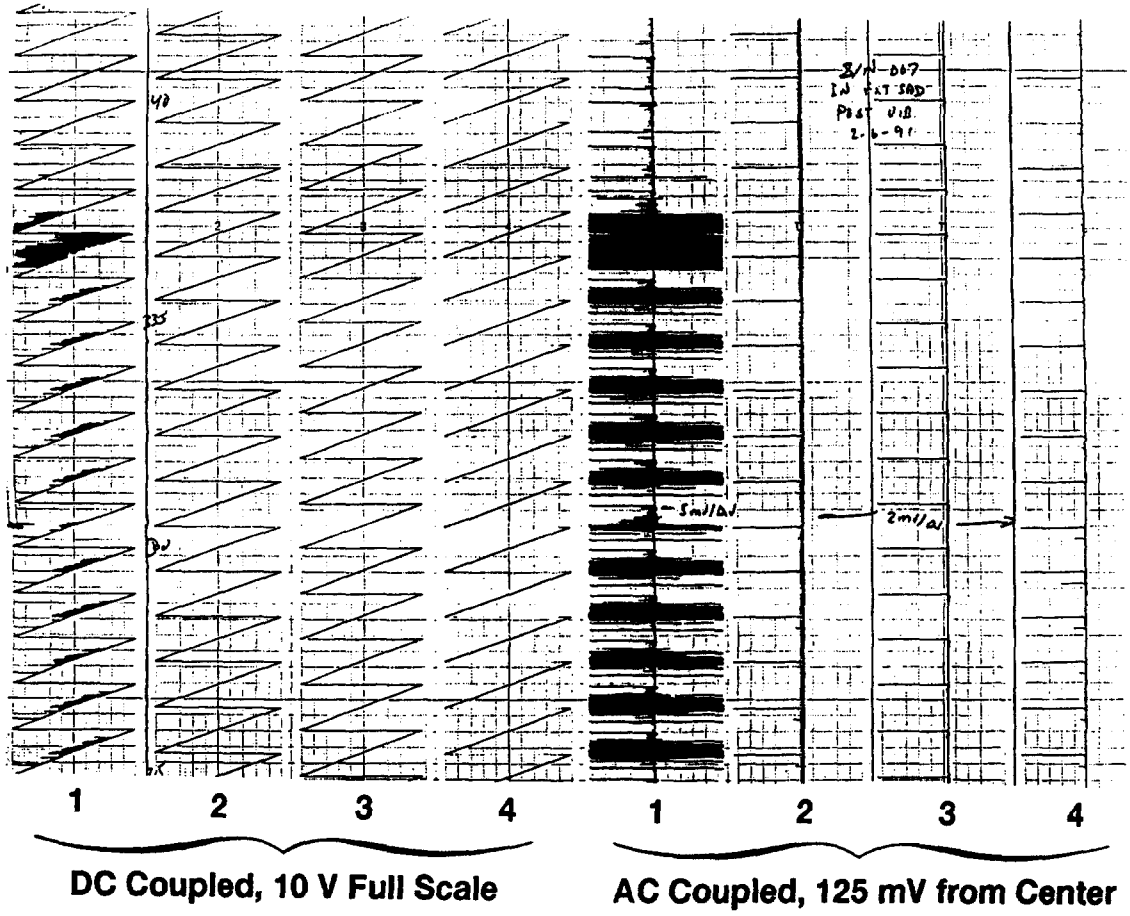

Chart Record of Noise on Pot SN 007 after Vibration, Elements 1 through 4.

Figure 6

Element Damage from Vibration at Wiper Contact Dwell Point

Figure 7

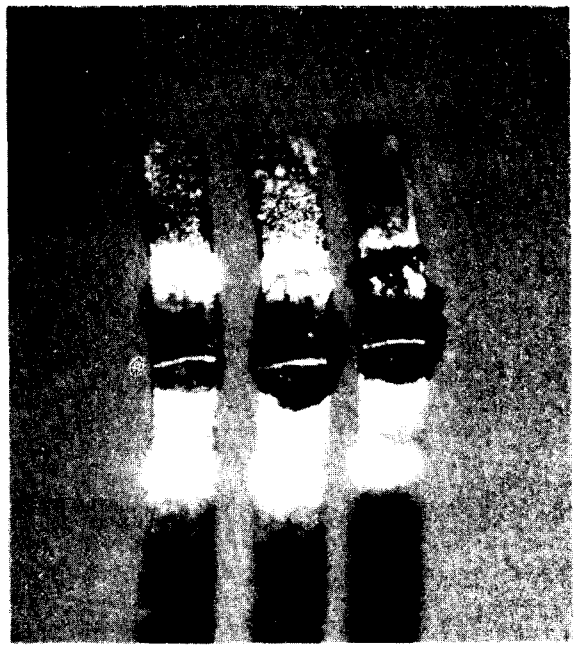

Oil and Wear Debris Slurry on SN 006 Wiper Contacts

Figure 8

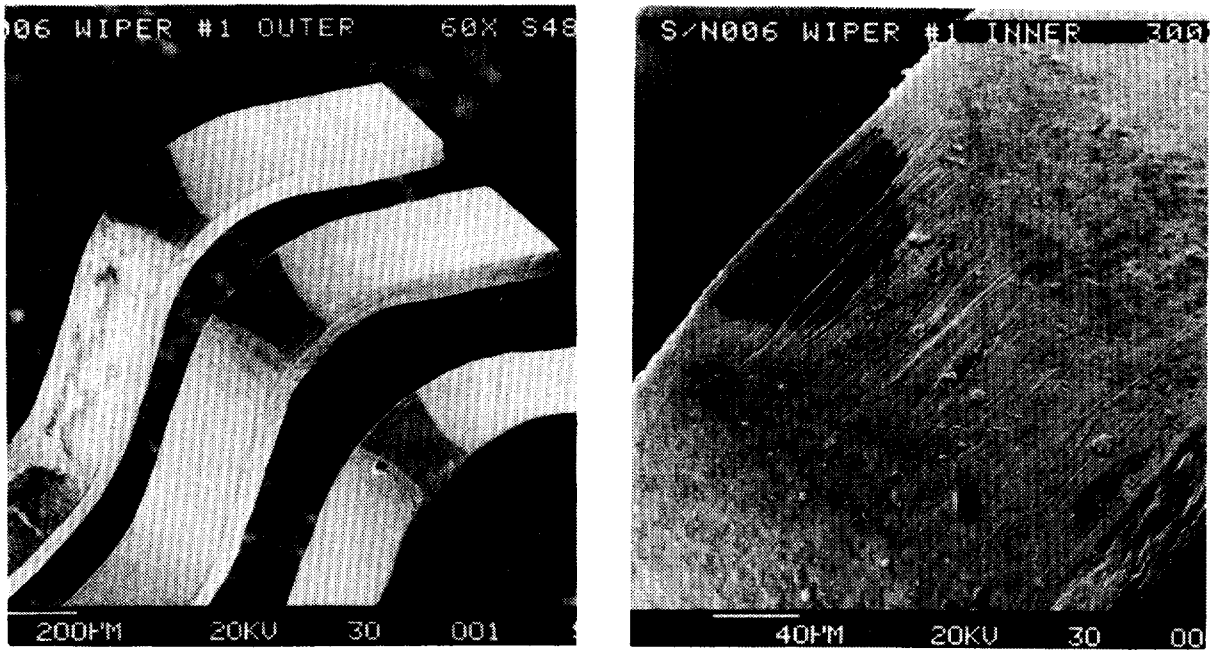

SEM Photo of SN 006 Wiper Contact Wear

Figure 9

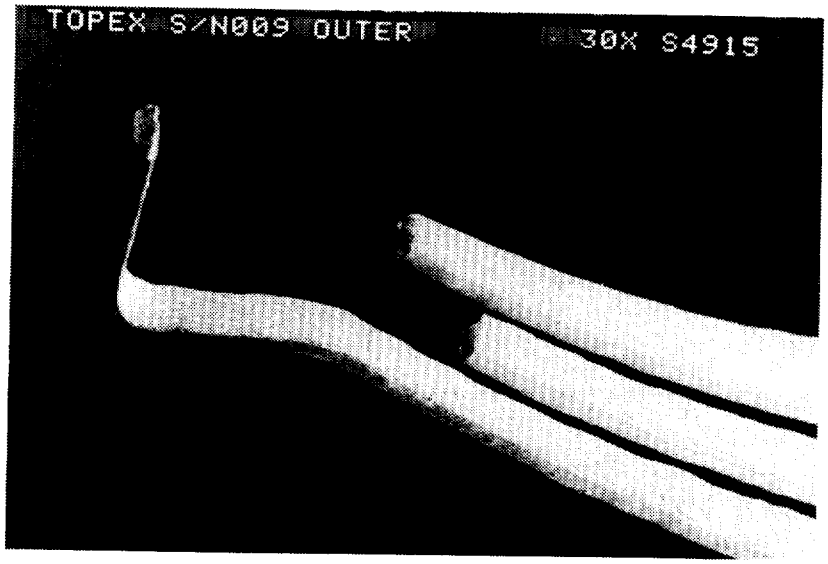

SEM Photo of SN 009 Fractured Wiper

Figure 10

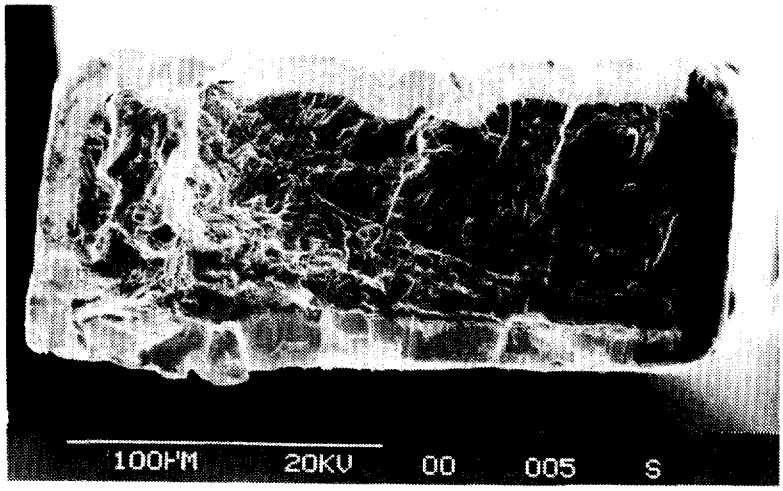

**SEM Photo of Fracture Plane,
Showing Gold Plated Outer Layer**

Figure 11

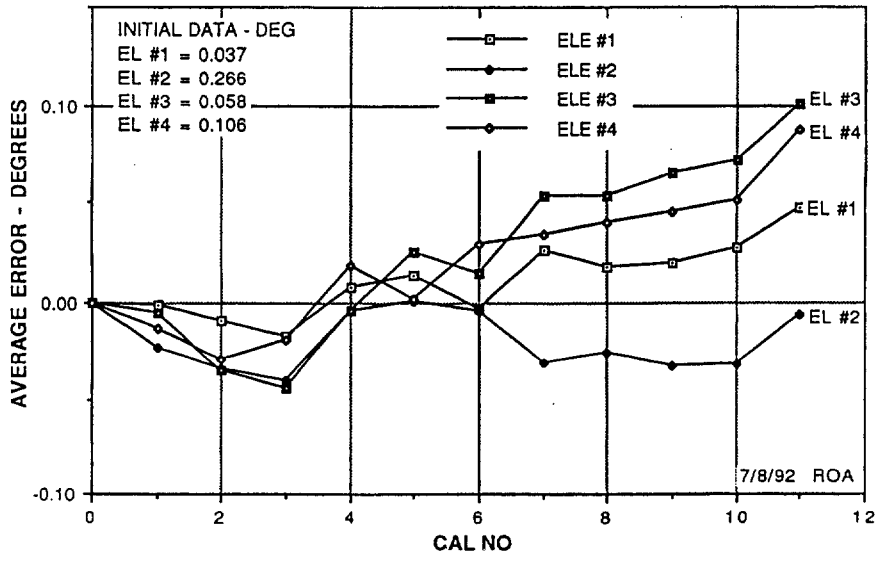

Life Test Calibration Trend for SN 016 Pot Elements

Figure 12

THE GALILEO HIGH GAIN ANTENNA DEPLOYMENT ANOMALY

Michael R. Johnson
California Institute of Technology
Jet Propulsion Laboratory
Pasadena, California

ABSTRACT

On April 11, 1991, the Galileo spacecraft executed a sequence that would open the spacecraft's High Gain Antenna. The antenna's launch restraint had been released just after launch, but the antenna was left undeployed to protect it from the heat of the sun. During the deployment sequence, the antenna, which opens like an umbrella, never reached the fully deployed position. The analyses and tests that followed allowed a conclusive determination of the likely failure mechanism and pointed to some strategies to use for recovery of the high gain antenna.

INTRODUCTION

The Galileo spacecraft's mission is to drop a probe (the Huygens Probe) into the atmosphere of Jupiter and then tour the Jovian system for two years, gathering a wealth of data on the system's structure, composition, and environments. The spacecraft was launched from Kennedy Space Center aboard the Space Shuttle on October 18, 1989. Galileo's trajectory carried it toward Venus for a gravity assist on February 10, 1990. The spacecraft then flew by Earth for a second gravity assist on December 8, 1990, and it flew by Earth again on December 8, 1992 for a third gravity assist. The spacecraft is currently on its way toward a December 1995 arrival at Jupiter.

The Galileo spacecraft (Figure 1) is a spin stabilized spacecraft and has three Earth-to-spacecraft communications antennas for commanding and returning spacecraft telemetry. Two of the antennas are low gain and the third is a high gain. One of the low gain antennas was used only during the portion of the mission that the spacecraft was inside Earth's orbit. This antenna, called the Low Gain Antenna-2 (LGA-2), faces the opposite direction of the other two antennas and is deployable and retractable. The remaining two antennas, the High Gain Antenna and the Low Gain Antenna-1, are part of the same assembly and face the same direction. During the portion of the mission that took the spacecraft close

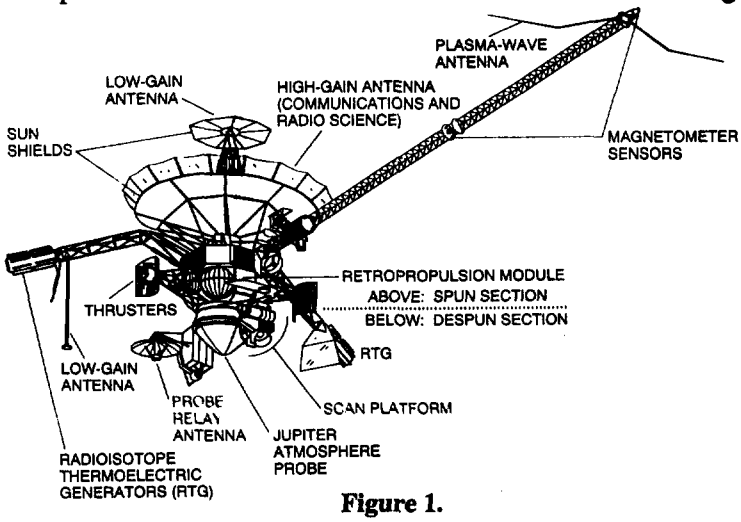

Figure 1.
Galileo Spacecraft Configuration

Figure 2.
High Gain Antenna
Stowed Position

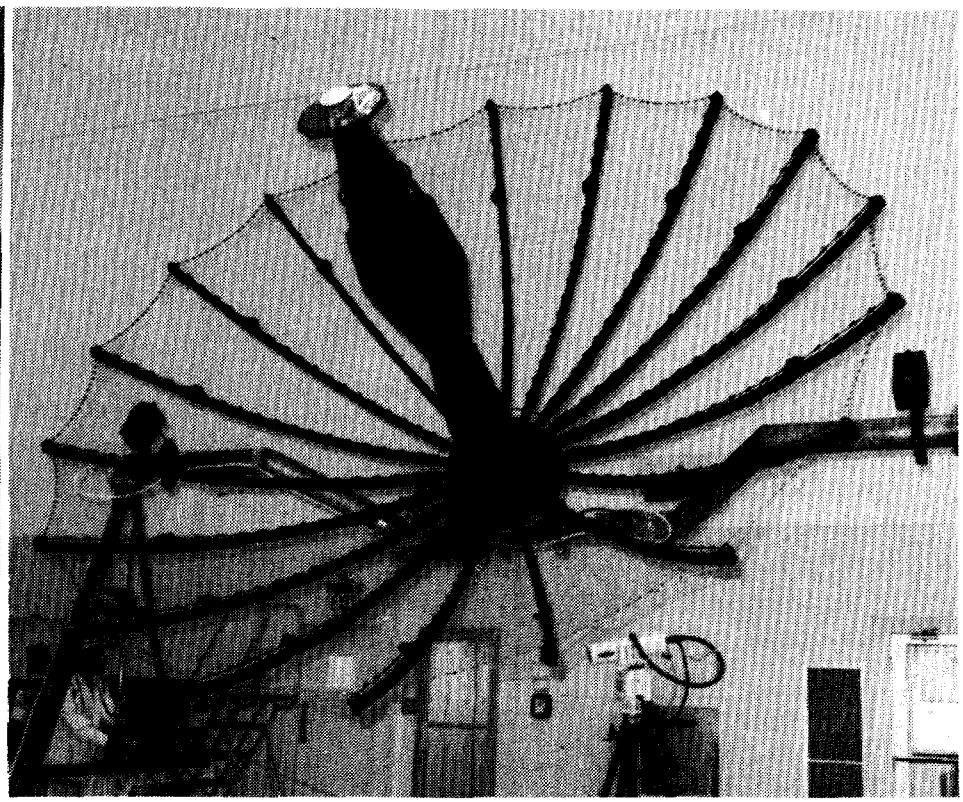

Figure 3.
High Gain Antenna
Deployed Position

to the sun, the High Gain Antenna (HGA) had to be protected from the direct sun. To do this, a sunshade was put on the tip of the antenna structure and the antenna was left in the undeployed position until April 1991 when the sun-to-spacecraft distance was large enough to present no thermal danger to the HGA.

The Galileo High Gain Antenna is shown in Figure 2 in the stowed position, and Figure 3 shows the antenna in the deployed position. The HGA is deployed and stowed by a mechanism located in the base of the antenna called the Mechanical Drive System (MDS). This system consists of a Dual Drive Actuator[1] (DDA), a 0.5 inch (12.7 mm) diameter, eight threads per inch (0.125 in, 3.175 mm pitch) ballscrew/ballnut assembly, a carrier assembly, 18 pushrods, and 18 ribs. (Figure 4) The ribs have a gold-plated wire mesh connected to them that stretches and forms the reflector surface when the antenna is fully deployed. Figure 5 shows the Mechanical Drive System in the fully deployed position. The lower end of the ballscrew is supported by a bearing housing containing a radial roller bearing and two roller thrust bearings. As the ballscrew is turned by the DDA, the carrier, which is prevented from rotating by the pushrods, moves toward the DDA. This motion results in the pushrods forcing the ribs to rotate about their pivot point and open out like an umbrella. The motion of the ribs pulls the wire mesh out and stretches it tight, creating the reflector surface. The ribs open out until each rib fitting contacts a mechanical stop, preventing any further deployment of the rib. The continued motion of the carrier compresses a spring on each of the pushrods, preloading the ribs against their stops, and

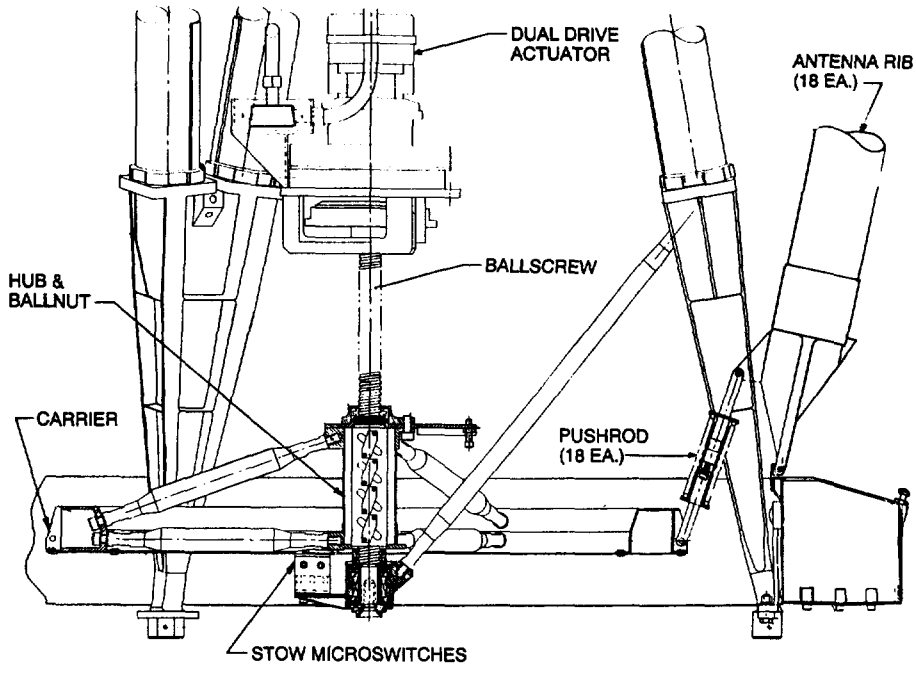

Figure 4.
Galileo High Gain Antenna Mechanical Drive System (Stowed)

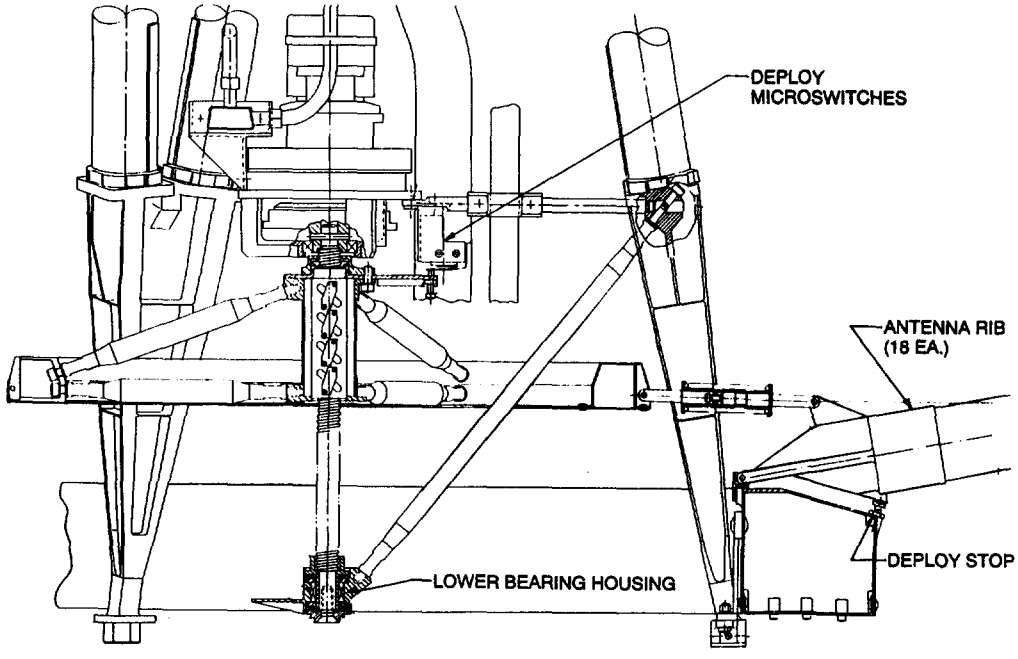

Figure 5.
Galileo High Gain Antenna Mechanical Drive System (Deployed)

continues until the pushrods pass over center. This maintains a constant preload on the ribs in the deploy direction after the DDA is shut off at the fully deployed position.

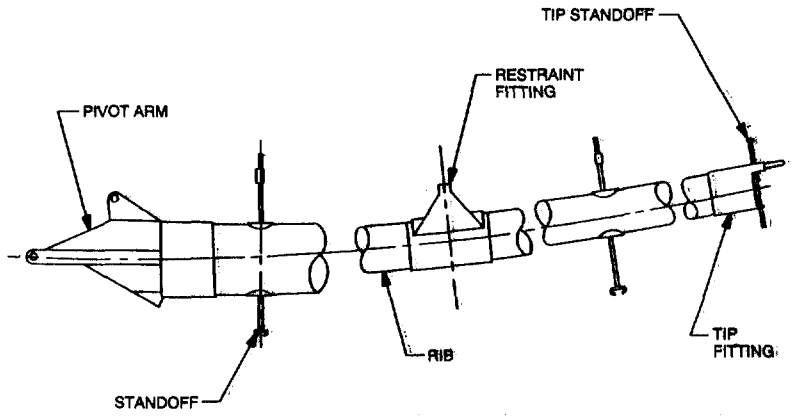

Figure 6.
Rib Assembly

Figure 6 depicts a rib assembly sectioned to show the pertinent components. The ribs are restrained during launch at the restraint fitting by a spoke assembly which is held in place by the Central Release Mechanism (Figure 7). This mechanism is opened by a spring when the retaining shaft, held in place by a Non Explosive Initiator (NEI), is released. After launch, the Central Release Mechanism (CRM) is actuated, releasing all 18 spokes and allowing the MDS to deploy the antenna. For launch, the spoke assemblies are each preloaded to 378 N (85 lb) and this preload is reacted by two pin-socket combinations called the mid-point restraint (inset, Figure 8). Both pins are titanium 6Al-4V with spherical ends that engage the sockets. The pin receptacle design is shown in Figure 9. One receptacle is a cone, the other is a V-groove, they both have included angles of 90 degrees, and they are both made from Inconel 718. The reason for the different receptacle designs was to avoid multiple load paths in case the pins did not have the exact same separation as the receptacles. The two receptacles balance the tension from the spoke preload, the cone locates the rib in the plane of the receptacles, and the V-groove reacts any rotation about the cone receptacle. The tip restraint of the ribs is a pin (shown in Figure 6) in a tuning-fork-like receptacle. This design prevents rotations of the ribs about their mid-point restraints and allows the ribs to move out freely during deployment.

Antenna Transportation History

The antenna was built at the HARRIS Corporation in Melbourne, Florida. The ribs were then stowed with the launch preload of 378 N (85 lb) and shipped by ground transportation to the Jet Propulsion Laboratory (JPL) in California. The shipping method supported the antenna by its flight interface horizontally (cantilevered) in the shipping container. The antenna was tested at JPL and then shipped by ground transport to Kennedy Space Center (KSC) for launch in May 1986. The Challenger disaster prevented Galileo from launching in 1986, and so the spacecraft and antenna were returned to JPL. The flight antenna was again returned to KSC for launch in October 1989.

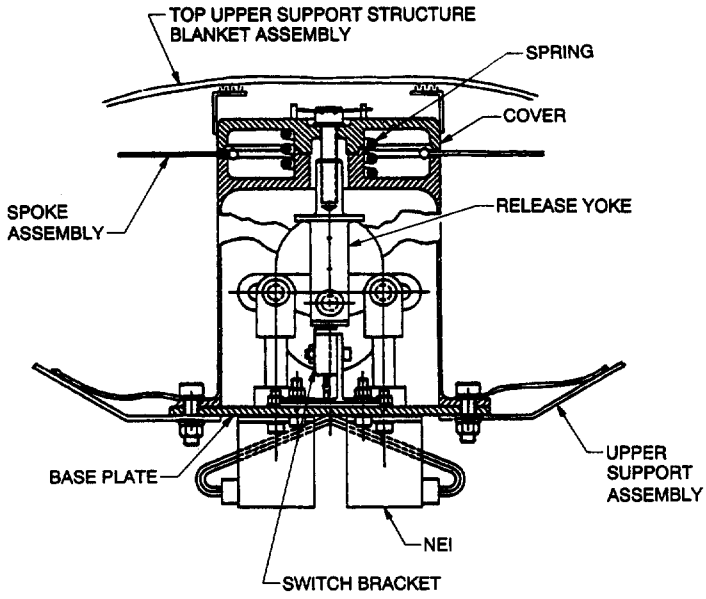

Figure 7.
Central Release Mechanism

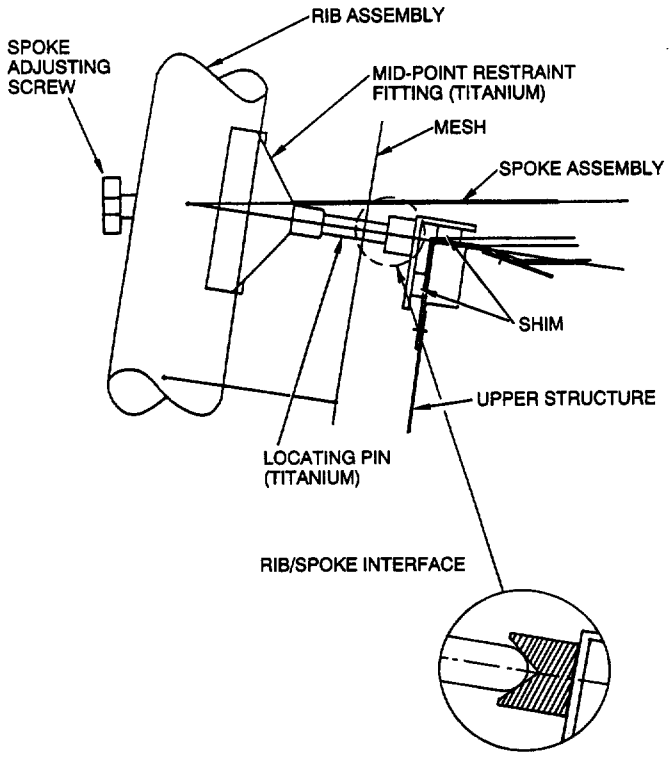

Figure 8.
Rib/Spoke Interface

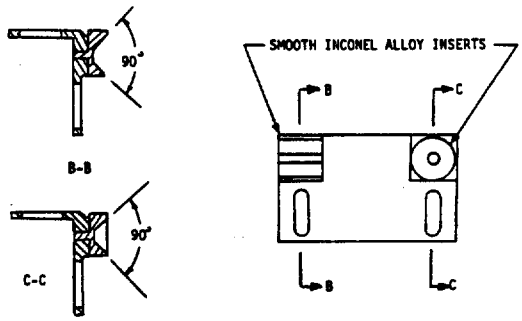

Figure 9.
Receptacle Design

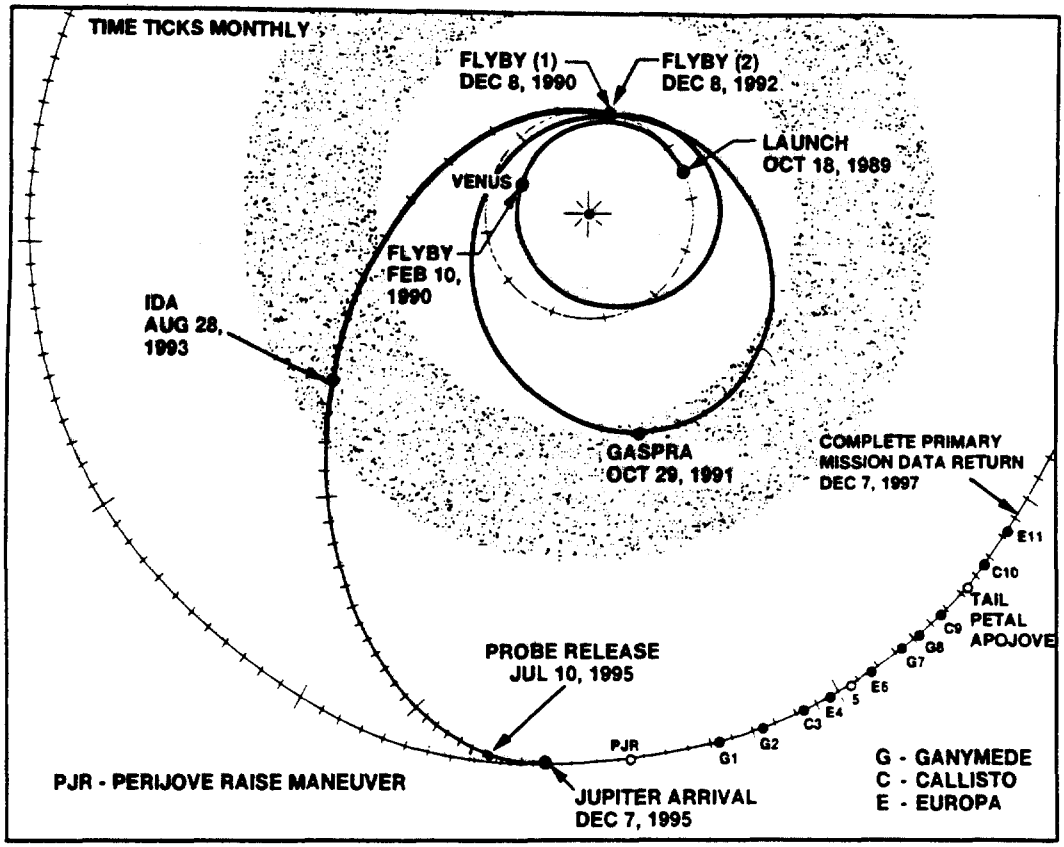

Figure 10.
Galileo Mission Timeline

Galileo Flight History and the Deployment Anomaly

The Galileo mission timeline is shown in Figure 10. The spacecraft was launched on October 18, 1989 and during the launch sequence, the Central Release Mechanism on the HGA was actuated. Telemetry from the spacecraft indicated that the CRM had released properly. The antenna was left in the stowed position so it would not be damaged by the intense sunlight during the early portion of the mission when Galileo would be at sun relative distances of less than one astronomical unit. The spacecraft reached Venus for a gravity assist on February 10, 1990 and then swung around for another gravity assist at Earth on December 8, 1990. This put Galileo on a trajectory that would bring it around for a third and final gravity assist at Earth on December 8, 1992. By April 1991 the spacecraft had reached a point in its mission where it would no longer be thermally risky to deploy the HGA. On April 11, 1991 Galileo executed a sequence to open the High Gain Antenna. The sequence energized the HGA deployment motors (both motors on the Dual Drive Actuator) for eight minutes. A nominal deployment time would have been about 165 seconds with both motors on the DDA operating properly. The deployment time, if one motor/gear train had failed, would have been about 330 seconds. When the antenna reached the fully deployed position, a set of redundant microswitches would have shut down power to the drive motors. The sequence was set to operate the motors for eight minutes to protect the motors from

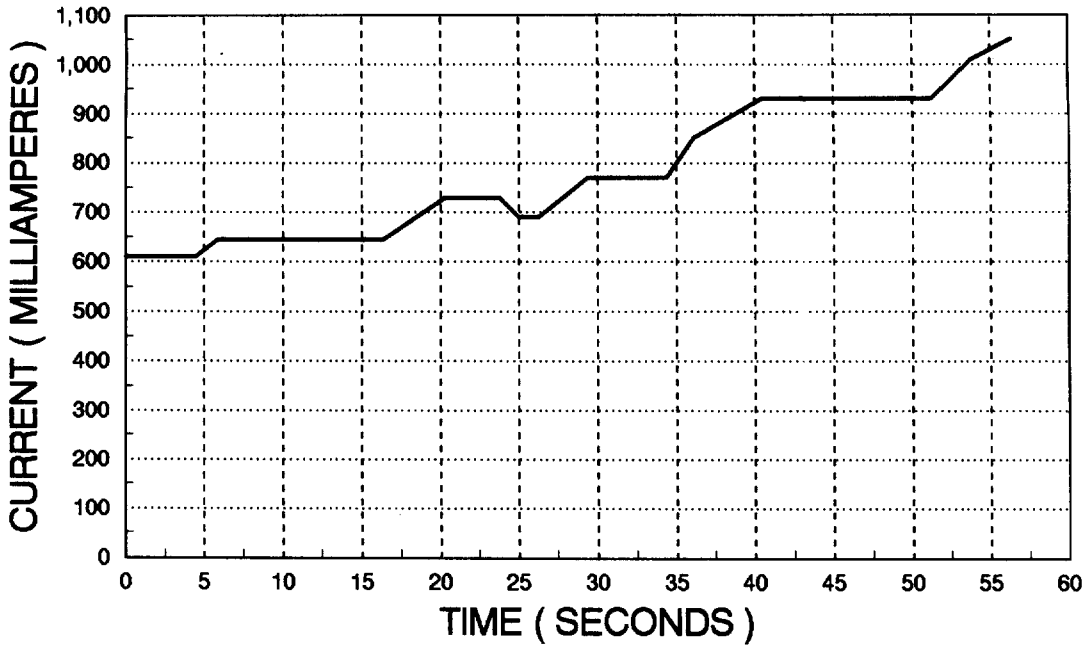

Figure 11.
Motor Current Telemetry
(Start : 19:51:23 spacecraft time)

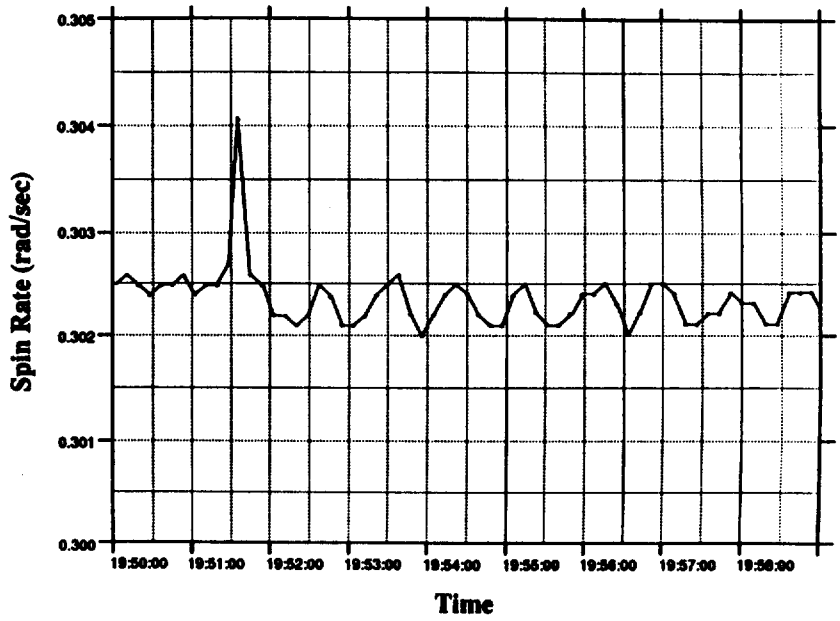

Figure 12.
Spin Detector Telemetry

overheating (if stalled) and to allow enough time for a single motor operating at cold temperature to fully deploy the antenna. The motor current telemetry received from the spacecraft is shown in Figure 11. The current drawn by the motors started higher than expected and continued to rise until it leveled off 56 seconds after initiation.

The other telemetry significant to the anomaly received from Galileo during the HGA deploy attempt are a spike in the Spin Detector output (Figure 12), a reduction in the output of the Sun Gate at certain clock angles (Figure 13), a decrease in the spin rate, and an increase in the wobble of the spacecraft. The Spin Detector is a very sensitive accelerometer mounted on the spinning portion of the spacecraft. This sensor is used to detect the spin rate of the spacecraft. At eight seconds after the start of the deployment, a sudden acceleration occurred and produced the Spin Detector output spike shown in Figure 12. Figure 13 shows the output of the Sun Gate after the deploy attempt. The Sun Gate is a detector that is used to protect the spacecraft from exceeding an angle of 15 degrees between the sun and Galileo's long axis. This was necessary to protect the Galileo during the portion of the mission when it was close to the sun. During the HGA deploy attempt, the Sun Gate output dropped at a spacecraft clock angle of 265 degrees. The clock angle is an angular position measurement on the spacecraft with the origin at the rotational center of Galileo and in a plane perpendicular to the HGA long axis. Also, the decrease in spin rate was not enough for a fully deployed antenna (due to the increase in the antenna's moment of inertia) and the reason for the increase in wobble was not initially understood.

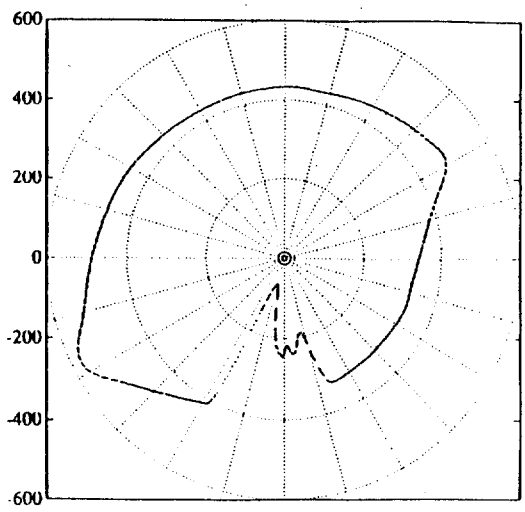

Figure 13.
Sun Gate Output vs. Clock Angle

DATA ANALYSIS

The first conclusion that can be drawn from the Sun Gate data is that the output was reduced by the shadow of an antenna rib. Analysis of the Sun Gate's location with respect to the antenna shows that only one rib can shadow the Sun Gate and that this rib can only shadow it at deployment angles of 34 to 43 degrees given the spacecraft-to-sun angle at the time of the deploy attempt (5.39 degrees). Analysis of the amount of obscuration of the Sun Gate indicated that the one rib that can shadow the Sun Gate was deployed about 35 degrees from its stowed position.

The motor current telemetry indicated that the motors stalled at 56 seconds after initiation. The telemetry was then used to determine how far the ballscrew in the Mechanical Drive System had rotated from the stowed position. The motors on the DDA are brushless dc motors. The DDA, therefore, has the speed-torque-current relationship shown in Figure 14.

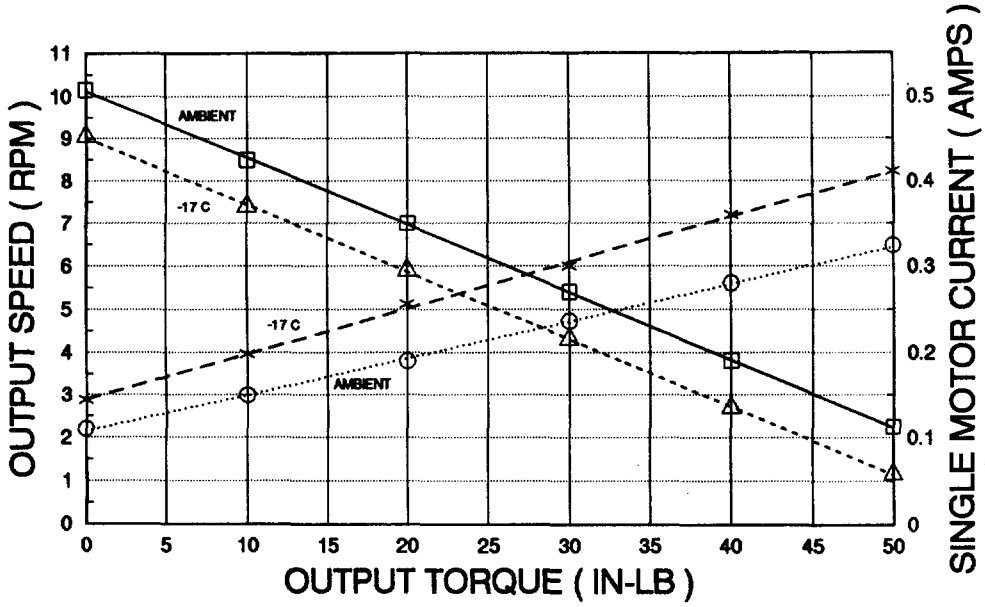

Figure 14.
Dual Drive Actuator Performance

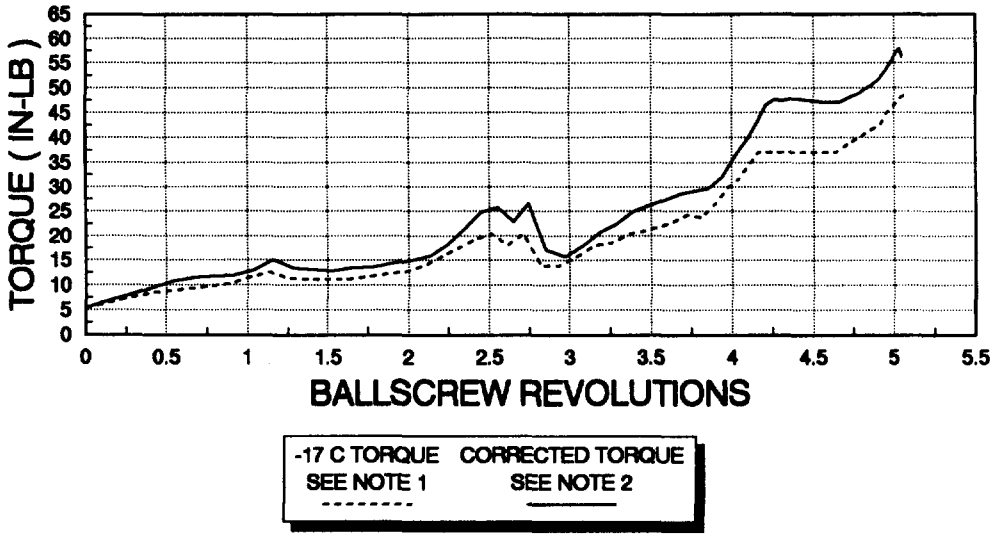

Figure 15.
Torque vs. Ballscrew Revolutions
for the High Gain Antenna Deployment Anomaly

This allows the expression of speed as a function of current. Utilizing this relationship, the current telemetry from the spacecraft, and integrating over time allowed the determination of the ballscrew position as a function of time. Taking into account the granularity of the current telemetry, converting the current telemetry to torque, and plotting this as a function of ballscrew revolutions resulted in the curve shown in Figure 15. The data indicates that the ballscrew rotated just over five turns. (A full deployment requires 25 rotations of the ballscrew.) Converting the five rotations to carrier movement and then to rib rotation indicates that the ribs could not have deployed to an angle greater than 11 degrees, which is inconsistent with the Sun Gate data. The way the ribs are connected to the carrier allows for an asymmetric deployment of the ribs if one or more ribs are restrained by something. After several tests on the spare antenna, it was determined that the most likely configuration of the antenna was three ribs restrained at their stowed position. This would allow the opposite rib (over the Sun Gate) to deploy to the position indicated by the Sun Gate data. Also, the number of ballscrew revolutions and the torque required to deploy the antenna under these conditions is consistent with the current telemetry. Figure 16 is a photograph of the spare antenna in the three restrained rib configuration. This asymmetrical configuration is also consistent with the amount of reduction in the spin rate and the increase in wobble.

The Spin Detector spike occurred at a time in the deployment that coincided with an increase in torque for the DDA. The initial thinking that the spike was due to the release of some other restrained ribs was not consistent with the increase in torque required from the drive system.

After the shape of the antenna was determined, the design was dissected to find what could possibly be holding the ribs in the stowed position. Four possibilities survived this analysis. They were:

1. The tip shade (sunshade mounted on the tip of the antenna to protect it during the early part of the flight) snagged in the wire mesh.
2. Restraint of the Mechanical Drive System (MDS).
3. Retention of the rib tips in their tuning-fork-like sockets.
4. Retention of the ribs at the mid-point restraint due to friction, cold welding, or adhesion.

Tests performed on the spare antenna to snag the tip shade were totally unsuccessful. No configuration of tangling the tip shade in the wire mesh could be found that would restrain the ribs at the stowed position. All attempts resulted in significant rotation of the restrained ribs from the stowed position, allowing a much greater number of ballscrew revolutions before stalling the Dual Drive than indicated by the current telemetry.

Restraint of the MDS was eliminated due to the order in which testing and assembly occurred at Kennedy Space Center. The area around the MDS was closed and no longer

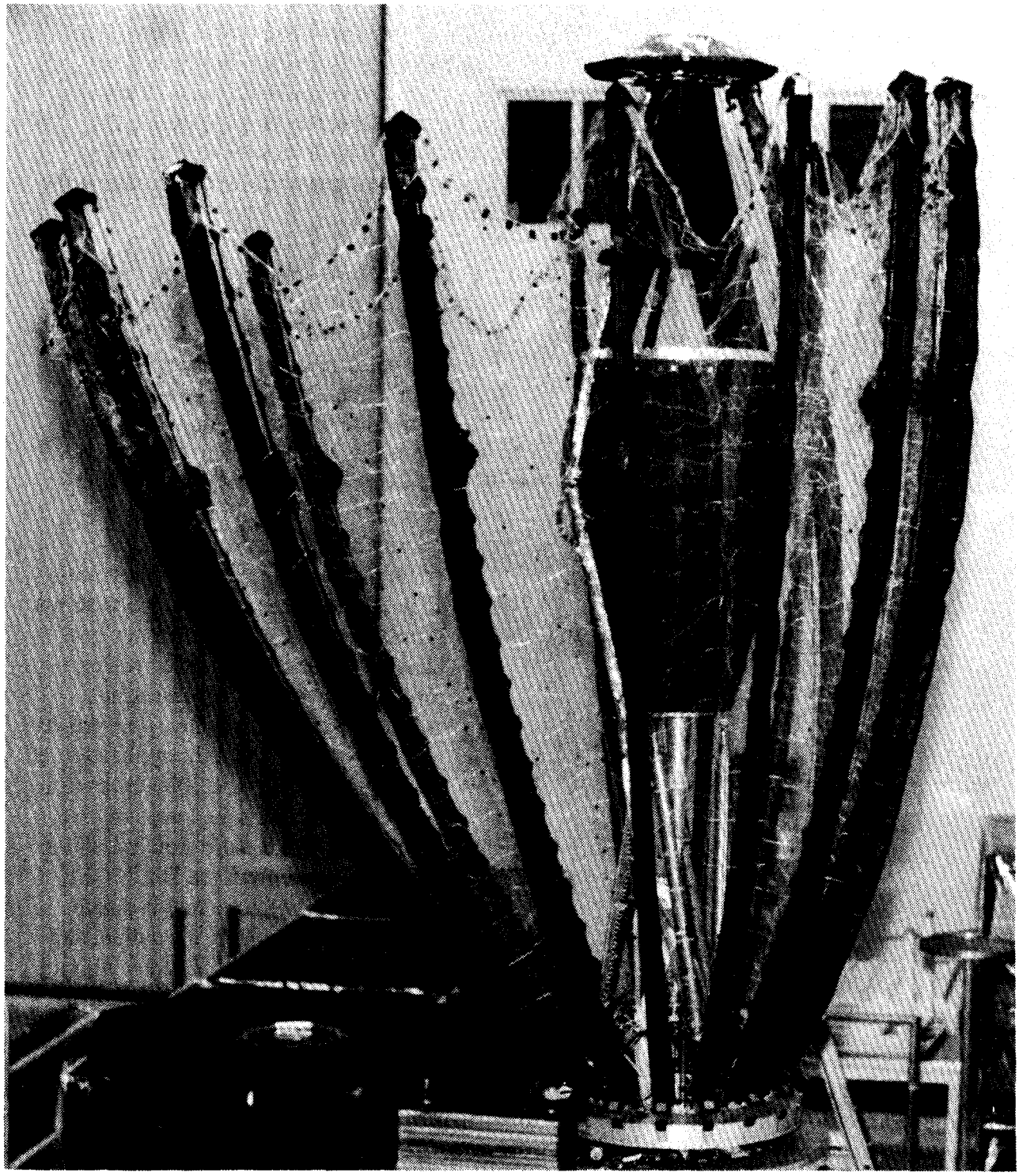

Figure 16.
Galileo High Gain Antenna
Asymmetric Deployment Configuration

accessible prior to several deploy tests of the flight antenna. Also, this area was not accessible during installation of the antenna on the spacecraft.

Retention of the rib tips in their tuning-fork sockets was very unlikely due to the pre-launch testing that had been performed. The tuning forks would have to have been damaged after the final deployment test or in flight. A failure of this type would also cause a slower increase in the torque required from the DDA (due to the stiffness of the ribs) during the deploy attempt than was indicated by the current telemetry. This left as the first choice of failure the mid-point restraint pins and sockets. If friction was responsible for restraining the pins, it would require a coefficient of friction greater than one.

The next mystery was how the MDS and the structure were able to carry the load generated by the stalled motors. The Dual Drive stall torque output during the deploy attempt was about 6.33 N-m (56 in-lb). A test was performed on a mock-up of the MDS to determine how it would respond to the odd loading condition created by the antenna. The test fixture shown in Figure 17 was used to apply moment, axial, and shear loads to the "carrier plate" individually and in combination. The results of these tests showed that shear and axial loads do not significantly affect the efficiency of a ballscrew. Moment loads, however, result in very significant losses in a ballscrew/ballnut assembly. The graphs in Figure 18 show that the application of a moment of 339 N-m (3000 in-lb) to a ballnut results in torque losses of 4.18 N-m (37 in-lb), or more than half of the available torque from the DDA. This large amount of torque loss is due to jamming of the balls in the ballnut and sliding contact of the ballscrew with the ballnut body. Also, it was found that further losses occurred at the lower bearing housing (see Figure 5), due to the sliding contact of the ballscrew with the stationary outer housing. The needle roller bearing in the lower housing is not capable of supporting a large moment load, allowing the ballscrew to rotate relative to the housing and come in contact with it. The result of these torque losses was that very little torque was available to move the ribs against their restraints.

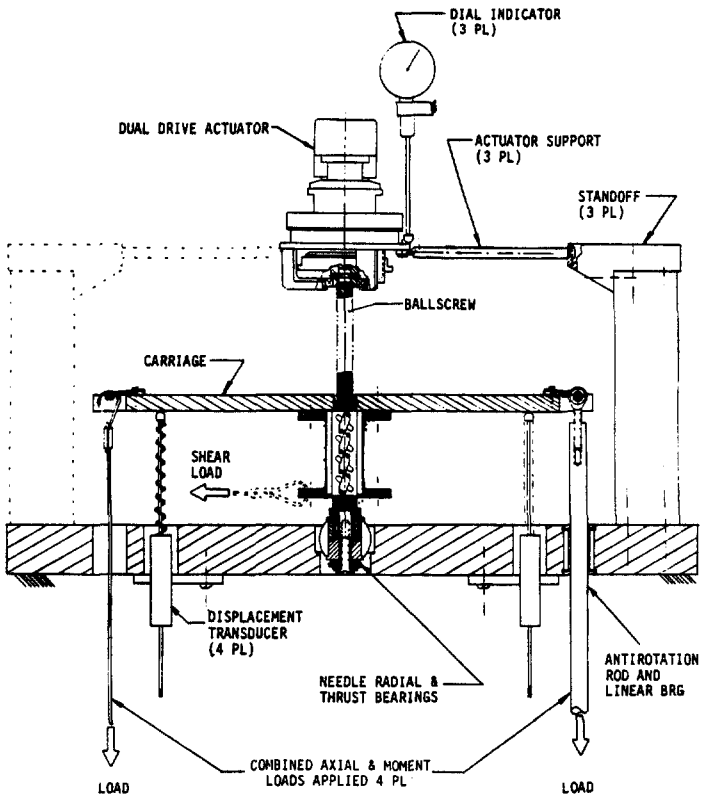

Figure 17.
Mechanical Drive System
Loading Fixture

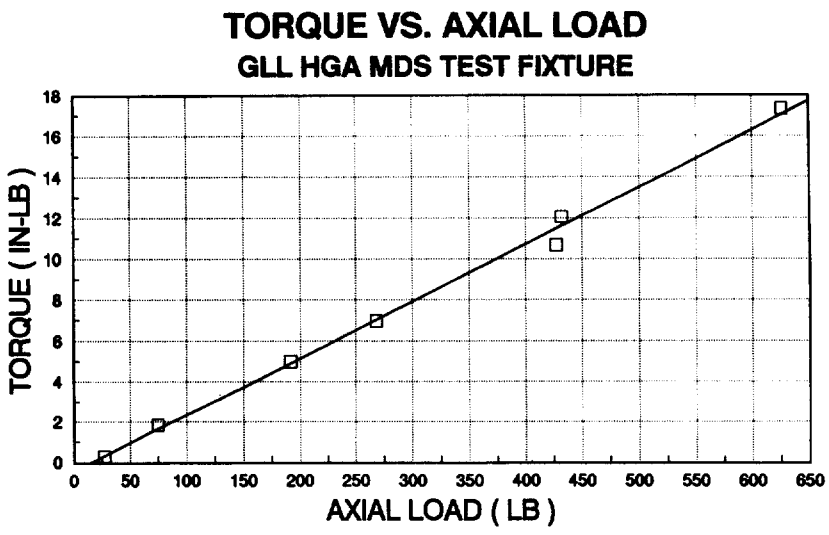

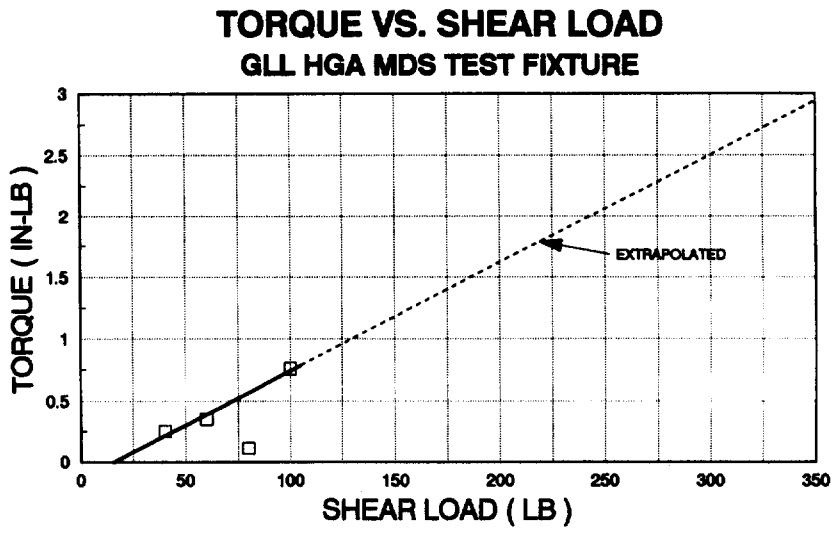

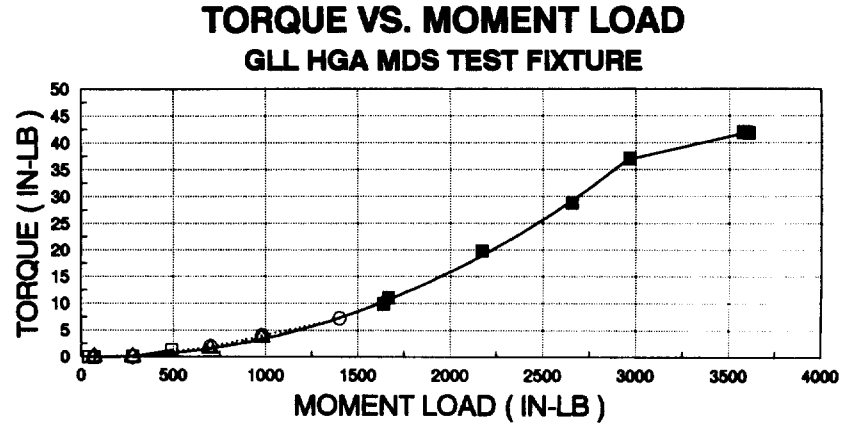

Figure 18.
Mechanical Drive System
Test Fixture Results
(Torque required to turn ballscrew with the specified loads applied)

RECOVERY TECHNIQUES AND ATTEMPTS

The first suggestion made to get the antenna open was to restow it and try the deployment again. The Dual Drive Actuator, although capable of bi-directional operation, was not wired on the spacecraft to stow the antenna. This operation required human assistance to roll the wire mesh in order to prevent the mesh from snagging on itself or other portions of the antenna. Also, it was later learned through ground testing on the spare antenna that the lower bearing housing torque losses increase every time the antenna is stowed and redeployed, resulting in less and less DDA torque available to overcome the rib restraint. This increase in torque losses is due to the rotating steel ballscrew galling the stationary aluminum housing. The galling changes the surface finish of the aluminum so much that the torque required to turn the ballscrew increases. The testing showed that after just five deploy and stow cycles, the amount that the ballscrew could be rotated from the stow position was less than half the original amount of five revolutions.

The first attempt at breaking loose the antenna was to rotate the spacecraft away from the sun and then toward the sun. The thermal expansion and contraction of the antenna structure would be much greater than the expansion of the ribs and would cause a significant change in the forces at the mid-point restraints. A computer analysis of the pin-socket joints indicated that after several (4 to 6) thermal cycles of the antenna, the pins might come out of the sockets due to infinitesimal sliding each time the forces changed from the temperature cycle. This analysis assumed friction was holding the pins in the sockets. After seven thermal turns, there was no indication that the rib pins were "walking" out of their sockets.

The next recovery technique used was to swing the LGA-2 and impart a shock to the spacecraft structure. The LGA-2 swings 145 degrees at about five RPM and then hits a hard stop. The Low Gain Antenna-2 mast is approximately 2 meters long with the low gain antenna mounted on the end. The moment of inertia of this assembly is very large and imparts a significant impulse to the spacecraft structure. The LGA-2 was swung six times with no results.

The final recovery technique tried to date was to pulse the HGA Dual Drive motors at 1.25 and 1.875 Hertz. It was found during testing that the Dual Drive Actuator has a mode of oscillation that is due to the coupling of the motor armature inertia and the gearbox stiffness. The result of this mode is that the DDA can produce a pulsing torque at the output shaft that is forty percent greater than the stall torque value. When the pulsing was performed on a DDA in the spare High Gain Antenna, the antenna also responded at the same frequencies. The combination of the DDA and the antenna was able to turn the ballscrew another 1.5 revolutions beyond the stall point. This significantly increased the force on the mid-point restraint pins to a pullout force of 18 N (4 lb) and a shear force of 213 N (48 lb). These forces were high enough to elastically deform the ribs and pull them out of the bottom of the tuning-fork receptacles if they had been restrained there. The forces applied to the ribs on the Galileo spacecraft, after completion of the DDA pulsing, conclusively eliminate the tip

fittings as a possible source of restraint. The ribs are therefore restrained at the mid-point restraints.

PIN AND SOCKET ANALYSIS

Several pin and socket pairs were removed from the spare HGA for evaluation and testing.[2] The spare HGA had been through a significant amount of vibration testing, which causes relative motion between the pins and sockets. The sockets were made of Inconel 718 with a surface finish of 0.2 microns RMS (8 micro inch RMS). The pins were made from titanium 6Al-4V and were finished with the Tiodize type II and the Tiolube 460 processes. These processes consist of putting an anodize coating on the titanium and following this with a molybdenum disulfide coating for dry lubrication.

A conical socket and its associated pin are shown in Figure 19. The contact area on the conical receptacle shows a transfer of some drylube from the pin, which was expected. The surface shows no indications of damage of any kind. The surface of the pin also shows no damage. There is a barely visible ring on the spherical surface where the pin made line contact with its receptacle. The Hertzian contact stresses on this surface were well within the operating capability of the pin and its surface coatings.

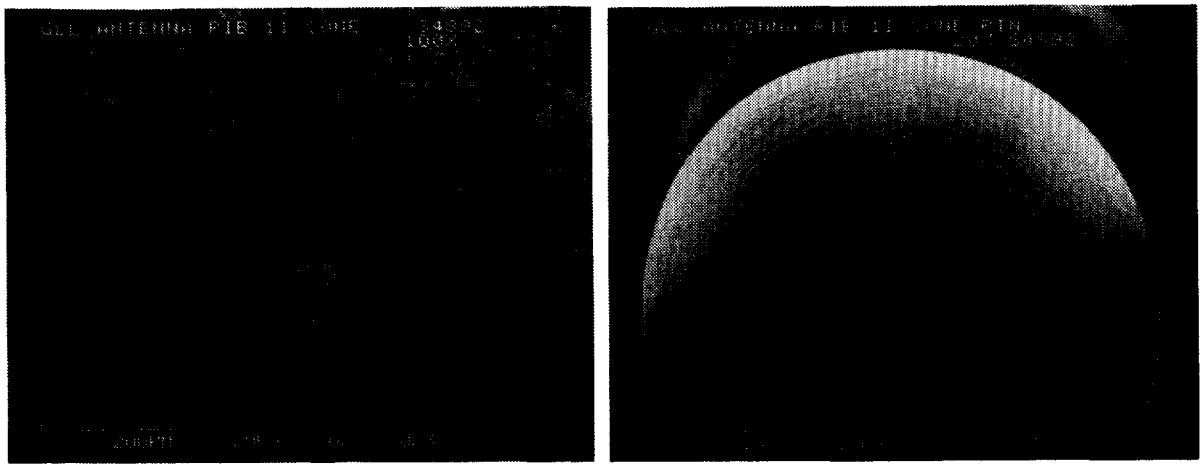

Figure 19.
Cone Socket and Pin

A V-groove socket and its mating pin are shown in Figure 20. These are from the same rib as the cone and pin shown in Figure 19. The surface of the pin is plastically deformed to a flat spot, as shown by the arrow. Although X-ray diffraction scans of the surface show the presence of MoS2 on the contact area, scans of some other pins from other ribs showed no presence of MoS2 on their contact patches. This indicates that the deformation of the surface destroyed the Tiolube and Tiodize coatings. The contact stresses actually exceeded the capability of the pin coatings by about five times. A higher magnification of the upper spot on the V-groove receptacle in Figure 20 is shown in Figure 21. The surface has been

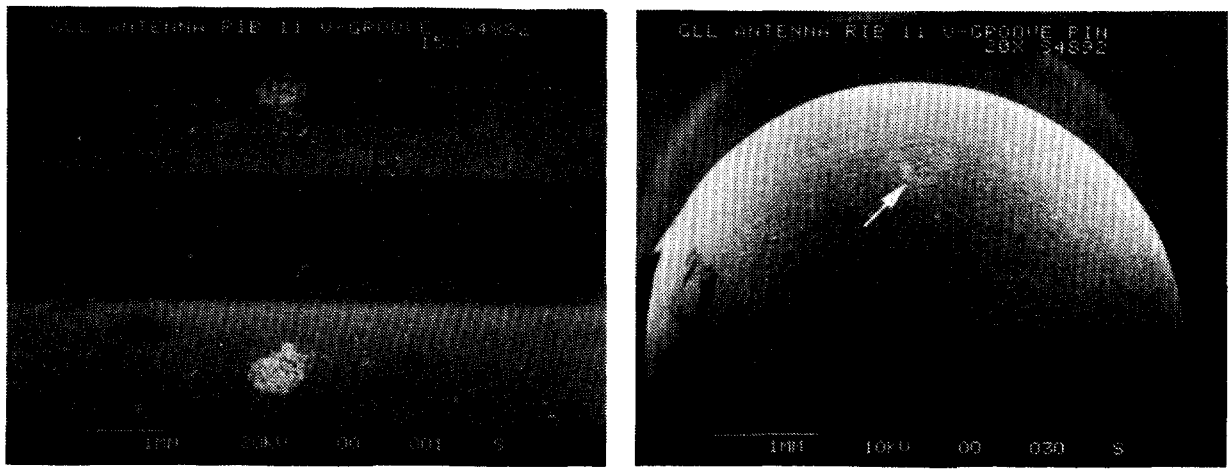

Figure 20.
V-Groove Socket and Pin

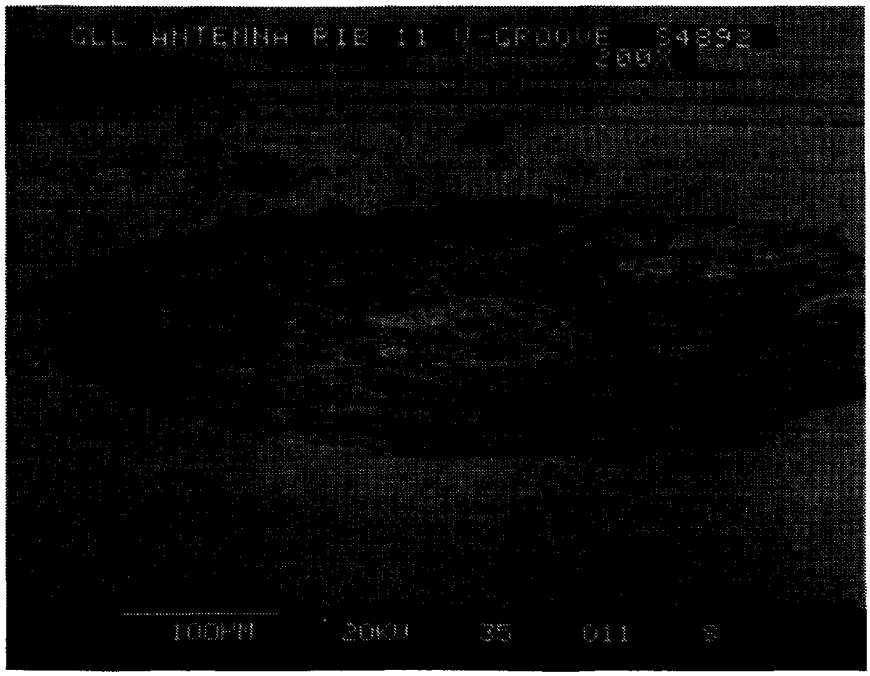

Figure 21.
Magnification of Upper Spot
on V-Groove Socket in Figure 20

deformed and worn away. Scans of the contact surface on the receptacle show a large amount of Ti 6Al-4V, indicating a transfer of base material from the titanium pin.

A series of tests was performed at NASA Lewis Research Center on the friction properties of drylubed and bare titanium against Inconel 718.[3] The results of these tests showed that if the two surfaces are displaced relative to each other under load and in air, then displaced relative to each other under load in a vacuum, the sliding friction between the surfaces increases nearly ten times. When a drylubed and anodized pin was operated in an atmosphere, the drylube surface was quickly destroyed and, as a result, exposed the base titanium. The testing also showed that with an atmosphere present to continue to react with the bare titanium as it was worn by sliding contact, the friction coefficient never exceeded 0.35. However, once a pin's drylube was damaged by operation in air and then operated in a vacuum, the surfaces started to gall and produce coefficients of friction in excess of 1.0.

RIB RETENTION MECHANISM

The first time the ribs were stowed to their full preload, plastic deformation of the contact points on the V-groove pins destroyed the ceramic coating on the titanium that was the bonding surface for the drylube material. During the four trips across the country the antenna was exposed to enough of a vibration environment to cause relative motion between the pins and sockets. This motion was amplified by the cantilever mounting of the antenna in its shipping container. The pins that were on the top and bottom (with the antenna horizontal) saw the greatest amount of relative motion with respect to their sockets. Since this occurred in an atmosphere, the drylube surfaces on the pins were worn. During vibration testing of the antenna at JPL, further damage to the drylube occurred. The vibration testing was done along the same axis as the gravity vector during ground transport, causing the same pins and sockets to experience the greatest amount of relative motion. By launch, the drylube was probably completely worn off the contact points between the pins and V-groove sockets. After launch, the spacecraft was exposed to a vibration environment from the upper stage that caused more relative motion of the pins and sockets. Since this occurred in a vacuum with bare titanium pins (due to the destruction of the contact patch on the V-groove receptacles), the pins and sockets galled together requiring more force to deploy the ribs than can be generated by the MDS.

Also, several other ribs spaced around the antenna were stuck by this same mechanism at the start of the deployment. Since the ballscrew did not have a large moment applied to it due to the spacing of the ribs, the ballscrew generated enough force to eject most of the ribs (which explains the acceleration detected by the Spin Detector). When the only ribs remaining stuck were on one side of the antenna, the ballscrew moment started increasing significantly, increasing the torque losses in the drive system. The increased losses, coupled with the reduction of force at the pins and sockets on the remaining stuck ribs, ended up stalling the DDA before the forces were large enough to eject the last three ribs.

The failure mechanism requires a special set of circumstances in a specific order to cause the deployment anomaly. The events necessary to produce the failure of the Galileo HGA are summarized, in the required order of sequence, below:

1. Generate a high enough contact stress to plastically deform the titanium pins and break the ceramic coating that was used to bond the drylube.
2. Produce relative motion between the pins and sockets in an atmosphere to remove the damaged coating and drylube from the contact areas and to produce a rough surface on the mating parts.
3. Produce relative motion between the pins and sockets in a vacuum to remove the oxidized and contaminated titanium from the surface of the pins and then gall both parts so the friction is very high.
4. Produce an asymmetric deployment of the ribs so that the ballscrew has a large moment applied to it and cannot produce the force necessary at the mid-point restraint to eject the ribs.

Without the relative motion of the pins and sockets in a vacuum, (number 3 above) the lower coefficient of friction of the interface in air allowed all ground deployment tests of the antenna to be perfectly successful due to the V-groove socket internal angle of 90 degrees. As long as there is an atmosphere to react with any free titanium generated by any relative motion, the friction between the pins and sockets is maintained at a value that will not prevent the antenna from deploying. Also, a vacuum deployment test without the relative motion of the parts in the vacuum, would also be successful due to the oxides and contaminants on the bare titanium pins. A vacuum deployment of the flight antenna was done and was successful because of the lack of relative motion between the pins and sockets in the vacuum.

CONCLUSIONS

The high contact stresses on the V-groove pin/socket interfaces destroyed the integrity of the lubricant film and started the chain of events that led to the deployment anomaly. The conical sockets and pins were exposed to all of the same environments as the V-groove sockets and pins, but the lubricant surface was not breached. A low enough friction level was maintained such that the conical sets did not inhibit the antenna deployment. The main difference between the cone sockets and V-groove sockets is the contact stress level.

The use of drylube, specifically molybdenum disulfide, on a mechanism that is going to be operated in an atmosphere should be carefully evaluated. The wear rate of the MoS2 in air is so much higher than in a vacuum that any coatings could be worn out by in-air testing and not provide the desired lubrication when needed. The pins and sockets on the HGA that received the greatest amount of relative motion due to the shipping method were the same ones that were exercised most by the vibration testing. These are also the same pins and sockets that are stuck on the spacecraft. One solution to the problem of ambient testing

wearing out the lubricant coating would be to replace the lubricated components just prior to launch so there is a virgin lubricant surface for the flight operation.

The failure of the Galileo HGA was not detectable with in-air testing, due to the choice of titanium for the pin material. Since this material reacts with oxygen so readily, the in-air friction change, due to the damaged surfaces, was not detectable because the higher friction coefficient (0.35 vs. 0.05) was not high enough to be restrained by the 90 degree included angle of the receptacles. As a result, more deployment tests in air would only have worn out the drive system. Also, the vacuum deployment test of the flight antenna did not exhibit this failure mode due to the lack of pin and socket relative motion. The test conditions were not adequate for finding this problem, indicating that just a functional test in vacuum is not always appropriate.

EPILOGUE

Although the Galileo spacecraft has no operating high gain antenna, workarounds using the Low Gain Antenna (LGA-1), new data compression techniques, and the spacecraft's recorder have been developed that will meet 70 percent of the mission objectives (Reference 4).

REFERENCES

1. Packard, D. T. : " Dual Drive Actuators ," Proceedings of the 16th Aerospace Mechanisms Symposium, p. 123, May 1982.
2. Lewis, D. F. : Materials Analysis in Support of the Galileo High Gain Antenna (HGA) Deployment Anomaly, Jet Propulsion Laboratory Internal Document JPL D-9814, November 1992.
3. Miyoshi, K. and Pepper, S. V. : " Properties Data for Opening the Galileo's Partially Unfurled Main Antenna ," Test Report, NASA Lewis Research Center, 1992.
4. O'Neil, W. J.; Ausman Jr., N. E.; Johnson, T. V.; Landano, M. R.; Marr, J. C. : " Performing the Galileo Jupiter Mission with the Low Gain Antenna (LGA) and an Enroute Progress Report ," 44th Congress of the International Astronautical Federation, IAF-93.Q.5.411, October 1993.

ACKNOWLEDGEMENTS

The work presented in this paper is the culmination of a two-year investigation involving the talents of many people at the Jet Propulsion Laboratory.

This work was performed at the Jet Propulsion Laboratory, California Institute of Technology, under a contract with the National Aeronautics and Space Administration. Reference herein to any specific commercial product, process, or service by trade name, trademark, manufacturer, or otherwise, does not constitute or imply its endorsement by the United States Government or the Jet Propulsion Laboratory, Pasadena, California.

Tiolube 460 and Tiodize are registered trademarks of the Tiodize Company, Incorporated, Huntington Beach, California.

IMPLEMENTATION OF HEATERS ON THERMALLY ACTUATED SPACECRAFT MECHANISMS

John D. Busch and Michael D. Bokaie
TiNi Alloy Company
San Leandro, California

ABSTRACT

This paper presents general insight into the design and implementation of heaters as used in actuating mechanisms for spacecraft. Problems and considerations that were encountered during development of the Deep Space Probe and Science Experiment (DSPSE) solar array release mechanism are discussed. Obstacles included large expected fluctuations in ambient temperature, variations in voltage supply levels, outgassing concerns, heater circuit design, materials selection, and power control options. Successful resolution of these issues helped to establish a methodology which can be applied to many of the heater design challenges found in thermally actuated mechanisms.

INTRODUCTION

The aerospace industry's trend away from pyrotechnic devices is resulting in the development of new non-explosive actuator technologies. Many of these new devices are thermally actuated mechanisms which convert heat into kinetic work. Paraffin actuators and shape memory alloys represent two examples of flight qualified, thermally actuated technologies. Although such actuators are typically simple in construction, re-usable, and safe to handle, implementation of the heating elements which govern actuation is not trivial. The vacuum of space, variations in spacecraft temperatures and supply voltages, and minimum outgassing requirements all work against the design of a simple heater. Design and implementation are further complicated by the frequent necessity of maintaining intimate contact between the heater and an element in motion. This paper uses the development of Frangibolt^{R} heaters for the DSPSE solar array release to chronicle the design and development issues that were addressed in successfully implementing spacecraft mechanism heaters.

The Frangibolt is a non-explosive release device which uses shape memory alloy (SMA) to forcefully break a bolt in tension [1]. Figure 1 illustrates the device, showing a notched bolt element passing through a

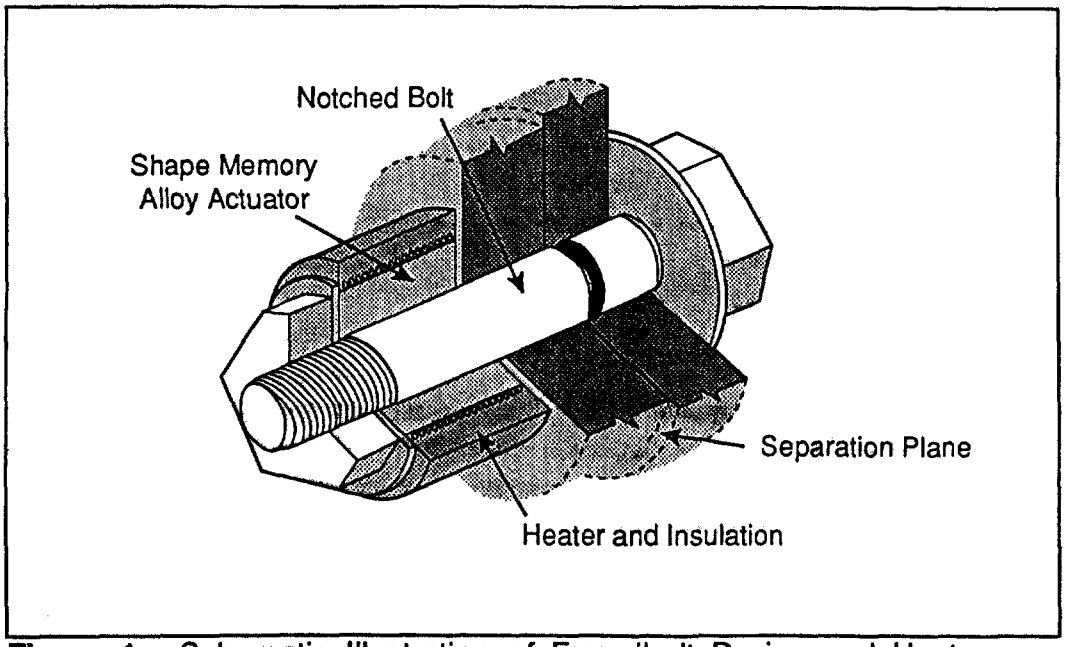

Figure 1: Schematic Illustration of Frangibolt Device and Heater Location

compressed SMA cylinder. When the SMA is heated above its transformation temperature, it recovers to its original length thereby stretching the bolt to failure. It is the heater which mounts to the outer surface of the SMA cylinder that inspired this paper. Using the Frangibolt heater design as a case study, issues common in designing, developing, and qualifying such devices are highlighted and discussed.

SPACECRAFT MECHANISMS AND HEATERS

The number of commercially available mechanisms which are thermally actuated is growing. In addition to the conventional applications of heaters on board spacecraft, such as for thermal control and temperature management, the push for non-pyrotechnic actuators is leading toward more challenging applications for heaters in the control of mechanical devices. Thermal energy is the basic trigger on such technologies as shape memory alloys, paraffin, low melting temperature alloys, and fusible links. Table I summarizes the operation and uses of these technologies.

Thermal actuators which can be operated by joule heating, such as burn-wires and small SMA wires, have an obvious advantage with respect to heater implementation: the element itself is the heater. However, for larger SMA elements, paraffin actuators, and low melting temperature alloy devices, a separate heater must be provided.

TABLE I: Thermally Actuated Spacecraft Mechanisms

Technology	Typical Method of Heating: Joule	External	Real Applications
SMAs	Yes	Yes	Frangibolt, pin pullers, latch releases
Paraffin	No	Yes	Pin pullers/actuators
Low Melting Temp. Alloys	No	Yes	Active dampers
Fusible Links	Yes	No	Pin pullers, separation nuts

TYPICAL SPACECRAFT SPECIFICATIONS

Two of the most important criteria in accepting a heater for spaceflight are that it provide ample heat energy under all expected conditions and that it not exceed the specified outgassing limits. This is a significant challenge in view of the potentially wide variations in supply voltages and ambient temperatures. Table II presents some of the basic requirements as they applied to the use of Frangibolt heaters on DSPSE, the Advanced Release Technologies (ARTS) project, and the Total Ozone Mass Spectrometer (TOMS) satellite. Much of the difficulty in designing these heaters stemmed from the requirement by all three spacecraft that power be provided from an unregulated voltage supply. Combining the effects of variations in ambient temperature with an unpredictable power level presented a significant challenge in developing heater integrity.

TABLE II: Heater Specifications

Temperature to Reach:	150°C
Expected Voltage	
Minimum:	24 volts
Maximum:	36 volts
Max. Current Allowed:	5 amps
Expected Temperature	
Minimum:	-50°C
Maximum:	+50°C
NASA Outgassing (SP-R-0022A)	
Total Mass Loss:	< 1.0%
CVCM:	< 0.1%
Redundancy:	Yes

For a heating element with a 10 Ω resistance, the specified 22 to 34 volt range translates directly into 56 to 130 watts of power delivered. This is a variation of ± 40% from the mean. Variations in temperature from -50 to +50°C imply that the total increase in temperature required to effect actuation can vary by 100°C. Depending on the heat capacity of the component(s) to

be heated, this can represent a significant amount of energy. Therefore, design of the heater must allow for the possible variations in both the power delivered as well as the component's temperature. This must be achieved without exceeding the NASA outgassing standards.

ESTABLISHING HEATING REQUIREMENTS

Calculating the heat energy required to increase the temperature of a component or substance to a specific level is relatively straight forward. Ascertaining the rate of heat loss from the system is more difficult and depends on temperature gradients and paths of escape. Thermal actuators which can be heated very quickly, such as SMA wires and burn-wire devices, are not as prone to heat loss since the duration of the heating event is relatively short. For actuators requiring longer heating times, the rate of heat loss becomes much more important.

Three basic factors make up the heat input requirements: heat capacity, latent heat of transformation, and expected heat loss. That is

$$Q_{IN} = Q_{STORED} + Q_{TRANSFORMATION} + Q_{LOST} \quad (1)$$

Paraffin and SMA actuators undergo phase transformations which absorb appreciable quantities of heat energy. Burn-wire devices, however, typically fail in tension before the material changes phase into the molten state and thus the latent heat of transformation is negligible.

The stored energy term is described simply by the expression:

$$Q_1 \text{ (joules)} = m \bullet c_p \bullet (T_{FINISH} - T_{START}) \quad (2)$$

The second term, if a phase transformation is expected, can be calculated by:

$$Q_2 \text{ (joules)} = m \bullet \lambda \quad (3)$$

where m is the mass of the heated element, c_p is its specific heat capacity, and λ is its latent heat of transformation. The minimum power requirement is then determined by dividing the total heat energy ($Q_1 + Q_2$) by the desired response time. To this must then be added the expected rate of heat loss.

Using the DSPSE Frangibolt hardware as a specific example, the SMA actuator requires 1475 joules of heat energy to increase its temperature to 150°C from the coldest expected temperature (-50°C), and 575 joules to undergo the phase transformation. Thus, not including heat losses, a total of 2050 joules is needed. To actuate the SMA cylinder in 1 minute under these conditions, the power consumption would be 2050/60 J/sec = 34 watts.

Simple estimates of heat loss out of the SMA cylinder were made by examining two paths of escape: conduction out of each exposed end and radiation away from the outer surface. In the case of the DSPSE application, one end of the SMA actuator had only the bolt head in its conduction path, while the other end had an aluminum flange which was integrally attached to the spacecraft frame. Titanium washers were used on each end in part as thermal insulators. Only the end which was in contact with the attachment flange was considered in the analysis of heat loss.

Using Equation (4), the conduction losses out of the SMA cylinder and across the titanium washer and aluminum flange were estimated.

$$q_C \text{ (watts)} = \frac{k \bullet A \bullet (T_{SMA} - T_{FLANGE})}{t} \quad (4)$$

where k is thermal conductivity, A is the surface area, and t is the thickness of the insulating material(s). The conducted loss out of the system, assuming in worst case a 200°C gradient, was predicted to be 32 watts. Equation (5) was then used to estimate maximum possible heat loss due to radiation,

$$q_R \text{ (watts)} = \sigma \bullet A \bullet (T_1^4 - T_2^4) \quad (5)$$

where σ is the Stefan-Boltzmann constant = 5.67 x 10^{-12} W/cm^2-K^4, A is now the outside surface area, and T_1 and T_2 represent the two facing temperatures in degrees kelvin. For the DSPSE Frangibolt device, this was calculated to be 2.5 watts, indicating that losses by radiation were small.

After making the estimates described above, the conclusion was drawn that 2100 joules of heat energy was required to sufficiently heat up the actuator from its coldest possible starting temperature, approximately 35 watts of additional heat would be lost to the environment, and power delivered must be adequate over the entire range of 24 to 36 volts. To determine power consumption, the maximum allowable actuation time under worst case conditions (24 volts) was assumed to be 80 seconds. Using Equation (6),

$$\begin{aligned} \text{Power} &= Q/T + q_{LOSS} \\ &= 2100/80 + 35 \\ &= 61 \text{ watts} \end{aligned} \quad (6)$$

This implies that at 24 volts, 35 watts is lost to the environment via conduction and radiation while 26 watts is available for heating the SMA actuator. At 36 volts, the same 35 watts is lost but now 104 watts is available for heating. This factor of 4 difference in available heat energy exemplifies the challenge in heater design.

Continuing with this example, the SMA surface watt density which results from this power variation ranges from 4 to 9 watts/cm^2. Watt density is typically a very important factor in the design of a heater as it will often limit the choices available in selecting the materials for construction and insulation. This is discussed in more detail later in the paper.

HEATER TECHNOLOGIES CONSIDERED

Since radiation and conduction are the only two modes of heat transfer that can be considered for spacecraft heater applications, it was simple to narrow the choice to conduction transfer. Using only radiation transfer would have required, under ideal conditions, bringing a surface concentric about the SMA cylinder to a temperature of 1000°C or above. This was not considered a desirable feature within a reusable spacecraft mechanism.

Focusing on conductive approaches to heat transfer, there were again two alternatives: chemical and resistive. Commonly used chemical heaters comprise a cold-rolled steel tube packed with a slow burning pyrotechnic composition. Such heaters can provide 5500 to 26,000 joules of heat energy in 1 to 3 seconds. The fact that these chemical heaters are one shot devices, with no provision for pre-flight testing, significantly reduces their attractiveness to spacecraft applications. However, where significant heat is required to be delivered in a short duration and with minimal electrical energy consumption, they are certainly a viable alternative.

Four basic types of resistive heating elements were investigated for the Frangibolt mechanism:

a) wrapped wire
b) band heaters
c) etched foil
d) cable heaters

The first approach explored consisted of wrapping the SMA cylinder with Nichrome wire, sandwiched between two layers of Kapton tape. The desired watt density could be achieved by varying wire diameter and number of wraps. The performance, however, was less than desirable. The temperature of the Nichrome element was sufficiently high so as to "burn" a cavity within the insulation that resulted in the wire shifting and occasionally shorting between wraps. After two or three cycles, these heaters became unreliable.

The second type of heater examined was the band heater. These are commercially available units with stainless steel or mica jackets containing the heating wire element(s) and packed with a high temperature insulation (typically an MgO filler). A variation on this design was also tested that comprised a stainless steel tube in which the walls were packed with the filler and heating elements. In both cases, the inside diameter of the heater, no

matter how intimately pressed against the SMA cylinder, would expand away from the SMA surface, thus breaking its conductive path. This effect was doubled when the actuator began to recover: the SMA grows in length to break the bolt, but must decrease in diameter to conserve volume. Therefore, shortly after the heater was turned on, it lost intimate contact with most of the SMA cylinder and thereby thermal conduction was drastically reduced. This effect was observed only during tests in vacuum, because convection heat transfer during atmospheric tests produced false positives.

Etched foil heating elements appear the most sophisticated, but are in fact simple to manufacture and easy to install on flat or curved surfaces. They are also more flexible than other heater configurations, which can be important for applications requiring physical movement of the heated element. Figure 2 shows a photograph of the etched foil element used on the Frangibolt actuator. Power output is determined by the thickness of the foil, its width and total length. The serpentine patterns are designed on a CAD system, a mask is made, and then the foil is etched using standard lithography techniques. A major benefit of this approach is that the heating element has a large surface area in contact with the heated component, whereas wire elements can have at best a line contact with the heated surface. The disadvantage of the etched foil, as will be discussed later, is that it is prone to buckling when adhered to a surface that contracts and expands through a large percentage.

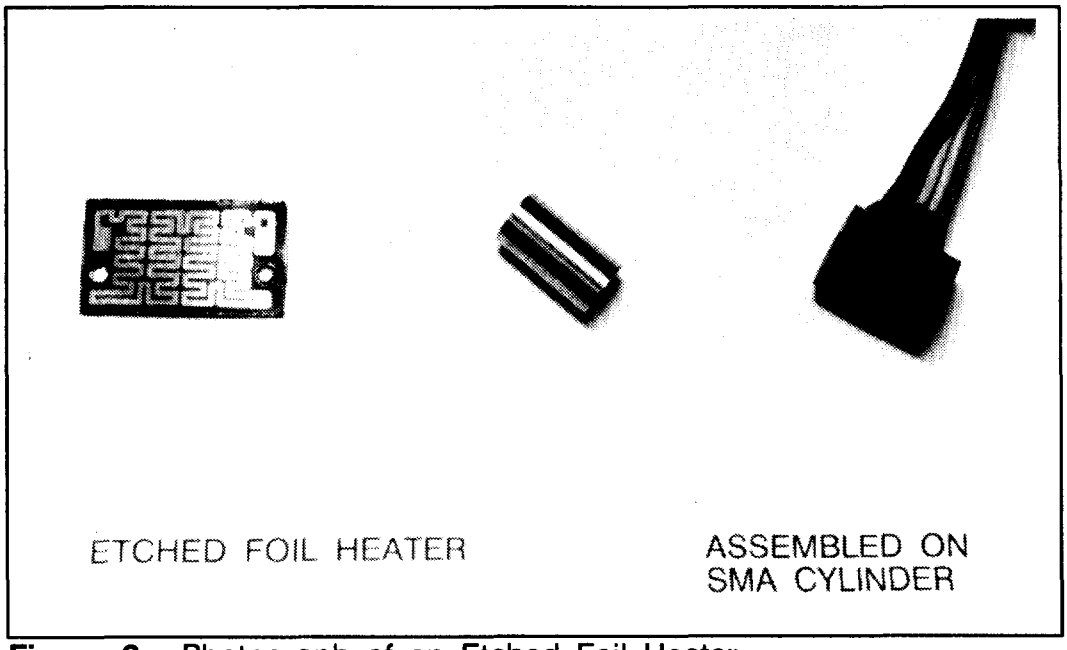

Figure 2: Photograph of an Etched Foil Heater

Cable heaters are thin walled stainless steel tubes which comprise the heating wire and insulative filler. These tubes can be drawn down to diameters as small as 1.5 mm. During the Frangibolt investigation, two different types of cable heaters were tested: a 3 mm diameter tube with a flattened edge (to provide a "D" shaped cross-section) and a small 1.5 mm diameter tube. Both were wrapped in helical fashion around the SMA cylinder. The larger of the two behaved similarly to the band clamps described above; despite the flattened surface to maximize contact, it still tended to grow away from the SMA surface. The smaller cable heater was wound into a helix to a diameter just smaller than the SMA cylinder (see Figure 3). Even as the heater increased in temperature, its elastic propensity to decrease in diameter kept it in good conductive contact with the cylinder.

Other types of heaters that are available, but which were not investigated for the Frangibolt, include cartridge, ceramic fiber, strip and radiant heaters. The cartridge heater incorporates a Nichrome wire element and MgO filler inside an Incoloy sheath. Commercially available diameters range from 3 to 25 mm, and lengths can range from 3 to 180 cm. These cartridges can be

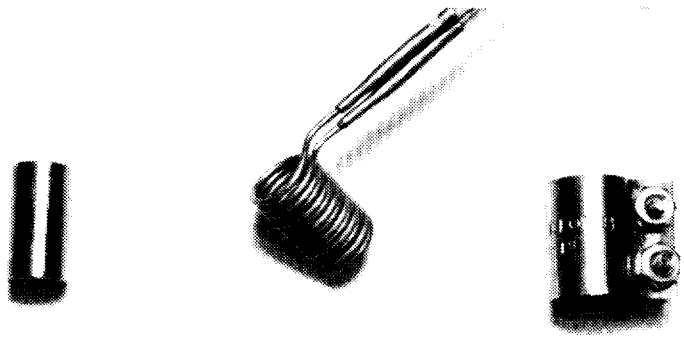

1.5 mm REDUNDANT CABLE HEATERS
WITH CLAMP

Figure 3: Photograph Showing Cable Heater

heated to 870°C with a maximum watt density of 62 watts/cm^2. Ceramic fiber heaters provide for very high temperature operation, incorporating iron-chromium-aluminum heating elements within a matrix of ceramic fiber insulation. Operating temperatures can be as high as 1200°C and watt densities as high as 4.6 watts/cm^2. Strip heaters are flat plate stainless steel sheaths containing heater wire or etched foil elements within mineral or mica insulation. The watt densities can be as high as 15 watts/cm^2 and temperatures can go to 760°C. The commercially available radiant heaters are

larger in size and use either radiating panels or quartz tubes with reflectors. Radiant heater temperatures typically range from 540°C to 1100°C, and watt densities can range from 1.5 to 6.2 watts/cm^2. [2]

EMBEDDING THE HEATING ELEMENTS

Integrating the heater with the component or substance to be heated also requires careful consideration. Clamping a helical heater to the surface of an SMA cylinder as shown in Figure 3 poses little difficulty and minimal concern for outgassing. Embedding an etched foil heater in Kapton or silicone rubber, however, requires close examination of watt densities and material limitations. Table III presents the watt densities of several standard insulation materials [3].

TABLE III: Comparison of Heater Insulation Materials

	Max. Watt Densities @		
	-50°C	+50°C	+150°C
Mica	17.0 W/cm^2	17.0	15.5
Silicone Rubber	9.3	7.8	3.1
Kapton	7.8	6.2	0.8
Nomex	5.1	1.6	0

Kapton insulation was tried with minimal success. An etched foil heating element was sandwiched between two layers of kapton film and bonded with an FEP filler. The total thickness of the assembly was approximately 0.2 mm. Contact between the Kapton and SMA surface was achieved with a high temperature adhesive. Initial tests using a watt density of 4 watts/cm^2 resulted in burning of the Kapton film and failure of the heating element. Adhesion to the SMA surface was maintained, but local hot spots created some gaseous discharge.

A single stage silicone rubber was then analyzed. This heater was constructed by vulcanizing the etched foil heater (shown in Figure 2) directly to the SMA surface with a sandwich structure of thin silicone rubber sheets. This assembly was then placed in a mold and an outer jacket of silicone rubber was vulcanized in place. The resulting heater exhibited excellent adhesion qualities to the SMA cylinder even after numerous mechanical and thermal cycles. The benefit of silicone in this application is that it easily tolerates the 3% strain compression and elongation of the SMA actuator without delamination. The disadvantage is that it is more prone to outgassing if the heater(s) were to remain on indefinitely.

To identify the limitations of the selected silicone rubber, a thermal gravimetric analysis was performed on a sample piece. Figure 4 shows that the material is stable to approximately 370°C, after which the total mass loss exceeds 1% [4]. Based on this data, the upper temperature limit of the silicone rubber during use was defined to be 300°C. This provided a 150°C margin above the temperature required to actuate the SMA cylinder under all possible conditions. To meet the NASA outgassing standards, the assembled actuators needed only to be heated in vacuum at 125°C for 24 hours.

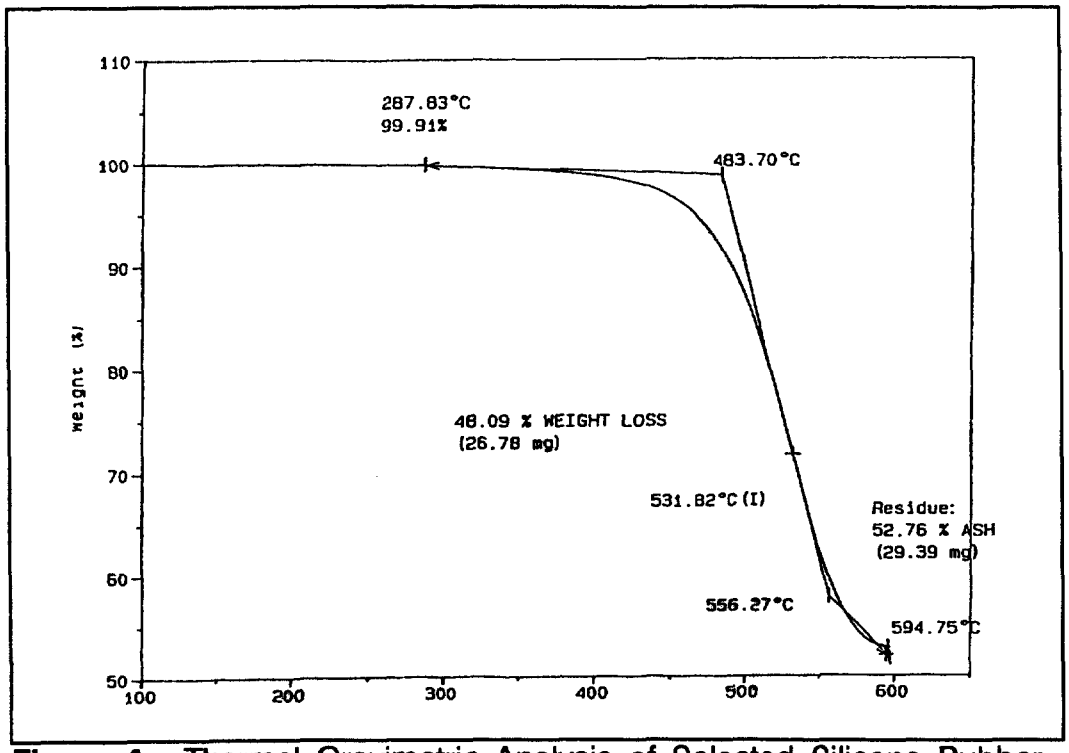

Figure 4: Thermal Gravimetric Analysis of Selected Silicone Rubber

The silicone rubber heater provided the best heat transfer and easily tolerated the compression and elongation of the SMA cylinder. Even so, it was decided that a second heater design would be provided for applications hypersensitive to outgassing. The second design uses the small helical cable heaters described above. This unit provided the same watt density against the SMA surface, yet could reach temperatures of up to 900°C with effectively no outgassing.

CONTROLLING THE HEATING ELEMENTS

Another important consideration in applying heaters on spacecraft mechanisms is the method of control and shut-off. Since these heaters will

be operated remotely under computer command, the simplest of control schemes should be used to ensure high reliability. Five different approaches were investigated for the Frangibolt system:

1) Timer
2) Deployment switch
3) Self-regulating resistance element
4) Thermal cut-out
5) Thermocouple feedback

Timing circuits are used in most spacecraft heater applications as a safety measure to ensure that the duration of the event is limited. This has been the case in most uses of the Frangibolt and High Output Paraffin actuators. If the heaters are left on too long, they will likely outgas and deteriorate. Thus, additional control elements may be added in series with the timing circuit to ensure that overheating does not occur, especially during ground tests of flight hardware.

For the TOMS satellite, TRW elected to use only a timing circuit to control the Frangibolt heaters. It was their determination after performing thermal vacuum tests that actuation from worst case conditions would occur within 60 seconds. Further, even if the hot extreme case was encountered (+50°C and 34 volts), the 60 seconds on time would not result in undesirable outgassing. Therefore, the TOMS satellite will supply power to the primary heaters for 60 seconds each, and then, after a specified waiting period, to the secondary circuits for 60 seconds each.

For the DSPSE satellite, NRL chose to add a deployment switch through which the heater power passed. The heaters automatically turned off upon release of the solar panels, thereby eliminating the chance of overheating the heating elements.

Self-regulating resistive elements have been applied to heaters for many years, but with only limited success. The material is usually made from nickel-iron alloys which increase in resistance proportionally with their temperature. The temperature coefficient of resistance for these materials is typically 0.25% per °C. The disadvantage of this technology in practice is that there is a high in-rush current, followed by a quick decrease in current flow, and then little additional ability to control temperature. Applications which do benefit from self-regulating heaters are those with constant heat loads, a wide range of acceptable temperatures, and low watt density requirements.

Another type of heater control considered was the thermal cut-off (TCO) switch. At a predetermined temperature, these switches interrupt current flow. The solid state devices can interrupt currents up to 40 amperes and will range in size from 0.8 to 6.2 cm^3 [5]. The TCO was not incorporated in the Frangibolt heater design because of the physical size. To incorporate such a switch within the silicone rubber molding around the SMA cylinder would have doubled the size of the actuator.

A control scheme that was short-lived during the initial investigation was that of using a thermocouple embedded in the heater to complete a control loop. For critical temperature maintenance this may be a necessary requirement, but for thermally actuated devices this was considered too complex. Demanding complicated electronics to drive single event mechanical systems is contrary to the philosophy of simplifying spacecraft mechanisms. Therefore, it was necessary to find simpler and even more reliable means for controlling the Frangibolt heaters, such as the timer and deployment switch combination.

SELECTED HEATER DESIGN FOR DSPSE

The final configuration of the Frangibolt heaters for use on DSPSE was defined in conjunction with NRL. The etched foil heating element design using the low outgassing silicone rubber insulation was selected. Electrical redundancy was provided by using two heater circuits on each SMA cylinder in an over/under manner. This increased the surface area for each heating element which, in turn, reduced the watt density demanded of the heaters. As mentioned above, DSPSE incorporated deployment switches on each solar panel to turn power off immediately after actuation. Power was supplied from an unregulated bus and temperatures of the release mechanisms were expected to range from -10°C to +50°C. Actuation times of the flight units during pre-flight tests confirmed that each heater worked as expected.

FAILURE MODES OBSERVED AND PROBLEMS RESOLVED

During the two years of developing the Frangibolt heaters, only three failure modes were observed. These failures resulted from localized buckling of the etched foil elements, an inferior electrical connection to one heater circuit, and overheating of the silicone rubber jacket. None of these problems was inherent to the mechanism design, but rather to the design, fabrication, and use of the heating elements.

One of the benefits discussed regarding non-pyrotechnic spacecraft mechanisms is their ability to be re-used in most instances. For thermally actuated devices, this means that the heaters must be re-usable and yet remain reliable. Numerous compression and elongation cycles performed on Frangibolt prototypes revealed localized hot spots within the heaters and, on two occasions, failure of the etched foil element due to excessive buckling. This was caused by having segments in the etched foil serpentine pattern which were too long in the direction of the compression and elongation strain.

Although the silicone rubber conforms easily to the 3% strain deformation, the etched foil material does not. Initial prototypes, which had longitudinal runs as long as 70% of the cylinder's length, exhibited buckling directly in the middle of each longitudinal segment. This buckling occurred within the first four cycles and created localized areas where the heating foil delaminated from the silicone rubber. The points of delamination caused the hot spots that were observed.

This problem was solved by redesigning the etched foil pattern so as to minimize the length of any longitudinal segments. Figure 2 shows the second of three revisions of this serpentine pattern. The longer segments are all oriented in a circumferential manner, leaving only short segments in the longitudinal direction. This pattern eliminates the buckling problem by providing the necessary compliance against repeated compression and elongation.

The second failure encountered was that of a poor electrical connection between a lead wire and an etched foil element. Close examination revealed that bonding the wire to the thin pad is a difficult manual operation, and that better screening procedures were required during its manufacture. Since the addition of an in-process inspection of this joint, no further failures have been experienced.

Overheating of the silicone rubber jacket was the third failure mode observed. This resulted from continuing to apply power at high voltages to the secondary circuit after the point of actuation. The heater was optimized as much as possible to operate effectively over the entire specified voltage range and from any anticipated temperature. However, even though the units operated effectively from -50°C at 24 volts (61 watts) and from +50°C at 36 volts (136 watts), the latter condition, when applied to the secondary heaters, created the potential for an excessive rise in temperature. If this high power level was driven through the secondary heater after actuation had occurred, the temperature would rise to 300°C within an additional 15 to 20 seconds. Beyond this point, outgassing would exceed the levels accepted by NASA.

The overheating problem was solved three different ways. For the TOMS application, the maximum sustained voltage level under load does not exceed 34 volts, and thus the problem does not manifest itself. For DSPSE, the specified voltage range did extend to 36 volts. Therefore, incorporation of the deployment switches ensured that the heaters would shut off immediately upon actuation. For future satellites, where high voltages are anticipated and no deployment switch is desired, use of the stainless steel heater configuration shown in Figure 3 would provide the heat requirement without the concern for outgassing.

CONCLUSIONS

Two different approaches were developed to heat an SMA cylinder in a vacuum for spacecraft applications. The course of designing and refining these heaters identified important considerations which are applicable to most applications of heaters on spacecraft (see Figure 5). These include designing heaters to accommodate large fluctuations in voltage supply and temperature, providing direct intimate contact to either stationary or moving components, and minimizing outgassing potential during use. It was concluded that silicone rubber heaters offer relatively high watt densities and are extremely flexible. Stainless steel cable heaters provide very high temperatures with no outgassing, but are not as efficient in thermal transfer. Implementation of heaters on spacecraft mechanisms will often require that the driving circuit be limited to a timer and simple shut-off scheme. Use of sophisticated controls for single event heater operation is generally discouraged.

ACKNOWLEDGEMENTS

The authors wish to thank Mr. Bill Purdy of the Naval Research Laboratory and Mr. Howard Eller of TRW for their assistance during the past two years in testing and evaluating the Frangibolt heaters. The extra effort provided by Watlow Electric in optimizing the heater designs is also gratefully acknowledged. This work was sponsored in large part by a contract with the Naval Research Laboratory.

REFERENCES

1. J.D. Busch, W.E. Purdy, and A.D. Johnson, "Development of a Non-Explosive Release Device for Aerospace Applications," Proceedings of the 26th Aerospace Mechanisms Symposium, NASA Goddard Space Flight Center, May 13-15, 1992.

2. Watlow Electric Mfg. Co. Product Catalog #9293, St. Louis, MO.

3. Minco Products, Inc. product bulletin HS-201 on Thermofoil Heaters, Minneapolis, MN, 1991.

4. Thermal Gravimetric Analysis was performed by TRW, Redondo Beach, CA.

5. Raychem Corporation PolySwitch product catalog, RDE and RBE families.

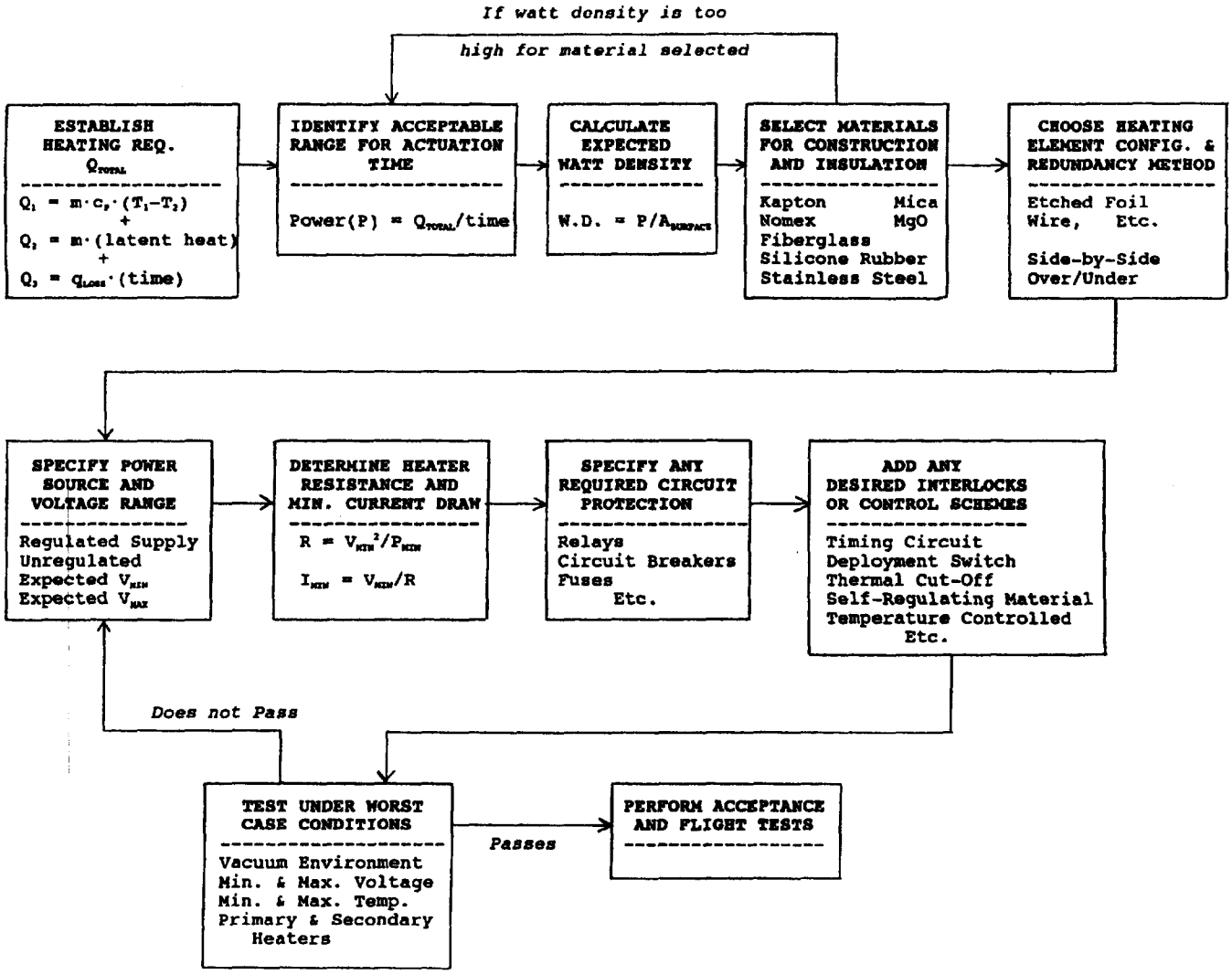

Figure 5: Suggested Heater Design Methodology for Spacecraft Mechanisms

PAYLOAD HOLDDOWN AND RELEASE MECHANISM

Dale Chaput, Mark Visconti, Michael Edwards, and Tom Moran
G&H Technology, Inc.
Camarillo, California

ABSTRACT

A payload holddown and release mechanism, designated the Model 1172, was designed and built at G&H Technology during the winter of 1992/1993. The mechanism is able to restrain and release a 45-pound payload with minimal tipoff. The payload is held in place by a stainless steel band and released using electrically triggered non-explosive actuators. These actuators provide reliable operation with negligible shock and no special handling requirements. The performance of the mechanism was demonstrated in two flight tests. Data showed pitch and yaw tipoff rates of less than 0.07 radian (4 degree) per second. The Model 1172 design is an efficient replacement for conventional payload deployment devices, especially where low transmitted shock is required.

INTRODUCTION AND BACKGROUND

Common methods of payload retention and release, including pyrotechnic joints and V-bands and Marmon clamps held by explosive release devices, present definite risks when used on critical missions. Release of non-symmetrical retention can impart perturbations and undesirable motion to the payload. Pyrotechnic device shock can affect sensitive on-board equipment. The Model 1172 holddown and release mechanism was designed to alleviate these problems.

The mechanism design evolved from the separation and retention methods used on a series of electrically actuated umbilical disconnect devices developed for use on the Minuteman III reentry vehicle, the Peacekeeper, Small ICBM and Space Shuttle Programs. These devices

had non-explosive actuators integrated into their design. Electro-mechanical actuators locked the spring-loaded connector plug and receptacle together until separation was required. An electrical signal triggered the actuators, releasing the connector halves so that spring energy can drive them apart.

The design elements that provided successful connector retention and release were viewed as possible solutions to the similar requirements of space payload holddown and release. A mechanism integrating spring loading and non-explosive actuators could cushion and capture a payload during flight and release it on command. A preliminary design for a payload holddown mechanism of this type was initiated for the kinetic energy weapon program known as SABIR in 1989.

A new design, using a simplified version of these principles of holddown and release, was developed for Rockwell for use on the LEAP program. The design parameters and performance goals for the device are presented below:

- Retention and separation for a 20.25 kg (45 pound) payload
- 102 ±25.4 cm/sec (40± 10 inch/second) payload separation velocity
- 20 year storage life
- <0.122 radian (7°) per second payload tipoff rate
- 5 kilogram (11 pounds) weight

The Model 1172 is shown in Figure 1.

MECHANISM DESCRIPTION

The main elements of the Model 1172 holddown and release mechanism are:

- A spring-loaded deployment plate, a ring of 14 collet fingers with Belleville spring washers for preload clamping
- A 27.9 centimeter (11 inch) diameter housing that steps down to a 22.9 centimeter (9 inch) diameter for payload interface.
- A steel retention band for collet retention, and
- A pair of non-explosive actuators.

The 22.9 centimeter (9-inch) diameter deployment plate mounts inside the housing. The housing is hard-mounted on the booster. The deployment plate is attached to a shaft that floats within a linear bearing positioned on the housing centerline. The spring-loaded collet fingers, actuators, and steel band retain an asymmetrical payload until separation is required. An overall view of the holddown and release mechanism is provided in Figure 2.

The payload mounts directly on the deployment plate which is shaped to match the countours of the payload's aft end. The hub of the deployment plate is preloaded by a compression spring. Payload retention is accomplished by fourteen collet fingers spaced along the circumference of the housing. The upper edge of each finger is notched to fit and grasp a flange on the payload. The collet fingers are preloaded by a stack of Belleville spring washers mounted in the housing. The washers are concentric with the fingers.

A stainless steel band is wrapped around the outside of the collet fingers and tightened to lock the collet fingers onto the payload flange. The band has small wedge-shaped steel pieces welded to each of its ends. The angular surfaces on these pieces form ramps that are held against matching bosses on the collet housing. Pins from a pair of non-explosive actuators lock the steel band ends against the housing. This is shown in Figure 3.

Upon receipt of an electrical signal, the non-explosive actuators are triggered. This pulls the pins, unlocks the steel band, and releases the payload. The spring load on the deployment plate pushes the payload away at the design velocity, with minimal rotation and tipoff. A linear bearing and shaft system controls the deployment plate motion, restricting it to travel along the housing's vertical axis and providing a stop. A shroud around the mechanism covers it and retains the steel band after payload deployment.

The total mechanism weight is 5 kilograms (11 pounds) and includes the deployment plate, housing, and hardware. All of the materials used in the mechanism, including lubricants used on the aligning shafts, are rated for exposure to the space environment.

OPERATION - HOLDDOWN

The Model 1172 must securely restrain the payload during launch and flight. This is accomplished by a steel band retainer and the system of peripheral collet fingers.

The aluminum deployment plate is shaped and sized to accept the contours of the payload and acts as a cradle for it prior to release. The deployment plate assembly mounts inside the collet flight housing, a circular unit that, using fasteners, attaches directly to the booster. The housing is also made from aluminum alloy. Holddown is illustrated in Figure 4.

The deployment plate assembly is centered on a spring-loaded ball bushing linear bearing. The weight of the payload and plate assembly compresses the deployment spring that is concentric with the linear bearing. The linear bearing shaft extends through the collet flight housing as the spring is compressed. Shaft extension is completed when the deployment plate is completely recessed within the housing.

Three additional deployment alignment shafts are attached to the deployment plate. These also extend through the flight housing and prevent rotational motion of the deployment plate about the mechanism's centerline.

Fourteen collet fingers are located along the 22.9 centimeter (9 inch) periphery of the flight housing. Each finger has a small notch which is positioned to slip over and retain a flange on the payload. The bases of the aluminum alloy fingers have a conical shape and are centered in cavities spaced around the housing. Each of the collet fingers is uniformly preloaded through forces exerted by Belleville spring washers stacked at their bases.

A stainless steel retention band wrapped around the exterior of the flight housing collet fingers holds them in position so they grip and retain the payload flange. The band is sized, with an ample safety factor, to withstand the collet finger radial loading imparted by force from the Belleville washers. Each end of the band has a wedge-shaped locking ramp that is attached by TIG welding. As this welding process causes partial annealing in localized areas of the band, the band design is based on working stresses well below the yield strength of heat treated 17-7 stainless steel.

Pins from a pair of non-explosive actuators trap the 5.24 radian (30°) locking ramps on the band ends against bosses on the collet housing. The actuator pins restrain the band, keeping the deployment plate and payload in place on the housing. For the 20 kg (45 pound) payload, the collet finger Belleville spring system payload preload is 34,500 newtons (7,700 pounds). This results in the collet fingers imposing a 4,000 newton (900 pound) preload on the band.

Statically indeterminate methods were used to determine the collet retention forces needed to secure the payload during flight. The maximum loading on the collet fingers, the stress on the retention band, and the side loading on the actuator retention pins were calculated. Representative free body diagrams of the critical elements are shown in Figure 5.

Assembly of the mechanism requires special tools to preload the Belleville washers so the collet fingers can engage the payload flange. The retention band is brought over the collet fingers and properly positioned using an engagement tool. The tool prevents over-stressing of the retention band as it is tightened against the individual collet fingers. Another tool holds the deployment plate in place, seated against its spring, as the band is positioned and locked. A safety plate is used to prevent danger from the spring-loaded collet fingers if the band assembly is accidentally released during assembly.

During preflight ground handling, launch, and flight the collet fingers and Belleville washers resist any forces that might cause unwanted payload separation. The non-explosive actuator pin puller assemblies are not affected by flight vibration and shock and can not be triggered by stray electrical signals. The mechanism reliably holds the payload in full contact with the deployment plate and collet flight housing until separation from the booster is desired.

The Model 1172 separation mechanism has a pair of D-sub connectors mounted in the deployment plate. These serve as quick disconnect umbilical connectors, allowing the transfer of data and power between the booster and payload while it is restrained. They are symmetrically arranged to minimize their effect on tipoff rate when separation occurs.

OPERATION - SEPARATION

Separation is initiated by an electrical trigger signal. The signal, usually 4.5 amperes at 5 Vdc, causes the non-explosive actuators to pull their pins away from each end of the stainless steel band. The actuators are sized so that they have sufficient force to overcome the side loading from the band and withdraw the pins. Without the pins retaining them, the band ends slip off the bosses on the collet housing and the band springs loose.

The unrestrained band can no longer hold the collet fingers. The force exerted by the Belleville spring washers bottoms the 14 collet fingers in their cavities. This movement strips the gripping notches on the collet fingers away from the payload flange. The collet fingers move simultaneously, insuring a uniform release of the load so that the payload tipoff rate is kept to a minimum. This release initiates deployment.

Figure 6 illustrates the holddown and release mechanism at the moment when the actuator has pulled the pin and freed the retainer band.

The design is redundant, using two non-explosive actuators as pin pullers. The band is released if either pin is pulled by its actuator or if both pins are pulled at the same time. The addition of the second, redundant pin puller increases the mechanism's predicted reliability to .99998. A single actuator design would have a reliability of .9998.

With the retainer band removed, the energy stored in the deployment spring is released. This pushes the deployment plate and accelerates the payload forward, away from the booster. The quick disconnect connectors come apart as the deployment plate begins to move away from its recessed position in the housing.

The movement of the deployment plate and payload is controlled by an alignment shaft and linear bearing on the plate centerline and three other alignment shafts. The alignment shaft and low friction ball bushing linear bearing maintain precision centering of the payload on the booster as the deployment plate and payload gain velocity. The other alignment shafts are equi-spaced around a common diameter of the deployment plate. They prevent rotational and angular motion.

This design maintains close alignment and minimizes the tipoff rate upon separation.

Movement of the deployment plate is halted when a mechanical stop on the bearing washer comes into contact with the flight housing. The payload continues its movement with the velocity imparted at separation by the deployment spring. The Model 1172 is sized to deploy a 20 kilogram (45 pound) payload at 76 to 127 centimeters per second (30 to 50 inches per second).

Figure 7 illustrates the holddown and release mechanism as the payload is deployed.

A shroud surrounds the collet housing and captures the steel retention band after it is released. The pin pullers, deployment plate, springs, and other parts of the mechanism stay with the booster after release. Separation occurs without gas release, debris, or other pollution.

NON EXPLOSIVE ACTUATOR PIN PULLERS

The operation of the payload holddown/separation mechanism is based on the performance and reliability of the non-explosive actuators used to restrain and release the retention band. The actuators belong to a family of lightweight devices that have been successfully used in numerous sophisticated space systems.

These actuators use a wire-wrapped split spool assembly to control the release of spring energy. The two-piece spool, with insulator assembly, is held together by a wrap of spring-tempered stainless steel wire set at a predetermined tensile load. One end of the steel wire is tied directly to a spool half. The other end is attached to the resistive link wire which is part of the insulator assembly. The resistive wire is also connected to a pair of electrical contacts.

The wrapped spool is used to restrain a moveable shaft under spring tension. In the absence of an electrical signal, the spools remain bound together under the predetermined and precise tensile load. The spool's restraining grip is constant and resistant to outside vibration, temperature extremes, and other shocks. Severe transportation and launch environments will not loosen the winding or impair the spool's

ability to restrain or release. This has been demonstrated by developmental and qualification testing for numerous programs.

However, when the mission critical event is required -in this case separation- actuation will be triggered by the arrival of the appropriate signal. This is done by applying electrical or laser power between the contacts tied to the resistive link wire. The power causes the temperature of the wire to rise, bringing with it a loss in tensile strength. When its strength drops below the imposed tensile load, the link wire breaks. This loosens and releases the wire wrapped around the spools. The two spool halves quickly separate and the spring-loaded shaft, which had been restrained, is now free to move.

Figure 8 illustrates the sequence of operation in these actuators.

The actuators will not actuate or "fire" if the current applied to the link wire is 0.6 ampere or less. This prevents operational failures of the devices from stray or induced signals. Actuation at current levels above one ampere is time dependent. Lower current levels must be applied for a longer duration to generate sufficient heat to lower the link wire strength below the tensile loading. High current levels can cause very rapid triggering. The units are rated for operation at 5 volts dc and 5 amperes with separation resulting within 20 milliseconds.

Spool separation releases the stored spring energy to move the shaft, in this case a pin. The actuator springs are sized to overcome the sideload placed on the pins as they restrain the retention band. The released actuator springs drive the pins free of the separation mechanism's steel circumferential band and allow deployment of the payload.

These actuators perform with negligible shock imparted to the adjoining structure. Although they act as "one-shot" devices during a mission, the spools may be fired and replaced, allowing them to be ground-tested with little difficulty. They contain no age-sensitive materials and can be stored for long periods of time with no degradation in performance. Their non-explosive nature eliminates the need for special handling, training, and safety precautions.

TEST/FLIGHT HISTORY

The test history of the Model 1172 separation mechanism consists of development, characterization, and demonstration testing. Development tests were conducted to refine and improve the design, and characterization tests were used to verify the mechanism performance. Use of the separation mechanism was demonstrated by Rockwell in its LEAP kinetic energy weapon program.

Development testing consisted of 30 tests to evaluate the mechanism and its design features. Several improvements were made as a result of this testing and release experience. The steel retainer band was widened to provide an increased margin of safety. Both brazing and spot welding were tried as methods of attaching the ramped ends to the retainer band. These methods proved unreliable and were replaced with TIG welding of the ends, resulting in a strong secure metal joint. Additional improvements were made to the band and band loading. Two extra collet fingers were added to provide more uniform loading of the non-symmetrical payload flange and to prevent the retainer band from making direct contact with the payload housing. The band mounting was also modified to control the collet preloading. This important factor is, in practice, very difficult to establish with precision. This was achieved by micro-adjustments in the lock ramps at the band ends prior to welding the ramps. Lastly, a shroud enclosing the periphery of the mechanism was added as a safety measure to capture the retainer band after payload separation.

Characterization testing of the mechanism included side load tests to verify the clamping force of the mechanism to the payload and drop tests to evaluate the payload tipoff and ejection velocity. Results of the side load testing agreed with predictions. Drop testing provided a means of evaluating the payload ejection tipoff and velocity in a 1 g gravitational field. The mechanism was inverted and interfaced with a simulated payload. The mechanism was then actuated, and the payload was released. Film data of the drops provided the means of determining the ejection tipoff and velocity. The 1 g acceleration was taken into account in determining the ejection velocity. The tipoff data agreed with expectations, and pushoff springs were characterized and selected to provide the required ejection velocities for the LEAP flight tests.

The Model 1172 was used by Rockwell to retain and eject payloads for a hover test and two LEAP flights. For the hover test, the mechanism was incorporated to demonstrate its integration and function with a Rockwell payload by separating an umbilical from the payload. For both of the LEAP flights (flown in June and September 1993), the mechanism was flown in space and ejected payloads of approximately 20 kilograms (45 pounds). Tipoff and ejection velocity data were obtained from the September test and were within expectations. This data is presented below:

Measurement	Planned	Actual
Ejection velocity	101.6 ± 25 cm/sec (40±10 in/sec)	88.4 cm/sec (34.8 in/sec)
Tipoff,		
Pitch	<0.122 radian/sec (<7 degrees/sec)	0.06 radian/sec (3.5 degrees/sec)
Yaw	<0.122 radian/sec (<7 degrees/sec)	0.01 radian/sec (0.6 degree/sec)
Roll	N/A N/A	0.129 radian/sec (7.4 degrees/sec)

SUMMARY

The Model 1172 payload holddown and release mechanism was designed, developed, and flight tested. Using non-explosive actuators, the mechanism was able to restrain a payload through launch and flight and release it upon command. The actuators required no special handling, eliminating assembly, transportation, and range safety problems. They operated without causing pollution or imparting significant shock to the payload.

The mechanism design uses a retention band and collet fingers to restrain a spring-loaded deployment plate and payload. The band provides a preload at the attachment points. The system has operational redundancy which, with the simple electro-mechanical nature of the actuators, provides a very high reliability.

The design can be easily adapted to payloads of other sizes and configurations. Adjustment of the size and number of collet fingers, as well as the band, can be made to accommodate smaller and larger

payloads, as well as changes in launch loading. To optimize weight savings, the basic design and collet fingers can also be integrated directly into the missile or booster without the need for a collet housing.

The Model 1172 demonstrated a tipoff rate of 0.06 radian (3.5 degrees) per second on the pitch axis and less than 0.017 radian/second (1 degree) on the yaw axis during flight testing. It provides a new and alternate method of payload holddown and release, especially in situations where imparted shock, safety, and reliability are concerns.

ACKNOWLEDGMENTS

Portions of the work described in this report were undertaken for Rockwell International under its contract with the U.S. Air Force Phillips Laboratory. That effort is part of the LEAP Program, sponsored by the Ballistic Missile Defense Office. Timothy J. Crowley of Rockwell International, Canoga Park, CA, provided the LEAP Program flight test data used in this report.

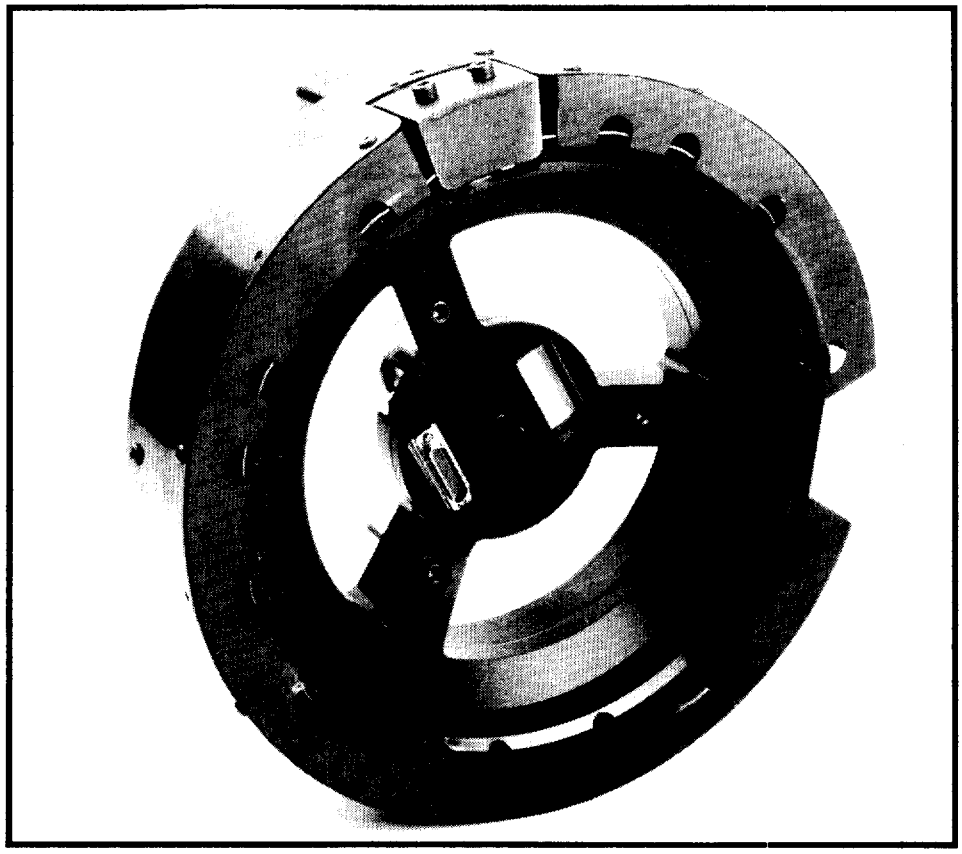

Figure 1: Model 1172 Holddown and Release Mechanism

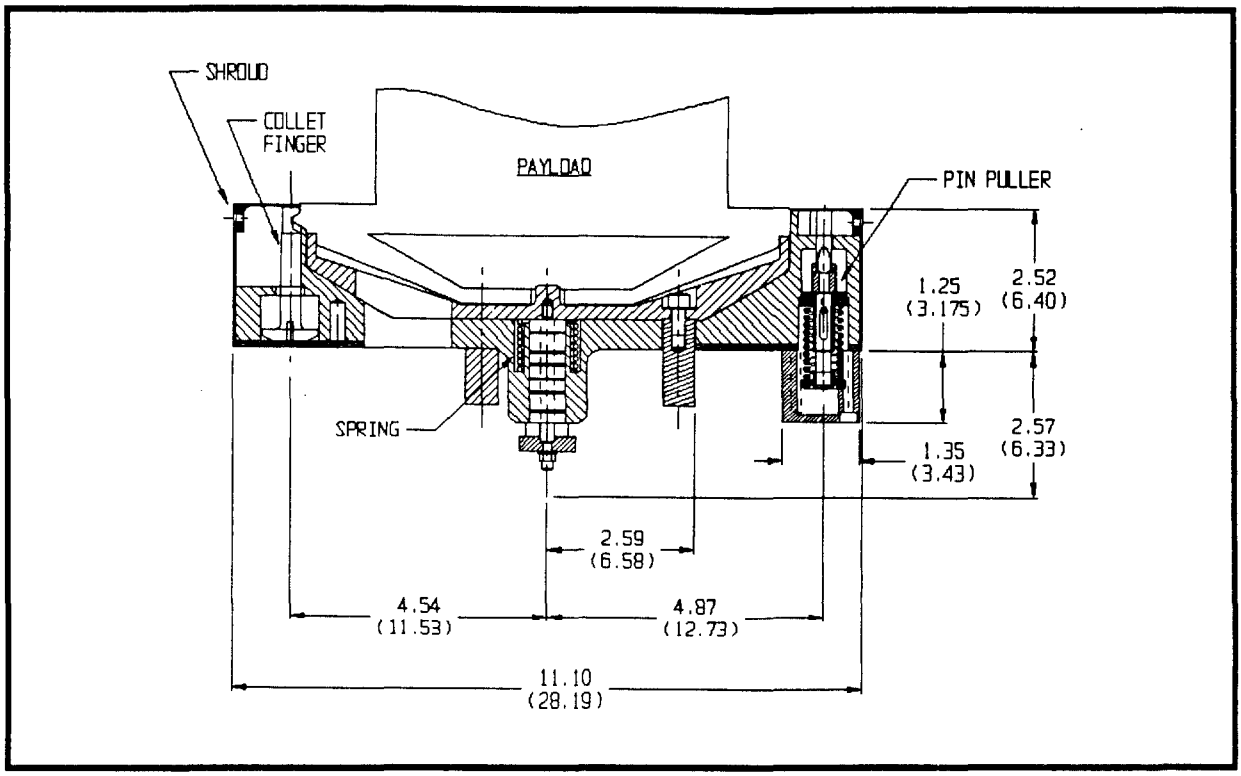

Figure 2: - Holddown and Release Mechanism (HDRM)

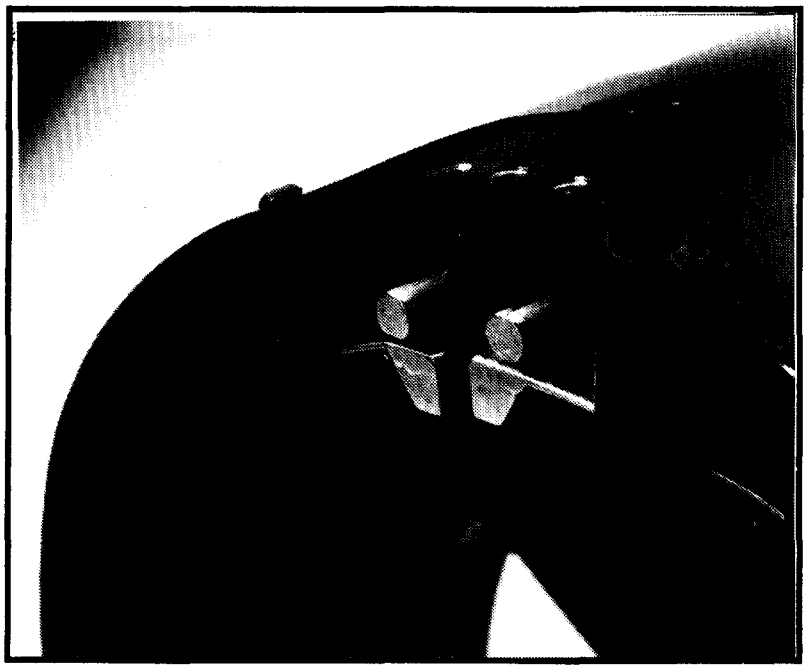

Figure 3: Retainer Locking Mechanism

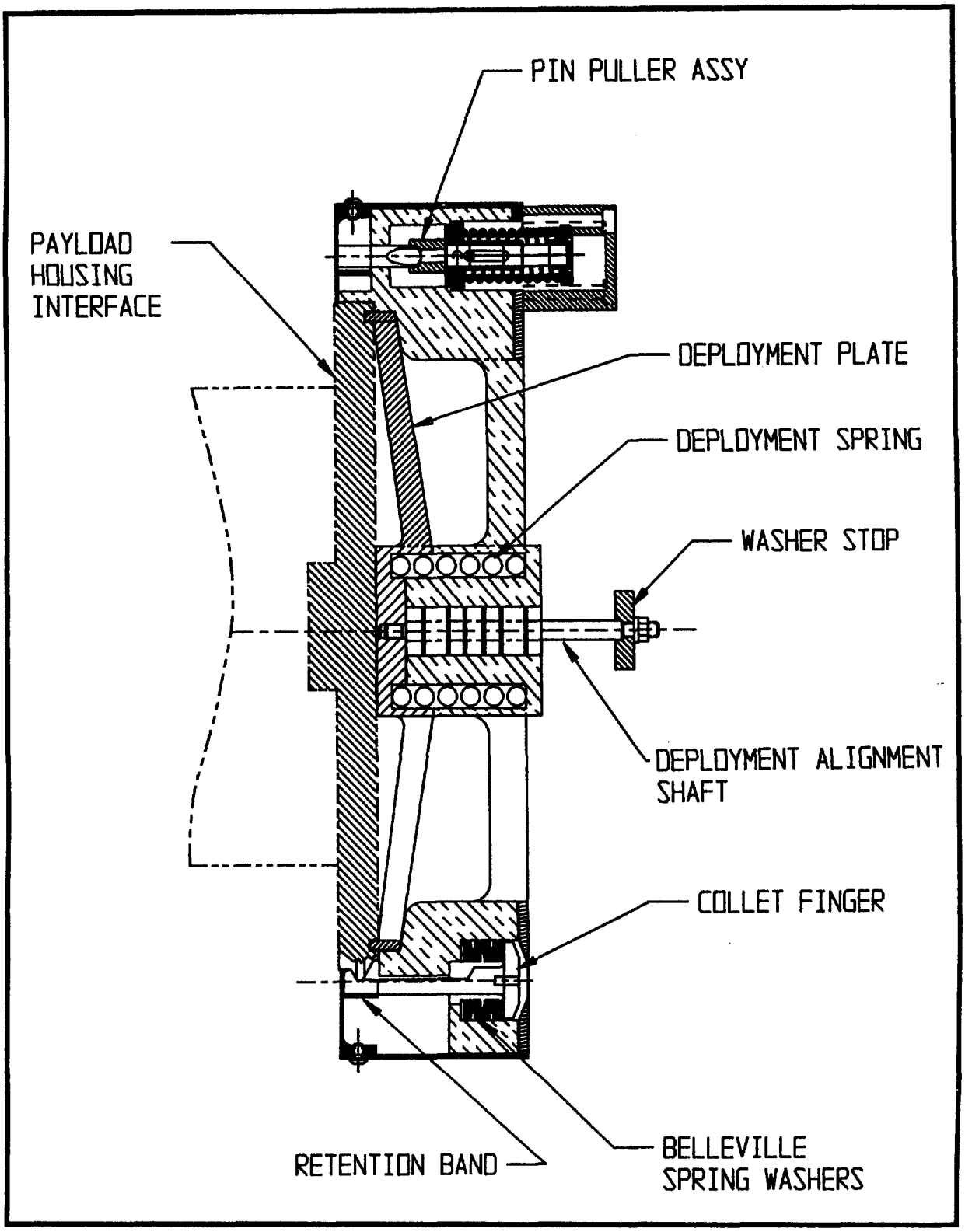

Figure 4: Holddown and Release Mechanism - During Holddown

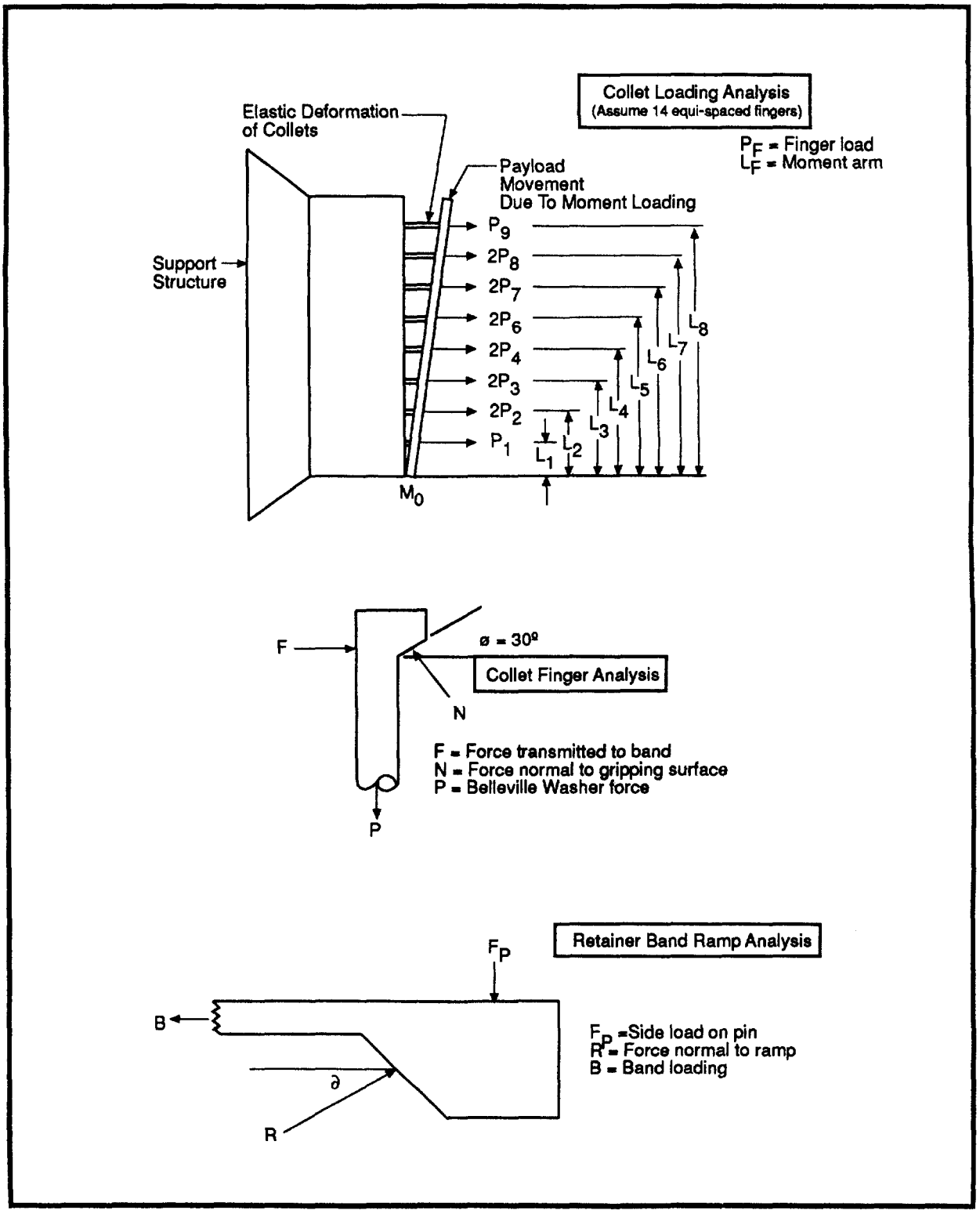

Figure 5: HDRM - Typical Free Body Diagrams

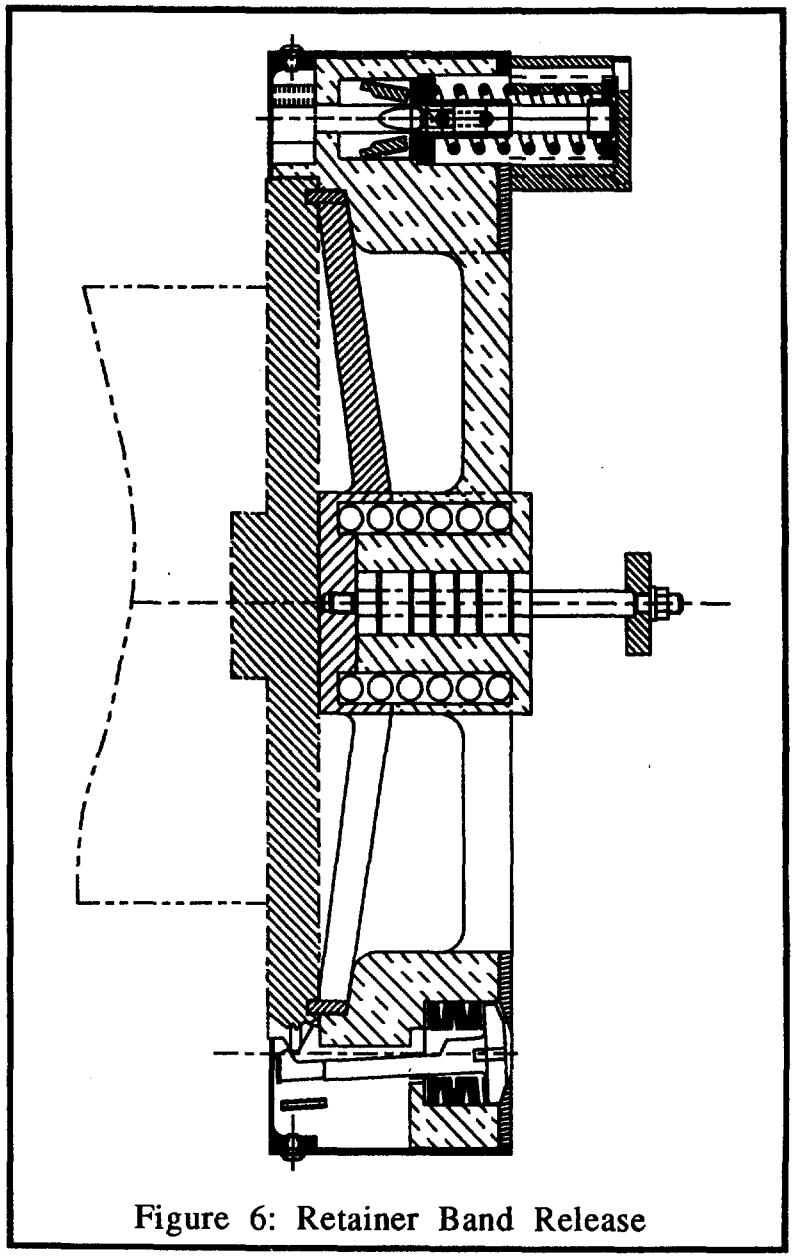

Figure 6: Retainer Band Release

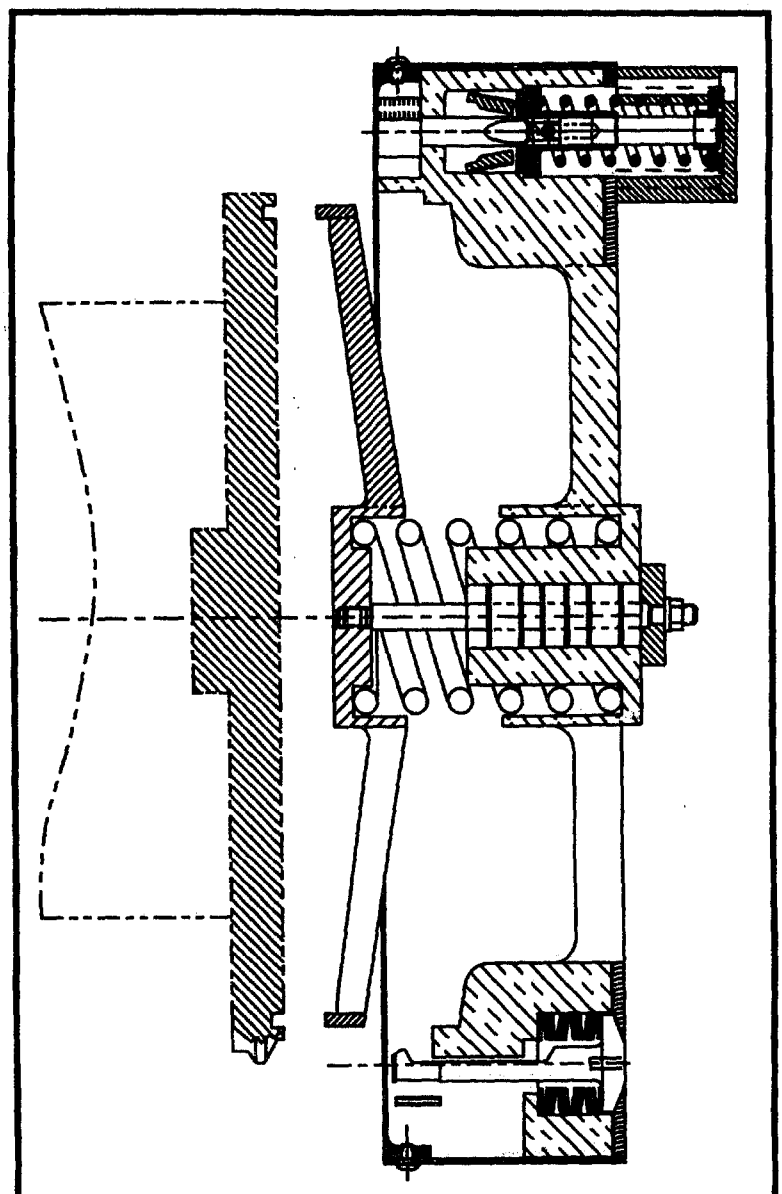

Figure 7: Payload Deployment

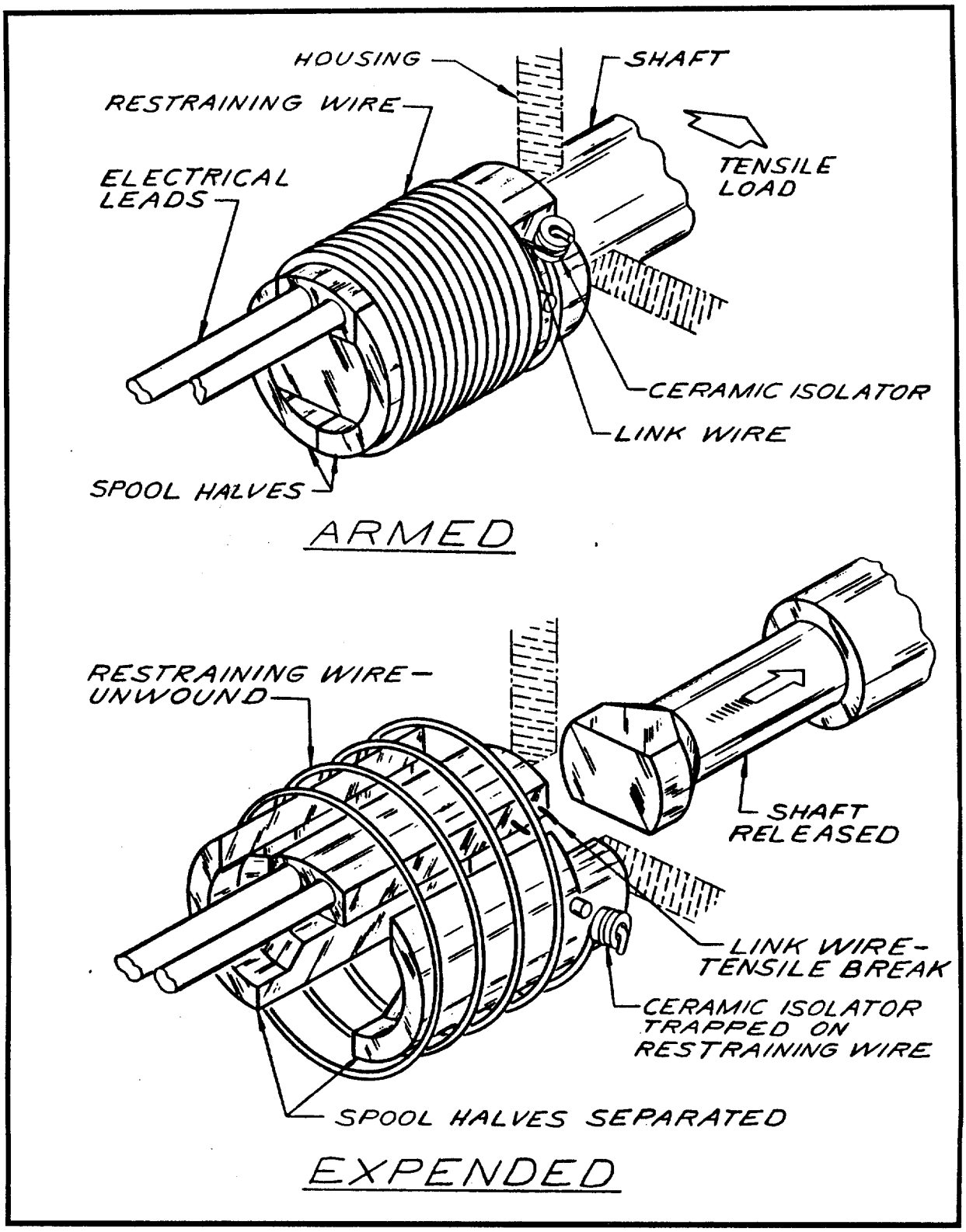

Figure 8: Non-Explosive Actuator Operation

ADVANCED RELEASE TECHNOLOGIES PROGRAM

Bill Purdy
Naval Research Lab
Washington, DC

Abstract

The objective of the ARTS program was to develop lighter and less expensive spacecraft ordnance and release systems that answer to the requirements of a wide variety of spacecraft applications. These improvements were to be evaluated at the spacecraft system level, as it was determined that there were substantial system-level costs associated with the present ordnance and release subsystems. New, better devices were to be developed, then flight qualified, then integrated into a flight experiment in order to prove the reliability required for their subsequent use on high-reliability spacecraft. The secondary goal of the program was to quantify the system-level benefits of these new subsystems based upon the development program results.

Three non-explosive release mechanisms and one laser-diode-based ordnance system were qualified under the program. The release devices being developed were required to release high preloads because it is easier to scale down a release mechanism than to scale it up. The laser initiator developed was required to be a direct replacement for NASA Standard Initiators, since these are the most common initiator in use presently. The program began in October, 1991, with completion of the flight experiment scheduled for February, 1994. This paper will: 1) provide an overview of the ARTS program, 2) discuss the benefits of using the ARTS components, 3) introduce the new components, 4) compare them with conventional systems and each other, and 5) provide recommendations on how best to implement them.

Program Overview

The ARTS program had two distinct phases: Phase 1) development and evaluation, and Phase 2) qualification and flight experiment production. An industry survey was done to evaluate many components in the early stages of research and development. The three most promising release devices and the most promising laser ordnance system were selected for phase 1 development. The selected devices were then developed to meet the level of reliability needed for flight production. Phase 1 concluded with a thorough test series to measure the devices' performance envelopes. Phase 2 took the phase 1 designs, made any minor modifications desired after the envelope testing, and then built a single lot of flight and qualification hardware. This hardware was then qualified and used to build a flight

experiment. One of the release mechanisms was rejected for phase 2 after phase 1 exposed inadequacies. The integration of the flight experiment required undergoing range safety reviews and interfacing with the host vehicle. This process exposed many issues, for example, living with current limits from the host vehicle. The production of the flight hardware and experiment proved to be very valuable in that it required us to be truly ready for flight. The overall two-phase process resulting in a flight build worked out quite nicely.

The spacecraft system-level benefits take the form of reduced production costs and result from three key factors: 1) reduced safety efforts, 2) reduced weight, and 3) reduced pyroshock environment. Neither the laser ordnance nor the non-explosive release devices is sensitive to Electro-Magnetic Interference (EMI) thus eliminating most of the safety hazards associated with today's pyrotechnically driven spacecraft components. The insensitivity to EMI allows the elimination of heavy shielding from the firing harness design. The bulk of the weight savings, which can add up to as much as 9 kilograms (20 pounds) on a large spacecraft, results from eliminating this shielding. The non-explosive release mechanisms have a pyroshock output of about one fourth of today's pyromechanical release devices. This characteristic allows spacecraft designers to seriously look at eliminating much pyroshock testing since the levels for almost all of its components will follow this 75% reduction.

A detailed cost analysis was performed comparing production and processing costs for a large satellite with conventional systems and the same satellite design using an ARTS-based system. The analysis showed that the ARTS system cost $1.1 million per satellite and that the conventional system cost $1.6 million per satellite. The satellite had already been built with conventional systems so its production costs were accurately known. The dominant savings were: 1) elimination of much of the labor required to get safety approvals, 2) the cost of weight to orbit, and 3) the elimination of a vehicle-level pyroshock acceptance test.

Frangibolt[1]

The Frangibolt release mechanism, developed by TiNi Alloy Company in San Leandro, California, and the Naval Center for Space Technology, uses the shape-memory alloy, nitinol, to break a notched bolt in tension upon command to effect a release operation (see Figure 1). The nitinol collar is compressed before installation so that when heated, it elongates to its original length, stretching the bolt until it fails in tension at the notch. A pair of 10-ohm etched foil heaters encased in a common silicone jacket

[1] Frangibolt is a registered trademark of the TiNi Alloy Co., San Leandro, CA

molded onto the nitinol actuator operates with a 24 to 36 volt DC supply typical of most spacecraft power systems. The advantages of the Frangibolt are that it is: 1) very simple, with only one moving part; 2) safe to use; 3) very lightweight; and 4) it produces a low pyroshock output. The disadvantage of the Frangibolt is that it takes from 10 to 60 seconds to operate and is incapable of releasing two locations simultaneously. The Frangibolt was discussed extensively in a paper presented at the 1992 Aerospace Mechanisms Symposium.

The Frangibolt is useful for roughly half the release tasks on typical spacecraft. This system is not capable of releasing several joints simultaneously, nor releasing at a specific time within 1 second. The Frangibolt is especially well suited to releasing items such as solar arrays and hinge-mounted deployables. The Frangibolt has been qualified to operate at 24 to 36 volts from -50°C to 50°C. The Frangibolt has been qualified for typical lifetimes of up to 25 releases by operating several of them 50 times.

The development program was focused on verifying the reliability of the Frangibolt over a wide range of supplied power and operating temperatures. The requirements of high watt density and wide voltage range coupled with large actuator deformations resulted in a very challenging heater design. The development also had a heavy emphasis on optimizing the fatigue strength of the bolt while keeping its breaking properties at their desired levels. The final design of the notched bolt was qualified by testing it to 4.5 million fatigue cycles in a bolted joint that was preloaded to 6670 N (1500 lb) and subjected to ±6670 N (1500 lb) applied load. The development process highlighted the fact that the Frangibolt is sensitive to compliance in the joint it is clamping. We determined that the Frangibolt installation must be procedurally controlled to verify proper joint assembly and that the actuator has been properly compressed. After long consideration of this sensitivity, it was decided to lengthen the actuator for the flight build in order to provide more margin on actuator stroke. The development process for the Frangibolt was successful in showing its reliability and capabilities.

The Frangibolt was used in both the ARTS flight experiment and in releasing the solar arrays on the Deep Space Probe Science Experiment (DSPSE) spacecraft (also known as Clementine 1). The DSPSE spacecraft will be launched in January, 1994. The Frangibolt acceptance testing consists of: 1) measuring the force and elongation to failure of 10% of the lot of notched bolts, and 2) verifying that the force and stroke output of each actuator exceeds the worst-case bolt breaking strength and elongation. This lot testing on the bolts showed the breaking strength variability, defined as

the standard deviation divided by the mean, to be 2% and the elongation variability to be 9%.

It was shown that the Frangibolt needed to be turned off by a switch activated by the solar array release during its implementation into the DSPSE spacecraft. This prevented the Frangibolt heater from being left on too long and overheating. The Frangibolt had to operate over a wide range of voltages and temperatures so its actuation time was expected to range from 10 to 60 seconds which prevented using a timer to turn it off. The DSPSE solar arrays remain closed for 7 days on orbit before they are opened. The arrays get very hot in this time period so the actuator had to be kept cool enough to prevent it from actuating prematurely. This was accomplished by mounting the actuator against an aluminum plate on the spacecraft side of the interface and using a titanium plate on the solar array to block heat from getting to the actuator. This arrangement kept the actuator at 45°C with the array at 100°C and the spacecraft at 25°C. The importance of a good installation procedure with several cross checks was found to be very important during the DSPSE integration.

Fusible Link

The Fusible Link, jointly developed by Boeing Space and Defense Mechanisms Research Department, in Seattle, Washington and the Naval Center for Space Technology, fuses a strap made of nitinol to unlock a preloaded link to perform a release operation (see Figure 2). When a 30 amp (minimum), 3 volt AC current is applied to heat the nitinol fusing element it weakens and breaks within 300 ± 50 milliseconds, unlatching the two jaws which allows the tensioned link to be pulled out of the separable joint. The DC voltage supply of a typical spacecraft is centrally converted to AC and is fed to a 9:1 transformer located on each Fusible Link, which steps the current up to the required level. Nitinol is used as the fusing element for its properties of high strength, high electrical resistivity and excellent corrosion resistance, rather than utilizing its shape memory effect. The advantages of the Fusible Link are: 1) that it is mechanically simple, 2) is safe to use, 3) has a low pyroshock output, and 4) that it is capable of releasing multiple locations simultaneously. The disadvantages are that 1) it requires a power conditioning circuit to create the high current AC, and 2) that it is the largest of the new devices.

The Fusible Link is designed to release one or more loads of up to 6670 N (1500 lb) simultaneously over a temperature range of -50°C to 100°C with voltage supplied to the power converter at 24 to 36 VDC. This design should be scalable to higher and lower loads, with size and power increasing or decreasing accordingly. The Fusible Link's release motion is very simple mechanically with no sliding friction opposing the motion of the jaws or link, which are its only moving parts. There is moderate complexity in the

DC to AC power converter although it is a relatively simple electrical circuit. An extractor must be used to pull the link out of the separation joint quickly and reliably. A Fusible Link can be used for 50 or more releases with no degradation although it requires replacing the fuse after each operation.

The development process included several iterations on both the mechanical and electrical design. The largest hurdle cleared in the design process was developing the AC heating method necessary to open the fuse fast enough to support the simultaneity requirement. At first, we could not make the fuse draw enough current out of the power converter. We discovered that the inductance of the fuse was as large as its resistance and this was preventing the fuse from drawing the large current it needed. This came as quite a surprise to we mechanical engineers who barely understand DC electricity. The solution to this problem was to redesign the fuse such that it could be located adjacent to the transformer to minimize the inductive loop area of this high current portion of the circuit. Several flexure-mounted jaw designs were tried in the interest of simplicity before they were ultimately rejected in favor of a hinged jaw design; the flexure-mounted jaw is shown in Figure 2. The bending of the flexure, coupled with the high tension loads, resulted in excess stress on the flexure. Ultimately, the development process proved the Fusible Link to be very reliable over the wide range of operating conditions required.

The qualification testing operated the Fusible Link at the required temperature extremes with the required supply voltage extremes. The flight experiment had a 5 ampere current limit imposed on it, which turned out to be a tight constraint when operating the Fusible Link at 36 VDC since the Fusible Link also had to draw enough current to fire quickly at 24 VDC. The acceptance testing required for the Fusible Link consists of electrical measurements, then verifying release while monitoring current draw and time to fire for normal performance. The time to fire is proportional to joint preload as well as to the required fuse temperature rise, so consistent preload control on the fuse installation and separation joint preloading is important for maintaining release simultaneity.

Non-Explosive Separation Nut

The Non-Explosive Separation Nut, developed and qualified independently by G&H Technology, Inc. in Camarillo, California, utilizes their previously qualified Non-Explosive Actuators (NEAs) to unlatch a spring-powered separation nut (see Figure 3). Current is passed across the bridgewires of two redundant NEAs releasing them, which in turn unlocks the release housing of the separation nut that is then driven upward by a spring to disengage the thread segments, thus releasing a preloaded bolt. The advantages of this device are that: 1) it operates within 10 to 20 milliseconds, 2) is safe to use, 3) that it produces a low pyroshock. The

disadvantage of the device is that it contains several moving parts and one highly loaded sliding surface.

The Non-Explosive Separation Nut is qualified to release up to 16,000 N (3500 lb) within 20 milliseconds which supports requirements for release of multiple points simultaneously. The device has been qualified from -150°C to 121°C with a 4.5 amp minimum current while at a 20,000 N (4500 lb) preload. The NEA has been separately qualified as a 3.5 amp all-fire device. This development and qualification took place prior to the nut's implementation in the ARTS program. The nut exhibited the same performance, tendencies and sensitivities as standard separation nuts during its integration into ARTS. The Non-Explosive Separation Nut was shown to be a direct replacement for comparable capability pyrotechnic separation nuts. The acceptance testing for the nuts consisted of releasing them with a mechanical, hand-operated replacement for the NEA at one and at two times their nominal preload of 11,100 N. The Non-Explosive Separation Nut design's scalability to larger preloads is unfortunately limited by the sizing of the release spring. It is expected that a 9.5-mm ($^3/_8$) bolt will be the largest practical size for this basic design. Other designs utilizing NEAs for higher preloads are presently under development.

Laser Ordnance System

The laser ordnance system, jointly developed by Ensign Bickford Aerospace Corporation in Simsbury, Connecticut, and the Naval Center for Space Technology, ignites explosive cartridges using lasers rather than electrically heated bridgewires. A two-watt laser diode fires down a fiber optic harness into an explosive cartridge igniting the explosive mix with light energy. The advantages of this system over electrically ignited ordnance are: 1) that it is much less sensitive to EMI and RFI, 2) that it is safer than conventional ordnance, and 3) that its fiber optic harness is much lighter than a shielded ordnance wire harness.

The laser ordnance system is sized towards replacing electrically ignited NASA Standard Initiators (NSIs). The system consists of the Laser Standard Initiator, a fiber optic firing harness, and firing electronics, including the high-power laser diodes. Figure 4 shows the system schematically. The system is designed to meet all of the NSI and range safety specifications. The firing electronics are all built to typical spacecraft high reliability standards.

The development effort focused on electrical design and initiator fabrication techniques. The laser diode and fiber optic cable technologies were already mature. The critical design issues for the initiator were consistency of all-fire power levels and in duplicating the explosive output

of the NSI. One important deviation from the NSI design was to manufacture the initiator housing from stainless steel rather than from Inconel, which significantly reduced manufacturing costs. This initiator is being tested to show that it can be qualified to the NSI specification. The ARTS program could not afford to test the large quantities of initiators required to qualify the design to the NSI specification. The electronics are being qualified at this writing to operate at 24 to 32 VDC from -5°C to 45°C.

Flight Experiment

A flight experiment shown in Figure 5 containing all of the ARTS devices is in production and will have completed protoflight acceptance testing by February, 1994. The experiment will then be installed on a host spacecraft and will await launch. The experiment contains a four-channel laser ordnance firing system, two laser standard initiator fired bolt cutters (only two of the laser ordnance channels are used in orbit), two Frangibolts, two Non-Explosive Separation Nuts, and two Fusible Links and their DC to AC power converter. The experiment has eight small preloaded plates that are individually deployed upon release of the ARTS devices. These deployments are verified by hall effect sensors. We used hall effect sensors to evaluate them as a replacement for microswitches. One of each of the two devices will be operated within two months of launch and the second of each of the devices will be operated approximately one year after launch.

The production of a flight experiment proved to be a very useful tool by forcing us to truly complete the development process. All of the issues that effect a component's design and usage from spacecraft interfaces to ground safety to testing and many others had to be successfully addressed. Additionally, staking one's reputation on a device working in space is excellent motivation to dot all the i's and cross all the t's. The dominating requirement for the experiment, other than reliability, was that it pose minimal risk to the host spacecraft. This led to the configuration used wherein all release devices and electronics are packaged inside a common housing, thus protecting the host from any potential mechanical mishap. Another key requirement was the 5 amp current limit set by the host's power bus. Most of the release devices prefer 3 to 4 amps at the low bus voltage of 24 VDC, which can result in a normal current draw exceeding 5 amps at the high bus voltage of 36 V. We had to put a current limiting system in to protect the host at high bus voltages. While this current limit was imposed by designing the experiment around an existing spacecraft, living with it exposed some of the system-level issues that must be dealt with in using these high-current devices. One of the key results of the experiment is to get range safety approval and recognition of the safety benefits of these new systems.

Release Device Comparisons

These new devices are very competitive with one another and with existing components. Pyrotechnically operated devices are presently the most commonly used release mechanisms. The following discussion will compare the components and discuss which tasks are best suited to which devices. This discussion shows that explosively powered devices can and should be replaced for most applications. There are two major divisions in classes of release mechanisms. The first is high versus low release loads. I feel that this is a fuzzy boundary somewhere between 1100 to 4500 N (250 to 1000 lb). The ARTS program targeted the high load release category on the theory that it would be easier to scale down than up. The second major division is whether or not multiple devices must release simultaneously. The following chart exemplifies these divisions.

REQUIREMENTS	OPERATION	COMMON METHOD
High Load, Simultaneous	Spacecraft Release	Pyro Sep Nut
High Load, Non-Simultaneous	Structure Release	Pyro Bolt Cutter
Low Load, Simultaneous	Payload Jettison	Pyro Pin Puller
Low Load, Non-Simultaneous	Solar Array Release	Pyro Pin Puller

There are relatively few types of mechanisms capable of releasing the high loads. There is a larger variety of devices for the lower load applications. The comparison will only compare the ARTS components with the most common devices in use today. Slow devices, typically heat actuated, are usually well suited to the non-simultaneous applications and poorly suited to the simultaneous release applications. These slow devices can sometimes be applicable if an additional release device located in the center of the deployable is operated after all of the load carrying devices have already been released. The faster devices can handle all of the tasks, however, they require higher current than the paraffin release devices and are more complex than the Frangibolts. The pyrotechnic systems in use today are very reliable although they carry the baggage of pyroshock, safety costs, and heavy firing systems.

The ultimate evaluation of a component's worth should be made at the spacecraft-system level. This level is where the elimination of explosives really shines. Of course, all of the devices have to be highly reliable to make the comparison meaningful. The use of laser ordnance is very appealing over conventional ordnance for its reduced weight and safety costs. However the maximum benefit comes from eliminating high pyroshock sources in conjunction with the reduced cost and weight. This analysis leads to the ARTS program approach of eliminating all ordnance possible and firing the remaining ordnance with lasers. These selections also have to take into account factors such as fitting into existing or similar designs, weight versus cost priorities, and other like considerations. The large costs

and weights associated with conventional ordnance make it very unappealing for most new designs.

RELEASE DEVICE	ADVANTAGES	DISADVANTAGES	COMMENT
HIGH AND LOW LOAD APPLICATIONS			
ELEC. PYRO DEVICES • SEPARATION NUTS • EXPLOSIVE BOLTS • BOLT CUTTERS AND PINPULLERS FOR LOW LOADS	• SIMULTANEOUS • PYRO & DEVICE HERITAGE	• HIGH SAFETY COSTS • HIGH FIRING SYSTEM WEIGHT • HIGH PYROSHOCK • MODERATE COMPLEXITY IN MECHANISM	• GOOD TRACK RECORD • ALL SIZES AVAILABLE
LASER PYRO DEVICES • SEPARATION NUTS • EXPLOSIVE BOLTS • BOLT CUTTERS AND PINPULLERS FOR LOW LOADS	• SIMULTANEOUS • DEVICE HERITAGE • REDUCED SYSTEM COST & WEIGHT	• HIGH PYROSHOCK	• EASY TO RETRO-FIT INTO EXISTING SYSTEMS • SIMILAR COMPLEXITY TO ELEX SYSTEMS
FRANGIBOLT	• REDUCED SYSTEM COST & WEIGHT • LOW PYROSHOCK • LOW COMPLEXITY	• NOT SIMULTANEOUS WITHOUT ADD'L DEVICE	• WOULD NEED RESIZING FOR >9000 NEWTONS
FUSIBLE LINK	• REDUCED SYSTEM COST & WEIGHT • LOW PYROSHOCK • SIMULTANEOUS	• MODERATE COMPLEXITY IN FIRING CIRCUIT	• WOULD NEED RESIZING FOR >9000 NEWTONS
NON-EXPLOSIVE SEPARATION NUT	• REDUCED SYSTEM COST & WEIGHT • LOW PYROSHOCK • SIMULTANEOUS	• MODERATE COMPLEXITY IN MECHANISM	• DIRECT REPLACEMENT FOR SEPARATION NUT • WOULD NEED RESIZING FOR >16000 NEWTONS
LOW LOAD APPLICATIONS ONLY			
NON-EXPLOSIVE ACTUATOR-BASED DEVICES • EXCLUDING SEPARATION NUT	• REDUCED SYSTEM COST & WEIGHT • LOW PYROSHOCK • SIMULTANEOUS • NEA IS LOW COMPLEXITY	• MODERATE COMPLEXITY IN SOME OF THE MECHANISMS	• WIDE VARIETY OF DEVICES
PARAFFIN PIN PULLER	• REDUCED SYSTEM COST & WEIGHT • LOW PYROSHOCK	• MODERATE COMPLEXITY IN MECHANISM • NOT SIMULTANEOUS WITHOUT ADD'L DEVICE	• WIDE VARIETY OF DEVICES

Only the Non-Explosive Separation Nut and the Fusible Link are capable of achieving simultaneity without using explosives. The Non-Explosive Separation Nut has more mechanical complexity while the Fusible Link has more electrical complexity. The Frangibolt is the simplest and lightest of the new devices. Laser ordnance is similar in complexity to conventional, electrical ordnance systems but it is much safer and lighter in weight. There is a large variety of non-explosive release mechanisms for the lower load applications so there is very little need to consider explosive devices for these applications.

Future Work

The ARTS program will have future work in working with spacecraft manufacturers and customers to integrate the new devices into space systems. The ARTS program is also hoping to undertake the development of

a non-explosive isolation valve capable of being used on spacecraft carrying large quantities of hazardous liquid propellants. This device would be driven from closed to open upon command, providing a hermetic seal in both states. The valve would have a parent metal seal when in the closed state which is required for safe ground processing. The program would complete a full development and qualification if it is funded.

Conclusions & Recommendations

The benefits of the ARTS components can be maximized by proper application. All explosives that can be eliminated should be eliminated. The remaining explosives should be fired with laser systems. The ARTS devices do not need shielded firing harnesses, so the shielding should be eliminated to maximize weight savings. Safe and arm systems can be reduced to a simple electrical power turn-on connector. Pyroshock testing can be greatly reduced if not eliminated from spacecraft system-level acceptance tests. The shock isolators now used on some spacecraft components can be eliminated.

The ARTS program resulted in several lessons learned. The foremost lesson was that wide voltage swings are very difficult to accommodate for heat-actuated mechanisms. It is important to evaluate requiring the spacecraft electronics to limit this voltage swing somewhat. Producing true flight hardware is a great tool to force thoroughness into the development of components. Testing to the limits of the performance envelope is a very valuable development process to find the strengths and weaknesses of a device. On a specific level, we found that good joint design and installation procedures are important to the reliability of the Frangibolt. We also found that AC heating circuits can be susceptible to inductive losses. The development process and production of the flight experiment verified our assertions that these systems could greatly reduce spacecraft costs when used correctly.

All of the tasks of a spacecraft ordnance system could be performed with a lighter, more economical system utilizing the ARTS-developed components. The implementation philosophy would be to replace all pyrotechnically driven release devices with non-explosive release devices and to fire the remaining ordnance with the laser ordnance system. The primary thrust of the ARTS program has been to create economic savings including the inherent cost savings of weight reductions. These goals have been met with flight hardware being the verification. The ARTS program will conclude with flight-proven spacecraft components ready for implementation on production spacecraft with minor resizing of the components as required. Questions about this program should be directed to William Purdy of the Naval Center for Space Technology in Washington, DC at 202-767-0529.

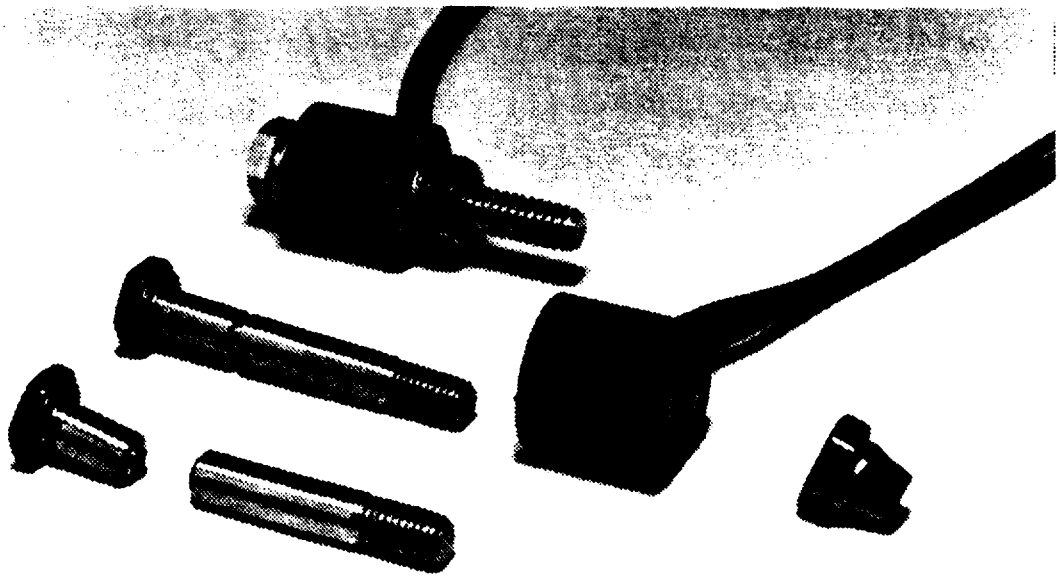

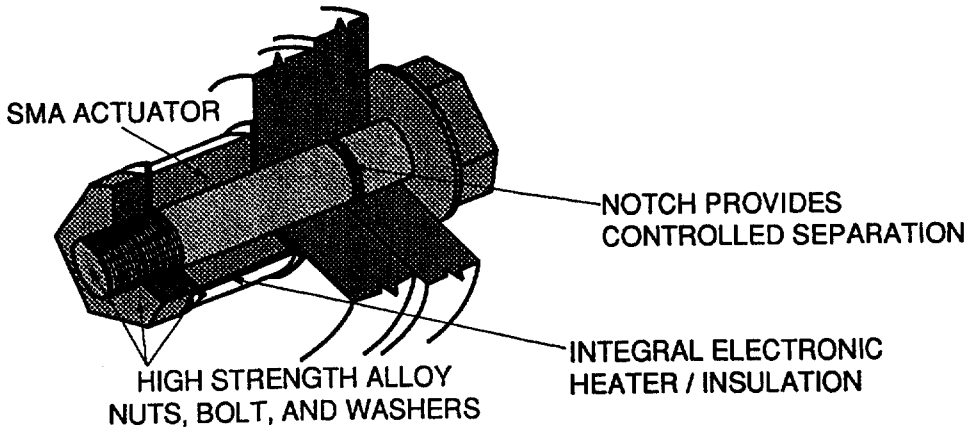

Figure 1: Frangibolt

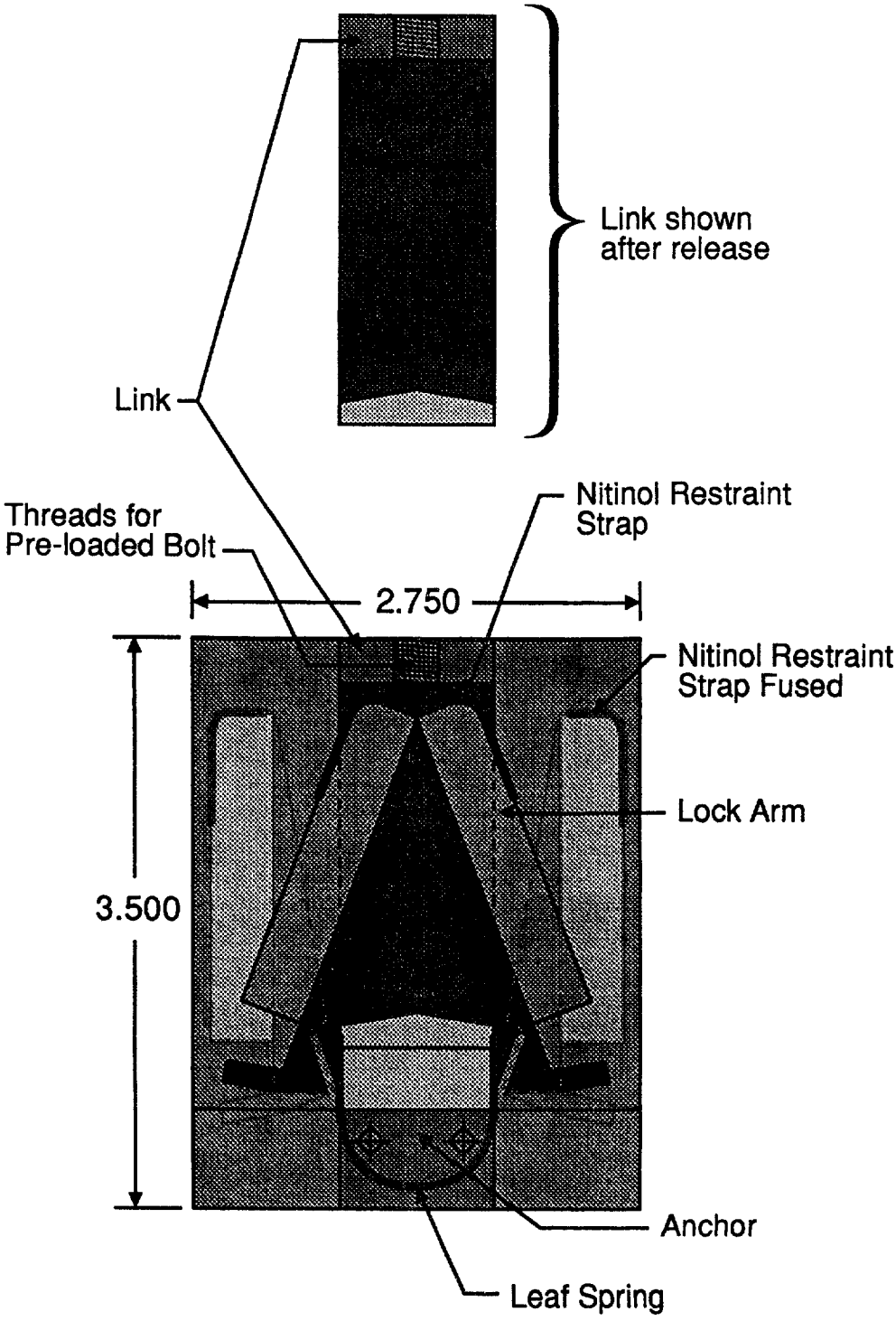

Figure 2: Fusible Link

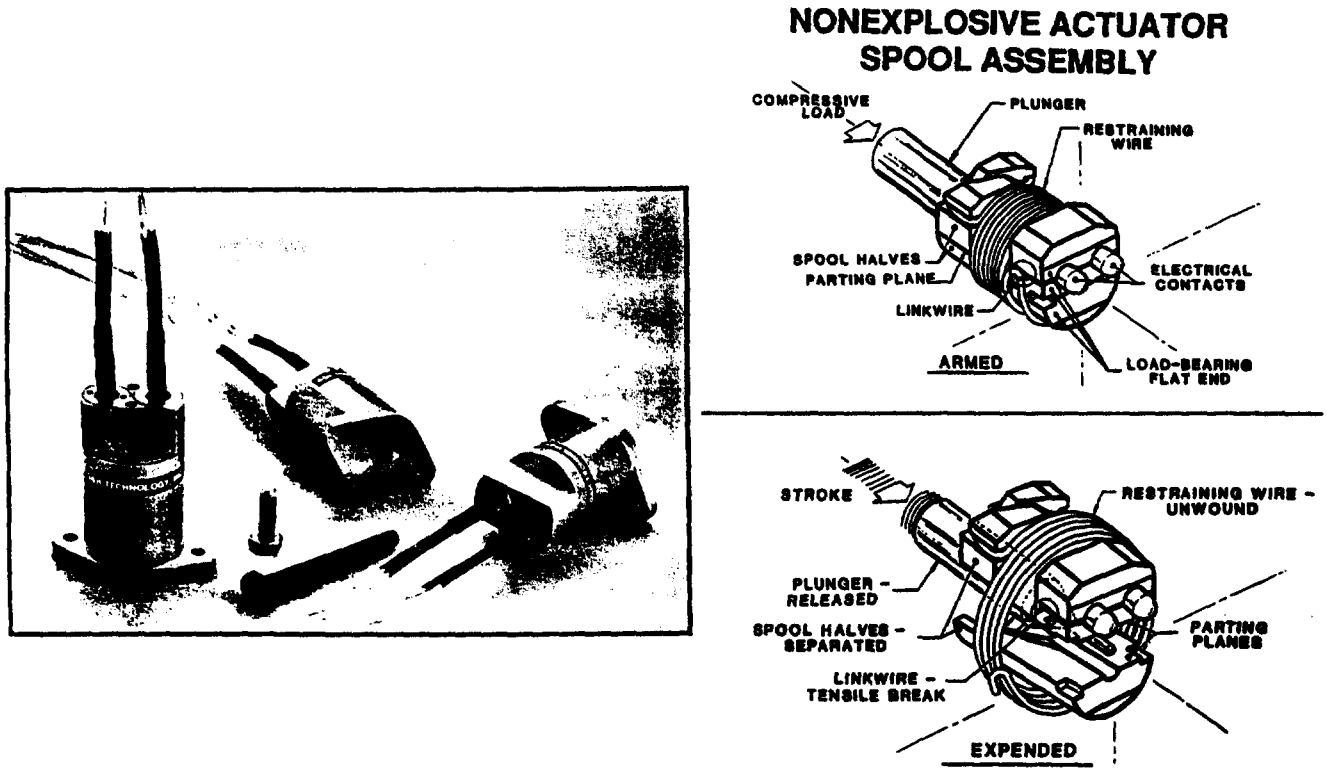

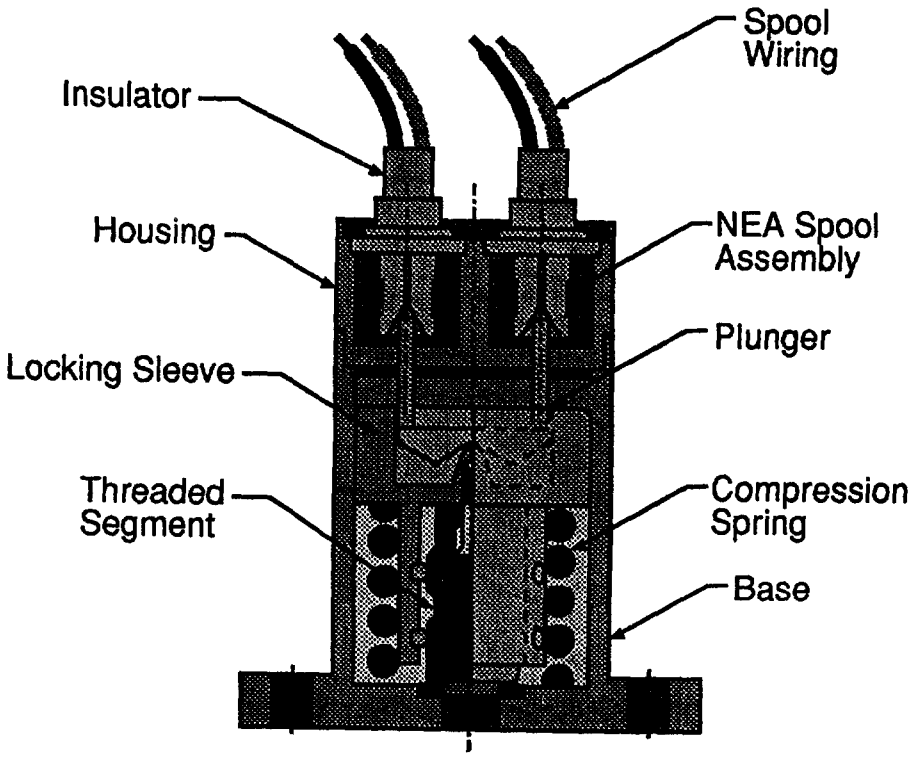

Figure 3: Non-Explosive Separation Nut

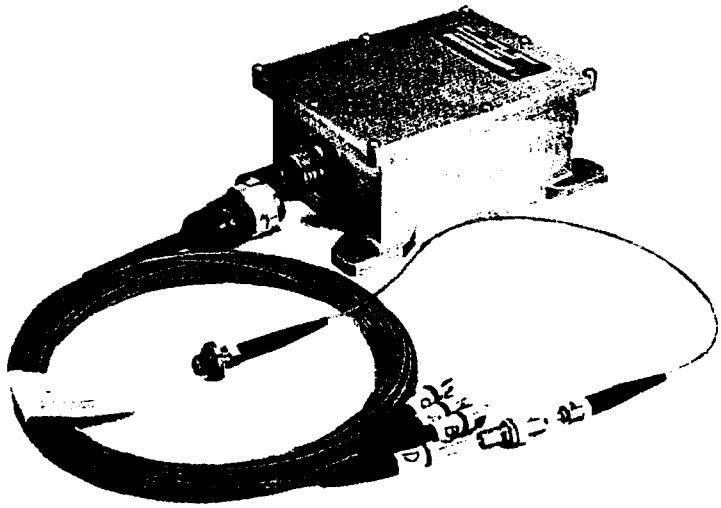

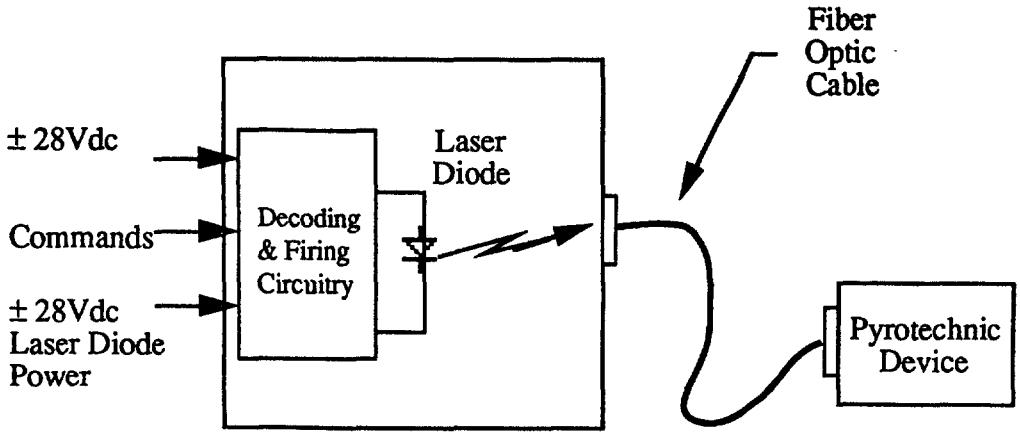

Figure 4 Laser Ordnance System

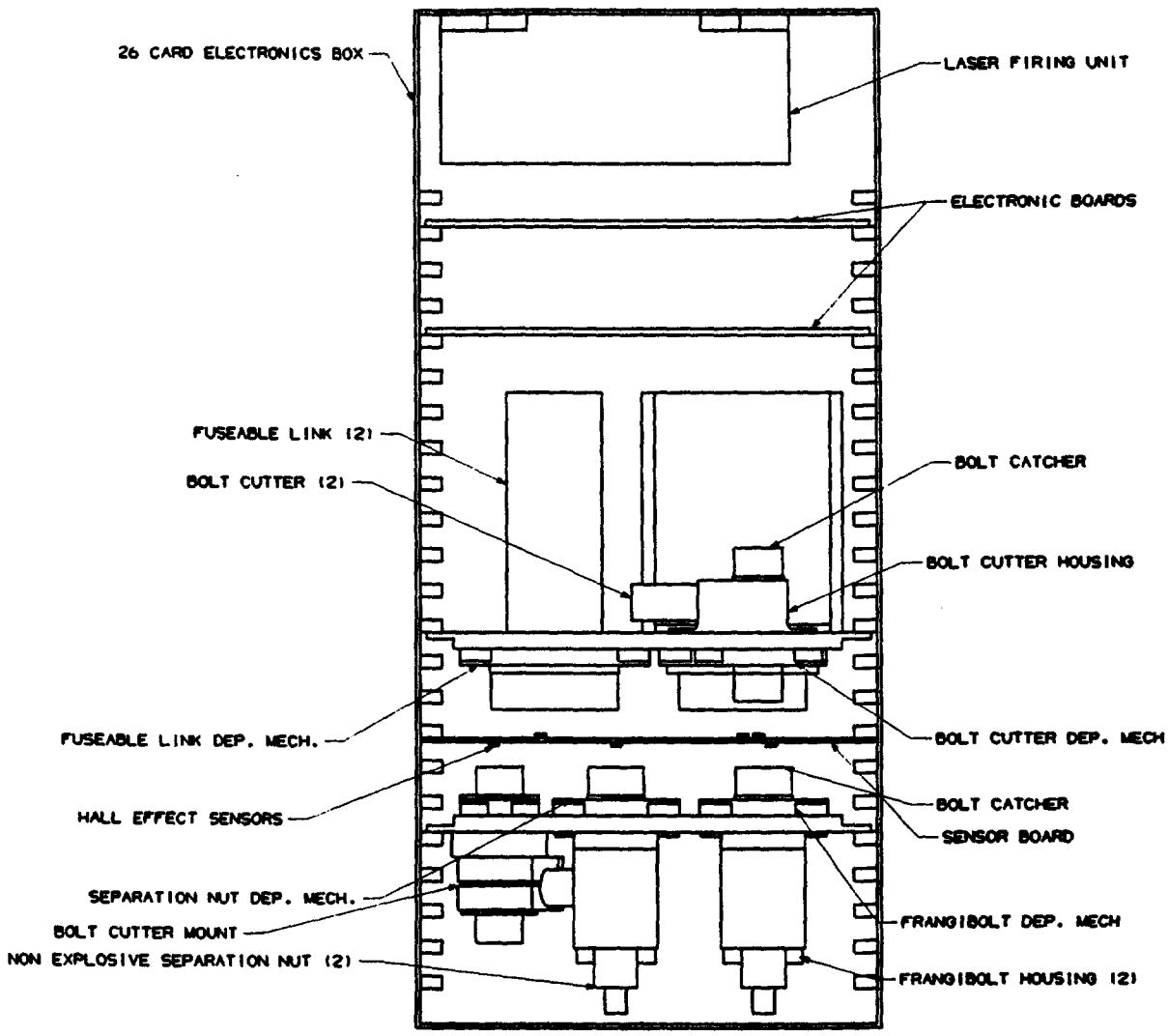

Figure 5 ARTS Flight Experiment

LOAD-LIMITING LANDING GEAR FOOTPAD ENERGY ABSORPTION SYSTEM

Chris Hansen and Ted Tsai
Structures and Mechanics Division
NASA Johnson Space Center
Houston, Texas

ABSTRACT

As a precursor to future manned missions to the moon, an inexpensive, unmanned vehicle that could carry small, scientific payloads to the lunar surface was studied by NASA. The vehicle, called the Common Lunar Lander, required extremely optimized structural systems to increase the potential payload mass. A lightweight energy-absorbing system (LAGFEAS), which also acts as a landing load-limiter was designed to help achieve this optimized structure. Since the versatile and easily tailored system is a load-limiter, it allowed for the structure to be designed independently of the ever-changing landing energy predictions. This paper describes the LAGFEAS system and preliminary verification testing performed at NASA's Johnson Space Center for the Common Lunar Lander program.

INTRODUCTION

As NASA looks toward the future and the goal of a permanent manned presence on the moon, several smaller steps must be taken to achieve this goal. A scientific survey of the lunar surface, more detailed than the Apollo missions could accomplish, must be undertaken. One proposed way of performing this task is with a group of small, unmanned landing vehicles that could carry various scientific payloads to the lunar surface. A telescope, a soil sampler, or a small remote rover could be delivered and could carry out the necessary exploration. NASA imagined a common vehicle, capable of multiple tasks, and dubbed this vehicle the Common Lunar Lander (see Figure 1). This lander had to be inexpensive, which meant the use of a small, commercial launch vehicle such as McDonnell-Douglas' Delta rocket was necessary. The lander must also be extremely efficient to deliver the greatest payload mass possible to the moon. In 1992, the Structures and Mechanics Division at NASA's Johnson Space Center underwent a six-month design study to explore the feasibility of designing and flying such a vehicle.

As the study progressed, it was found that the structure of the vehicle became a major driving force toward the vehicle's efficiency. All of the vehicle's components were attached to the structure, and therefore had to be integrated into the structure. Any inefficiencies in the structural design would be amplified in effect by all of the other system components. In addition to these difficulties, the landing environment for which the structure had to be designed was very difficult to quantify early in the project. The loads induced into the lander and its payload are a function of the mass of the lander, the impact velocity of the lander, the surface properties, the vehicle's inertia, the radar quality, and many other factors. To make a truly optimized structure, this load environment must be well understood, and early in the design process this is not the case. Since the load environment is a

strong function of the design itself, a very intensive, time-consuming iterative design process must be used to achieve the most optimum vehicle design.

Since much of the problem was centered on quantifying the landing load environment, a unique solution to the problem was created. The solution was called the Load-limiting Landing Gear Footpad Energy Absorption System, or LAGFEAS. Typical landing shock absorbers are velocity dependent and heavy. The LAGFEAS provides a simple, easily modified, and load-limiting mechanism to absorb the landing shock. Because the system is load-limiting, the maximum load input into the structure is not dependent on the landing velocity or vehicle mass, only on the parameters of the energy absorbing system itself. This offers a great advantage to the designer. A maximum load value can be chosen and the rest of the structure can be designed. As long as enough stroke is allowed, the G-levels seen by the structure and the payload can be controlled. With the maximum loads known, the rest of the structure can be designed long before landing velocities or vehicle weight can be accurately determined. With this system in place, the Common Lunar Lander design was initiated.

Landing Requirements

The expected mass and landing velocities of the lander were conservatively evaluated. These velocities corresponded to the lander's ability to land with a functioning radar device and the energy absorption system must remove all the energy present in the lander. This energy is in the form of kinetic energy, which is a function of the velocity in two directions; a vertical direction, and a horizontal direction. The energy absorption system must remove all the energy present in the system for it to complete its function under all reasonable landing conditions. During the early phase of the design, two stringent requirements were placed on the landing system:

1. One footpad must be capable of absorbing all of the energy present in the lander system.

2. The g-loading experienced during the landing phase must remain at or below the same g-loading experienced by the lander during the launch phase.

Requirement number 1 above is placed on the landing gear system to account for any unexpected landing conditions. If a large rock or ditch is hit, then one landing gear could conceivably be expected to absorb a majority of the energy. The lander has three legs, and all three landing pads would nominally act in absorbing energy, but by assuming that one energy absorbing pad can absorb the entire landing energy, a degree of safety is obtained for many varied and unexpected landing conditions.

Requirement number 2 is placed on the landing system in order to allow the future payloads and the lander itself to be designed. Since some of those future payloads are expected to be highly sensitive and potentially fragile, such as a

telescope, the loading on those payloads must be kept as low as possible. The loads experienced by the payloads during launch are well known and pre-determined by the launch vehicle choice, therefore, by assuming that the landing loads must be equal to or lower than the loads seen at launch, a reasonable requirement for the landing loads is obtained.

The g-load seen by the structure is a function of the force applied to the vehicle to slow it down, and the stroke over which that force is applied. Therefore, since the maximum g-loading on the lander is determined by parameters of the landing energy absorption system alone and is relatively independent of other environmental conditions. Because both the energy and the strength requirements are defined, it is possible to design a landing gear energy absorption system. Due to the relatively small stroking distances needed, based on landing velocities, the approach taken on designing a system was to place all energy absorption in the footpads. This precludes the use of shock absorbers in the leg members which can be heavy and in some cases more complicated. This is a new approach for lunar-type landers which have used shock absorbers as the main energy dissipater. However, the design team felt that a significant weight savings could be obtained by utilizing the approach of placing all of the energy absorption in the footpads.

Energy Absorption System

A unique system has been designed that satisfies all the energy absorption requirements. Figure 1 shows the proposed Common Lunar Lander and the location of the Energy Absorption System. Figure 2 shows the major components of the system, to be described in detail in the following section.

Friction Rod and Washers

The main component of the system uses the friction between a traveling rod and press-fit washers to absorb the vertical energy. As shown in Figure 3, the washers are pressed onto the rod and spaced some distance apart. The kinetic energy of the applied loading can be resisted at the desired load level and dissipated through heat generated by the traveling friction. The washers are initially picked up one at a time, by varying the spacing and the number of the washers, the onset rate and the total friction load can be controlled. The friction rod/washer system was originally developed by NASA for use in the Apollo command-module couch struts. The design used a series of small washers placed on a 9.5 mm (3/8 inch) rod as the energy absorber and provided an acceptable g level and onset rate to the crewmen. The right materials are crucial to the success of the system. Material compatibility, especially the relative hardness between the rod and washers, is important. Various materials and lubricants were considered and tested. The best material combination found was 718 Inconel rods (heat treated to Rc 40) and fully annealed 416 stainless steel (SST) washers (R_B 83). The two materials have relatively equal Young's modulus but the yielding strength of the rod is three times that of the washers. Drill rod, 17-4 PH stainless steel rod and 304 stainless steel washers were all tested and discarded because of galling and thermal effects. To achieve the desirable frictional coefficient, a boundary

(thin-film) lubrication was applied. For the thin-film, boundary lubrication, the friction coefficient falls within the range of 0.05 to 0.15. The highest friction coefficient occurs when the interface pressure becomes so great that the lubricant film can no longer support the load. Some wear will occur, however, the wear should not be visible to the eye and severe wear is abnormal and visible. Various lubricants including high-quality oils and greases were tested without success. Finally, the Miller Stephenson dry-film lubricant MS-122 successfully produced the desired results and proved to be highly repeatable.

For the application of the landing gear energy absorber, the sizes of the rod and washers have to be drastically increased compared to the Apollo tests. To meet the strength (bending and buckling) and deformation requirements, the diameter of rod was increased to more than 2.8 cm (1.1 in). To optimize the weight of the system, the rod was also hollowed. The outer diameter of the washers were designed to be twice their inner diameter and the inner diameter of the washers were manufactured to 3% less than the outer diameter of the rod. The elastic limit on the strain of the SST washer material is 0.1%. Based on analysis, the 3% interference will result in plastic yielding of the entire washer. Using the Von Mises yielding criteria, the normal compression between the washer and rod is approximately 80% of the yielding strength while the entire washer has already been plastically deformed. The washer works like a stiff but elastic rubber band which provides a constant normal force (grasping force) between the washer and rod. The plastic strain will not reach the point of rupture because the fully annealed washer has an ultimate strain of 30%. The elastic springback of the washer is also an important factor for consideration. Because of the high stiffness of the washer material, the load will vanish quickly if the rod diameter (nominal 284.5 mm) decreases 0.03 mm. The maximum allowable variation of rod diameter in manufacturing is defined to be 0.005 mm (0.0002 in) (15% of the elastic springback). Due to this small tolerance and the fact that the inconel rod has a higher thermal expansion coefficient than the SST washer, thermal effects may not be ignored. The interface compression will be significantly reduced or completely released if the system is exposed to a relatively low temperature. A light weight insulation cover or heaters can be added to resolve the problem.

The inner edge of the washers are also rounded (0.25 mm radius) to help in the installation and prevent galling. When a washer is stroked, the applied loading has to overcome the initial static friction of the washer. Afterwards, the washer will move at a lower and constant sliding friction. The thickness of the washer shall not be too great to induce a high static friction. A thicker washer also requires higher installation load. However, the washer may buckle or warp if it is too thin. The washer thickness for the Common Lunar Lander energy absorber will be between 3.8 to 5.1 mm. The washer tested for the design concept was 5.1 mm. A 3.8-mm-thick washer may be even more suited for the system, but has never been tested due to lack of resources. As stated previously, boundary lubrication generally yields coefficients of friction in the range of $\mu = 0.05$ to 0.15. The friction coefficient is dependent on various parameters including the stroking velocity. After the basic design of the energy absorber is established, the best way of obtaining and verifying the friction load of the design is to perform the actual hardware testing.

Because of a resources constraint, the testing program was performed in a very limited fashion. Nevertheless, the tests were considered very successful. By using the available materials in the shop, four test specimens were manufactured, assembled and tested. The sizes of the test specimens are tabulated in Table 1 below.

Table 1. Sizes of Washers and Rod Test Specimen

	Outer Radius, Ro, mm	Inner Radius, Ri, mm	Thickness, Plate, mm		
Washer	27.559	13.780	5.080		
			Thickness, Tube, mm	Length, cm	Washer-Rod Interference
Rod #1	14.133	6.350	7.772	26.67	2.50 %
Rod #2	14.133	7.938	6.198	26.67	2.50 %
Rod #3	14.282	7.938	6.350	26.67	3.50 %
Rod #4	14.282	9.119	5.156	26.67	3.51 %

The purpose of the test was to verify the concept and to evaluate the maximum load and the total energy absorption of the design. Because of the flexibility of the design, the sizing of the washers-and-rod system can be easily modified and tailored to meet the final design requirements. Four 5.08-mm-thick washers were installed on each rod, the 2.50% interference sufficient to induce a full plastic deformation of the washer. The washers were spaced 5.08 mm apart using the installation procedure shown in Figure 4. A static stroking test (0.38 $^{mm}/_{s}$ rate) was also performed to record the static and sliding friction loads during the installation of the washers. A typical load vs. displacement curve for a single washer (rod #4) is shown in Figure 5. Under the low stroking speed, the static friction load was 8563 N (1925 lb) and sliding friction was 2224 N (500 lb) for the washer. A dynamic weight-drop test was consequently performed. As shown in Figure 6, the total weight (2847 N (640 lb)) and the drop height (39.80 cm) were determined based on the kinetic energy and landing velocity. Because the available stroking distance of the rods was limited, each specimen was tested to half of the design landing energy (1133 N•m) with the same landing velocity (279.4 $^{cm}/_{s}$). A typical result (load vs. displacement) of the drop test is also shown in Figure 6 (for rod #4). The maximum load of the washer stack was about 17.79 kN (4000 lb) with additional spikes of a single washer. A specimen was tested at a higher energy level (50.8 cm drop height) and the maximum stroking distance was 12.7 cm for the washer on the bottom of the stack. The design capability for the legs of Common Lunar Lander was 12 kN (2700 lb), however, by using thinner washers, the system should easily meet the specific design requirements. No additional tests were performed.

Horizontal Energy Absorption

To absorb the energy in the horizontal direction, a material deformation system is used. Several materials were considered, but the material selected

would be a honeycomb-type material. This type of material crushes in a way that also creates a load-limiting system. Once the honeycomb crushes to a certain load value, it continues to crush up to 70 percent of its volume at a constant load. The load will never go above this value until 70 percent of the material has been crushed. As long as enough material has been used, this system will act as a predictable load-limiter in the same fashion as the friction washers. In the system, the friction rod is enclosed within the footpad. Inside the footpad, a block of honeycomb material surrounds the rod. The rod is free to move inside of this material, being able to freely slide along the top of a stiff, honeycomb plate. When a side load is placed on the footpad from impact, the rod will crush through the honeycomb sections, absorbing the necessary energy. The bottom of the footpad will also be shaped to allow the pad to slide along the surface as much as possible. This sliding helps dissipate energy and gives the system more capability. To the bottom of the friction rod is attached a small sliding plate that is allowed to rotate with a ball joint. This allows the sliding plate to remain in contact with the honeycomb top plate at all times. The honeycomb is contained in a restraining cylinder. A very good material candidate is available commercially under the brand name DUOCEL®, and is an isotropic foam metal. The parent material can be selected and heat treated from a variety of materials and processes, including most forms of aluminum. The foam metal behaves in the same fashion as honeycomb under compressive loads. This load-limiting behavior retains the unique nature of the energy absorption system. The foam metal may be cut into sections to avoid placing portions of the metal into tension as the rod crushes through. The general mechanical properties under compression of the DUOCEL® were evaluated with three tests. Each specimen was 10.16 cm by 3.81 cm by 1.91 cm in size made of an aluminum alloy. The porosity of the specimen was 3.937, 7.874 and 15.748 pores per cm and the density was 8%, 12% and 12% respectively. Each specimen was compressed with the Instron machine with a rate of 0.2 $^{mm}/_{s}$. The results showed a constant stress portion extending over a 50% strain range for all three tests. A typical stress-strain curve of the test results is shown in Figure 7. The DUOCEL® is certainly the leading candidate for the horizontal energy absorber.

Yielding Rod Energy Absorption System

Another method of absorbing the horizontal energy has also been proposed. The **yielding rod** energy absorption system is shown in Figure 8. The system also uses the friction washers and rod to absorb the vertical energy. However, instead of letting the rod stroke through the washers, this system uses a stationary rod with traveling washers. The horizontal landing energy is absorbed by the plastic bending of a yielding rod. Crushable honeycomb materials are also used for the additional cushion and energy absorption. The solid circular section of the rod provides a high capability for plastic bending. The yielding rod basically replaces the metal foam of the previous system as the horizontal load-limiter and the energy absorber. Located at the root of a cantilever beam, the rod will carry the maximum bending moment from the lateral loading. The rod is sized based on the load and the energy requirement. The strong (F_{ty} = 1165 MPa) and tough (e_{ult}=16%) Inconel 718 was selected for the yielding rod. Based on the loading

and energy requirements, and the moment capability at full plasticity (plastic bending moment) of the circular rod, the size of the rod was determined. For the design environment of the Common Lunar Lander, the radius of the rod was analyzed to be 11.68 mm. The rod would be required to bend by only 45 degrees to absorb the entire horizontal energy for the worst case of landing. The outer diameter of the tubular friction rod was 16.51 mm, which provided far stronger sectional properties than the yielding rod. The horizontal loading on the structure is limited by the plastic bending strength of the yielding rod and the minimum length of the footpad (moment arm) during and after stroking. A bend guide is also included in the system. Based on the radius of the bend guide and the size of the yielding rod, the maximum/ minimum elongation of the rod can be easily evaluated. Many tough materials can also be considered for the yielding rod application, depending on the loading and energy environments. When the horizontal landing energy becomes significantly high, this system is advantageous in weight saving.

CONCLUSIONS

In 1992, The Structures and Mechanics Division at NASA's Johnson Space Center underwent a design study to determine the feasibility of building a Common Lunar Lander which met certain, strict requirements. These requirements meant that innovative solutions had to be found to increase the lander's structural and operational efficiencies and decrease the system's mass. The LAGFEAS was designed with this goal in mind. To prove that the system is workable, and ultimately a benefit to the lander, a significant amount of testing would be necessary. Due to funding problems and finally a cancellation of the project, this testing was never completed. However, it was felt by the authors that this system was a unique approach to the problem of absorbing impact energy from landing systems and therefore deserved to be presented to the mechanisms community.

Using the plastically deformed washers to control the frictional force between the friction rod and the washers creates a system that is by design very tolerant of temperature fluctuations. In some extreme cases, a low temperature environment can affect the friction force between the rod and the washers. In these cases, a lightweight thermal insulation would solve this problem. In addition, it is felt that the coefficient of friction between the rod and the washer can also be carefully controlled in a vacuum environment. The problem of cold-welding of the materials can be avoided through the use of a captured dry-lubricant between the rod and the washers, also part of the original design. Further thermal-vacuum chamber tests would be performed to verify the system's functionality during future development tests.

REFERENCES

1. Common Lunar Lander Detailed Design Study, Structural Design and Integration Report to the Artemis Engineering Team, NASA document number JSC-26094.

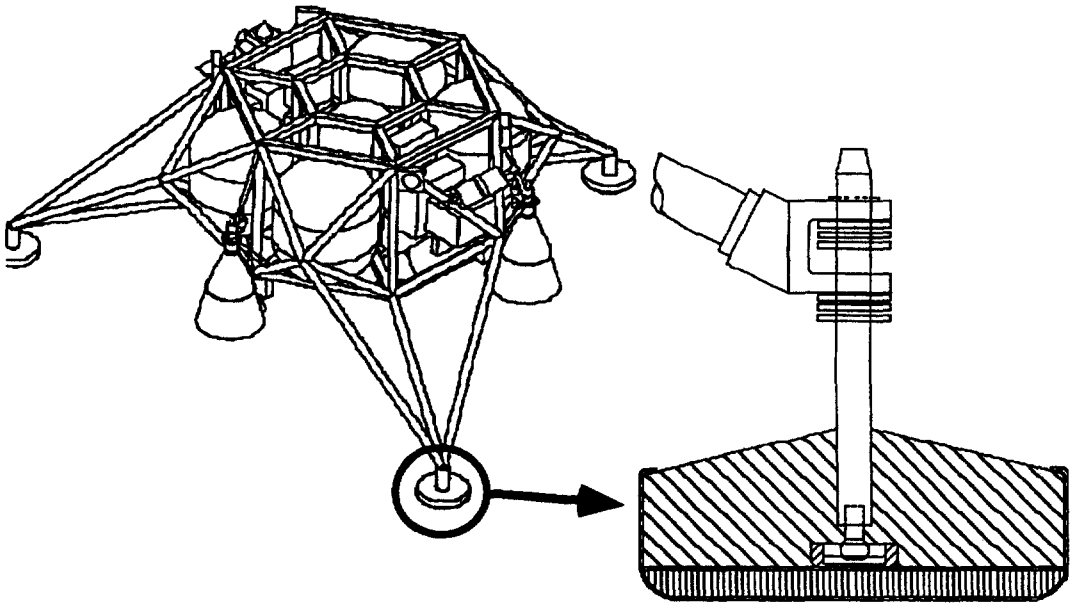

Figure 1: Common Lunar lander with Energy Absorption System at Inset.

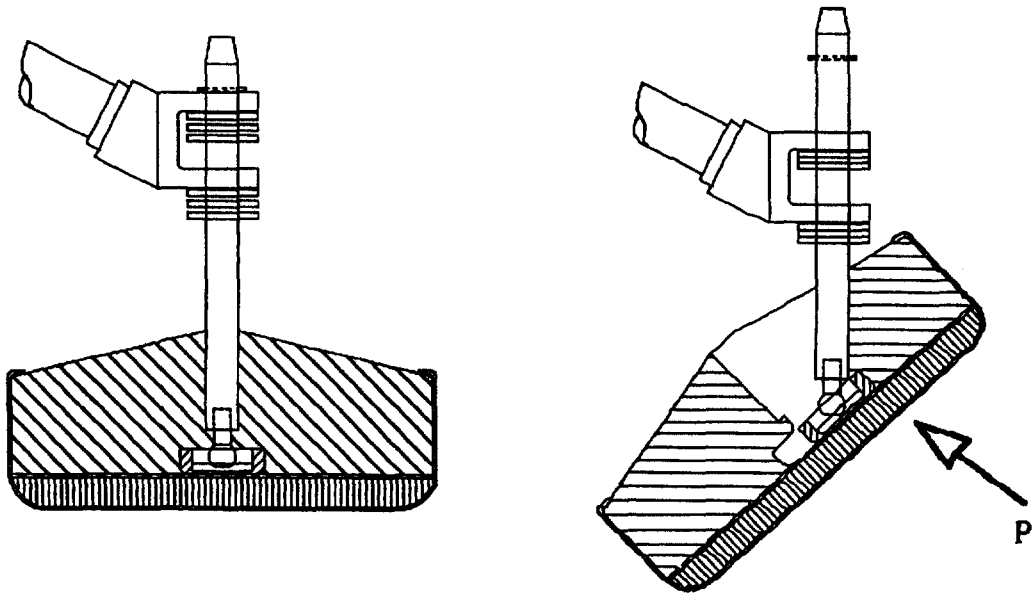

Figure 2: Landing Gear Footpad Energy Absorption System

Apply interference fit beyond the material elastic limit to induce a full over-strain of the washer; The ductile material will not rupture with sufficient ultimate strain

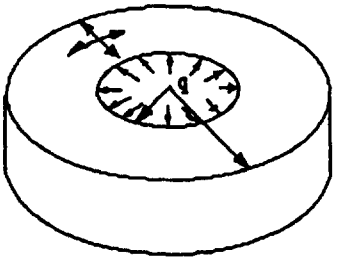

Yielding Criteria (Von Mises)

$$\tau_{max\ shear} = \frac{\sigma_1 - \sigma_2}{2} = \frac{\sigma_\theta - \sigma_r}{2} = \frac{\sigma_{yield}}{\sqrt{3}}$$

The interference normal compression q becomes

$$q = \frac{\sigma_{yield}}{\sqrt{3}} \left(2\ ln \frac{R_o}{R_i}\right)$$

The interface normal force N is

$$N = 2\,\pi\,R_0\,t\,q$$

The ideal washer friction F becomes

$$F_{static\ or\ sliding} = N\,\mu_{static\ or\ sliding}$$

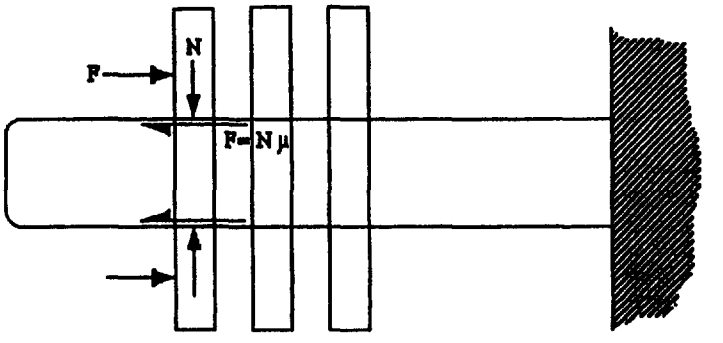

Figure 3: Washers and Rod Energy Absorption System

Step (1) Clean and lubricate one rod; Install one washer

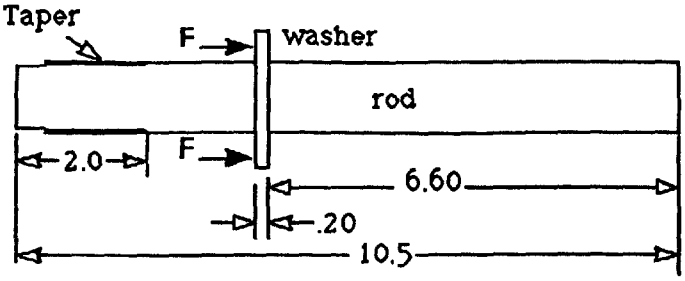

Step (2) After a minimum 24 hours, clean and lubricate the rod;
Perform load and stroking test (.015 inch/sec rate)

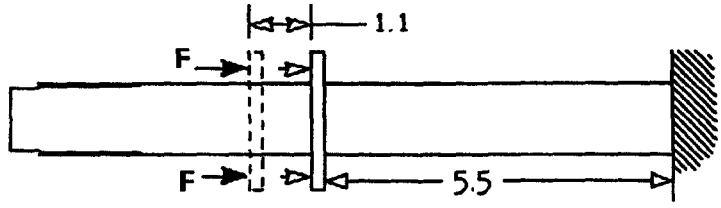

Step (3) Clean and lubricate the rod; install 3 more washers

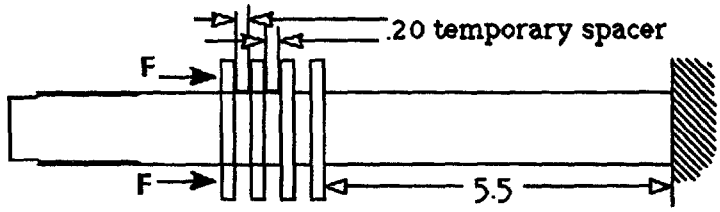

Figure 4: Configuration of Washers and Rod Test Specimen

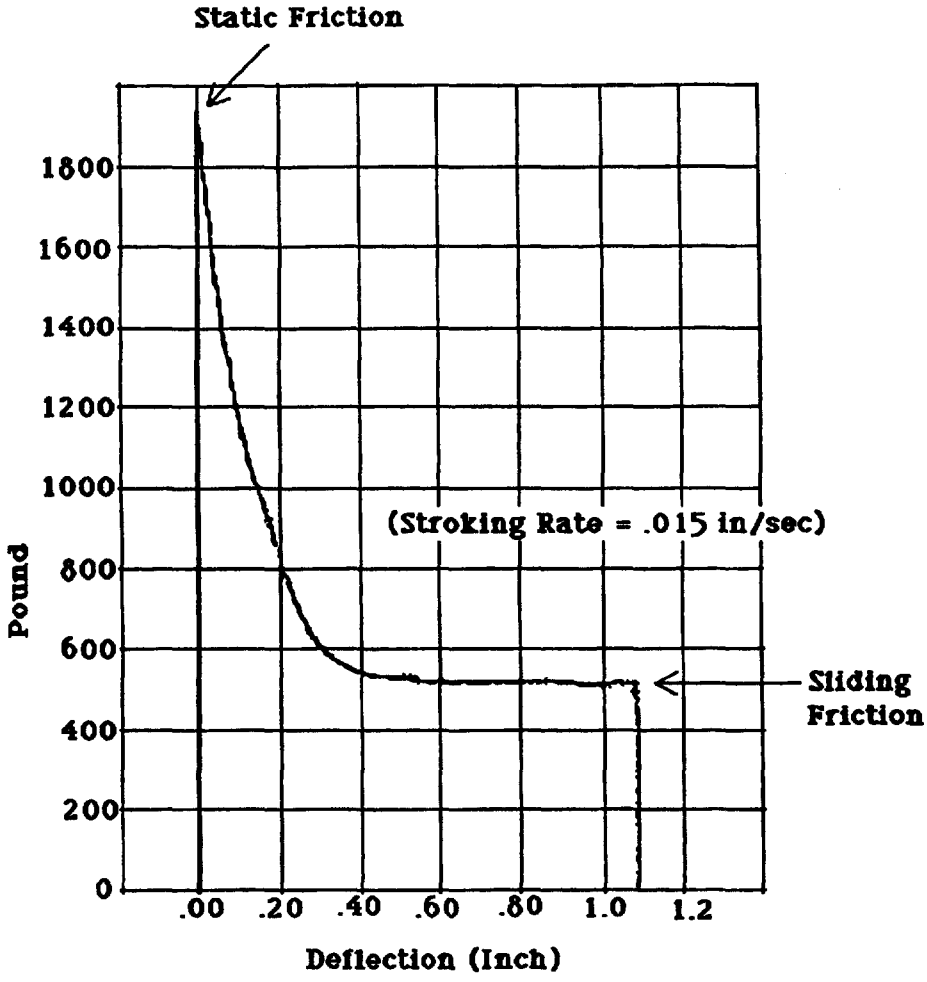

Figure 5: Typical Load Vs. Displacement Curve for a Single Washer

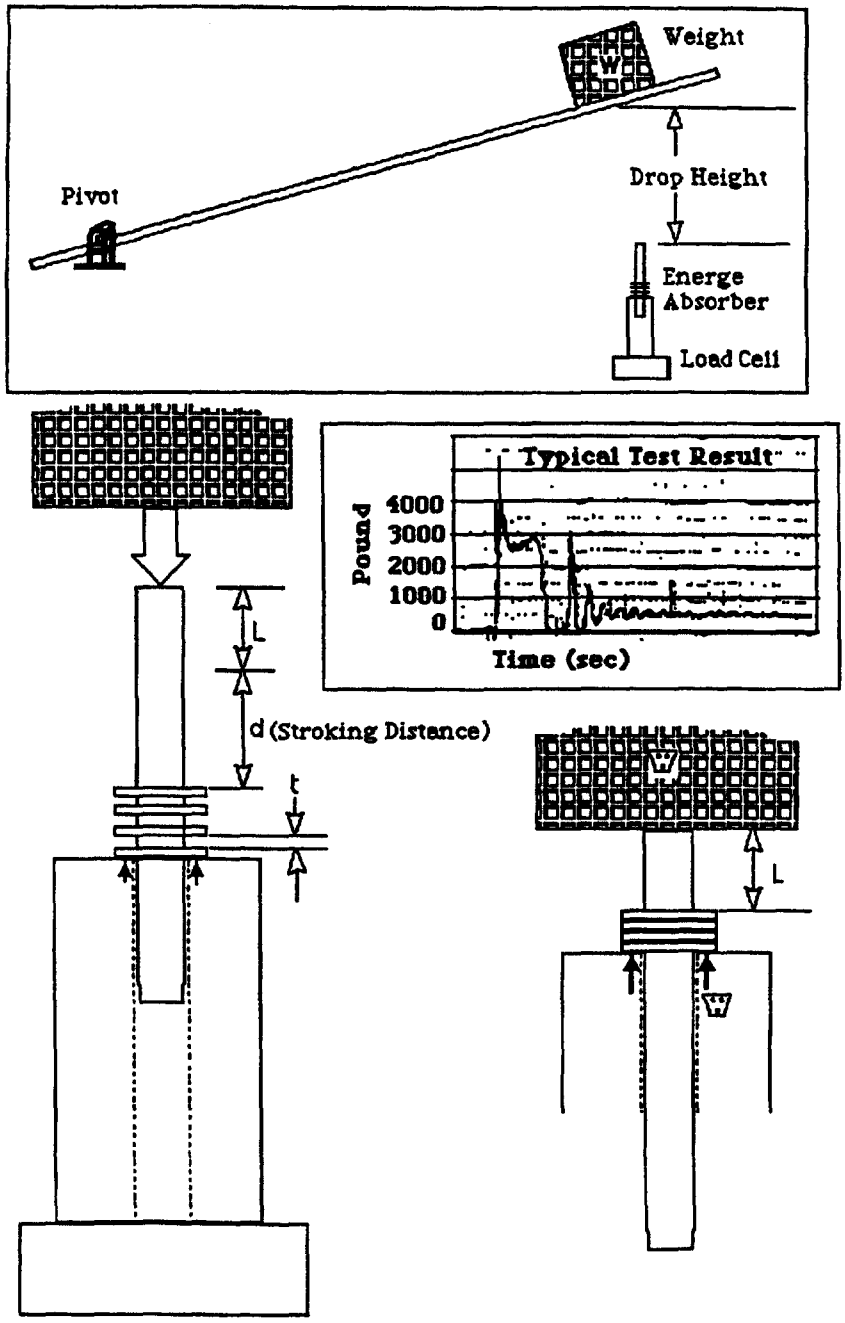

Figure 6: Dynamic Weight-Drop Test

- Rigid, highly porous and permeable and has a controlled density of metal per unit volume
  - Independently variable porosity from 10 to 40 pores per inch
  - Independently variable density from 3 to 20 percent of Aluminum
- Completely isotropic load response
- High strength to weight ratio
- Impact energy absorption application with constant stress portion extends over a 50 percent strain range

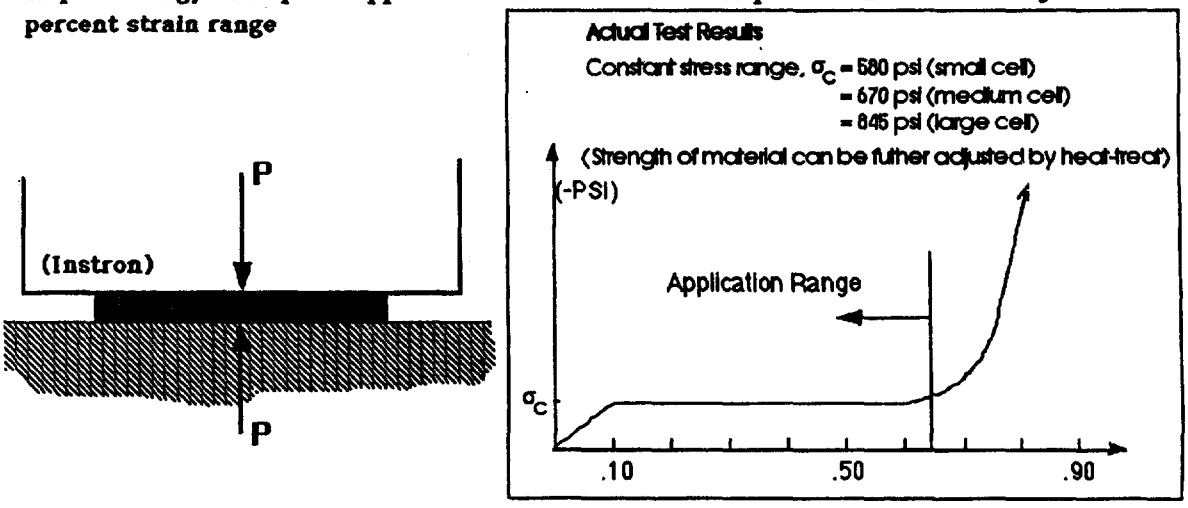

Figure 7: Typical Properties of Isotropic Open-Cell Foam Metal

- The primary vertical landing energy is absorbed by friction washers and rod
- The horizontal landing energy is absorbed by crushable honeycomb and plastic bending of a yielding rod

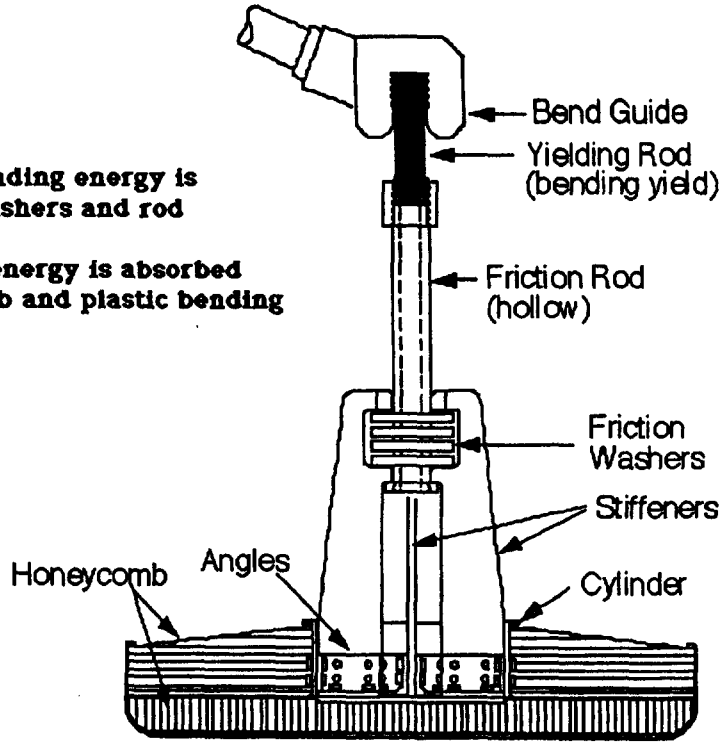

Figure 8: Yielding Rod Energy Absorption System

REPORT DOCUMENTATION PAGE

Form Approved
OMB No. 0704-0188

1. AGENCY USE ONLY (*Leave blank*)	2. REPORT DATE	3. REPORT TYPE AND DATES COVERED
	May 1994	Conference Publication

4. TITLE AND SUBTITLE

28th Aerospace Mechanisms Symposium

5. FUNDING NUMBERS

WU–506–43–41

6. AUTHOR(S)

Douglas A. Rohn, compiler

7. PERFORMING ORGANIZATION NAME(S) AND ADDRESS(ES)

National Aeronautics and Space Administration
Lewis Research Center
Cleveland, Ohio 44135–3191

8. PERFORMING ORGANIZATION REPORT NUMBER

E–8667

9. SPONSORING/MONITORING AGENCY NAME(S) AND ADDRESS(ES)

National Aeronautics and Space Administration
Washington, D.C. 20546–0001

10. SPONSORING/MONITORING AGENCY REPORT NUMBER

NASA CP–3260

11. SUPPLEMENTARY NOTES

Proceedings of a symposium cosponsored by NASA Lewis Research Center and Lockheed Missiles and Space Company, Inc., Sunnyvale, California 94088, and held at the Cleveland Marriott Society Center, Cleveland, Ohio, May 18–20, 1994. Responsible person, Douglas A. Rohn, organization code 5230, (216) 433–3325.

12a. DISTRIBUTION/AVAILABILITY STATEMENT

Unclassified - Unlimited
Subject Category 15

12b. DISTRIBUTION CODE

13. ABSTRACT ***(Maximum 200 words)***

The proceedings of the 28th Aerospace Mechanisms Symposium, which was hosted by the NASA Lewis Research Center and held at the Cleveland Marriott Society Center on May 18, 19, and 20, 1994, are reported. Technological areas covered include actuators, aerospace mechanism applications for ground support equipment, lubricants, pointing mechanisms joints, bearings, release devices, booms, robotic mechanisms, and other mechanisms for spacecraft.

14. SUBJECT TERMS

Spacecraft components; Array deployment; Robotics; End effectors; Actuators; Dampers; Reaction compensation; Pointing mechanisms; Antenna deployment; Booms

15. NUMBER OF PAGES

462

16. PRICE CODE

A20

17. SECURITY CLASSIFICATION OF REPORT	18. SECURITY CLASSIFICATION OF THIS PAGE	19. SECURITY CLASSIFICATION OF ABSTRACT	20. LIMITATION OF ABSTRACT
Unclassified	Unclassified	Unclassified	